Sivas Cumhuriyet University

Cumhuriyet Science Journal

Year: 2021

No: 4

Vol: 42

Cumhuriyet

Science

Journal

Volume: 42   Number: 4   Year: 2021

Cumhuriyet Science Journal (CSJ)

Assoc. Prof. Dr. Duran KARAKAŞ

dkarakas@cumhuriyet.edu.tr

Subjects: Inorganic Chemistry, Theoretical Chemistry

Institution: Sivas Cumhuriyet University

Assoc. Prof. Dr. Yaşar ÇAKMAK

ycakmak@cumhuriyet.edu.tr

Subjects: Applied Mathematics

Institution: Sivas Cumhuriyet University

Assoc. Prof. Dr. Sevgi DURNA DAŞTAN

sdurna@cumhuriyet.edu.tr

Subjects: Moleculer Biology

Institution: Sivas Cumhuriyet University

Assist. Prof. Dr. Didem ALTUN

didemaltun@cumhuriyet.edu.tr

Subjects: Engineering sciences

Institution: Sivas Cumhuriyet University

CONTENTS

PAGES

Identification and validation of key genes associated with smoking-induced lung adenocarcinoma development through bioinformatics analysis and predictions of small-molecule drugs

Hamid CEYLAN [1,*] (iD)

[1]*Atatürk University, Faculty of Science, Department of Molecular Biology and Genetics, 25240, Erzurum, TURKEY*

Abstract

Although smoking is known to be the leading risk factor for lung cancer, it is still unclear how normal cells turn cancerous in cigarette smokers. This study aimed to identify key molecular drivers that contributed to the progression and prognosis of lung adenocarcinoma (LUAD) in cigarette smokers, as well as screen, correlated small molecule therapeutic drugs by bioinformatics analysis. Gene expression profile was obtained from the Gene Expression Omnibus (GEO) database. Differentially expressed genes (DEGs) between current smokers without cancer and never smokers were identified and were analyzed to identify gene ontologies, pathways, protein-protein interaction (PPI) networks, hub genes, and prognostic potentials. Finally, effective small-molecule compounds were screened by the Connectivity Map (CMap) database. A total of nine genes were screened out as the critical among the DEGs from the PPI network. Overall survival analysis revealed that high mRNA expression of ACTR2 and ANAPC10 were significantly associated with the LUAD. Furthermore, three candidate small-molecule drugs for manipulating LUAD progression were predicted. Identification of critical genes involved in disease development and candidate drugs to combat it can lead us to better diagnosis and targeted therapy strategies. The results of the present study may provide insight into the mechanisms underlying LUAD pathogenesis development risk in cigarette smokers and may provide potential targets for prevention.

1. Introduction

Lung cancer is the second most frequently diagnosed cancer type in 2020 (2.2 million new cases; 11.4%) and the common reason for cancer-related deaths (1.8 million deaths; 18%) [1]. About 85% of patients were diagnosed with the non-small cell lung cancer (NSCLC) subtype. Lung adenocarcinoma (LUAD), a subtype of NSCLC, is responsible for about 40% of all lung cancer cases [2]. For this reason, determining the molecular drivers and mechanisms underlying cancer progression in LUAD is considered very important in terms of diagnosis and developing effective treatment approaches.

Smoking is an extremely important risk factor, which causes approximately 80-90% of lung cancer cases worldwide and is the highest source of cancer-related deaths in humans [3]. Individuals with a history of smoking are tens of times more likely to develop LC than never smokers. Lung cancer-related genomic alterations have a distinct difference between smokers and non-smokers [4]. However, information on the underlying molecular mechanisms that contribute to lung tumor formation in smokers is still quite insufficient.

Polygenic or multifactorial diseases, including cancer, arises as a result of complex interactions of multiple genes [5]. Given the complexity observed in cancer pathophysiology, alterations in the whole genome and transcriptome should be taken into account for effective treatment [6]. Identifying differentially expressed genes by analyzing DNA microarray datasets using bioinformatics tools is considered an approach that has the potential to reveal specific mechanisms and molecular events precisely in terms of disease management [7, 8]. This approach can provide a strong framework for understanding how a pathological process is regulated, as well as identifying

biomarkers that can be used in diagnosis, and identifying potential therapeutic targets and tools.

In this study, it was aimed to investigate the global gene expression differences in bronchial epithelial samples of current smokers and never smokers to elucidate the biological mechanisms underlying lung adenocarcinoma that may be caused by smoking. The selected microarray dataset was analyzed and the DEGs were identified. A PPI network was created to elucidate important relationships between DEGs and identify key genes, and also the expression and prognostic potential of key genes were studied. Finally, candidate small molecules that can be used in the prevention of smoking-induced LUAD development were predicted.

2. Methods

2.1. Microarray data processing and identification of DEGs

The gene expression profile (GSE19027) [9] was downloaded from the NCBI GEO (http://www.ncbi.nlm.nih.gov/geo) public repository. In this study, to detect genes whose expression is altered only by smoking, datasets from never-smokers and datasets from patients who smoke but do not have cancer were selected. A total of 25 bronchial epithelial tissue samples (6 never smokers and 19 current smokers without cancer) were used for analysis. Identification of DEGs between smokers and non-smokers was performed using the GEO2R web tool (https://www.ncbi.nlm.nih.gov/geo/geo2r/). The cut-off criteria were set as follows $|LogFC| > 1.5$ and $p < 0.05$.

2.2. PPI network construction and module analysis

STRING (Search Tool for the Retrieval of Interacting Genes; https://string-db.org/) database was employed to evaluate the interrelationships between DEGs. Cytoscape software was used to analyze and visualize the PPI network. Finally, Molecular Complex Detection (MCODE) plugin of Cytoscape was used to filter central modules in the PPI network.

2.3. Hub gene selection and analysis

CytoHubba plugin of Cytoscape was used to identify the hub genes. The Database for Annotation, Visualization and Integrated Discovery database (DAVID; https://david.ncifcrf.gov/home.jsp) application was used to perform GO (gene ontology)

and Kyoto Encyclopedia of Genes and Genome (KEGG) pathway enrichment analysis of hub genes.

2.4. Survival analysis and validation of hub genes

To confirm the reliability of the hub genes, their expressions were validated using GEPIA (Gene Expression Profiling Interactive Analysis) database [10]. In addition, GEPIA and Kaplan-Meier [11] survival curves of overall survival were used to analyze prognostic potentials and survival differences of the hub genes.

2.5. Candidate small molecule drugs prediction

The CMAP online tool (https://www.broadinstitute.org/connectivity-map-cmap) which contains whole genomic expression profiles for small active molecular inferences, was used to mine potential small molecules. Hub genes probesets in GSE19027 between smokers and non-smokers samples were used as inputs to the CMap database. Compounds were selected as potential therapeutic agents for smoking-induced LUAD after ranking them according to their negative connectivity enrichment scores.

3. Results

3.1. Identification of DEGs

Based on the cut-off criteria a total of 1092 DEGs were screened, including 313 upregulated and 779 downregulated genes in the smoker samples compared to non-smoker samples.

3.2. Network construction and screening of hub genes

According to acquired information from the STRING database, a total of 966 nodes and 4119 edges were mapped in the network. A significant module (MCODE score >10) including 69 nodes and 364 edges was identified in the PPI network (Figure 1). The top 20 genes were ranked using four calculation algorithms of the CytoHubba plugin including Maximal Clique Centrality (MCC), Maximum Neighborhood Component (MNC), Degree, and Betweenness. Finally, nine intersecting genes (*ACTR2, ANAPC10, CXCL8, CXCR4, DAB2, GNG11, PTGDR2, SOCS3,* and *VAMP3*) of the top 20 ranked DEGs were selected as hub genes (Table 1, Figure 2).

Table 1. Top 20 genes evaluated in the PPI network. Intersecting genes are shown in bold.

Gene	MCC	Gene	MNC	Gene	Degree	Gene	Betweenness
GNG11	4037681.0	GNG11	26.0	GNG11	27.0	CXCL8	1692,21
LPAR1	3674790.0	CXCL8	19.0	CXCL8	19.0	GNG11	1153,11
DRD4	3634320.0	COL7A1	18.0	COL7A1	18.0	TGFB1	849,85
CXCL8	3634224.0	LPAR1	17.0	LPAR1	17.0	TGFA	757,71
GNAI3	3633864.0	CXCR4	15.0	CXCR4	15.0	SOCS3	683,25
GRM2	3633842.0	GRM1	14.0	GRM1	14.0	COL7A1	635,85
HTR1D	3633840.0	DRD4	13.0	PTGDR2	13.0	ACTR2	602,41
CXCR4	3629058.0	PTGDR2	13.0	SOCS3	13.0	CXCR4	441,50
PTGDR2	3628814.0	SOCS3	13.0	DRD4	13.0	ANAPC10	363,00
SOCS3	3628808.0	GNAI3	12.0	ADRBK1	12.0	COL2A1	246,51
ANAPC10	3628802.0	GRM2	12.0	GNAI3	12.0	DAB2	212,35
VAMP3	3628802.0	ADRBK1	12.0	GRM2	12.0	ADM	167,87
CLTB	3628802.0	HTR1D	11.0	VAMP3	12.0	SEC24D	155,40
CLTCL1	3628802.0	ANAPC10	11.0	HTR1D	11.0	VAMP3	131,61
ACTR2	3628801.0	CLTB	11.0	ANAPC10	11.0	IL13	91,75
DAB2	3628801.0	CLTCL1	11.0	CLTB	11.0	ADRBK1	71,23
KLHL20	3628800.0	TGFA	11.0	CLTCL1	11.0	PTGDR2	66,04
KCTD7	3628800.0	VAMP3	10.0	ACTR2	11.0	GRM1	65,33
FBXO21	3628800.0	ACTR2	10.0	DAB2	11.0	STX17	60,76
ARIH2	3628800.0	DAB2	10.0	TGFA	11.0	SEC22B	60,76
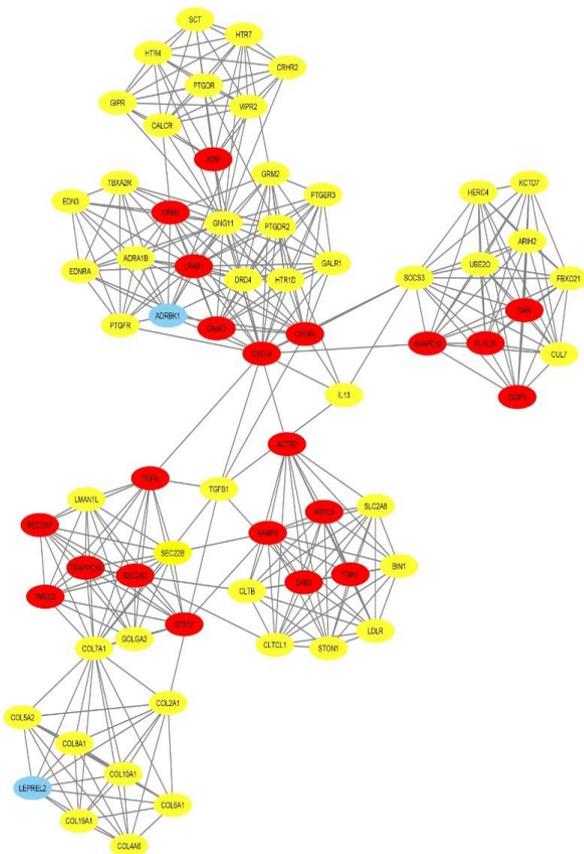
Figure 1. Top module from PPI network. Red nodes represent upregulated genes, and yellow nodes represent downregulated genes.
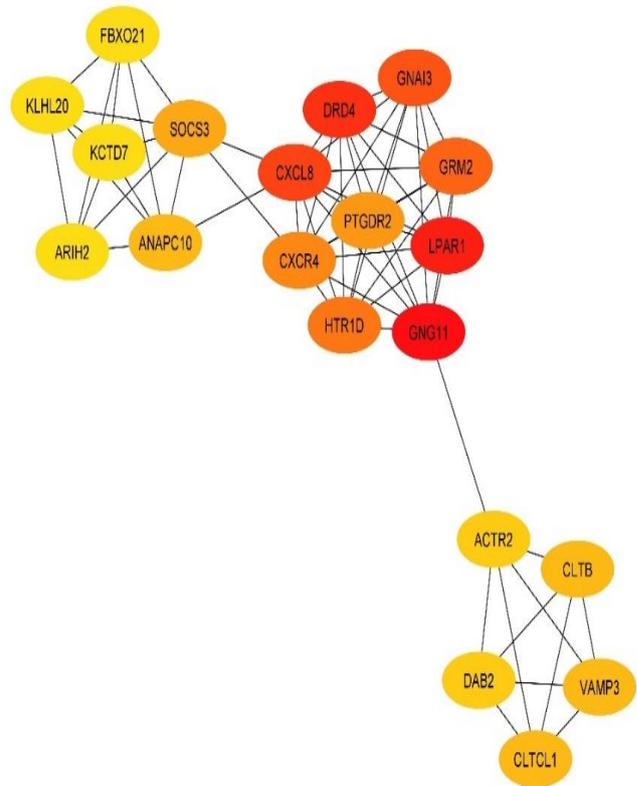
Figure 2. Visualization of the hub genes using cytoHubba plugin. Color grade red to yellow represents MCC scores.

3.3. GO and KEGG pathway enrichment analysis

GO term enrichment results revealed that DEGs are significantly enriched in BP (biological process) and CC (cellular component). As indicated in Table 2, the hub genes were mainly enriched in calcium-mediated signaling, G-protein coupled receptor signaling pathway, chemotaxis, chemokine-mediated signaling pathway, and movement of cell or subcellular component at BP. the hub genes were significantly enriched in clathrin-coated vesicle membrane, intracellular, and clathrin-coated vesicle at CC. In addition, KEGG pathway enrichment results showed that the hub genes were significantly enriched in two pathways including Chemokine signaling pathway and Pathways in cancer (Table 2).

Table 2. KEGG pathway enrichment analysis of hub genes. GO; Gene Ontology, BP; biological process, CC; cellular component, MF; molecular function, KEGG; Kyoto Encyclopedia of Genes and Genomes.

Category	GO Term	p-value
BP	calcium-mediated signaling	2,50E-04
BP	chemotaxis	1,40E-03
BP	G-protein coupled receptor signaling pathway	7,00E-03
BP	chemokine-mediated signaling pathway	3,30E-02
BP	movement of cell or subcellular component	4,00E-02
CC	clathrin-coated vesicle membrane	4,80E-03
CC	intracellular	1,70E-02
CC	clathrin-coated vesicle	2,50E-02
KEGG	Chemokine signaling pathway	1,00E-02
KEGG	Pathways in cancer	4,20E-02

3.4. Validation of hub genes

Prognostic potentials of nine hub genes were evaluated by survival analysis using the Kaplan-Meier plotter and GEPIA. The results demonstrated that among the hub genes only *ACTR2* and *ANAPC10* expression levels significantly associated (p<0.005) with the OS of patients with LUAD. Increased *ACTR2* and *ANAPC10* expression could result in a worse OS rate in LUAD patients (Figure 3a-b and d-e). It was also determined that the expressions of these hub genes were higher in LUAD tissues compared to normal tissues (Figure 3c-f). In fact, in the analysis of the GSE19027 dataset, it was also found that the *ACTR2* and *ANAPC10* mRNA levels in smokers increased 3.83-fold and 3.11-fold in smokers compared to non-smokers, respectively. The results indicate that these genes can be effective prognostic factors for LUAD.
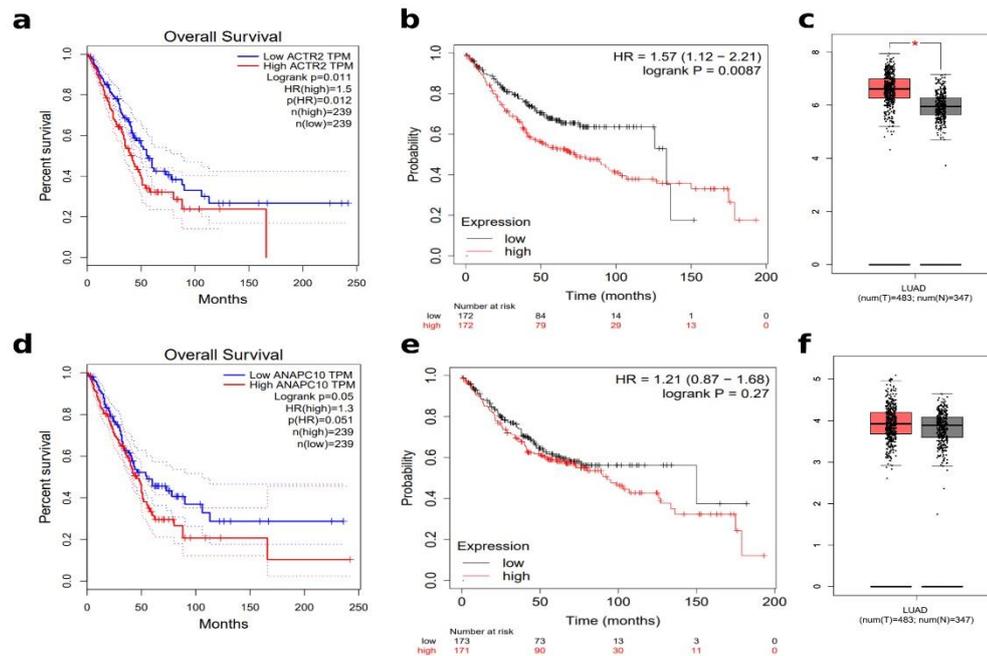
Figure 3. Survival curves and expression boxplots of the hub genes. Overall survival analyses of *ACTR2* using GEPIA **(a)** and Kaplan-Meier plotter **(b)** database. Overall survival analyses of *ANAPC10* using GEPIA **(d)** and Kaplan-Meier plotter **(e)** database. Validation of the expression levels (mRNA) of *ACTR2* **(c)** and *ANAPC10* **(f)** in LUAD samples and normal lung samples using the GEPIA platform.

3.5. Candidate small-molecule drugs screening

To identify candidate small-molecular drugs that could be used to control LUAD progression, prognosis-related DEGs (*ACTR2* and *ANAPC10*) were submitted to the CMap. The related six small molecule drugs with highly significant correlations (p<0.01 and higher negative connectivity score) are listed in Table 3. Among these small molecules, MS-275, domperidone, and clomifene showed a higher negative correlation with a smaller p-value.

Table 3. CMap analysis results.

Rank	CMap name	Mean	N	Enrichment	p-value	Specificity	% non-null
1	MS-275	-0,921	2	-0,991	0,00026	0,0617	100
2	domperidone	-0,884	2	-0,981	0,00076	0	100
3	clomifene	-0,878	2	-0,981	0,00082	0,015	100
10	fusaric acid	-0,836	2	-0,956	0,00414	0	100
11	seneciphylline	-0,865	2	-0,951	0,00531	0,0324	100
16	pancuronium bromide	-0,826	2	-0,94	0,00752	0,0216	100

4. Discussion

According to World Health Organization (WHO) reports, non-communicable diseases (NCDs), including cardiovascular diseases, stroke, cancer, and chronic lung disease are responsible for almost 70% of deaths globally [12]. However, it has been shown that almost half of cancer-related deaths can be prevented by modifying lifestyle behaviors or avoiding main risk factors including malnutrition, alcohol consumption, and tobacco use. In addition, early detection of cancer is a highly effective and long-term strategy in reducing the global cancer burden. The most common lethal tumor in the world, lung cancer, causes 1.6 million deaths each year and accounts for 19.4% of the total cancer-related deaths [13]. NSCLC, one of the two main subtypes of lung cancer, comprises 85% of all lung cancers. NSCLC is also classified into three subtypes: large cell carcinoma, squamous cell carcinoma, and adenocarcinoma [14]. Lung adenocarcinoma (LUAD) is the most common type of lung cancer (around 40% of all) [15]. However, underlying mechanisms responsible for the initiation, development, and metastasis of the disease are still poorly understood. Therefore, identifying the molecular drivers associated with LUAD development may contribute to the development of new approaches for early diagnosis and disease management. In this study, a total of 9 significantly dysregulated genes between current smokers without cancer and never smokers were identified in the GEO dataset GSE19027 using bioinformatics analysis. Finally, nine genes were screened out as hub genes. Among them, it was found that overexpression of *ACTR2* and *ANAPC10* were significantly associated with shorter patients' survival.

Different types of mammalian cells, including fibroblasts, hematopoietic cells, and embryonic cells, have their directional motility, also known as cell migration, which plays an essential role in the physiologic functions [16]. However, abnormal cytoplasmic protrusions, such as lamellipodia, can mediate cancerous cells to migrate and metastasize in a coordinated manner in malignant cells [17]. The Arp2/3 (Actin-related protein 2: ACTR2 and 3: ACTR3) complex is responsible for lamellipodium formation and thus involved in the movement of many types of cells. Deletion and RNA-mediated interference (RNAi) studies on Arp2/3 complex have also indicated that this complex is essential for cell migration [18, 19]. Previous studies also demonstrated that the Arp2-positive cells with higher levels of ACTR2 were accumulated within the tumor tissue [20]. Anaphase-promoting complex (APC/C), consisting of 11–13 highly conserved subunits, marks target cell cycle proteins for degradation. ANAPC10, a subunit of the APC/C complex, displays an essential role in substrate recognition [21]. Recent studies, such as that performed by Wang et al. [22] discovered that *ANAPC10* is overexpressed in NSCLC cell lines and promotes the proliferation of cells. They also showed that the knockdown of *ANAPC10* significantly inhibited the migration of NSCLC cells. Taken together, *ACTR2* and *ANAPC10* may be a valuable clinical indicator of lung adenocarcinoma development and progression.

Based on the small-molecule analysis, a set of small-molecule that could reverse smoking-induced abnormal gene expression that can lead to the LUAD development was determined. According to CMap predication, it was found that the drug signatures significantly correlates with *ACTR2* and *ANAPC10*

gene signatures. Among these, MS-275, also known as entinostat is a histone deacetylase inhibitor (HDACi) that increases acetylated histones and leads to transcriptional suppression [23]. Moreover, recent studies also reported that MS-275 potentiated and facilitated inhibitory effects of different antitumor suppressors in lung adenocarcinoma [24]. Furthermore, other noteworthy molecules and bioactive metabolites we found are listed in Table 3.

In summary, this study was designed to identify critical genes that might be involved in the smoking-associated LUAD progression. In addition, a group of small molecules that can increase efficacy in LUAD therapy have been identified. However, future experimental investigations are needed to validate the predicted molecules.

Conflicts of interest

The authors state that there is no conflict of interests.

References

[1] Sung H., Ferlay J., Siegel R.L., Laversanne M., Soerjomataram I., Jemal A., Bray F., Global Cancer Statistics 2020: GLOBOCAN estimates of incidence and mortality worldwide for 36 cancers in 185 countries, *CA: Cancer J. Clin.*, 71(3) (2021) 209-249.

[2] Bender E., Epidemiology: the dominant malignancy, *Nature*, 513 (2014) S2-S3.

[3] Hammouz R.Y., Kostanek J.K., Dudzisz A., Witas P., Orzechowska M., Bednarek AK., Differential expression of lung adenocarcinoma transcriptome with signature of tobacco exposure, *J. App. Genet.*, 61 (2020) 421-437.

[4] Herbst R.S., Morgensztern D., Boshoff C., The biology and management of non-small cell lung cancer, *Nature*, 553 (2018) 446-454.

[5] Ducray F., Honnorat J., Lachuer J., DNA microarray technology: principles and applications to the study of neurological disorders, *Rev. Neurol.*, 163 (2007) 409-420.

[6] Sahin U., Derhovanessian E., Miller M., Kloke B.P., Simon P., Löwer M., Bukur V., Tadmor A.D., Luxemburger U., Schrörs B., Personalized RNA mutanome vaccines mobilize poly-specific therapeutic immunity against cancer, *Nature*, 547 (2017) 222-226.

[7] Li L., Lei Q., Zhang S., Kong L., Qin B., Screening and identification of key biomarkers in hepatocellular carcinoma: evidence from bioinformatic analysis, *Oncol. Rep.*, 38 (2017) 2607-2618.

[8] Liu W., Ouyang S., Zhou Z., Wang M., Wang T., Qi Y., Zhao C., Chen K., Dai L., Identification of genes associated with cancer progression and prognosis in lung adenocarcinoma: Analyses based on microarray from Oncomine and The Cancer Genome Atlas databases, *Mol. Genet. Gen. Med.*, 7 (2019) e00528.

[9] Wang X., Pittman G.S., Bandele O.J., Bischof J.J., Liu G., Brothers J.F., Spira A., Bell D.A., Linking polymorphic p53 response elements with gene expression in airway epithelial cells of smokers and cancer risk, *Hum. Genet.*, 133 (2014) 1467-1476.

[10] Tang Z., Li C., Kang B., Gao G., Li C., Zhang Z., GEPIA: a web server for cancer and normal gene expression profiling and interactive analyses, *Nucleic Acids Res.*, 45 (2017) W98-W102.

[11] Győrffy B., Surowiak P., Budczies J., Lánczky A., Online survival analysis software to assess the prognostic value of biomarkers using transcriptomic data in non-small-cell lung cancer, *PLoS One.*, 8 (2013) e82241.

[12] World Health Organization, *Noncommunicable Diseases Country Profiles – WHO Global Report, Geneva: WHO*, (2018).

[13] Forum of International Respiratory Societies. The Global Impact of Respiratory Disease – Second Edition. Sheffi eld, European Respiratory Society (2017).

[14] Zappa C., Mousa S.A., Non-small cell lung cancer: current treatment and future advances, *Transl. Lung Cancer Res.*, 5 (2016) 288-300.

[15] Denisenko T.V., Budkevich I.N., Zhivotovsky B., Cell death-based treatment of lung adenocarcinoma, *Cell Death Dis.*, 9 (2018) 1-14.

[16] Yamaguchi H., Lorenz M., Kempiak S., Sarmiento C., Coniglio S., Symons M., Segall J., Eddy R., Miki H., Takenawa T., Molecular mechanisms of invadopodium formation: the role of the N-WASP–Arp2/3 complex pathway and cofilin, *J. Cell. Biol.*, 168 (2005) 441-452.

[17] Kurisu S., Suetsugu S., Yamazaki D., Yamaguchi H., Takenawa T., Rac-WAVE2 signaling is involved in the invasive and metastatic phenotypes of murine melanoma cells, *Oncogene.*, 24 (2005) 1309-1319.

[18] Sawa M., Suetsugu S., Sugimoto A., Miki H., Yamamoto M., Takenawa T., Essential role of the C. elegans Arp2/3 complex in cell migration during ventral enclosure, *J. Cell. Sci.*, 116 (2003) 1505-1518.

[19] Hudson A.M., Cooley L., A subset of dynamic actin rearrangements in Drosophila requires the Arp2/3 complex, *J. Cell. Biol.*, 156 (2002) 677-687.

[20] Semba S., Iwaya K., Matsubayashi J., Serizawa H., Kataba H., Hirano T., Kato H., Matsuoka T., Mukai K., Coexpression of actin-related protein 2 and Wiskott-Aldrich syndrome family verproline-homologous protein 2 in adenocarcinoma of the lung, *Clin. Cancer Res.*, 12 (2006) 2449-2454.

[21] Marrocco K., Criqui M.C., Zervudacki J., Schott G., Eisler H., Parnet A., Dunoyer P., Genschik P., APC/C-mediated degradation of dsRNA-binding protein 4 (DRB4) involved in RNA silencing, *PLoS One.*, 7 (2012) e35173.

[22] Wang Y., Han T., Gan M., Guo M., Xie C., Jin J., Zhang S., Wang P., Cao J., Wang J-B. A novel function of anaphase promoting complex subunit 10 in tumor progression in non-small cell lung cancer, *Cell Cycle.*, 18 (2019) 1019-1032.

[23] Gerson S.L., Caimi P.F., William B.M., Creger R.J., Pharmacology and molecular mechanisms of antineoplastic agents for hematologic malignancies, Hematology (Seventh Edition), Elsevier, (2018) 849-912.

[24] Luo B.L., Zhou Y., Lv H., Sun S.H., Tang W.X., MS-275 potentiates the effect of YM-155 in lung adenocarcinoma via survivin downregulation induced by miR-138 and miR-195, *Thorac. Can.*, 10 (2019) 1355-1368.

Effects of EGFR inhibitor AG 1478 on MDA-MB-231 and MCF-7 breast cancer cells

Nazlıcan İŞLEN [1] *Mehmet Rıfkı TOPÇUL* [2, *]

[1] *Istanbul University, Institute of Science, Department of Biology. Istanbul/Turkey.*
[2] *Istanbul University, Faculty of Science, Department of Biology. Istanbul/Turkey.*

Abstract

In this current study, antiproliferative effect of EGFR inhibitor AG1478 was investigated in human breast cancer cell lines. MDA-MB-231 and MCF-7 cell lines were used respectively as triple negative breast cancer and Luminal A breast cancer model. To this end cell viability, cell index values by xCELLigence Real-Time Cell Analysis DP instrument and mitotic index analysis were used. The results of the current study showed that AG1478 had cytostatic effects on both of cell lines. The IC50 concentration was determined as 50 µM for MDA-MB-231 and 20 µM for MCF-7 cell line. IC50 concentration was used for mitotic index parameter. IC50 concentrations decreased the mitotic index values of both of cell lines. There were significant differences between the control and the experimental groups ($p<0.05$). The results of the present study suggest that AG1478 may serve as a promising treatment option for breast cancer.

1. Introduction

Breast is a bilateral organ which is diagnosed with the highest number of malignancies in women and has major changes in size, shape and function during adolescence, pregnancy, breastfeeding, and postmenopausal periods [1]. It is a heterogeneous disease with various risk factors and clinical features. Although it is generally known as female disease, it is reported that researches can also develop in men [2]. Incidence rate increases with age up to 45-50 years. Lifetime estrogen exposure is one of the most important risk factors. Early menarche, late menopause, late and a small number of pregnancies, postmenopausal hormone replacement therapy, xenoestrogens and childlessness prolong the exposure to estrogen [3]. On the other hand, age, family history, the use of oral contraceptives, radiation exposure, alcohol use and benign breast disease are among the risk factors for breast cancer [4]. The prolonged exposure to estrogen and the prolongation of proliferation times increase the number of cells that can be mutated and start to proliferation of the cells that begin to tumour. Signals that cause differentiation of breast ductal cells, especially during pregnancy and other strong signals cause intense apoptosis of the

alveolar and ductal cells after weaning. These cycles may be involved in the elimination of tumor cells and purification of tissue. Therefore, it is thought that many pregnancies at an early age can have a strong protective effect with long periods of breastfeeding [5, 6].

BRCA genes encode various proteins involved in the DNA repair mechanism. The germline mutations in BRCA genes are associated with breast cancer. In the examined populations, mutations on the BRCA-1 and BRCA-2 genes caused a high increase in the risk of breast cancer. However, the incidence of mutations in the BRCA-2 gene is higher than in the BRCA-1 gene [7]. BRCA1 and BRCA2 have different functions. While the protein encoded by the BRCA 1 gene is involved in estrogen receptor signaling pathway, the BRCA2 gene is involved in terminal differentiation of mammary epithelial cells [8, 9].

Epidermal Growth Factor Receptor (EGFR), a transmembrane protein, binds to peptide growth factors of the Epidermal Growth Factor (EGF) family to activate [10, 11]. EGF binds to EGFR to stimulate cell growth, proliferation and differentiation. EGFR overexpression gives tumors an aggressive phenotype and it is common in many types of solid tumors [12]. EGF and EGFR are involved in many aspects of the

---

development of carcinomas [13, 14]. Studies have shown that overexpression of the EGF receptor plays an important role in pathological processes such as tumorigenesis and progression. Overexpression of EGFR is associated with poor prognosis and reduced survival, especially in different types of carcinomas [15-17].

In recent years, EGFR has an important role in cancer treatment studies. Tyrosine kinase inhibitors and monoclonal antibodies are molecules that target EGFR. It binds competitively to the ATP pocket of EGFR to inhibit tyrosine kinase activity. In contrast, antibodies competitively inhibit ligand binding to EGFR and thus inhibit receptor activation [18]. The majority of protein tyrosine kinase inhibitors disrupt signal transduction by binding the enzyme to the ATP binding pocket and are currently used in clinical trials [19]. AG 1478 is a specific epidermal growth factor receptor tyrosine kinase inhibitor used in laboratory studies [20]. In recent years, targeted treatment approaches have replaced classic methods in breast cancer, as in many cancers [21].

In this study, it was aimed to investigate the antiproliferative effects of the EGFR inhibitor AG1478 on triple negative and luminal A breast cancer cell lines.

2. Materials and Methods

2.1. Cell culture

MDA-MB-231 cells were cultured in DMEM (high glucose) (Sigma) containing 10% fetal bovine serum (Sigma), 100 µg/ml streptomycin (Ulugay), 100 IU/ml penicillin (Pfizer), amphotericin B (Sigma) at 37°C in humidified atmosphere of 5% CO_2. TMCF-7 cells were cultured in RPMI-1640 medium containing 10% fetal bovine serum (Sigma), 100 µg/ml streptomycin (Ulugay), 100 IU/ml penicillin (Pfizer), amphotericin B (Sigma). 37°C in an atmosphere humidified with 5% CO_2 for both cell types. The pH of the medium was adjusted to 7.2 with sodium bicarbonate.

2.2. Seeding of cells

In order to calculate the relative viability, seeding was made in 96-well plates with 30,000 cells / 200 µl medium per well. Sterile round coverslips were placed in each well of 24-well plates for the mitotic index parameter. Cell seeding was carried out at 150,000 cells / 300 µl medium per well. After the cells adhered to the coverslips, 500 µl of medium was added to each well. The cells were prepared for the experiment by continuing the incubation in a mixture of 95% air and 5% CO_2 at 37°C for 24 hours.

2.3. Preparation of inhibitor concentrations

The experiments were carried out at different concentrations of EGRF inhibitor AG 1478 and at different time intervals. AG 1478 hydrochloride (Tocris) is stored as 10 mg powder at -20°C. AG 1478 was dissolved with DMSO to obtain a 10mM stock solution and stored at + 4°C during the experiments. Concentrations to be applied to cells in experiments were obtained by diluting the stock solution with tissue culture medium.

2.4. Cell viability (MTT)

The cytotoxicity of AG 1478 on the cells as a result of the application of different doses was evaluated with the MTT test. Different concentrations of AG 1478 were applied to the cells. At the end of the experiment periods, the medium from the wells was removed and 40 µl MTT (5mg / ml) was added. After waiting for 4 hours, 160 µl DMSO was added to the wells with MTT and left for 1 hour incubation in shaker. After the dissolution of the formed formazan crystals by this process, the absorbance values of the experimental groups were measured by spectrophotometer at 570 nm by taking the 690 nm wavelength as reference.

2.5. xCELLigence real-time cell analysis (RTCA): cytotoxicity

The basic principle of the xCELLigence RTCA-DP system is that as the amount of cells adhering to the surface of the gold-coated E-Plate increases, the resistance against current increases and as the amount of cells adhered to the surface decreases, its resistance decreases. Cell proliferation and cell death can be recorded continuously and in real time through the xCELLingence RTCA-DP system.

16-well E-Plate was used to evaluate the cell index parameter. Later, 5,000 cells in 100 µl medium for MDA-MB-231 cells and 10,000 cells in 100 µl medium for MCF-7 cells were seeded in each well. After seeding process, E-Plates were incubated for 20 minutes in a sterile working cabinet at room temperature and then placed in xCELLigence DP device and incubation continued at 37°C and 5% CO_2 ambient conditions. After cell seeding was performed on the E-Plates, the xCELLigence DP device was commanded to take measurements every 15 minutes. Approximately 24 hours after cell seeding, in 1/3 of the proliferation phase of the cells, the medium in the E-plates was replaced with the medium containing inhibitors, and measurements were taken at 15 minutes intervals for 72 hours. Graphs of concentration and

time dependent cell index values were transferred to the computer screen.

2.6. Mitotic index (MI)

The preparations prepared according to the experimental groups were first hydrolyzed with 1 N HCl at room temperature for 1 minute and then with 1 N HCl at 60°C for 10 minutes. After the hydrolysis process, Feulgen method was applied to the preparations for 1 hour. These preparations were then washed 3 times with the washing solution of the Feulgen method for 2 minutes each and air dried. After the preparations dried, they were stained with Giemsa dye for 2 minutes. Late prophase, metaphase, anaphase and telophase phases were counted in order to determine the mitosis index (MI) values of the preparations ready for counting. Since the early prophase stage is morphologically similar to the cells in the interphase group, it was evaluated together with this stage. The applied inhibitor concentration was evaluated as three preparations for each time and the MI values were determined by counting an average of 3,000 cells from each preparation.

2.7. Statistical evaluation

Concentrations applied to all experimental groups and values of cell kinetics parameters determined according to time were evaluated relative to control groups and each other. One-way ANOVA test was applied to the values determined from the experimental groups. While the significance of the groups with respect to the control was evaluated with the DUNNETT's test, the significance of the groups with each other was evaluated with the t-test. Statistical evaluations were based on $p < 0.05$ significance level.

3. Results and Discussion

3.1. Determination of optimal concentration with cell viability analysis

In order to determine the changes caused by AG 1478 in the mitochondrial dehydrogenase enzyme activity of MDA-MB-231 and MCF-7 cell lines, initially 50 µM, 100 µM, 150 µM inhibitor concentrations were used in the cultured cells for 24 hours. The absorbance values obtained from the experimental series conducted in parallel with the control group without inhibitor applied were shown in Tables 1 and 2.

Table 1. Absorbance values of mitochondrial dehydrogenase activity of MDA-MB-231 cells treated with AG 1478 at concentrations of 50 µM, 100 µM ve 150 µM for 24 h ($p < 0.05$).

Experimental Groups	Absorbance Values (450-690 nm)
Control	$561{,}636 \times 10^{-3} \pm 0{,}014$ SD
50 µM	$289{,}5 \times 10^{-3} \pm 0{,}011$ *
100 µM	$266{,}15 \times 10^{-3} \pm 0{,}009$ *
150 µM	$184{,}1 \times 10^{-3} \pm 0{,}008$ *

Table 2. Absorbance values of mitochondrial dehydrogenase activity of MCF-7 cells treated with AG 1478 at concentrations of 20 µM, 100 µM ve 150 µM for 24 h ($p < 0.05$).

Experimental Groups	Absorbance Values (450-690 nm)
Control	$561{,}636 \times 10^{-3} \pm 0{,}014$ SD
20 µM	$288{,}166 \times 10^{-3} \pm 0{,}012$ *
100 µM	$180 \times 10^{-3} \pm 0{,}008$ *
150 µM	$143{,}166 \times 10^{-3} \pm 0{,}007$*

When the absorbance values are examined viability values were 51,8% for 50 µM; 43,63 for 100 µM and 32,95 for 150 µM compared to control group which was considered as 100% for MDA-MB-231 cell. For MCF-7 cell line these values were 51,76% for 20 µM; 45,42 for 100 µM and 37,94 for 150 µM (Figure 1 and 2).
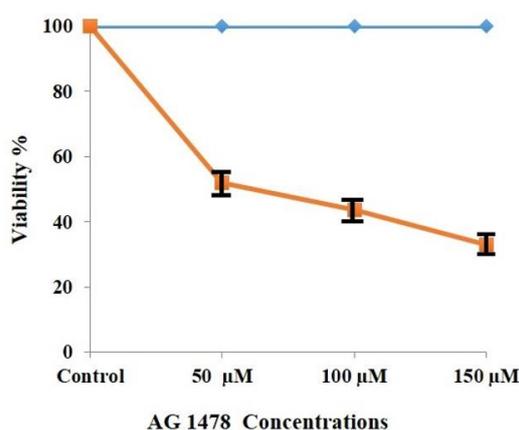
Figure 1. Percent viability values of MDA-MB-231 cells treated with 50 µM, 100 µM, 150 µM AG 1478 for 24 h ($p < 0.05$).
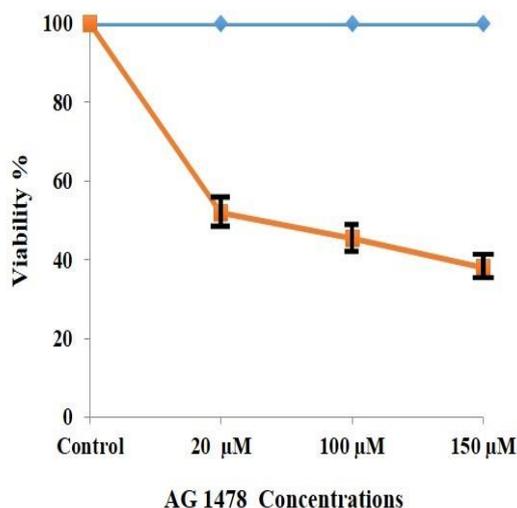
Figure 2. Percent viability values of MCF-7 cells treated with 50 μM, 100 μM, 150 μM AG 1478 for 24 h (p<0.05).

According to the data obtained, it is seen that 50 μM AG 1478 for the MDA-MB-231 cell line and 20 μM AG 1478 for the MCF-7 cell line were the IC50 concentrations that cause the death of half of the cells.

3.2. xCELLigence Real-Time Cell Analysis (RTCA): cytotoxicity

When the cell index values obtained from the real-time cell analysis system as a result of the application of AG 1478 to the MDA-MB-231 cell line at concentrations of 50 μM, 100 μM and 150 μM to the MCF-7 cell line at 20 μM, 100 μM and 150 μM concentrations were examined, inhibitor appeared to have antiproliferative effects on cells. The curves of the graph of the cell index values, when compared with the standard curves, suggest that all the applied AG 1478 concentrations produced a cytostatic effect in both cell lines (Figure 3 and 4).
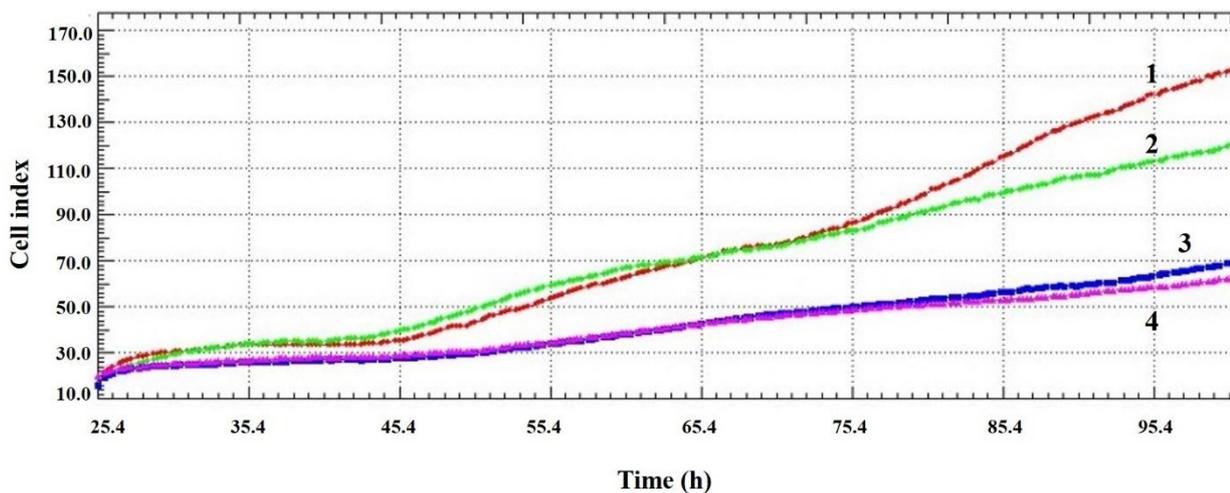
Figure 3. Graph of cell index of MDA-MB-231 cells treated with AG 1478 at concentrations of 50 μM, 100 μM ve 150 μM (Line 1: Control, Line 2: 50 μM, Line 3: 100 μM , Line 4: 150 μM).
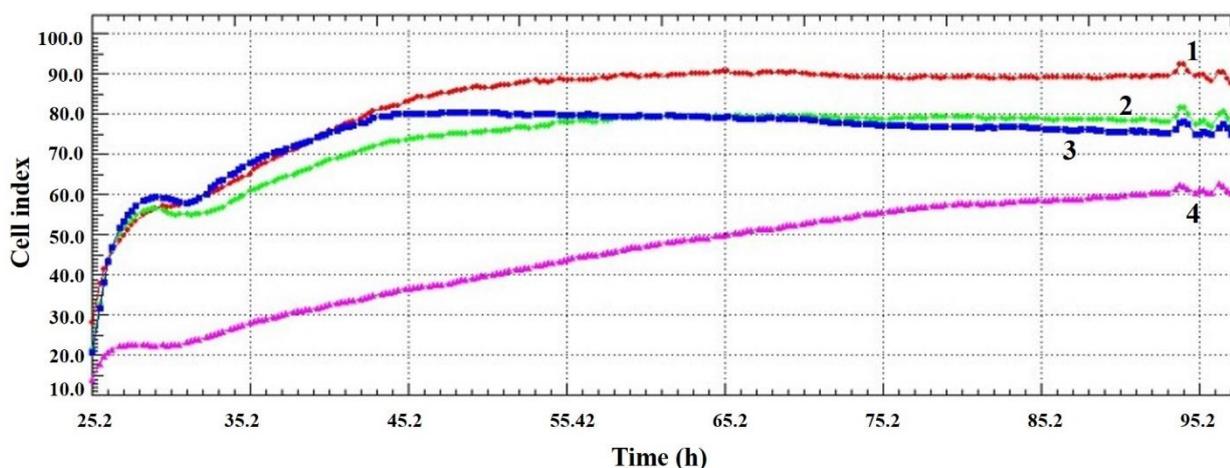
Figure 4. Graph of cell index of MCF-7 cells treated with AG 1478 at concentrations of 20 μM, 100 μM ve 150 μM (Line 1: Control, Line 2: 20 μM, Line 3: 100 μM , Line 4: 150 μM).

3.4. Mitotic index (MI)

In order to determine the change in mitotic index values as a result of the application of AG 1478 on cells; inhibitor concentrations of 50 μM were applied to MDA-MB-231 cells and 20 μM to MCF-7 cells, which were cultured for 0-72 hours. The mitotic index values obtained as a result of the experiment conducted in parallel with the control group without inhibitors are shown in Table 3 and Table 4. As seen in Figure 5 and Figure 6, mitotic index values of MDA-MB-231 and MCF-7 cells decreased significantly depending on time as a result of AG 1478 application.

Table 3. Mitotic index valuees of MDA-MB-231 cells treated with AG 1478 at concentrations of 50 μM for 0-72 h ($p<0.05$).

Time (h)	Mitotic Index (%)	
	Control	50 μM
24	6,13±0,03[SD]	2,6±0,02*
48	6,6±0,04	0,93±0,01*
72	6,7±0,03	0,34±0,01*

Table 4. Mitotic index valuees of MCF-7 cells treated with AG 1478 at concentrations of 20 μM for 0-72 h ($p<0.05$).

Time (h)	Mitotic Index (%)	
	Control	50 μM
24	4,7 ± 0,02[SD]	2,08 ± 0,02*
48	5,8 ± 0,03	2,06 ± 0,01*
72	5,4 ± 0,03	1,8 ± 0,01*

4. Discussion

Developing the treatment methods of cancer, one of the most important diseases of our age, directing the treatments to specific targets in line with the purposes of increasing the effectiveness of the methods used and eliminating the side effects increases the survival chances of the patients.

Triple negative breast cancer has a poor prognosis and an aggressive phenotype. It is insensitive to drugs that target hormone receptors and human epidermal growth factor receptor 2. Therefore, the development of an effective therapeutic reagent to treat triple negative breast cancer is required [22].

Bishop et al. observed that in their studies examining the sensitivity of cancer cells against different inhibitors of the EGFR family, it was observed that HER1 and MAPK signaling in all HER1-expressing cells was inhibited by AG 1478. In this study, in cell lines with high HER1 expression and where AG 1478

mediates the arrest of cells in the G1 phase. It has been observed that at low concentrations the inhibitor potentially inhibits both HER1 phosphorylation and the MAPK pathway, whereas cell lines expressing low HER1 require higher inhibitor concentrations for the same effects [23].

In this study, different concentrations of AG 1478 were applied to triple negative and Luminal A breast cancer cell lines and evaluated with xCELLigence Real Time Cell Analysis System. As a result of the comparison of the obtained cell index values and the curves obtained from these values with the standard curves, it is suggested that the AG 1478 have a cell growth inhibitory effect for both cell lines. This situation is in accordance with the fact that AG 1478, mentioned in the above literature, mediates the pause in the G1 phase.

In Zhang et al.'s study on MCF-7 and MDA-MB-231 cell lines have been shown that AG1478 was able to inhibit the activation of EGFR, ERK1 / 2 and AKT signaling pathways, and although the two cell lines expressed EGFR at different levels, the inhibitor had similar antiproliferative activity on cell lines [24].

Studies with AG 1478 show that this inhibitor has antitumor activity. In *in vitro* studies, the inhibitor showed significant antiproliferative effects on glioblastoma, leiomyoma, colorectal carcinoma and nasopharyngeal carcinoma cells [25-28]. It has also been shown to sensitize tumors to the cytotoxic effect of cisplatin and temozolomide or to the monoclonal antibody mAb 806, which is an anti-EGFR antibody [29-31].

The use of EGFR/HER1 inhibitor AG 1478 with HER2 inhibitor has been shown to synergistically reduce cell viability in breast cancer [32]. It has been shown that the use of tamoxifen with AG 1478 in breast cancer patients inactivates the EMT program that plays a role in the metastasis process [33]. Treatments of the EGFR inhibitor AG1478 in SkBr3 cells have been shown to abolish the cytochrome P450 1B1 (CYP1B1) expression [34].

In recent years, many studies have found that estrogen and estrogen receptors play critical roles on breast tumors. ER and / or progesterone receptors are expressed in approximately 70% of breast tumors [35]. Tsonis et al. showed that the coordinated action of ERs with EGFR and / or IGFR in the expression of bioactive ECM macromolecules that play a role in cancer progression is very important and powerful agents for endocrine therapies [36].

In this study; The effect of EGFR inhibitor AG 1478 on MDA-MB-231 as a triple negative breast cancer model and MCF-7 cell lines used as a Luminal A breast cancer model was evaluated using cell kinetics parameters such as cell viability, cell index, and mitotic index. The data obtained as a result of the study show that there is a significant decrease in cell viability, cell index, mitotic index values depending on time.

These data suggest that treatments for EGFR in breast cancer and other cancer types will have positive results in cancer treatment. The findings show that treatment strategies can be developed by targeting HER1 in HER2-negative cancer types that are difficult to treat, such as triple negative breast cancer. It is also thought to be useful in the treatment of treatment-resistant cancers.

Acknowledgment

Conflicts of interest

The authors state that did not have conflict of interests.

References

[1] Russo J., Russo I.H., Development of The Human Breast, *Maturitas*, 49(1) (2004) 2-15.

[2] Bahreyni A., Samani S.S., Rahmani F., Behnam-Rassouli R., Khazaei M., Ryzhikov M. et al., Role of Adenosine Signaling in The Pathogenesis of Breast Cancer, *Journal of Cellular Physiology*, 233(3) (2018) 1836-1843.

[3] Topçul M., Çetin İ., Breast Cancer, Cancer: Disease of the Age, In: (Ed.) Ahmed M El-Sharkawy, Chapter 19, OMICS Group eBooks, Foster City, USA, (2015) 1-21.

[4] Board P.C.G.E., Genetics of Breast and Gynecologic Cancers (PDQ®), (2016).

[5] Schulz W.A., Breast Cancer, In: Schulz WA (Ed.). Molecular Biology of Human Cancers, Springer, Germany, (2005) 357-382.

[6] Weber G.F., Epithelial Tumors, In: Weber GF (Ed.). Molecular Mechanisms of Cancer, Springer, USA, (2007) 441-524.

[7] Tryggvadottir L., Olafsdottir E.J., Gudlaugsdottir S., Thorlacius S., Jonasson J.G., Tulinius H. et al., BRCA2 Mutation Carriers, Reproductive Factors and Breast Cancer Risk, *Breast Cancer Research*, 5(5) (2003) R121.

[8] Narod S.A., Modifiers of Risk of Hereditary Breast and Ovarian Cancer, *Nat. Rev. Cancer*, 2 (2002) 113-123.

[9] Vidarsson H., Mikaelsdottir E.K., Rafnar T., Bertwistle D., Ashworth A., Eyfjord J.E. et al., BRCA1 and BRCA2 Bind Stat5a and Suppress Its Transcriptional Activity, *FEBS Letters*, 532(1-2) (2002) 247-252.

[10] Yarden Y., Ullrich A., Growth Factor Receptor Tyrosine Kinases, *Annu Rev Biochem.*, 57 (1988) 443-478.

[11] Normanno N., De Luca A., Bianco C., Strizzi L., Mancino M., Maiello M.R. et al., Epidermal Growth Factor Receptor (EGFR) Signaling in Cancer, *Gene*, 366(1) (2006) 2-16.

[12] Demirelli F.H., Hedefe yönelik kanser tedavisi ve monoklonal antikorlar, *Antibiyotik ve Kemoterapi Derneği (ANKEM) Dergisi*, 19 (2005) 123-125.

[13] Mehrabi M., Mansouri K., Soleymani B., Hoseinkhani Z., Shahlaie M., Khodarahmi R., Development of A Human Epidermal Growth Factor Derivative with EGFR-Blocking and Depleted Biological Activities: A Comparative *In Vitro* Study Using EGFR-Positive Breast Cancer Cells, *International Journal of Biological Macromolecules*, 103 (2017) 275-285.

[14] Cadena D.L., Gill G.N., Receptor Tyrosine Kinases, *FASEB J.*, 6 (1992) 2332-2337.

[15] Pawlowski V., Revillion F., Hebbar M., Hornez L., Peyrat J.P., Prognostic Value of The Type I Growth Factor Receptors in A Large Series of Human Primary Breast Cancers Quantified with A Real-Time Reverse Transcription polymerase Chain Reaction Assay, *Clin. Cancer Res.*, 6 (2000) 4217-4225.

[16] Gullick W.J., Prevalence of Aberrant Expression of The Epidermal Growth Factor, *Br. Med. Bull.*, 47 (1991) 87-98.

[17] Mao R.D., Tan Y.M., Expressions of EGFR and p16 Protein in Nasopharyngeal Cancer, *Pract. J. Cancer*, 14 (1999) 182-184.

[18] Gan H.K., Walker F., Burgess A.W., Rigopoulos A., Scott A.M., Johns T.G., The Epidermal Growth Factor Receptor (EGFR) Tyrosine Kinase Inhibitor AG1478 Increases the Formation of Inactive Untethered EGFR Dimers, *Journal of Biological Chemistry*, 282(5) (2007) 2840-2850.

[19] Al-Obeidi F.A., Lam K.S., Development of Inhibitors for Protein Tyrosine Kinases, *Oncogene*, 19(49) (2000) 5690-5701.

[20] Johns T.G., Luwor R.B., Murone C., Walker F., Weinstock J., Vitali A.A. et al., Antitumor Efficacy of Cytotoxic Drugs and The Monoclonal Antibody 806 Is Enhanced by The EGF Receptor Inhibitor AG1478, *Proceedings of the National Academy of Sciences*, 100(26) (2003) 15871-15876.

[21] Topçul M.R., Çetin İ., Endpoint of Cancer Treatment: Targeted Therapies, *Asian Pacific Journal of Cancer Prevention*, 15(11) (2014) 4395-4403.

[22] Kawai M., Nakashima A., Kamada S., Kikkawa U., Midostaurin Preferentially Attenuates Proliferation of Triple-Negative Breast Cancer Cell Lines Through Inhibition of Aurora Kinase Family, *Journal of Biomedical Science*, 22 (1) (2015) 48.

[23] Bishop P.C., Myers T., Robey R., Fry D.W., Liu E.T., Blagosklonny M.V., et al., Differential Sensitivity of Cancer Cells to Inhibitors of The Epidermal Growth Factor Receptor Family, *Oncogene*, 21 (2002) 119-127.

[24] Zhang Y.G., Du Q., Fang W.G., Jin M.L., Tian X.X., Tyrphostin AG1478 Suppresses Proliferation and Invasion of Human Breast Cancer Cells, *International Journal of Oncology*, 33(3) (2008) 595.

[25] Zhu X.F., Liu Z.C., Xie B.F., Li Z.M., Feng G.K., Yang D. et al., EGFR Tyrosine Kinase Inhibitor AG1478 Inhibits Cell Proliferation and Arrests Cell Cycle in Nasopharyngeal Carcinoma Cells, *Cancer Letters*, 169(1) (2001) 27-32.

[26] Nagane N., Levitzki A., Gazit A., Cavanee W.K., Huang H.J., Drug Resistance of Human Glioblastoma Cells Conferred by A Tumour Specific Mutant Epidermal Growth Factor Receptor Through Modulation of Bcl-XL and Caspase 3-Like Proteases, *Proc. Natl. Acad. Sci. USA*, 95(10) (1998) 5724-5729.

[27] Shushan A., Rojansky N., Laufer N., Klein B.Y., Shlomai Z., Levitzki R. et al., The AG1478 Tyrosine Kinase Inhibitor Is An Effective Suppressor Of Leiomyoma Cell Growth, *Hum. Reprod.*, 19 (2004) 1957-1967.

[28] Partik G., Hochegger K., Schörkhuber M., Marian B., Inhibition of Epidermal-Growth-Factor-Receptor-Dependent Signalling by Tyrphostins A25 and AG1478 Blocks Growth and Induces Apoptosis in Colorectal Tumour Cells *In Vitro*, *J. Cancer Res. Clin. Oncol.*, 125 (1999) 379-388.

[29] Lei W., Mayotte E.J., Levitt L.M., Enhancement of Chemosensitivity and Programmed Cell Death by Tyrosine Kinase Inhibitors Correlates with EGFR Expression in Non-Small Cell Lung Cancer Cells, *Anticancer Res*., 19 (1999) 221-228.

[30] He H.Y., Fang W.G., Zheng J., You J.F., Heng W.J., Li Y., Mechanisms of Mitogen Activated Protein Kinase Phosphatase-5 Regulation Growth and Invasion of A Human Prostate Cancer Cell Line, *Natl. Med. J. China*, 83 (2003) 1812-1817.

[31] Nakamura H., Takamori S., Fujii T., Ono M., Yamana H., Kuwano M. et al., Cooperative cell growth inhibition by combination treatment with ZD1839 (Iressa) and trastuzumab (Herceptin) in non-small-cell lung cancer, *Cancer Lett*., 230 (2005) 33-46.

[32] Yi H., Wu M., Zhang Q., Lu L., Yao H., Chen S et al., Reversal of HER2 Negativity: An Unexpected Role for Lovastatin in Triple-Negative Breast Cancer Stem Cells, *J. Cancer*, 11(13) (2020) 3713-3716.

[33] Tian M., Schiemann W.P., GF-β Stimulation of EMT Programs Elicits Non-genomic ER-α Activity and Anti-estrogen Resistance in Breast Cancer Cells, *J. Cancer Metastasis Treat.*, 3 (2017) 150-160.

[34] Cirillo F., Pellegrino M., Malivindi R., Rago V., Avino S., Muto L., GPER is involved in the regulation of the estrogen-metabolizing CYP1B1 enzyme in breast cancer, *Oncotarget*, 8(63) (2017)106608-106624.

[35] Lim E., Metzger-Filho O., Winer E.P., The Natural History of Hormone Receptor-Positive Breast Cancer, *Oncology*, 26 (2012) 688-694.

[36] Tsonis A.I., Afratis N., Gialeli C., Ellina M.I., Piperigkou Z., Skandalis S.S. et al., Evaluation of The Coordinated Actions of Estrogen Receptors with Epidermal Growth Factor Receptor and Insulin-Like Growth Factor Receptor in The Expression of Cell Surface Heparan Sulfate Proteoglycans and Cell Motility in Breast Cancer Cells, *FEBS Journal*, 280(10) (2013) 2248-2259

Influences of basal media, growth regulators, explant type and photoperiod on callus competency and pigmentation of *Alkanna orientalis* L.

Cennet YAMAN [1,*] 🆔 , *Allah BAKHSH* [2, 4] 🆔 , *Serkan URANBEY* [3] 🆔

[1] *Yozgat Bozok University, Agriculture Faculty, Department of Field Crops, Yozgat/TURKEY*
[2] *Niğde Ömer Halisdemir University, Faculty of Agricultural Sciences and Technologies, Department of Agricultural Genetic Engineering, Niğde/TURKEY*
[3] *Ankara University, Faculty of Agriculture, Department of Field Crops, Ankara/TURKEY*
[4] *University of the Punjab, Centre of Excellence in Molecular Biology, , Lahore, Pakistan*

Abstract

The goal of this research was in-vitro callus induction and red pigment production of Alkanna orientalis as a medicinal herb which belongs to Boraginaceae family containing valuable naphthoquinone derivates. The two different explants (leaf and leaf base) were subjected to abiotic factors such as different nutrient media (MS, B5 and M9), light and plant growth regulators (IAA and IBA). High frequency reproducible, prolific and compact calli formation was obtained from MS and B5 media supplemented with IAA, whereas high pigmentation was found in leaf base explants on M9 medium. Leaf base explant and dark conditions were found more effective for both callus formation and pigment production. The pigmentation at IBA was more than IAA, and the maximum level of pigmentation was observed on M9 medium with a combination of 1.0 mg/l IBA under dark. The factors that may be the most influential in the production of callus and red color pigment from A. orientalis have been determined. A. orientalis may be considered to be alternative plants for the A/S (alkannin/shikonin) production in vitro.

1. Introduction

Boraginaceae family including some important *Alkanna, Arnebia, Echium, Lithospermum* and *Onosma* genus are well known as medicinal and dye plants containing valuable secondary metabolites such as hydroxynaphthoquinone pigments (alkannin, shikonin) and their derivatives [1]. The genus Alkanna with 50 species is an important member of the family [2]. Turkey is also one of the most important gene centres for the genus represented in the flora of Turkey by 41 taxa belonging to 36 species with an 80% endemism rate [3]. *Alkanna* species are spread out in Mediterranean coast, Central, Eastern and Western Anatolia of Turkey the genus naturally grows in rocky, sandy and steppe habitats [4]. The most important phytochemical constituents of Alkanna taxa consist of isohexenylnaphthazarins, mainly alkannin, shikonin and other derivatives such as acetylalkannin, propionylalkannin, isobutylalkannin, angelylalkannin, β,β-Dimethylacrylalkannin, isovalerylalkannin and

others [5-7]. The species are ethnobotonically used for many therapeutic and non-therapeutic purposes in worldwide. Their roots of the species are multipurpose utilized in industries as a natural source of red pigments, including dye of cosmetics, food and textiles [8, 9]. Moreover, they are evaluated for treatment of a wide range of disorders such as a natural remedy to prevent and to treat ulcers, wounds, various dermatological diseases, fever, inflammation, aging and herpes [6, 9, 10]. The scientific literature demonstrated the chemo-preventive [11], antiproliferative [8], anticancer [12], wound healing [13], antimicrobial [14], antipyretic, antinociceptive and sedative [15] properties of *Alkanna* species root bark.

The biotechnological approaches such as cell/tissue culture have been efficiently used as alternative renewable source for the industrially large-scale commercial production of these pharmaceutical compounds resembling those accumulated in the root bark of the original plants [16-19]. Many studies have

reported that the bioactive compounds obtained from tissue culture techniques are minimal for production time and the cost of labor than those obtained from field-grown plants [20, 21]. Callus, suspension and root culture among tissue culture techniques are efficient approach to produce fast, stable and prolific secondary metabolites [22]. Callus cultures were successfully applied to produce secondary metabolites for many plant species. The induction of regenerative and compact callus is accomplished by differential application of various plant growth regulators (PGRs) types and control of conditions in the culture medium [23]. Different plant tissue culture approaches such as different basal media, combinations and concentrations of PGRs, explant types, have been used to increase the production of A/S and its derivatives [24] along with genetic manipulation [25]. Commercial production of A/S and its derivatives were first produced by callus culture of *Lithospermum erythrorhizon* [26]. It is also reported that A/S and it derivatives might be produced using tissue culture techniques for different species, e.g., callus culture of *Alkanna tinctoria* [27], suspension culture of *Alkanna orientalis* [17], callus culture and suspension culture of *Arnebia hispidissima* [28], suspension culture of *Echium italicum* L. [29], root and suspension culture of *Lithospermum canescens* [30], as well as callus culture of *Onosma bulbotrichom* [18].

Alkanna orientalis (L.) Boiss var. *orientalis* is a perennial deciduous herb with red-pigmented roots [31], and grows in wild regions of Mediterranean. Up to date, there are limited callus differentiation and shoot regeneration literatures about the production of *in vitro* secondary metabolites in *Alkanna* species [17, 32]. In our previous study, callus induction and regeneration capacity of *Alkanna orientalis* were achieved using different type and concentrations cytokine/auxin combination [32]. However, it is necessary to develop reliable and efficient methods to increase the frequency of induction of morphogenesis in calli. The present study also aimed to improve suitable and prolific callus culture system and red pigmentation in *Alkanna orientalis* using different nutrient basal media and growth regulators.

2. Materials and Methods

2.1. Material

The seeds of *Alkanna orientalis* (L.) Boiss var. orientalis were collected from Yozgat Bozok University Campus (1339 m, 39° 46′ 45″N, 34° 47′ 38″E) in June 2017, Yozgat province, in Turkey (Figure 1) dried at room temperature for 7 days and kept under 4 °C.

Figure 1. *Alkanna orientelis* at its natural habitat in Yozgat province of Turkey

2.2. Seed surface sterilization

Seed sterilization and inoculation were performed as described by Yaman et al. [32]. The seeds of *A. orientalis* were thoroughly washed in a running tap water for 30 min. Then, the seeds were surface sterlizated with 20% (v/v) commercial bleach (Axion) containg sodium hypochlorite (0.4-0.5%) for 20 min and rinsed three times with de-ionized sterile water. Subsequently, surface sterilized seeds were kept in sterile distilled water for 1 h to remove the hard and thick shell of seeds. The thick cortex of seeds was gently removed using sterile scalpel.

2.3. Germination and explant isolation

The surface sterilized seeds were germinated and cultured on MS [33] medium with vitamins supplemented with 0.25 mg/L BAP (6-benzylaminopurine), 0.5 mg/L Kn (kinetin), 1.0 mg/L IAA (indol acetic acid), 30 g/L sucrose and 6 g/l agar as previously described by Yaman et al. [32]. The pH was adjusted to 5.7-5.8 using 1 M NaOH. The plantlets of rosette plant growing from the germinated seeds were subcultured on the same medium after 15 days. The leaf and leaf base (the part where the leaf attaches to the stem) were excised from 4-week-old in vitro propagated seedlings. Leaf (2-3 mm width) and leaf base (1-2 mm length) of the species were cultured on MS, Gamborg B5 (B5) [34], and M9 [24] basic basal media containing 30 g/l sucrose and 0.5, 0.1 and 2.0 mg/l IAA alone or indol butyric acid (IBA).

2.4. Culture conditions

The pH of all media was adjusted to 5.7-5.8 using 1 N NaOH followed by the addition of agar. The medium-containing flasks were then autoclaved at 121°C under 103 kPa for 20 min. Plant growth regulator (PGR)-free medium (MS0, B50 and M90) was used as the control.

All of the leaf and leaf base explants were separately inoculated onto these media. All cultures were separately incubated at 24 - 25 °C under 60% humidity. Each application was cultured in two different lighting conditions as follows: a 16/8 hrs photoperiod with 35 µmol m2/s light intensity delivered by cool white fluorescent (1) and darkness (2) conditions. Callus induction and pigmentation from explants in each application were recorded after 6 week from culture initiation. Also, the rosette plantlets developing from the germinated seeds of *A. orientalis* cultured separately MS, B5 and M9 mediums supplemented with 0.25 mg/L BAP, 0.5 mg/L Kn, 1.0 mg/L, 30 g/L sucrose under light. After 30 days, the observation of the seedlings growing on these three nutrient media was taken.

2.5. Experimental design and statistical analysis

Experiments were conducted in a completely randomized design and repeated three and each experiment consisted of 10 explants per Petri dishes (90 × 90 mm). The statistical comparison was conducted using version IBM SPSS statistics 20. Data given in percentage were subjected to arcsine (_X) transformation before statistical analysis. Duncan's multiple range tests was used to determine the significance at $P < 0.05$.

3. Results and Discussion

3.1. Effects of MS basal media on compact, prolific callus induction and pigmentation

The prolific callus induction and pigmentation from the leaf and leaf base explants of *Alkanna orientalis* were tested using different concentrations of IAA and and IBA on MS basal medium under light and darkness conditions.and all data were given in Table 1. Callus regeneration was significantly affected by different doses of IAA/IBA and darkness and light conditions and explant types. There were also statistically significant interactions between these parameters at $P < 0.05$.

Under darkness conditions, mean callus formation ratio (81.3%) was higher than the light application (34.6%). As the source of explant, the leaf base explant showed a higher callogenezis with 76.4% than the leaf explant (39.4%). Among auxin types, IAA was more effective on callus induction than IBA (42.5%), callus formation increased with increasing concentrations of IAA and IBA. Bagheri et al. [18] reported that callus initiation of *Onosma bolbutrichum* on MS media supplemented with increasing of IAA concentration in media increased and pigment production was observed on the entire surface of the callus tissue. In this study, the callus formed a brown color pigment. Leaf base explant exhibited 100% callus formation in all doses of IAA in darkness conditions and 2.0 mg/l IBA. 100 % callus regeneration was only achieved on the medium containing 2.0 mg/l IAA under light conditions. They also formed brownish-lack pigment, not red. Gharehmatrossian et al. [35] defined that callus of *Onosma sericeum* on MS media supplemented with 0.5 mg/1 IAA and 3.0 mg/l BAP under darkness were semi hard and black color.

Table 1. Effects of MS medium containing different doses of IAA and IBA on callus regeneration (%) of *A. orientalis* under light and darkness conditions

PGRs	Concentration (mg/l)	Light		Darkness		Mean	Mean
		Leaf	Leaf base	Leaf	Leaf base		
	0	0.0b	0.0e	0.0c	0.0c		
IAA	0.5	0.0b	53.3c	87.5a	100a	60.2b	
	1.0	40.0a	86.7b	93.8a	100a	80.6a	73.3
	2.0	25.0ab	100.0a	91.7a	100a	79.2a	
	Mean	21.7C	80.0B	91.0AB	100A		
IBA	0.5	0.0b	20.0d	4.2c	70.8b	23.8b	
	1.0	0.0b	0.0e	33.3b	95.8a	32.3b	42.5
	2.0	0.0b	90.0b	95.8a	100a	71.5a	
	Mean	0.0C	36.7B	44.4B	88.9A		
Mean		10.8C	58.3B	68.1B	94.4A		
Mean		34.6		81.3			
Leaf						39.4	
Leaf base						76.4	

The duncan comparisons of the difference between the data were showed with lower case letters in the line and upper case letters in the column

3.2. Effects of B5 basal media on compact, prolific callus induction and pigmentation

The responses of the leaf and leaf base of *A. orientalis* to different doses of IAA and IBA in B5 basal medium under light and darkness conditions were investigated and the data were given in Table 2.

As a result of the analysis, light/darkness conditions, explant source and auxin types showed different effects on callus induction. A higher rate of callus formation was observed in dark condition (66.0%) than light condition (36.8%). The leaf base explant produced a higher callus formation (80.8%) than the leaf explant (22.0%). B5 medium containing different concentrations of IAA produced higher mean callus ratio (60.1%) than B5 medium supplemented with various concentarations of IBA (42.7%). Leaf base explant exhibited 100% callus formation on BG medium including 0.5-1.0 mg/l of IAA and 1.0-2.0

mg/l IBA at darkness conditions, 0.5 mg/l IAA and 2.0 mg/l IBA under the light conditions. Leaf explant only gave 100% callus formation in 1.0 mg/l IAA under darkness conditions. The color of calli was brownish-lack pigment. Bagherieh-Najjar and Nezamdoos [36] stated same findings for pigment production from *Onosma dichroantha* in B5 medium. Similarly, Zare et al. [29] reported that the calli in B5 medium supplemented with 1 mg/L IAA and 1 mg/L kinetin failed to produce pigments and B5 medium appeaed to lack such potential which seems to be a key determinant factor for hydrophobic metabolites (naphthazarin derivatives etc.) that require a lipophilic adsorbent.

Electrostatic interactions between chemical species vary depending on the pH of the aqueous solution. In the extraction experiments, the interaction between the analyte and the selected chemical medium should be high.

Table 2. Effect of B5 medium containing different doses of IAA and IBA on callus regeneration (%) from leaf explant of *A. orientalis* under light/darkness conditions

PGRs	Concentration (mg/l)	Light		Darkness		Mean	Mean
		Leaf	Leaf base	Leaf	Leaf base		
	0.0	0.0b	0.0d	0.0c	0.0d		
IAA	0.5	0.0b	100a	0.0c	100a	50.0	
	1.0	0.0b	53.3bc	100a	100a	63.3	60.1
	2.0	26.7a	78.3b	75.0b	87.5b	66.9	
	Mean	8.9C	77.2AB	58.3B	95.8A		
IBA	0.5	0.0b	56.7bc	0c	66.7c	30.8b	
	1.0	0.0b	26.7c	0c	100a	31.7b	42.7
	2.0	0.0b	100a	62.5b	100a	65.6a	
	Mean	0.0C	61.1B	20.8C	88.9A		
Mean		4.5D	69.2B	20.8C	77.4A		
Mean		36.8		66.0			
Leaf						22.0	
Leaf base						80.8	

The duncan comparisons of the difference between the data were showed with lower case letters in the line and upper case letters in the column

3.2. Effects of M9 basal media on compact, prolific callus induction and pigmentation

The callus initiation and red pigment production from the leaf and leaf base of *A. orientalis* to different doses of IAA and IBA in M9 nutrient medium in light and darkness conditions were examined and the data were given in Table 3 and Table 4.

Table 3. Effect of M9 medium containing different doses of IAA and IBA on callus regeneration (%) from leaf explant of *A. orientalis* under light/darkness conditions

PGRs	Concentration (mg/l)	Light			Darkness		
		Callus rate	Nigrescence	Red pigment formation	Callus rate	Nigrescence	Red pigment formation *
IAA	0.0	0.0	+	0	0.0	+	0
	0.5	0.0	+	0	0.0	+	0
	1.0	0.0	+	0	0.0	+	0
	2.0	0.0	+	0	0.0	+	0
IBA	0.5	0.0	+	0	0.0	+	1
	1.0	0.0	+	0	0.0	+	1
	2.0	0.0	+	0	0.0	+	1

* 0, no red color. 1, 2, 3 and 4 denote the intensity of red color

As shown in Tables 3 and 4, virtually no callus was produced from both explants cultured at all dose concentrations of IAA and IBA in M9 medium light and dark conditions. Also, the leaf and leaf base explants cultured under light condition turned black in all nutrient medium. Zhang et al. [37] notified that white light completely blocked the biosynthesis of shikonin and its derivatives that produce the red pigment in the cells cultured in M9 medium.

Table 4. Effect of M9 medium containing different doses of IAA and IBA on callus regeneration (%) from leaf base explant of *A. orientalis*

PGRs	Concentration (mg/l)	Light			Darkness		
		Callus rate	Nigrescence	Red pigment formation	Callus rate	Nigrescence	Red pigment formation*
IAA	0.0	0.0	+	0	0.0	+	1
	0.5	0.0	+	0	0.0	+	1
	1.0	0.0	+	0	0.0	+	1
	2.0	0.0	+	0	0.0	+	1
IBA	0.5	0.0	+	0	0.0	+	2
	1.0	0.0	+	0	0.0	+	4
	2.0	0.0	+	0	0.0	+	3

* 0, no red color. 1, 2, 3 and 4 denote the intensity of red color

When the culture of both explants under dark conditions is examined, leaf explant formed a red pigment in all concentrations of IBA. But, all concentrations of IAA were not effective on pigment production from leaf explants. The leaf base explant generated red color pigment in all concentrations of IAA and IBA. Densities of color pigments were evaluated as 1, 2, 3 and 4 from less to more, respectively. While the color pigment density of leaf base explants in IAA growth regulator was at the level of 1 (Figure 2A), it was recorded that the leaf base explants cultured in all doses of IBA was formed the higher red pigment density (Table 4). The highest red pigment density, level 4, was determined in leaf base explants in 1.0 mg/l IBA under darkness conditions (Figure 2B). Among the various auxin types analyzed, many researcher indicated that IBA was more effective than IAA and NAA (a-naphthalene acetic acid) in inducing roots for *Arnebia hispidissima* containing shikonin in its root [38, 39]. Bagheri et al. [18] noted that IAA had lower callus induction than 2,4 D, whereas it was more effective to produce naphthoquinone pigments from callus of *Onosma bulbotrichom*, and, as the IAA concentration increased, the pigmentation in the calli decreased.

Figure 2. The red pigmentation from *A. orientelis* in M9 medium A) The red color pigment (level 1) in leaf base explants in IAA under darkness conditions B) The red color formation (level 4) from leaf base explants on M9 medium containing 1.0 mg/l IBA under darkness conditions after 4 weeks of culture initiation

In generally, the rosette plantlets developing from the germinated seeds of *A. orientalis* cultured separately MS, B5 and M9 media supplemented with 0.25 mg/L BAP, 0.5 mg/L Kn, 1.0 mg/L, 30 g/L sucrose under light. As indicated in Figure 3. M9 medium was found to be more effective on red pigment production of *A. orientalis* than MS and B5 media *in vitro* seedlings of *A. orientalis*. Previous studies clearly demonstrated that M9 medium had a higher level of red pigment production than MS, B5 and other media, in tissue culture of Boraginaceae species containing naphthazarin compounds in their roots [17, 36, 38].
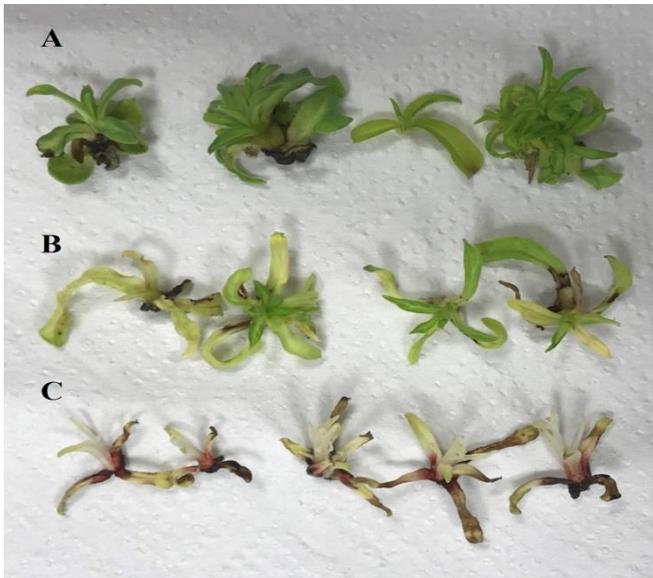
Figure 3. *In vitro* seedlings of *A. orientalis* in different nutrient media under light conditions at the end of the 30 days of culture (A: MS, B: B5, C: M9)

Also, Fang et al. [40] recorded that no pigmentation was visible in hairy roots of *Lithospermum erythrorhizon* cultured in B5 medium under light condition, whereas distinct red color was apparent upon visual inspection when hairy roots were transferred into M9 medium in the dark conditions. The current work supports the studies developed by

Fang [40] and Fujita [24] to produce industrially large quantities of important naphthazarine compounds (red pigment). For the production of red color pigments, primarily the cell proliferation culture of plant cells should be done on B5 nutrient medium, then these cells should be transferred to M9 liquid medium for red pigment production. In contrast to B5 medium, M9 medium lacks ammonium ions that are known to inhibit biosynthesis of naphthazarin and its derivatives [24]. Interestingly, although light signals mostly stimulate the biosynthesis of secondary metabolites [41], the red pigment production in analyzed all medium is completely inhibited under white light.

In our study the pigmentation was observed on nearly all explants in all nutrient media tested in the first week, however, the pigmentation density and color changed according to the nutrient medium, growth regulator and explant types in the following days. Similarly, Gupta et al. [42] reported that light had a negative effect on shikonin production in M9 medium in *Arnebia* sp., but even in light condition, shikonin production increased up to the first 4 days and inhibited in the following days, however, continued to increase in dark conditions.

Explant source is of great importance for plant regeneration and commercially secondary metabolite production of cell/organ through plant tissue culture. In species belonging to Boraginaceae, leaf and root explants are generally used to produce shikonin and its derivatives. The leaf base explants were higher regeneration capacity and pigmentation ability than the leaf in all tested applications. Yaman et al. [32] also recorded that both stem and leaf base explants induced high compact callus production (>86.0%) of *Alkanna orientalis* and *Alkanna sieheana* in all media under light.

Conclusion

In this study, the callus and red pigment production from leaf and leaf base *A. orientalis* in three basal nutrient media (MS, B5 and M9) supplemented with various concentrations of IAA or IBA under light and darkness conditions were examined. MS was the most suitable nutrient medium for both callus growth and brown pigment production (non-red). B5 medium was better for callus growth, but not well for pigment production. M9 medium was also found to be the best nutrient medium for red pigment production, but not a suitable nutrient medium for callus growth. In all media tested, leaf base explant showed higher regeneration capacity and pigmentation ability than leaf explant. Also, the findings of this study revealed that IAA had a powerful effect on callus induction,

while IBA was more effective on pigmentation. These data presented here are useful for large-scale *in vitro* micropropagation of *A. orientalis* for *in vitro* production of its valuable phytochemical compounds.

Acknowledgment

Conflicts of interest

The authors state that did not have conflict of interests.

References

[1] Boulos J.C., Rahama M., Hegazy M.F., Efferth T., Shikonin derivatives for cancer prevention and therapy, *Cancer Letter*, 459 (2019) 248–267.

[2] Mahmoudi S.Z., Seyedabadi M., Esfahani H.R.M., Amanzadeh Y., Ostad S.N., Anti-inflammatory and analgesic activity of *Alkanna bracteosa* and *Alkanna tricophila*, *Nat. Prod. Res.*, 26(6) (2012) 564-569.

[3] Güner A., Aslan S., Ekim T., Vural M., Babaç T., Türkiye Bitkileri Listesi, İstanbul:NGBB and Flora Araştırmaları Derneği Yayını, (2012).

[4] Davis P.H., Mill R.R., Tan K., Flora of Turkey and the East Aegean Islands, 6. Edinburgh: Edinburgh University press, (1988).

[5] Assimopoulou A.N., Karapanagiotis I., Vasiliou A., Kokkini S., Papageorgiou V.P., Analysis of alkannin derivatives from *Alkanna* species by high-performance liquid chromatography/photodiode array/mass spectrometry, *Biomed. Chromatogr.*, 20 (2006) 1359-1374.

[6] Papageorgiou V., Assimopoulou A., Ballis A., Alkannins and shikonins: a new class of wound healing agents, *Curr. Med. Chem.*, 15(30) (2008) 3248-3267.

[7] Assimopoulou A.N., Sturm S., Stuppner H., Papageorgiou V.P., Preparative isolation and purification of alkannin/shikonin derivatives from natural products by high speed counter-current chromatography, *Biomed. Chromatogr.*, 23(2) (2009) 182-198.

[8] Tung N.H., Du G., Wang C., Yuan C., Naphthoquinone components from *Alkanna tinctoria* (L.) Tausch Show significant antiproliferative effects on human colorectal cancer cells, *Phytotherapy Research*, 27 (2012) 66-70.

[9] Jaradat N.A., Zaid A.N., Hussen F.M., Issa L., Altamimi M., Fuqaha B., Nawahda A., Assadi M., Phytoconstituents, antioxidant, sun protection and skin anti-wrinkle effects using four solvents fractions of the root bark of the traditional plant *Alkanna tinctoria* (L.), *Eur. J. Integr. Med.*, 21 (2018) 88-93.

[10] Abdel-Gelil O.E.A., Atwa N.A., Moustafa A.R.A., Mansour S.R., *Alkanna* species: a promising herbal medicine and its uses, *Journal of Food Science and Nutrition Research*, 2 (2009) 309-315.

[11] Tung N.H., Wang C.Z., Du G.J., Yuan C.S., Uto T., Shoyama Y., Chemopreventive activity of naphthoquinones from *Alkanna tinctoria* (L.) Tausch in human colorectal cancer cells, *J. Gastroenterol Hepatol Res.*, 5(4) (2016) 2115-2121.

[12] Rashan L., Hakkim L., Fiebig H.H., Al-Balushi M., *In vitro* anti-proliferative activity of the *Rubia tinctorum* and *Alkanna tinctoria* root extracts in panel of human tumor cell lines, *Jordan J. Biol. Sci.,* 11(5) (2018) 489-494.

[13] Ogurtan Z., Hatipoglu F., Ceylan C., The effect of Alkanna tinctoria Tausch on burn wound healing in rabbits, *Deutsche tierärztliche Wochenschrift*, 109(11) (2002) 481-485.

[14] Alwahibi M.S., Perveen K., Chemical analysis by GC-MS and *in vitro* antibacterial activity of *Alkanna tinctoria* extracts against skin infection causing bacteria, *Biomedical Research,* 28(18) (2017) 7946-7949.

[15] Salih M., Mohammed M.S., Basudan O., El Tahir K.E.H., Osman B.I., Ahmed W.J., Evaluation of antipyretic, antinocieptive and sedative effects of *Tribulus terrestris*, *Mimosa pigra* and *Alkanna tinctoria* methanolic extracts, *J. Phytopharm.,* 5 (2016) 1-3.

[16] Piekoszewska A., Ekiert H., Zubek S., Arbutin production in *Rutagraveolens* L. and *Hypericum perforatum* L. *in vitro* cultures. *Acta Physiologiae Plantarum,* 32 (2010) 223-229.

[17] Mahjouri S., Movafeghi A., Zare K., Kosari-Nasab M., Nazemiyeh H., Production of naphthoquinone derivatives using two-liquid-phase suspension cultures of *Alkanna orientalis*, *Plant Cell, Tissue and Organ Culture (PCTOC),* 124 (2016) 201-207.

[18] Bagheri F., Tahvilian R., Karimi N., Chalabi M., Azam M., Shikonin production by callus culture of Onosma bulbotrichom as active pharmaceutical ingredient, *Iran J. Pharm. Sci.*, 17(2) (2018) 495-504.

[19] Fu J., Zhao H., Bao J., Wen Z., Fang R., Fazal A., Yang M., Liu B., Yin T., Pang Y., Lu G., Qi J., Yang Y., Establishment of the hairy root culture of *Echium plantagineum* L. and its shikonin production, *3 Biotech,* 10 (2020) 429.

[20] Ahmad S., Garg M., Tamboli E.T., Abdin M.Z., Ansari S.H., *In vitro* production of alkaloids: Factors, approaches, challenges and prospects, *Pharmacogn. Rev.,* 7 (13) (2013).

[21] Krol A., Kokotkiewicz A., Szopa A., Ekiert H., Luczkiewicz M., Bioreactor-grown shoot cultures for the secondary metaboliteproduction. In: Ramawat, K.G., Ekiert, H.M., Goyal, S. (Eds.) Plant Cell and Tissue Differentiation and Secondary Metabolites: Fundamentals and Applications, Springer International Publishing, Cham, (2020) 1-62.

[22] Praveen N., Murthy H.N., Effects of macroelements and nitrogen source on biomass accumulation and withanolide - A production from cell suspension cultures of *Withania somnifera* (L.) Dunal, *Plant Cell, Tissue and Organ Culture (PCTOC),* 104(1) (2011) 119-124.

[23] Passinbo H.C., Meira P.R., David J.P., Mesquita P.R., Vale A.E. Rodrigues F.M., Pereira P.A.P., De Santana J.R.F., De Oliveira F.S., De Andrade J.B., David J.M., Volatile organic compounds obtained by in vitro callus cultivation of *Plectranthus ornatus* Codd. (Lamiaceae), *Molecules,* (2013) 10320-10333.

[24] Fujita Y., Hara Y., Ogino T., Suga C., Production of shikonin derivatives by cell suspension cultures of *Lithospermum erythrorhizon*: I. Effects of nitrogen sources on the production of shikonin derivatives, *Plant Cell Rep.*, 1(2) (1981) 59-60.

[25] Boehm R., Sommer S., Li S.M., Heide L., Genetic engineering on shikonin biosynthesis: expression of the bacterial ubiA gene in *Lithospermum erythrorhizon*, *Plant Cell Physiol.,* 41 (2000) 911-919.

[26] Tabata M., Mizukami H., Hiraoka N., Konoshima M., Pigment formation in callus cultures of *Lithospermum erythrorhizon*, *Phytochemistry,* 13 (1974) 927-932.

[27] Urbanek H., Katarzyna Bergier K., Marian Saniewski M., Patykowski J., Effect of jasmonates and exogenous polysaccharides on production of alkannin pigments in suspension cultures of *Alkanna tinctoria*, *Plant Cell Rep.*, 15(8) (1996) 637-641.

[28] Singh B., Sharma R.A., Antioxidant and antimicrobial activities of *Arnebia hispidissima*, *Am. J. Adv. Drug Deliv.,* 2(2) (2014) 224-237.

[29] Zare K.H., Nazemiyeh H., Movafeghi A., Khosrowshahli M., Motallebi-Azar A., Dadpour M., Omidi Y., Bioprocess engineering of *Echium italicum* L.: Induction of shikonin and alkannin derivatives by twoliquid- phase suspension cultures. *Plant Cell, Tissue and Organ Culture (PCTOC),* 100(2) (2010) 157-164.

[30] Tatsumi K., Yano M., Kaminade K., Sugiyama A., Sato M., Toyooka K., Aoyama T., Sato F., Yazaki K., Characterization of shikonin derivative secretion in *Lithospermum erythrorhizon* hairy roots as a model of lipid-soluble metabolite secretion from plants, *Front. Plant Sci.,* 7 (2016) 1066.

[31] Akgun I., Ganzera M., Gur C., Senol S., Korkmaz K., Bedir E., Determination of naphthazarin derivatives in 16 *Alkanna* species by RP-LC using UV and MS for detection, *Chromatographia*, 70 (2009) 963–967.

[32] Yaman C., Uranbey S., Ahmed H.A., Özcan S., Tugay O., Başalma, D., Callus induction and regeneration of *Alkanna orientalis* var. *orientalis* and *A. sieheana*, *Bangladesh J. Bot.*, 48 (2019) 633–640.

[33] Murashige T, Skoog F., A revised medium for rapid growth and bio assays with tobacco tissue cultures, *Physiol. Plant.*, 15 (1962) 473–497.

[34] Gamborg, O. L., Miller, R. A., Ojima, K., Nutrient requirements of suspension cultures of soybean root cells, *Exp. Cell Res.*, 50 (1968) 151.

[35] Gharehmatrossian S., Popov Y., Ghorbanli M., Safaeian S., Iranbakhsh A., Phytochemical and morphological evidences for shikonin production by plant cell cultures of *Onosma sericeum* Willd, *Braz. Arch. Biol. Technol.,* 59 (2016) 1-7.

[36] Bagherieh-Najjar M., Nezamdoost T., Optimization of shikonin production in *Onosma dichroantha* callus using response surface methodology, *Plant Cell, Tissue and Organ Culture (PCTOC),* 126 (2016) 399–409.

[37] Zhang W.J., Su J., Tan M.Y., Liu G.L., Pang Y.J., Shen H.G., Qi J.L., Yang Y., Expression analysis of shikonin-biosynthetic genes in response to M9 medium and light in *Lithospermum erythrorhizon* cell cultures, *Plant Cell, Tissue and Organ Culture (PCTOC),* 101 (2010) 135-142.

[38] Shekhawat M.S., Shekhawat N.S., Micropropagation of *Arnebia hispidissima* (Lehm). DC. and production of alkannin from callus and cell suspension culture, *Acta Physiol. Plant.,* 33 (2011) 1445-1450.

[39] Pal M., Chaudhury A., High Frequency Direct Plant Regeneration, Micropropagation and Shikonin Induction in *Arnebia hispidissima*, *J. Crop Sci. Biotechnol.,* 13(1) (2010) 13-20.

[40] Fang R, Wu F, Zou A, Zhu Y, Zhao H, Zhao H., Liao Y., Tang R., Yang T., Pang Y., Wang X., Yang R., Qi J., Lu G., Yang Y., Transgenic analysis reveals LeACS-1 as a positive regulator of ethylene-induced shikonin biosynthesis in *Lithospermum erythrorhizon* hairy roots, *Plant Mol. Biol.,* 90 (2016) 345-358.

[41] Abbasi B., Tian C., Murch S., Saxena P., Liu C., Light-enhanced caffeic acid derivatives biosynthesis in hairy root cultures of *Echinacea purpurea*, *Plant Cell Rep.*, 26 (2007) 1367-1372.

[42] Gupta K., Garg S., Singh J.,, Kumar M., Enhanced production of naphthoquinone metabolite (shikonin) from the cell suspension culture of *Arnebia* sp. & its up-scaling through bioreactor, *3 Biotech*, 4(3) (2014) 263-273.

The therapeutic potential of targeting HDAC6 with Tubastatin A in TFK-1 and EGI-1 cholangiocarcinoma cells

Münevver YENİGÜL[1] , *Emel Başak GENCER AKÇOK [2], **

[1]*Abdullah Gul University, Graduate School of Engineering and Science, Bioengineering Department, Kayseri, TURKEY*
[2]*Abdullah Gul University, Faculty of Life and Natural Sciences, Molecular Biology and Genetics Department, Kayseri, TURKEY*

Abstract

Cholangiocarcinoma (CCA) is a highly aggressive and invasive malignancy with a poor diagnosis because of the resistance, relapse and limited therapy. Histone deacetylases (HDAC) are a class of enzyme that have important roles in epigenetic modulations. These enzymes are intensely studied and HDAC inhibitors are considered as potent anticancer agents in both solid tumors and hematological malignancies. HDAC inhibitors can affect and induce different mechanisms such as cell cycle arrest, differentiation, and cell death. In this study, we aim to investigate the cytotoxic effect of Tubastatin A, which is a selective HDAC6 inhibitor, on cholangiocarcinoma cell lines, TFK-1 and EGI-1, by MTT assay. Besides, it was aimed to examine the impact on colony formation potential of the cells. The effect of the inhibitor on cell cycle distribution was also examined by using flow cytometry. Tubastatin A has significantly decreased the colony formation and changed cell cycle progression. Taken together, our results suggest that Tubastatin A could be a potent inhibitor against cholangiocarcinoma. On the basis of these results, further mechanistic studies are required to elucidate the antineoplastic activity of Tubastatin A.

1. Introduction

Cholangiocarcinoma is a malignancy that is originating from biliary duct. It stands for the 10-20% of all liver cancers and it is the second most seen hepatic malignancy [1]. The process of development of CCA involves various mechanisms including alterations in oncogenic signaling pathways, genetic changes, epigenetic mechanisms and chromosomal abnormalities. [2].

Epigenetic modifications have crucial roles in tumor progression. These epigenetic changes include DNA methylation and histone modifications, such as acetylation, and regulates important events such as chromatin structure remodeling and regulation of gene expression [3]. In particular, the enzyme histone deacetylase (HDAC), which removes the acetyl group from histone proteins surrounding DNA, makes DNA less reachable to transcription factors. By doing so, it is considered as an important epigenetic regulator for chromatin remodeling and gene expression [4]. Therefore, any dysregulation in the function of

HDACs in cancer cells can lead to suppression of genes involved in the regulation of important cellular events such as cell differentiation, angiogenesis, apoptosis and cell proliferation [5]. Histone deacetylases are highly expressed in both normal cholangiocytes and cholangiocarcinoma cells [6].

There are different members of HDAC family of enzymes [7]. HDAC6 is a unique cytoplasmic enzyme that was shown to interact with and deacetylate tubulin, and then in turn having a regulatory role in cell migration [8]. The overexpression of HDAC6 has been identified in a variety of other cancer cell lines and mouse tumor models and induce oncogenic cell transformation [9]. HDAC6 is an isoform of HDACs that is considered as enhancing CCA cell growth [10].

Selective HDAC6 inhibitors, such as ACY1215 and tubastatin-A, significantly inhibited CCA cell growth both in vitro and in vivo [11,12]. Tubastatin A is a selective HDAC6 inhibitor that has shown promising effects for cancer therapy in many studies. Tubastatin A reduced cell migration and colony-forming capacity of cells in glioblastoma cells and showed a reversing

effect of epithelial-to-mesenchymal transition [13]. Tubastatin A was investigated on CCA in the aspect of primary cilia formation in malignant transformation and CCA animal model was used to demonstrate the decrease in tumor growth. Different CCA cell lines were used to demonstrate the decrease in cell proliferation upon pharmacological inhibiton of HDAC6 with Tubastatin A [11].

In the current study, it is aimed to investigate the effects of HDAC6 inhibition in cholangiocarcinoma cells by using a selective inhibitor, Tubastatin A. TFK-1 and EGI-1 CCA cell lines were investigated against Tubastatin A for the first time for its anti-cancer properties.

2. Materials and Methods

2.1. Chemicals

MTT (M2128-500MG) reagent and the HDAC inhibitor Tubastatin A (SML0044-5MG) was purchased from Sigma. A 5 mM stock of Tubastatin A solution in DMSO (dimethylsulfoxide) was prepared according to the recommendations of the supplier and the main stocks were stored at -20°C. The RPMI 1640, fetal bovine serum, penicillin/streptomycin, and PBS (Phosphate Saline Buffer) were obtained from Euro Clone, Biological Industries, Euro Clone, and Gibco, respectively. The crystal violet that was used to stain the colonies was purchased from Serva chemicals. RNAse enzyme (R5503) and the propidium iodide dye (P4170) were also obtained from Sigma for use in cell cycle analysis.

2.2. Cell lines and maintenance

Human CCA cell lines, TFK-1 and EGI-1, were obtained from German National Resource Center for Biological Material (DSMZ). Cells were cultured in RPMI medium supplemented with 10% FBS and 100 U/mL penicillin/streptomycin and maintained at 37°C in 5% CO_2.

2.3. Cell proliferation

Antiproliferative effects of Tubastatin A were determined by MTT cell proliferation assay on the indicated cell lines. This test is based on the principle that metabolically active cells convert the MTT ((3-(4,5-dimethylthiazol-2-yl)-2,5-diphenyltetrazolium bromide) molecule into insoluble formazan salts and measuring the resulting color at 570 nm [14]. Briefly, 96-well plate were seeded with 10000 cells/well containing 200 µl of growth medium in the absence and presence of increasing concentrations of Tubastatin A. After 48 hours of incubation, 10 µl of

MTT reagent was added to each well and incubated for extra 4 hours. The 96-well plates were centrifuged at 1800 rpm for 10 minutes and the formed formazan crystals was dissolved with 100 µl of DMSO. Formazan intensities was read in the spectrophotometer at a wavelength of 570 nm by Varioskan™ LUX multimode microplate reader (Thermo Scientific™). The proliferation graphs were plotted and the IC_{50} (drug concentration that inhibits cell growth by 50%) concentration calculated for Tubastatin A.

2.4. Colony formation assay

Cholangiocarcinoma cell lines, TFK-1 and EGI-1, were seeded in triplicates into 6-well plates (2000 and 1000 cells/well, respectively) and treated with Tubastatin A (10 µM and 50 µM). The cells were cultured in a humidified incubator at 37°C with 5% CO_2 for 14 days. By the end of 14 days, the medium was removed and the colonies were fixed with 4% paraformaldehyde and then stained with 0.1% crystal violet for 30 minutes at room temperature. After the staining, excess dye was removed using distilled water to improve the visualization of the colonies. After the digital images of the colonies were obtained with the camera, colony counts were made using ImageJ software.

2.5. Cell cycle analysis

Cell cycle analyzes of TFK-1 and EGI-1 cells treated with Tubastatin A were performed by flow cytometry and $1x10^6$ cells were incubated with the inhibitor for 48 hours. Cells were washed with 1 ml of cold PBS (pH=7.4) and centrifuged. Then, 4 ml of 70% ethanol was added to the cells and the cells were kept in a -20°C for at least 24 hours. Afterwards, cell pellet was homogenized in 5 ml of cold PBS, washed and centrifuged. Cell pellets were then washed with 1 ml of PBS/Triton X-100, followed by the addition of 100 µl of RNase-A and incubated at 37°C for 30 minutes. Finally, 100 µl of propidium iodide was added and left at room temperature for 10 minutes. Cell cycle analysis was performed by fluorescence-activated cell sorting (FACS).

2.6. Statistical analysis

The results are presented as mean ± standard deviation (SD). The statistical significance was detected using a one-way analysis of variance (ANOVA) for Dunnett's assay compared to the untreated controls. Statistical analysis was performed using GraphPad Prism 8.0.2 program.

3. Results

3.1 Antiproliferative effect of Tubastatin A on TFK-1 and EGI-1 cholangiocarcinoma cells

The cytotoxic effect of Tubastatin A was examined on TFK-1 (Figure 1A) and EGI-1 (Figure 1B) cholangiocarcinoma cells. The cells were treated with concentrations varying between 0.0025 - 10 µM for TFK-1 cells and 0.1-50 µM for EGI-1 cells for 48 hours. Tubastatin A decreased cell viability in a time and concentration dependent manner when compared to the untreated control (P<0.001). The IC_{50} value for Tubastatin A, which is the drug concentration that inhibits cell growth by 50%, was calculated as 15 µM and 20 µM for TFK-1 and EGI-1 cells, respectively.
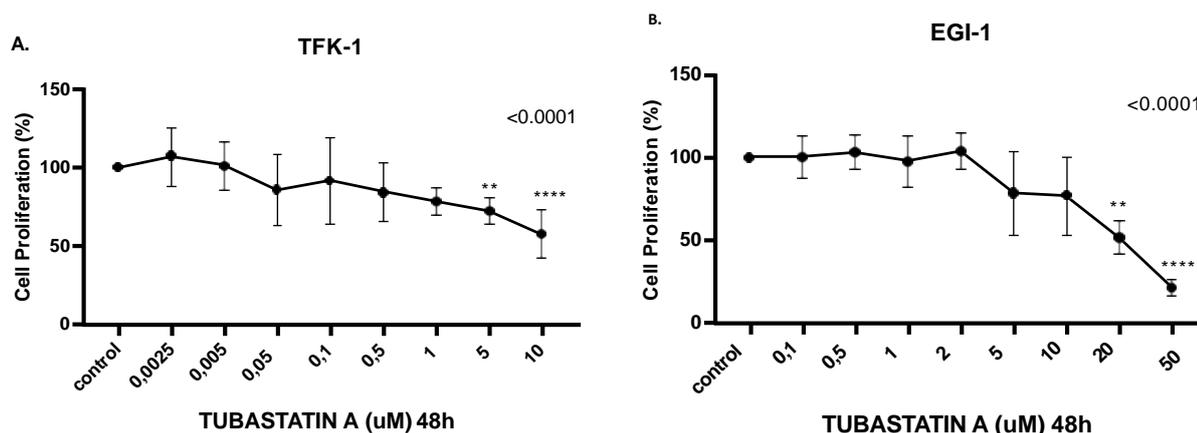
Figure 1. The cytotoxic effect of Tubastatin A on TFK-1 (A) and EGI-1 (B) cells with increasing concentrations for 48 hours. The standard deviation was done on the number of replicates, which is 3 wells per treatment and the experiment was done three times (n=3). (**= $P \leq 0.01$, ****= $P \leq 0.0001$)

3.2 The effect of Tubastatin A on the clonogenicity of cholangiocarcinoma cells

Clonogenic potential of TFK-1 and EGI-1 cholangiocarcinoma cells has been evaluated for 14 days after using two different Tubastatin A concentrations. Tubastatin A treatment caused a decrease in the number of colonies when compared to untreated or DMSO treated control cells (Figure 2).
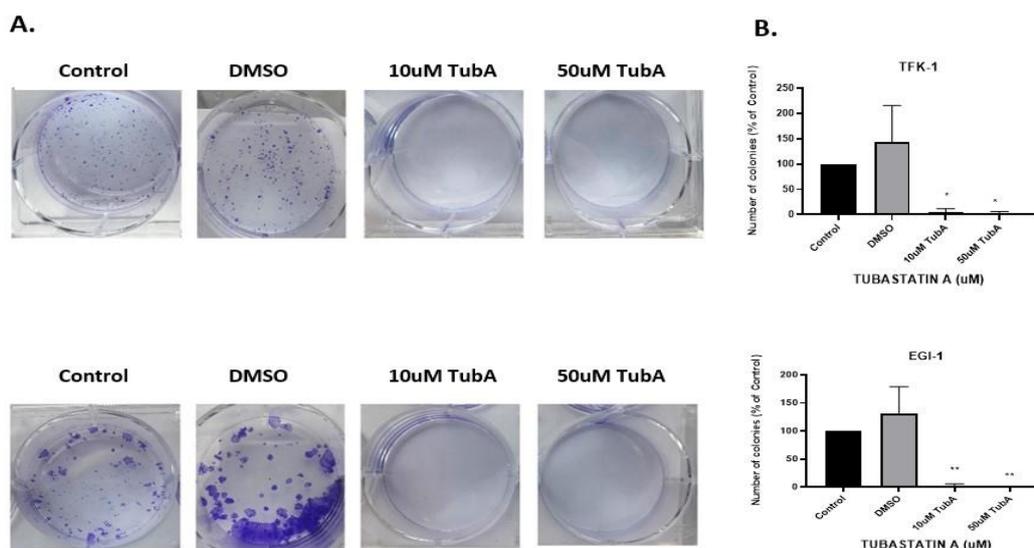
Figure 2. The impact of Tubastatin A on the clonogenicity of cholangiocarcinoma cells. (A) Representative images of clonogenic assays in TFK-1 (upper panel) and EGI-1 (lower panel) cells with different concentrations of Tubastatin A (TubA). (B) The effect of the different treatments on the clonogenic effect on TFK-1 and EGI-1 cells. (*= $P \leq 0.05$, **= $P \leq 0.01$)

3.3 The impact of Tubastatin A on cell cycle distribution

TFK-1 and EGI-1 cells were treated with 10 μM and 50 μM Tubastatin A in complete medium for 48 hours and cell cycle progression was analyzed by fluorescence-activated cell sorting (FACS) analysis (Figure 3). For EGI-1 cells, Tubastatin A treatment demonstrated cell cycle arrest in G2/M phase and the cell population in G0/G1 phase was also decreased by 9 % and 12 % in 10 μM and 50 μM Tubastatin A treatment, respectively. In TFK-1 cells, Tubastatin A did not show a significant effect on cell cycle progression when compared to untreated control cells.
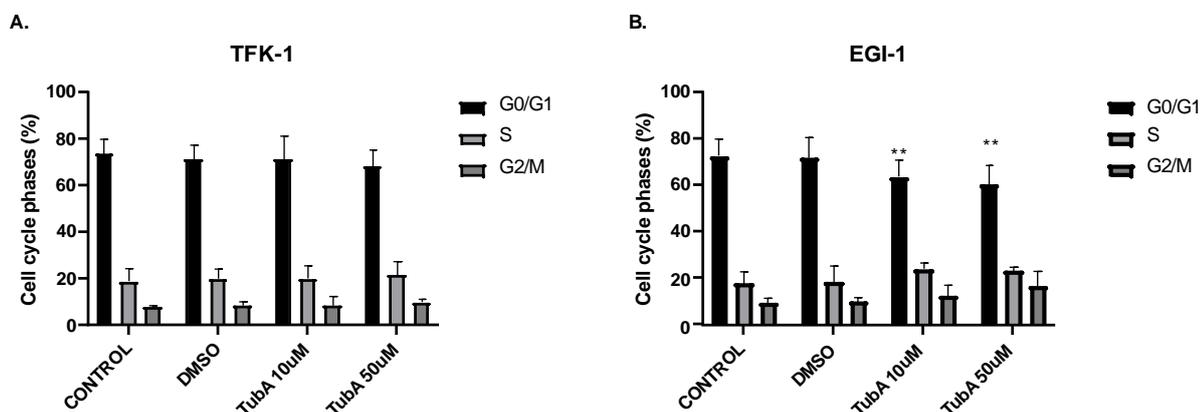
Figure 3. The effect of Tubastatin A on the cell cycle progression. The TFK-1 (A) and EGI-1 (B) cells were treated for 48 hours with 10 μM and 50 μM Tubastatin A (TubA), the cells were harvested, fixed, and stained with propidium iodide. Then the cells were analyzed by flow cytometer. Two independent experiments were performed, combined and analyzed. ** indicates that there is a significant (** = $P \leq 0.01$) difference between control and Tubastatin A administrations.

4. Discussion

In this study, we aimed to investigate the effects of selective HDAC6 inhibitor, Tubastatin A, on TFK-1 and EGI-1 CCA cell lines. Antiproliferative effects of Tubastatin A on CCA cells using MTT assay were determined and a dose dependent cell proliferation decrease was detected. Furthermore, the colony formation assay revealed a significant reduction in colony number depending on the Tubastatin A concentration. Further insight for the cytotoxic mechanism of Tubastatin A, we examined the cell cycle progression by flow cytometry. The cells were shown to be arrested in G2/M phase for EGI-1 cells but there was no significant change in TFK-1 cells.

Cholangiocarcinoma is a highly aggressive and metastatic form of adenocarcinoma with a poor prognosis and mortality rate because of heterogeneity, limited therapy options and developing resistance. It is the second most common type of liver cancer with a rate of 10-20% among all liver cancer types. The chemotherapy options of CCA are mostly gemcitabine and cisplatin, which are considered as a first-line therapy [15]. Some combinational therapies are also done but the overall survival is increased mildly ameliorated [16] and there is a requirement for novel treatment strategies for CCA.

Epigenetics changes involve the DNA and histone modifications which results in changes of genetic expression without changing the DNA sequence. The posttranslational modifications of histone proteins that are tightly bound to the DNA is a significant epigenetic mechanism [4]. These modifications involve acetylation and methylation of certain lysine residues on histone proteins. The histone acetylation causes a change in transcription activity, loosening the compactly packed nucleosome and this process results in the increase in gene expression in many cases [17]. This effect is reversed by histone deacetylation and this reaction is catalyzed by histone deacetylase (HDAC) enzymes. The involvement of epigenetic regulations in various types of diseases, like cancer, got the attention on developing novel strategies targeting epigenetic modifications that has been studied widely [18,19]. HDAC inhibitors show promising effects by causing hyperacetylation and inhibiting the removal of acetyl groups from the lysine residues [20]. Their potential as anticancer agents lead the FDA approval of HDAC inhibitors. HDAC6 is a class II inhibitor that induces cell proliferation in CAA cells and is over expressed in CCA patients [11,12]. HDAC inhibition caused the downregulation of the malignant properties of CCA cells. Many studies demonstrated and suggested the potency of selective HDAC6 inhibition not only for

CCA but also in various types of malignancies like gastric cancer [21], glioblastoma [13], pancreatic cancer [22], colorectal cancers [23]. These selective inhibitors exert anticancer effect by different mechanisms. It has been suggested that Tubastain A enhances temozolomide-induced apoptosis in glioblastoma cells, while treatment affects Hedgehog signaling, thereby reducing glioblastoma progression. [13]. In another study, CCA was used as a model and it was shown that the primary cilia were reduced upon HDAC6 overexpression. The inhibition of HDAC6 and restoration of cilia formation resulted in inhibition of tumor growth [11].

Colony forming capability of cancer cells is a valuable indicator of reproductive potential of living single cancer cells. Tubastatin A was reported to decrease the 2D colony number by 50% in glioblastoma cells [13] and inhibited colony formation in triple negative human breast epithelial/cancer cell lines [24]. Similarly, in this study, decreasing colony formation was also observed in cells treated with Tubastatin A.

HDAC inhibitors are potential anti-cancer agents, and this effect sometimes manifests as cell cycle progression and sometimes cell cycle arrest. This cytoplasmic enzyme also has a nonhistone target, such as tubulin, which plays an important role in cell division and microtubule formation [25]. HDAC6 inhibition was shown to have similar variable effects on cell cycle in three different melanoma cell lines. HDAC6 inhibitors, including Tubastatin A, caused G1 arrest accompanied by changes of cell population in G2 fraction. Although Tubastatin A and other HDAC6 inhibitors were applied to same cancer type but different cell lines, variable effects were observed [26]. In this current study, Tubastatin A induced G2/M arrest for EGI-1 cells and decreased the cell population in G0/G1. On the contrary, the cell population in S phase increased compared to the control. Interestingly, Tubastatin A administration did not have a significant effect on cell cycle distribution. The cell cycle results in the present study is in line with the results that is observed in this previously discussed study [26] that the inhibitor caused different impacts on cell cycle in different CCA cell lines. These observations suggest that Tubastatin A may alter different cell cycle regulatory proteins depending on the type of CCA cell line.

In conclusion, our study demonstrated that the selective inhibitor Tubastatin A exhibits an antiproliferative effect towards TFK-1 and EGI-1 cholangiocarcinoma cells. Tubastatin A's antiproliferative activity is thought to be mediated by its impact and inhibition on clonogenicity of these cells. In addition, the EGI-1 cells were arrested in the G2/M phase upon increasing concentrations of Tubastatin A. Collectively our results show that HDAC6 inhibition with Tubastatin A leads a decrease in cell proliferation, colony formation and cell cycle arrest. Clearly it is important to evaluate the effect of the inhibitor mechanistically. These results provide a starting point for further studies. The focus of future work might be combinational treatments of Tubastatin with different inhibitors that target different pathways. After the validation of conclusions that would be brought, it could be a subject of a multiple inhibitor therapy for CCA. Although there is a need for follow-up studies and further investigation, our results suggest that HDAC6 could be potential therapeutic targets for treating cholangiocarcinoma, and administration of selective inhibitor, Tubastatin A, could be a potential therapeutic approach for cholangiocarcinoma.

Acknowledgment

Conflicts of interest

The authors declare that there is no conflict of interest.

References

[1] Pant K., Peixoto E., Richard S. Gradilone, S. A., Role of Histone Deacetylases in Carcinogenesis: Potential Role in Cholangiocarcinoma, *Cells*, 9(3) (2020) 780.

[2] Rizvi S., Gores G. J., Pathogenesis, diagnosis, and management of cholangiocarcinoma, *Gastroenterology*, 145(6) (2013) 1215-29.

[3] Dawson M. A., Kouzarides T., Cancer epigenetics: From mechanism to therapy, *Cell*, 150(1) (2012) 12-27.

[4] Weinhold B., Epigenetics: the science of change, *Environ. Health Perspect.*, 114(3) (2006) 160-7.

[5] Li Y., Seto E., HDACs and HDAC inhibitors in cancer development and therapy, *Cold Spring Harb. Perspect. Med.*, 6(10) (2016) a026831.

[6] Sriraks R., Limpaiboon T., Histone deacetylases and their inhibitors as potential therapeutic drugs for cholangiocarcinoma–cell line findings, *Asian Pacific J. Cancer Prev.*, 14(4) (2013) 2503-2508.

[7] Dokmanovic M., Clarke C., Marks P. A., Histone deacetylase inhibitors: Overview and perspectives, *Molecular Cancer Research*, 5(10) (2007) 981-989.

[8] Hubbert C., Guardiola A., Shao R., Kawaguchi Y., Ito A., Nixon A., Yoshida M., Wang X. F., Yao T. P., HDAC6 is a microtubuleassociated deacetylase, *Nature,* 417(6887) (2002) 455-458.

[9] Sakamoto K. M., Aldana-Masangkay G. I., The role of HDAC6 in cancer, *Journal of Biomedicine and Biotechnology*, 2011 (2011) 875824.

[10] Gradilone S. A., Pisarello M. J., LaRusso N. F., Primary Cilia in Tumor Biology: The Primary Cilium as a Therapeutic Target in Cholangiocarcinoma, *Curr. Drug Targets*, 18(8) (2015) 958-963.

[11] Gradilone S. A., Radtke B. N., Bogert P. S., Huang B. Q., Gajdos G. B., LaRusso N. F., HDAC6 inhibition restores ciliary expression and decreases tumor growth, *Cancer Res.*, 73(7) (2013) 2259-2270.

[12] Gradilone S. A., Gradilone S. A., Habringer S., Masyuk T. V., Howard B. N., Masyuk A. I., Larusso N. F., HDAC6 is overexpressed in cystic cholangiocytes and its inhibition reduces cystogenesis, *Am. J. Pathol*, 184(3) (2014) 600–608.

[13] Urdiciain A., Erausquin E., Meléndez B., Rey J. A., Idoate M. A., Castresana J. S., Tubastatin A, an inhibitor of HDAC6, enhances temozolomide-induced apoptosis and reverses the malignant phenotype of glioblastoma cells, *Int. J. Oncol*, 54(5) (2019) 1797-1808.

[14] Marks D. C., Belov L., Davey M. W., Davey R. A., Kidman A. D., The MTT cell viability assay for cytotoxicity testing in multidrug-resistant human leukemic cells, *Leuk. Res.*, 16(12) (1992) 1165-1173.

[15] Rizvi S., Khan S. A., Hallemeier C. L., Kelley R. K., Gores G. J., Cholangiocarcinoma-evolving concepts and therapeutic strategies, *Nature Reviews Clinical Oncology*, 15(2) (2018) 95-111.

[16] Valle J., Wasan H., Palmer D. H., Cunningham D., Anthoney A., Maraveyas A., Madhusudan S., Iveson T., Hughes S., Pereira S. P., Roughton M., Bridgewater J., ABC-02 Trial Investigators., Cisplatin plus Gemcitabine versus Gemcitabine for Biliary Tract Cancer, *N. Engl. J. Med.*, 362(14) (2010) 1273-81.

[17] Eberharter A., Becker P. B., Histone acetylation: A switch between repressive and permissive chromatin. Second in review on chromatin dynamics, *EMBO Rep.*, 3(3) (2002) 224-9.

[18] Egger G., Liang G., Aparicio A., Jones P. A., Epigenetics in human disease and prospects for epigenetic therapy, *Nature*, 429(6990) (2004) 457-63.

[19] Cheng Y., He C., Wang M., Ma X., Mo F., Yang S., Han J., Wei X., Targeting epigenetic regulators for cancer therapy: Mechanisms and advances in clinical trials, *Signal Transduct. Target. Ther.,* 4 (2019) 62.

[20] Bates S. E., Epigenetic Therapies for Cancer, *N. Engl. J. Med.*, 383(7) (2020) 650-663.

[21] Dong J., Zheng N., Wang X., Tang C., Yan P., Zhou H. B., Huang J., A novel HDAC6 inhibitor exerts an anti-cancer effect by triggering cell cycle arrest and apoptosis in gastric cancer, *Eur. J. Pharmacol.,* 828 (2018) 67-79.

[22] Wang G., He J., Zhao J., Yun W., Xie C., Taub J. W., Azmi A., Mohammad R. M., Dong Y., Kong W., Guo Y., Ge Y., Class I and Class II Histone Deacetylases Are Potential Therapeutic Targets for Treating Pancreatic Cancer, *PLoS One,* 7(12) (2012) e52095.

[23] Won H. R., Ryu H. W., Shin D. H., Yeon S. K., Lee D. H., Kwon S.H., A452, an HDAC6-selective inhibitor, synergistically enhances the anticancer activity of chemotherapeutic agents in colorectal cancer cells, *Mol. Carcinog.*, 57(10) (2018) 1383- 1395.

[24] Su Y., Hopfinger N. R., Nguyen T. D., Pogash T. J., Santucci-Pereira J., Russo J., Epigenetic reprogramming of epithelial mesenchymal transition in triple negative breast cancer cells with DNA methyltransferase and histone deacetylase inhibitors, *J. Exp. Clin. Cancer Res.*, 37(1) (2018) 314.

[25] Li Y., Shin D., Kwon S. H., Histone deacetylase 6 plays a role as a distinct regulator of diverse cellular processes, *FEBS Journal*, 280(3) (2013) 775-93.

[26] Woan K. V., Lienlaf M., Perez-Villaroel P., Lee C., Cheng F., Knox T., Woods D. M., Barrios K., Powers J., Sahakian E., Wang H. W., Canales J., Marante D., Smalley K. S. M., Bergman J., Seto E., Kozikowski A., Pinilla-Ibarz J., Sarnaik A., Celis E., Weber J., Sotomayor E. M., Villagra A., Targeting histone deacetylase 6 mediates a dual anti-melanoma effect: Enhanced antitumor immunity and impaired cell proliferation, *Mol. Oncol.*, 9(7) (2015) 1447–1457.

Antimicrobial activity screening of a series of taurine derivatives

*Özlem AKGÜL[1], * ID, Çağlar AKGÜNLÜ [2] ID, Hatice BİLER [3] ID, Ayşegül ATEŞ [4] ID,*
Şafak ERMERTCAN [4] ID

[1]*Ege University, Faculty of Pharmacy, Department of Pharmaceutical Chemistry, İzmir, TURKEY.*
[2]*Manisa City Hospital, Manisa, TURKEY.*
[3]*Gercüş State Hospital, Batman, TURKEY.*
[4]*Ege University, Faculty of Pharmacy, Department of Pharmaceutical Microbiology, İzmir, TURKEY.*

Abstract

In this study, a series of taurinamide derivatives 1–18 were assessed for their in vitro antimicrobial activity. Enterococcus faecalis, which is the third most commonly isolated nosocomial pathogen among hospital infections, was found to be more susceptible to the tested compounds than other pathogens. Two of the tested compounds, 1 and 18, showed promising activity against E. faecalis, with minimal inhibitory concentrations (MICs) of 128 and 64 µg/mL, respectively. On the other hand, compound 3 was distinguished from other compounds by its better activity against G(−) Escherichia coli bacteria, with a MIC of 512 µg/mL. None of the compounds displayed better activity than the standard drugs Ciprofloxacin and Fluconazole.

1. Introduction

Taurine is the only free and non-proteogenic amino acid in mammalian species. Indeed, as an organoelement isostere of amino acids, taurine possess sulfonic acid instead of carboxylic acid, which imparts permeability, acidity, and biological activities different from those of conventional amino acids [1–4]. Besides taurine's wide range of biological activities, it also possesses antibacterial, antifungal, and antiviral effects [5,6]. The antibacterial effect of taurine is believed to depend on the formation of low cytotoxic taurinechloramine (TCA) formation during inflammation process of the body (Figure 1) [7,8]. Moreover, a stable derivative of TCA which is known as NVC-422 (*N,N*-dichloro-2,2-dimethyltaurine) was reported as a broad spectrum antibacterial agent that reached to phase II clinic studies however didn't approve as a drug substance (Figure 1) [9,10]. In the search for finding effective antimicrobial taurine derivatives, Winterbottom et al. functionalized taurine's sulfonic acid as a secondary or tertiary sulfonamide and connected its amino group to pantothenic acid in an amide form to obtain pantolytaurinamide derivatives (Figure 1). These derivatives were tested for their antiplasmodial and antibacterial activities and reported to have promising results [11]. In another study, the sulfonic acid moiety of taurine was converted to its primary sulfonamide analog and introduced into a meropenem structure via an amide connection (Figure 1). This final compound was reported to increase the in vivo efficacy and stability of the parent compound meronepem [1]. Those studies indicate that taurine is a promising building block that can be used in antimicrobial drug development that has reached an impasse in recent years. This problem is mostly the result of resistance mechanisms that pathogens have developed to existing chemical structures. According to the World Health Organization, bacterial resistance has become a worldwide threat that will cause 10 million deaths per year by 2050 [12]. As a result; finding new structures distinct from the known antibiotic scaffolds, would be useful for averting resistance. From this point of view; taurine serves a distinctive feature for medicinal chemists.
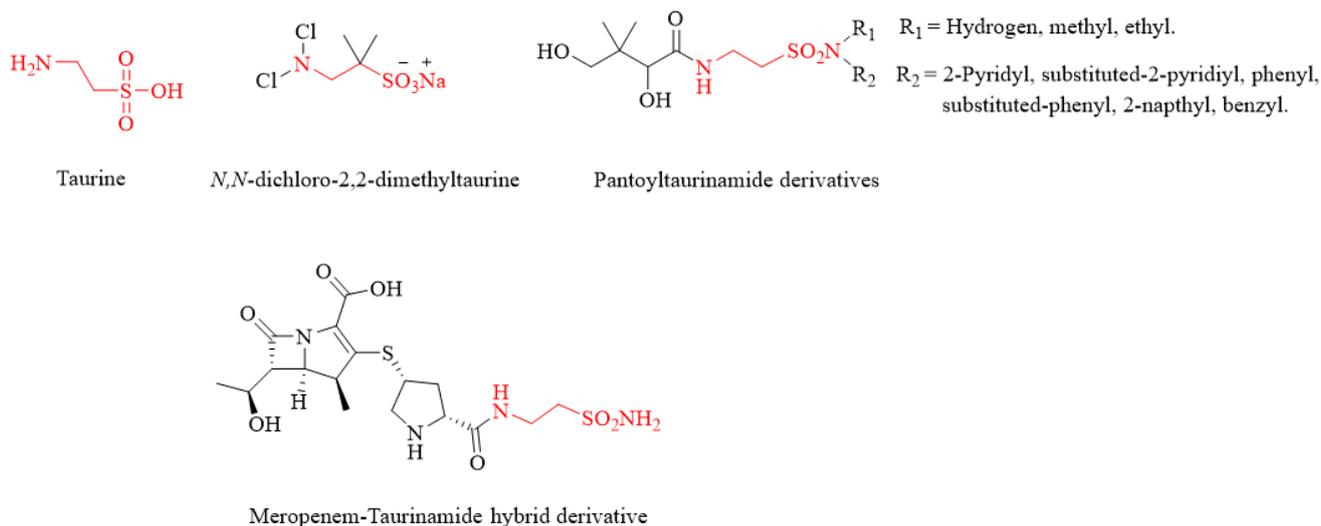
Figure 1. Taurine and its biologically active derivatives.

In our previous study, we added a phthalimido moiety to taurine via its amine while functionalizing it with either hydrogen, a substituted aniline, or morpholine from its sulfonic acid group to achieve primary, secondary, and tertiary sulfonamides, respectively (Figure 2). Synthesized molecules were evaluated for their antimicrobial and antifungal features. Interestingly, among the tested compounds, two compounds having methyl and methoxy moieties on a phenyl ring displayed fairly good activity equal to gentamicin with a minimum inhibitory concentration (MIC) of 4 µg/mL [13]. This result prompted us to continue our research on taurine derivatives to investigate the key structural requirements for obtaining effective antimicrobial agents. For improving the biological activity of a known compound, ring opening is the most well-known strategy that has been used from the beginning of drug discovery [14]. This method is believed to change the flexibility, binding energy, membrane penetration, and absorption of the previously investigated scaffold, thus providing additional contacts with the proposed biological targets. Pursuing this strategy herein, we decided to investigate the amide derivatives of taurinamide as open analogs of phthalamide. Pursuing this strategy herein, we decided to investigate the amide derivatives of taurinamide as open analogs of phthalamide (Figure 3). For this purpose, we functionalized the sulfonic acid part of taurine as primary, secondary (with aniline and 4-methoxyaniline substitution), or tertiary sulfonamides (with morpholine substitution) and coupled the amine group with substituted benzoic acids to obtain amide derivatives. Compounds **1–4** and **6–17** were evaluated for their cytotoxic activities and presented in our previous study, whereas we report **5** and **18** here for the first time. None of the compounds have been previously inspected for their antimicrobial activity [15].

A=CH₃   MIC= 4 µg/mL
A=OCH₃   MIC= 4 µg/mL
A= H   MIC=128 µg/mL
A=SO₂NH₂   MIC=256 µg/mL

MIC=256 µg/mL

MIC=1024 µg/mL
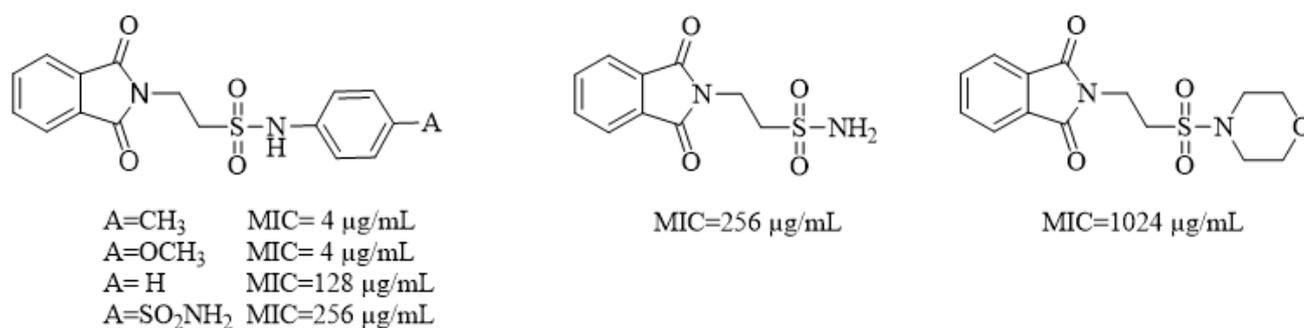
Figure 2. The general structure and antimicrobial activities of previously discovered taurine derivatives.
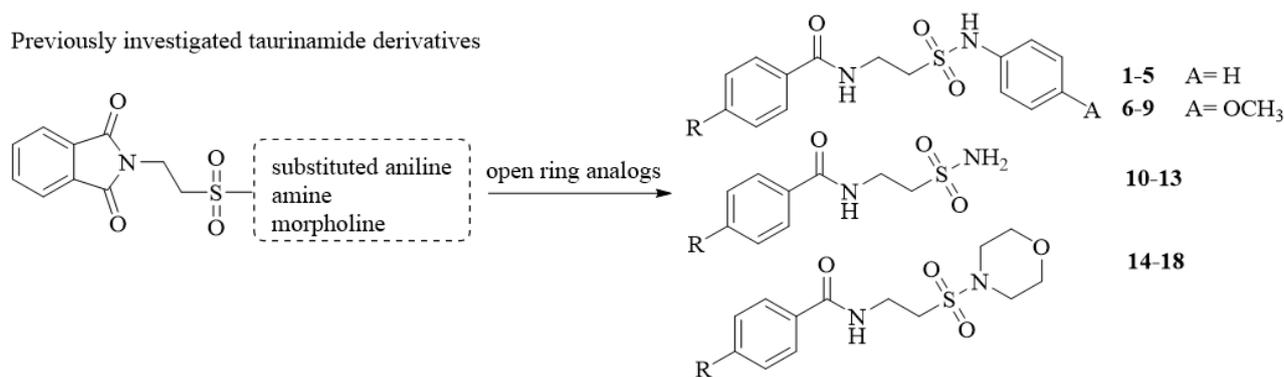
Figure 3. The drug design strategy.

2. Materials and Methods

2.1. Chemistry

Sigma-Aldrich and Interlab (Germany) were the suppliers of the anhydrous solvents and all reagents that were used in our studies. Agilent 600 MHz PremiumCOMPACT NMR spectrometer was used for examining ^{1}H and ^{13}C NMR spectra and DMSO-d_6 was used as a solvent. Parts per million (ppm) unit was used to report chemical shifts and the coupling constants (J) were stated in Hertz (Hz). Splitting patterns were assigned as; s (singlet); d (doublet); t (triplet); m (multiplet); $br\ s$ (broad singlet). Merck silica gel F-254 plates were utilized for analytical thin-layer chromatography (TLC). Flash chromatography purifications were implemented by using Merck silica gel 60 (230–400 mesh ASTM) as the stationary phase. Stuart$^{®}$ (SMP30) melting point apparatus was used to detect melting points of the compounds in open capillary tubes whereas the values were uncorrected. Elemental analyses (C, H, N, and S) were functioned with a Leco TruSpec CHNS Micro analyzer (Leco Corporation, St. Joseph, MI, USA) and outcomes were within ± 0.4% of calculated values.
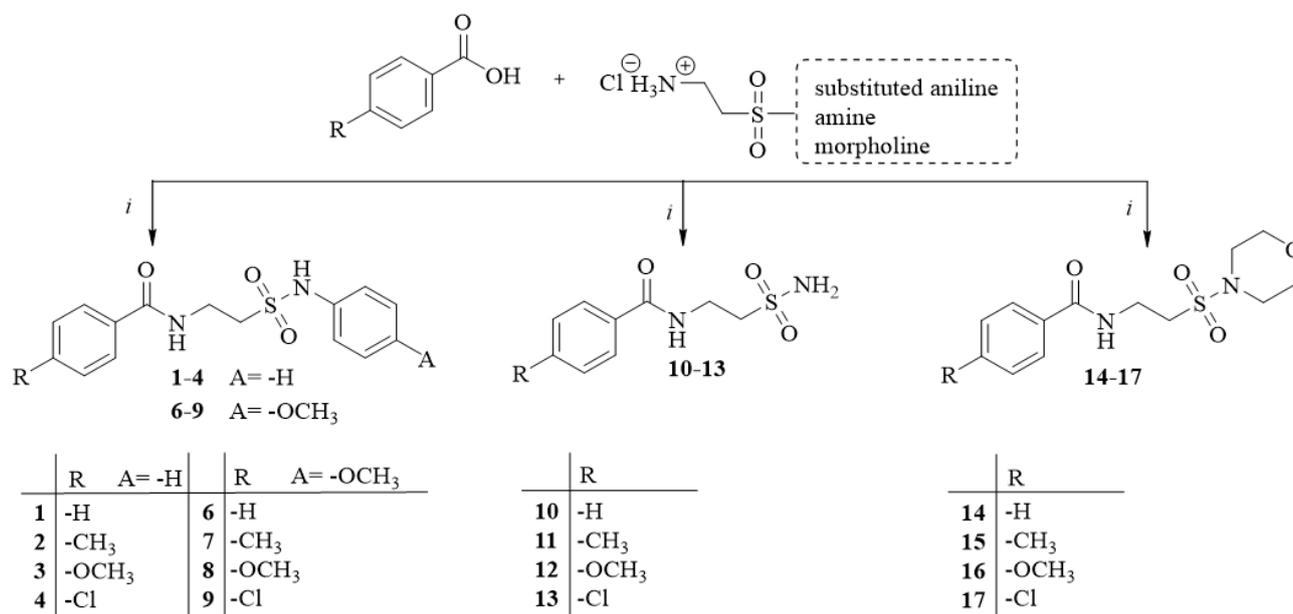
Figure 4. Synthesis of compounds 1-4, 6-17 [15].
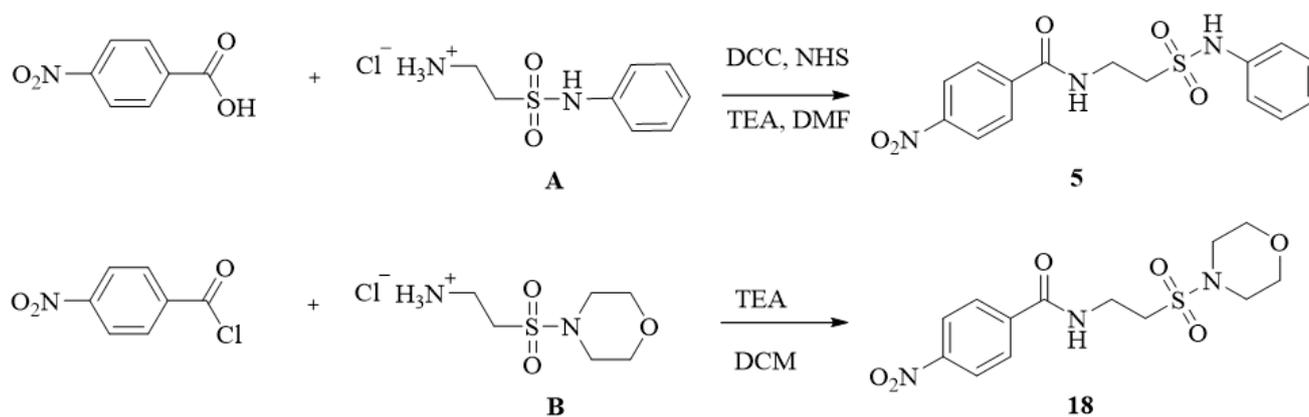
Figure 5. Synthesis of compounds **5** and **18**.

2.2. Synthesis of the Final Compounds 5 and 18

2.2.1. Synthesis of 4 – nitro – *N* - (2 - (*N* – phenylsulfamoyl) ethyl) benzamide (5).

2-(*N*-phenylsulfamoyl)ethanamine hydrochloride salt (**A**) was synthesized according to procedure that was described before [13, 15]. 4-Nitrobenzoic acid (1 mmol), *N,N′*-dicyclohexylcarbodiimide (DCC, 1.1 mmol) and *N*-hydroxysuccinimide (NHS, 1 mmol) were dissolved in dimethylformamide (DMF) and stirred for half an hour. 2-(*N*-phenylsulfamoyl)ethanamine hydrochloride salt (**A**, 1 mmol) and trimethylamine (NEt$_3$, 2 mmol) was added to this reaction mixture and stirred at room temperature. The reaction was pursued with TLC and the solvent was evaporated after the starting compounds consumed. The resulted solid was subjected to extraction by using ethyl acetate (EtOAc), dilute hydrochloric acid (dil. HCl) and dilute sodium bicarbonate (dil. NaHCO$_3$) solution. The ethyl acetate phase was evaporated, and the residue exposed to flash column chromatography (EtOAc: Hxn 2:1). The related fractions were collected and evaporated to give the final compound **5**.

Yellow solid. Yield 25%. Mp: 173.2 °C; ^{1}H NMR (400 MHz, DMSO-d_6) δ: 3.43-3.39 (m, 2H, CH$_3$), 3.73-3.68 (m, 2H, CH$_2$), 7.16-7.12 (m, 1H, CH$_2$), 7.27-7.25 (m, 2H, Ar-H), 7.37-7.33 (m, 2H, Ar-H), 8.04 (d, *J* 8.8 Hz, 2H, Ar-H), 8.34 (d, *J* 8.8 Hz, 2H, Ar-H), 8.95-8.93 (m, 1H, NH), 9.89 (br s, 1H). ^{13}C NMR (100 MHz, DMSO-d_6) δ: 35.3 (Aliph-C), 50.3 (Aliph-C), 120.7 (2 × Ar-C), 124.4 (2 × Ar-C), 124.9 (Ar-C), 129.5 (2 × Ar-C), 130.2 (2 × Ar-C), 138.8 (Ar-C), 140.4 (Ar-C), 150.0 (Ar-C), 165.5 (C=O). IR υ$_{maks}$ (cm^{-1}): 3381, 3108 (N-H stretching), 1654 (amide I band), 1548 (amide II band), 1326 (SO$_2$ asymmetric stretching), 1135 (SO$_2$ symmetric stretching). Elemental analysis calculated (%) for C$_{15}$H$_{15}$N$_3$O$_5$S: C, 51.57; H, 4.33; N, 12.03; S, 9.18. Found: C, 51.69; H, 4.31; N, 12.01; S, 9.52.

2.2.2. Synthesis of *N*-(2-(morpholinosulfonyl) ethyl)-4-nitrobenzamide (18).

2-(morpholinosulfonyl)ethanamin hydrochloride salt (B) was synthesized according to procedure that was described before [13, 15]. 4-Nitrobenzoyl chloride (1 mmol), 2-(morpholinosulfonyl)ethanamin hydrochloride salt (B, 1 mmol) was reacted with 4-nitrobenzoyl chloride by using NEt$_3$ (2 mmol) as a base in dichloromethane (DCM) solution at room temperature. The reaction was followed with TLC and the solvent was removed *in vacuo* after the starting compounds consumed. The mixture put through to flash column chromatography by using EtOAc: Hxn (2:1) solvent system and the pertinent fractions were collected and evaporated to obtain the final compound 18 as a yellow solid that was crystallized from isopropanol.

Yellow solid. Yield 20%. Mp: 199.5 °C; ^{1}H NMR (400 MHz, DMSO-d_6) δ: 3.23-3.20 (m, 4H, CH$_2$), 3.40-3.39 (m, 2H, CH$_2$), 3.74-3.67 (m, 6H, CH$_2$), 8.10 (d, *J* 8.6 Hz, 2H, Ar-H), 8.37 (d, *J* 8.5 Hz, 2H, Ar-H), 9.07-9.04 (m, 1H, NH). ^{13}C NMR (100 MHz, DMSO-d_6) δ: 34.9 (Aliph-C), 46.1 (Aliph-C), 47.4, 66.7, 124.5 (2 × Ar-C), 129.5 (2 × Ar-C), 140.5 (Ar-C), 150.0 (Ar-C), 165.61 (C=O). IR υ$_{maks}$ (cm^{-1}): 3399, 3070 (N-H stretching), 1657 (amide I band), 1524 (amide II band), 1320 (SO$_2$ asymmetric stretching), 1148 (SO$_2$ symmetric stretching). Elemental analysis calculated (%) for C$_{13}$H$_{17}$N$_3$O$_6$S: C, 45.48; H, 4.99; N, 12.24; S, 9.34. Found: C, 45.51; H, 4.79; N, 12.09; S, 9.43.

2.3. Antimicrobial activity

2.3.1. Determination of minimum inhibitory concentration (MIC)

Staphylococcus aureus (ATCC 29213), Enterococcus faecalis (ATCC 29212), Escherichia coli (ATCC 25922), Pseudomonas aeruginosa (ATCC 27853),

Candida albicans (ATCC 90028) and Candida parapsilosis (ATCC 22019) were used in this experiments. All bacteria and yeast strains were stored in Brain-Heart Infusion Broth (Merck, Germany) with 10% glycerol at -80 °C. The antibacterial and antifungal activity of taurinamide derivatives were performed for each strain using broth microdilution method according to the European Committee on Antimicrobial Susceptibility Testing (EUCAST) criteria [16]. Bacteria and yeast strains were grown on Mueller-Hinton Agar (Merck, Germany) and Sabouraud Dextrose Agar (Oxoid, UK) at 37 °C for 24 h, respectively. Bacteria and yeast colonies were taken with sterile swabs and then, these colonies were suspended with sterile physiological saline in glass tubes. The bacterial and fungal cells density in tubes were prepared to 0.5 McFarland by densitometer (Biosan, DEN-1), and the suspensions were diluted at rate of 100-fold and 10-fold for bacteria and yeasts, respectively. Mueller-Hinton broth (Merck, Germany) (50 μl) and RPMI (Sigma, UK) with 2% of glucose (RPMI 2% G) were added into the each well of sterile 96-well microdilution plates for bacteria and yeasts,

respectively. 50 μl from each of the tubes compassing the corresponding concentration of new compounds were included into first wells each column of the microdilution plate. The medium and compound in the first well of each vertical line was mixed using sterile pipette and serial dilutions were accomplished. Diluted bacterial and yeast suspensions were added each well of plate with 50 μL, and the microplates were incubated for 24 h at 37 °C. Growth control for each organisms and sterility control for medium are also tested as positive and negative controls. The final concentrations of the compounds were ranged from 2048 to 64 μg/mL. *Ciprofloxacin* (Santa Cruz, US) and *Fluconazole* (Sigma, UK) were used as reference agents for antibacterial and antifungal activities, respectively. Quality control ranges were also evaluated according to EUCAST. Microdilutions was performed with triplicates for each substances and DMSO, which is used as a solvent, was also tested separately for antibacterial and antifungal activity. After incubation period, MICs were defined the lowest concentration of synthesized compounds, which prohibits macroscopic microbial growth.

Table 1 *In vitro* MICs (μg/mL) of compounds **1–18** against selected bacterial and fungal strains.

1-5 A= H Phenyl derivatives
6-9 A= OCH₃ Methoxy derivatives
10-13 Sulfonamide derivatives
14-18 Morpholine derivatives

Compound		Bacterial strains				Fungal strains	
		Gram (+)		Gram (-)			
	R	*S. a.*	*E. f.*	*E. c.*	*P. a.*	*C. a.*	*C. p.*
1	-H	1024	128	2048	1024	1024	1024
2	-CH₃	2048	2048	1024	1024	2048	2048
3	-OCH₃	1024	2048	512	1024	>2048	>2048
4	-Cl	1024	2048	1024	1024	2048	>2048
5	-NO₂	2048	512	1024	1024	>2048	>2048
6	-H	2048	2048	1024	1024	1024	1024
7	-CH₃	2048	1024	1024	1024	1024	1024
8	-OCH₃	2048	2048	1024	1024	1024	1024
9	-Cl	2048	2048	1024	1024	2048	>2048
10	-H	2048	2048	1024	1024	1024	1024
11	-CH₃	2048	2048	1024	1024	1024	1024
12	-OCH₃	2048	2048	1024	1024	1024	1024
13	-Cl	2048	2048	1024	1024	1024	1024
14	-H	2048	2048	204 8	1024	1024	1024
15	-CH₃	2048	256	1024	1024	>2048	>2048
16	-OCH₃	1024	2048	>2048	>2048	>2048	>2048
17	-Cl	>2048	1024	2048	2048	>2048	>2048
18	-NO₂	1024	64	1024	1024	>2048	>2048
Ciprofloxacin		0.25	1	0.008	0.5	nt	nt
Fluconazole		nt	nt	nt	nt	32	2

S.a: Staphylococcus aureus ATCC 29213, *E. f.: Enterococcus faecalis* ATCC 29212, *E.c.: Escherichia coli* ATCC 25922, *P.a.: Pseudomonas aeruginosa* ATCC 27853, *C. a.: Candida albicans* ATCC 90028, *C. p.: Candida parapsilosis* ATCC 22019.
nt: not tested.

3. Results and Discussion

3.1. Chemistry

The final compounds 1–4 and 6–22 were obtained according to the procedure described previously (Figure 4) [13, 17, 18]. Compounds 5 and 18 reported here were synthesized by using different reaction mediums and are reported here for the first time (Figure 5). The starting compounds 2-(*N*-phenylsulfamoyl)ethanamine hydrochloride salt (A) and 2-(morpholino sulfonyl)ethanamine hydrochloride salt (B) were synthesized by following the previously described method [13]. 4-Nitro-*N*-(2-(*N*-phenylsulfamoyl)ethyl)benzamide (5) was obtained by a coupling reaction of A with 4-nitrobenzoic acid in the presence of DCC, NEt₃, and NHS in DMF solution. The treatment of 2-(morpholinosulfonyl)ethanamine hydrochloride salt (B) with 4-nitrobenzoyl chloride and NEt₃ in DCM solution yielded with *N*-(2-(morpholinosulfonyl)ethyl)-4-nitrobenzamide (18) as a raw product. This product was purified by utilizing a column chromatography method and required crystallization from an appropriate solvent. Finally, the intended molecules were achieved in 20–25% yields as yellow solids. The results of the ^{1}H and ^{13}C NMR, IR, and elemental analysis were coherent with the intended structures (*cf.* experimental section).

3.2. Antimicrobial activity

Final compounds were tested for their *in vitro* antibacterial and antifungal activities against two G(+) bacteria, *Staphylococcus aureus* and *Enterococcus faecalis;* two G(−) bacteria, *Escherichia coli* and *Pseudomonas aeruginosa*; and two fungal strains, *Candida albicans* and *C. parapsilosis* by employing broth microdilution method, with *Ciprofloxacin* and *Fluconazole* used as as reference agents for antibacterial and antifungal activities. The data in Table 1 were analyzed to evaluate the effects of substitutions on the designed skeleton.

Considering G(+) *S. aureus*; the antimicrobial activities of compounds 1, 3, and 4 bearing phenyl and 16, and 18 comprising morpholine group on the sulfonamide unit of the molecule were weak but 2-fold better than those of the other compounds.

E. faecalis was found to be susceptible to phenyl derivative 1 with a MIC of 128 µg/mL. Introduction of an electron withdrawing nitro group (compound 5) to 1 decreased the activity 4-fold (MIC=512 µg/mL), whereas other substitutions as in compounds 2, 3, and 4 diminished the activity (MIC=2048 µg/mL). The methoxy derivative 12 demonstrated a 2-fold more potent activity (MIC=1024 µg/mL) relative to that of its congeners 11, 13, and 14. Considering morpholine derivatives 14–18; the best antibacterial activity was observed with compound 18 bearing an electron-withdrawing nitro substitution with a MIC of 64 µg/mL against *E. faecalis*. Replacement of nitro in 18 with an electron-donating methyl 15 and chloro group 17 decreased the activity 2- and 4-fold (MIC=256 and 1024 µg/mL), respectively. On the other hand, compounds 14 and 16 demonstrated a weak activity against *E. faecalis* (MIC=2048 µg/mL).

Considering G(−) *E. coli* bacteria, among the phenyl derivatives, compound 3 having methoxy substitution was found to be the most potent analog, with a MIC of 512 µg/mL. Compounds 2, 4 and 5 were equipotent inhibitors with a MIC of 1024 µg/mL, whereas compound 1 displayed a poorer activity profile relative to that of the other phenyl derivatives 1–5. On the other hand 1–5 exhibited the same MICs of 1024 µg/mL against G(−) *P. aerıgonasa* bacteria. The rest of the molecules 6–13, 15, and 18 displayed equipotent activity with MICs of 1024 µg/mL against both of the G(−) bacteria.

Considering the fungal strains *C. albicans* and *C. parapsilosis*, among the phenyl derivatives (1–5), 1 was found to have the best activity, with a MIC of 1024 µg/mL. Introduction of a chloro or methoxy group to 1 decreased the activity 2-fold against *C. albicans*, whereas neither of the fungal strains susceptible to the other phenyl analogs. Among the methoxy derivatives 11–14, nonsubstituted derivative 11 and electron-donating methyl and methoxy-substituted derivatives (12 and 13, respectively) exhibited the same activity profiles, with MICs of 1024 µg/mL. The activity was found to be diminished with the introduction of a chloro group, as in 14. Interestingly, all of the primary sulfonamide derivatives 15–18 exhibited the same activity profile against fungal strains, with MICs of 1024 µg/mL. The morpholine derivative 19 exhibited antifungal activity, with a MIC of 1024 µg/mL, whereas introduction of electron-withdrawing and -donating groups to 19 diminished the activity against both of the fungal strains. It is interesting to note that fungal strains were found to gain greater susceptibility to all of the nonsubstituted final compounds 1, 6, 10, and 14 than their previously investigated phthalimide derivatives [19]. However, none of the compounds exhibited better activity than the reference drugs *Ciprofloxacin* and *Flucanozole*.

4. Conclusion

A series of taurinamide derivatives 1-18 were assessed for their *in vitro* antimicrobial activity. Interestingly, compound 3 was distinguished from other compounds due to its better activity against G(–) *E. coli* bacteria, with a MIC of 512 μg/mL. On the other hand, *E. faecalis* was found to be more susceptible than the other pathogens to the tested compounds. In recent years, *Enterococcus* has emerged as a serious nosocomial pathogen having intrinsic antibiotic resistance [20]. For this reason, *Enterococcus* has become the target of antimicrobial drug development studies. In our antimicrobial screening test, the best activity was observed for nitro-substituted morpholine derivative 18, with a MIC of 64 μg/mL against *E. faecalis*. The same bacteria were also moderately inhibited by nonsubstituted phenyl derivative 1 and methyl-substituted morpholine derivative 15, with MICs of 128 and 256 μg/mL, respectively. However, none of the compounds exhibited low MICs against the tested bacterial strains, as observed with previously investigated phthalamide derivatives [13]. On the other hand, it is interesting to note that; fungal strains were found to gain increased susceptibility to all of the nonsubstituted final compounds 1, 6, 10, and 14 compared to their phthalimide derivatives which were previously reported (Figure 2) [13]. These results seem to be uncorrelated with the lipophilicity of the drugs. As a result, expanding the substitution patterns of the derivatives or trying different functionalization strategies would provide more insights to design effective antimicrobial agents.

Acknowledgment

Conflicts of interest

The authors have declared no conflict of interest.

References

[1] Grygorenko O. O., Biitseva A. V., Zhersh S., Amino Sulfonic Acids, Peptidosulfonamides and Other Related Compounds, *Tetrahedron*, 74(13) (2018) 1355–1421.

[2] Chung M., Malatesta P., Bosquesi P., Yamasaki P., Santos J. L. dos, Vizioli E., Advances in Drug Design Based on the Amino Acid Approach: Taurine Analogues for the Treatment of CNS Diseases, *Pharmaceuticals*, 5(10) (2012) 1128–1146.

[3] Gupta R. C., Taurine Analogues and Taurine Transport: Therapeutic Advantages, in: Oja, S.S., Saransaari, P., (Eds.), Taurine 6. Springer US, New York, NY (2006) 449–467.

[4] Ripps H., Shen W., Review: Taurine: A 'Very Essential' Amino Acid, *Mol. Vis.*, 18 (November) (2012) 2673–2686.

[5] Chen K., Zhang Q., Wang J., Liu F., Mi M., Xu H., Chen F., Zeng K., Taurine Protects Transformed Rat Retinal Ganglion Cells from Hypoxia-Induced Apoptosis by Preventing Mitochondrial Dysfunction, *Brain Res.*, 1279 (2009) 131–138.

[6] Vanitha M. K., Baskaran K., Periyasamy K., Saravanan D., Ilakkia A., Selvaraj S., Venkateswari R., Mani B. R., Anandakumar P., Sakthisekaran D., A Review on the Biomedical Importance of Taurine, *Int. J. Pharma Res. Heal. Sci.*, 3(3) (2015) 680–686.

[7] Gottardi W., Nagl M., N-Chlorotaurine, a Natural Antiseptic with Outstanding Tolerability, *J. Antimicrob. Chemother.*, 65(3) (2010) 399–409.

[8] Nagl M., Hess M. W., Pfaller K., Hengster P., Gottardi W., Bactericidal Activity of MicromolarN-Chlorotaurine: Evidence for Its Antimicrobial Function in the Human Defense System, *Antimicrob. Agents Chemother.*, 44(9) (2000) 2507–2513.

[9] Gottardi W., Debabov D., Nagl M., N-Chloramines, A Promising Class of Well-Tolerated Topical Anti-Infectives, *Antimicrob. Agents Chemother.*, 57(3) (2013) 1107–1114.

[10] Jekle A., Yoon J., Zuck M., Najafi R., Wang L., Shiau T., Francavilla C., Rani S. A., Eitzinger C., Nagl M., Anderson M., Debabov D., NVC-422 Inactivates Staphylococcus Aureus Toxins, *Antimicrob. Agents Chemother.*, 57(2) (2013) 924–929.

[11] Winterbottom R., Clapp J. W., Miller W. H., English J. P., Roblin R. O., Studies in Chemotherapy. XV. Amides of Pantoyltaurine 1,. *J. Am. Chem. Soc.*, 69(6) (1947) 1393–1401.

[12] de Kraker M. E. A., Stewardson A. J., Harbarth S., Will 10 Million People Die a Year Due to Antimicrobial Resistance by 2050?, *PLOS Med.*, 13(11) (2016) e1002184.

[13] Akgül Ö., Öztürk İ., Aygül A., Ermertcan Ş., Synthesis and Antimicrobial Activity of Some Taurinamide Derivatives, *Marmara Pharm. J.*, 21(2) (2017) 361–361.

[14] Sun H., Tawa G., Wallqvist A., Scaffold-Hopping Provides Both a Conceptual and Practical Route for Generating New Lead Series and Chemistries with Improved Efficacy and Pharmacokinetic Properties Based on Known Drugs and Drug-Target Interactions Classification of Scaffold-Hopping Approaches, *Drug Discov. Today*, 17(7-8) (2012) 310-324.

[15] Akgül Ö., Erdoğan M. A., Birim D., Kayabaşı Ç., Gündüz C., Armağan G., Design, Synthesis, Cytotoxic Activity, and Apoptosis Inducing Effects of 4- and N-Substituted Benzoyltaurinamide Derivatives, *Turkısh J. Chem.*, 44(6) (2020) 1674–1693.

[16] European Committee on Antimicrobial Susceptibility Testing, Routine and Extended Internal Quality Control for MIC Determination and Disk Diffusion as Recommended by EUCAST, *Eucast*, Version 10 (2020) 1–20.

[17] Akgül Ö., Kilic F. S., Erol K., Pabuccuoglu V., Synthesis and Anticonvulsant Activity of Some N-Phenyl-2-Phtalimidoethanesulfonamide Derivatives, *Arch. Pharm. (Weinheim).*, 340 (12) (2007) 656–660.

[18] Akgül Ö., Angeli A., Vullo D., Carta F., Supuran C. T., Unconventional Amino Acids in Medicinal Chemistry: First Report on Taurine Merged within Carbonic Anhydrase Inhibitors, *Bioorg. Chem.*, 103 (2020) 104236.

[19] Akgül Ö., Ateş, Ayşegül, Ermertcan Ş., Antimicrobial Activity Evaluation of Newly Synthesized N,N-Disubstituted Taurinamidobenzenesulfonamide Derivatives, *J. Turkish Chem. Soc. Sect. A Chem.*, 8(1) (2021) 323–330.

[20] López-Rojas P., Janeczko M., Kubiński K., Amesty Á., Masłyk M., Estévez-Braun A., Synthesis and Antimicrobial Activity of 4-Substituted 1,2,3-Triazole-Coumarin Derivatives, *Molecules*, 23(1) (2018) 199.

Investigation of the effect of paracetamol against glutamate-induced cytotoxicity in C6 glia cells

*Murat DOĞAN [1], * Kenan YILDIZHAN [2]*

[1] *Sivas Cumhuriyet University, Faculty of Pharmacy, Department of Pharmaceutical Biotechnology, Sivas / TURKEY*
[2] *Van Yüzüncü Yıl University, Faculty of Medicine, Department of Biophysics, Van / TURKEY*

Abstract

Paracetamol is an active metabolite with analgesic and antipyretic properties of phenacetin, which is sold without a prescription in our country and in many countries. However, the effect of paracetamol on oxidative stress due to glutamate-induced cytotoxicity remains unclear. This study aims to investigate the effect of an appropriate dose of paracetamol on nitric oxide and increased oxidative stress as a result of glutamate-induced cytotoxicity in C6 cells. The cells were divided into 4 groups as Control group, Glutamate group, Paracetamol group, and Paracetamol+Glutamate group. Cell viability rate between groups was measured by XTT assay. Oxidative stress and antioxidant levels were measured with TOS and TAS elisa kits. Paracetamol at all concentrations significantly increased cell viability in C6 cells (p < 0.001). Paracetamol also increased TAS levels (p < 0.01) while significantly decreased TOS levels (p < 0.001). In addition, paracetamol was observed to decrease TNF-α and NO levels (p < 0.001). In conclusion, paracetamol has protective feature on glutamate-induced cytotoxicity in C6 glial cells by suppressing oxidative stress. The results of this study show that when the appropriate dose of paracetamol is used, it can be a crucial promoter agent in glutamate toxicity-induced neurodegeneration.

1. Introduction

Glutamate, a proteinogenic amino acid, is a crucial neurotransmitter for excitatory signals in the mammalian central nervous system (CSN). However, the CSN also has many functional tasks with memory, cognition, and learning. Glutamate has an important role in the development of the CSN, containing migration, synapse induction, and differentiation [1]. However, intracellular glutamate concentration is in the millimolar (mM) interval, and excess glutamate is released out of the cell. Although glutamate is a necessary neurotransmitter for the continuation of the functions in the CNS, high concentrations of glutamate in the CNS cause neurodegeneration [2]. There can be many factors for neurodegeneration. One of them is excessive glutamate release. The result of excessive glutamate accumulating in the environment is the prolonged activation of glutamate receptors, as well as intracellular calcium overload, protease activation, mitochondrial dysfunction, increased ROS formation in response to an increase in intracellular calcium concentration, and neurodegeneration is observed in

the CNS [3, 4]. In studies on glutamate toxicity, it has been associated with many neurodegenerative diseases and has been indicated to have a significant role in the damage mechanism [5, 6].

Glia cells are essential for providing a healthy environment for neurons in the CNS. In addition, excessive glia cell activation; it can cause many pathological conditions in the CNS such as ischemic stroke, Alzheimer's and Parkinson's Disease, Multiple Sclerosis. Oxidative stress (OS) is the most striking common feature in the formation of these damages [7]. Recent studies have shown that OS has significant actions on neuronal damage in various neurodegenerative diseases [8, 9]. It has been stated that the result of excessive extracellular glutamate level causes the depletion of the amount of intracellular glutathione (GSH), thus reducing the antioxidant level and causing the oxidant/antioxidant balance to deteriorate. It has been emphasized that this causes neuronal damage in the CNS through various mechanisms [10]. In a study conducted to understand the effect pathway of glutamate toxicity in C6 cells, which we used in our study, it was emphasized that the

cells went to apoptosis due to the decrease in intracellular antioxidant level after glutamate incubation and the increase in OS [11]. Again, in a different in vitro study using C6 cells, apoptotic cell death was observed in these cells due to the increase in OS as a result of glutamate excitotoxicity [12]. Paracetamol is an active metabolite of phenacetin, which can be sold over-the-counter in our country and many other countries, with analgesic and antipyretic properties [13]. Paracetamol is a centrally acting drug that selectively inhibits nervous system cyclooxygenase (COX) [14], which inhibits prostaglandin synthesis. Other central mechanisms based on spinal serotonergic pathways may also be involved in the action mechanism of paracetamol. It is possible that the mechanism of action of paracetamol is using central mechanisms other than inhibition of prostaglandin synthesis. Animal studies have shown that the antinociceptive efficacy of paracetamol is reduced when serotoninergic pathways are damaged, depleted or blocked [15, 16]. Considering that increased glutamate-dependent cytotoxicity in the CNS causes neuronal damage, it will be important to develop a protective therapeutic approach against glutamate-induced excitotoxicity of neuronal cells. Paracetamol is one of the most widely used over-the-counter drugs in the world. These recently discovered effects have been significantly detected in vitro. It is thought that important therapeutic effects will be seen with the use of this drug in appropriate doses with new studies to be done [16, 17]. In this study, we investigated the effect of paracetamol against the increase in oxidative stress in the cytotoxicity model we created in glutamate-induced C6 cells. The main hypothesis of this study is that paracetamol reduces glutamate toxicity and oxidative stress on C6 cells. In this way, it will be shown that paracetamol has a protective feature on glutamate-induced cytotoxicity in C6 glial cells by suppressing oxidative stress.

2. Materials and Methods

2.1. Cell culture

Rat glioma cell (C6) line was used in the study because it is suitable for glutamate-dependent cytotoxicity [18]. C6 (CCL-107TM) cell line was obtained from the American Type Culture Collection (ATCC®, Manassas, VA, USA). The growth medium consisted of DMEM supplemented with FBS (10 %) and penicillin/streptomycin (1 %). C6 cells were cultured in 5 % CO_2 at 37 ºC. Paracetamol and glutamate were dissolved in isotonic saline and prepared freshly on the days of the experiment. Control group: no treatment was applied, Glutamate group: 10 mM glutamate was added and incubated for 24 hours, Paracetamol group: Different doses of paracetamol (5, 10, 20 and 40 µg/mL) were added and incubated for 24 hours, Paracetamol + Glutamate group: 1 hour after adding different doses of paracetamol (5, 10, 20 and 40 µg/mL) with 10 mM glutamate was incubated for 24 hours. In a study, glutamate toxicity group were formed to the single concentration of glutamate (10 mM) used to model the gliotoxicity [18]. Based on the literature, we used glutamate at a concentration (10 mM) in this study.

2.2. Cell viability assay

In order to investigate the protective effect of paracetamol against glutamate cytotoxicity on C6 cells, the cell viability rate was checked, for this purpose, XTT (Abcam, UK) assay was performed. C6 cells were seeded in 96-well plates (10×10^3 cells each well) in 100 µL DMEM. On the base of the litarature 1 hour after adding different doses of paracetamol (5, 10, 20 and 40 µg/mL), 10 mM glutamate was added to each well and incubated for 24 hours [15, 18]. After the 24 hour incubation period was over, 50 µL of the XTT reagent mixture was added to the C6 cells in a 96-well plate and then incubated at 37°C for 4 hours. The absorbance value for the XTT determination was measured at 450 nm using a microplate reader (Multiskan PLUS, Thermo Scientific). All tests were read by repeating three times.

2.3. Preparation of cells homogenates

All groups were transferred to different sterile falcon tubes. These tubes were centrifuged at 2000 rpm for 10 minutes. Tubes were brought into sterile laminar flow, supernatants were removed. The cell pellet remaining at the bottom of the tubes was diluted to 1×10^6/mL by adding PBS (pH: 7.4). The cell structure was lysed via freeze-thaw repetition and the cytoplasmic ingredients were withdrawn. The mixture was centrifuged at 4000 rpm for 10 minutes. The supernatant remaining in the upper part of the tubes was taken with the help of sterile pipettes and collected in various sterile tubes. Total protein levels in the study groups were measured with the Bradford protein assay kit (Merck Millipore).

2.4. Measurement of total antioxidant status (TAS), total oxidant status (TOS), tumor necrosis factor-alpha (TNF-α) and nitric oxide (NO) levels in the C6 cells

Glutamate toxicity induction of TAS, TOS, TNF-α and NO levels in the supernatants of C6 cells was determined by ELISA kits (BT Lab). These analyzes were performed considering the protocols determined by the companies for commercial kits. Samples

incubated at 37 °C for 60 minutes were placed in 96-well plates. Standard and supernatant samples were inserted to the plate and incubated for 60 minutes. After the washing step, staining solutions were added and incubated for 15 minutes. Stop solution was inserted and absorbances were read at 450 nm on an ELISA microplate reader (Thermo Fisher Scientifc).

2.5. Statistical analysis

Study results were indicated as mean ± SEM (standard error of mean). Data analyzes were performed with SPSS Version 22. Data were evaluated using a one-way analysis of variance (ANOVA) and a posthoc Tukey test. $p < 0.05$ was determined statistically significant.

3. Results

3.1. Effect of paracetamol on C6 cell viability

In this study, cell viability was investigated in study groups using different doses to determine the effect of paracetamol against glutamate-toxicity. For this, XTT cell viability kit was used. Cell viability was determined in C6 cells treated with both control and glutamate at different doses (5-40 µg/mL) for paracetamol. C6 cells were initially pre-treated with doses of paracetamol (5, 10, 20 and 40 µg/mL) for 60 minutes and incubated with or without glutamate (10 mM) for the next 24 hours. Pre-incubation of C6 cells with glutamate for 24 hours substantially reduced cell viability compared to untreated cells (control group) ($p<0.001$; Figure 1). However, paracetamol doses tested appeared to increase cell survival in C6 cells compared to C6 cells incubated with glutamate ($p<0.001$; Figure 1)
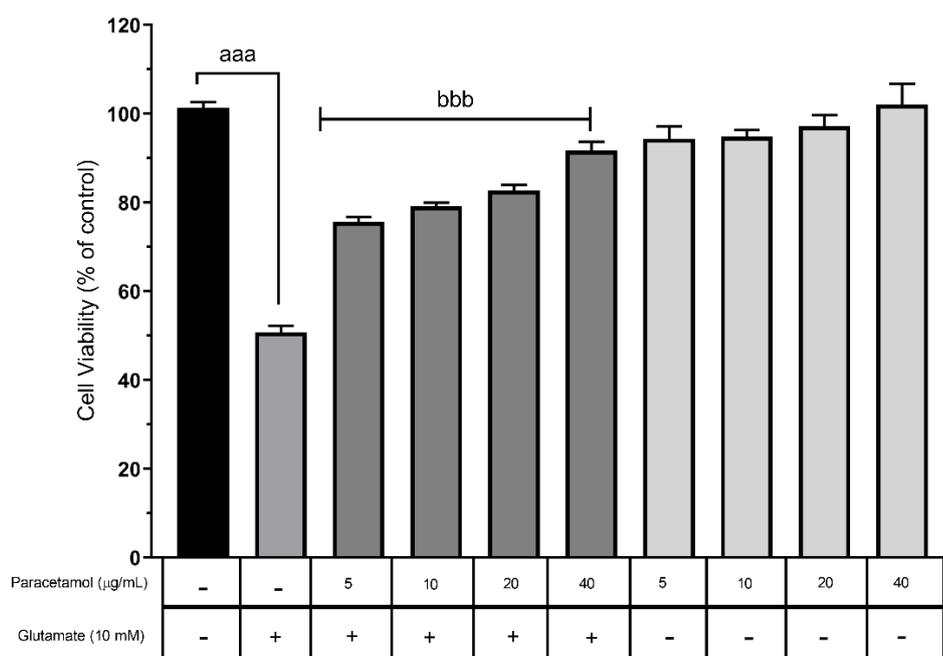
Figure 1. Effect of paracetamol on cell viability after glutamate-induced cytotoxicity in the C6 cells. $^{aaa}p \leq 0.001$ as compared to control-untreated group; $^{bbb}p \leq 0.001$ compared to glutamate-treated group.

3.2. Effect of paracetamol on TAS and TOS levels in C6 cells

The changes in TAS and TOS levels in cells against glutamate cytotoxicity of paracetamol in the groups formed were measured with the Elisa kits. TAS levels were significantly reduced between the groups when the glutamate-treated group was compared to the control and Paracetamol+Glutamate groups ($p<0.001$; Figure 2A). There was no statistically significant difference between the control group and the

Paracetamol+Glutamate group (Figure 2A). When the glutamate-treated group was compared to the control and Paracetamol+Glutamate groups between the groups, it was observed that the TOS level increased considerably ($p<0.001$; Figure 2B). No statistically significant difference was found between the control group and the Paracetamol+Glutamate group (Figure 2B).
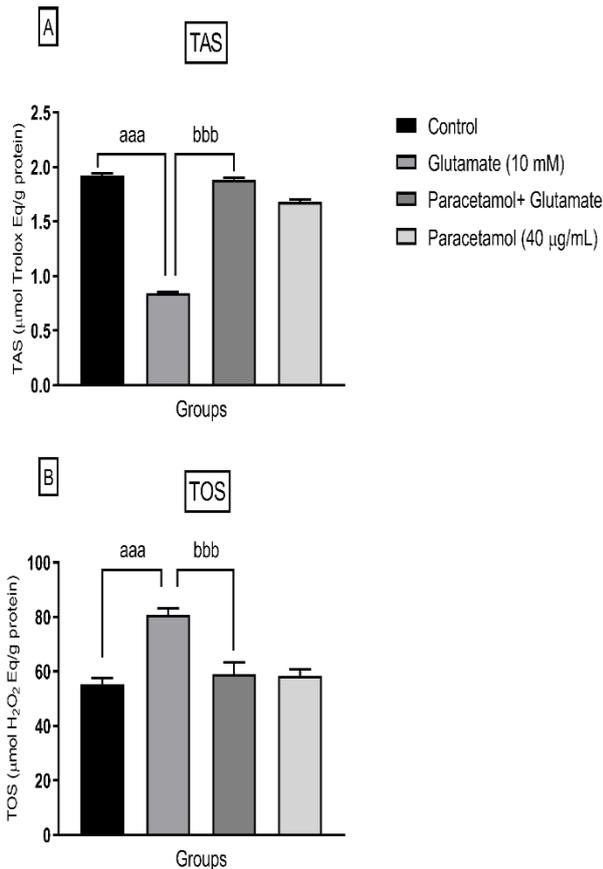
Figure 2. Effect of paracetamol on TAS and TOS levels in C6 cells after glutamate-induced cytotoxicity. aaap≤ 0.001 as compared to control group; bbbp≤ 0.001 compared to glutamate-treated group.

Figure 3. Effect of paracetamol on TNF-α and NO levels in C6 cells after glutamate-induced cytotoxicity. aaap≤ 0.001 as compared to control group; bbbp≤ 0.001 compared to glutamate-treated group.

3.3. Effect of paracetamol on TNF-α and NO levels in C6 cells after glutamate-induced cytotoxicity

ELISA commercial kits were used to investigate the effect of paracetamol on TNF-α and NO levels in glutamate-induced C6 cells. TNF-α levels were substantially increased between the groups when the glutamate-treated group was compared to the control and Paracetamol+Glutamate groups (p<0.001; Figure 3A). There was no statistically considerable difference between the control group and the Paracetamol+Glutamate group (p>0.05; Figure 3A). When the glutamate-treated group was compared to the control and Paracetamol+Glutamate groups between the groups, the NO level increased significantly (p<0.001; Figure 3B). No statistically significant difference was found between the control group and the Paracetamol+Glutamate group (p>0.05; Figure 3B).

4. Discussion

In our study, the effect of pre-treatment of paracetamol using different doses against glutamate-dependent toxicity, which we induced in vitro, was investigated. It was observed that pretreatment with paracetamol increased cell viability and reduced cell death against glutamate-dependent cytotoxicity in C6 cells (Figure 1). Also, Paracetamol pretreatment decreased TOS levels and increased TAS level in C6 cells. In addition, paracetamol pretreatment was also observed to suppress TNF-α and NO levels. Although glutamate is one of the most crucial neurotransmitters for CSN, its depolarization in neurons causes excitotoxicity if its extracellular concentration increases. It has been mentioned in the literature that glutamate in excitotoxicity causes NOS regulation, mitochondria dysfunction, ROS production, ER stress as a result of intracellular Ca^{2+} increase [18, 19]. In the study conducted by Gundogdu et al, a significant decrease in cell viability was detected in primary cortical neuron cells with glutamate toxicity. An increase in cell

viability was detected following the application of parietin to primary cortical neuron cells with toxicity [1]. In a study performed by Das et al melatonin receptor 1 appeared to be involved in the protection of C6 cells from excitotoxic and oxidative damage [12]. Similarily in our study, paracetamol had significant protective effect against glutamate-induced cytotoxicity and oxidative stress. In a study the effect of salmon calcitonin against glutamate-induced cytotoxicity was investigated in C6 cell line. It was observed that there was an increase in NOS and NO levels in cells [18]. In another study examining the protective effect of Thiamine against glutamate-induced cytotoxicity in C6 cell line, an increase was observed in MDA levels after glutamate incubation, while a decrease was observed in SOD and CAT levels. It was observed that the use of thiamine increased cell viability by reducing the oxidant damage caused by the use of glutamate [20]. In a study performed by Park et al, it was determined that glioma cells with glutamate toxicity increased OS, mitochondrial dysfunction and ER stress. It was observed that after the use of alpha-lipoic acid, OS, mitochondrial dysfunction and ER stress were reduced [21]. In support of the studies in the literature, we also observed that the TAS level increased and TOS level decreased in the paracetamol group compared to the glutamate group in C6 cells, in the use of paracetamol against cytotoxicity caused by glutamate in our study (Figure 2).

TNF-α is a very important proinflammatory cytokine in the regulation of inflammation in the CNS. It is actually expressed at low levels by different other cells, including neurons, without a pathological condition. However, in case of any pathological or inflammation, its secretion also increases in other cells, especially in microglia cells, which are local defense cells in the CNS. For this reason, it is accepted as an important indicator in determining a damage mechanism that may occur in the CNS [9, 23]. Marchetti et al, found very important findings about TNF- α expression in their study on glutamate toxicity. As a result, they stated that it may be an inflammation marker [23]. In our study, we observed that the TNF- α level, which increased after glutamate toxicity, decreased after paracetamol treatment. This shows that paracetamol can be an important therapeutic agent for glutamate toxicity (Figure 3A). In a study performed by Lesage et al on primary hippocampal cell culture, they showed that there is an increase in NO with glutamate toxicity. They argued that preventing the increased NO level could be an important approach in reducing the damage [24]. In our study, we observed that the NO level, which increased after glutamate toxicity, decreased after paracetamol treatment (Figure 3B).

Our study results and literature studies showed that paracetamol can reduce cell death in C6 cells. This protective effect of paracetamol appears to occur with the suppression of oxidative stress and NO pathways. Therefore, the use of appropriate dose of paracetamol may be protective in CNS disorder and may be selected as a beneficial therapeutic agent in neurodegenerative disorders.

5. Conclusions

The findings of this study showed that the use of appropriate dose of paracetamol reduced cellular damage against glutamate-dependent cytotoxicity in C6 cells. It is seen that this protective effect of paracetamol is revealed by the suppression of oxidative stress and NO pathways. Therefore, the use of appropriate doses of paracetamol may be protective against glutamate toxicity that may occur in CNS disorders and can be used as a useful therapeutic agent in neuronal damage-related damage. However, further in vitro and in vivo studies are needed to answer questions about the possible mechanisms of action of paracetamol in glutamate toxicity.

Acknowledgement

Conflict of Interest

The authors declare that they have no conflict of interest.

References

[1] Gündoğdu G., Şenol O., Demirkaya A.K., Glutamat Eksitotoksisitesi Oluşturulan Primer Kortikal Nöron Kültürlerinde Parietinin Nöroprotektif Etkisinin İncelenmesi, *Atatürk Üniversitesi Veteriner Bilimleri Dergisi*, 13(2) (2018) 165-173.

[2] Lewerenz J., Maher P., Chronic Glutamate Toxicity in Neurodegenerative Diseases-What Is the Evidence?, *Front Neurosci*., 9 (2015) 469.

[3] Rego A.C., Oliveira C.R., Mitochondrial Dysfunction and Reactive Oxygen Species in Excitotoxicity and Apoptosis: Implications for the Pathogenesis of Neurodegenerative Diseases, *Neurochem Res*., 28(10) (2003) 1563-1574.

[4] Taşkın T., Dogan M., Yilmaz B.N., Senkardes I., Phytochemical screening and evaluation of antioxidant, enzyme inhibition, anti-proliferative and calcium oxalate anti-crystallization activities of Micromeria fruticosa spp. brachycalyx and Rhus coriaria, *Biocatalysis and Agricultural Biotechnology*, 27 (2020) 1-7.

[5] Butterfield D.A. Pocernich C.B., The Glutamatergic System and Alzheimer's Disease: Therapeutic Implications, *CNS Drugs,* 17(9) (2003) 641-652.

[6] Wang J., Wang F., Mai D., Qu S., Molecular Mechanisms of Glutamate Toxicity in Parkinson's Disease, *Front Neurosci.*, 14 (2020) 585584.

[7] Yıldızhan K., Nazıroğlu M., Microglia and Its Role in Neurodegenerative Diseases, *Journal of Cellular Neuroscience and Oxidative Stress,* 11(2) (2019) 861-873.

[8] Penugonda S., Mare S., Goldstein G., Banks W.A., Ercal N., Effects of N-Acetylcysteine Amide (NACA), a Novel Thiol Antioxidant against Glutamate-Induced Cytotoxicity in Neuronal Cell Line Pc12, *Brain Res.*, 1056(2) (2005) 132-138.

[9] Yildizhan K., Naziroglu M., Glutathione Depletion and Parkinsonian Neurotoxin Mpp(+)-Induced Trpm2 Channel Activation Play Central Roles in Oxidative Cytotoxicity and Inflammation in Microglia, *Mol. Neurobiol.*, 57(8) (2020) 3508-3525.

[10] Wen X., Huang A., Hu J., Zhong Z., Liu Y., Li Z., Neuroprotective Effect of Astaxanthin against Glutamate-Induced Cytotoxicity in HT22 Cells: Involvement of the Akt/Gsk-3beta Pathway, *Neuroscience*, 303 (2015) 558-568.

[11] Kato S., Negishi K., Mawatari K., Kuo C.H., A Mechanism for Glutamate Toxicity in the C6 Glioma Cells Involving Inhibition of Cystine Uptake Leading to Glutathione Depletion, *Neuroscience*, 48(4) (1992) 903-914.

[12] Das A., Belagodu A., Reiter R.J., Ray S.K., Banik N.L., Cytoprotective Effects of Melatonin on C6 Astroglial Cells Exposed to Glutamate Excitotoxicity and Oxidative Stress, *J. Pineal Res.*, 45(2) (2008) 117-24.

[13] Clissold S.P., Paracetamol and Phenacetin, *Drugs,* 32 Suppl. 4. (1986) 46-59.

[14] Botting R., Cox-1 and Cox-3 Inhibitors, *Thrombosis research,* 110(5-6) (2003) 269-272.

[15] Graham G.G., Scott K.F., Mechanism of Action of Paracetamol, *American Journal of Therapeutics,* 12(1) (2005) 46-55.

[16] Graham G.G., Davies M.J., Day R.O., Mohamudally A., Scott K.F., The Modern Pharmacology of Paracetamol: Therapeutic Actions, Mechanism of Action, Metabolism, Toxicity and Recent Pharmacological Findings, *Inflammopharmacology,* 21(3) (2013) 201-232.

[17] Toussaint K., Yang X.C., Zielinski M.A., Reigle K.E., Sacavage S.D., Nagar S., Raffa R.B., What Do We (Not) Know About How Paracetamol (Acetaminophen) Works?, *Journal of Clinical Pharmacy and Therapeutics,* 35(6) (2010) 617-638.

[18] Taskiran A.S., Ergul M., The Effect of Salmon Calcitonin against Glutamate-Induced Cytotoxicity in the C6 Cell Line and the Roles the Inflammatory and Nitric Oxide Pathways Play, *Metab Brain Dis.*, 36(7) (2021) 1985-1993.

[19] Kritis A.A., Stamoula E.G., Paniskaki P.A., Vavilis T.D., Researching Glutamate - Induced Cytotoxicity in Different Cell Lines: A Comparative/Collective Analysis/Study, *Front Cell Neurosci.*, 9 (2015) 91.

[20] Ergul M., Taskiran A.S., Thiamine Protects Glioblastoma Cells against Glutamate Toxicity by Suppressing Oxidative/Endoplasmic Reticulum Stress, *Chem. Pharm. Bull. (Tokyo),* 69(9) (2021) 832-839.

[21] Park E., Gim J., Kim D.K., Kim C.S., Chun H.S., Protective Effects of Alpha-Lipoic Acid on Glutamate-Induced Cytotoxicity in C6 Glioma Cells, *Biol. Pharm. Bull.*, 42(1). (2019) 94-102.

[22] Neniskyte U., Vilalta A., Brown G.C., Tumour Necrosis Factor Alpha-Induced Neuronal Loss Is Mediated by Microglial Phagocytosis, *FEBS Lett.*, 588(17) (2014) 2952-2956.

[23] Marchetti L., Tumor Necrosis Factor (Tnf)-Mediated Neuroprotection against Glutamate-Induced Excitotoxicity Is Enhanced by N-Methyl-D-Aspartate Receptor Activation. Essential Role of a Tnf Receptor 2-Mediated Phosphatidylinositol 3-Kinase-Dependent Nf-Kappa B Pathway, *J. Biol. Chem.*, 279(31) (2004) 32869-32881.

[24] Lesage A.S., Peeters L., Leysen J.E., Lubeluzole, a Novel Long-Term Neuroprotectant, Inhibits the Glutamate-Activated Nitric Oxide Synthase Pathway, *Journal of Pharmacology and Experimental Therapeutics,* 279(2) (1996) 759-766.

Synthesis, molecular docking, *in silico* ADME and antimicrobial activity studies of some new benzimidazole-triazole derivatives

Asaf Evrim EVREN [2] (iD), *Ismail ÇELİK* [3, *] (iD), *Ulviye ACAR ÇEVİK* [1] (iD)

[1]Anadolu University, Faculty of Pharmacy, Department of Pharmaceutical Chemistry, Eskisehir/ TURKEY
[2]Bilecik Seyh Edebali University, Vocational School of Health Services, Bilecik/ TURKEY
[3]Erciyes University, Faculty of Pharmacy, Department of Pharmaceutical Chemistry, Kayseri/TURKEY

Abstract

In this study, new benzimidazole-triazole derivatives were synthesized in two steps. First, 4-benzaldehyde derivatives are synthesized by reacting 1,2,4-triazole ring and 4-fluorobenzaldehyde. In the last step, the benzimidazole ring was obtained with *o*-phenylenediamine derivatives under microwave radiation. The structures of synthesized compounds were confirmed by ^{1}H-NMR, ^{13}C-NMR, infrared spectroscopy, mass spectroscopy, and elemental analysis. Antimicrobial activity of synthesized compounds is associated with six different types of bacteria *(Escherichia coli* ATCC 35218, *E.coli* ATCC 25922, *Klebsiella pneumoniae* NCTC 9633, *Pseudomonas aeruginosa* ATCC 27853, *Salmonella typhimurium* ATCC 13311, *Staphylococcus aureus* ATCC 25923), and four different Candida (*C. albican*s ATCC 24433, *C. glabrata* ATCC 90030, *C. krusei* ATCC 6258, *C. parapsilosis* ATCC 22019). Synthesized compounds showed weak antibacterial activity. However, 3a, 3b, and 3c compounds against *C. albicans* of the Candida species were found to show promising activity. Given the effect of substituents on antifungal activity, it is seen that the compounds 3a, 3b, and 3c carry chlorine, methyl, and fluoro substituents on the benzimidazole ring attract attention with higher activities. Molecular docking studies of 3a, 3b, and 3c were performed Schrödinger Glide XP against Candidas' sterol 14-alpha demethylase (CYP51), and estimated ADME calculations were analyzed.

1. Introduction

Antimicrobial resistance (AMR) has become a global problem in recent years. The World Health Organization's Global Antimicrobial Resistance Monitoring System (GLASS) report in 2016-2017 shows that *Escherichia coli*, *Klebsiella pneumoniae*, *Staphylococcus aureus*, *Streptococcus pneumoniae*, and Salmonella species are the most commonly reported resistant bacteria [1]. Due to this increasing antimicrobial resistance, the treatment of microbial diseases has become a challenging process. The conscious use of existing antibiotics and the development of new antimicrobial agents have gained importance against this development of resistance. Therefore, drug development studies have gained a reputation [2].

The benzimidazole core is a vital ring system in medicinal chemistry. This ring system is primarily used to develop compounds belonging to a wide range of therapeutic classes such as antimicrobial, anticancer, antioxidant, antiasthmatic and antiallergic,

antiprotozoal, antidiabetic, anti-inflammatory, antiparasitic [3-12]. The benzimidazole scaffold is an important structure that plays a crucial role in drug discovery due to its similarity to the purine ring, which forms the structure of nucleotide bases, is an important pharmacophore group found in the structure of many biologically active compounds [13,14]. The structure of 1,2,4-triazole is another important ring found in the structure of many drugs such as triazolam, alprazolam, etizolam, rizatriptan, fucozole, and efnaconazole. Fluconazole and itraconazole to first generation triazoles; vorikonazole, posakonazole, isavukonazole, albaconazole and ravukonazole are examples of second-generation triazoles [15,16]. Since the benzimidazole ring is a purine analog and antifungal drugs contain a triazole ring, it was thought that the hybridization of these two rings would create significant antifungal activity.

In the light of this information, ten new benzimidazole-triazole derivatives were synthesized, their antimicrobial activity was evaluated, and molecular

docking against *C. albicans'* sterol 14-alpha demethylase (CYP51) and estimated ADME studies of compounds 3a, 3b, and 3c were performed.

2. Materials and Methods

2.1. Chemistry

Microwave-assisted 4-(1,2,4-triazol-1-yl) benzaldehyde and 4-(1,2,4-triazol-3-yl)thio) benzaldehyde synthesis (Method A):

1*H*-1,2,4-triazole (1 mol) and 3-mercapto-1*H*-1,2,4-triazole (1 mol) and 4-fluoroenzaldehyde (1.1 mol) were enclosed in the vial with the volume of 30 mL, and 10 mL dimethylformamide (DMF) was added and dissolved. K_2CO_3 (1 mol) was added as a catalyst and heated under the reversing cooler (reflux). The reaction mixture was held in the microwave synthesis reactor for 15 minutes under the temperature of 200 °C and the pressure of 10 bar. At the end of the reaction period, the vial content is poured into the ice water, and the product is preceded, washed with plenty of water, dried, and crystallized from ethanol.

Microwave-assisted 2-(4-(1,2,4-triazol-1-yl) phenyl)-1,3-benzimidazole synthesis (Method B):

Into the microwave synthesis reactor vial (30 mL), methyl 4-(1,2,4-triazol-1-yl)benzaldehyde (0.03 mol) and 4-(1,2,4-triazol-3-yl)thio)benzaldehyde (0.03 mol), sodium disulfide (0.03 mol) and DMF (10 mL) were added. The reaction mixture was kept in a microwave synthesis reactor at 240 °C under 10 bar pressure for 5 minutes. At the end of this period, the mixture was removed from the reactor, and 5-chloro or 5-fluoro-1,2-phenylenediamine (0,03 mol) was added. The reaction was subjected to microwave irradiation for another 5 minutes under the same conditions. At the end of the reaction period, the product was precipitated by pouring into ice water, filtered, washed with plenty of water, and crystallized from ethanol.

2-(4-(1H-1,2,4-triazol-1-yl)phenyl)-5-chloro-1-benzimidazole (3a)
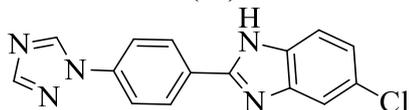
M.p.: 190 °C, yield: 87.5%. IR (ATR) v_{max}(cm⁻¹): 3134.33 (N-H voltage band), 1653.00 – 1500.62 (C=C and C=N voltage bands), 839.03 (1.4-dissected non-resynthetic deformation tape). ¹H-NMR (300 MHz, DMSO-d₆): δ= 7.24 (1H, s, Aromatic CH), 7.56-7.64 (4H, m, Aromatic CH), 8.07-8.18 (3H, m, Aromatic CH), 8.34 (1H, s, Aromatic CH), 13.23 (1H, s, NH). ¹³C-NMR (75 MHz, DMSO-d₆): δ=111.58,

113.23, 118.79, 120.11, 120.70, 122.76, 123.40, 127.82, 128.45, 131.20, 137.80, 144.93, 145.17. Anal Calcd for $C_{15}H_{10}N_5Cl$: C:61.12977; H:3.07789; N:23.76288. Found: C: 61.3534; H:3.0756; N:23.7089. Mass (ES) m/z: 296 [% 100, M+1].

2-(4-(1H-1,2,4-triazol-1-yl)phenyl)-5-methyl-1-benzimidazole (3b)
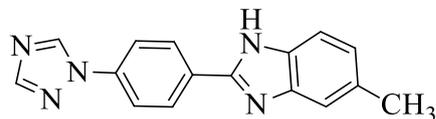
M.p.: 314 °C, yield: 82.6%. IR (ATR) v_{max}(cm⁻¹): 3101.54 (N-H voltage band), 1654.92 – 1438.90 (C=C and C=N voltage bands), 839.03 (1.4-dissected non-flaxformation tape). ¹H-NMR (300 MHz, DMSO-d₆): δ= 2.43 (3H, s, CH₃), 7.68 (2H, d, J=8.49 Hz, Aromatic CH), 7.95 (1H, s, Aromatic CH), 8.03 (2H, d, J=8.76 Hz, Aromatic CH), 8.17 (2H, d, J=8.49 Hz, Aromatic CH), 8.32 (2H, d, J=8.76 Hz, Aromatic CH), 12.87 (1H, s, NH). ¹³C-NMR (75 MHz, DMSO-d₆): δ=21.81, 120.04, 124.16, 127.55, 128.10, 129.40, 130.08, 130.20, 130.66, 131.33, 131.72, 133.69, 137.37, 144.80. Anal Calcd for $C_{16}H_{13}N_5$: C:70,0589; H:4,409; N:25,532. Found: C:69,8994; H:4,403; N:25,5091. Mass (ES) m/z: 276 [% 100, M+1].

2-(4-(1H-1,2,4-triazol-1-yl)phenyl)-5-fluoro-1-benzimidazole (3c)
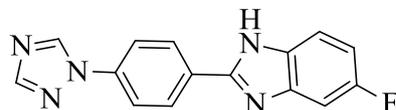
M.p.: 306 °C, yield: 84.4%. IR (ATR) v_{max}(cm⁻¹): 3103.46 (N-H voltage band), 1654.92 – 1440.83 (C=C and C=N voltage bands), 837.11 (1.4-dissected non-flax deformation band). ¹H-NMR (300 MHz, DMSO-d₆): δ= 7.69 (2H, d, J=8.46 Hz, Aromatic CH), 7.95 (1H, s, Aromatic CH), 8.06 (2H, d, J=8.76 Hz, Aromatic CH), 8.17 (2H, d, J=8.46 Hz, Aromatic CH), 8.33 (2H, d, J=8.76 Hz, Aromatic CH), 13.16 (1H, s, NH). ¹³C-NMR (75 MHz, DMSO-d₆): δ=120.09, 127.68, 128.27, 129.46, 129.57, 129.75, 130.29, 131.25, 131.61, 131.72, 134.27, 137.64, 144.88. Anal Calcd for $C_{15}H_{10}N_5F$: C:64.74457; H:3.259896; N:25.16805. Found: C:64.85; H:3.25456; N:25,1745. Mass (ES) m/z: 280 [% 100, M+1].

2-(4-(1H-1,2,4-triazol-1-yl)phenyl)-1-benzimidazol-5-yl phenyl methanone (3d)
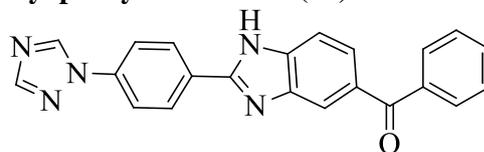
M.p.: 250 °C, yield: is 85%. IR (ATR) v_{max}(cm^{-1}): 3116.97 (N-H voltage band), 1653.00 – 1386.82 (C=C and C=N voltage bands),839.03 (1.4-dissected non-resuming deformation tape). ^{1}H-NMR (300 MHz, DMSO-d$_6$): δ= 7.59-7.63 (2H, m, Aromatic CH), 7.67-7.70 (2H, m, Aromatic CH), 7.90-7.94 (3H, m, Aromatic CH), 8.05-8.07 (2H, m, Aromatic CH), 8.23-8.26 (3H, m, Aromatic CH), 8.40-8.43 (2H, m, Aromatic CH). ^{13}C-NMR (75 MHz, DMSO-d$_6$): δ=114.80, 117.11, 120.06, 124.41, 127.92, 128.53, 129.41, 129.70, 129.92, 131.20, 134.34, 137.66, 144.89, 152.28, 152.61, 158.81, 162.90, 170.38. Anal Calcd for $C_{22}H_{15}N_5O$: C:72.51666; H:3.872507; N:19,21997. Found: C:72.60; H:3.8691; N:19.22366. Mass (ES) m/z: 366 [% 100, M+1].

2-(4-(1H-1,2,4-triazol-1-yl)phenyl) -1-benzimidazole-5-carboxylic acid (3e)
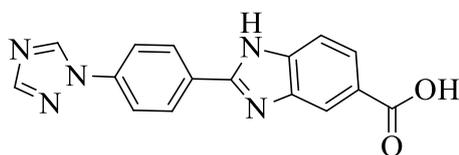
M.p.: 85 °C, yield: 86.7%. IR (ATR) v_{max}(cm^{-1}): 3095.75 (N-H voltage band), 1651.07 – 1500.62 (C=C and C=N voltage bands),831.32 (1.4-dissected non-resuming tape). ^{1}H-NMR (300 MHz, DMSO-d$_6$): δ= 7.76-7.78 (2H, m, Aromatic CH), 7.95 (1H, s, Aromatic CH), 8.08-8.09 (2H, m, Aromatic CH), 8.20-8.23 (2H, m, Aromatic CH), 8.36-8.39 (2H, m, Aromatic CH), 9.56 (1H, s, OH). ^{13}C-NMR (75 MHz, DMSO-d$_6$): δ=120.14, 122.17, 124.42, 125.43, 127.99, 128.63, 129.94, 130.60, 131.15, 131.72, 132.58, 138.51, 144.97, 162.75. Anal Calcd for $C_{16}H_{11}N_5O_2$ C:63.15552; H:3.312382; N:23.01595. Found: C:63,1855; H:3.3252; N:23.0678. Mass (ES) m/z: 306 [% 100, M+1].

2-(4-((1H-1,2,4-triazol-3-yl)thio)phenyl)-5-chloro-1-benzimidazole (3f)
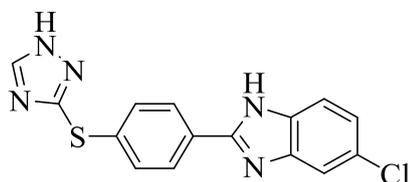
M.p.: 265 °C, yield: 84.3%. IR (ATR) v_{max}(cm^{-1}): 3086.11 (N-H voltage band), 1517.98 – 1454.33 (C=C and C=N voltage bands), 842.89 (1.4-dissected non-flaxformation tape). ^{1}H-NMR (300 MHz, DMSO-d$_6$): δ= 7.05-7.12 (1H, m, Aromatic CH), 7.42-7.61 (2H, m, Aromatic CH), 8.07 (2H, d, J=8.76 Hz, Aromatic CH), 8.30 (1H, s, Aromatic CH), 8.32 (2H, d, J=8.76 Hz, Aromatic CH), 9.42 (1H, s, NH), 13.16

(1H, s, NH). ^{13}C-NMR (75 MHz, DMSO-d$_6$): δ= 104.95, 110.90, 112.26, 112.73, 120.12, 128.28, 129.49, 138.05, 142.98, 153.10, 153.12, 157.77, 160.80. Anal Calcd for $C_{15}H_{10}N_5SCl$: C:55,13152; H:2.775878; N:21.43119. Found: C:55,20321; H:2.77654; N:21.45458. Mass (ES) m/z: 328 [% 100, M+1].

2-(4-((1H-1,2,4-triazol-3-yl)thio)phenyl)-5-methyl-1-benzimidazole (3g)
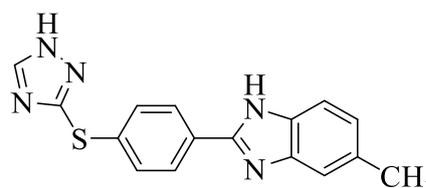
M.p.: 153.7 °C, yield: 84.3%. IR (ATR) v_{max}(cm^{-1}): 3116.97 (N-H voltage band), 1606.0 – 1500.26 (C=C and C=N voltage bands), 840.96 (1.4-dissected non-rectal deformation band). ^{1}H-NMR (300 MHz, DMSO-d$_6$): δ= 2.43 (3H, s, CH$_3$), 7.03-7.06 (1H, m, Aromatic CH), 7.40 (1H, s, Aromatic CH), 7.49 (2H, d, J=8.19 Hz, Aromatic CH), 8.06 (2H, d, J=8.76 Hz, Aromatic CH), 8.32 (2H, d, J=8.76 Hz, Aromatic CH), 9.41 (1H, s, NH). ^{13}C-NMR (75 MHz, DMSO-d$_6$): δ= 21.79, 112.28, 115.94, 120.07, 124.28, 128.11, 128.28, 129.93, 132.06, 137.79, 142.93, 150.33, 152.15, 153.08. Anal Calcd for $C_{16}H_{13}N_5S$: C:62.72633; H:3.947846; N:22.85953. Found: C:62,7212; H:3.9489; N:22.8345. Mass (ES) m/z: 308 [% 100, M+1].

2-(4-((1H-1,2,4-triazol-3-yl)thio)phenyl)-5-fluoro-1-benzimidazole (3h)
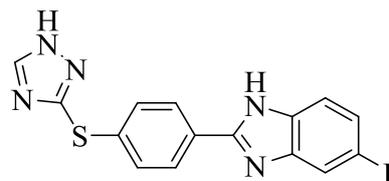
M.p.:. 232.7 °C, yield: 79.4%. IR (ATR) v_{max}(cm^{-1}): 3113.11 (N-H voltage band), 1606.70 – 1508.33 (C=C and C=N voltage bands),839.03 (1.4-dissected non-flaxformation tape). ^{1}H-NMR (300 MHz, DMSO-d$_6$): δ= 7.05-7.12 (1H, m, Aromatic CH), 7.40-7.44 (1H, m, Aromatic CH), 7.59-7.64 (1H, m, Aromatic CH), 8.06 (2H, d, J=8.73 Hz, Aromatic CH), 8.30 (1H, s, Aromatic CH), 8.33 (2H, d, J=8.76 Hz, Aromatic CH), 9.42 (1H, s, NH). ^{13}C-NMR (75 MHz, DMSO-d$_6$): δ=110.79, 111.12, 112.28, 120.12, 121.90, 128.29, 128.54, 129.46, 138.07, 142.99, 153.13, 157.67, 160.79. Anal Calcd for $C_{15}H_{10}N_5SF$: C:58.05477; H:2.923064; N:22.56754. Found: C:58,025; H:2.9236; N:22,556. Mass (ES) m/z: 312 [% 100, M+1].

2-(4-((1*H*-1,2,4-triazol-3-yl)thio)phenyl)-1-benzimidazole-5-carboxylic acid (3i)
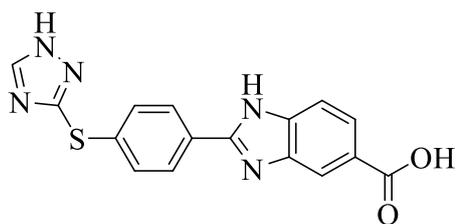
M.p.: 318.8 °C, yield: 78.8%. IR (ATR) v_{max}(cm^{-1}): 3124.68 (N-H voltage band), 2929.87 (C-H voltage band), 1658.7 8 – 1516.05 (C=C and C=N voltage bands),840.96 (1.4-non-plane deformation band that resembles dissectitis). ^{1}H-NMR (300 MHz, DMSO-d$_6$): δ= 7.67 (1H, d, J=8.46 Hz, Aromatic CH), 7.85-7.87 (1H, m, Aromatic CH), 8.08 (2H, d, J=8.73 Hz, Aromatic CH), 8.21 (1H, s, Aromatic CH), 8.30 (1H, s, Aromatic CH), 8.37 (2H, d, J=8.73 Hz, Aromatic CH), 9.43 (1H, s, OH). ^{13}C-NMR (75 MHz, DMSO-d$_6$): δ=112.24, 120.12, 121.93, 124.21, 124.86, 125.24, 128.62, 129.18, 138.32, 143.03, 152.99, 153.14, 162.80, 168.28. Anal Calcd for C$_{16}$H$_{11}$N$_5$SO$_2$: C:57,13472; H:2.996603; N:20.82177. Found: C:57,304; H:2.9998; N:20.8565. Mass (ES) m/z: 338 [% 100, M+1].

(2-(4-((1*H*-1,2,4-triazol-3-yl)thio)phenyl)-1-benzimidazol-5-yl)phenyl)methanone (3j)
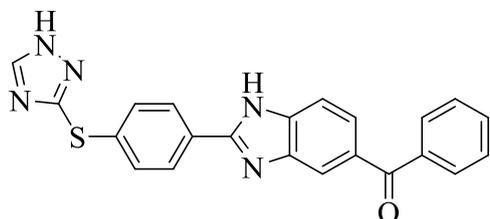
M.p.: 272.6 °C, yield: 82.6%. IR (ATR) v_{max}(cm^{-1}): 3109.25 (N-H voltage band), 1639.49 (C=O voltage band), 1612.49 - 1514.12 (C=C and C=N voltage bands), 839.03 (1.4-non-flax plane deformation band resemsounding to dissectitis). ^{1}H-NMR (300 MHz, DMSO-d$_6$): δ= 7.57-7.58 (2H, m, Aromatic CH), 7.65-7.71 (2H, m, Aromatic CH), 7.75-7.78 (3H, m, Aromatic CH), 7.98 (1H, s, Aromatic CH), 8.07 (2H, d, J=8.79 Hz, Aromatic CH), 8.30 (1H, s, Aromatic CH), 8.37 (2H, d, J=8.76 Hz, Aromatic CH), 9.43 (1H, s, NH). ^{13}C-NMR (75 MHz, DMSO-d$_6$): δ=112.52, 120.14, 120.88, 121.98, 124.85, 128.30, 128.65, 128.89, 129.06, 129.94, 131.63, 132.59, 138.39, 138.50, 143.04, 153.15, 153.36, 196.04. Anal Calcd for C$_{22}$H$_{15}$N$_5$SO: C:66.6514; H:3.5593; N:17.6654. Found: C:66,605; H:3.5569; N:17.6584. Mass (ES) m/z: 398 [% 100, M+1].

2.2. Antimicrobial activity studies

To recreate microorganism strains, the fungi are removed from -85 °C to petri dishes with Sabouraud Dextrose Agar (Sigma Aldrich), the bacteria were planted in petri dishes containing Mueller Hinton Agar (MHA-Sigma Aldrich) and left to incubate for 24 hours at 37 °C. Bacteria were taken from the colonies, transferred to tubes containing Mueller Hinton Broth (MHB), and fungi were transferred to tubes with RPMI and left to incubate for 24 hours at 37 °C. After incubation, turbidity was adjusted according to McFarland no: 0.5 (10^8 CFU/mL) tube.

The compounds to be tested were weighed at 10 mg and transferred to sterile vials, and 1 mL of pure dimethyl sulfoxide (DMSO) was added to them. Compounds were fully dissolved within the DMSO and became a homogeneous mixture.

Microtitration plates (Brand) with 96 "U" type wells were used for the experiment. Prepared compound mixtures were transferred to the wells respectively in the concentration range of 1000 to 1.95 µg/mL with serial dilution of 100 µL with the help of micropipettes. After all, concentrations are transferred to the wells, 100 µL pipettes are made of microorganism cultures. The last column is divided into microorganism control, and the last row is divided into fattening location control. After these procedures, the lids of the microtitration plates were closed and incubated at 37 °C for 24 hours, and at the end of this period, 20 µL of resazurin solution was added to the wells to better observe the presence or absence of growth in the wells. It was then incubated at 37 °C for 3 hours for coloration. At the end of the incubation period, the lowest concentration at which growth was observed, that is, the minimum inhibitory concentration (MIC) was determined as µg/mL. Experiments were repeated in pairs in parallel. Ketoconazole was used as a standard antifungal agent, and chloramphenicol was used as an antibacterial. [12.] Resazurin, which is used as a metabolic indicator in evaluating test results, was tried by Alamar Blue on many cell types 50 years ago, and its effectiveness has been proven. It is more preferred than other indicators to dissolve easily in water, be stable in cell culture, not toxic, and easily pass through cell membranes. Resazurin is a blue-colored paint that does not give fluorescence. It is reduced by living organisms and transformed into a pink-colored resorufin metabolite that gives fluorescence. Thanks to this feature, it offers the possibility to evaluate the control of reproduction in each well in the microtitration petri dishes as a result of activity studies both by observing the color change in the well and by fluorometric reading [13].

2.3. Molecular docking studies

Sterol 14-alpha demethylase (CYP51) (PDB ID: 5TZ1, resolution 2.00 Å) was selected for molecular docking for possible interactions of 3a, 3b, and 3c compounds with *C. albicans* [17]. Molecular docking studies were carried out with Schrödinger Maestro version 12.8. Heteroatoms found except HEM in enzyme structure were removed and prepared with Protein Preparation Wizard. The compounds were drawn with ChemDraw Professional 17.0 and prepared with LigPrep. Based on the cocrystal VT1 of the 5TZ1 structure, grid box was created x: 70.87, y: 66.28, z: 4.42 coordinates, and 20*20*20 Å^3 size by Receptor Grid Generation. Molecular docking analyses were performed with Glide XP [18]. 2D and 3D imaging were performed with Maestro 12.8.

2.4. ADME prediction

Computational prediction of absorption, distribution, metabolism, and excretion (ADME) of compounds 3a, 3b, and 3c, which are the three most active compounds against *C. albicans*, were performed with SwissADME online tools (http://www.swissadme.ch/) [19].

3. Results and Discussion

The structures of 10 original compounds 3a-3j, which were synthesized with microwave-assisted, were elucidated by data on ^{1}H-NMR, IR and mass spectroscopic methods and elemental analysis results. With the microwave synthesis used, reaction times are shortened, efficiency is increased, less resources are used, and it is more environmentally friendly and economical. Spectrum assessments were given under the heading of the relevant spectroscopic method. IR studies of 10 new triazole-derived compounds synthesized within the scope of the project were elucidated with the help of spectroscopic data. When the chemical structures of synthesized compounds are examined, all synthesis compounds have an aromatic ring system. The voltage band bee of the C=C and C=N groups carried by these rings was obtained in the range of 1386.82 – 1654.92 cm$^{-1.}$ Another structure commonly found in all synthesis products is the 1,4-dissected and benzene rings. The specific non-plane deformation bands for this ring were obtained in the range of 831.32 - 842.89 cm$^{-1.}$ Another structure commonly found in all synthesis products is the voltage bands of the N-H group in the range of 3086.11 – 3134.33 cm^{-1}. In the ^{1}H-NMR spectra, the -CH$_3$ group protons of compounds 3b and 3g on 5th position of benzimidazole ring were observed at 2.43 ppm as a singlet. A broad singlet due to NH proton of the benzimidazole ring was recorded around at 13 ppm. NH proton of the triazole ring was observed around at 9 ppm. The signals belonging to aromatic protons were found at 7.03–8.43 ppm. The mass spectrums of synthesized compounds were drawn by positive ionization technique using electron spray method. Therefore, peaks with a numerical value greater than the calculated molecular weights (molecular ion peaks; M+1 peaks) are expected to be observed in the spectrums. When the spectrums are examined, it is seen that the M+1 peaks obtained by the molecular weights of the compounds are compatible as expected. Percentage analyses of C, H, N elements were performed for the compounds covered by the study. The results indicate a deviation of 0.4% between theoretically calculated element percentages and experimental findings. This finding is an indication that the compounds contain minimal impurities.
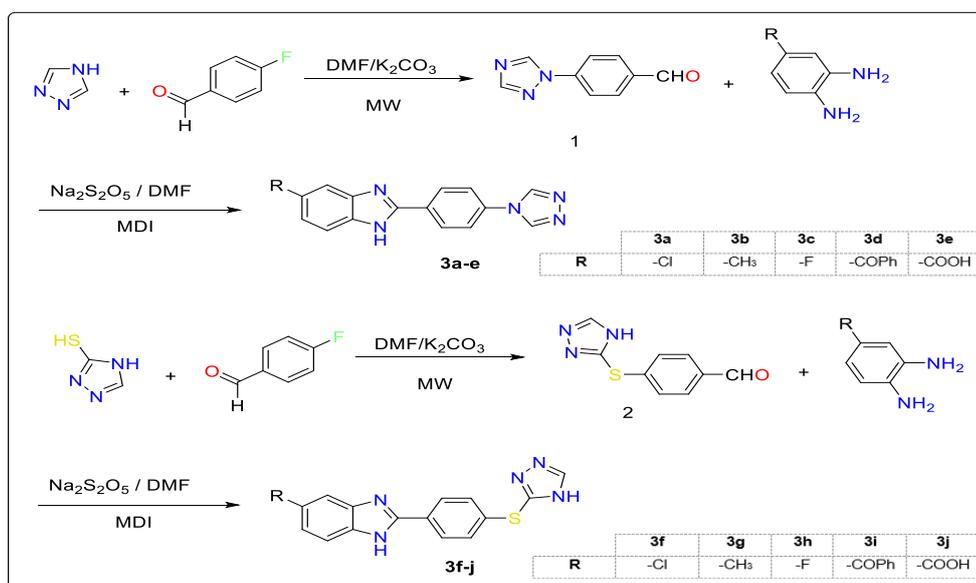
Figure 1. General synthesis pathways of the target compounds

The synthesis of 10 new benzimidazole compounds synthesized as antimicrobial agents was performed in two steps. First, two products were obtained: triazole and 4-fluorobenzaldehyde and 4-(1,2,4-triazol-1-yl)benzaldehyde and 4-(1,2,4-triazol-3-yl)benzaldehyde. The aldehyde derivatives were obtained in the first step were reacted with *o*-phenylenediamine products under microwave radiation, and the benzimidazole ring system was closed. When designing the compounds, five compounds with triazole-related sulfur structures and five compounds that do not carry sulfur were synthesized, and the activities of compounds with two different structures were evaluated. The synthesis pathways of the compounds are given in Figure 1.

The synthesis of the compounds performed was elucidated by various spectroscopic methods. Antibacterial activity results of synthesized compounds were given in Table 1, and antifungal activity results were given in Table 2. *E. coli* ATCC 35218 *(E.coli 1)*, *E. coli* ATCC 25922 *(E.coli 2)*, *K. pneumoniae* NCTC 9633 *(Kp)*, *P. aeruginosa* ATCC 27853 *(Pa)*, *S. typhimurium* ATCC 13311 *(St)*, *S.*

aureus ATCC 25923 *(Sa)* bacterial type is used. Chloramphenicol was used as a reference drug. When the results of the activity were evaluated, it was seen that the compounds were ineffective against the types of bacteria tested.

Antibacterial and antifungal activities of synthesized compounds have been tested using microdilution methods reported by the Clinical & Laboratory Standards Institute (CLSI). As a result of microbiological studies, MIC values were obtained by fluorometric measurement using resazurin solution. In this study, a more reliable, repeatable, more standardized spectroscopy method was used in the evaluation of antimicrobial test results instead of the methods of determining the MIC value detected by the eye based on the color change of a particular indicator. For this purpose, the fluorometric method modified from the CLSI method, which is available taking into account the aforementioned properties of resazurin, has been successfully applied as mentioned. According to the antimicrobial results obtained, synthesized compounds were not antibacterially effective in *in vitro* medium conditions (3a-3j for MIC: >1mg/mL).

Table 1. MIC (μg/mL) values for synthesized compounds

Comp.	*E.coli* [1]	*E.coli* [2]	*Kp*	*Pa*	*St*	*Sa*
3a	>1mg/mL	>1mg/mL	>1mg/mL	>1mg/mL	>1mg/mL	>1mg/mL
3b	>1mg/mL	>1mg/mL	>1mg/mL	>1mg/mL	>1mg/mL	>1mg/mL
3c	>1mg/mL	>1mg/mL	>1mg/mL	>1mg/mL	>1mg/mL	>1mg/mL
3d	>1mg/mL	>1mg/mL	>1mg/mL	>1mg/mL	>1mg/mL	>1mg/mL
3e	>1mg/mL	>1mg/mL	>1mg/mL	>1mg/mL	>1mg/mL	>1mg/mL
3f	>1mg/mL	>1mg/mL	>1mg/mL	>1mg/mL	>1mg/mL	>1mg/mL
3g	>1mg/mL	>1mg/mL	>1mg/mL	>1mg/mL	>1mg/mL	>1mg/mL
3h	>1mg/mL	>1mg/mL	>1mg/mL	>1mg/mL	>1mg/mL	>1mg/mL
3i	>1mg/mL	>1mg/mL	>1mg/mL	>1mg/mL	>1mg/mL	>1mg/mL
3j	>1mg/mL	>1mg/mL	>1mg/mL	>1mg/mL	>1mg/mL	>1mg/mL
Chloramphenicol	≤1,95 μg/mL	≤1,95 μg/mL	3,9 μg/mL	250 μg/mL	≤1,95 μg/mL	15,62 μg/mL

Escherichia coli ATCC 35218 (E.coli [1]),Escherichia coli ATCC 25922 (E.coli [2]), Klebsiella pneumoniae NCTC 9633 (Kp), Pseudomona aeruginosa ATCC 27853 (Pa), Salmonella typhimurium ATCC 13311 (St), Staphylococcus aureus ATCC 25923 (Sa).

It was also found that compounds other than 3a, 3b, and 3c were again not effective against any *Candida* species. However, compounds 3a, 3b, and 3c show activity only against *C. albicans*. The MIC value of

ketoconazole against *C. albicans* was 7.8 mg/mL, while the compounds were 3.9 mg/mL, 7.8 mg/mL, and 3.9 mg/mL, respectively.

Table 2. MIC (µg/mL) values for synthesized compounds

Compound	*Ca*	*Cg*	*Ck*	*Cp*
3a	3.9 µg/mL	>1mg/mL	>1mg/mL	>1mg/mL
3b	7.8 µg/mL	>1mg/mL	>1mg/mL	>1mg/mL
3c	3.9 µg/mL	>1mg/mL	>1mg/mL	>1mg/mL
3d	>1mg/mL	>1mg/mL	>1mg/mL	>1mg/mL
3e	>1mg/mL	>1mg/mL	>1mg/mL	>1mg/mL
3f	>1mg/mL	>1mg/mL	>1mg/mL	>1mg/mL
3g	>1mg/mL	>1mg/mL	>1mg/mL	>1mg/mL
3h	>1mg/mL	>1mg/mL	>1mg/mL	>1mg/mL
3ı	>1mg/mL	>1mg/mL	>1mg/mL	>1mg/mL
3j	>1mg/mL	>1mg/mL	>1mg/mL	>1mg/mL
Ketoconazole	7,8 µg/mL	≤1,95 µg/mL	≤1,95 µg/mL	≤1,95 µg/mL

Candida albicans ATCC 24433 *(Ca), Candida glabrata* ATCC 90030 *(Cg), Candida krusei* ATCC 6258 *(Ck), Candida parapsilosis* ATCC 22019 *(Cp)*

Antifungal activity test of the compounds was performed against four different *Candida* species: *C. albicans* ATCC 24433 *(Ca), C. glabrata* ATCC 90030 (Cg), *C. krusei* ATCC 6258 *(Ck), C. parapsilosis* ATCC 22019 *(Cp).* Ketoconazole was used as a reference drug. When we looked at the results of antifungal activity, it was seen that the compounds coded 3a, 3b, and 3c stand out. In particular, compounds with a code of 3a and 3c were twice as effective as the reference drug with a value of 3.9 µg/mL. The 3b compound had an activity equal to ketoconazole with a value of 7.8 µg/mL MIC. When looking at the structures of compounds 3a, 3b, and 3c, the presence of chlorine and fluorine substituent in the benzimidazole ring caused a significant increase in activity. Especially when compared with the activities of sulfur-containing compounds due to triazole, it was seen that the presence of sulfur reduces activity.

Contrary to the current study, in our previous studies [14,15] , it was seen that the sulfur atom was in a bridge position both within the ring system and between the aliphatic carbon chain and the ring system in compounds showing antimicrobial activity. In addition, the fact that the sulfur atom was attached to the acetamide residue in previous studies also explains the differences in the chemotherapeutic effect. As a result of the study, ten new compounds were synthesized in which two ring systems known to be antimicrobial effective were used together. Although synthesized compounds have no antibacterial effectiveness, they appear to give hope in antifungal activity. In future studies, it is aimed to reach more effective compounds with different modifications through this main structure.

Molecular docking studies were carried out with Schrödinger Glide XP against sterol 14-alpha demethylase (CYP51) enzyme of 3a, 3b, and 3c compounds that showed activity against *C. albicans*. CYP51 (PDB ID: 5TZ1) cocrystal VT1 redocking was performed to ensure validation of the molecular docking process and to compare synthesized compounds. The RMSD between the cocrystal natural pose and the redocking docking pose was 1.6393 Å. The RMSD value of less than 3 Å is considered suitable for molecular docking. As shown in Table 3, compounds 3a, 3b, and 3c produced lower docking scores than cocrystal, while VT1 gave a lower glide emodel value than compounds.

Table 3. Glide XP molecular docking interaction energies (kcal/mol) of 3a, 3b, and 3c against *C. albicans'* sterol 14-alpha demethylase (CYP51)

Comp.	Docking score	XP GScore	Glide emodel
3a	-8.749	-9.262	-65.704
3b	-6.077	-6.662	-60.415
3c	-7.518	-7.877	-63.733
VT1*	-6.291	-6.293	-112.080

*VT1: cocrystal of 5TZ1

Protein-ligand interactions and binding poses of the 3a, 3b, and 3c compounds on the CYP51 active site were examined. As shown in Figure 2, an H bond of 2.11 Å between the 3a compound and Met508, pi-pi stacking interactions with Tyr118, Hie377, Phe233, generated hydrophobic interactions with Pro230, Leu376, Tyr64, Phe228, and Tyr505. The 3b compound generated hydrophobic interactions with Tyr118 with pi-pi

stacking, Leu300, Tyr132, Phe380, and Met508. The 3c compound formed hydrophobic interactions with Ser378 (2.33 Å) and Hie377 (1.91 Å), pi-pi stacking with Hie377 and Phe233, Pro230, Leu376, Met508, Leu121, and Ile379.

It's always helpful to do some theoretical calculations so that drug design, research, and development will have fewer problems in terms of ADME. In this direction, the physiochemical, drug-likeness, pharmacokinetics, lipophilicity, and medicinal chemistry parameters of the 3 most active compounds against *C. albicans* were calculated using SwissADME online tools. Details are shown in Table 4. The molecular weight of compounds 3a, 3b, and 3c was between 279 g/mol and 395 g/mol. According to all lipophilicity calculations, compounds 3a, 3b, and 3c were below the logP value. Their solubility in water was moderately soluble to soluble. There was high GI absorption and BBB permeant. It complied with all of the limiting rules of Lipinski, Ghose, Veber, Egan, and Muegge. PAINS, Brenk, Leadlikeness values in all three compounds were suitable and synthetic accessibility was in the easy class.
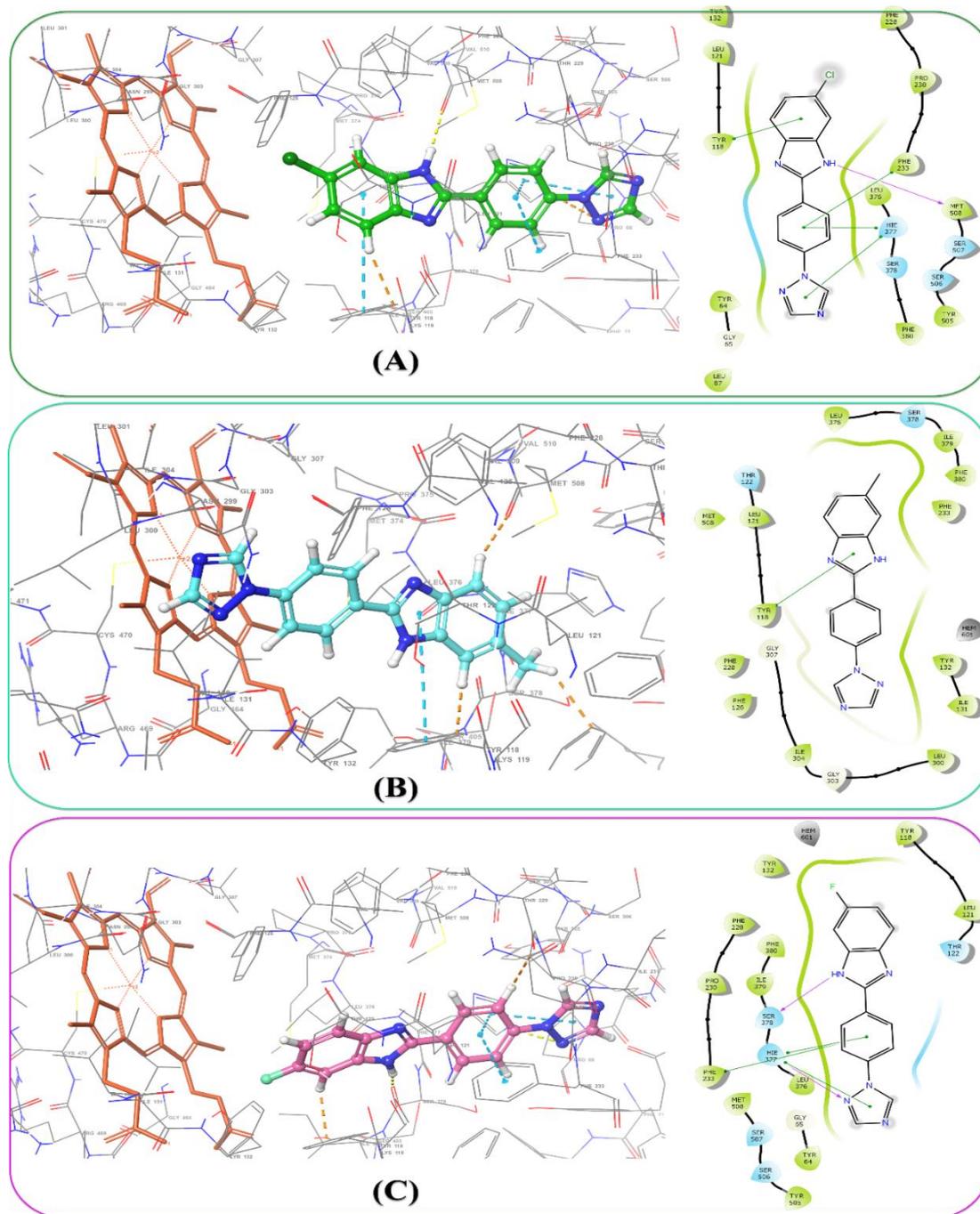
Figure 2. 3D binding poses and 2D schematic protein-ligand interactions of compounds (A) **3a**, (B) **3b**, and (C) **3c** in the active site of *C. Albicans*' sterol 14-alpha demethylase (PDB ID: 5TZ1)

Table 4. Physiochemical, drug-likeness, pharmacokinetics, lipophilicity, and medicinal chemistry parameters of compounds 3a, 3b, and 3c obtained from SwissADME.

Physicochemical Properties			
Formula	$C_{15}H_{10}ClN_5$ (3a)	$C_{16}H_{13}N_5$ (3b)	$C_{15}H_{10}FN_5$ (3c)
Molecular weight	295.73 g/mol	275.31 g/mol	279.27 g/mol
Num. heavy atoms	21	21	21
Num. arom. heavy atoms	20	20	20
Num. rotatable bonds	2	2	2
Num. H-bond acceptors	3	3	4
Num. H-bond donors	1	1	1
Molar Refractivity	81.46	81.41	76.40
TPSA	59.39 Å²	59.39 Å²	59.39 Å²
Lipophilicity			
Log $P_{o/w}$ (iLOGP)	2.17	2.16	2.02
Log $P_{o/w}$ (XLOGP3)	3.52	3.25	2.99
Log $P_{o/w}$ (WLOGP)	3.46	3.12	3.37
Log $P_{o/w}$ (MLOGP)	2.99	2.72	2.87
Log $P_{o/w}$ (SILICOS-IT)	3.08	2.95	2.86
Consensus Log $P_{o/w}$	3.05	2.84	2.82
Water Solubility			
Log S (ESOL)	-4.46	-4.17	-4.03
Class	Moderately soluble	Moderately soluble	Moderately soluble
Log S (Ali)	-4.45	-4.17	-3.90
Class	Moderately soluble	Moderately soluble	Soluble
Pharmacokinetics			
GI absorption	High	High	High
BBB permeant	Yes	Yes	Yes
CYP1A2 inhibitor	Yes	Yes	Yes
CYP2C19 inhibitor	Yes	Yes	Yes
CYP2C9 inhibitor	No	No	No
CYP2D6 inhibitor	No	No	No
CYP3A4 inhibitor	No	No	No
Log K_p (skin permeation)	-5.60 cm/s	-5.67 cm/s	-5.88 cm/s
Druglikeness			
Lipinski	Yes; 0 violation	Yes; 0 violation	Yes; 0 violation
Ghose	Yes	Yes	Yes
Veber	Yes	Yes	Yes
Egan	Yes	Yes	Yes
Muegge	Yes	Yes	Yes
Medicinal Chemistry			
PAINS	0 alert	0 alert	0 alert
Brenk	0 alert	0 alert	0 alert
Leadlikeness	No; 1 violation: XLOGP3>3.5	Yes	Yes
Synthetic accessibility	2.08	2.12	2.21

4. Conclusion

In this study, 10 new triazole bearing benzimidazole derivatives were designed and synthesized, and their structures were elucidated by IR, ^{1}H NMR, ^{13}C NMR, mass spectral analysis, and elemental analysis. It was tested against some gram-positive and negative bacteria and found no significant antibacterial activity. In contrast, in antifungal activity experiments with *C. albicans, C. glabrata, C. krusei,* and *C. parapsilosis,* compounds 3a (3.9 µg/mL), 3b (7.8 µg/mL), and 3c (3.9 µg/mL) were used as reference drug ketoconazole (7.8 µg/mL) showed the same or higher activity. In addition, molecular docking of 3a, 3b, and 3c compounds against *C. albicans*' sterol 14-alpha demethylase (CYP51) enzyme was performed with Glide XP, and their binding energies of -9.262 kcal/mol, -6.662 kcal/mol, and -7.877 kcal/mol were obtained, respectively. Theoretical ADME calculations of the 3a, 3b, and 3c were made, and the compounds were found to have good lipophilicity, moderate water solubility, and within the limiting rules of Lipinski, Ghose, Veber, Egan, and Muegge.

Acknowledgment

Conflicts of interest

The authors declare that there are no conflicts of interest.

References

[1] Willyard C., The Drug-Resistant Bacteria That Pose The Greatest Health Threats, *Nature*, 543 (7643) (2017) 15.

[2] Bansal Y., Kaur M., Bansal G., Antimicrobial Potential Of Benzimidazole Derived Molecules, *Mini Rev. Med. Chem.,* 19(8) (2019) 624-646.

[3] Acar Cevik U., Kaya Cavusoglu B., Saglik B.N., Osmaniye D., Levent S., Ilgin S., Ozkay Y., Kaplancikli Z.A., Synthesis, Docking Studies And Biological Activity Of New Benzimidazole-Triazolothiadiazine Derivatives As Aromatase Inhibitor, *Molecules*, 25(7) (2020).

[4] Evren A.E., Tekinkoca S., Yurttas L., Synthesis And Antimicrobial Activity Of Some New N-(1h-Benzimidazol-2-Yl)-2-Mercaptoacetamide Derivatives, *Lett. Drug Des. Discov.*, 15(2) (2018) 154-159.

[5] Evren A.E., Yurttas L., Yılmaz-Cankilic M., Synthesis Of Novel N-(Naphthalen-1-Yl)Propanamide Derivatives And Evaluation Their Antimicrobial Activity, *Phosphorus Sulfur*, 195(2) (2019) 158-164.

[6] Aouad M.R., Soliman M.A., Alharbi M.O., Bardaweel S.K., Sahu P.K., Ali A.A., Messali M., Rezki N., Al-Soud Y.A., Design, Synthesis And Anticancer Screening Of Novel Benzothiazole-Piperazine-1,2,3-Triazole Hybrids, *Molecules*, 23 (11) (2018).

[7] Garuti L., Roberti M., Malagoli M., Rossi T., Castelli M, Synthesis And Antiproliferative Activity Of Some Benzimidazole-4, 7-Dione Derivatives, *Bioorg. Med. Chem. Lett.,* 10(19) (2000) 2193-2195.

[8] Ayhan-Kılcıgil G., Kus C., Özdamar E.D., Can-Eke B., Iscan M., Synthesis And Antioxidant Capacities Of Some New Benzimidazole Derivatives, *Arch. Pharm.,* 340(11) (2007) 607-611.

[9] Can O.D., Osmaniye D., Demir Ozkay U., Saglik B.N., Levent S., Ilgin S., Baysal M., Ozkay Y., Kaplancikli Z.A., Mao Enzymes Inhibitory Activity Of New Benzimidazole Derivatives Including Hydrazone And Propargyl Side Chains, *Eur. J. Med. Chem.,* 131 (2017) 92-106.

[10] Vinodkumar R., Vaidya S.D., Kumar B.V.S., Bhise U.N., Bhirud S.B., Mashelkar U.C., Synthesis, Anti-Bacterial, Anti-Asthmatic And Anti-Diabetic Activities Of Novel N-Substituted-2-(4-Phenylethynyl-Phenyl)-1h-Benzimidazoles And N-Substituted 2 [4-(4, 4-Dimethyl-Thiochroman-6-Yl-Ethynyl)-Phenyl)-1h-Benzimidazoles, *Eur. J. Med. Chem.,* 43(5) (2008) 986-995.

[11] Torres-Gómez H., Hernández-Núñez E., León-Rivera I., Guerrero-Alvarez J., Cedillo-Rivera R.,

Moo-Puc R., Argotte-Ramos R., Del Carmen Rodríguez-Gutiérrez M., Chan-Bacab M.J., Navarrete-Vázquez G., Design, Synthesis And In Vitro Antiprotozoal Activity Of Benzimidazole-Pentamidine Hybrids, *Bioorg. Med. Chem. Lett.,* 18(11) (2008) 3147-3151.

[12] Shingalapur R.V., Hosamani K.M., Keri R.S., Hugar M.H., Derivatives Of Benzimidazole Pharmacophore: Synthesis, Anticonvulsant, Antidiabetic And Dna Cleavage Studies, *Eur. J. Med. Chem.,* 45(5) (2010) 1753-1759.

[13] Saglik B.N., Sen A.M., Evren A.E., Cevik U.A., Osmaniye D., Kaya Cavusoglu B., Levent S., Karaduman A.B., Ozkay Y., Kaplancikli Z.A., Synthesis, Investigation Of Biological Effects And In Silico Studies Of New Benzimidazole Derivatives As Aromatase Inhibitors, *Z Naturforsch C J Biosci*., (2020).

[14] Evren A.E., Yurttas L., Ekselli B., Akalin-Ciftci G., Synthesis And Biological Evaluation Of 5-Methyl-4-Phenyl Thiazole Derivatives As Anticancer Agents, *Phosphorus Sulfur,* 194(8) (2019) 820-828.

[15] Beyzaei H., Khosravi Z., Aryan R., Ghasemi B., A Green One-Pot Synthesis Of 3 (5)-Substituted 1, 2, 4-Triazol-5 (3)-Amines As Potential Antimicrobial Agents, *Journal Of The Iranian Chemical Society*, 16(12) (2019) 2565-2573.

[16] Pappas P.G., Kauffman C.A., Andes D., Benjamin D.K., Calandra T.F., Edwards J.E., Filler S.G., Fisher J.F., Kullberg B.J., Ostrosky-Zeichner L., Reboli A.C., Rex J.H., Walsh T.J., Sobel J.D., Infectious Diseases Society Of, A. Clinical Practice Guidelines For The Management Of Candidiasis: 2009 Update By The Infectious Diseases Society Of America, *Clin. Infect. Dis.,* 48(5) (2009) 503-535.

[17] Hargrove T.Y., Friggeri L., Wawrzak Z., Qi A., Hoekstra W.J., Schotzinger R. J., Lepesheva G.I., Structural analyses of Candida albicans sterol 14α-demethylase complexed with azole drugs address the molecular basis of azole-mediated inhibition of fungal sterol biosynthesis. *J. Biolog. Chem.,* 292(16) (2017) 6728-6743.

[18] Friesner R.A., Murphy R.B., Repasky M.P., Frye L.L., Greenwood J.R., Halgren T.A., Mainz D.T., Extra precision glide: Docking and scoring incorporating a model of hydrophobic enclosure for protein-ligand complexes, *J. Med. Chem.,* 49(21) (2006) 6177-6196.

[19] Daina, A., Michielin, O., Zoete, V., SwissADME: a free web tool to evaluate pharmacokinetics, drug-likeness and medicinal chemistry friendliness of small molecules, *Scientific reports*, 7(1) (2017) 1-13.

Synthesis, characterization and biological activity evaluation of novel thiazole derivatives containing acetic acid residue as selective COX-1 inhibitors

*Derya OSMANİYE [1, 2] * (iD) , Begüm Nurpelin SAĞLIK [1, 2] (iD)*

[1] *Department of Pharmaceutical Chemistry, Faculty of Pharmacy, Anadolu University, Eskişehir / TURKEY*
[2] *Doping and Narcotic Compunds Analysis Laboratory, Faculty of Paharmacy, Anadolu University, Eskişehir / TURKEY*

Abstract

The fact that the side effect profiles of the COX inhibitors available in the market is very high and most of these side effects are caused by non-selective inhibitors increases the need for new selective COX-1 inhibitors. In this study, carried out to develop a new COX-1 inhibitor, the thiazole ring system was preferred because of its known activity in the vary different field. Additionally, The acid residue, which is in the structure of the most commonly used COX inhibitors such as ıbuprofen and flurbiprofen, was synthesized. 2-(4-((4-(Substituted phenyl)thiazol-2-yl)amino)phenyl)acetic acid (3a-3c) series consisting of 3 new compounds was synthesized. The structures of the obtained compounds were elucidated using ^{1}H-NMR, ^{13}C-NMR and mass spectroscopy data. The *in vitro* COX inhibitory activity of the compounds was determined using fluorimetric methods. Among the synthesized compounds, the compound **3c** showed similar activity with the reference drug against the COX-1 enzyme. When the selective COX-1 inhibitory potentials of the synthesized compounds are examined, compound **3c** comes to the fore. According to the results of this study, it is recommended to investigate the selective COX-1 inhibitory activities of new compounds to be synthesized with modifications to be made on the active derivative in the project.

1. Introduction

Cyclooxygenase (COX) enzymes; are integral membrane proteins containing heme as cofactors. There are two isoforms of the COX enzyme called COX-1-2. COX-2 is restricted in the nuclear membrane and endoplasmic reticulum (ER), whereas COX-1 is found in the ER. Both enzymes convert arachidonic acid to prostaglandins, but they differ from each other in their distribution and physiological roles in the organism. The amino acid sequences are 60-65% identical. COX-1 covers 576 amino acids; COX-2 covers 587 amino acids. The COX-1 enzyme is encoded by gene located on the ninth chromosome. It is found in almost all tissues under physiological conditions. COX-1 produced in platelets is involved in the formation of thromboxane responsible for platelet aggregation. It is commonly found in the gastric mucosa. It is responsible for the formation of cytoprotective prostaglandins. By stimulating the synthesis of vasodilator prostaglandins (PGI2, PGE2 and PGD2) in the kidney, it plays a role in regulating blood flow, reducing vascular resistance, expanding renal blood vessels and increasing organ perfusion [1-3].

The selectivity to COX-1 has benefits, such as inhibition of platelet TXA2 produc-tion and absence of gastrointestinal toxicity, while non-selective COXs inhibitors have opposing cardiovascular side effectsdue to their action as reducers of prostacyclin (PGI2) biosynthesis, which has cardio protective influence presence a vasodilator and a potentplatelet aggregation inhibitor [4-8]. Therefore, within the scope of this study, it is planned to evaluate the synthesis and biological activities of new selective COX-1 inhibitors.

Thiazoles have diverse applications in drug improvement for treatment inflammation, allergies, HIV infections, hypertension, bacterial infections, hypnotics, schizophrenia, and pain as fibrinogen receptor antagonists with antithrombotic activity [9-19]. It was thought that such an active ring would be chosen as the main structure and a positive contribution

to the activity would be made. In addition, acetic acid residue was added to the structure to increase COX-1 selectivity. Thus, it is thought that many side effects caused by non-selective COX inhibitors can be combated.

It is important to develop studies to develop new drugs in the pharmaceutical industry of our country. The discovery of a new drug may become a reality as a result of academic studies. As a matter of fact, projects to find an effective new compound are intensively carried out by pharmaceutical chemists in our country. In this study, considering the potential analgesic effect of the thiazole ring system, 3 new compounds were synthesized. In the design of the target compounds in the study, a biologically active thiazole ring was considered as a constant, and aromatic systems were placed on both sides. One of these aromatic systems has been substituted with acetic acid. The aim here is to provide the acidic structure found in most COX-1 inhibitors. Synthesis compounds were subjected to efficacy tests for COX inhibition. % inhibition values and IC_{50} values were recorded. A halogen-substituted benzene ring is placed on the other side. Here, the contribution of the fluorine atom in flurbiprofen to the activity was tried to be caught. At the same time, a compound containing chlorine atom instead of fluorine atom was also synthesized and it was desired to examine how halogens would affect the activity among themselves.

2. Materials and Methods

2.1. Chemistry

All reagents were purchased from commercial suppliers and used as such.^{1}H-NMR and ^{13}C-NMR, (nuclear magnetic resonance) were performed using Bruker DPX 300 FT-NMR spectrometer and Bruker DPX 75 MHz spectrometer, respectively (Bruker Bioscience, Billerica, MA, USA). Coupling constants (*J*) were stated in Hertz (Hz). Mass spectra were verified on an APCI-MS (Advion, New York, USA) using the APCI method.

2.1.1. Synthesis of 2-(4-Aminophenyl)acetic acid hydrochloride (1)

2-(4-aminophenyl)acetic acid (0.03 mol) was dissolved in water (20 ml). A solution of HCl in water was added in 2-(4-aminophenyl)acetic acid solution in water as portions. It was decided that the reaction was complete by applying TLC. Before this reaction was terminated, the next step was passed.

2.1.2. Synthesis of [4-(carbamothioylamino)phenyl]acetic acid (2)

KSCN (0.036 mol) was added to the reaction content obtained in the synthesis of 2-(4-Aminophenyl)acetic acid hydrochloride. The reaction mixture was refluxed for 10 hours. After achievement of the reaction, the solvent was evaporated, and the hastened compound was filtered.

2.1.3. Synthesis of target compounds (3a-3c)

Compound **2** (0.001 mol) and appropriate 2-bromoacetophenone (0.001 mol) were refluxed in EtOH for 8 hours. After completion of the reaction, the precipitated product was filtered, dried recrystallized from EtOH.

2-(4-((4-(4-Fluorophenyl) thiazol-2-yl)amino)phenyl) acetic acid (3a)

Harvest: 83 %, ^{1}H-NMR (DMSO-d_6, 300 MHz): δ = 3.33 ppm (s, 2H, –CH$_2$–), 7.20 ppm (d, 2H, *J*=8.7 Hz, phenyl), 7.22-7.28 ppm (m, 3H, Thiazole+phenyl), 7.57 ppm (d, 2H, *J*=8.7 Hz, phenyl), 7.95 ppm (dd, 2H, J_1=5.6 Hz, J_2=8.9 Hz, phenyl), 10.23 ppm (s, 1H, -NH). ^{13}C-NMR (DMSO-d_6, 75 MHz): δ =45.53 ppm, 102.70 ppm, 115.91 ppm (*J*=21.6 Hz), 117.19 ppm, 128.09 ppm (*J*=7.9 Hz), 130.20 ppm, 131.35 ppm, 131.69 ppm (*J*=3.4 Hz), 139.46 ppm, 149.45 ppm, 162.05 ppm (*J*=244.3 Hz), 163.95 ppm, 174.51 ppm. APCI-MS [M+H]$^+$: C$_{17}$H$_{13}$FN$_2$O$_2$S; calculated:329.1; found:329.7.

2-(4-((4-(2,4-Difluorophenyl) thiazol-2-yl)amino) phenyl)acetic acid (3b)

Harvest: 79 %, ^{1}H-NMR (DMSO-d_6, 300 MHz): δ = 3.26 ppm (s, 2H, –CH$_2$–), 7.16 ppm (d, 1H, *J*=2.6 Hz, phenyl), 7.18-7.21 ppm (m, 3H, Thiazole+ phenyl), 7.34 ppm (td, 1H, J_1=2.6 Hz, J_2=9.2 Hz, phenyl), 7.54 ppm (d, 2H, *J*=8.7 Hz, phenyl), 8.13 ppm (td, 2H, J_1=6.9 Hz, J_2=8.9 Hz, phenyl), 10.36 ppm (bronsted singlet, 1H, -NH). ^{13}C-NMR (DMSO-d_6, 75 MHz): δ =44.83 ppm, 104.96 ppm (t, *J*=26.7 Hz), 106.9 ppm (d, *J*=13.8 Hz), 112.39 ppm (d, *J*=23.7 Hz), 117.20 ppm, 119.55 ppm, 130.11 ppm, 131.22 ppm, 132.70 ppm, 139.08 ppm, 143.32 ppm, 159.97 ppm (dd, J_1=12.8 Hz, J_2=250.2 Hz), 161.61 ppm (dd, J_1=12.7 Hz, J_2=245.1 Hz), 163.37 ppm, 175.09 ppm. APCI-MS [M+H]$^+$: C$_{17}$H$_{12}$F$_2$N$_2$O$_2$S; calculated:347.1; found:347.7.

2-(4-((4-(2,4-Dichlorophenyl)thiazol-2-yl)amino) phenyl) acetic acid (3c)

Harvest: 80 %, ^{1}H-NMR (DMSO-d_6, 300 MHz): δ = 3.21 ppm (s, 2H, –CH$_2$–), 7.17 ppm (d, 2H, *J*=8.5 Hz, phenyl), 7.35 ppm (s, 1H, Thiazole), 7.49-7.54 ppm (m, 3H, phenyl), 7.68 ppm (d, 1H, *J*=2.1 Hz, phenyl),

7.97 ppm (d, 1H, *J*=8.7 Hzr, phenyl), 10.37 ppm (s, 1H, -NH). ^{13}C-NMR (DMSO-*d₆*, 75 MHz): δ =47.35 ppm, 110.63 ppm, 119.38 ppm, 130.27 ppm, 132.29 ppm, 132.30 ppm, 132.45 ppm, 134.16 ppm, 134.77 ppm, 135.06 ppm, 135.20 ppm, 141.20 ppm, 148.14 ppm, 165.39 ppm, 177.01 ppm. APCI-MS [M+H]$^+$: $C_{17}H_{12}Cl_2N_2O_2S$; calculated:379.0; found:379.6.

2.2. Biological activity

The in vitro inhibition power of the synthesized compounds against COX-1/COX-2 isoenzymes was restrained by means of fluorometric COX-1 and COX-2 inhibitor screening kits (Biovision, Switzerland) according to the builder's orders [20,21]. The assay was founded on the fluorometric discovery of prostaglandin G2, the middle product made by the COX enzymes. The *in vitro* COX-1 and COX-2 inhibition assay procedure was carried out as previously declared by our research group [22, 23].

2.3. Molecular docking

Molecular docking studies were carried out using a structure-based protocol to reveal the binding mechanisms of compound 3c to the active site of the COX-1 enzyme. For this purpose, the crystal structure of COX-1 crystallized with flurbiprofen (PDB ID: 1EQH) [24] was extracted from the Protein Data Bank

database [25]. Docking studies were performed as reported in previous studies [26-29].

3. Results and Discussion

3.1. Chemistry

The compounds 3a-3c were obtained as presented in Scheme 1. Firstly, 2-(4-Aminophenyl)acetic acid hydrochloride (1) was obtained by means of reaction between 2-(4-aminophenyl)acetic acid and HCl solution. This salt-forming reaction was proceeded by very careful dropwise addition. An ice bath was used while adding the HCl solution. Secondly, [4-(carbamothioylamino)phenyl]acetic acid (2) was synthesized using potassium thiocyanate. Continuing this reaction without terminating the first reaction medium significantly shortens the experiment time. The purpose of this event is to eliminate the possibility of decomposition of the substance we obtain in the form of salt in the time it takes until the water end. Finally, the resulting compound (2) and the appropriate 2-bromoacetophenone were reacted to synthesize the target compounds. The structures of the gained compounds were demonstrated by means of spectroscopic methods, such as, ^{1}H-NMR, ^{13}C-NMR and APCI-MS (Supplementary Data).
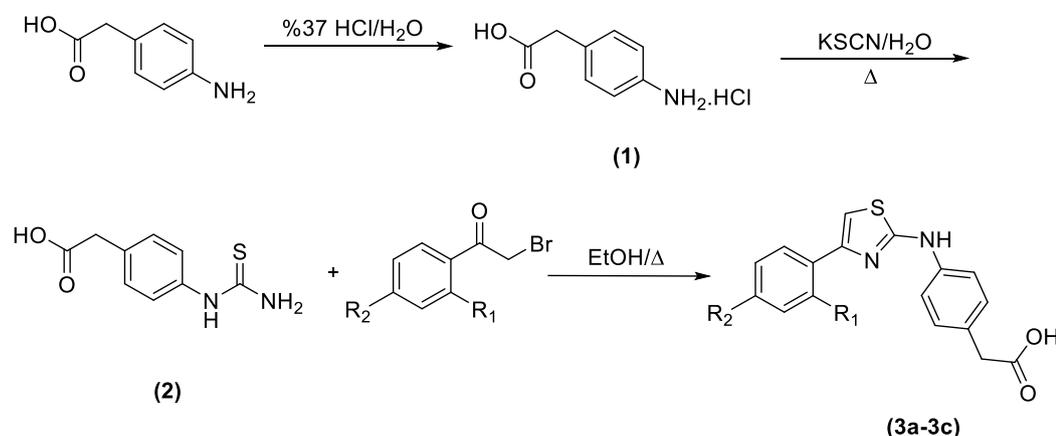
Compounds	R₁	R₂
3a	-H	-F
3b	-F	-F
3c	-Cl	-Cl

Scheme 1: Synthesis pathway of obtained compounds (3a-3c)

3.2. Biological activity

The fluorometric COX enzymes inhibition assay was applied to determine the inhibition power of all the synthesized thiazole derivatives [20-22]. The enzyme activity procedure was performed conferring to the

inhibition fractions and concentrations of the derivatives as two steps. The first step of the enzyme inhibition assay was performed by means of the applications of 10^{-3} and 10^{-4} M of the produced compounds and reference drugs. The results of this

step were given in Table 1. The compounds which presented more than 50% inhibitory activity at 10^{-4} M concentration were designated for the another step of inhibition procedure and this step was performed using their additional concentrations by serialized dilutions (extending from 10^{-5} M to 10^{-9} M). The percent inhibition rates (at 10^{-3} M to 10^{-9} M) and the semi highest inhibitory concentration (IC$_{50}$) principles of the designated compounds were given in Table 1.

Firstly, it could be said by looking Table 1 that all compounds showed higher inhibition power against COX-1 enzyme. None of the compounds displayed more than 50% inhibition at 10^{-4} M concentration on COX-2 enzyme. On the other hand, compound 3c demonstrated more than 50% inhibitory activity on COX-1 enzyme and the second step of enzyme

inhibition assay was carried out with further concentrations of this compound to calculate the IC$_{50}$ value Among the synthesized derivatives, compound 3c was found to be the most active agent with an IC$_{50}$ value of 2.518±0.120 µM. When this value compared to that of reference drugs, it was seen that compound 3c displayed similar potent inhibition profile with ibuprofen (IC$_{50}$=2.450±0.135µM).

Compound 3c has chlorine substituent unlike other compounds. According to the activity results, it is seen that the chlorine substituent contributes positively to the activity compared to the fluorine substituent. Docking studies with COX-1 enzyme active site and compound 3c were performed to explain how this contribution might be.

Table 1. %Inhibition of the synthesized compounds, ibuprofen, celexocib and nimesulide against COX-1 and COX-2 enzymes

Compounds	COX-1 % Inhibition		COX-1 IC$_{50}$ (µM)	COX-2 % Inhibition		COX-2 IC$_{50}$ (µM)	Selectivity	Selectivity index (SI)
	10^{-3} M	10^{-4} M		10^{-3} M	10^{-4} M			
3a	97.796 ±1.450	62.750 ±1.108	>10	92.345 ±1.702	40.643 ±0.932	>100	COX-1	>10
3b	94.247 ±1.632	67.159 ±1.023	>10	93.473 ±1.465	40.943 ±0.815	>100	COX-1	>10
3c	97.458 ±1.957	89.365 ±1.234	2.518 ±0.120	95.216 ±1.258	49.108 ±0.902	>100	COX-1	>39.714
Ibuprofen	98.152 ±1.058	89.361 ±1.245	2.450 ±0.135	98.234 ±1.208	88.155 ±1.348	5.326 ±0.218	COX-1	2.174
Celecoxib	-	-	-	92.327 ±1.425	85.485 ±1.303	0.132 ±0.005	COX-2	-
Nimesulide	-	-	-	97.821 ±1.214	89.575 ±1.049	1.684 ±0.079	COX-2	-

3.3. Molecular docking

As mentioned in the COX enzymes inhibition power assay, compound 3c was found to be the most active derivative in the series on COX-1 enzyme. Therefore, docking studies were performed to prove its inhibition power by using *in silico* method. Through insertion studies, further information on the binding mode of compound 3c and evaluation of the effect of structural modifications on inhibitory activity against COX-1 enzyme could be sought. The X-ray crystal structure of COX-1 (COX-1 PDB Code: 1EQH) [24] retrieved from Protein Data Bank database [25] was used in the docking procedure. The rendered docking poses of compound 3c were presented in Figures 1-2. With the COX-1 enzyme active site of compound 3c; its 2-dimensional interaction is presented in Figure-1, and its 3-dimensional interaction is presented in Figure-2.

When Figure 1 is examined, the OH group of the acetic acid group formed a hydrogen bond with Tyr385 in the

active site. It explains the selective effect of these compounds. The nitrogen of the thiazole ring formed a hydrogen bond with Arg120. Again, this ring exhibits π-π interaction with both Arg120 and Tyr355.

When examined compound 3c from the point of chemical structure, it was understood that compound 3c had the 2,4-dichlorophenyl ring differ from the additional obtained compounds. Furthermore, this studies demonstrated that the chlorine atom particularly at the 4nd situation of the phenyl ring was very crucial aimed at binding to the active site of the enzyme and so giving high inhibitory activity on COX-1. For the reason that, it was detected that there was a halogen bond between the chlorine atom at the 4nd location of the phenyl ring and the Arg83 (Figure 2). All these detected connections explained why compound 3c exhibited a good profile.
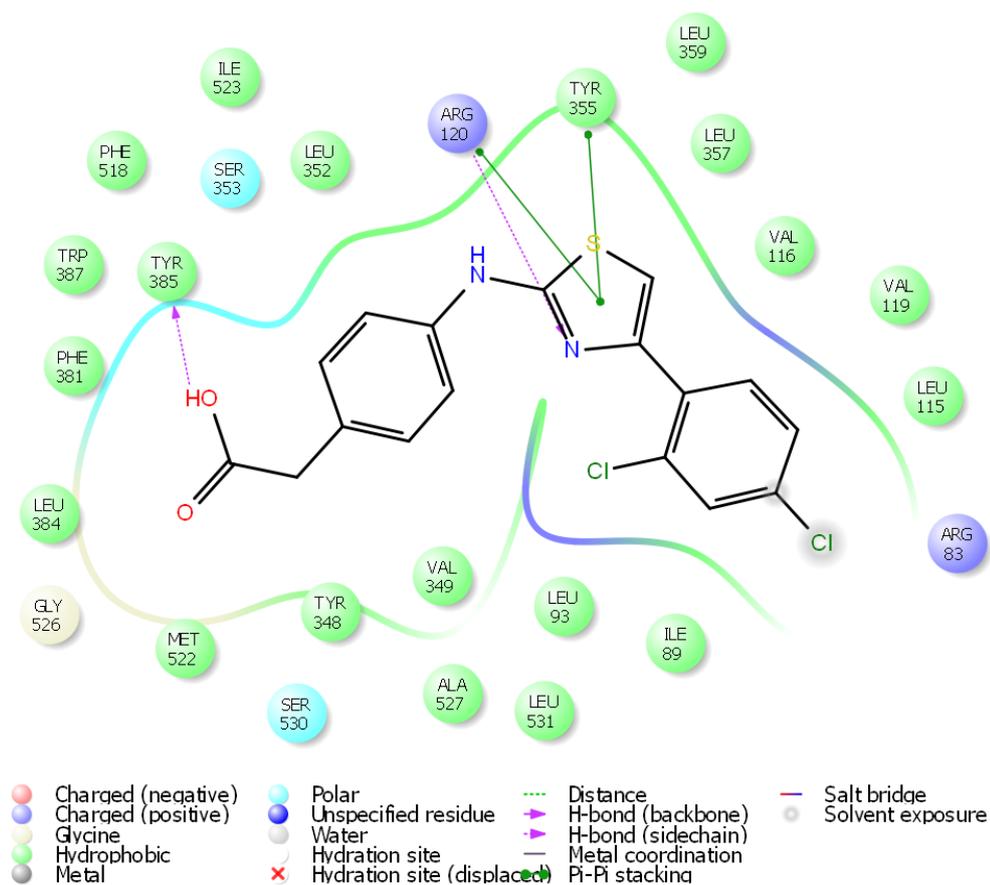
Figure 1. The 2D interacting mode of compound **3c** in the active region of ovis COX-1 enzyme (PDB ID:1EQH)
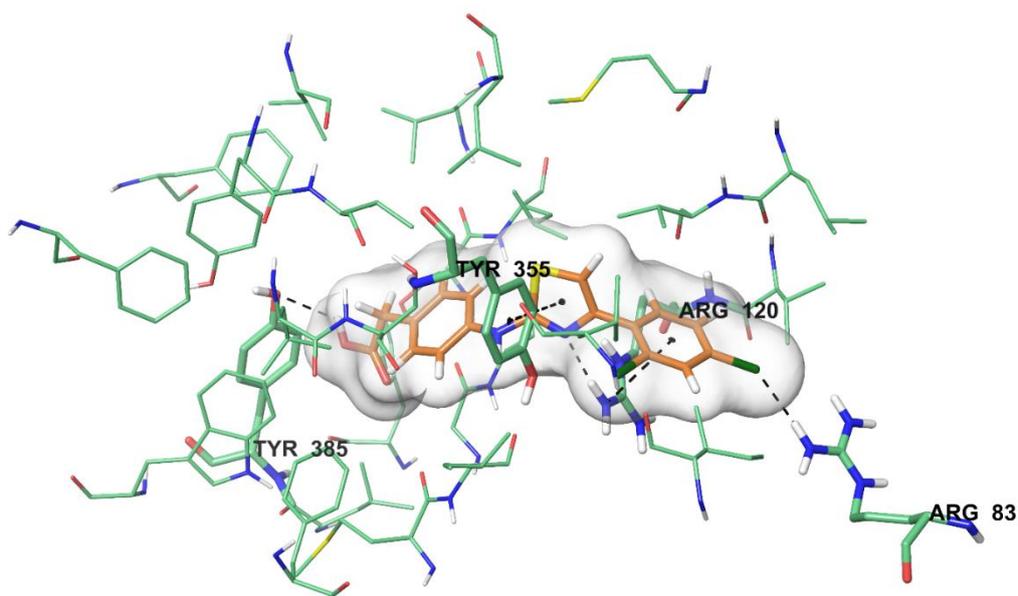
Figure 2. The 3D interacting mode of compound **3c** in the active region of ovis COX-1 enzyme (PDB ID:1EQH). The inhibitor colored with orange, and the important residue, colored with green, in the active site of the enzyme are presented by tube model.

4. Conclusion

Putting a new treatment into the service of humanity requires a long and meticulous work process lasting 12-15 years. Thanks to the new treatments put into service after these studies, people's lives are extended, their quality of life increases and important ways are covered in the fight against deadly diseases. While the average human lifespan in the world was at the age of 40 at the beginning of the 20th century, one of the important factors in reaching the age of 70 today is the development of new drugs and putting them at the service of humanity. The main purpose of drug development is to make a change in people's lives for the better. With each drug developed, it is necessary to obtain a preventive, curative or reducing effect on the signs and symptoms of the disease.

It is important to develop studies to develop new drugs in the pharmaceutical industry of our country. The discovery of a new drug may become a reality as a result of academic studies. As a matter of fact, projects to find an effective new compound are intensively carried out by pharmaceutical chemists in our country.

In this proposed study, the chain will form the first link in the long process for the discovery of a new drug. The promising results of the study give time to reach more active compounds.

Found in 1899, Aspirin® (Acetylsalicylic acid) is the first example of NSAID drugs. In the following years, many anti-inflammatory compounds such as ibuprofen, indomethacin, diclofenac and naproxen were developed and offered for treatment. The mechanism of action of NSAIDs is inhibition of prostaglandin (PG) synthesis by inhibition of cyclooxygenase enzymes and lipoxygenase. There is an urgent need to use new and safe anti-inflammatory drugs for common chronic inflammatory disorders such as rheumatoid arthritis.

In this study, considering the potential analgesic effect of the thiazole ring system, 3 new compounds were synthesized. The structures of the obtained compounds were elucidated by ^{1}H-NMR, ^{13}C-NMR and mass spectroscopic methods. Synthesis compounds were subjected to efficacy tests for COX inhibition. % inhibition values and IC_{50} values were recorded. The results showed that all compounds exhibited selective COX-1 inhibition. In addition, compound 3c exhibited similar inhibitory potential to a drug with widespread clinical use, such as ibuprofen. Therefore, according to the results of this study, it is recommended to investigate the analgesic activities of the new compounds to be synthesized in future studies by adhering to the synthesis methods used within the scope of the project.

When looking at the data obtained, the fact that the compounds show selective COX-1 inhibition. Compound 3c is very important for this activity areas. In summary, structural modifications can be further made on the basis of the new thiazoles to look for compounds with higher inhibitory activity against the human COX-1 enzyme.

Acknowledgment

Conflicts of interest

The authors declare no conflict of interest, financial or otherwise.

References

[1] Abdellatif K.R., Abdelall E.K., Fadaly W.A., Kamel G. M., Synthesis, Cyclooxygenase Inhibition, and Anti-Inflammatory Evaluation of Novel Diarylheterocycles with a Central Pyrazole, Pyrazoline, or Pyridine Ring, *Med. Chem. Res.*, 24(6) (2015) 2632-2644.

[2] Abdellatif K.R., Abdelgawad M.A., Elshemy H.A., Alsayed S.S., Kamel, G., Synthesis and Anti-Inflammatory Evaluation of New 1, 3, 5-Triaryl-4, 5-Dihydro-1H-Pyrazole Derivatives Possessing an Aminosulphonyl Pharmacophore, *Arch. Pharm. Res.*, 38(11) (2015) 1932-1942.

[3] Kankala S., Kankala R.K., Gundepaka P., Thota N., Nerella S., Gangula M.R., Guguloth H., Kagga M., Vadde R., Vasam C.S., Regioselective Synthesis of Isoxazole–Mercaptobenzimidazole Hybrids and Their In Vivo Analgesic and Anti-Inflammatory Activity Studies, *Bioorg. Med. Chem. Lett.*, 23(5) (2013) 1306-1309.

[4] Perrone M.G., Lofrumento D.D., Vitale P., De Nuccio F., La Pesa V., Panella A., Calvello R., Cianciulli A., Panaro M.A., Scilimati A. Selective Cyclooxygenase-1 Inhibition by P6 and Gastrotoxicity: Preliminary Investigation, *Pharmacology*, 95(1-2) (2015) 22-28.

[5] Vitale P., Panella A., Scilimati A., Perrone M.G., COX-1 Inhibitors: Beyond Structure Toward Therapy, *Med. Chem. Rew.*, 36(4) (2016) 641-671.

[6] G Perrone M., Scilimati A., Simone L., Vitale P. Selective COX-1 inhibition: A therapeutic target to be reconsidered, *Curr. Med. Chem.*, 17(32) (2010) 3769-3805.

[7] Mitchell J.A., Kirkby N.S., Eicosanoids, Prostacyclin and Cyclooxygenase in the Cardiovascular System, *Br. J. Pharmacol.*, 176(8) (2019) 1038-1050.

[8] Perrone M.G., Miciaccia M., Vitale P., Ferorelli S., Araújo C.D.C.B., de Almeida G.S., Domingos T.F.S., Silva L.C.R.P., Padula M., Cabral L.M., Sathler P.C., Bonaccorso C., Fortuna C.G., Scilimati A. An Attempt to Chemically State the Cross-Talk Between Monomers of COX Homodimers by Double/Hybrid Inhibitors Mofezolac-Spacer-Mofezolac and Mofezolac-Spacer-Arachidonic Acid, *Eur. J. Med. Chem.*, 209 (2021) 112919.

[9] Haragave K.D., Hess F.K. Oliver J.T., *N*-(4-Substituted-Thiazolyl) Oxamic Acid Derivatives, New Series of Potent, Orally Active Antiallergy Agents, *J. Med. Chem.*, 26(8) (1998) 1158–1163.

[10] Sharma R.N., Xavier F.P., Vasu K.K., Chaturvedi S.C., Pancholi S.S., Synthesis of 4-Benzyl-1,3-Thiazole Derivatives as Potential Anti-Infammatory Agents: An Analogue-Based Drug Design Approach, *J. Enzym. Inhibit. Med. Chem.*, 24 (2009) 890–897.

[11] Bell F.W., Cantrell A.S., Hoegberg M., Jasknas S.R., Johansson N.G., Jordan C.L., Kinnick M.D., Lind P., Morin J.M., Noreen R., Öberg B., Palkowitz J.A., Parrish C.A., Pranc P., Sahlberg C., Ternansky R.J., Vasileff R.T., Vrang L., West S.J., Zhang H., Morin Jr J.M., Phenethylthiazolethiourea (PETT) Compounds, A New Class of HIV-1 Reverse Transcriptase Inhibitors. 1. Synthesis and Basic Structure-Activity Relationship Studies of PETT Analogs, *J. Med. Chem.*, 38(25) (1995) 4929-4936.

[12] Patt W.C., Hamilton H.W., Taylor M.D., Ryan M.J., Taylor Jr D.G., Connolly C.J., Doherty A.M., Clutchko S.R., Sircar I.., Steinbaugh B.A., Batley B.L., Painchaud C.A., Rapundalo S.T., Michniewicz B.M., Sircar I., Structure-Activity Relationships of a Series of 2-Amino-4-Thiazole-Containing Renin Inhibitors, *J. Med. Chem.*, 35(14) (1992) 2562-2572.

[13] Tsuji K., Ishikawa H., Synthesis and Anti-Pseudomonal Activity of New 2-Isocephems with a Dihydroxypyridone Moiety at C-7, *Bioorg. Med. Chem. Lett.*, 4(13) (1994) 1601-1606.

[14] Ergenç N., Çapan G., Günay N.S., Özkirimli S., Güngör M., Özbey S., Kendi E. Synthesis and Hypnotic Activity of New 4-Thiazolidinone and 2-Thioxo-4, 5-

Imidazolidinedione Derivatives, *Arch. Pharm.*, 332(10) (1999) 343-347.

[15] Jaen J.C., Wise L.D., Caprathe B.W., Tecle H., Bergmeier S., Humblet C.C., Heffner T.G., Meltzer L.T., Pugsley T.A. 4-(1, 2, 5, 6-Tetrahydro-1-Alkyl-3-Pyridinyl)-2-Thiazolamines: A Novel Class of Compounds with Central Dopamine Agonist Properties, *J. Med. Chem.*, 33(1) (1990) 311-317.

[16] Carter J.S., Kramer S., Talley J.J., Penning T., Collins P., Graneto M.J., Seibert K., Koboldt C.M., Masferrer K.J., Zweifel B., Synthesis and Activity of Sulfonamide-Substituted 4,5-Diaryl Thiazoles as Selective Cyclooxygenase-2 Inhibitors, *Bioorg. Med. Chem. Lett.*, 9(8) (1999) 1171-1174.

[17] Rudolph J., Theis H., Hanke R., Endermann R., Johannsen L., Geschke F.U., Seco-Cyclothialidines: New Concise Synthesis, Inhibitory Activity Toward Bacterial and Human DNA Topoisomerases, and Antibacterial Properties, *J. Med. Chem.*, 44(4) (2001) 619-626.

[18] Badorc A., Bordes M.F., de Cointet P., Savi P., Bernat A., Lalé A., Petitou M., Maffrand J.P., Herbert J.M., New Orally Active Non-Peptide Fibrinogen Receptor (Gpiib-Iiia) Antagonists: Identification of Ethyl 3-[N-[4-[4-[amino [(ethoxycarbonyl)imino]methyl]phenyl]-1,3-thiazol-2-yl]-N-[1-[(ethoxycarbonyl)methyl] piperidin-4-yl]amino]propionate (SR 121787) as a Potent and Long-Acting Antithrombotic Agent, *J. Med. Chem.*, 40(21) (1997) 3393-3401.

[19] Khidre R.E., Radini I.A.M., Design, Synthesis and Docking Studies of Novel Thiazole Derivatives Incorporating Pyridine Moiety and Assessment as Antimicrobial Agents, *Scientific Reports*, 11(1) (2021) 1-10.

[20] Biovision COX-1 Fluorescent Inhibitor Screening Kit (Catalog No: K548-100) manual, http://www.biovision.com/manuals/K548.pd f.

[21] Biovision COX-2 Fluorescent Inhibitor Screening Kit (Catalog No: K547-100) manual, http://www.biovision.com/manuals/K547.pd f.

[22] Kaya Çavuşoğlu B., Sağlık B.N., Acar Çevik U., Osmaniye D., Levent S., Özkay Y., Kaplancıklı Z. A., Design, Synthesis, Biological Evaluation, and Docking Studies of Some Novel Chalcones as Selective COX-2 Inhibitors, *Arch. Pharm.*, 354(3) (2021) 2000273.

[23] Sağlık B.N., Osmaniye D., Levent S., Acar Çevik U., Çavuşoğlu Kaya B., Özkay Y., Kaplancıklı Z. A., Design, Synthesis and Biological Assessment of New Selective COX-2 Inhibitors Including Methyl Sulfonyl Moiety, *Eur. J. Med. Chem.*, 209 (2021) 112918.

[24] Selinsky B.S., Gupta K., Sharkey C.T., Loll P.J., Structural Analysis of NSAID Binding by Prostaglandin H2 Synthase: Time-Dependent and Time-Independent Inhibitors Elicit Identical Enzyme Conformations, *Biochemistry*, 40(17) (2001) 5172-5180.

[25] RCSB, Protein Data Bank. Biological Macromolecular Structures Enabling Breakthroughs in Research and Education, Available at: rcsb.org/structure/1EQH. Retrieved June 2, 2021

[26] Maestro, Maestro, version 10.6, Schrödinger, LLC, New York, NY, (2016).

[27] Schrödinger, LLC, New York, NY, (2016).

[28] LigPrep, Schrödinger, LLC, New York, NY, (2016).

[29] Glide, Schrödinger, LLC, New York, NY, (2016).

Electrochemical investigation of DNA and Capecitabine interaction using glassy carbon electrode (GCE)

Derya KIZILOLUK[1], iD , Gültekin GÖKÇE [2] iD, Şenay ÇETİNUS [3] iD*

[1]*Sivas Cumhuriyet University, Faculty of Science, Department of Biochemistry, Sivas/TURKEY*
[2]*Sivas Cumhuriyet University, Faculty of Pharmacy, Department of Basic Pharmacy Sciences, Analytical Chemistry, Sivas/TURKEY*
[3]*Sivas Cumhuriyet University, Faculty of Science, Department of Biochemistry, Sivas/TURKEY*

Abstract

In recent years, studies with biosensors have increased in order to better understand the mechanisms of anticancer drug action. Thus, studies to examine interactions with DNA using biosensors have gained momentum. In our study, it was investigated that Capecitabine (CPT), an anticancer drug, and glassy carbon electrode (GCE) interaction by using electrochemical methods. The interaction of CPT with calf thymus DNAs (dsDNA, ssDNA) immobilized on the electrode surface was analyzed by exploiting changes in the oxidation signals of the guanine base. The immobilization of DNA on the electrode surface has been optimized. Optimal DNA concentration and optimal interaction times were found. Electrochemical impedance spectroscopy technique was used for impedimetric measurements.
The results obtained confirmed that the ct-DNAs were immobilized on the electrode surface. Detection limit (DL) was found as 17.54 µg / mL for interaction capecitabine with ds-DNA and was found 17.12 µg / mL for interaction capecitabine with ss-DNA.

1. Introduction

Structures obtained by adding biological substances to an electrochemical sensor device are called biosensors. [1-3]. Sensors using DNA as recognition surface are called DNA biosensors [3-5]. These biological structures are used to determine the interaction mechanisms of some drugs or substances that target DNA. It also helps to illuminate the effects of these drugs on DNA [3-7].

Analyzing of DNA - drug interaction using these new methods is important in terms of enabling new drug designs [7]. The rapid and reliable determination of the interactions of drug molecules has anticancer properties with DNA is of great importance for drug development studies [8]. Antitumor drugs that act by binding to DNA help to examine whether many different compounds have anticancer drug properties [9]. Many different techniques have been developed to examine the interaction of compounds with nucleic acids. This technique may allow some parts of the drug molecule to bind to DNA through hydrogen bonds and

van der Waals interaction or other interactions. Drug molecules must be functional in order to interact with target DNA. The biological functions of the drug can be explained according to the functional groups it contains. It will be possible to devise a new class of compounds with the necessary structures to increase or change the activity of a drugs. [10-13].

Today, the determination of drug-DNA interaction can be successfully performed using electrochemical DNA biosensors. Studies examining the effect of drugs on DNA have analyzed drug-dependent changes in the measured signals. [3, 12]. This change in signal may be due to the DNA base, or it may be due to changes in the drug signal. This result indicates a reliable interaction between analyte and DNA [3, 5,13].

In our research, the interaction of the capecitabine with GCEs with or without DNA modification were investigated. Capecitabine binding capacity determined by reduction in guanine base signal [3,13-15]. Subsequently, by changing the capecitabine concentration, variables such as guanine signal response, interaction times and reproducibility were

examined [16]. There is no study in the literature investigating the effect of capecitabine on DNA using GCE. It is believed that our study will complete the deficid in the literature.

2. Materials and Methods

2.1 Devices

All measurements were performed using the electrochemical workstation SP-150 from Bio132 Logic Science Instruments (France), connected to the EC-Lab software V.11.25. Conventional three-electrode system was used. Glassy carbon electrode (GCE) was used as indicator electrode; Ag/AgCl was used as reference electrode and platinum wire was used as counter electrode. Balance (Precisa XB 220A), Sound vibration cleaner (Bandelin Sonorex), pH-meter (WTW InolabpH 720), Magnetic stirrer (AGE velp), Vortex (Velp scientifics), Potentiostat μ-AUTOLAB type III (GPES ve FRA Modülleri – EcoChemie, Hollanda).

2.2 Chemicals

Acetic acid (CH_3COOH, 98%), Hydrochloric acid (HCl, 37%), Sodium chloride (NaCl), Capecitabine (CPT), Sodium Hydroxide (NaOH), Calf thymus ds DNA, Calf thymus ss DNA were obtained from Sigma-Aldrich (Missouri, USA). Potassium ferrocyanide ($K_4[Fe(CN)_6]$), Potassium ferricyanide ($K_3[Fe(CN)_6]$), Sodium phosphate dibasic (Na_2HPO_4), Potassium hydrogen phosphate (KH_2PO_4), Di potassium monophosphate (K_2HPO_4), Ethanol (C_2H_6O, 98%), Tris(hydroxymethyl)aminomethane hydrochloride ($C_4H_{11}NO_3$), Trisma hydrochloric acid (Trisma-HCl), EDTA ($C_{10}H_{16}N_2O_8$) disodium salt were purchased from Merck-sigma Aldrich (Saint-Quentin-Fallavier, France). All solutions in the study were prepared in deionized Milli- Q water (Millipore, Bedford, MA, USA) (18 Mega-ohms). Experimental studies were carried out at room temperature (25.0 ± 0.5) °C.

2.2.1. Preparation of the solutions

18 ohm ultrapure water was used in the preparation of all buffer solutions. After the buffer solutions were prepared, they were stored in plastic bottles in the refrigerator.

Preparation of 0.05 M phosphate buffer solution (pH 7.4; PBS):

The 0.05 M phosphate buffer solution used during the measurements contained 1.36 g (0.01 mol) KH_2PO_4, 6.96 g (0.04 mol) K_2HPO_4 and 1.168 g NaCl (0.02 mol) per liter. The pH value of the prepared buffer solution is about 7.4. If necessary, the pH of the solution was

adjusted to 7.4 with a pH meter by the addition of 0.1 M NaOH and/or 0.1 M HCl. Then, 5 mM phosphate buffer solution was prepared by diluting the 0.05 M phosphate buffer solution prepared as a stock [3].

Preparation of 0.50 M acetate buffer solution (pH 4.8; ABS, from liquid):

Some ultrapure water was added to the 500mL flask. 28.9 mL of concentrated acetic acid solution was taken. The balloon was added onto the water in the flask. It was made up to 500 mL with ultrapure water and poured into a 1 liter beaker with a stirrer. The mixer was started and the pH meter was started. 1 M NaOH solution was added until the pH was 4.81. Then 1.168 g of NaCl was weighed and added. When the pH was 4.8, the solution was poured into a 1L flask and made up to 1L with ultrapure water [3].

Preparation of 0.02 M Tris HCl buffer solution (pH 7.0; TBS):

The 0.02 M Tris HCl buffer solution used contains 3.152 g Trisma HCl and 1.168 g NaCl (0.02 mol) per liter. Adjustment of the pH of the solution to 7.0 was accomplished by adding 0.1 M NaOH and/or 0.1 M HCl, by measuring with a pH meter [3].

Preparation of 0.01 M Tris-HCl, 1 mM EDTA buffer solution (pH 8.0; Tris-EDTA):

The 0.01 M Tris-HCl used contains 1.576 g Trisma HCl and 0.372 g EDTA per liter of 1 mM EDTA buffer solution. Adjustment of the pH of the solution to 8.0 was accomplished by adding 0.1 M NaOH and/or 0.1 M HCl, by measuring with a pH meter [3].

Preparation Capecitabine solution:

Until the purchased Capecitabine was completely dissolved, the previously prepared buffer solution ABS was added to the bottle containing the drug, when the dissolution was complete, the stock concentration of the drug was calculated and put into eppendorf tubes in 50 μL volumes for later use and stored at 4°C. In order to minimize the exposure of the drug to light, it was worked as quickly as possible during preparation and the prepared drug solution was kept in a refrigerator in a box that will not be exposed to light [3].

Preparation DNA solutions:

DNA from calf thymus gland (= Calf Thymus DNA); double-stranded DNA (dsDNA) stock solutions; 1000 μg/mL was prepared with TE solution (10 mM Tris-HCl, 1mM EDTA, pH 8.0) and stored below zero. Ct dsDNA dilute solution was prepared with 0.5 M Acetate buffer (pH 4.8). In order to minimize the exposure of the solution to light, it was stored in a refrigerator at -20 °C in an opaque box [3, 5].

Single-stranded DNA (= ssDNA) solution was also prepared as described above for ct dsDNA and stored in the refrigerator at -20 ˚C.

2.3. Method

Preparation of electrodes and immobilization of DNA on electrodes were performed as reported in the current literature [3]. In addition, the interaction of DNA with the drug was also made as reported in the current literature [3, 4]. Each study was repeated at least 5 times.

Glassy carbon electrode was polished with pure water include small alumina powders until a mirror-like bright image was formed. Afterwards, carbon dust and polishing dust were removed from the surface by ultrasonication. Surface activation of the glassy carbon electrode was carried out in ABS (acetate buffer solution) by applying +0.50 V for 60 seconds. The buffer solution was changed by aborting the system for the last 5 seconds and the measurement was continued in PBS (phosphate buffer solution) [1,2,11]. These prepared electrodes are suitable for one use only. For this reason, the electrodes are prepared and activated fresh each time before use.

Glassy carbon electrode was prepared for the experiment with the differential pulse voltammetry technique using a potentiostat device, as stated in the current

2.4. Electrochemical impedance spectroscopy (EIS) measurements

Optimization steps for DNA immobilization on the GCE surface and optimization steps for the interaction of DNA immobilized GCEs with CPT were performed as stated in the current literature [3]. In addition, the preparation of the solutions in the EIS experiments and the measurement technique were also performed as reported in the existing literature [3].

3. Results and Discussion

3.1. DNA immobilization to the active GCE surface

Passive adsorption for GCE was chosen as the immobilization technique. The ct ds-DNA and ct ss-DNA were interacted with the activated GCE. The concentrations of the immobilized ct ds-DNA were kept constant and the most appropriate time for immobilization was optimized (Figure 1). The optimum amount of ct ds-DNA for immobilization keeping the optimal interaction time of the immobilized DNA constant was optimized (Figure 2). As stated in the literature measurements were made over guanine signals [3,4].

The immobilization parameters (time and concentration) on the GCE surface for ct ds DNA and ct ssDNA were separately optimized.
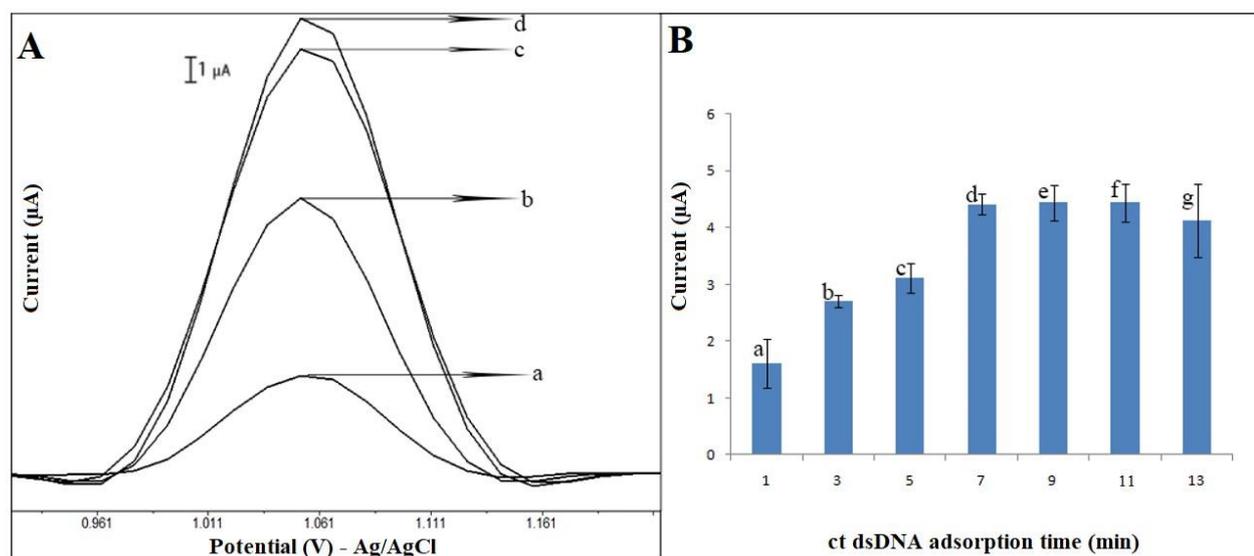
Figure 1. (A) Voltammogram and (B) Histogram for ct ds-DNA immobilized on the GCE surface at different time

When the voltammogram and histogram in Figure 1 is examined, it is seen that the interaction times for immobilization of ct ds-DNA on the GCE surface are compared. When the voltammogram of different interaction times such as a)1, b)3, c)5, d)7, e)9, f)11, g)13 min was examined, it was found that the most appropriate interaction time in terms of reproducibiliy to be 9 min.

Figure 2. (A) Voltammogram and (B) Histogram for ct ds-DNA immobilized on the GCE surface at different concentration.

When the voltammogram and histogram in Figure 2 is examined, it is seen that the interaction concentrations for the immobilization of ct ds-DNA on the GCE surface are compared. When the voltammogram of ct ds-DNA prepared at different concentrations such as a) without DNA, b)24, c)30, d)36, e)42, f)48, g)54 μg /mL is examined, it was concluded that the most appropriate interaction concentration in terms of reproducibility to be 42 μg /mL. The signal marked with (a) in the histogram is the received signal (without DNA) for GCE with no DNA immobilized.

When the optimization procedures were repeated for ct ss-DNA immobilization on the GCE surface, it was determined that the ct ss-DNA was immobilized on the GCE surface in an optimal 9 min. And the concentration of ct ss-DNA was determined to be 36 μg/mL (also not shown in the figure).

3.2. Interaction between immobilized DNA and CPT

DNA (ct ds-DNA and ct ss-DNA) immobilized GCE was kept at different times in CPT solutions at constant volume and different concentrations. Optimum interaction time (Figure 3) and optimum interaction amount (Figure 4) for ct ds-DNA –CPT interaction were found as indicated in the current literatüre [3].
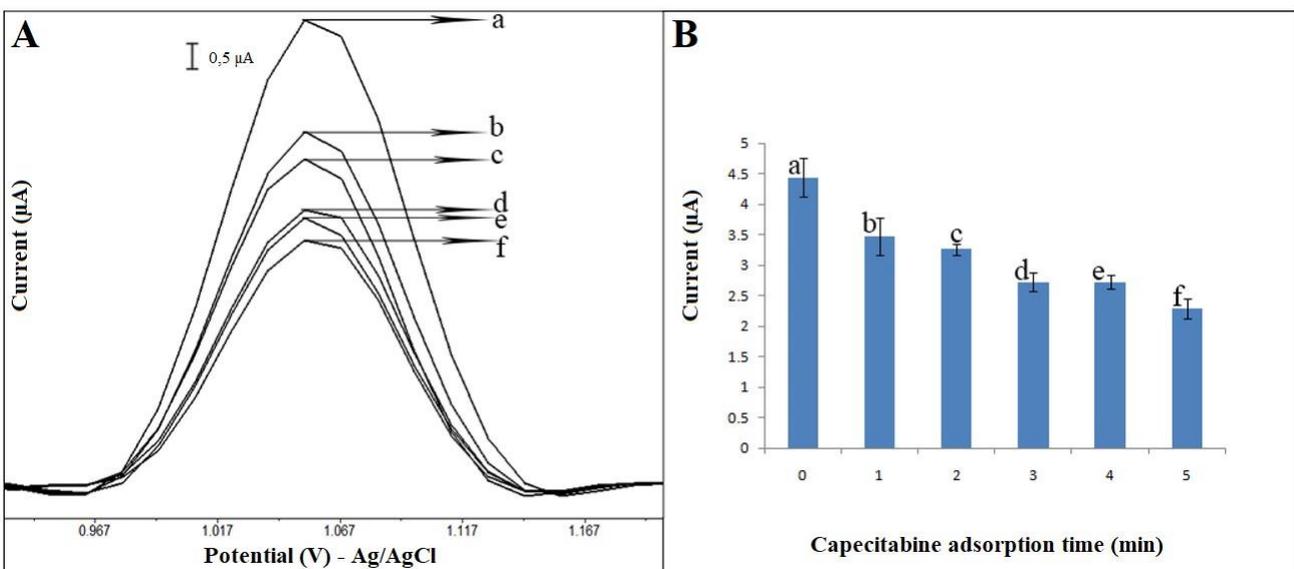
Figure 3. (A) Voltammogram and (B) Histogram of the effect of capecitabine immobilization time on response.

When the voltammogram and histogram in Figure 3 are examined, it is seen the interaction of ct ds DNA immobilized GCEs in CPT solution at different times such as a)0, b)1, c)2, c)3, d)4, e)5min. The signal marked with (a) in the histogram is only that of ct ds-DNA immobilized GCE. In other words, it is the measurement signal taken without interacting with the electrode CPT (without CPT, with ct- dsDNA). When the measured guanine signals were compared, the optimum interaction time was found to be 4 min.
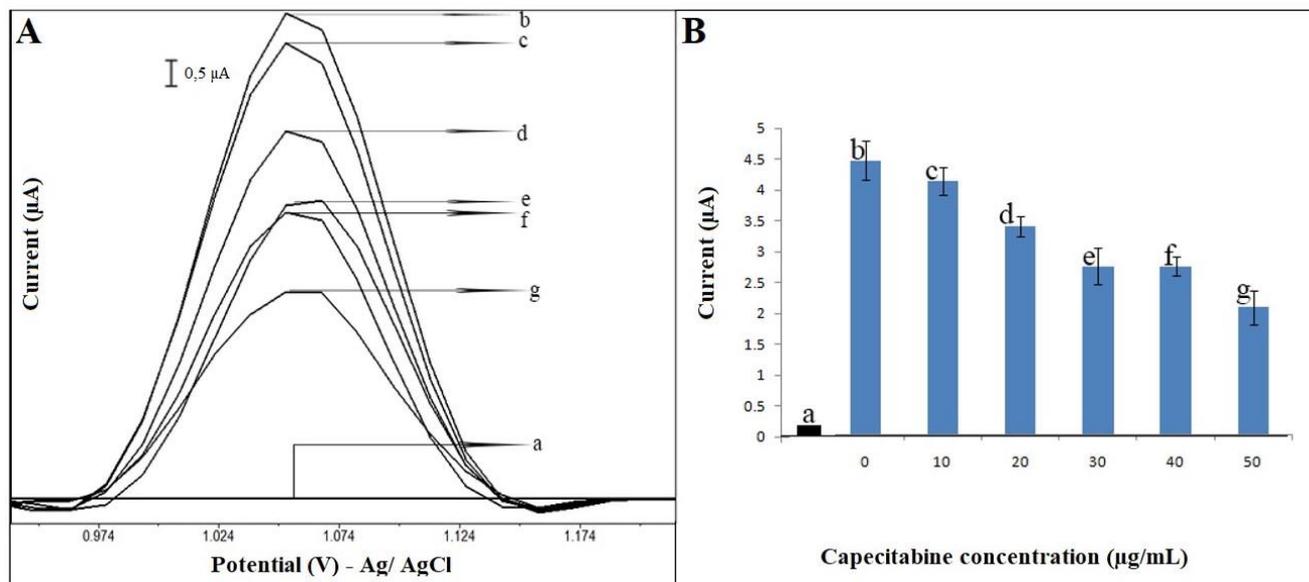
Figure 4. (A) Voltammogram and (B) Histogram of the effect of capecitabine concentration on response.

When the voltammogram and histogram in Figure 4 are examined, it is seen that the interaction signals of ct ds-DNA immobilized GCEs with different concentrations of CPT solutions such as (a) without both ct dsDNA and CPT (b)0 (c) 10 (d) 20 (e) 30 (f) 40 µg/mL are compared. The signal marked by (a) in the histogram is the signal of GCE that has not been immobilized ct ds-DNA and that has not interacted with the CPT. Likewise, the signal marked (b) in the histogram is the signal before to interaction with CPT of DNA immobilized GCEs (without CPT, with ct-ds DNA). When the measured guanine signals were compared, the optimum CPT concentration was found to be 40 µg/mL.

When optimization procedures were repeated for CPT interaction with ct ss-DNA immobilized GCEs, it was determined that the optimum CPT concentration was 40µg/mL and the optimum CPT interaction time was 3 min (also not shown in the figure).

Standard graphs of the interaction of ct ds-DNA and ct ss - DNA with capecitabine are given in Figure 5 and Figre 6.
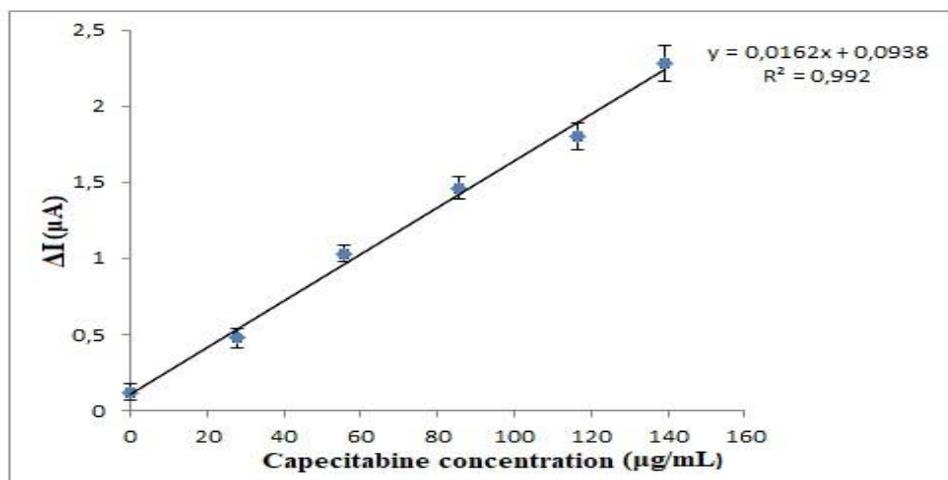
Figure 5. Calibration curve of CPT concentration change upon interaction of ct - ds DNA immobilized GCE and CPT
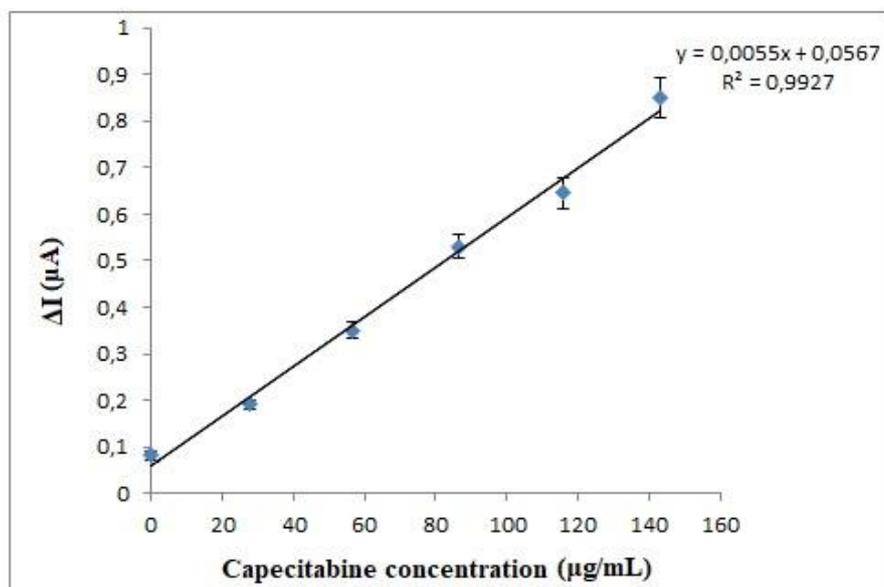
Figure 6. Calibration curve of CPT concentration change upon interaction of ct - ss DNA immobilized GCE and CPT

Detection limits were calculated as reported in the available literature [3].The lowest detection limit for ct ds-DNA-CPT interaction was 17.54 μg/mL, and the lowest detection limit for ct ss-DNA-CPT interaction was found as 17.12 μg/mL [3].

3.3. Result of electrochemical impedance (EIS) experiments

The electrode was activated according to the method described in 2.3 (electrode activation process). Differently, EIS measurements were made using FRA (Frequency Analyzer) software instead of DPV technique. Analyzes based on impedance values obtained by measuring current in the cell at constant potential and at different frequencies with the impedimetric technique were performed. Measures were taken by EIS for activated GCE, ct dsDNA immobilized GCE, and GCE after ct dsDNA – CPT interaction. Nyquist curves were drawn using values close to the mean value.

The procedures described above were repeated for ct ss-DNA. The results obtained are given in Figure 7 and Figure 8.

When the Histogram in Figure 7 is examined, it is seen that a) pret (activated) GCE resistance, b) ct dsDNA immobilized GCE resistance, and c) GCE resistance after interaction CPT with ct dsDNA immobilized to GCE surface are compared.

It was observed that there was an increase in the resistance of the GCE surface after ct dsDNA was immobilized compared to its previous state (only after surface activation).
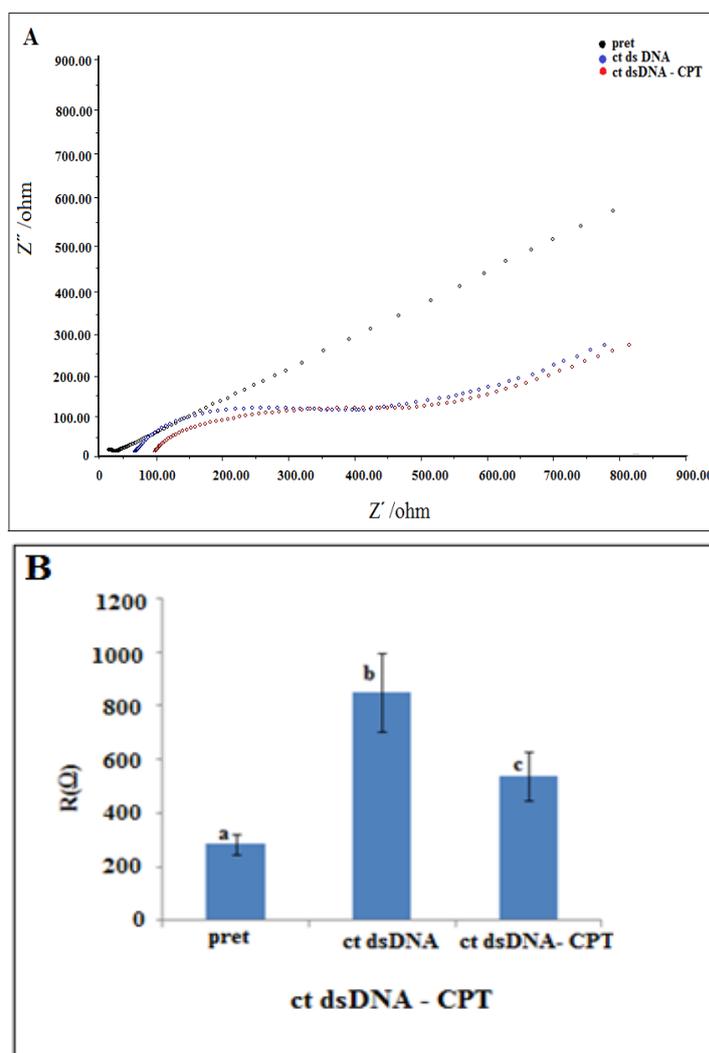
Figure 7. (A) Nyquist curve (B) Histogram of resistance of ct ds- DNA immobilized GCE and CPT interaction to transferred current load

Afterwards, a decrease in electrode resistance was observed after the interaction of CPT with ct dsDNA on the GCE surface. So, we can say that the conductivity of activated GCE is higher than that of ct dsDNA immobilized GCE and than that of GCE that happening interaction ct dsDNA with CPT on its surface.
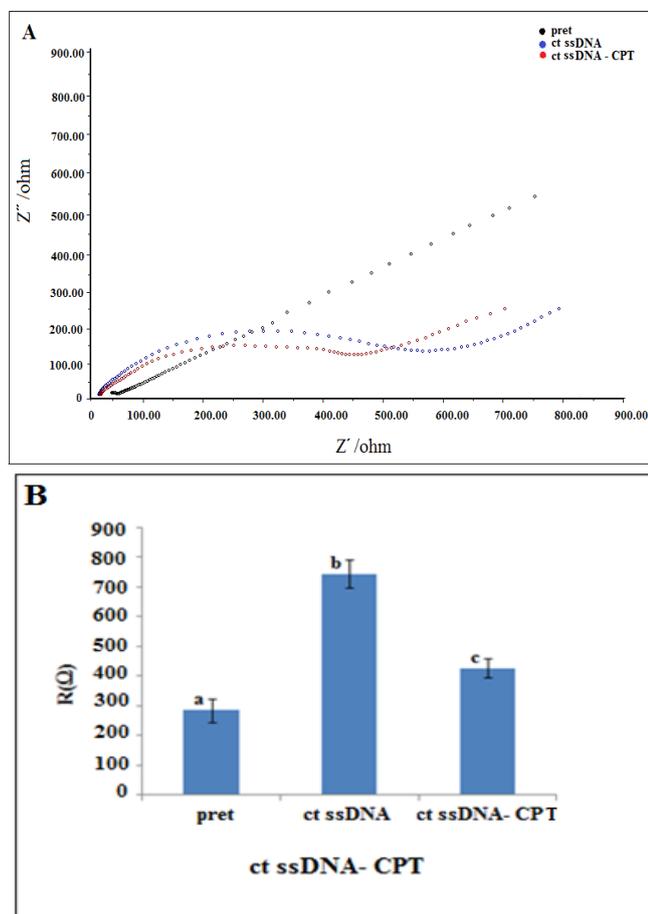
Figure 8. (A) Nyquist curve (B) Histogram of resistance of ct ss- DNA immobilized GCE and CPT interaction to transferred current load

When the Histogram in Figure 8 is examined, it is seen that a) pret (activated) GCE resistance, b) ct ssDNA immobilized GCE resistance, and c) GCE resistance after interaction CPT with ct ssDNA immobilized to GCE surface are compared. It was observed that there was an increase in the resistance of the GCE surface after ct ssDNA was immobilized compared to its previous state (only after surface activation). Afterwards, a decrease in electrode resistance was observed after the interaction of CPT with ct ssDNA on the GCE surface So, we can say that the conductivity of activated GCE is higher than that of ct ssDNA immobilized GCE and than that of GCE that happening interaction ct ssDNA with CPT on its surface.

When the measurements made with the impedimetric technique for both ct dsDNA and ct ssDNA are examined, it is seen that similar results are obtained. In addition, an increase in load transfer resistance was observed (Figure 7B and Figure 8B). We can say that in both types of DNA (ct dsDNA, ct ssDNA) DNA immobilization on the electrode surface and then interaction with the drug (CPT) cause differentiations on the electrode surface.

EIS experiments have shown that the interactions on the GCE face depend on two parameters (conductivity and resistance) that are inversely proportional to each other. As it is known, there is an inverse relationship between resistance and conductivity. Therefore, we can say that the conductivity decreases with increasing resistance.

If the histograms are interpreted in the light of this information; An increase in resistance was observed after DNAs (ct ds-DNA and ct ss-DNA) were immobilized on the GCE surface. And then, a decrease in resistance was observed with DNA-CPT interaction on the DNA-immobilized GCE surface (same results were found for both DNAs). Therefore, we can interpret that the conductivity of activated GCE is higher than that of DNA (ct ds-DNA and ct ss-DNA) immobilized GCE, and the conductivity of the DNA immobilized GCE surface decreases with CPT interaction.

In other words, by using these measurements, we can get information about whether the electrode surface is covered with DNA and whether the DNA-CPT interaction has taken place. Therefore, a decrease in the oxidation signal of guanine base was observed as the CPT concentration increased. This reduction indicates that CPT interacts with DNA, which is consistent with studies in the literature [11].

The optimal immobilization conditions of DNA to the GCE surface were determined. The optimal interaction time was found for 9 min (ct ds-DNA and ct ss-DNA), optimal DNA concentration 42 μg / mL (ct ds-DNA) and 36 μg / mL (ct ss-DNA).

Optimization experiments of DNA immobilized GCE and CPT interaction were performed. The optimized interaction time was 4 min and 3 min, respectively, and the optimized interaction amount was found to be 40 μg / mL for both DNAs.

As a result, we can say that capecitabine has an effect on DNA. We also believe that it will be an important electrochemical method for quantification of drugs such as capecitabine in biological materials.

Acknowledgment

Conflicts of interest

The authors state that did not have conflict of interests.

References

[1] Özsöz M., Erdem A., Kara P., Kerman K., Özkan D., Electrochemical biosensor for the detection of interaction between arsenic trioxide and DNA based signal, *Electroanal.*, 15 (7)(2003) 613- 619.

[2] Wang J., Electrochemical nucleic acid biosensors, *Analytica Chimica Acta.*, 469 (1)(2002) 63-71.

[3] Elik A., Gökçe G., Bostancı E., Kızıloluk D., Electrochemical Determination of Interaction between Anticancer Drug Epirubicin and DNA by DNA Biosensors, *Cumhuriyet Sci. J.*, 38(3) (2017) 525-534.

[4] Kızıloluk D., Gökçe G., Akkuş Çetinus Ş., Electrochemical Determination of the Interaction between Anticancer Drug Capecitabine and DNA by Carbon Paste Electrode, *Journal of Scientific Perspectives,* 4(1) (2020) 1-12.

[5] Wang J., Rivas G., Cai X., Palecek E., Nielsen P., Shiraishi H., Dontha N., Luo D., Parrado C., Chicharro M., Farias PAM., Valera FS., Grant DH., Özsöz M., Flair MN., DNA electrochemical biosensors for environmental monitoring. A Review, *Anal. Chim. Acta*, 347(1-2) (1997) 1-8.

[6] Erdem A., A Review: Nanomaterial-based electrochemical DNA sensing strategies, *Talanta*, 74(3) (2007) 318-325.

[7] Nawaz H., Rauf S., Akthar K., Khalid A.M., Electrochemical DNA biosensor for the study of ciprofloxacin–DNA interaction, *Analytical Biochemistry*, 354(1) (2006) 28–34.

[8] Kuralay F., Erdem A., Abacı S., Ozyoruk H., Yildiz A., Characterization of redox polymer based electrode and electrochemical behavior for DNA detection, *Analytica Chimica Acta.*, 643(1-2) (2009) 83-89.

[9] Karadeniz H., Erdem A., Calıskan A., Pereira C. M., Pereira E. M., Ribiero. J.A., Electrochemical sensing of silver tags labelled DNA immobilized onto disposable graphite electrodes, *Electrochem. Commun.*, 9(9) (2007) 2167-2173.

[10] Yan F., Erdem A., Meric B., Kerman. K., Özsöz M., Sadik O.A., Electrochemical DNA biosensor for the detection of specific gene related to Microcystis species, *Electrochemistry Communications*, 3(5) (2001) 224-228.

[11] Wang. J., Rıvas G., Fernandes J. R., Jıang M., Paz. J.L.L., Waymıre R., Nıelsen T.W., Getts R.C., Adsorption and detection of DNA dendrimers at carbon electrodes, *Electroanal.*, 10(8) (1998) 553-556.

[12] Mikkelsen S. R., Electrochemical biosensors for DNA sequence detection- a review, *Electroanal.*, 8(1) (1996) 15-19.

[13] Rauf S., Goodıng J.J, Akthar K., Ghaurı M.A, Rahman M., Anwar M.A., Khalıd A.M., Electrochemical approach of anticancer drugs–DNA interaction, *Journal of Pharmaceutical and Biomedical Analysis*, 37(2) (2005) 205–217.

[14] Palecek E., From Polarography of DNA to Microanalysis with Nucleic Acid Modified Electrodes, *Electroanal*, 8(1) (1996) 7-14.

[15] Wang L., Lın L., Ye B., Electrochemical studies of the interaction of the anticancer herbal drug emodin with DNA, *Journal of Pharmaceutical and Biomedical Analysis,* 42(5) (2006) 625–629.

[16] Erdem A., Kerman K., Meriç B., Akarca U.S., Özsöz M., DNA Electrochemical biosensor fort he detection of short DNA sequences related to the hepatitis B virüs, *Elektroanal.*, 11(8) (1999) 586-587

The effects of *f*CNT and oxidation on the OGG/*f*CNT double networked hydrogel

Serbülent TÜRK [1, 2,]* (ID)

[1]*Sakarya University, Biomedical, Magnetic and Semi Conductive Materials Research Center (BIMAS-RC), Esentepe Campus, 54187 Sakarya/TURKEY*
[2]*Sakarya University, Biomaterials, Energy, Photocatalysis, Enzyme Technology, Nano & Advanced Materials, Additive Manufacturing, Environmental Applications and Sustainably Research & Development Group (BIOENAMS R&D Group), 54187, Sakarya/TURKEY*

Abstract

Double networked (DN) hydrogel systems consisting of *f*CNT and OGG have been successfully developed by ionic crosslinking. OGG was synthesized and mixed with *f*CNT to obtain DN hybrid hydrogel with improved modulus and $T_{gelation}$. The effects of H_2O_2 oxidation and *f*CNT addition on the gelling and physico-chemical features of the prepared OGG-*f*CNT hydrogels were investigated. The OGG and prepared OGG-*f*CNT DN hydrogels were characterized by SEM, FTIR, zeta potential, contact angle, and $T_{gelation}$ measurements to evaluate H_2O_2 oxidation and CNT effects on the physicochemical properties. While the degree of $T_{gelation}$ after oxidation is successfully reduced below physiological temperature, this temperature was further lowered by mixing with *f*CNT. The synthesized DN hydrogel showed an increasing modulus from 1389 Pa to 4895 Pa with *f*CNT. The morphological structure of the OGG-*f*CNT DN hydrogel system was significantly affected by the addition of *f*CNT. This study for the OGG-*f*CNT hydrogel system demonstrated the interaction between components and the properties of a three-dimensional GG structure can be affected by oxidation and the presence of *f*CNT. The obtained observations from this study may be necessary for the application of GG as a biomaterial in tissue engineering and drug carrier in delivery systems.

1. Introduction

Hydrogels are a subject that continues to increase rapidly and attracts attention from scientists [1]. The spatial harmony of the liquid form of the gel systems between the implant formed and the randomly shaped places, their drug loading capabilities, and adjustable modulus values put hydrogels among essential research topics in the biomedical field [2]. On the other hand, in cell cultivation studies, the rapid gelation process is at the forefront as it causes a uniform distribution of the transplanted cells into the biomaterial [3]. All these ideal features of hydrogels bring with it more prospects and research to develop new hydrogel materials to meet the ever-increasing requisitions of tissue engineers and biomaterials. Since hydrogels are water-containing 3D structures, they are also used in drug release applications such as wound healing, especially due to their ability to encapsulate water-soluble drug molecules. In addition, it is also used in the field of tissue engineering by adding additions to the hydrogels in accordance with the mechanical strength of the target tissue.

Gellan gum (GG) is an extracellular polysaccharide, water-soluble, anionic and contains α-L-rhamnose (Rhap), β-D-glucose (Glcp), β-D-glucuronic acid (GlcpA), and β-D-glucose (Glcp) repeating units [4]. Due to its biological, physical, and chemical behavior, a suitable heat and acid resistant biomaterial, and its biodegradability, biocompatibility, and low cytotoxicity, GG has been explored its use in nanomedicine, bioengineering, and tissue engineering [5–7]. Physicochemical modification facilitates the applications of GG in different fields. Produced on an industrial scale at low cost, GG is also used in wound dressing preparation to prevent postoperative wound formation and suppress adhesions [8].

Homogeneous distribution of thermally reversible gelling GG can be obtained at 85-90°C [9]. The 3D mesh formation begins with lowering the temperature, with many free random GG coils interacting with the

junction areas to form a double helix structure. With the complexation of multiple cations supporting the strengthening of the hydrogel architecture, adjacent carboxyl groups can help the gelation process. However, some disadvantage of physical cross-linking of GG include gelling temperature incompatibility with most cell therapy strategies, in-vivo instabilities over time due to the exchange of cations. Therefore, many studies have been performed examining how to improve its stability and lower the gelation temperature [10].

Since the Tgelation of pure GG is too high (>42°C) for injectable cell carriers, it must be brought to physiological temperature (~37.5°C) so that it can transport cells and be used in minimally invasive injectable applications. In addition, since they have poor mechanical strength, their strength needs to be improved for successful applications as tissue engineering scaffolds and carrier materials [11]. Modifying the structure of GG with the use of cross-linking agents (e.g., (1-ethyl-3-(3-dimethylaminopropyl)carbodiimide) that are toxic to cells causes a long gelation time. In this study, it is assumed that the design of a system that can both add strength and obtain a double network structure and the oxidation of GG can overcome these limitations and improve its functional properties.

Oxidation is an ideal method for adding carboxyl groups, increasing water solubility, and reducing the gelling temperature to physiological values. Due to the poor solubility of pure carbon nanotube (CNT), functionalized CNT (*f*CNT) with oxygen-containing functional groups on its surface is often used as supplementary material for biomedical applications. For instance, because of a great number of active hydroxyl groups on both oxidized GG and *f*CNT chain, the interconnection occurs between them, resulting in the ionic cross-linking of *f*CNT OG form stable hydrogels. This study aims to develop a hydrogel composed of different concentrations of *f*CNT and OGG to promote convenient features for the reasons mentioned above. To achieve this purpose, it has been oxidized the GG with H_2O_2 and then to obtain a DN hydrogel through the −H bond reactions it has been further combined OGG with *f*CNT. Investigations have shown that there is no hydrogel study in the literature examining the properties of OGG-*f*CNT structure oxidation and CNT addition.

2. Materials and Methods

2.1. Materials

Gellan gum (GG, trade name Phytagel), hydrogen peroxide (H_2O_2, 30% in aqueous), copper sulfate ($CuSO_4$), multi-walled carbon nanotube (CNT), and calcium chloride ($CaCl_2$), were purchased from Sigma Aldrich. Throughout the study, purified water obtained by Millipore Milli-Q was used in the synthesis and solution preparation steps.

2.2. Synthesize of oxidized GG

To synthesize the OGGs, 2 g of GG was dissolved in 60 mL of deionized water at 85°C in a sealed bottle to prevent water loss. After cooling to 50°C, 0.05% $CuSO_4$ solution (4 mL) was added, and 30% H_2O_2 was added at different rates (20, 40, and 60 mL) with stirring, then allowed to react at room temperature for 48 h. After the prepared mixture was dialyzed to remove H_2O_2 and Cu^{2+}, the lyophilization step was started. After freezing at −20°C for 12 h, it was lyophilized (BIOBASE) at 15Pa for 2 days at −50°C. After that, the lyophilized hydrogels were stored in sealed bottles. The OGGs were denoted as OGG_1, OGG_2, and OGG_3 when the rates of H_2O_2 were 20, 40, and 60 mL, respectively.

2.3. Preparation of OGG-*f*CNT DN hydrogels

Lyophilized OGG and *f*CNT were dissolved in deionized water at rates of 2.5% (w/v) and 1% (w/v), respectively, under constant mixing for 15 min at 85°C. The *f*CNT was obtained by functionalizing CNT by refluxing it with nitric acid, as in our previous study [12]. To prepare GG-*f*CNT, OGG_1-*f*CNT, OGG_2-*f*CNT, and OGG_3-*f*CNT hydrogels for each sample 15 mg/mL of *f*CNTs mixing with 1% w/v OGG, OGG_1, OGG_2, and OGG_3, respectively. To obtain the well-dispersed *f*CNT in the DN hydrogel, *f*CNT was sonicated by probe sonication (Q Sonica Sonicator) in distilled water for 10 min at an amplitude of 15% in pulsed mode (1.0 seconds pulse on/off) and then transferred into the hot OGG solutions. Afterward, 0.1% (w/v) $CaCl_2$ was added and stirred for 15 minutes to produce cross-linked hydrogels. The prepared solutions were cooled to room temperature to obtain three-dimension OGG-*f*CNT DN hydrogels.

2.4. Characterization of hydrogels

Molecular groups and bindings in pure gellan gum (PGG), oxidized GGs, and prepared OGG-*f*CNT samples were characterized using FTIR (Spectrum Two Perkin-Elmer Co.). The prepared samples were

scanned at 4 cm^{-1} resolution in the 4000 cm^{-1}-400 cm^{-1} wavelength range.

Gelation temperature of PGG and OGGs and OGG-*f*CNT were measured according to the inverting approach. The OGG-*f*CNT hydrogel solutions were added to the centrifuge tubes after dissolving in the distilled water at 85°C. Tubes were then incubated in a temperature-monitored water bath (Nuve, ST 30) to determine the gelation point. The temperature of the water bath, which was initially kept higher than the T$_{gelation}$ to avoid gelation of samples, was gradually lowered. The tubes (n=5) in which the samples were placed before gelation was removed from the water bath for observation after the temperature stabilized every 5 min and the current temperature at which the solutions lost their fluidity was recorded as the T$_{gelation}$.

The morphologies of hydrogels were investigated by scanning electron microscopy (SEM, JEOL, JMS 6060). Lyophilized hydrogels were cut into suitable pieces before observation. After fixation on conductive carbon tapes, they were analyzed after coating them with a thin layer of gold by sputtering (Polaron CS7620) to ensure conductivity. Pore sizes were measured with Image J software using SEM micrographs of lyophilized OGG-*f*CNT hydrogels.

PGG, OGGs, and OGG-*f*CNT were dissolved in distilled water at a concentration of 0.1% (w/v) at 70°C. The zeta potentials of the samples were then measured at 25°C (Nano-Plus).

4 µl of distilled water was dropped on the lyophilized hydrogel with the help of a Hamilton syringe, and contact angles were measured using a goniometer (Attention) with sessile drop method at room temperature. Since the porosity in the surface morphology may affect the contact angle, the measurements of the samples pressed into flat surfaces were carried out to obtain a flat surface by minimizing the effects of the porous morphology of the lyophilized samples. Average contact angle values collected 5 s

after drop deposition were obtained using a video-enabled optical system.

The rheological properties of OGG-*f*CNT DN hydrogels were investigated after they were placed in the measuring cell of the rheometer and covered with paraffin oil to avoid the evaporation of the water in it. Sweep tests of angular frequency (ω) with a frequency range between 1 and 100 rad s^{-1} of OGG-*f*CNT DN hydrogels adjusted at 0.5 mm thickness and fixed at 1% strain (γ) were performed at 25°C.

3. Results and Discussion

It has been analyzed that the FTIR spectrums of PGG and OGGs have characteristic peaks around 3367, 2912, 1727, 1609, 1405, and 1029 cm^{-1}, as can be seen from Fig. 1 (a). While the band formed at approximately 2912 cm^{-1} corresponds to the C−H stretching vibrations of sugar, the peaks corresponding to the symmetric and asymmetric stretching vibrations of the carboxyl groups of the salt form were observed at 1405 cm^{-1} and 1609 cm^{-1}, respectively. The band belonging to the C−O−C stretch was observed around 1029 cm^{-1}. A new characteristic peak around 1727 cm^{-1} in the spectra of all OGGs was analyzed, which was followed to become more pronounced in proportion to oxidation. It is known that the peak around 1715 cm^{-1} corresponds to the C=O stress peaks of aldehydes, esters, and carboxylic acids. Peaks belonging to the carboxylic group were observed in the dissociated form at 1727 cm^{-1} and in the salt form at around 609 cm^{-1}-1405 cm^{-1} [13]. Thus, a new characteristic peak increase of about 1727 cm^{-1} appeared for all OGGs, indicating the formation of carboxylic groups in OGGs after oxidation. [14]. The new peak intensity increase, indicating that the amounts of carboxyl groups in the OGGs increased with increasing oxidation degree, demonstrated successful incorporation of carboxyl groups into GG.
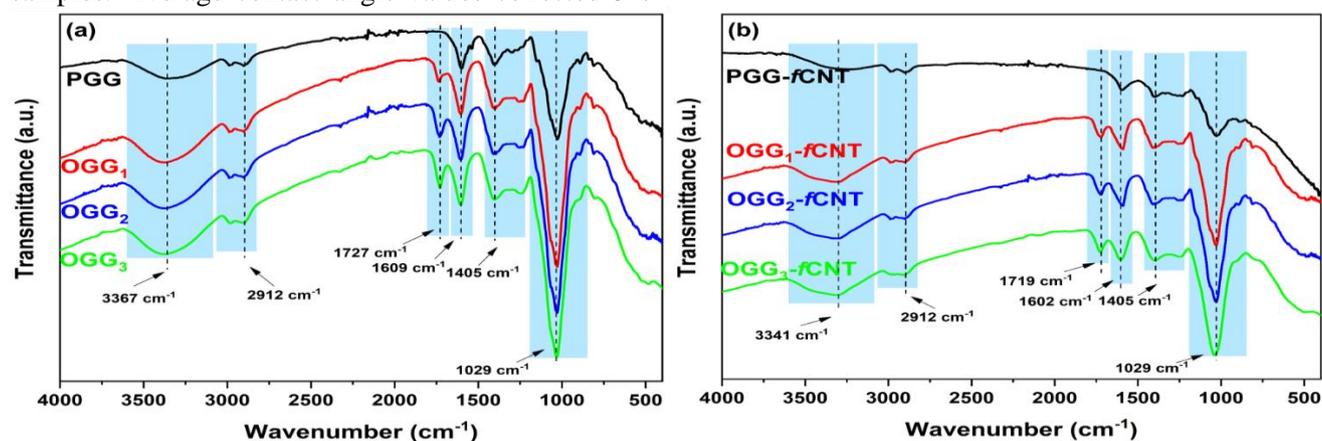
Figure 1. (a) FTIR spectra of PGG, OGG$_1$, OGG$_2$, and OGG$_3$,. (b) FTIR spectra of OGG-*f*CNT DN hydrogels.

Fig. 1b was FTIR spectra of OGGs/fCNT hydrogels. No noticeable difference was appeared between the groups, only a slight shift after DN hydro-gelation. The peak at 1719 cm^{-1} indicates that OGG participates in the gelation and takes place in the hydrogels prepared by preserving its original structure.

As can be seen in Fig. 2a, $T_{gelation}$ values of PGG, OGG$_1$, OGG$_2$, and OGG$_3$ samples prepared at 2.5% (w/v) concentration differ. PGG exhibited a high gelling temperature of 43°C, while the gelling temperatures of OGG$_1$, OGG$_2$, and OGG$_3$ were 39°C, 32°C, and 29°C, respectively. After oxidation, the $T_{gelation}$ temperatures of GG significantly reduced with the increase of H$_2$O$_2$ amount.

Fig. 2b shows how $T_{gelation}$ values change with the addition of fCNT. It was observed that the $T_{gelation}$ temperature of the OGG$_3$-fCNT sample obtained by adding fCNT to the OGG$_3$ sample, which has a high oxidation degree, was the lowest. Decreasing the $T_{gelation}$ temperatures of OGG samples with fCNT can be attributed to the inhibition of the electrostatic interaction between the OGG chains. It is thought that the temperature of the gelation phenomenon, which considers the formation of stabilized double helix junction sites, decreases by increasing the interaction in unit volume with the oxidation of hydroxyl groups of GG and addition of fCNT.

Figure 2. (a) Gelation temperature of PGG, OGG$_1$, OGG$_2$, and OGG$_3$. (b) Gelation temperature of PGG-fCNT, OGG$_1$-fCNT, OGG$_2$-fCNT, and OGG$_3$-fCNT. (n= 5).

As presented in Table 1, the charge density of PGG, OGGs, and OGG/fCNT DN hydrogels was characterized by measuring their zeta potential values. The zeta potentials of the PGG, GG samples showed a negative value because of the presence of carboxyl groups in the repeating units of the molecules. In addition, after oxidation, OGG$_1$-OGG$_3$ samples were characterized as having lower negativities with zeta potentials in the range of −12.4 mV to −28.3 mV. These increased negative zeta potential values were attributed to incorporating more carboxyl groups. In addition, it was observed that the charge densities of OGG-fCNT DN hydrogels increased with the addition of CNT. This decrease in zeta potential supports the presence of oxygen-containing functional groups on the fCNT surface. With the increase of functional groups containing oxygen in the hybrid hydrogel, it was found as −16.2, −27.1 and −31.4 for OGG$_1$, OGG$_2$ and OGG$_3$, respectively, after fCNT addition. Therefore, OGG-fCNT products with DN structure can

be obtained containing OGG, which has the desired negativity for oxidation and application with fCNT.

Table 1. Zeta potential of pristine, oxidized, and fCNT added DN structured hydrogels.

Hydrogels	Zeta-potential (mV)
PGG	−8.2±0.3
OGG$_1$	−12.4±0.2
OGG$_2$	−22.6±0.8
OGG$_3$	−28.3±0.9
PGG-fCNT	−11.6±0.2
OGG$_1$-fCNT	−16.2±0.5
OGG$_2$-fCNT	−27.1±0.8
OGG$_3$-fCNT	−31.4±1.1

To investigate the effect of *f*CNT addition on morphology, OGG$_3$ and OGG$_3$-*f*CNT hydrogels were examined by SEM, as shown in Fig. 3. Prepared cylindrical hydrogels (a1 and b1) were lyophilized and morphologically analyzed after cutting to the appropriate size. It has been observed that the hydrogels prepared with interconnected and homogeneous porosity have different pore sizes. While the pore size of the OGG$_3$ hydrogel was found to be 523±87 μm, the pore size of the OGG$_3$-*f*CNT hydrogel after the addition of *f*CNT decreased to 238±43 μm and was observed to be more compact than OGG$_3$. There was no apparent phase separation in OGG$_3$-*f*CNT, and the results support that *f*CNT is homogeneously dispersed into the hydrogel network with a porous structure. The structure of OGG$_3$-*f*CNT with uniform and small pores has been attributed to the increased crosslinking density in its structure.
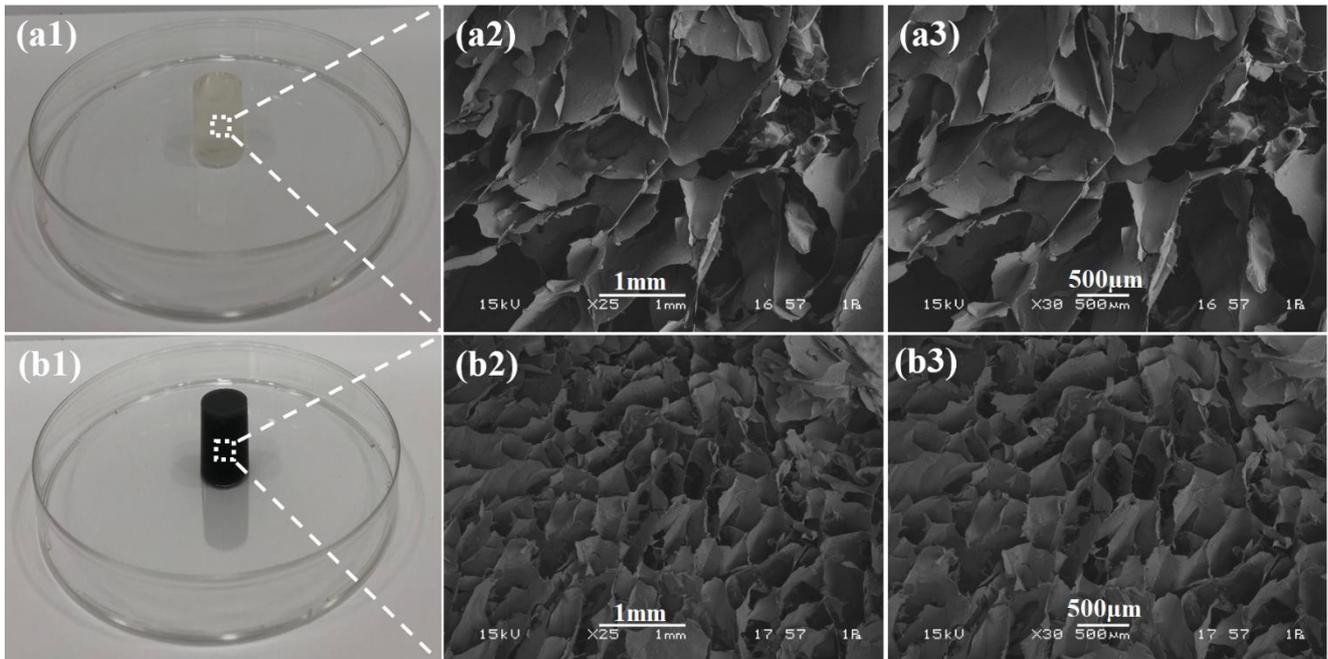
Figure 3. Prepared cylindrical (a1) OGG$_3$ and (b1) OGG$_3$-*f*CNT hydrogels, and SEM images of the cross-section of lyophilized (a2, a3) OGG$_3$ hydrogels and (b2, b3) OGG$_3$-*f*CNT hydrogels.

The storage (*G'*) and loss modulus (*G''*) of OGG$_3$ and OGG$_3$-*f*CNT DN hydrogels at a constant test temperature of 25°C were investigated depending on the frequency as seen in Fig. 4.
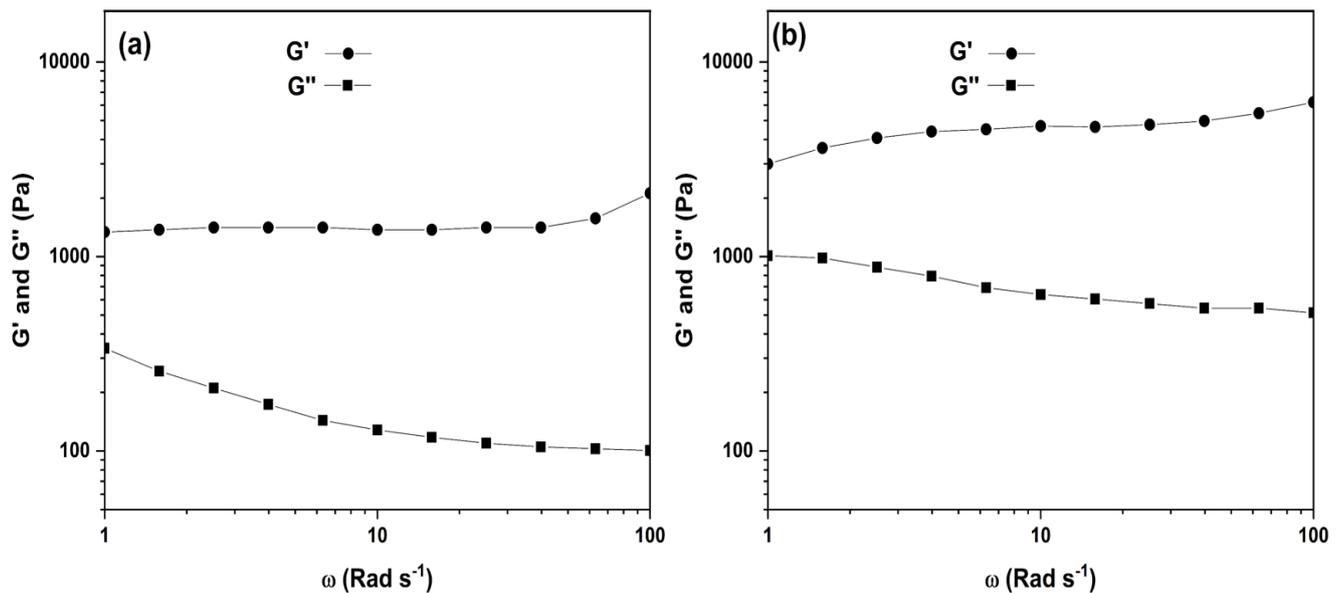
Figure 4. Storage modulus (*G'*) and loss modulus (*G''*) of the prepared (a) OGG$_3$ and (b) OGG$_3$-*f*CNT hydrogels.

When the modulus values of both hydrogels are examined, G'' is lower than G' indicates that the hydrogel samples exhibit a solid-like behavior. It was observed that hydrogels with higher modulus values were obtained after the increase of the G' value after the addition of fCNT. For example, at a frequency of 40 rad s^{-1}, the mean modulus for OGG without CNT was 1389 Pa, while it increased to an average of 4895 Pa after fCNT addition. This result shows that with CNT, the G' and G'' values can be adjusted to the desired values for the OGG/fCNT DN hydrogel. The OGG-fCNT hydrogel produced for engineering bone tissue requires a strong and relatively hard gel, or, conversely, for applications of tissues such as heart or corneal tissue, which requires a much softer and more elastic gel, can be adjusted. These site-related factors need to be considered when optimizing a hydrogel to culture a specific tissue. Based on this result, the adjustment of the properties of the OGG-fCNT hydrogel produced to suit the tissue to be cultured and the in vitro modulus of the hydrogels that reflect the in vivo environment can be performed. As shown in Fig. 5, measurements of contact angle five seconds after drop deposition on all gel types' surfaces were performed to investigate the oxidation and fCNT effects further. When the contact angles of the pristine (a1) and oxidized GG samples (a1-a4) were examined, it was observed that the contact angle decreased as a result of oxidation. This decrease is attributed to the increase of oxygen-containing functional groups formed due to oxidation on the surface. In the fCNT added hydrogel samples, it was concluded that the wettability of the hydrogel samples was increased by the addition of fCNT because of the presence of oxygen-containing functional groups on the surface of fCNT. Since the contact angle is related to the

interactions between the material and the water molecules, it is generally concluded that the water interacts less with the unoxidized and fCNT-free GG hydrogel sample.

Hydrogen peroxide (H_2O_2), which has a pKa of 11.6, is more acidic than water and decomposes into the unstable perhydroxyl anion (HOO^-) with heat. Then, it reacts with H_2O_2 to form a highly reactive hydroxyl radical (HO•). The formation steps of these reactions are shown in Equations 3.1, 3.2, and 3.3 as follows:

$$H_2O_2 \rightarrow H^+ + HOO^- \tag{3.1}$$

$$HOO^- \rightarrow HO^- + (O) \tag{3.2}$$

$$H_2O_2 + HOO^- \rightarrow HO \cdot + H_2O + O_2^- \tag{3.3}$$
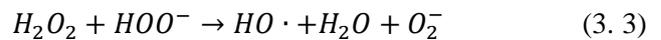
Free hydroxyl radicals (HO•) abstract hydrogen atoms from GG's C_6 and form –COOH groups. As mentioned above, hydroxyl groups are formed due to oxidation steps, including the oxidation steps of C6 hydroxyl to carbonyl groups and carboxyl groups. The GG oxidation steps from the presence of H_2O_2 are shown in Scheme1a.

Scheme 1b showed that DN hydrogels were prepared by cross-linking fCNT and calcium cross-linked OGG. The oxidation reaction increased the cross-linking allowed for both entangled networks formation. Gelation is mainly because of the H bond reaction between OGG and fCNT. In the DN hydrogel system, OG was pretreated with Ca^{2+} for physical crosslinking since known that the presence of the cation is required to form a stable hydrogel via electrostatic interaction. Mixed with $CaCl_2$, linked by H bonds, DN hydrogels were also ionically cross-linked via electrostatic interactions.
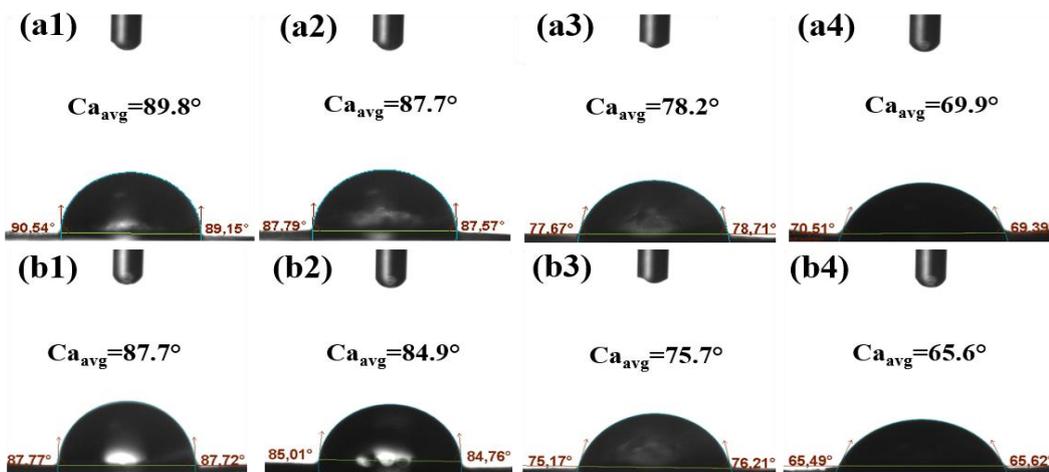
Figure 5. Contact angle measurements of (a1) PGG, (a1) OGG, (a2) OGG$_1$, (a3) OGG$_2$, (a4) OGG$_3$ hydrogel samples before fCNT addition and (b1) PGG-fCNT, (b2) OGG$_1$-fCNT, (b3) OGG$_2$-fCNT, and (b4) OGG$_3$-fCNT hydrogel samples after fCNT addition.
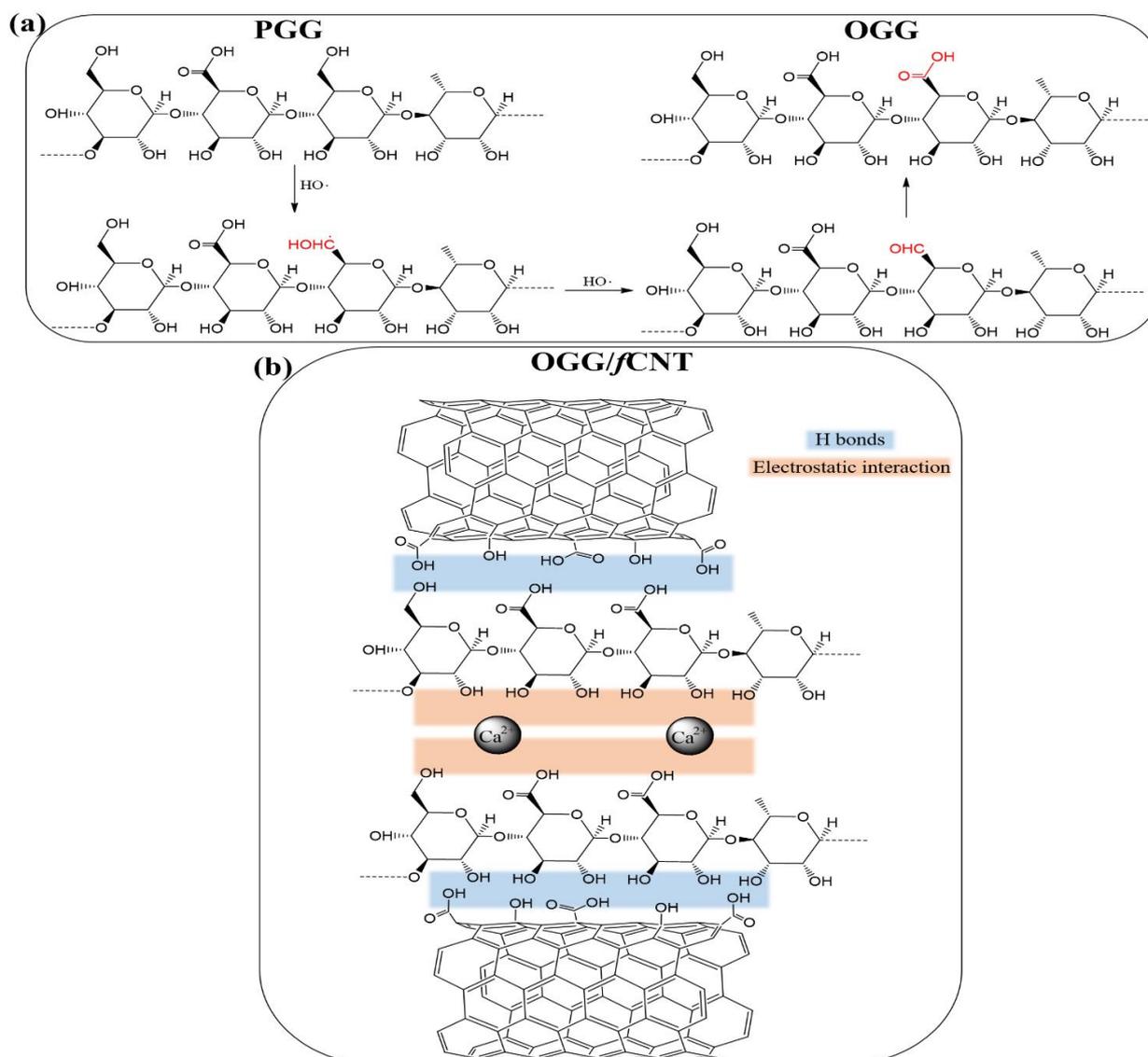
Scheme 1. (a) The overall reaction of GG oxidation in the presence of H_2O_2. (b) Demonstration of structure and interactions in double networked OGG/*f*CNT hydrogels.

In this study, a new hydrogel was successfully developed with oxidation gellan and *f*CNT. The DN structure was formed by the ionic cross-linking method, including both Ca^{2+} cross-linking and hydrogen bonding. The results obtained from the modulus and $T_{gelation}$ were found to be promising for the prepared hydrogel, as it has a wide range of use and adjustable properties. FTIR, Zeta, and contact angle measurements confirmed the successful incorporation of carboxyl groups into GG molecules. The OGG-*f*CNT hydrogel exhibited a higher wettability with increasing oxidation amount.

Moreover, the gelation temperature and zeta potential of OGGs significantly changed depending on *f*CNT addition and degree of oxidation. The added *f*CNT greatly influenced the morphology of fabricated OGG-

*f*CNT hydrogel. The OGG$_3$-*f*CNT hydrogel showed a high modulus compared to 4895 Pa for OGG without *f*CNT and was 1389 Pa. As a result, this study presents innovative hydrogel composed of OGG and *f*CNT that can be used as biomaterials in tissue engineering and as carriers in various drug delivery systems as potential applications.

It is believed that in future studies, GG-based hydrogels obtained with the addition of CNT, which is known to be conductive, will also take part in self-healing strain sensor studies and will be a strong candidate as a new material for use in sensitivity studies against sensitive movements such as pulse, which is one of the requirements of this field.

Acknowledgments

Conflicts of interest

The authors state that they did not have any conflict of interests.

References

[1] Mondal S., Das S., Nandi A.K. , A review on recent advances in polymer and peptide hydrogels, *Soft Matter*, 16 (2020) 1404–1454.

[2] Dorishetty P., Dutta N.K., Choudhury N.R., Bioprintable tough hydrogels for tissue engineering applications, *Advances in Colloid and Interface Science,* 281(102163) (2020) 1-23.

[3] Yang J., Zhang Y.S., Yue K., Khademhosseini A. , Cell-laden hydrogels for osteochondral and cartilage tissue engineering, *Bone Research,* 5(17014) (2017) 1–20.

[4] Bonifacio M.A., Cometa S., Cochis A., Gentile P., Ferreira A.M., Azzimonti B., Procino G., Ceci E., Rimondini L., De Giglio E. , Antibacterial effectiveness meets improved mechanical properties: Manuka honey/gellan gum composite hydrogels for cartilage repair, *Carbohydrate Polymers,* 198 (2018) 462–472.

[5] Kouhi M., Varshosaz J., Hashemibeni B., Sarmadi A., Injectable gellan gum / lignocellulose nano fi brils hydrogels enriched with melatonin loaded forsterite nanoparticles for cartilage tissue engineering : Fabrication, characterization and cell culture studies, *Materials Science & Engineering C,* 115(111114) (2020) 1–12.

[6] Palumbo F.S., Federico S., Pitarresi G., Fiorica C., Giammona G. , Gellan gum-based delivery systems of therapeutic agents and cells, *Carbohydrate Polymers,* 229(115430) (2020) 1-19.

[7] Liu S., Qiu Y., Yu W., Zhang H. , Highly Stretchable and Self-Healing Strain Sensor Based on Gellan Gum Hybrid Hydrogel for Human Motion Monitoring, *ACS Applied Polymer Materials,* 2(3) (2020) 1325–1334.

[8] Zhang X., Pan Y., Li S., Xing L., Du S., Yuan G., Li J., Zhou T., Xiong D., Tan H., Ling Z., Chen Y., Hu X., Niu X. , Doubly crosslinked biodegradable hydrogels based on gellan gum and chitosan for drug delivery and wound dressing, *International Journal of Biological Macromolecules,* 164 (2020) 2204–2214.

[9] Osmałek T.Z., Froelich A., Jadach B. , Rheological investigation of high-acyl gellan gum hydrogel and its mixtures with simulated body fluids, *Journal of Biomaterials Applications*, 32(10) (2018) 1435–1449.

[10] Mohammadinejad R., Kumar A., Ranjbar-Mohammadi M., Ashrafizadeh M., Han S.S., Khang G., Roveimiab Z. , Recent Advances in Natural Gum-Based Biomaterials for Tissue Engineering and Regenerative Medicine: A Review, *Polymers,* 12(176) (2020) 1-38.

[11] Wang D., Li C., Gong Y., Wang C., Lai R.C., Su K., Zhang F., Wang D. , An improved injectable polysaccharide hydrogel : modified gellan gum for long-term cartilage regeneration in vitro, *Journal of Materials Chemistry,* 19(14) (2009) 1968–1977.

[12] Türk S., Altınsoy I., Çelebi Efe G., Ipek M., Özacar M., Bindal C. , 3D porous collagen/functionalized multiwalled carbon nanotube/chitosan/hydroxyapatite composite scaffolds for bone tissue engineering, *Materials Science & Engineering C*, 92 (2018) 757–768.

[13] Lu Y., Zhao X., Fang S. , Characterization, Antimicrobial Properties and Coatings Application of Gellan Gum Oxidized with Hydrogen Peroxide, *Foods*, 8(31) (2019) 1–12.

[14] Wang P., Luo Z., Xiao Z. , Preparation, physicochemical characterization and in vitro release behavior of resveratrol-loaded oxidized gellan gum/resistant starch hydrogel beads, *Carbohydrate Polymers*, 260(117794) (2021) 1-10.

The effect of strontium carbonate additive on the production of graphitic boron nitride using modified O'connor method

Muhammed ÖZ [1], * (ID)

[1]*Bolu Abant İzzet Baysal University, Department of Chemistry and Chemical Processing Technology, Bolu/ TURKEY*

Abstract

In this study, it was investigated that whether the graphitic boron nitride was successfully synthesized by adding strontium carbonate (within the different amount of 20-40%) using O'Connor method which is the one of the solid-state methods or not. Fourier transform infrared spectroscopy FTIR, powder X-ray diffraction (XRD), energy-dispersive X-ray spectroscopy (EDS) and scanning electron microscopy (SEM) methods were used to clarify the formation of boron nitride structure. Inter and intra-layer BN vibration movements of gBN were determined by FTIR method. Also, peaks belonging to the gBN formation were observed in the XRD analysis, and the distance between the layers was found to be close to both the theoretical values and data of commercially produced BN structure. The morphological examination was performed with SEM, and the planar properties of structure were determined. In addition, the EDS measurements supported that the crystal structure of powders include only nitrogen and boron atoms. In the light of these methods, it has been determined that the graphitic BN was able to synthesize at a lower temperature and in a more regular crystal structure compared to the O'Connor method with strontium carbonate additives.

1. Introduction

Boron chemicals have been great importance in last two decates since the recent studies have intensified on these compounds that are produced from boron. At the same time, the boron compounds have a wide range of uses in many branches of industry, especially nuclear field, defense industry, jet and rocket fuel, soap, detergent, solder, photography, textile dyes, glass fiber and paper industry [1-3]. Boron nitride is a syththetic compound of boron and nitrogen atoms that are isoelectronic to the carbon analogue when they form a compound. Both are adjacent to the carbon atom in periodic table with atomic numbers 5 and 7, respectively. Boron nitride is an extraordinary synthetically produced chemical in the field of materials science due to its bonding behavior and can be found in many different crystal structures [4].

Boron nitride (in all its forms), which is naturally encountered in trace amounts, is a commercially valuable compound for industrial applications like other boron compounds because of its unique chemical and physical properties [4-6]. Moreover, the graphite-like BN is a technologically important compound due to its properties such as high temperature stability, low dielectric constant, high thermal conductivity, high mechanical strength, hardness and chemical inertness [3]. It is synthesized by the solid-state reaction of boron compounds (boron oxide, boric acid, metal borates) and nitrogen compounds (urea, melamine, cyanamide etc.) at high temperatures (> 1600 ° C) in nitrogen or ammonia gas atmosphere [7-8].

The layered-planar structure of BN is named as hexagonal crystalline morphology and is similar to graphite; for this reason, it is often referred to as "white graphite". In addition, the boron nitride has various crystal structures depending on the bond hybridization between boron and nitrogen atoms. Graphitic boron nitride (gBN), hexagonal boron nitride (hBN), turbostratic boron nitride (tBN), amorphous boron nitride (aBN) and rhombohedral boron nitride (rBN) are sp^2 hybridized while the cubic boron nitride (cBN) or borazone, and wurzite boron nitride (wBN) are sp^3 hybridized [4]. Besides, there are BN classifications according to the production methods such as ion-bombed boron nitride (iBN), boron nitride (eBN), amber boron nitride (aBN), Showa Denko's cubic

boron nitride (sBN), pyrolytic boron nitride (pBN) [4,5,9].

Various chemical additives, mostly metal salts, are used during the synthesis of graphitic BN, [10-12]. For example, the effects of metal carbonates on hBN layered structures are discussed in detail by Öz et al. [10-12]. In this scope, the metal carbonates were used to reduce the activation energy to increase the crystallinity, crystallite size and yield of hBN samples. It has been found that the critical properties of hBN synthesized by the applied methods were noted to increase significantly in the presence of metal carbonates [8-11]. In this study, synthesis of gBN was performed using the modified O'Connor method [7] by addition of strontium carbonate into the reaction mixture. The experimental findings showed that the positive effect of strontium carbonate addition on the crystal structure of gBN was determined at the relatively lower preparation temperature than that of O'Connnor method.

2. Materials and Methods

Graphitic boron nitride was synthesized by using 1/2 ratio of boron oxide (Fluka, 97 %)-urea (Fluka, 99 %) mixture with the addition proportions (20, 30 and 40%) of $SrCO_3$ (Alfa Aesar, 99.9%) according to the O'Connor method. In the first stage, boron oxide, urea and $SrCO_3$ were mixed homogeneously and pre-heat treatment was applied at 200 ° C for 2 hours. In the second stage, the intermediate product obtained in the first step was annealed under ammonia (Linde Co. 99.9%) gas atmosphere at 1450 ° C for 3 hours. In the third stage, the room-temperature-cooled samples were purified by heating in 100 mL 1 M HCl (Merck, 37%) solution. In the last stage, the structure of products was examined using Fourier transform infrared spectroscopy (FTIR), powder X-ray diffraction (XRD), energy-dispersive X-ray spectroscopy (EDS) and scanning electron microscopy (SEM) methods. KBr discs containing 2 % sample were prepared, and the vibration movements in the range of 400-4000 cm⁻¹ were determined with Shimadzu 8400S FTIR spectrometer. The powder gBN was investigated by XRD (a Rigaku Multiflex + XRD 2kW diffractometer with a CuKα target) in the range of 10º and 90º at 2θ angles. Surface imaging analysis and EDS were performed with JEOL JST-6400 SEM after gold coating of the products.

3. Results and Discussion

The methods that used for the synthesis of boron nitride have great importance since the additives used as the dopant in mixture lead to discrete properties.

Constructive effect of metal carbonates on BN formation has signficaty been deduced in literature when the metal carbonates are used as catalysts [8-11]. In these previous studies, the formation of layered structure and growth of graphitic boron nitride particles in the presence of metal carbonates were explained by the catalytic effect, however the catalyst-solvent effect was not discussed before. This effect has been determined in the previous studies to improve the synthesis positively depending on the increament of surface area and especially solvent-solute balance of additive [8-12]. It is anticipated that the successful results were obtained with the use of carbothermic methods [13, 14]. Therefore, in this study, the $SrCO_3$ compound which was not previously used as additive was preferred due to the positive contribution of metal carbonates on the synthesis of BN [10]. In this context, the $SrCO_3$ was added in different molar ratios (20, 30, and 40%) during the synthesis of BN to determine lowest concentration for the formation of highly crystalline boron nitride. The instrumental methods such as the FTIR, XRD and SEM were used to impress the formation of BN. Meanwhile, the first identifation of samples has been investigated by the FTIR where the chemical bond vibrational modes of BN structure are apparently designated in this analysis method. The gBN with the form of sp^2 hypritized hexagons adjacent to each other is settled as lamellar or multilayer structure. Therefore, in the spectra two main peaks derived form the in-plane and out of plane interactions were observed at the wavenumbers of 1400 cm⁻¹ and 800 cm⁻¹, respectively [15]. Moreover, the synthesized samples have weak end-groups peaks derived from the N-H and B-OH vibrational modes at approximately 3500 cm⁻¹ accompanied to main vibrational modes of B-N (Figure 1). In addition, the crystalline morphology can be estimated from the FTIR spectra. Accordingly, Fig. 1 indicated the hexagonal (graphitic) form due to the range of the main peaks. In contrast to hexagonal form, the cubic morphology included the sharp peak in the wave number range of 1000-1100 cm⁻¹. In the spectra, the peak identified for cubic form did not exist while the observed peak values indicated the graphitic form as the conformation of gBN formation. The values are in accordance with the range given in the literature [16].

XRD crystallography is a method used to study the atomic and molecular structure of a crystal. Besides, the chemical bonds, irregularities in the crystal structure, distances between layers, lattice parameters and average positions of the atoms in the crystals can easily be determined by measuring the angles and amplitudes of diffracted beams.
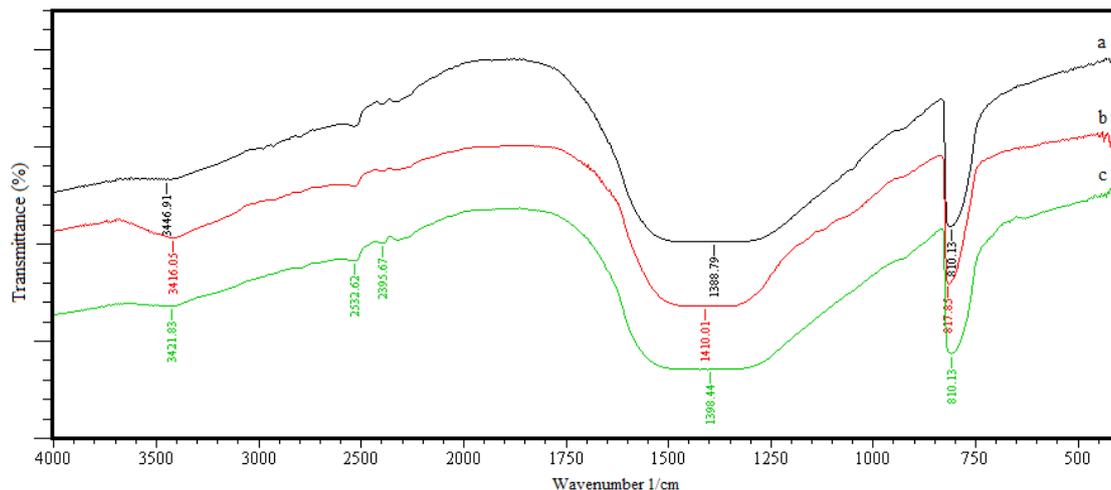
Figure 1. FTIR spectra of gBN obtained in presence of SrCO₃ additive: a) 40 %, b) 30 %, c) 20 %,

In this respect, the XRD analysis was performed to clarify the fundamental crystallographic properties such as the lattice parameters, inter-layer distance and crystal plane alignment of gBN samples. Meanwhile, the crystallite composition of products synthesized by adding SrCO₃ was examined and compared with the ICDD 34-421 card containing the main peaks of Miller indices of pure gBN [17]. The original XRD diffractogram of gBN structure includes the characteristic planes: 002, 100, 101, 102, 004, 110 and 112 [18]. The presence of whole identified planes in the sample diffractograms was the evidence of gBN formation (Figure 2). As a result of the imrovement of gBN crystal structure, the corresponding peak intensities were found to increase considerably when the dopant level of SrCO₃ concentation was chosen 20 % and more.
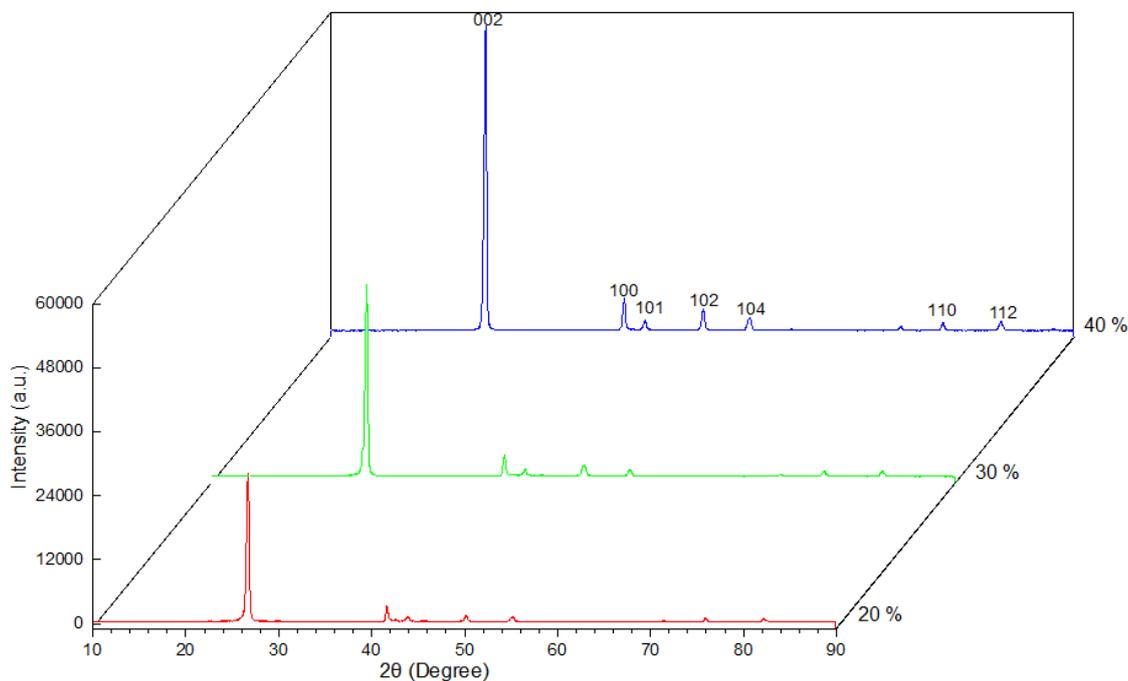
Figure 2. XRD diffractogram of gBN samples synthesized in presence of 20 %, 30 % and 40 % SrCO₃

In addition, the XRD experimental findings enable us to calculate the lattice cell parameters from the least squares method with the measured inter-layer distance "*d*" values and *hkl* planes for hexagonal unit cell structure [10]. The lattice parameters for the hexagonal (graphitic) systems have "a" and "b" values that are equal to each other, and one can see the calculated lattice values of "*a*", "*b*", "*c*" and "*d*" in Table 1.

According to the table, the results of lattice parameter calculations were found to be close to the original literature values ($a = b$=0.2504 nm, c = 0.6656 nm, d = 0.3328 nm) for all the gBN samples produced in presence of $SrCO_3$ (Table 1) [19]. The samples preapred by the $SrCO_3$ addition levels of 20 % and 40 % possessed closer values while the compound produced by 30 % had sligtly higher than the literature values (Table 1). Consequently, the good aggrements were obtained in terms of lattice parameters when 20 % or more strontium carbonate was used.

Table 1. Lattice parameters and average rain size values of gBN

		Amount of additive (%)		
		20	30	40
Lattice Parameters (nm)	a	0.2504	0.2506	0.2504
	c	0.6656	0.6676	0.6658
	d	0.3328	0.3338	0.3329
Average Grain Size (nm)		56,90	44,25	92,00

XRD measurements are also used to calculate crystallite and average grain size parameters by Debye-Scherrer equation (Eq. 1)

$$L = \frac{K \; \lambda}{\beta \; \cos \; \theta} \qquad \text{Eq. (1)}$$

where K is the shape factor (which is 0.941), L is the average grain size, λ is the wavelength, B is the FWHM of the Bragg peak and θ is the Bragg angle [20]. It is determined that the grain sizes of gBN samples appreciated as accrual at the amount of $SrCO_3$ that the sample prepared by 40 % dopant level exhibits the highest average crystallite size among the samples. Moreover, 20 % addition level of $SrCO_3$ into the sample mixture also improved the grain size in contrast to undoped or plain mixtures.

The scanning electron microscopy (SEM) method was applied to clarify the surface morphology of $SrCO_3$ added gBN samples after the purification process [21]. SEM images include homogenous bulk gBN as shown in Fig. 3 and the structure consists of 1-3 µm particles formed from the coagulation of sub-particles. The average grain sizes of sub-particles calculated from the XRD diffractograms were found as approximately 100 nm where 10 to 30 small particles cause the greater particles by the agglomeration as well in SEM images. The SEM images include the hexagonal layaered gBN with uniform nature while there is not any strontium carbonate traces in the views as well as EDS measurements (Fig. 4). Besides, one can deduce from

the EDS measurements that the samples comprised of only boron and nitrogen elements while the gold existance is mainly derived from the coating process.
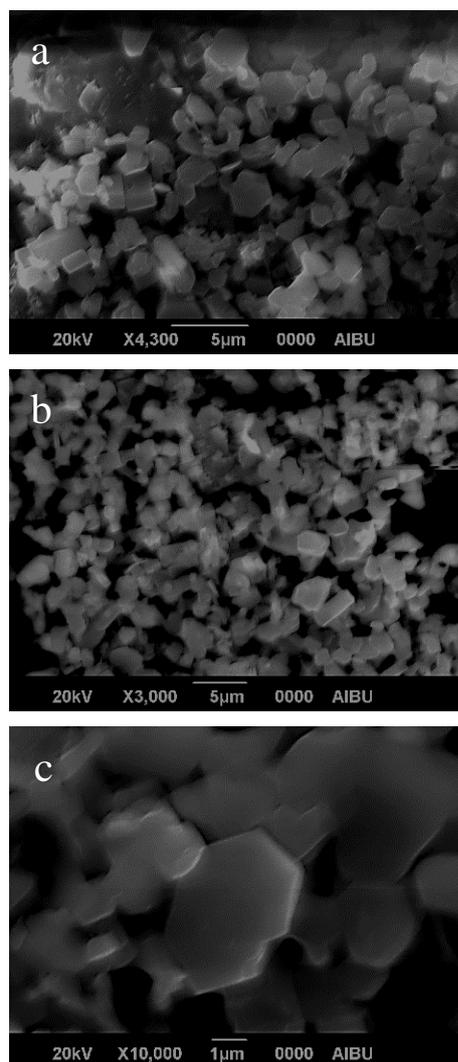
Figure 3. SEM images of the gBN synthesized in the presence of $SrCO_3$ with different magnifications a) 4300, b) 3000 and c) 10000 fold.
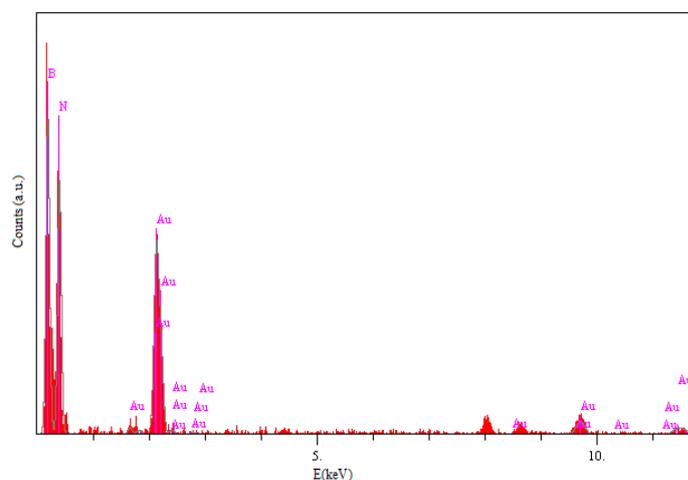
Figure 4. The EDS of the gBN synthesized in the presence of $SrCO_3$

3. Conclusion

In this study, it was aimed to determine both the effect of $SrCO_3$ additives on gBN formation and the lowest dopant amount for positively contribution to the ordered structure. In this context, the gBN samples were prepared by adding different concentration level of $SrCO_3$ (from 20% to 40% additive) at the temperature of 1450 °C by means of the O'Connor method. Powder samples have extensively been characterized by the stanrd characterization techniques such as the FTIR, XRD and SEM instrumental methods. According to all the experimental results obtained, it was determined that the favorable $SrCO_3$ contribution was in a range of about 20-40%.

According to FTIR studies, the presence of $SrCO_3$ content in the gBN crystal matrix caused an increase in the strength of the covalent bonds between boron and nitrogen atoms and a strong B-N lattice vibration in the flat plane. The absorbtion peaks at around 800 cm^{-1} and 1400 cm^{-1} in FTIR spectra verified the formation of the graphitic morphology. Besides, a wide peak was observed at around 3450 cm^{-1} wavenumber assigned for the N-H and O-H groups at the end of chains as a signal for the lateral structure.

Experimental findings from the XRD patterns show that the presence of $SrCO_3$ powder activates the gBN formation to overcome the internal stress in the crystalline structure (meaning the reduction of residual stresses). The lattice parameters determined from the XRD results for all the materials have been calculated and compared to the literature findings. It was observed that all the comparision results were found to be in good aggremet with each other. The inter-layer distance of hBN samples synthesized in this study was oserved to be approximately 0.333 nm that was attributed to close to the theoretical value. Moreover, the $SrCO_3$ content improving the crystallinity of gBN converts the crystal structure to the highly graphitic nature. Thus, new crsytal structure exhibitied relatively lower temperatures as compared to the material synthesized by O'Connor method (at 1600 °C). At this point, the dopant level affected positively not only the lattice parameters but also the grain size related to the formation of graphitic BN. In this respect, the highest crystal size of aproximately 92 nm was obtained in case of 40 % $SrCO_3$ additive level.

Acknowledgment

Conflicts of interest

The authors state that did not have conflict of interests.

References

[1] Mishima O., Era K., Electric Refractory Materials, ed. Y. Kumashiro, Marcel Dekker, Inc., New York (2000), 495.

[2] Lin Y., Connell J. W., Advances in 2D boron nitride nanostructures: nanosheets, nanoribbons, nanomeshes, and hybrids with graphene, *Nanoscale*, 4(22) (2012) 6908-6939.

[3] Zhi C., Bando Y., Tang C., Golberg D., Boron nitride nanotubes, *Materials Science and Engineering: R: Reports*, 70(3-6) (2010) 92-111.

[4] Paine R. T., Narula C. K., Synthetic routes to boron nitride, *Chemical Reviews*, 90(1) (1990) 73-91.

[5] Haubner R., Wilhelm M., Weissenbacher R., Lux B., High performance non-oxide ceramics II, in Boron Nitride Properties, Synthesis and Applications. Structure and Bonding Series, vol. 102 Springer, Berlin, (2002), 1–45.

[6] Kimura Y., Wakabayashi T., Okada K., Wada T., Nishikawa H., Boron nitride as a lubricant additive, *Wear*, 232(2) (1999) 199-206.

[7] O'connor T. E., Synthesis of boron nitride, *Journal of the American Chemical Society*, 84(9) (1962) 1753-1754.

[8] Thomas J. R., Weston N. E., O'connor T. E., Turbostratic1 boron nitride, thermal transformation to ordered-layer-lattice boron nitride, *Journal of the American Chemical Society,* 84(24) (1962) 4619-4622.

[9] Niedenzu K., Boron- Nitrogen Compounds, Academic Pres. Inc., Springer Verlag, (1965), 147-153.

[10] Öz M., Saritekin N. K., Bozkurt Ç., Yildirim G., Synthesis of highly ordered hBN in presence of group I/IIA carbonates by solid state reaction, *Crystal Research and Technology*, 51(6) (2016) 380-392.

[11] Öz M., Temperature dependency on crystallinity and durability of mineral dolomite doped nanocrystalline hexagonal boron nitride, *Journal of Inorganic and Organometallic Polymers and Materials*, 30(3) (2020) 758-766.

[12] Öz M., Bozkurt Ç., Kanbur Yılmaz B., Yıldırım G., Effect of borates on the synthesis of nanoscale hexagonal boron nitride by a solid-state method, *Microscopy Research and Technique*, 84(11) (2021) 2677–2684.

[13] Hubáček M., Sato T., Preparation and properties of a compound in the BCN system, *Journal of Solid State Chemistry*, 114(1) (1995) 258-264.

[14] Bartnitskaya T. S., Lyashenko V. I., Kurdyumov A. V., Ostrovskaya N. F., Rogovaya I. G., Effect of lithium on structure formation of graphite-like boron nitride with carbothermal synthesis, *Powder Metallurgy and Metal Ceramics*, 33(7) (1995) 335-340.

[15] Öz M., Characterization of Caesium Carbonate-Doped Porous Non-Activated Graphitic (Hexagonal) Boron Nitride and Adsorption Properties, *Arabian Journal for Science and Engineering*, 46(6) (2021) 5671-5680.

[16] Hagio T., Nonaka K., Sato T., Microstructural development with crystallization of hexagonal boron nitride, *Journal of Materials Science Letters*, 16(10) (1997) 795-798.

[17] Warren B. E., X-ray Diffraction, Courier Corporation, Dover Publications Inc., New York, (1990), 20-80.

[18] Pease R. S., An X-ray study of boron nitride, *Acta Crystallographica*, 3 (1952) 356-361.

[19] Hubáček M., Ueki M., Chemical reactions in hexagonal boron nitride system, *Journal of Solid State Chemistry*, 123(2) (1996) 215-222.

[20] Scherrer P., Bestimmung der Größe und der inneren Struktur von Kolloidteilchen mittels Röntgenstrahlen, Nachrichten von der Gesellschaft der Wissenschaften zu Göttingen Math.-Phys. Kl., 26(2) (1918) 98–100.

[21] Shimomura J., Funahashi T., Koitabashi T., Electron microscopy of hexagonal boron nitride powder, *Journal of Materials Science*, 30(12) (1995) 3193-3199.

Major and trace element enrichment in Kızıldere formation (Arsuz-Hatay)

Esef KILINÇ [1], * 🆔 , *Meryem YEŞİLOT KAPLAN* [2], 🆔

[1]*Adıyaman University, Technology Transfer Office, Engineering Faculty, Adiyaman/ TURKEY*
[2]*Iskenderun Technical University, Department of Petroleum and Natural Gas Engineering, 31200, Iskenderun, Hatay/ TURKEY*

Abstract

The study area is in the Arsuz - HATAY region and the geochemical properties and deposition environment of the claystones in the Kızıldere Formation (Middle - Upper Miocene) were investigated in this study. Kızıldere Formation, which is common in Arsuz and İskenderun (Hatay) regions, has both bedrock and reservoir rock characteristics. It generally consists of a sequence of medium bedded sandstones and thin to medium bedded claystones. The average concentrations of major and trace elements in the samples taken from ten different points of the Arsuz region were determined (V-1180.65 ppm, Ni-219.83 ppm, Cr-149.26 ppm, Co-19.45 ppm, Cu-22.63 ppm, Rb-42.96 ppm, As-8.40 ppm, Zn-54.47 ppm, Sb- 0.61 ppm, Mo-1.28 ppm, Cd - (- 0.71) ppm, Pb- 5.68 ppm, U-1, It is 35 ppm, Ba-171.15 ppm, Li-24.64 ppm, Cs-3.06 ppm, S-325.48 ppm). V / Ni, Ni / Co, V (V + Ni), V / Cr, (Cu / Mo) / Zn ratios in claystones and increases in concentrations in trace elements (e.g. V, U, Ni) indicates that it precipitated in the marine-anoxic environment. In addition, in the distribution mapping drawn according to the trace elements Ni-U-Cu-Zn in the region, the paleo-environment changes with organic matter conservation were determined.

1. Introduction

The aim of the research is to determine the environmental conditions in Arsuz (Hatay) region by investigating the units in Kızıldere Formation. The study area includes of İskenderun-Arsuz of Hatay (Figure 1). Generally, field studies, petrography and geochemical analyzes are performed to determine the environmental conditions of a region [1]. Some of the analyzes are done to determine the amount of organic matter and are carried out to determine the cause of trace element enrichment in the environment conditions.

XRF (X-Ray Fluorescence Spectrometer), ICP-MS (Inductively Matched Plasma Mass Spectrometry) and AAS (Atomic Absorption Spectroscopy) analysis methods are used to determine trace elements [2]. The amount of trace elements in the environment, which are present together with the hydrocarbon in the samples in the research area, are determined with the results of trace element analysis, This data used in determining the oxic-anoxic-euxinic state environment is interpreted and concluded that it is suitable / unsuitable for the formation of hydrocarbon.

Trace elements are described as elements that are mostly less than 0.01% in amount in rocks. Interpretation of environmental conditions is determined by the amount of elements with trace element analysis and it is possible to identify new geothermal energy resources, source rocks that produce oil and natural gas, and new mineral deposits. In many published source rock potential studies, it has been observed that trace element enrichments are directly related to the high production of organic matter in the region [1, 2]. Environmental properties can also be determined with trace element analysis [2]. Studies that reveal the reservoir rock characteristics of the region where the Kızıldere Formation is located are related to geological, tectonic and sedimentological areas, but there is no study on the geochemical examination of the elements and determination of the source rock.

The terms oxic, anoxic/suboxic or euxinic are used depending on the amount of O_2 in environmental classifications. Anoxic environment is the most effective in enrichment of organic matter and H_2S is not present in the water column in this environment.

Researchers investigating the changes of organic matter under reducing conditions proved that the protection of organic matter increases under anoxic conditions where oxygen decreases [3, 4]. There are two approaches regarding the relationship between sedimentation rate or burial rate and the protection of organic matter in their studies by different researchers. The first of these is the increase in the protection of organic matter based on the increase in sedimentation rate. The other is the increase in organic matter due to the slow sedimentation rate [5].

The geochemical conditions of the depositional environment can be determined from the enrichment of trace metals and anoxic/euxinic environment correlations. If there is no Mo enrichment in the environment with U and V enrichment, it is interpreted that the environment is in anoxic/suboxic depositional conditions without free H_2S. Conversely, sediments with enrichments in U, V and Mo indicate euxinic conditions at the sediment-water interface or in the water column. Mo and Zn enrichments are related to TOC (Total Organic Carbon) and can be controlled very strongly by the environmental conditions of sedimentation [6].

It is known that organic matter accumulation does not occur with a single control mechanism. The redox conditions of the depositional environment can be oxic, suboxic, anoxic or euxinic, depending on the amount of oxygen in the environment. Trace element enrichments increase according to organic matter accumulation as a result of the decrease in the amount of oxygen in the environment. Trace elements such as Mo, Ni, Co, Cu, V, U, Th and Cr have been used in many studies to determine the paleo-redox environmental conditions.

The Miocene sequence unconformably deposited on ophiolites started with coarse clastics (Kalecik Formation). Reef limestones (Horu Formation) are lenticularly observed over the Kalecik Formation and the Kızıldere Formation consisting of a later sandstone-shale sequence has been deposited [7, 8, 9, 10].

Figure 1. Location map of the study area.

During the Messinian period, evaporitic sediments (Haymaseki Member) were deposited in the Kızıldere Formation due to the sea regression, and then the marine clasts of the Aktepe Formation were deposited in the region with transgression. The stratigraphic section of the region is given in Figure 2. Geological maps and fault lines are not shown since the samples were taken from near the surface.

Kızıldere Formation was named by Schmidt [7]. Kozlu [8] used "the Kızıldere Formation" name by adding the Miocene sequence located in the south of the region. The Kızıldere Formation consists of the sequence of gray-colored medium-thick layered sandstone and shale layers. Carbonized plant origin clastics are observed in almost every layer [11, 14]. It has been determined that the formation shows the source rock feature that can form an oil system in the region according to the total organic carbon and main-trace element contents [12, 13].

Figure 2. Generalized stratigraphic section of the region [14]

2. Material and Method

2.1. Field description of Kızıldere formation

The study area was deposited in the Neogene period and is located in Konacık, Tülek and Işıklı in Arsuz-İskenderun basin. Kızıldere Formation (Middle-Late Miocene) is typically observed in Konacık (Arsuz-HATAY) region. In the Kızıldere Formation, where sand and clay sequences are common, gray-yellow colored sandstones are medium-thick bedded between 10-50 cm and gray-colored claystones are thin-medium bedded between 2-30 cm (Figure 3A-B). The sequence of sandstone and claystone overlies the layered jibs deposits and the layer thicknesses of the jibs are 5-15 cm. The claystone layers are generally thinning from bottom to top, layer thicknesses on the lower parts of the profiles reach up to 102 cm. Tectonic cracks are commonly observed in the formation due to the effective post-Middle Miocene tectonism (Figure 3-B). Plant residuals can be seen with marls and jibs layers.
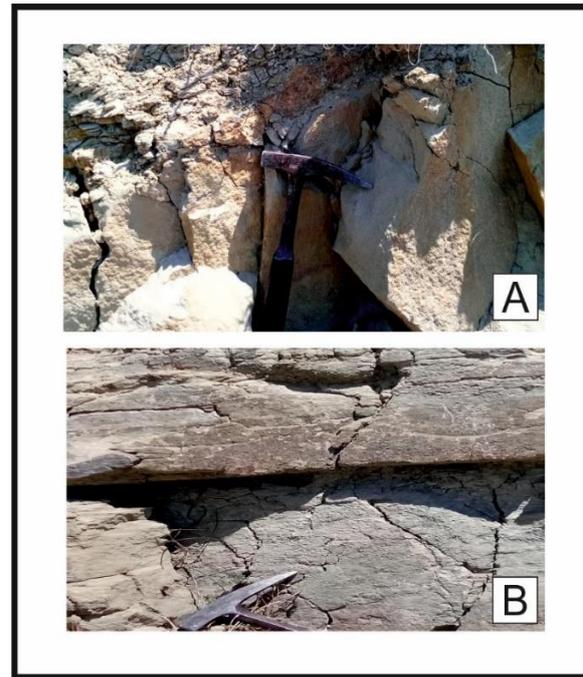
Figure 3. The field descriptions of the Kızıldere Formation, (A) medium-thick bedded, cracked sandstone layers sequenced claystone (B) cracks formed by tectonism in claystone-sandstone.

2.2. Trace elements and environmental descriptions of Kızıldere formation

Trace element concentrations in organic material rich sediments have been studied by many researchers [13, 15, 16, 17]. Consumption and enrichment of some elements such as V, Mo, Ni, Ba in sediments depend on environmental conditions. Changes in Ni, Co, Cu, U and V elements in Kızıldere Formation claystones have similarities.

Trace elements such as U, Zn, Ni and Cu and TOC (Total Organic Carbon) are enriched in the formation. Table 1 shows the main and trace elements in Kızıldere sandstones. The enrichment of U, V, Zn, Ni, Mo and Cu in claystones is an indication of anoxic conditions. It is known that the elements sensitive to redox are U, V and Mo, and other enriched elements depend on organic matters. U and Mo enrichments are indicators of oxygen consumption according to some researchers [15].

The U (Uranium) average values of the Kızıldere Formation are 1.224 ppm. Soua [15] compared the values in different claystone samples and indicated the trend of these values to an anoxic environment at the water-sediment interface of the formation. Pedersen and Calvert's [16] "productivity" model fits these Kızıldere Formation claystone data, and the increase in redox sensitive (U and V) and productivity (Ba, Cu and Ni) elements form the basis of the model.

Table 1. Main (Ca, K, Mg, Na) and trace (Rb,Cu, Cr, As, Zn, Sb, Co, Mo, Cd, Pb, U, Ba, Li, Cs, S, Ni, V) element contents of Kızıldere Formation claystones [17].

Sample	KD 1	KD 6	KD 7	KD 8	KD 9	KD 11	KD 13	KD 14	KD 15	KD 16	Mean
Ca (ppm)	18830	62870	69480	72410	93540	95290	102900	59510	54130	63110	74804.4
K (ppm)	48.23	8987	8658	7541	6832	7617	7492	7220	11070	7992	8156.56
Mg (ppm)	71630	29110	61290	36500	32670	33990	34350	23040	49580	42690	38135.6
Na (ppm)	407.2	12960	8186	7680	5221	7873	6959	17890	6500	11480	9416.56
Rb (ppm)	0.52	40.89	31.53	58.65	42.81	43.76	46.13	42.58	38.49	41.77	42.96
Cu (ppm)	134.49	20.91	13.09	34	26.43	31.31	21.66	21.65	17.01	17.56	22.63
Cr (ppm)	140.78	151.17	149.68	186.63	173.52	135.47	138.6	142.16	124.53	141.61	149.26
As (ppm)	1.68	7.43	9.19	8.25	12.02	10.46	7.91	8.61	5.13	6.56	8.4
Zn (ppm)	61.24	49.51	36.57	70.16	54.47	65.32	63.01	53.35	50.68	47.22	54.47
Sb (ppm)	0.21	0.62	0.57	0.67	0.78	0.9	0.5	0.49	0.41	0.52	0.61
Co(ppm)	189.24	22.18	15.02	17.63	18.23	19.27	19.56	25.67	23.02	14.46	19.45
Mo(ppm)	0.8	3.33	0.36	2	0.61	1.53	0.29	0.37	0.96	2.07	1.28
Cd(ppm)	-0.66	-0.68	-0.8	-0.61	-0.75	-0.55	-0.73	-0.78	-0.76	-0.7	-0.71
Pb(ppm)	-2.34	3.43	4.08	7.91	11.25	8.75	4.22	4.47	3.15	3.82	5.68
U(ppm)	0.12	1.61	0.94	2.13	1.11	1.24	1.2	1.07	1.33	1.49	1.35
Ba(ppm)	8.17	158.96	213.78	172.3	218.72	199.73	134.54	126.45	138.56	177.3	171.15
Li(ppm)	6.25	24.63	18.35	31	25.52	25	25.98	24.8	23.14	23.37	24.64
Cs(ppm)	0.08	3.26	1.63	4.47	2.95	2.76	3.34	2.57	3.18	3.34	3.06
S(ppm)	-67.19	341.38	34.6	354.48	377.16	403.41	280.05	269.35	272.77	286.1	325.48
Ni(ppm)	1809.05	212.41	149.79	249.63	185.84	235.56	249.36	292.49	200.15	203.21	219.83
V(ppm)	2482.95	1116.18	1104.31	1285.95	1175.41	1237.89	1222.9	1343.68	976.89	1162.63	1180.65

The average value of Cd (cadmium) in claystones is -0.70 ppm. This amount is below the Cd threshold. According to Pattan and Pearce [18], the negative result of Cd amounts in the measurements in the samples taken from the study area indicates that the environment is not oxic.

Many researchers have used Ni/Co, V/Cr and V/(V+Ni) indices to determine paleo-redox conditions. Jones and Manning [19] suggested that Ni/Co ratios <5 indicate oxic conditions, 5-7 disoxic conditions and> 7 anoxic-suboxic conditions. V/Cr ratios were determined to be <2 for oxic conditions, 2–4.25 for disoxic conditions, and> 4.25 for suboxic to anoxic conditions. Lewan (1984) noted that the V/(V+Ni) value should be greater than 0.5 for organic matter deposited under euxinic conditions. The average of Ni / Co, V/Cr and V/(V+Ni) ratios in Kızıldere Formation claystones are 11.45, 7.44 and 0.84, respectively, and all values indicate anoxic conditions. Kızıldere claystones were formed in anoxic environment according to the graph of Ni /Co and /(V+Ni) values [20, 21].

Ni/Co ratio is widely used to determine paleoredox conditions [19]. The average of Ni/Co ratios in Kızıldere claystone is 11.25 and indicates anoxic conditions (Figure 4.A-B).

Molybdenum (Mo), used as a indicator for depositional conditions, is associated with humic acids in organic matter. Mo concentrations increase with increasing anoxic conditions and the enrichment of Mo depends on the amount of organic matter and sulfidic conditions of the environment. According to Wedepohl [22], the average Mo value in claystones deposited under anoxic conditions is 2.6 ppm, and there is a Mo concentration close to this value in the Kızıldere Formation claystones and changes between 0.29-3.33 ppm (Figure 4.A).

Similarity is observed in Kızıldere claystones in concentrations measured from whole rock analyzes and enrichments in elements (Ni-Zn-Cu-U-V) which are the indicator of redox environment. The environmental sensitivities of these elements are compatible in all samples in terms of increase and decrease. Figure 4.C-D shows the variation of these elements.

There is usually a relationship between V/(V-Ni) and Ni/Co, indicating environmental properties [20]. In the graph shown in Figure 4.E, it is observed that Kızıldere claystones were deposited in anoxic environment.

Hallberg [23] noted that the Cu/Zn and (Cu+Mo)/Zn ratios are redox parameters. According to Hallberg [23], low Cu/Zn ratios indicate oxidizing conditions and high values indicate reduction conditions in sedimentation basins. Wedepohl [22] stated that the mean values of claystones are shallow marine sediments accumulated under oxidizing conditions.

The average Cu/Zn ratio in the Kızıldere Formation is 0.58, while the (Cu+Mo)/Zn ratio is 0.83.
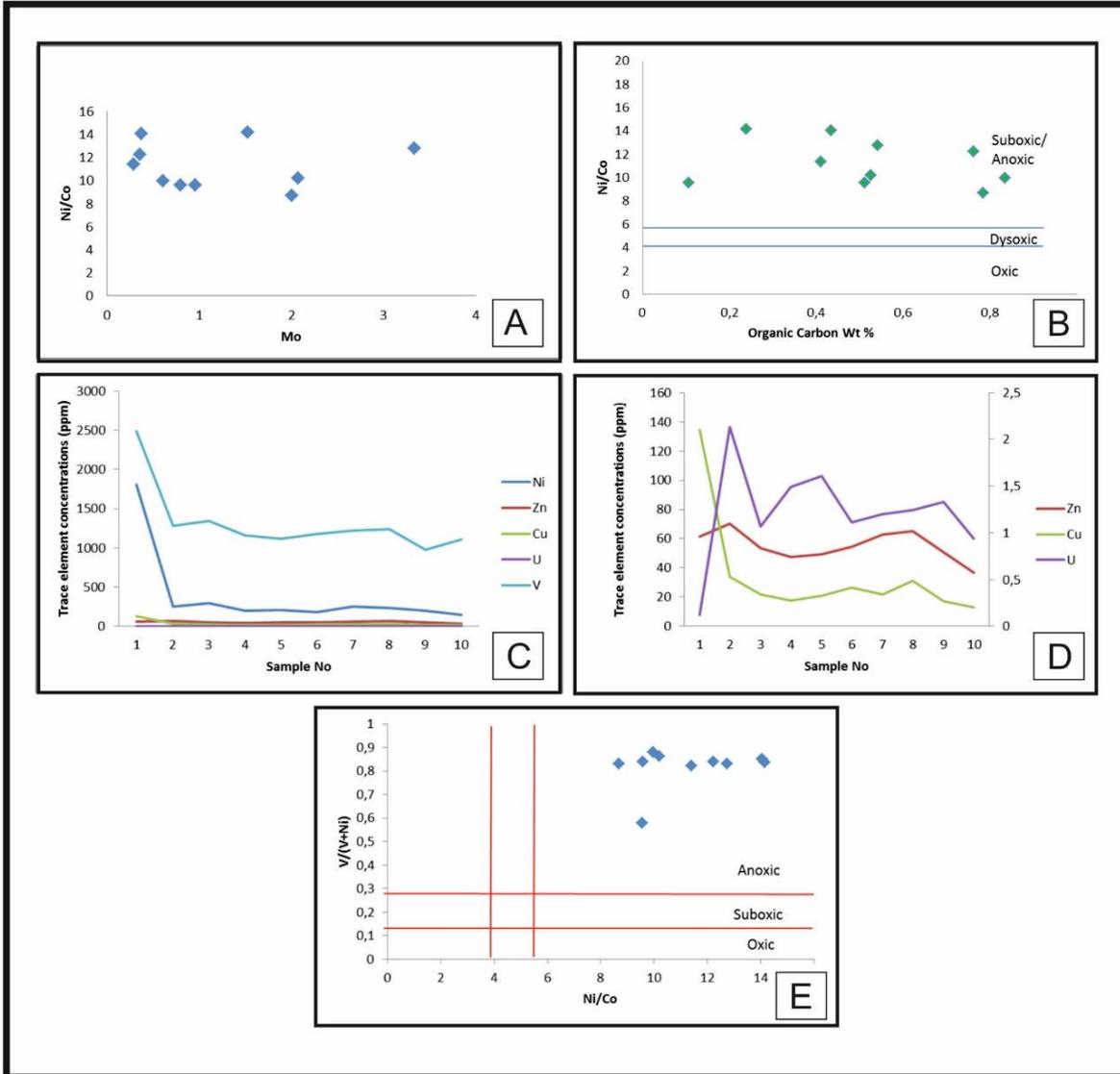
Figure 4. Environment indicators of trace elements A) Ni/Co –Mo plot, B) TOC-Ni/Co graph, C-D) comparison of similar environmental indicator elements, E) V/(V + Ni) -Ni /Co plot.

2.3. Regional distributions of elements

The regional distributions of the elements used in the environment interpretation in the region are shown in Figure 5. The distribution maps of these elements indicating the anoxic environment are similar and match with the TOC (Total Organic Carbon) distribution map. It is observed that the enrichments indicating anoxic values increase in the northeast direction of the region on the Ni-U-Cu-Zn distribution maps.

In Figure 5, the variations of the elements in the same coordinates are shown with contour maps depending on their quantities.
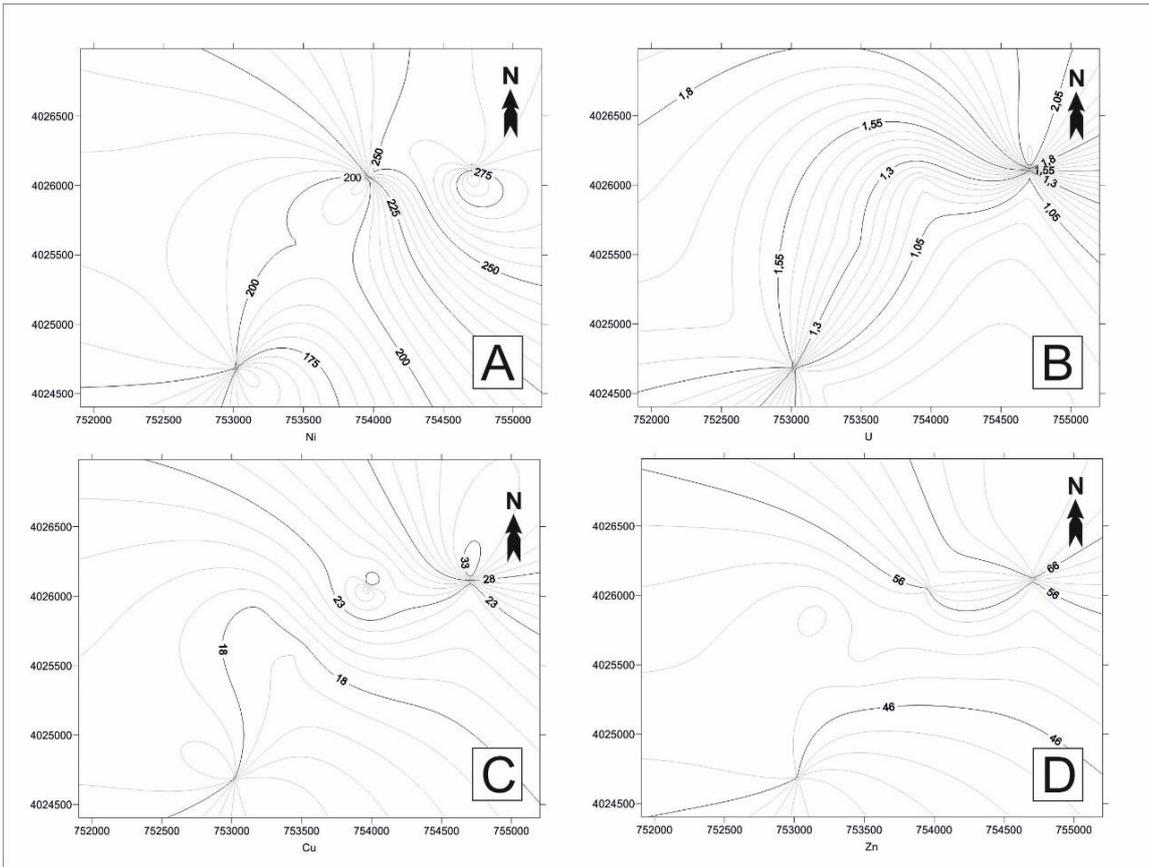
Figure 5. Contour maps of elements used as environmental indicator, A) Ni (nickel) contour map, B) U (uranium) contour map, C) Cu (copper) contour map, D) Zn (zinc) contour map.

3. Conslusions

It is important to determine the environmental conditions, especially the characteristics of claystones in hidrocarbon exploration areas. The Kızıldere Formation is important in the petroleum system as it has both reservoir and source rock properties, and trace element concentrations and environmental properties are revealed in this study. Increases in Ni-Zn-Cu-U-V elements, which are anoxic environment indicators, have been observed in Kızıldere Formation claystones, and Ni/Co -Mo, TOC-Ni / Co, V/(V + Ni) -Ni/Co values used as environment indicators proves that it precipitated in the environment. The similarities of the regional concentration distributions of these elements are also evidence of environmental changes. The similarities of the regional concentration distributions of these elements are also evidence of environmental changes. In addition, enrichment of trace elements that support the protection of organic matter content indicates that claystones may be source rock.

Acknowledgment

Conflicts of interest

The authors state that did not have conflict of interest.

References

[1] Schneider S., Hornung J., Hinderer M., Garzanti E., Petrography and Geochemistry of Modern River Sediments in an Equatorial Environment (Rwenzori Mountains and Albertine Rift, Uganda) Implications for Weathering and Provenance, *Sedimentary Geology*, 336 (2016) 106-119.

[2] Rollinson H. R., Using Geochemical Data: Evaluation, Presentation, Interpretation, Routledge, 2014.

[3] Gélinas Y., Baldock J.A., Hedges, J.I., Organic Carbon Composition of Marine Sediments: Effects of Oxygen Exposure on Oil Generation Potential, *Science*, 294 (2001) 145-148.

[4] Xie X., Borjigin T., Zhang Q., Zhang Z., Qin J., Bian L., Volkman, J. K., Intact Microbial Fossils in the Permian Lucaogou Formation Oil Shale, Junggar Basin, NW China, *International Journal of Coal Geology*, 146 (2015) 166-178.

[5] Kätz B.J., Controlling Factors on Source Rock Development a Review of Productivity, Preservation, and Sedimentation Rate, In: Harris, N.B. (eds), The Deposition of Organic Carbon Rich Sediments: Models, Mechanisms, and Consequences, *SEPM*, (2005) 282.

[6] Koca D., Sarı A., Koç Ş., Yavuz B., Koralay D.B., Denizel Kaynak Kayalarda Ana ve İz Element Zenginleşmelerine Türkiye'den Bir Örnek: Akkuyu Formasyonu (Orta Toroslar), Ankara, *Gazi Üniv. Müh. Mim. Fak. Der.*, 25(2) (2010) 243-256.

[7] Schmidt G.C., Stratigraphic Nomenclature for the Adana Region Petroleum District VII, Ankara, *Petroleum Administration Bull.*, 6 (1961) 47-63.

[8] Kozlu H., İskenderun Basen Jeolojisi ve Petrol Olanakları, TPAO Rapor no:1921, 1982.

[9] Kozlu H., Misis Andırın Dolaylarının Stratigrafisi ve Yapısal Evrimi. Ankara: Türkiye 7. Petrol Kongresi, (1987) 104-113.

[10] Yaşar E., Assessment of Petroleum geology of Iskenderun Basin, (2018) 200-206.

[11] Kozlu H., Doğu Akdeniz Bölgesinde Yer Alan Neojen Basenlerinin (İskenderun, Misis-Andırın) Tektono-stratigrafi Birimleri ve Bunların Tektonik Gelişimi. Adana: Yayınlanmamış Doktora Tezi, Çukurova Üniversitesi, Fen Bilimleri Enstitüsü, (1997) 189.

[12] Kılınç E., Yeşilot Kaplan M., Source Rock Characteritic of The Kızıldere Clays (ARSUZ-HATAY), *Cumhuriyet Sci. J.*, 39(2) (2018) 524-530.

[13] Kilinc E., Kaplan M.Y., Paleoenvironmental Conditions, Geochemistry and Hydrocarbon Potential of Kızıldere Formation (Hatay-Turkey), *Fresenius Environmental Bulletin*, 28(4A), (2019) 3516-3526.

[14] Tekin E., Varol B., Ayyıldız T., Kozlu H., İskenderun Havzası Messiniyen (Üst Miyosen) Evaporitlerinin Sedimantolojisi. Ankara: MTA 59. Türkiye Jeoloji Kurultayı, (2006) 191-192.

[15] Soua M., Productivity and bottom water redox conditions at the Cenomanian-Turonian Oceanic Anoxic Event in the southern Tethyan margin, Tunisia, *Revue Mediterraneenne de l'Environement*, 4 (2010) 653-664

[16] Pedersen T.F., Calvert S.E., Anoxia vs. productivity: what controls the formation of organic-carbon-rich sediments and sedimentary rocks, *American Association of Petroleum Geologists Bulletin*, 74 (1990) 454-466.

[17] Kılınç, E., Arsuz (Hatay) yöresi Kızıldere formasyonunun hidrokarbon potansiyelinin araştırılması, MS Thesis, İskenderun Teknik Üniversitesi, Mühendislik ve Fen Bilimleri Enstitüsü (2018) 96.

[18] Pattan J.N., Pearce N.J.C., Bottom water oxygenation history in southeastern Arabian Sea during the past 140 ka: Results from redox-sensitive elements, *Palaeogeography, Palaeoclimatology, Palaeoecology*, 280 (2009) 396-405.

[19] Jones B., Manning D.A.C., Comparison of geological indices used for the interpretation of palaeoredox conditions in ancient mudstones, *Chemical Geology*, 111 (1994) 111-129.

[20] Goldberg K., Humayun M., Geochemical paleoredox indicators in organic-rich shales of the Irati Formation, Permian of the Paraná Basin, southern Brazil, *Brazilian Journal of Geology*, 46(3) (2016) 377-393.

[21] Lewan M.D., Factors controlling the proportionality of vanadium and nickelin crude oils, *Geochimica et Cosmochimica Acta.*, 48 (1984) 2231-2238.

[22] Wedepohl K.H., Environmental influences on the chemical composition of shales and clays, In: Ahrens, L.H., Press, F.,Runcorn, S.K., Urey, H.C. (Eds.), *Physics and Chemistry of the Earth*, 8 (1971) 307-331.

[23] Hallberg R., Халлберг Р., A Geochemical Method for Investigation of Paleoredox Conditions in Sediments, *Ambio Special Report*, (4) (1976) 139-147.

Methylene blue adsorption capacity and coherent isotherm model of commercial activated carbon

*İlhan KÜÇÜK [1], ***

[1]Muş Alparslan University, Central Research Laboratories Application and Research Center, Muş/ TURKEY

Abstract

The use of dyes that pollute the earth and adversely affect the health of human beings is increasing day by day and it is important to remove them from nature. Methylene blue (MB), which is one of the most commonly used dyestuffs that affects natural life negatively, was the subject of this study. In this study, the adsorption mechanism of commercial activated carbon to remove MB was investigated. In the study, activated carbon was added to MB solution taken in different concentrations and the results were applied to ten different adsorption isotherms which are Langmuir, Freundlich, Temkin, Harkins-Jura, Halsey, Dubinin- Radushkevich, Janovich, Redlich-Peterson, Henry's and Hills. Adsorption isotherm graphs were drawn with the obtained results and constant parameters in adsorption isotherm equations were calculated through graphics. The adsorption mechanism was examined according to the correlation coefficients (R^2) from the graphs obtained. The highest correlation coefficients were calculated as 0,9993 and 0,9954 from Redlich-Peterson and Langmuir isotherm equations respectively. Adsorption isotherm was coherent Langmuir and maximum adsorption capacity was determined 208,3 mg/g.

1. Introduction

With the increasing world population, the need for the industrial sector was increased day by day. This need has contributed to development of industrial sector. With the developing industry, many products were produced and many wastes occurred from these products. Among these wastes, the materials that pollute the nature the most and affect human health are chemical materials. Chemical materials have entered our lives in many areas such as drugs, cleaning products and dyes. Paints find uses in many areas being manufactured textile, food, cosmetics, paper and paint. The waste and unused paints cause environmental pollution. Environmental pollution can be handled under three main group as soil, air and water pollution. These dyestuffs are mostly mixed with our soil or water and cause contaminations in drinking water. These pollution occurring in drinking water negatively affect human life. Besides, these pollutions adversely affect aquatic lives and cause food shortages due to the use of these creatures as food products. It is important to prevent these impurities and to clean the increasing pollution [1-3].

Dyestuffs usually have a complex and durable structure and are generally divided into 3 groups as anionic, cationic and ionic. MB is a type of cationic dye with a heterocyclic aromatic structure. MB generally uses such as paper, silk, wool leather, ink, cotton dyeing and photocopy paper production. Even very low concentration of MB causes intense colouring in the water. Due to the colour intensity, sunlight cannot pass through the water and aquatic microorganisms harm because of the lack of sunlight. Besides, although MB is not a completely toxic dye, it has negative effects on humans and living when exposed for a long time. General effects which have seen in humans can be listed as vomiting, dizziness, skin diseases, etc. [4-7].

There are many processes to remove dyes from the aqueous environment. These processes are generally chemical, biological and photocatalytic oxidation as well as coagulation-flocculation, filtration, adsorption, membrane separation and ion-exchange. Adsorption is the most used process among them. This technique is frequently used because it is an economical, efficient, easy to apply and effective process [4,8].

Adsorption is generally defined as the attachment of atoms, ions or molecules in one phase to another phase. Although liquid-solid phase is widely used in general, it is also used in phases such as liquid-liquid, liquid-gas and gas-solid systems. Clay, zeolite, bentonite, polymers and activated carbon are generally used as adsorbents in the adsorption process. It is important that the adsorbent used has high adsorption capacity, high surface area, easy accessibility and easy produce. Activated carbon is referable to other adsorbents in terms of high surface area, easy processing and easy availability compared to other adsorbents. In addition, activated carbons can be obtained commercially or easily synthesized. Activated carbon synthesis is generally obtained from agricultural wastes in recent years. Agricultural wastes are preferred because of their abundant easy access, low cost, easy storage and most importantly, their high carbon content [9-11].

The aim of this study is to determine methylene blue adsorption capacity and coherent isotherm model of commercial activated carbon. Also, it will be possible to compare other synthesized activated carbon samples in the literature and advantages and disadvantages of commercial activated carbon will be determined.

2. Materials and Methods

In this study, MB was used as the dye. MB is a cationic dye with the formula $C_{16}H_{18}N_3SCI$ and a molecular weight of 373,9 g mol^{-1}. The molecular structure of MB has dimensions of 1.43 nm in width, 0.40 nm in thickness, and 0.61 nm in depth [12]. The formula is shown in Figure 1.
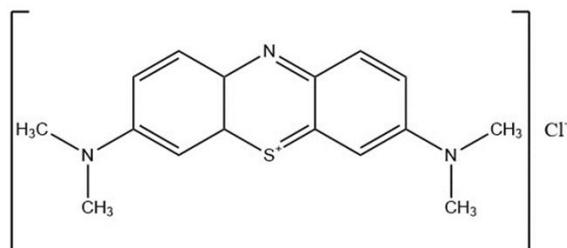
Figure 1. Methylene Blue

In this study, MB (ISOLAB C.I.52015, Turkey) was weighed 1 gram and added into a 1 litre volumetric flask and the total volume was completed to 1 litre. In this way, obtained a stock solution of 1000 ppm. The stock solution was diluted into 250ppm, 300 ppm, 350 ppm and 400 ppm solutions. The diluted solutions were taken into 100 ml flasks and 0,1 grams of active carbon was added. The mouths of the flasks were covered with paraffin and mixed for 24 hours in a miprolab brand mixer at 195 rpm. The highest peak value was determined by scanning the MB solutions in the

Agilent brand Cary-60 UV-VIS device between 200-800 nm as shown in Figure 2.

2.1. Adsorbance

The activated carbon used in this study was obtained commercially. Activated carbon is a product with code KIM-AC / 01CP / 091006 belonging to Kimetsan company (Turkey).
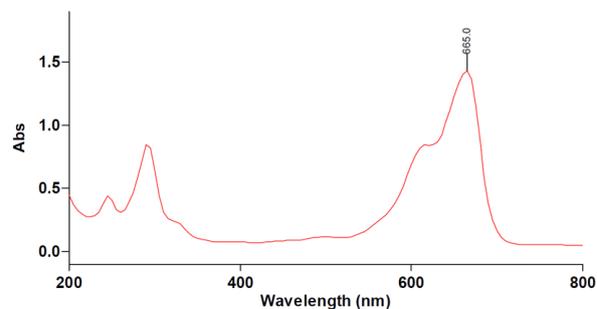
Figure 2. UV-Vis scanning of MB solution

2.2. Isotherm equations

2.2.1. Langmuir isotherm

Langmuir isotherm equation (Equation 1) was derived in 1918 by Irving Langmuir based on some assumptions. According to Irving Langmuir, adsorption takes place in a single layer and allows the calculation of the adsorption capacity. It also assumes that there is no interaction between the adsorbed molecules and that the entire adsorption field has the same energy. At the end of the adsorption process, the energy and adsorption rate is constant. In short, the maximum adsorption capacity is reached in the equilibrium state and the surface is covered in a single layer.

$$\frac{C_e}{q_e} = \frac{1}{b \times Q_o} \times \frac{C_e}{Q_o} \qquad (1)$$

According to this equation, C_e/q_e versus C_e is plotted. $1/q_m$ gives the slope, $1 / K_L \times q_m$ gives intercept. In the equation, Ce: The amount of MB remaining in the solution at the end of the adsorption (mg/L), qe: The amount of MB adsorbed on the activated carbon (mg/g), b: Langmuir constant, Q_o: The maximum amount of adsorbed substance forming a monolayer surface [13].

2.2.2. Freundlich isotherm

Freundlich isotherm equation (Equation 2) was derived in 1906 by Herbert Max Finley Freundlich. According to H.M. Finley Freundlich, the areas on the adsorbent have heterogeneous energy and may differ in the adsorption areas. In addition, adsorption takes place not in a single layer, but in a multi-layer.

$$q_e = K_F \; x \; C_e^{\frac{1}{n}} \tag{2}$$

The equation that occurred by linearization of Equation (2) is given in Equation 3.

$$logq_e = logK_F \; x \; \frac{1}{n}logC_e \tag{3}$$

$logC_e$ versus $logq_e$ is plotted according to the Freundlich equation. The slope is 1 / n and the intercept gives the $logK_F$ value. C_e: The amount of MB remaining in the solution at the end of the adsorption (mg/L), q_e: The amount of MB adsorbed on the activated carbon (mg/g), K_F shows the experimental adsorption capacity (1/mg), n adsorption density (without units) [14].

2.2.3. Temkin isotherm

Temkin isotherm assumes that there are adsorbent-adsorbate interactions. Very low and high concentration is ignored according to the model. In this model, the heat of adsorption decreases linearly. In other isotherms, this decrease is given logarithmically. The nonliner equation of the temkin isotherm is given in equation 4.

$$q_e = \frac{RT}{b_T}\ln(K_T C_e) \tag{4}$$

The equation that occurred by linearization of Equation (4) is given in Equation 5.

$$q_e = b_T lnK_T + b_T lnC_e \tag{5}$$

According to this equation, qe versus lnC_e is plotted. The slope gives b_T while the intercept gives the value of $b_T lnK_T$. According to this equation, q_e: MB adsorbed on activated carbon (mg/g), C_e: Indicates the amount of MB remaining in the liquid phase (mg/L). b_T is calculated from the value of RT/b. R is the ideal gas constant, T (°K) is the temperature and b is the temkin constant. K_T is the binding energy [15].

2.2.4. Harkins-Jura isotherm

According to Harkins-Jura isotherm model, there are micro and mesopores in the structure and multi-layer adsorption is available. Isotherm equation is given in equation 6.

$$\frac{1}{q_e{}^2} = \frac{B_H}{A_H} - \frac{1}{A_H}logC_e \tag{6}$$

According to this equation, $\frac{1}{q_e{}^2}$ versus log C_e is plotted. Slope gives $1/A_H$, intercept gives B_H/A_H values. Ce: The amount of MB remaining in the liquid phase in equilibrium (mg/L), qe: The amount of MB adsorbed on the activated carbon (mg/g), A_H, B_H are the isotherm constants [16].

2.2.5. Halsey isotherm

Halsey equation (Equation 7) is based on multi-layer adsorption with the adsorbate having micro and mesopores.

$$lnq_e = \frac{1}{n}lnk - \frac{1}{n}lnC_e \tag{7}$$

According to this equation, lnq_e versus lnC_e is plotted. The slope is 1/n, intercept is $\frac{1}{n}$ lnk. C_e: the amount of MB remaining in the liquid phase (mg/L), q_e: the amount of MB adsorbed on the activated carbon (mg/g), k value is the isotherm constant [16].

2.2.6. Dubinin- Radushkevich (D-R) isotherm

It is an equation derived based on the micropore volume filling theory put forward for gas phase adsorption. In this model, the adsorption is assumed to occur with the multilayer model. Generally, this model is used to calculate adsorption energy. Dubinin-Radushkevich isotherm equation is given in equation 8. Potential energy and adsorption energy calculation equations are given in equations 9 and 10, respectively.

$$lnq_e = lnq_m - K'\varepsilon^2 \tag{8}$$

$$\varepsilon = RTln(1 + \frac{1}{C_e}) \tag{9}$$

$$E = \frac{1}{\sqrt{2K'}} \tag{10}$$

lnq_e against the ε^2 (square of the potential energy) is plotted. q_m: theoretical adsorption capacity (mg/g) and from the intercept and slope of this line, the constants of qm and K are found, respectively. R: gas constant (8.314 J mol^{-1} K^{-1}), T: absolute temperature (°K), K': Isotherm constants related to adsorption energy, ε: potential Polanyi. The average adsorption energy (E) help us predict the adsorption mechanism. If the E value is 8-16 kj mol^{-1}, the adsorption process is characterized by ion exchange. If E <8 kj mol^{-1}, adsorption can be considered as physical, if 20 <E <40 kjmol^{-1}, adsorption can be considered chemical [17].

2.2.7. Janovich isotherm

According to the Janovich isotherm, Langmuir assumes that the isotherm is valid in adsorption. But it is assumed to be important in the interactions between the adsorbate and the adsorbent, which are not in the Langmuir isotherm. The Janovich equation is given in equation 11.

$$q_e = q_m(1 - e^{K_j C_e}) \tag{11}$$

$$lnq_e = lnq_m - K_j C_e \tag{12}$$

The equation that occurred by linearization of Equation (11) is given in Equation 12.

$\ln q_e$ versus C_e is plotted. Slope gives value K_j. qm: theoretical adsorption capacity (mg/g), qe: amount adsorbed to equilibrium (mg/g), Ce: amount remaining in equilibrium solution (mg/L), K_j is janovich's constant [18].

2.2.8. Redlich-Peterson isotherm

Redlich-Peterson isotherm is a mixture of two different isotherms, langmuir and Freundlich. Although the adsorption mechanism is a mixture, it assumes that adsorption takes place in a multi-layer. This isotherm equation is given in Equation 13.

$$\ln \frac{C_e}{q_e} = \beta \ln C_e - \ln A \tag{13}$$

$\ln \frac{C_e}{q_e}$ versus $\ln C_e$ is plotted. The slope gives β and intercept gives the value of lnA. Ce: amount remaining in equilibrium solution (mg/L), qe: amount adsorbed in equilibrium (mg/g), β and A are Redlich-Peterson constant [19].

2.2.9. Henry's isotherm

It is known as the most basic adsorption isotherm. This isotherm is generally valid at very low concentrations. It increases the adsorption capacity of the adsorbate by increasing the surface area. Henry's isotherm equation is given in equation 14.

$$q_e = K_{HE} X C_e \tag{14}$$

According to this equation, qe versus Ce is plotted. From the slope of the graph, the Henry constant K_{HE} is found. In the equation, qe: Amount adsorbed in equilibrium (mg/g), Ce: Amount remaining in the solution in equilibrium (mg/L) [19].

2.2.10. Hills isotherm

According to Hills isotherm model, homogeneous adsorbates are bound to adsorbents. Therefore, it affects other active sites on the surfaces of adsorbates and effect adsorption. The adsorption equation derived in this direction is given in equation 15.

$$\log \left(\frac{q_e}{q_{SH} - q_e} \right) = n_H \log C_e - \log K_D \tag{15}$$

$\log \left(\frac{q_e}{q_{SH} - q_e} \right)$ versus $\log C_e$ is plotted. In the resulting graph, n_H is found from the slope and K_D from intercept. In the equation, K_D and n_H hills constant, qe: adsorption amount of activated carbon (mg/g), Ce: Amount remaining in the solution in equilibrium (mg/L) [18].

3. Results and Discussion

Adsorption is similar to an equilibrium reaction. When the solution is brought into contact with a certain amount of adsorbate, the concentration of the adsorbed material in the solution decreases until it reaches equilibrium with those on the adsorbent surface. After the adsorption balance is established, the concentration of the adsorbed substance in the solution phase remains constant. The amount of adsorbed that can be retained by an adsorbent is a function of the concentration and temperature of the adsorbed. Generally, the amount of material adsorbed is determined as a function of the concentration at constant temperature. The result function called adsorption isotherm is obtained by plotting the amount of solute adsorbed, in unit adsorber weight, against the solute concentration remaining in the solution in equilibrium at constant temperature. Adsorption isotherms are essential for our understanding of how adsorption occurs. From the isotherms drawn using adsorption equations, it can be predicted how adsorption takes place. According to correlation coefficients in the adsorption isotherms drawn, it is decided which isotherm suits and how the adsorption takes place. If the correlation coefficient (R^2) has a value between 0 and 1, this indicates a positive relationship between the two variables. In other words, as the value of one variable increases, the other tends to increase. How clearly this relationship can be demonstrated depends on the value of R^2. If the value of R^2 is close to 1, the relationship between the two variables can be demonstrated well. However, as the value of R^2 approaches 0, it can be said that there may be only a weak relationship between the two variables or that the available data (or the sensitivity of the data) are insufficient to reveal such a relationship. At this point, it means that the adsorption mechanism of the isotherm is applied to a correlation coefficient close to 1. In this study, adsorption isotherms were drawn in order to learn the relationship between two variables. The adsorption isotherms drawn are given in Figure 3.
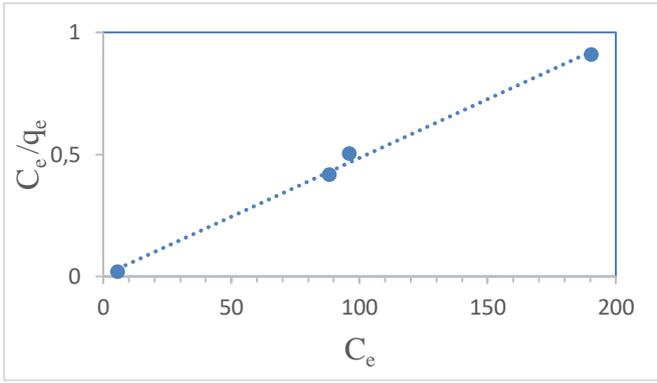
A
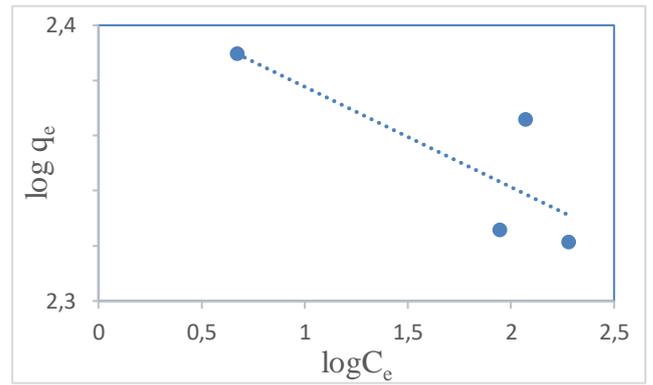
B
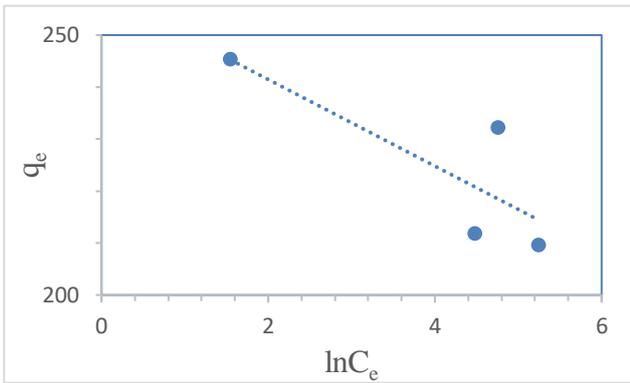
C
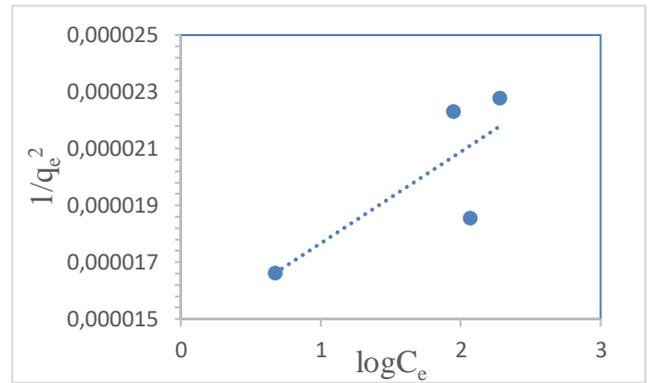
D
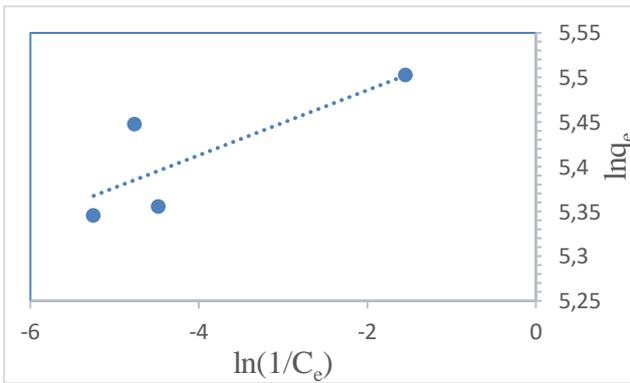
E
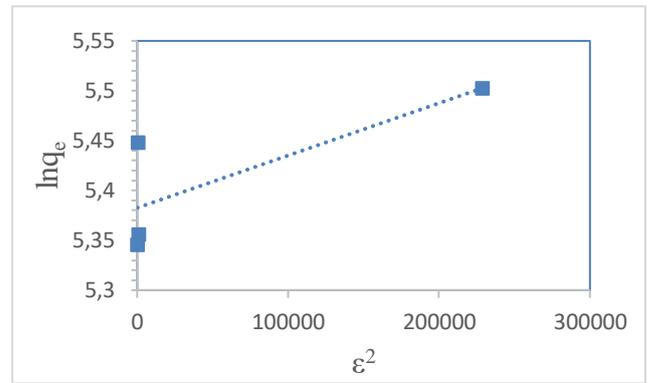
F
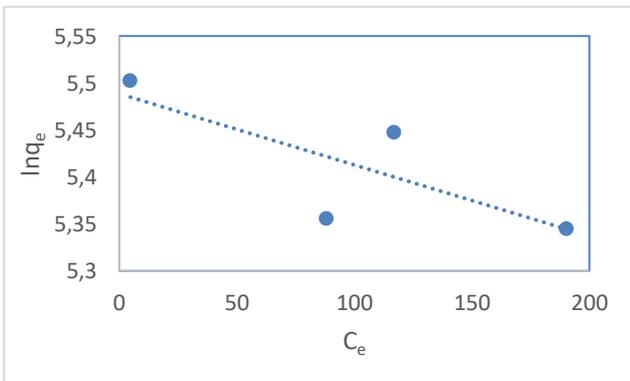
G
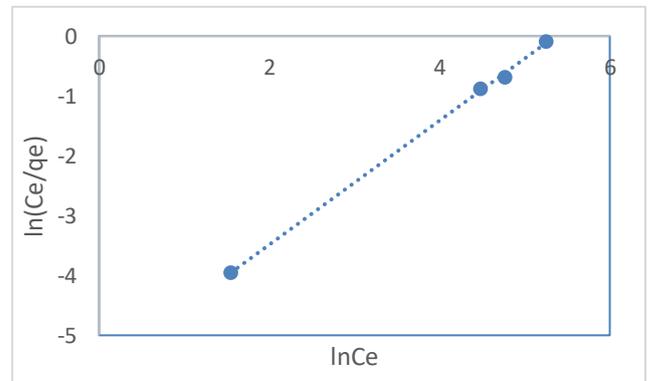
H
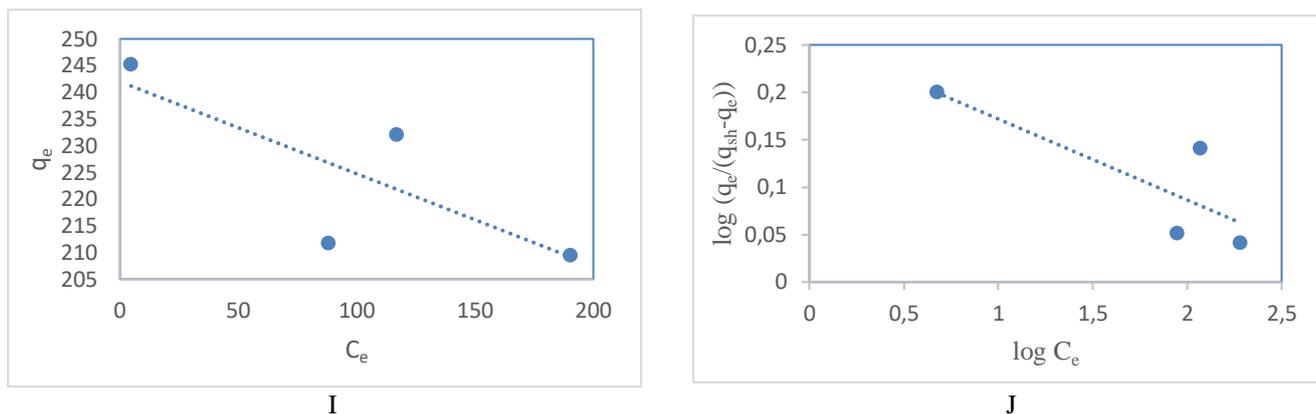
Figure 3. A. Langmuir Isotherm B. Freundlich Isotherm C. Temkin Isotherm D. Harkins-Jura Isotherm E. Halsey Isotherm F. Dubinin- Radushkevich Isotherm G. Janovich Isotherm H. Redlich-Peterson Isotherm I. Henry Isotherm J. Hills Isotherm

Using the correlation coefficients (R^2 values) obtained from the isotherm graphs shown in Figure 3, their applicability was evaluated and the R^2 values obtained for each isotherm are given in Table 1. In addition, the constants of each isotherm were determined by using the slopes and intercept of the graphics in Figure 3. These constants are also given in Table 1.

Table 1. Constant parametres and correlation coefficients

Langmuir		Freundlich		Temkin	
Q_o (mg/g)	208,3	K_F (L/mg)	259,47	$-b_T$ (J/mol)	8,33
b (L/mg)	1,26	n	27,47	$K_T x 10^{-14}$ (L/g)	3,51
R^2	0,9954	R^2	0,6503	R^2	0,665
Harkins-Jura		Halsey		Janovich	
$-A_H x 10^{-4}$	33	-n	0,17	q_m (mg/g)	241,89
$-B_H$	3,3	k	1,238	$K_j x 10^{-4}$ (L/g)	8
R^2	0,6214	R^2	0,6503	R^2	0,5934
Redlich-Peterson		Henry		Hills	
A (L/g)	259,48	$-K_{HE}$	0,172	$-n_H x 10^{-2}$	8
β	1,036	R^2	0,6006	K_D	1,8
R^2	0,9993			R^2	0,6703
D-R					
q_m (mg/g)	217,58				
$-K x 10^{-7}$ (mol²/j²)	5				
R^2	0,6285				
E (kj/mol)	1000				

According to Table 1, the correlation coefficients are listed as Redlich-Peterson > Langmuir > Hills >Temkin > Freundlich = Halsey >Harkins-Jura > Dubinin-Radushkevich >Henry >Janovich. When the correlation coefficients are examined, the closest isotherms to 1 are Redlich-Peterson and Langmuir isotherms. Therefore, since the correlation values of the adsorption mechanism are very close to each other, it can be assumed that it occurs according to Redlich-Peterson and Langmuir. When these two isotherm equations are examined, it is seen that the equations have similar properties. The Redlich-Peterson equation is based on the Langmuir equation and is obtained by combining this equation with the Freundlich equation. This equation obtained is similar to Freunlich's at high concentrations, while low concentrations are similar to Langmuir equation [20].

Table 2 demonstrates adsorption capacity of the different kinds of activated carbon used for MB removal.

Table 2. Adsorption capacity of different activated carbon

Adsorbent	Raw Metarial	Activation	Chemical/Gas	MB Adsorption Capacity	Ref.
Commercial Activated Carbon	-	-	$NiFe_2O_4$	167.45 mg/g	[22]
Activate Carbons	-	-	Silver Nanoparticles	416. 66 mg/g	[23]
Activated Carbon	Walnutt Shell	Physical Activation	CO_2	174,81 mg/g	[24]
Activated Carbon	*Platanus Orientalis*	Chemical Activation	$ZnCl_2$	138,88 mg/g	[25]
Activated Carbon	Almond Shell	Chemical Activation	$ZnCl_2$	201.40 mg/g	[26]
Activated Carbon	Sucrose	Chemical Activation	KOH	1666.66 mg/g	[27]
Activated Carbon	Almond Shells	Chemical Activation	H_2SO_4	131.58 mg/g	[28]
Activated Carbon	Peach Kernel Shells	Physical Activation	CO_2	3,67 mg/g	[29]
Activated Carbon	Pistachio Shell	Physical Activation	CO_2	93,45 mg/g	[30]
Commercial Activated Carbon	-	-	-	208,3 mg/g	This Study

4. Conclusions

MB adsorption has been studied on commercially obtained activated carbon and applied to 10 different adsorption isotherms to understand the adsorption mechanism. The adsorption mechanism was estimated by examining their suitability to the isotherm equations on the line of the obtained results. The suitability of the isotherm equations was determined according to the correlation coefficients (R^2) of the isotherms. The two isotherms with the highest correlation coefficients were Redlich-Peterson and Langmuir. Since the correlation coefficients of other isotherm graphs are very low, the adsorption mechanisms in which the equations are explained are not correct for this study. Since the Redlich Peterson equation has the highest correlation coefficient, it can be thought that the adsorption mechanism occurs in this way. However, since this equation consists of a mixture of two different equations which are Langmuir and Freundlich equations, it is necessary to investigate which isotherm the equation integrate. The linear state of the Redrich-Peterson equation is shown in equation 13. Since the constant value of β in this equation is approximately equal to 1, the equation is reduced to the Langmuir equation [18,21]. In this case, the adsorption mechanism in the study integrate the definition of Langmuir. Adsorption took place in a single layer with a homogeneous adsorbent surface.

Conflicts of interest

The author declares that there is no conflict of interest.

References

[1] Yemiş F., Yenil N., Metilen mavisi ve alizarin'in lüminesans spektrometresi ile asitlik sabitlerinin tayini ve bazı metal duyarlılıklarının incelenmesi, *SUJEST,* 6(2) (2018) 317-330.

[2] Saheed I. O., Adekola F. A., Olatunji G. A., Sorption study of methylene blue on activated carbon prepared from jatropha curcas and terminalia catappa seed coats, *JOTCSA,* 4(1) (2017) 375-394.

[3] Yılmaz N., Alagöz O., Nar kabuklarından kimyasal aktivasyon ile hazırlanan aktif karbon üzerinde metilen mavisinin adsorpsiyonu, *ECJSE,* 6(3) (2019) 817-829.

[4] Kaya N., Yıldız Z., Ceylan S., Preparation and characterisation of biochar from hazelnut shell and its adsorption properties for methylene blue dye, *Journal of Polytechnic*, 21(4) (2018) 765-776.

[5] Aldemir A., Kul A. R., Isotherm, kinetic and thermodynamic studies for the adsorption of methylene blue on almond leaf powder, *Cumhuriyet Sci. J.,* 41(3) (2020) 651-658.

[6] Dilekoğlu M. F., Harran Ovası tarım arazileri etrafında bulunan urfa taşı'nın metilen mavisi boyar maddesi adsorpsiyonu, *Turk J. Agric. Res.,* 5(1) (2018) 19-30.

[7] Coskun R., Savci S., Delibas A., Adsorption properties of activated almond shells for methylene blue, *Environ. Sci. Technol.,* 1(2) (2018) 31-38.

[8] Bayar S., Adsorption of methylene blue onto natural clay, *GUSTIJ.*, (2018) 8 (2): 264-272.

[9] Erşan M., Güler Ü. A., Doğan H., Sarraj B., Kolemanit destekli nzvı kullanılarak sulu çözeltilerden metilen mavisinin giderimi, *NOHU J. Eng. Sci.,* 9(1) (2020) 114-127.

[10] Kaykıoğlu G., Dalmış İ.S., Piroliz uygulanmış çeltik sapları ile sulu çözeltilerden renk giderimi, *Doğ. Afet Çev. Derg.*, 6(1) (2020) 37-48.

[11] Namal O.Ö., Kayısı çekirdeği kabukları ile sulu çözeltiden metilen mavisi adsorpsiyonuna partikül boyutunun etkisi, *NOHU Journal of Engineering Sciences*, 7(2) (2018) 566-571.

[12] Wang Y., Peng Q., Akhtar N., Chen X., Huang Y., Microporous carbon material from fish waste for removal of methylene blue from wastewater, *Water Sci. Technol.*, 81(6) (2020) 1180-1190.

[13] Basar C. A., Applicability of the various adsorption models of three dyes adsorption onto activated carbon prepared waste apricot, *J. Hazard. Mater.*, B135 (2006) 232–241.

[14] Erkurt F. E., Balcı B., Reaktif Black 5 boyar maddesinin aktif karbon üzerine adsorpsiyonunun kinetik ve adsorpsiyon modelleri kullanılarak incelenmesi, *Çukurova University Journal of the Faculty of Engineering and Architecture*, 30(1) (2015) 257-269.

[15] Aldemir A., Kul A. R., Elik H., Isotherm, kinetic and thermodynamic ınvestigation into methylene blue adsorption onto pinecone

powder, *Int. J. Environ. Sci. Technol.*, 14(4) (2019) 183-192.

[16] Saloğlu D., Mikro kirletici naproksenin atık sulardan spirulina platensis ile modifiye edilmiş kitosan-polivinilalkol biyokompozitleri ile adsorpsiyonu., *BEU Journal of Science*, 8(2) (2019), 506-520.

[17] Okumuş Z.Ç., Doğan T.H., Biyodizeldeki suyun reçine ile uzaklaştırılması: adsorpsiyon izotermi, kinetiği ve termodinamik incelemesi, *EJOSAT,* 15 (2019) 561-570.

[18] Al-Ghouti M. A., Da'ana D. A., Guidelines for the use and interpretation of adsorption isotherm models: a review, *J. Hazard. Mater.*, 393(5) (2020) 122383.

[19] Ayawei N., Ebelegi A. N., Wankasi D., Modelling and interpretation of adsorption isotherms, *Hindawi Journal of Chemistry,* (2017) 11.

[20] Foo K.Y., Hameed B.H., Insights into the modeling of adsorption isotherm systems, *Chem. Eng. J.*, 156 (2010) 2–10.

[21] Eder S., Müller K., Azzari P., Arcifa A., Peydayesh M., Nyström L., Mass transfer mechanism and equilibrium modelling of hydroxytyrosol adsorption on olive pit–derived activated carbon, *Chem. Eng. J.,* 404 (2021) 126519.

[22] Ceyhan A.A., Baytar O., Metilen mavisinin magnetik NiFe$_2$O$_4$/aktif karbon nanokompoziti ile adsorpsiyonu: kinetik ve izoterm, *Selcuk Univ. J. Eng. Sci. Tech.*, 6(2) (2018) 227-241.

[23] Altıntığ E., Soydan Ö.F., Metheylene blue adsorption and preparation silver bound to activated carbon with sol-gel methods, *Sakarya University J. Sci.,* 22(6) (2018) 1812-1819.

[24] Küçük İ., Önal Y., Başar C.A., The activated carbon from walnut shell using CO$_2$ and methylene blue removal, *DUJE.*, 12(2) (2021) 297-308.

[25] Toprakcı O., Toprakcı A.K., Okkay H., Methylene Blue removal by activated carbon from platanus orientalis leaves, *International Journal of Environment and Geoinformatics,* 8(3) (2021) 283-289.

[26] Teğin Ş.Ö., Şahin Ö., Baytar O., İzgi M.S., Preparation and characterization of activated carbon from almond shell by microwave-assisted using ZnCl$_2$ activator, *Int. J. Chem. Technol.,* 4(2) (2020) 130-137.

[27] Kazak Ö., Single-step pyrolysis for producing activated carbon from sucrose and its properties for methylene blue removal in aqueous solution, *Environmental Research & Technology,* 4(2) (2021) 165-175.

[28] Coskun R., Savci S., Delibas A., Adsorption properties of activated almond shells for methylene blue (MB), *Environmental Research & Technology,* 1(2) (2018) 31-38.

[29] Küçük İ., Önal Y., Low cost activated carbon synthesis, characterization and adsorption applications, *Naturengs,* 1(2) (2020) 32-38.

[30] Küçük İ., Önal Y., Başar C.A., The production and characterization of activated carbon using pistachio shell through carbonization and CO2 activation, *JOTCSB.*, 2(1) 2019 35-44.

Investigation of the catalytic effect of metal-metal oxide structure in the catalysts used in hydrogen production by electrolysis of water

Özkan AYDIN [1,*] (iD)

[1]*Osmaniye Korkut Ata University, Faculty of Engineering, Department of Chemical Engineering, Osmaniye / TURKEY*

Abstract

Hydrogen, which is obtained by water splitting using the electrolysis method, is one of the cleanest and most environmentally friendly energy carriers. However, since this production method is expensive, it is not preferred in industrial hydrogen production. Researchers working on this subject have intensified their studies to reduce costs. One of the most important factors determining the cost is the development of effective and inexpensive cathode and anode materials. In this study, the catalysts obtained by electrochemical deposition of nickel on the graphite rod, cobalt oxide using the drag effect and electrochemical platinum deposition on it, were used as the cathode material. The surface characterizations of the obtained catalysts were carried out using SEM and XRD techniques. The electrochemical properties of the catalysts were analyzed using electrochemical impedance spectroscopy, linear sweep voltammetry and potentiodynamic polarization methods. It was determined that the most effective nickel deposition time is 10 seconds, CoO content is 1.9 mg and platinum deposition time is 45 seconds. The initial potential for the hydrogen evolution reaction of the catalyst which has the highest catalytic efficiency was 75 mV and current density was determined as 500 mA cm^{-2} at the cathodic 0.5 V$_{SHE}$ overvoltage.

1. Introduction

In the world, the effects of global warming caused by greenhouse gases in the atmosphere caused by fossil fuels used to meet the world's increasing energy needs are being felt day by day. [1, 2]. Therefore, the demand for clean and renewable energy sources is increasing day by day. [3]. Hydrogen is preferred as an alternative clean energy source to fossil fuels due to its high energy density, abundance, and environmental friendliness. [4, 5]. There are many methods for producing hydrogen. About 50% of global hydrogen demand is met by natural gas steam reform, 30% by oil reform, 18% by coal gasification, 3.9% by electrolysis of water and 0.1% by other sources [6-9]. To eliminate the negative effects of fossil fuel use on the environment, human health and climate, it is necessary to produce hydrogen from clean and abundant sources with environmentally friendly methods. [10-14]. The name of this hydrogen production method is green hydrogen production. Hydrogen production by electrolysis of water is one of the green production technologies. The purity of the hydrogen obtained by this method is quite high. However, one of the main

problems of this production method is that the production cost is high compared to other methods. Developing effective and inexpensive cathode and anode materials in electrolysis processes has an important place in terms of cost. Therefore, researchers focused on the development of catalysts for a low-cost effective anode and cathode material. [15]. Different combinations of catalysts are formed using a single metal[16-18], binary [19-24], ternary metal alloys [25-27] or metal oxides[28-31]. These combinations can be obtained by attaching to the support electrode with different applications such as metallurgical sintering method [24], electrochemical deposition method [32-34], slurry application method [35] or spray coating method [31, 36]. In these applications, nickel-based catalysts are one of the most widely used metals because they are electrochemically advantageous and relatively inexpensive. [37-41]. Another element that is frequently used in the reactions of obtaining hydrogen by the electrolysis of water is cobalt and its oxide compounds. [31, 42-44] . Noble metals are often added in trace amounts to reduce the hydrogen evolution overvoltage. [45]. Platinum is one of the

noble metals most capable of producing hydrogen among these noble metals.

In this study, metallic nickel (Ni) was electrochemically deposited on a graphite rod (C). It is known that metal oxides create a synergistic effect with metals. [30]. Therefore, during metallic nickel deposition, nano-structured cobalt oxide (CoO) was added to the nickel deposition bath and suspended in the solution to attach the surface by the drag effect. Finally, trace amounts of platinum (Pt) were electrochemically deposited on the Ni-CoO combination. The obtained catalysts were electrochemically analyzed for hydrogen evolution reaction in alkaline medium using electrochemical impedance spectroscopy (EIS), linear sweep voltammetry (LSV), and potentiodynamic polarization techniques.

2. Experimental Method

2.1. Material and method

Cylindrical graphite rods of 10 cm length were used as support electrodes in the experiments. These rods are insulated with polyester material, leaving only the lower ends open. The area of this active circular part that remains open is 0.283 cm^2. Before each experiment, these rods were sanded with 1200 grit sandpaper, then washed with distilled water, acetone and again with distilled water, respectively. The cobalt oxide nanoparticles used in the study were synthesized as follows; 50 ml 0.6 M $Co(NO_3)_2 . 6H_2O$ (Fluka, $\geq$

98%) at 50℃ which was filled into a burette was added to 50 ml 3.2 M NaOH (Sigma-Aldrich, $\geq$ 99%) at 50℃ which is mixed dropwise. Then, 50 ml H_2O_2 (Merck , 50 % w/w) was added dropwise by using burette to this stirred solution. The precipitate was filtered off and washed with distilled water. The resulting precipitate was dried at 110℃ for 10 hours [46]. Electrochemical deposition and analyzes were performed using potentiostat (Gamry interface 1000E).

Three electrode techniques were used for electrochemical analyzes. Here, Pt sheet with a surface area of 2 cm^2 as the anode (CE), Ag / AgCl as the reference electrode, and catalysts loaded on the graphite rod as the cathode (WE) were used. In these analyses, 1.0 M KOH solution was used as the electrolyte. EIS, LSV and potentiodynamic polarization techniques were used to determine the catalytic efficiency for hydrogen production. EIS measurements were obtained in the frequency range of 10^6 to 0.01 Hz with an amplitude of 10 mV. LSV measurements were made at a scan rate of 1 mV s^{-1} between 0 V and cathodic 0.5 V.

2.2. Experimental

Graphite rods were electrochemically coated with a current density of 340.0 mA cm^{-2} in a nickel bath, the composition of which is given in Table 1. Therefore, three different deposition times (10, 60, and 110 s) were applied and denoted as **Ni$_t$.** Here t represents the nickel deposition time.

Table 1. Compositions of electrochemical deposition baths for Ni and Pt.

	NiSO$_4$ .6H$_2$O	H$_3$BO$_3$	NiCl$_2$.6H$_2$O	K$_2$PtCl$_6$	Total Volume
Ni Bath	30 g	1.25 g	1 g	---	100 mL
Pt Bath	---	---	---	0,1M (pH=1)	100 mL

After determining the most effective deposition time for nickel, CoO nanoparticles were added into the nickel bath and suspended solution was obtained. In this way, while nickel deposition is done electrochemically, CoO is also deposited on the surface with the drag effect. In this section, five different CoO amounts (0.1 mg, 1.0 mg, 1.3 mg, 1.9 mg, and 3.7 mg CoO) were prepared and the obtained catalysts were denoted as Ni$_t$-CoO$_{(Xmg)}$. Here x represents the amount of CoO added to the nickel-plating bath. Finally, platinum (Pt) was electrochemically deposited on Ni$_t$-CoO$_{(Xmg)}$ catalyst.

In this section, metallic platinum was deposited with a current density of 3,53 mA cm^{-2} in three different deposition times (15, 30, and 45 s). This obtained catalyst was denoted as Ni$_t$-CoO$_{(Xmg)}$_Pt$_t$.

After the Ni$_t$, Ni$_t$-CoO$_{(Xmg)}$, and Ni$_t$-CoO$_{(Xmg)}$_Pt$_t$ catalysts were prepared, the efficiency of the obtained catalysts in terms of hydrogen production was analyzed using EIS, LSV and potentiodynamic polarization techniques. Total hydrogen production for the best catalysts was calculated using a reverse burette[28]. Hydrogen produced at the cathode was collected in the reverse burette and after one hour the

total volume of hydrogen produced was measured. Experiments were carried out at 20 ℃ and under 736 mmHg pressure. Pt electrode was used as the anode and 1.0 M KOH solution was used as the electrolyte. Surface characterization and elemental analyses of the catalysts were carried out with Field emission scanning electron microscope (FEI Quanta 650 Field Emission SEM) coupled with energy dispersive X-ray (EDX). The powder XRD measurements were performed with PANalytical EMPYREAN, 2θ angle between 5° and 90°.

3. Results and Discussion
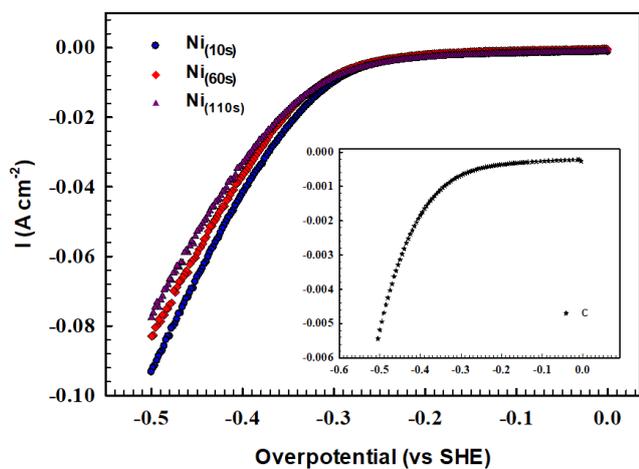
Figure 1. LSV diagrams of C, $Ni_{(10s)}$, $Ni_{(60s)}$, and $Ni_{(110s)}$ catalyst.

EIS measurements at the overvoltage region provide information about the charge transfer resistance of catalyst for hydrogen evolution reaction. The Nyquist graphs obtained for the prepared catalysts at -0.3 V_{SHE} in 1.0 M KOH solution were given in Fig. 2. The Nyquist graph for C is given in the inset graph. When Fig. 2 is examined, it is seen that all catalysts have a time constant due to charge transfer resistance and $Ni_{(10s)}$ catalyst has the lowest charge transfer resistance.

It is known that metal-metal oxide composition has positive effects for catalysts used in hydrogen production [28]. Therefore, the effect of CoO on the HER was investigated by adding to the catalyst structure. Metal oxides are usually attached to the catalyst structure using conductive adhesives such as Polyvinylidene fluoride and carboxymethyl cellulose. These adhesives create additional resistance. To avoid such negative effects, CoO nanoparticles were added to the catalyst structure by the drag effect during electrochemical nickel deposition. Different amounts of CoO (0.1 mg, 1 mg, 1.3 mg, 1.9 mg, and 3.7 mg CoO) were added to the nickel deposition bath to obtain a suspended CoO nickel bath.

The LSV technique was used to characterize all the catalysts obtained for hydrogen evolution reaction (HER). The overvoltage-current density curves for different nickel-deposition times on the graphite rod (C) given in Fig. 1 were taken at a scan rate of 1 mV s^{-1} and in the range of 0 V and cathodic 0.5 V_{SHE}. When Fig. 1 is examined, the initial potential of the HER for C is -0.35 V. Initial potentials of HER for $Ni_{(10s)}$, $Ni_{(60s)}$ ve $Ni_{(110s)}$ were shown in Fig. 1 as -0.26 V, -0.30 V and -0.29 V, respectively.

Comparing the curves, it is seen that the highest cathodic current density and the lowest overvoltage for HER belong to $Ni_{(10s)}$ catalyst.

The effect of CoO attachment during nickel deposition was investigated for HER using LSV and EIS techniques. The overvoltage (vs. SHE) – current density plots of catalysts defined as Ni_t-CoO$_{(Xmg)}$ was given Fig. 3. When the figure is examined, the initial potentials of hydrogen evolution for $Ni_{(10s)}$, $Ni_{(10s)}$-CoO$_{(0.1mg)}$, $Ni_{(10s)}$-CoO$_{(1.0mg)}$, $Ni_{(10s)}$-CoO$_{(1.3mg)}$, $Ni_{(10s)}$-CoO$_{(1.9mg)}$ ve $Ni_{(10s)}$-CoO$_{(3.7mg)}$ catalysts were obtained as -0.26 V, -0.32 V, -0.34 V, -0.28 V, -0.22 V, and -0.27 V, respectively. Comparing the curves obtained for the prepared catalysts at -0.3 V_{SHE} overvoltage, it was determined that the highest current density was 19.6 mA cm^{-2} and the lowest overvoltage for HER was -0.22 V. These values belong to $Ni_{(10s)}$-CoO$_{(1.9mg)}$ catalyst.
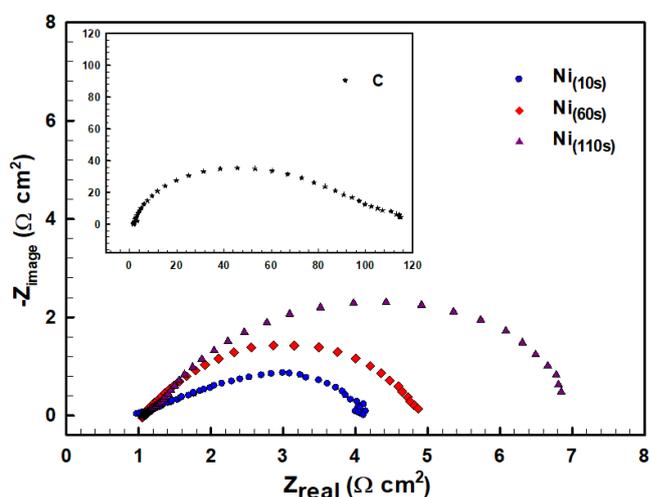
Figure 2. Nyquist diagrams of C, $Ni_{(10s)}$, $Ni_{(60s)}$ ve $Ni_{(110s)}$ catalyst
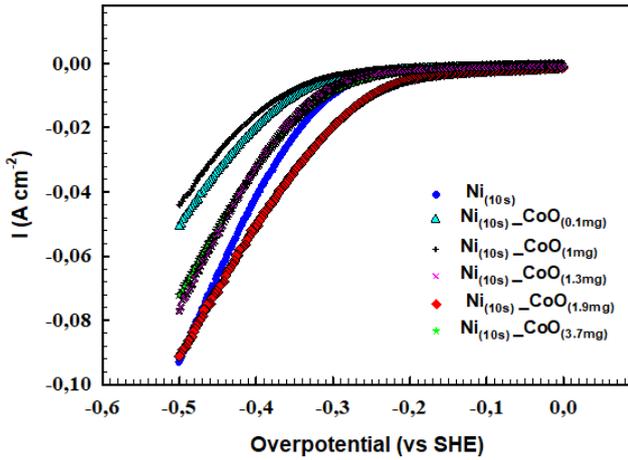
Figure 3. LSV diagrams of $Ni_{(10s)}$, $Ni_{(10s)}$-$CoO_{(0.1mg)}$, $CoO_{(1.0mg)}$, $Ni_{(10s)}$-$CoO_{(1.3mg)}$, $Ni_{(10s)}$-$CoO_{(1.9mg)}$ and $Ni_{(10s)}$-$CoO_{(3.7mg)}$ catalysts

EIS measurements for $Ni_{(10s)}$, $Ni_{(10s)}$-$CoO_{(0.1mg)}$, $Ni_{(10s)}$-$CoO_{(1.0mg)}$, $Ni_{(10s)}$-$CoO_{(1.3mg)}$, $Ni_{(10s)}$-$CoO_{(1.9mg)}$ and $Ni_{(10s)}$-$CoO_{(3.7mg)}$ catalysts were taken in 1.0 M KOH solution and -0.3 V_{SHE} overvoltage were given in Fig. 4. When the curves in Fig. 4 were compared, it is seen that the lowest charge transfer resistance (2.6 Ω cm^2) belongs to $Ni_{(10s)}$-$CoO_{(1.9mg)}$ catalyst.
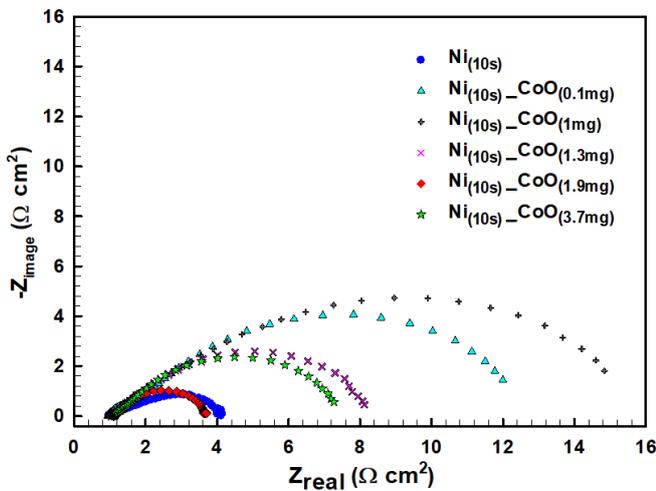
Figure 4. Nyquist diagrams of $Ni_{(10s)}$, $Ni_{(10s)}$-$CoO_{(0.1mg)}$, $Ni_{(10s)}$-$CoO_{(1.0mg)}$, $Ni_{(10s)}$-$CoO_{(1.3mg)}$, $Ni_{(10s)}$-$CoO_{(1.9mg)}$ and $Ni_{(10s)}$-$CoO_{(3.7mg)}$ catalysts

One of the noble metals, Pt, was electrochemically deposited on the $Ni_{(10s)}$-$CoO_{(1.9mg)}$ catalyst to increase the catalytic efficiency. Since it is a metal with high catalytic efficiency but expensive, so deposition times are kept short. Metallic Pt was deposited at a current density of 3.53 mA cm^{-2} in three different deposition times (15, 30 and 45 s). Prepared Ni_t-$CoO_{(Xmg)}$_Pt_t catalysts were electrochemically analyzed for HER activity using LSV and EIS techniques. Fig. 5 shows the overvoltage (vs. SHE) – current density plots of catalysts identified as Ni_t-$CoO_{(Xmg)}$_Pt_t. When the

figure is examined, the starting potentials of hydrogen evolution of catalysts $Ni_{(10s)}$-$CoO_{(01.9mg)}$, $Ni_{(10s)}$-$CoO_{(1.9mg)}$_Pt_{15}, $Ni_{(10s)}$-$CoO_{(1.9mg)}$_Pt_{30}, and $Ni_{(10s)}$-$CoO_{(1.9mg)}$_Pt_{45} are seen as -0.22 V, -0.13 V, -0.10 V and -0.075 V, respectively. When the curves at -0.3 V_{SHE} overvoltage were compared for the prepared catalysts, the highest cathodic current density was found to be 80.0 mA cm^{-2} and the lowest overvoltage value for HER was - 75 mV. These values belong to $Ni_{(10s)}$-$CoO_{(1.9mg)}$_Pt_{45} catalyst.

To determine the catalytic activities of the platinum deposited catalysts, EIS measurements were taken at -0.3 V_{SHE} overvoltage. Nyquist plots for $Ni_{(10s)}$-$CoO_{(01.9mg)}$, $Ni_{(10s)}$-$CoO_{(1.9mg)}$_Pt_{15}, $Ni_{(10s)}$-$CoO_{(1.9mg)}$_Pt_{30}, and $Ni_{(10s)}$-$CoO_{(1.9mg)}$_Pt_{45} catalysts were given in Fig. 6. When the figure is examined, it is seen that the lowest charge transfer resistance belongs to $Ni_{(10s)}$-$CoO_{(1.9mg)}$_Pt_{45} catalyst and is 0.35 Ω cm^2.
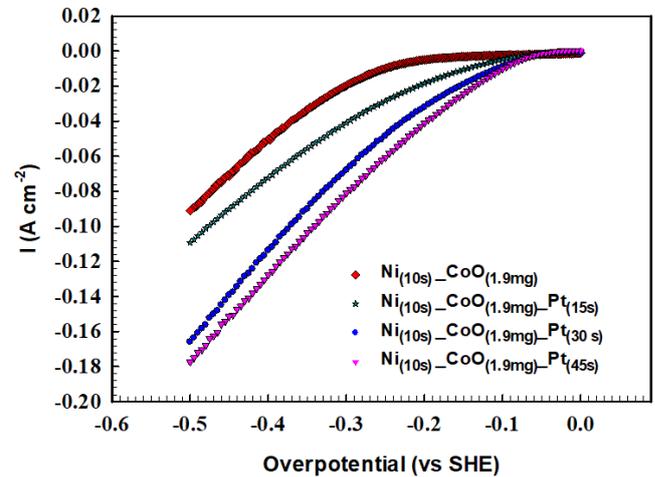
Figure 5. LSV diagrams of $Ni_{(10s)}$-$CoO_{(01.9mg)}$, $Ni_{(10s)}$-$CoO_{(1.9mg)}$_Pt_{15}, $Ni_{(10s)}$-$CoO_{(1.9mg)}$_Pt_{30}, and $Ni_{(10s)}$-$CoO_{(1.9mg)}$_Pt_{45} catalysts.
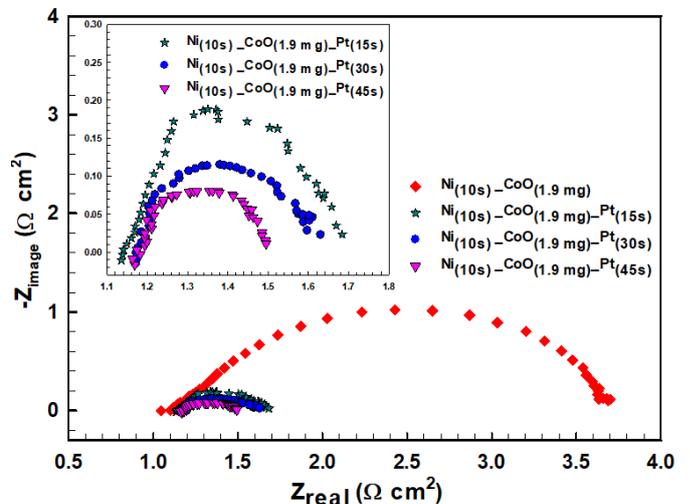
Figure 6. Nyquist diagrams of $Ni_{(10s)}$-$CoO_{(01.9mg)}$, $Ni_{(10s)}$-$CoO_{(1.9mg)}$_Pt_{15}, $Ni_{(10s)}$-$CoO_{(1.9mg)}$_Pt_{30}, and $Ni_{(10s)}$-

$CoO_{(1.9mg)}$_Pt_{45} catalysts. Comparisons of the LSV curves of $Ni_{(10s)}$-$CoO_{(1.9mg)}$_Pt_{45} catalyst and 20% (w/w) Pt/C catalysts purchased commercially from ERDES Technology ve Chemistry Company in terms of HER are given in Fig. 7.
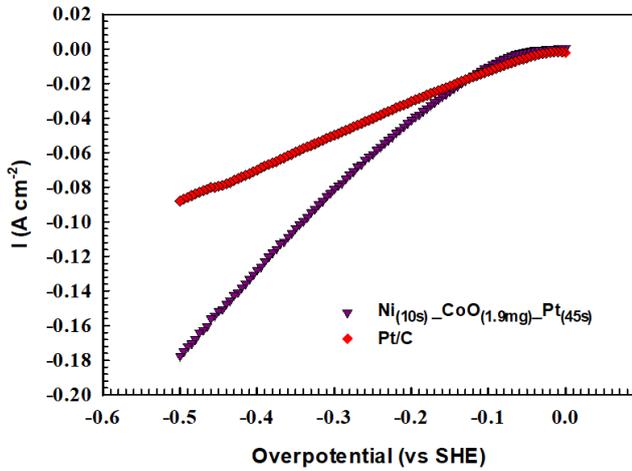
Figure 7. LSV diagrams of Pt/C and $Ni_{(10s)}$-$CoO_{(1.9mg)}$_Pt_{45} catalysts

Initial potentials for HER of commercial Pt/C catalyst and $Ni_{(10s)}$-$CoO_{(1.9mg)}$_Pt_{45} catalyst were measured as cathodic 28 mV and 75 mV, respectively. The Pt/C catalyst appears to be more efficient when comparing the initial potentials for hydrogen evolution. However, the current densities of Pt/C and $Ni_{(10s)}$-$CoO_{(1.9mg)}$_Pt_{45} catalyst at -0.5 V_{SHE} overvoltage were measured as 88 mA cm^{-2} and 500 mA cm^{-2}, respectively. This shows that the current density of $Ni_{(10s)}$-$CoO_{(1.9mg)}$_Pt_{45} catalyst at -0.5 V_{SHE} overvoltage is 5 times higher than the commercial catalyst.

The potentiodynamic polarization technique for catalysts $Ni_{(10s)}$, $Ni_{(10s)}$-$CoO_{(1.9mg)}$, and $Ni_{(10s)}$-$CoO_{(1.9mg)}$_Pt_{45} was applied at a scan rate of 10 mV s^{-1}, in 1.0 M KOH solution in the range of 0 to 300 mV. Obtained data are graphed in Fig. 8. Current densities at some overvoltages, 50, 100 and 200 mV were used to compare the catalytic efficiency. Current densities at given overvoltages, Tafel constant (b) and i_0 (-a/b), were given in Table 2.

Table 2. Electrochemical data obtained from cathodic potentiodynamic polarization curves at different potentials.

	-η_{50} (mA cm^{-2})	-η_{100} (mA cm^{-2})	-η_{200} (mA cm^{-2})	i_0 (mA cm^{-2})	b (mV dec^{-1})
$Ni_{(10s)}$	2.87	2.80	2.58	3.11	288.71
$Ni_{(10s)}$-$CoO_{(1.9mg)}$	2.73	2.62	2.29	2.97	248.62
$Ni_{(10s)}$-$CoO_{(1.9mg)}$-$Pt_{(45s)}$	2.84	2.32	1.39	4.04	73.53

When the current densities obtained at a constant overvoltage are compared, it is seen that the $Ni_{(10s)}$-$CoO_{(1.9mg)}$_Pt_{45} catalyst has a higher catalytic activity than the others. When the Tafel constant (b) values given in Fig. 8 are compared, the b values of $Ni_{(10s)}$ and $Ni_{(10s)}$-$CoO_{(1.9mg)}$ catalysts have a value greater than 120, and the b value for $Ni_{(10s)}$-$CoO_{(1.9mg)}$_Pt_{45} catalyst is less than 120. It can be understood that the hydrogen adsorption mechanism for the three catalysts is controlled according to Volmer- Heyrovsky mechanism. It is also seen that the rate determining reaction step for catalysts $Ni_{(10s)}$ and $Ni_{(10s)}$-$CoO_{(1.9mg)}$ is Volmer and the rate determining reaction step for catalyst $Ni_{(10s)}$-$CoO_{(1.9mg)}$_Pt_{45} is Heyrovsky mechanism.

Hydrogen evolution experiments in 1.0 M KOH solution using Pt/C, C, $Ni_{(10s)}$, $Ni_{(10s)}$-$CoO_{(1.9mg)}$ ve $Ni_{(10s)}$-$CoO_{(1.9mg)}$_Pt_{45} catalysts were carried out for 1 hour and at a current density of 200 mA cm^{-2}.
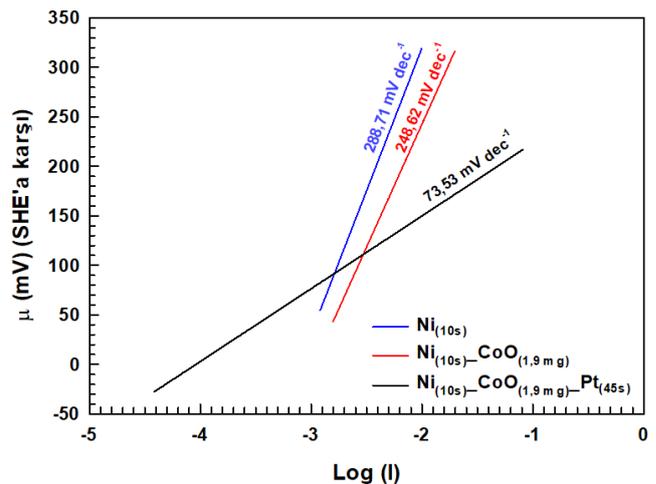
Figure 8. Cathodic potentiodynamic polarization curves of $Ni_{(10s)}$, $Ni_{(10s)}$-$CoO_{(1.9mg)}$, and $Ni_{(10s)}$-$CoO_{(1.9mg)}$_Pt_{45} catalysts obtained in 1.0 M KOH solution.

The results were given in Table 3. When the results are compared in terms of hydrogen production potential, it is seen that $Ni_{(10s)}$-$CoO_{(1.9mg)}$_Pt_{45} catalyst was more

effective. Considering the LSV curves in Fig. 7, it is seen that Pt/C is more effective at hydrogen output potential, but Ni$_{(10s)}$-CoO$_{(1.9mg)}$_Pt$_{45}$ catalyst was more effective at higher overvoltages ($\geq$ cathodic -150 mV). The hydrogen generation potentials in the overvoltage region in Table 3 confirm this.

Table 3. Hydrogen production amounts of catalysts.

	C	Ni$_{(10s)}$	Ni$_{(10s)}$-CoO$_{(1.9mg)}$	Ni$_{(10s)}$-CoO$_{(1.9mg)}$_Pt$_{45}$	Pt/C
Hydrogen Volume	82.8 mL cm^{-2}	85.4mL cm^{-2}	86.2 mL cm^{-2}	88.9 mL cm^{-2}	87.2 mL cm^{-2}

XRD measurements were made on the PANalytical EMPYREAN instrument. XRD measurements of Ni$_{(10s)}$-CoO$_{(1.9mg)}$_Pt$_{45}$ catalyst were given in Fig. 9. The peaks in the figure were defined using JCPDF No. 98-005-3781 (C), JCPDF No. 98-026-0169 (Ni), andJCPDF No. 98-010-5069 (Pt) reference cards. When the XRD graph was examined, two peaks belonging to C at 26.2 and 77.2, one peak belonging to Ni at 53.6 and two peaks belonging to Pt at 42.5 and 82.8 were determined. The peak of CoO was not observed in the XRD graph. This is because CoO was attached to the structure by the drag effect during nickel deposition, so it remained under the nickel plate. Observation of the C peak in the structure supports that the surface was not completely covered and a catalyst with a porous structure was obtained.
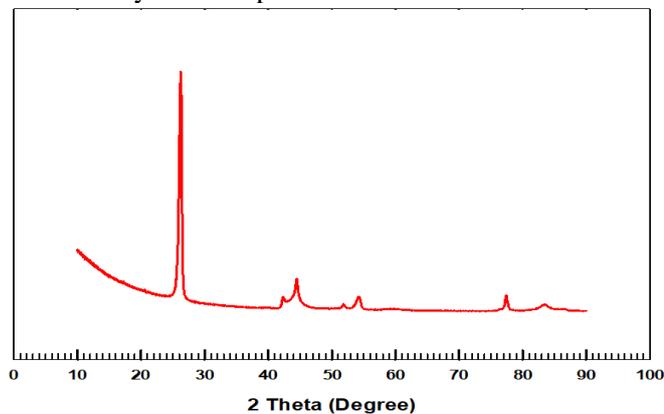
Figure 9. XRD pattern of Ni$_{(10s)}$-CoO$_{(1.9mg)}$_Pt$_{45}$ catalyst.

SEM images of C (a), Ni$_{(10s)}$ (b), Ni$_{(10s)}$-CoO$_{(1.9mg)}$ (c) ve Ni$_{(10s)}$-CoO$_{(1.9mg)}$_Pt$_{45}$ (d) catalysts taken with 10.0 kx magnification were given in Fig. 10. In Fig. 10a, carbon layers stacked on top of each other in the form of leaves are seen. Uniformly deposited nickel layers are shown in Fig. 10b. In Figure 10c, the presence of CoO in the structure is understood from the morphological differences in the structure due to the CoOs attached to the structure during nickel deposition. Finally, in Figure 10d, it is clearly seen that Pt is uniformly coated on the catalyst surface electrochemically, with a size of about 20-40 nm.
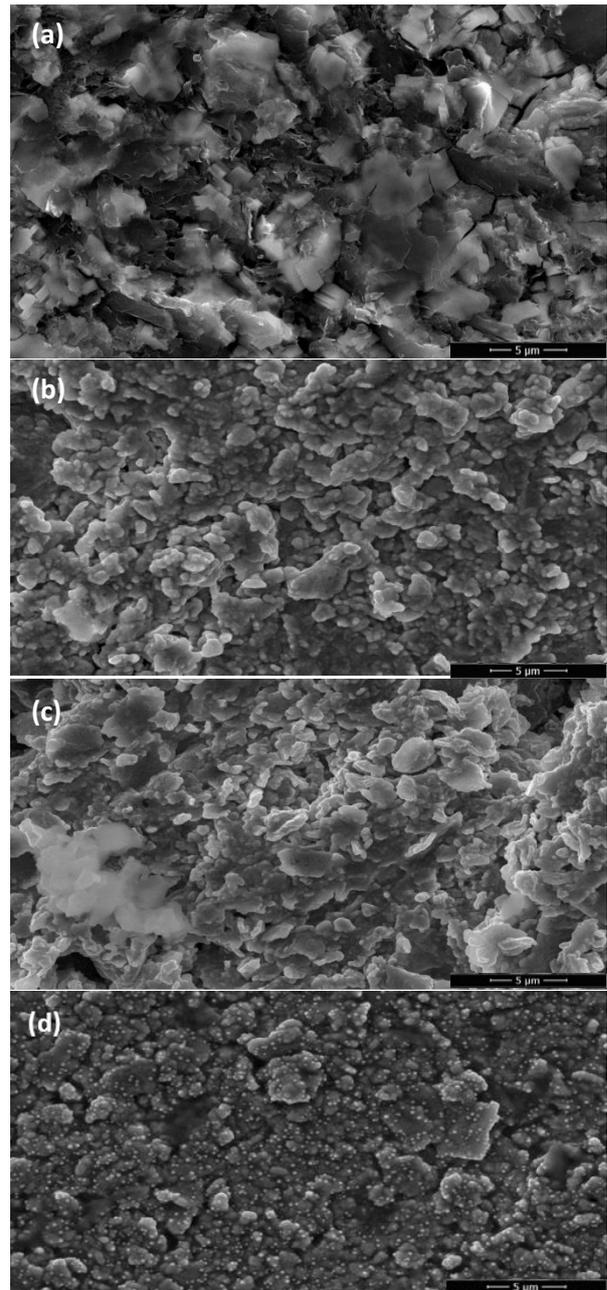
Figure 10. SEM images of C (a), Ni(10s) (b), Ni(10s)-CoO(1.9mg) (c), and Ni(10s)-CoO(1.9mg)_Pt45 (d) catalysts taken at 10.0 kx magnification.

In addition, the surface composition and surface homogenization characterization of $Ni_{(10s)}$-$CoO_{(1.9mg)}$_Pt_{45} catalyst using EDX and elemental
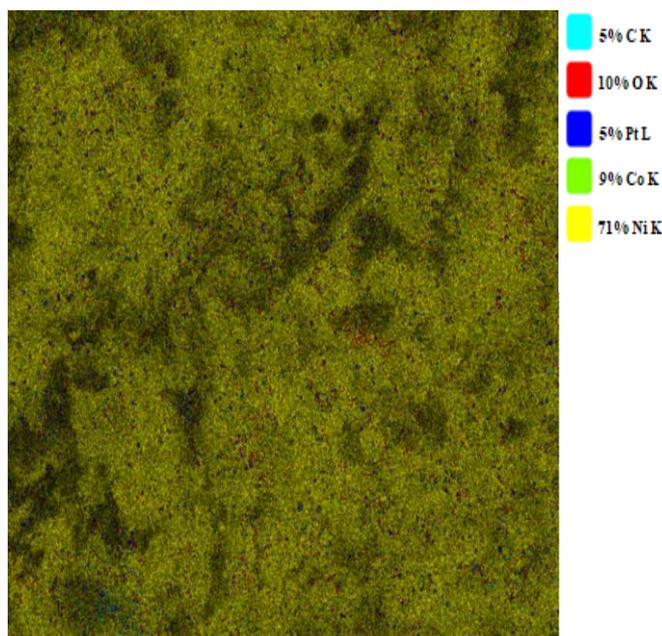
Figure 11. Mapping and EDX results of $Ni_{(10s)}$-$CoO_{(1,9mg)}$_Pt_{45} catalyst

Conclusions

In this study, catalysts with increased catalytic efficiency were obtained for HER by electrochemically deposited different compounds consisting of Ni, CoO and Pt on carbon support. All the obtained catalysts were analyzed by LSV and EIS techniques. In the nickel deposition process on carbon support, the most effective time for HER was determined as 10 seconds at 96 mA cm^{-2} and was shown as $Ni_{(10s)}$. CoO was added to the catalyst structure due to the catalytic efficiency-enhancing effect of metal-metal oxide structures for HER. In the process of adding CoO to the catalyst structure, the metal oxide was electrochemically deposited with a drag effect simultaneously during nickel deposition because avoid the negative effects of conductive adhesives. For deposition, different amounts of CoO were added to the Nickel bath and the most effective catalyst for HER was obtained when 1.9 mg of CoO was added, and it was symbolized as Ni(10s)-CoO(1.9mg). The catalytic activities of noble metals are known. To increase the catalytic efficiency, traces of noble metals (Pt) were added electrochemically to the catalyst structure. Because Pt is quite expensive compared to other metals. Therefore, different deposition times were applied and the Pt deposition time for the most effective catalyst was determined as 45 seconds and obtained catalyst was denoted as

mapping techniques were given in Fig. 11. When the figure is examined, it is seen that Nickel and CoO are uniformly deposited on the catalyst surface.

$Ni_{(10s)}$-$CoO_{(1.9mg)}$_Pt_{45}. Elemental and surface characterizations of the obtained catalysts were made using SEM-EDX and XRD devices. According to these analyzes, it was observed that Ni, CoO and Pt were homogeneously distributed on the surface. The hydrogen production capabilities of the obtained catalysts were tested with the reverse burette method and it was determined that the $Ni_{(10s)}$-$CoO_{(1.9mg)}$_Pt_{45} catalyst was more effective than the others. According to the potentiodynamic polarization technique, the hydrogen adsorption mechanism for the three catalysts is controlled by Volmer- Heyrovsky mechanism. It is also seen that the rate-determining reaction step for catalysts Ni(10s) and Ni(10s)-CoO(1.9mg) is Volmer and the rate-determining reaction step for catalyst $Ni_{(10s)}$-$CoO_{(1.9mg)}$_Pt_{45} is Heyrovsky mechanism.

Acknowledgment

Conflicts of interest

Related to the paper "Investigation of the Catalytic Effect of Metal-Metal Oxide Structure in the Catalysts Used in Hydrogen Production by Electrolysis of Water" submitted to the Cumhuriyet Science Journal, I declare that there is no financial/personal interest or belief that could affect our objectivity, and that no potential conflict exists.

References

[1] Höök M., Tang X., Depletion of fossil fuels and anthropogenic climate change—A review, *Energ Policy*, 52(1) (2013) 797-809.

[2] Luo M., Yi Y., Wang S., Wang Z., Du M., Pan J., Wang Q., Review of hydrogen production using chemical-looping technology, *Renewable and Sustainable Energy Reviews*, 81(2) (2018) 3186-214.

[3] Wang Y., Yang X., Wang Y., Catalytic performance of mesoporous MgO supported Ni catalyst in steam reforming of model compounds of biomass fermentation for hydrogen production, *International Journal*

of Hydrogen Energy, 41(40) (2016) 17846-57.

[4] Gong M., Wang D-Y., Chen C-C., Hwang B-J., Dai H., A mini review on nickel-based electrocatalysts for alkaline hydrogen evolution reaction, *Nano Research*, 9(1) (2016) 28-46.

[5] Zhang F., Zhao P., Niu M., Maddy J., The survey of key technologies in hydrogen energy storage, *International Journal of Hydrogen Energy,* 41(33) (2016) 14535-14552.

[6] Dincer I., Acar C., Review and evaluation of hydrogen production methods for better sustainability, *International Journal of Hydrogen Energy,* 40(34) (2015) 11094-11111.

[7] Muradov N., Veziroğlu T., From hydrocarbon to hydrogen–carbon to hydrogen economy, *International journal of hydrogen energy,* 30(3) (2005) 225-237.

[8] Arregi A., Amutio M., Lopez G., Bilbao J., Olazar M., Evaluation of thermochemical routes for hydrogen production from biomass: A review, *Energy Conversion and Management,* 165(1) (2018) 696-719.

[9] Holladay JD., Hu J., King DL., Wang Y., An overview of hydrogen production technologies, *Catalysis Today*, 139(4) (2009) 244-60.

[10] Levin DB., Chahine R., Challenges for renewable hydrogen production from biomass, *International Journal of Hydrogen Energy*, 35(10) (2010) 4962-4969.

[11] Bowen CT., Davis HJ., Henshaw BF., Lachance R., LeRoy RL., Renaud R., Developments in advanced alkaline water electrolysis, *International Journal of Hydrogen Energy,* 9(1) (1984) 59-66.

[12] Pu Z., Amiinu IS., Cheng R., Wang P., Zhang C., Mu S., Zhao W., Su F., Zhang G., Liao S., Sun S., Single-Atom Catalysts for Electrochemical Hydrogen Evolution Reaction: Recent Advances and Future Perspectives, Nano-*Micro Letters,* 12(1) (2020) 21.

[13] Danilovic N., Subbaraman R., Strmcnik D., Stamenkovic V., Markovic N., Electrocatalysis of the HER in acid and alkaline media, J*ournal of the Serbian Chemical Society,* 78(12) (2013) 2007-2015.

[14] Choquette Y., Brossard L., Lasia A., Menard H., Study of the Kinetics of Hydrogen Evolution Reaction on Raney Nickel Composite-Coated Electrode by AC Impedance Technique, *Journal of The Electrochemical Society,* 137(6) (1990) 1723-1730.

[15] Goranova D., Lefterova E., Rashkov R., Electrocatalytic activity of Ni-Mo-Cu and Ni-Co-Cu alloys for hydrogen evolution reaction in alkaline medium, *International Journal of Hydrogen Energy*, 42(48) (2017) 28777-28785.

[16] Farsak M., Kardaş G., Effect of current change on iron-copper-nickel coating on nickel foam for hydrogen production, *International Journal of Hydrogen Energy*, 44(27) (2019) 14151-14156.

[17] Solmaz R., Kardaş G., Fabrication and characterization of NiCoZn–M (M: Ag, Pd and Pt) electrocatalysts as cathode materials for electrochemical hydrogen production, *International Journal of Hydrogen Energy,* 36(19) (2011) 12079-12087.

[18] Farsak M., Aydın Ö., The snowflake-like structured CoO-Cu2O@ Fe/Ru catalyst for hydrogen fuel production, *International Journal of Energy Research*, 45(5) 2020 7561-7571.

[19] Hüner B., Farsak M., Telli E., A new catalyst of AlCu@ZnO for hydrogen evolution reaction, *International Journal of Hydrogen Energy*, 43(15) (2018) 7381-7387.

[20] Mkhondo N., Magadzu T., Surface properties of metal oxides and their role on electrochemical hydrogen storage of carbon nanotubes, *Digest journal of nanomaterials and biostructures*, 13(4) (2018) 921-929.

[21] Rios E., Poillerat G., Koenig JF., Gautier JL., Chartier P., Preparation and characterization of thin Co3O4 and MnCo2O4 films prepared on glass/SnO2:F by spray pyrolysis at 150 °C

for the oxygen electrode, *Thin Solid Films*, 264(1) (1995) 18-24.

[22] Wang K., Xia M., Xiao T., Lei T., Yan W., Metallurgically prepared NiCu alloys as cathode materials for hydrogen evolution reaction, *Mater Chem Phys.*, 186 (2017) 61-66.

[23] Solmaz R., Döner A., Kardaş G., Electrochemical deposition and characterization of NiCu coatings as cathode materials for hydrogen evolution reaction, *Electrochemistry Communications*, 10(12) (2008) 1909-1911.

[24] Telli E., Farsak M., Kardaş G., Investigation of noble metal loading CoWZn electrode for HER, *International Journal of Hydrogen Energy*, 42(36) (2017) 23260-23267.

[25] Tezcan F., Mahmood A., Kardaş G., Optimizing copper oxide layer on zinc oxide via two-step electrodeposition for better photocatalytic performance in photoelectrochemical cells, *Applied Surface Science,* 479 (2019) 1110-1117.

[26] Su D., Kim H-S., Kim W-S., Wang G., Mesoporous Nickel Oxide Nanowires: Hydrothermal Synthesis, Characterisation and Applications for Lithium-Ion Batteries and Supercapacitors with Superior Performance, *Chemistry – A European Journal*, 18(26) (2012) 8224-8229.

[27] Streckova M., Mudra E., Orinakova R., Markusova-Buckova L., Sebek M., Kovalcikova A., Sopcak T., Girman V., Dankova Z., Micusik M., Dusza J., Nickel and nickel phosphide nanoparticles embedded in electrospun carbon fibers as favourable electrocatalysts for hydrogen evolution, *Chem Eng J.,* 303 (2016) 167-181.

[28] Wen T-C., Kang H-M., Co–Ni–Cu ternary spinel oxide-coated electrodes for oxygen evolution in alkaline solution, *Electrochimica Acta*, 43(12) (1998) 1729-1745.

[29] Wang C., Li W., Lu X., Xie S., Xiao F., Liu P., Tong Y., Facile synthesis of porous 3D CoNiCu nano-network structure and their activity towards hydrogen evolution reaction, *International Journal of Hydrogen Energy,*

37(24) (2012) 18688-18693.

[30] Tsoncheva T., Tsyntsarski B., Ivanova R., Spassova I., Kovacheva D., Issa G., Paneva D., Karashanova D., Dimitrov M., Georgieva B., Velinov N., Mitov I., Petrov N., NixZn1-xFe2O4 modified activated carbons from industrial waste as catalysts for hydrogen production, *Microporous and Mesoporous Materials*, 285 (2019) 96-104.

[31] Tasic GS., Maslovara SP., Zugic DL., Maksic AD., Marceta Kaninski MP., Characterization of the Ni–Mo catalyst formed in situ during hydrogen generation from alkaline water electrolysis, *International Journal of Hydrogen Energy*, 36 (18) (2011) 11588-11595.

[32] Stoney GG., The tension of metallic films deposited by electrolysis, *Proceedings of the Royal Society of London Series A, Containing Papers of a Mathematical and Physical Character*, 82(553) (1909) 172-175.

[33] Rosalbino F., Delsante S., Borzone G., Angelini E., Electrocatalytic behaviour of Co–Ni–R (R=Rare earth metal) crystalline alloys as electrode materials for hydrogen evolution reaction in alkaline medium, *International Journal of Hydrogen Energy,* 33(22) (2008) 6696-6703.

[34] Nivetha R., Chella S., Kollu P., Jeong SK., Bhatnagar A., Andrews NG., Cobalt and nickel ferrites based graphene nanocomposites for electrochemical hydrogen evolution, *Journal of Magnetism and Magnetic Materials,* 448 (2018) 165-171.

[35] Hamdani M., Pereira MIS., Douch J., Ait Addi A., Berghoute Y., Mendonça MH., Physicochemical and electrocatalytic properties of Li-Co3O 4 anodes prepared by chemical spray pyrolysis for application in alkaline water electrolysis, *Electrochimica Acta,* 49(9-10) (2004) 1555-1563.

[36] Lačnjevac UČ., Jović BM., Jović VD., Radmilović VR., Krstajić NV., Kinetics of the hydrogen evolution reaction on Ni-(Ebonex-supported Ru) composite coatings in alkaline solution. *International Journal of Hydrogen Energy*, 38(25) (2013) 10178-10190.

[37] Lin H-K., Wang C-B., Chiu H-C., Chien S-H., In situ FTIR Study of Cobalt Oxides for the Oxidation of Carbon Monoxide, *Catalysis Letters,* 86(1) (2003) 63-68.

Approximation by the new modification of Bernstein-Stancu operators

Melek SOFYALIOĞLU[1,]* iD *, Kadir KANAT[1]* iD

[1]*Ankara Hacı Bayram Veli University, Polatlı Faculty of Science and Arts, Department of Mathematics, Ankara/TURKEY*

Abstract

The current paper deals with the new modification of Bernstein-Stancu operators which preserve constant and Korovkin's other test functions in limit case. We study the uniform convergence of the newly defined operators. The rate of convergence is investigated by means of the modulus of continuity, by using functions of Lipschitz class and by the help of Peetre-$\mathcal{K}$ functionals. Then a Voronovskaya type asymptotic formula for the newly constructed Bernstein-Stancu operators is presented. Finally, some graphs are given to illustrate the convergence properties of operators to some functions.

1. Introduction

Approximation theory concerns with the approximation of functions by the help of simpler calculated functions. Linear positive operators play a crucial role in this area. The well-known linear and positive operators are Bernstein operators [1], which are defined as

$$B_s(v; x) = \sum_{m=0}^{s} \binom{s}{m} x^s (1-x)^{s-m} v\left(\frac{m}{s}\right), \quad s \geq 1$$

for $v \in C[0,1]$ and $x \in [0,1]$. In 1983, Stancu [2] studied a generalization of Bernstein operators

$$S_s^{\alpha,\beta}(v; x) = \sum_{m=0}^{s} \binom{s}{m} x^m (1-x)^{s-m} v\left(\frac{m+\alpha}{s+\beta}\right)$$

with the condition $0 \leq \alpha \leq \beta$. After that, various versions of Bernstein operators are investigated by researchers such as [3-8]. Recently, a new modification of Bernstein operators is introduced by Usta [9] which unchanging constant test function and preserve Korovkin's other test functions t and t^2 in limit case by

$$B_s^*(v; x) = \frac{1}{s} \sum_{m=0}^{s} \binom{s}{m} (m - sx)^2 x^{m-1} (1-x)^{s-m-1} v\left(\frac{m}{s}\right).$$

And he proved the approximation properties of the $B_s^*(v; x)$ operators. Motivated by this work, we construct a modification of Bernstein-Stancu operators. The new modification of Bernstein-Stancu operators is presented for $v \in C[0,1]$ as follows:

$$B_s^{\alpha,\beta}(v; x) = \frac{1}{s} \sum_{m=0}^{s} \binom{s}{m} (m - sx)^2 x^{m-1} (1-x)^{s-m-1} v\left(\frac{m+\alpha}{s+\beta}\right), \tag{1}$$

where $0 \leq \alpha \leq \beta$, $x \in (0,1)$ and $s \geq 1$.

The aim of the current paper is to derive approximation properties for the operators (1) by working on Korovkin's theorem [10].

The rest of this paper is structured as follows: In Section 2, the certain elementary properties and uniform convergence of the newly constructed Bernstein-Stancu operators are investigated. In Section 3, the rate of convergence is studied, while Voronovskaya-type asymptotic formula is given in Section 4. In Section 5, the

numerical examples are illustrated to show the prosperousness of the theoretical results and the effectiveness of the defined operators. Finally, a brief conclusion about the paper is given in Section 6.

2. Approximation Properties of $B_s^{\alpha,\beta}$

In this part, we give some important auxiliary results which will be used in proving our main results of the following sections. First of all, we determine moments, central moments and some limit results for the operators (1).

Lemma 2.1 For every $x \in (0,1)$ and $0 \le \alpha \le \beta$, we write

$$B_s^{\alpha,\beta}(e_0;x) = 1,$$

$$B_s^{\alpha,\beta}(e_1;x) = \frac{s-2}{s+\beta}x + \frac{\alpha+1}{s+\beta},$$

$$B_s^{\alpha,\beta}(e_2;x) = \frac{s^2-7s+6}{(s+\beta)^2}x^2 + \frac{(5+2\alpha)s-6-4\alpha}{(s+\beta)^2}x + \frac{(\alpha+1)^2}{(s+\beta)^2},$$

$$B_s^{\alpha,\beta}(e_3;x) = \frac{s^3-15s^2+38s-24}{(s+\beta)^3}x^3 + \frac{(12+3\alpha)s^2-(48+21\alpha)s+36+18\alpha}{(s+\beta)^3}x^2$$
$$+ \frac{(13+15\alpha+3\alpha^2)s-14-18\alpha-6\alpha^2}{(s+\beta)^3}x + \frac{(\alpha+1)^3}{(s+\beta)^3},$$

$$B_s^{\alpha,\beta}(e_4;x) = \frac{1}{(\beta+s)^4(x-1)}(-1 + \alpha^4(x-1) + (10-8s)x + (-180+240s-61s^2)x^2 + (390-615s$$
$$+ 247s^2-22s^3)x^3 - (360-630s+317s^2-48s^3+s^4)x^4 + (120-226s+131s^2$$
$$- 26s^3+s^4)x^5 + 4\alpha^3(x-1)(1+(-2+s)x)$$
$$+ 6\alpha^2(x-1)(1+(-6+5s)x+(6-7s+s^2)x^2) + 4\alpha(x-1)(1+(-14+13s)x$$
$$+ 12(3-4s+s^2)x^2+(-24+38s-15s^2+s^3)x^3)),$$

where $e_m = t^m$ for $m = 0,1,2,3,4$.

Lemma 2.2 For every $x \in (0,1)$ and $0 \le \alpha \le \beta$, we have

$$B_s^{\alpha,\beta}(t-x;x) = -\frac{2+\beta}{s+\beta}x + \frac{\alpha+1}{s+\beta},$$

$$B_s^{\alpha,\beta}((t-x)^2;x) = \frac{-3s+6+4\beta+\beta^2}{(s+\beta)^2}x^2 + \frac{3s-(6+4\alpha+2(\alpha+1)\beta)}{(s+\beta)^2}x + \frac{(\alpha+1)^2}{(s+\beta)^2},$$

$$B_s^{\alpha,\beta}((t-x)^4;x) = \frac{1}{(\beta+s)^4(x-1)}(-1+\alpha^4(x-1)+2(5+2\beta-2s)x-(6\beta^2+\beta(60-40s)$$
$$+15(12-12s+s^2))x^2+(4\beta^3-6\beta^2(-7+3s)-40\beta(-5+4s)+5(78-83s$$
$$+9s^2))x^3-(12\beta^3+\beta^4-36\beta^2(-2+s)-40\beta(-6+5s)+15(24-26s+3s^2))x^4$$
$$+(8\beta^3+\beta^4+\beta(96-80s)-18\beta^2(-2+s)+5(24-26s+3s^2))x^5$$
$$-4\alpha^3(x-1)(-1+(2+\beta)x)+6\alpha^2(x-1)(1+(-6-2\beta+3s)x$$
$$+(6+4\beta+\beta^2-3s)x^2)-4\alpha(x-1)(-1+(14+3\beta-10s)x-3(12+\beta^2-$$
$$3\beta(-2+s)-10s)x^2+(24+6\beta^2+\beta^3-9\beta(-2+s)-20s)x^3)). \tag{2}$$

Proof.

With the help of the following equalities

$$B_s^{\alpha,\beta}(t-x;x) = B_s^{\alpha,\beta}(e_1;x) - xB_s^{\alpha,\beta}(1;x),$$

$$B_s^{\alpha,\beta}((t-x)^2;x) = B_s^{\alpha,\beta}(e_2;x) - 2xB_s^{\alpha,\beta}(e_1;x) + x^2B_s^{\alpha,\beta}(1;x),$$

$$B_s^{\alpha,\beta}((t-x)^4;x) = B_s^{\alpha,\beta}(e_4;x) - 4xB_s^{\alpha,\beta}(e_3;x) + 6x^2B_s^{\alpha,\beta}(e_2;x) - 4x^3B_s^{\alpha,\beta}(e_1;x) + x^4B_s^{\alpha,\beta}(1;x),$$

and with the help of Lemma 2.1, we get the desired results.

Lemma 2.3 We have following results

$$\lim_{s\to\infty} sB_s^{\alpha,\beta}(t-x;x) = -(2+\beta)x + \alpha + 1, \tag{3}$$

$$\lim_{s\to\infty} sB_s^{\alpha,\beta}((t-x)^2;x) = 3x(1-x), \tag{4}$$

$$\lim_{s\to\infty} s^2B_s^{\alpha,\beta}((t-x)^4;x) = 15(x-1)^2x^2. \tag{5}$$

Let the Banach space of all continuous functions v on $[0,1]$ is denoted by $C[0,1]$ endowed with the norm

$$\|v\| = \max_{x\in(0,1)}|v(x)|.$$

Theorem 2.1 For every $v \in C[0,1], x \in (0,1)$ and $0 \le \alpha \le \beta$

$$\left\|B_s^{\alpha,\beta}(v) - v\right\| \to 0, \tag{6}$$

uniformly as $s \to \infty$.

Proof.

It can be seen clearly from Lemma 2.1 that

$$\lim_{s\to\infty} B_s^{\alpha,\beta}(e_i;x) = t^i, \qquad i = 0,1,2.$$

Thus, we conclude the proof of the theorem thanks to the result of Korovkin's theorem [10].

3. Rate of Convergence

In this section, we study the rate of convergence with the help of modulus of continuity, by using functions that belong to Lipschitz class and with the help of Peetre-$\mathcal{K}$ functionals, respectively.

For $v \in C[0,1]$, the modulus of continuity is given by

$$\omega(v,\delta) := \sup_{|t-x|\le\delta} \sup_{x\in(0,1)} |v(t) - v(x)|, \quad \delta > 0.$$

Modulus of continuity of function v has the property as follows:

$$|v(t) - v(x)| \le \left(1 + \frac{(t-x)^2}{\delta^2}\right)\omega(v,\delta).$$

Theorem 3.1 For every $x \in (0,1)$, $v \in C[0,1]$ and $0 \le \alpha \le \beta$,

$$|B_s^{\alpha,\beta}(v;x) - v(x)| \le 2\omega(v,\delta_s(x)). \tag{7}$$

Here,

$$\delta_s(x) = \frac{\sqrt{\alpha^2 + 2\alpha + 1 + (3s - (6 + 4\alpha + 2(\alpha+1)\beta))x + (-3s + 6 + 4\beta + \beta^2)x^2}}{s+\beta}.$$

Proof.

$$\left|B_s^{\alpha,\beta}(v;x) - v(x)\right| = \left|\frac{1}{s}\sum_{m=0}^{s}\binom{s}{m}(m-sx)^2 x^{m-1}(1-x)^{s-m-1}v\left(\frac{m+\alpha}{s+\beta}\right) - v(x)\right|$$

$$\leq \frac{1}{s}\sum_{m=0}^{s}\binom{s}{m}(m-sx)^2 x^{m-1}(1-x)^{s-m-1}\left|v\left(\frac{m+\alpha}{s+\beta}\right) - v(x)\right|$$

$$\leq \frac{1}{s}\sum_{m=0}^{s}\binom{s}{m}(m-sx)^2 x^{m-1}(1-x)^{s-m-1}\left(1 + \frac{1}{\delta^2}\frac{(m+\alpha-x(s+\beta))^2}{(s+\beta)^2}\right)\omega(v,\delta)$$

$$= \left(1 + \frac{1}{\delta^2}\frac{\alpha^2+2\alpha+1+\left(3s-(6+4\alpha+2(\alpha+1)\beta)\right)x+\left(-3s+6+4\beta+\beta^2\right)x^2}{(s+\beta)^2}\right)\omega(v,\delta).$$

If we choose

$$\delta = \delta_s(x) = \frac{\sqrt{\alpha^2 + 2\alpha + 1 + (3s - (6 + 4\alpha + 2(\alpha + 1)\beta))x + (-3s + 6 + 4\beta + \beta^2)x^2}}{s+\beta},$$

then we achieve that

$$|B_s^{\alpha,\beta}(v;x) - v(x)| \leq 2\omega\left(v, \frac{\sqrt{\alpha^2 + 2\alpha + 1 + (3s - (6 + 4\alpha + 2(\alpha + 1)\beta))x + (-3s + 6 + 4\beta + \beta^2)x^2}}{s+\beta}\right),$$

which is the desired result.

Just now, we investigate the rate of convergence of $B_s^{\alpha,\beta}(v;x)$ by using functions of Lipschitz class. Let's recall that a function $v \in Lip_K(c)$ on $(0,1)$ if the inequality

$$|v(t) - v(x)| \leq K|t - x|^c \ ; \ \forall t, x \in (0,1) \tag{8}$$

holds.

Theorem 3.2 Let $v \in Lip_K(c)$, $0 < c \leq 1$, $0 \leq \alpha \leq \beta$, then we have

$$\left|B_s^{\alpha,\beta}(v;x) - v(x)\right| \leq K[\delta_s(x)]^c,$$

where

$$\delta_s(x) = \frac{\sqrt{\alpha^2 + 2\alpha + 1 + (3s - (6 + 4\alpha + 2(\alpha + 1)\beta))x + (-3s + 6 + 4\beta + \beta^2)x^2}}{s+\beta}.$$

Proof.

Let $v \in Lip_K(c)$, $0 < c \leq 1$ and $0 \leq \alpha \leq \beta$. By using (8) and the linearity and monotonicity of the operators $B_s^{\alpha,\beta}$ we have

$$\left|B_s^{\alpha,\beta}(v;x) - v(x)\right| \leq B_s^{\alpha,\beta}(|v(t) - v(x)|;x)$$

$$\leq KB_s^{\alpha,\beta}(|t - x|^c;x).$$

By taking $p = \frac{2}{c}$, $q = \frac{2}{2-c}$ in the Hölder's inequality, we get

$$\left|B_s^{\alpha,\beta}(v;x) - v(x)\right| \leq K\left\{B_s^{\alpha,\beta}((t - x)^2;x)\right\}^{\frac{c}{2}}$$

$$\leq K[\delta_s(x)]^c$$

immediately. If we choose

$$\delta_s(x) = \frac{\sqrt{\alpha^2 + 2\alpha + 1 + (3s - (6 + 4\alpha + 2(\alpha + 1)\beta))x + (-3s + 6 + 4\beta + \beta^2)x^2}}{s + \beta}$$

the proof is completed.

Lastly, we mention the rate of convergence of our operator $B_s^{\alpha,\beta}(v; x)$ by means of Peetre-$\mathcal{K}$ functionals. First of all, we give the following lemma:

Lemma 3.1 For $x \in (0,1)$, $v \in C[0,1]$ and $0 \leq \alpha \leq \beta$, we have

$$|B_s^{\alpha,\beta}(v; x)| \leq ||v||. \tag{9}$$

Proof.
From the definiton of $B_s^{\alpha,\beta}(v; x)$, we write

$$
\begin{aligned}
|B_s^{\alpha,\beta}(v; x)| &= \left| \frac{1}{s} \sum_{m=0}^{s} \binom{s}{m} (m - sx)^2 x^{m-1}(1-x)^{s-m-1} v\left(\frac{m+\alpha}{s+\beta}\right) \right| \\
&\leq \frac{1}{s} \sum_{m=0}^{s} \binom{s}{m} (m - sx)^2 x^{m-1}(1-x)^{s-m-1} \left| v\left(\frac{m+\alpha}{s+\beta}\right) \right| \\
&\leq ||v|| B_s^{\alpha,\beta}(1; x) \\
&= ||v||.
\end{aligned}
$$

Currently, we recall the properties of Peetre-$\mathcal{K}$ functionals. $C^2[0,1]$ is the space of the functions v, for which v, v' and v'' are continuous on $[0,1]$. We define classical Peetre-$\mathcal{K}$ functional as follows:

$$\mathcal{K}(v, \delta) := \inf_{u \in C^2[0,1]} \{||v - u||_{C[0,1]} + \delta ||u''||_{C[0,1]}\}$$

and second modulus of smoothness of the function is defined by

$$\omega_2(v, \delta) := \sup_{0 < h < \delta} \sup_{x, x+2h \in (0,1)} |v(x + 2h) - 2v(x + h) + v(x)|$$

where $\delta > 0$. By [11], it is known that for $A > 0$

$$\mathcal{K}(v, \delta) \leq A\omega_2(v, \sqrt{\delta}).$$

Theorem 3.3 Let $x \in (0,1)$, $v \in C[0,1]$ and $0 \leq \alpha \leq \beta$. Then we have for all $s \in \mathbb{N}$, there exists a positive constant A such that,

$$|B_s^{\alpha,\beta}(v; x) - v(x)| \leq A\omega_2(v, \alpha_s(x)) + 2\omega(v, \beta_s(x)),$$

where

$$\alpha_s(x) = \sqrt{\frac{3 + 6\alpha + 3\alpha^2 - 6\alpha(2 + \beta)x - 2(8 + 3\beta - 3s)x + (16 + 12\beta + 3\beta^2 - 6s)x^2}{2(s + \beta)^2}}$$

and

$$\beta_s(x) = \left| \frac{1 + \alpha - (2 + \beta)x}{s + \beta} \right|.$$

Proof.

Define an auxiliary operator $B_s^*: C[0,1] \to C[0,1]$ by

$$B_s^*(u; x) = B_s^{\alpha,\beta}(u; x) - u\left(\frac{(s-2)x+\alpha+1}{s+\beta}\right) + u(x). \tag{10}$$

From Lemma 2.1, we have

$$B_s^*(1; x) = 1$$

$$B_s^*(t - x; x) = B_s^{\alpha,\beta}((t - x); x) - \left(\frac{(s - 2)x + \alpha + 1}{s + \beta} - x\right) + x - x$$

$$= \left(-\frac{2+\beta}{s+\beta}x + \frac{\alpha+1}{s+\beta}\right) - \left(\frac{(s-2)x+\alpha+1}{s+\beta} - x\right) + x - x$$

$$= 0. \tag{11}$$

For a given function $u \in C^2[0,1]$, we have by the Taylor expansion that

$$u(t) = u(x) + (t - x)u'(x) + \int_x^t (t - m)u''(m)dm, \quad t \in (0,1). \tag{12}$$

Applying B_s^* operator to the both sides of the equation (12), we obtain

$$B_s^*(u; x) = B_s^*\left(u(x) + (t - x)u'(x) + \int_x^t (t - m)u''(m)dm; x\right)$$

$$= u(x) + B_s^*((t - x)u'(x); x) + B_s^*\left(\int_x^t (t - m)u''(m)dm; x\right).$$

So,

$$B_s^*(u; x) - u(x) = u'(x)B_s^*((t - x); x) + B_s^*\left(\int_x^t (t - m)u''(m)dm; x\right).$$

By using (10) and (11), we get

$$B_s^*(u; x) - u(x) = B_s^*\left(\int_x^t (t - m)u''(m)dm; x\right)$$

$$= B_s^{\alpha,\beta}\left(\int_x^t (t - m)u''(m)dm; x\right) - \int_x^{\frac{(s-2)x+\alpha+1}{s+\beta}}\left(\frac{(s-2)x+\alpha+1}{s+\beta} - m\right)u''(m)dm$$

$$+ \int_x^x \left(\frac{(s-2)x+\alpha+1}{s+\beta} - m\right)u''(m)dm. \tag{13}$$

Furthermore,

$$\left|\int_x^t (t - m)u''(m)dm\right| \le \int_x^t |t - m||u''(m)|dm \le ||u''||\int_x^t |t - m|dm$$

$$\le (t - x)^2||u''||, \tag{14}$$

and

$$\left|\int_x^{\frac{(s-2)x+\alpha+1}{s+\beta}}\left(\frac{(s - 2)x + \alpha + 1}{s + \beta} - u\right)u''(m)dm\right| \le ||u''||\int_x^{\frac{(s-2)x+\alpha+1}{s+\beta}}\left(\frac{(s - 2)x + \alpha + 1}{s + \beta} - m\right)dm$$

$$= \frac{||u''||}{2}\left(\left(\frac{(s-2)x+\alpha+1}{s+\beta}\right)^2 - 2\frac{(s-2)x+\alpha+1}{s+\beta}x + x^2\right)$$

$$= \frac{||u''||}{2}\left(\frac{(s-2)x+\alpha+1}{s+\beta} - x\right)^2. \tag{15}$$

Let's rewrite (14) and (15) in the absolute value of (13). Then we obtain

$$|B_s^*(u; x) - u(x)| \le ||u''||B_s^{\alpha,\beta}((t - x)^2; x) + \frac{||u''||}{2}\left(\frac{(s - 2)x + \alpha + 1}{s + \beta} - x\right)^2$$

$$= ||u''||\left(B_s^{\alpha,\beta}((t - x)^2; x) + \frac{1}{2}\left(\frac{(s-2)x+\alpha+1}{s+\beta} - x\right)^2\right)$$

$$= ||u''||\alpha_s^2(x),$$

where

$$\alpha_s(x) = \sqrt{B_s^{\alpha,\beta}\left((t-x)^2;x\right) + \frac{1}{2}\left(\frac{(s-2)x+\alpha+1}{s+\beta}-x\right)^2}$$

$$= \sqrt{\frac{3+6\alpha+3\alpha^2-6\alpha(2+\beta)x-2(8+3\beta-3s)x+(16+12\beta+3\beta^2-6s)x^2}{2(s+\beta)^2}}.$$

Now, we will find an upper bound for the auxiliary operator $B_s^*(u;x)$. In the light of the Lemma 3.1, we get

$$|B_s^*(u;x)| = |B_s^{\alpha,\beta}(u;x) - u\left(\frac{(s-2)x+\alpha+1}{s+\beta}\right) + u(x)|$$

$$\leq |B_s^{\alpha,\beta}(u;x)| + \left|u\left(\frac{(s-2)x+\alpha+1}{s+\beta}\right)\right| + |u(x)|$$

$$\leq 3||u||.$$

Accordingly,

$$|B_s^{\alpha,\beta}(v;x) - v(x)| = \left|B_s^*(v;x) - v(x) + v\left(\frac{(s-2)x+\alpha+1}{s+\beta}\right) - v(x) + u(x) - u(x)\right.$$

$$\left. + B_s^*(u;x) - B_s^*(u;x)\right|$$

$$\leq |B_s^*(v-u;x) - (v-u)(x)| + |B_s^*(u;x) - u(x)| + \left|v\left(\frac{(s-2)x+\alpha+1}{s+\beta}\right) - v(x)\right|$$

$$\leq 4||v-u|| + ||u''||\alpha_s^2(x) + \omega(v,\beta_s(x))\left(1 + \frac{\left|\frac{(s-2)x+\alpha+1}{s+\beta}-x\right|}{\beta_s(x)}\right)$$

$$= 4||v-u|| + ||u''||\alpha_s^2(x) + 2\omega\left(v,\left|\frac{(s-2)x+\alpha+1}{s+\beta}-x\right|\right), \tag{16}$$

where

$$\beta_s(x) = \left|\frac{(s-2)x+\alpha+1}{s+\beta}-x\right|$$

$$= \left|\frac{1+\alpha-(2+\beta)x}{s+\beta}\right|.$$

Finally, for all $v \in C^2[0,1]$ take the infimum of the equation (16). We achieve

$$|B_s^{\alpha,\beta}(v;x) - v(x)| \leq 4\mathcal{K}(u,\alpha_s^2(x)) + 2\omega(v,\beta_s(x)). \tag{17}$$

As a result, using the property of Peetre-$\mathcal{K}$ functional, we obtain

$$|B_s^{\alpha,\beta}(v;x) - v(x)| \leq A\omega_2(v,\alpha_s(x)) + 2\omega(v,\beta_s(x)). \tag{18}$$

Thus the proof is completed.

4. Voronovskaya-Type Theorem

In 1932, Voronovskaya [12] obtain the convergence speed of the the $B_s(v;x)$ operators to the function v. In this section, we give a Voronovskaya-type asymptotic formula for $B_s^{\alpha,\beta}(v;x)$ operators.

Theorem 4.1 Let v be integrable on the interval $(0,1)$, also u' and u'' exist at a fixed point $x \in (0,1)$. Then we have

$$\lim_{s\to\infty} s\left(B_s^{\alpha,\beta}(v;x) - v(x)\right) = (-(2+\beta)x+\alpha+1)v'(x) + \frac{3}{2}x(1-x)v''(x). \tag{19}$$

Proof.

By using the well-known Taylor's formula, we write

$$v(t) = v(x) + (t-x)v'(x) + \frac{(t-x)^2}{2}v''(x) + \mathcal{R}(t,x)(t-x)^2, \tag{20}$$

where $\mathcal{R}(t,x) := \frac{v''(\xi)-v''(x)}{2}$ is Peano form of the remainder term such that ξ lying between x and t. Also, $\lim_{t \to x}\mathcal{R}(t,x) = 0$. By applying $B_s^{\alpha,\beta}$ operators to (20), we get

$$B_s^{\alpha,\beta}(v;x) - v(x) = v'(x)B_s^{\alpha,\beta}((t-x);x) + \frac{v''(x)}{2}B_s^{\alpha,\beta}((t-x)^2;x)$$

$$+ B_s^{\alpha,\beta}(\mathcal{R}(t,x)(t-x)^2;x). \tag{21}$$

When we multiply (21) by s and take the limit as s goes to infinity, we achieve

$$\lim_{s \to \infty} s\left(B_s^{\alpha,\beta}(v;x) - v(x)\right) = \lim_{s \to \infty} sv'(x)B_s^{\alpha,\beta}((t-x);x) + \lim_{s \to \infty} s\frac{v''(x)}{2}B_s^{\alpha,\beta}((t-x)^2;x)$$

$$+ \lim_{s \to \infty} sB_s^{\alpha,\beta}(\mathcal{R}(t,x)(t-x)^2;x).$$

Considering Lemma 2.3, Eqn. (3) and Eqn. (4) we obtain

$$\lim_{s \to \infty} sv'(x)B_s^{\alpha,\beta}((t-x);x) = v'(x)\lim_{s \to \infty} sB_s^{\alpha,\beta}((t-x);x)$$

$$= v'(x)(-(2+\beta)x + \alpha + 1)$$

and

$$\lim_{s \to \infty} s\frac{v''(x)}{2}B_s^{\alpha,\beta}((t-x)^2;x) = \frac{v''(x)}{2}\lim_{s \to \infty} sB_s^{\alpha,\beta}((t-x)^2;x)$$

$$= \frac{v''(x)}{2}(3x - 3x^2).$$

Therefore, we have

$$\lim_{s \to \infty} s\left(B_s^{\alpha,\beta}(v;x) - v(x)\right) = (-(2+\beta)x + \alpha + 1)v'(x) + \frac{3}{2}x(1-x)v''(x)$$

$$+ \lim_{s \to \infty} sB_s^{\alpha,\beta}(\mathcal{R}(t,x)(t-x)^2;x). \tag{22}$$

In order to complete the proof, we need to prove that

$$\lim_{s \to \infty} sB_s^{\alpha,\beta}(\mathcal{R}(t,x)(t-x)^2;x).$$

Using the Cauchy-Schwarz inequality for the remainder term, we obtain

$$sB_s^{\alpha,\beta}(\mathcal{R}(t,x)(t-x)^2;x) \leq \sqrt{B_s^{\alpha,\beta}(\mathcal{R}^2(t,x);x)}\sqrt{s^2 B_s^{\alpha,\beta}((t-x)^4;x)}. \tag{23}$$

We already know the term $B_s^{\alpha,\beta}((t-x)^4;x)$ from Eqn. (2). Since $\mathcal{R}^2(.,x)$ is continuous at $t \in (0,1)$ and $\lim_{t \to x}\mathcal{R}(t,x) = 0$, we observe that

$$\lim_{s \to \infty} B_s^{\alpha,\beta}(\mathcal{R}^2(t,x);x) = \mathcal{R}^2(x,x) = 0. \tag{24}$$

Hence, by using (2), (23), (24) and positivity of the linear operators $B_s^{\alpha,\beta}$, we have

$$\lim_{s \to \infty} sB_s^{\alpha,\beta}(\mathcal{R}(t,x)(t-x)^2;x) = 0. \tag{25}$$

Finally, by substituting (25) in (22) we deduce

$$\lim_{s \to \infty} s\left(B_s^{\alpha,\beta}(v;x) - v(x)\right) = (-(2+\beta)x + \alpha + 1)v'(x) + \frac{3}{2}x(1-x)v''(x)$$

as desired.

5. Graphical Analysis

In this section, we show the convergence of the newly constructed operators $B_s^{\alpha,\beta}$ with function v.
Let the the function v be

$$v(x) = \tan\left(\frac{x}{16}\right)\left(\frac{x}{8}\right)^2\left(1 - \frac{x}{4}\right)^3.$$

We know that, the operators $B_s^{\alpha,\beta}$ have been given for the interval $(0,1)$. For this reason, we define the interval $[0 + \epsilon, 1 - \epsilon]$, where $\epsilon = 0.0001$.

Then for $\alpha = 1.01$ and $\beta = 1.02$, we have plotted the convergence of the B_s^* Bernstein operators [7] and newly constructed $B_s^{\alpha,\beta}$ Bernstein-Stancu operators to the function v in Fig. 1 for different s values.
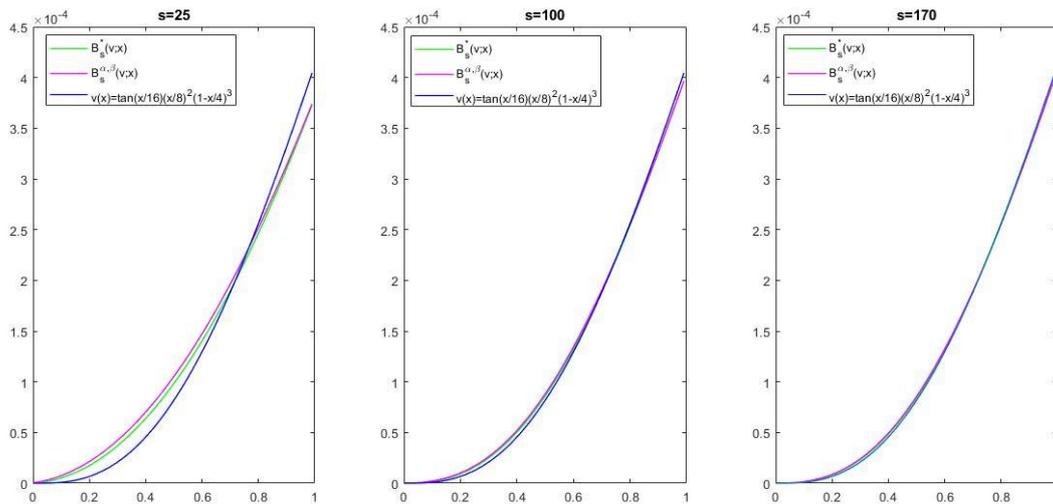
Figure 1. Convergence of $B_s^{\alpha,\beta}(v;x)$ and $B_s^*(v;x)$ to the function $v(x)$ for different values of s with fixed $\alpha = 1.01$, $\beta = 1.02$.

The maximum error estimation for operators $B_s^{\alpha,\beta}$ and B_s^* to the function $v(x) = \tan\left(\frac{x}{16}\right)\left(\frac{x}{8}\right)^2\left(1 - \frac{x}{4}\right)^3$ is presented in Table 1 for the interval $x \in [0 + \epsilon, 1 - \epsilon]$.

Table 1. Error estimation table

s	$\underset{x\in[0+\epsilon,1-\epsilon]}{\text{Max}}\lvert B_s^*(v;x) - v(x)\rvert$	$\underset{x\in[0+\epsilon,1-\epsilon]}{\text{Max}}\lvert B_s^{\alpha,\beta}(v;x) - v(x)\rvert$
25	$3.17794 \cdot 10^{-5}$	$3.05525 \cdot 10^{-5}$
75	$1.06654 \cdot 10^{-5}$	$1.05226 \cdot 10^{-5}$
100	$8.00549 \cdot 10^{-6}$	$7.92454 \cdot 10^{-6}$
170	$4.71371 \cdot 10^{-6}$	$4.68533 \cdot 10^{-6}$

For a second example, let the the function v be

$$v(x) = \frac{x^3}{3} - \frac{x^2}{10} + \frac{3x}{10}$$

and $[0 + \epsilon, 0.8 - \epsilon]$ where $\epsilon = 0.01$. Then for $\alpha = 0.01$ and $\beta = 0.1$, we have plotted the convergence of the $B_s^{\alpha,\beta}$ Bernstein-Stancu operators to the function v in Fig. 2 for $s = 170$.
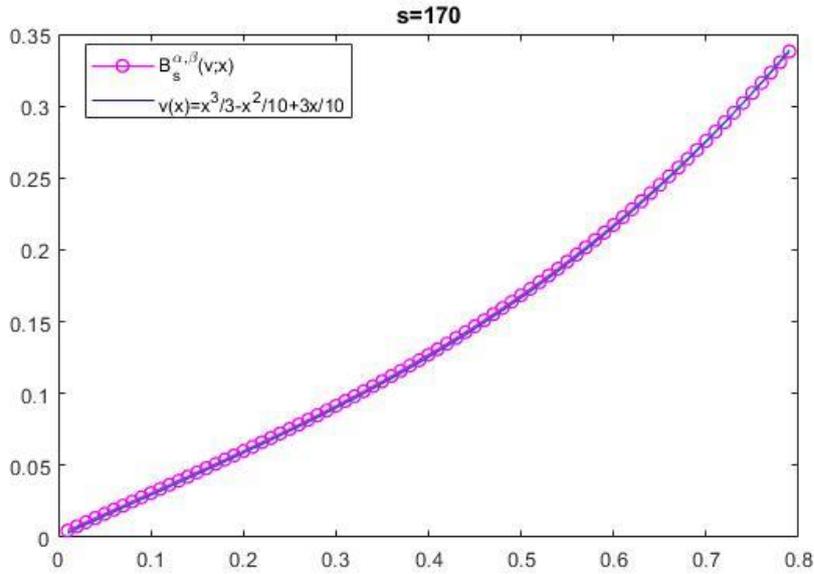
Figure 2. Convergence of $B_s^{\alpha,\beta}(v;x)$ for $s = 170$ with fixed $\alpha = 0.01, \beta = 0.1$.

The error estimation for operators $B_s^{\alpha,\beta}$ to the function $v(x) = \frac{x^3}{3} - \frac{x^2}{10} + \frac{3x}{10}$ is presented in Table 2 at the points x=0.1, 0.2, 0.4, 0.6 and x=0.79. Additionally, maximum error for Bernstein-Stancu operators to the function v is calculated for $x \in [0 + \epsilon, 0.8 - \epsilon], \ \epsilon = 0.01.$.

Table 2. Error estimation table

s	Error for x=0.1	Error for x=0.2	Error for x=0.4	Error for x=0.6	Error for x=0.79	$\underset{x\in[0+\epsilon,0.8-\epsilon]}{\text{Max}}\|B_s^{\alpha,\beta}(v;x) - v(\text{x})\|$
25	0.00962	0.00944	0.01114	0.00827	0.00663	0.01157
75	0.00313	0.00305	0.00373	0.00291	0.00210	0.00388
100	0.00234	0.00227	0.00280	0.00220	0.00156	0.00291
170	0.00137	0.00133	0.00164	0.00130	0.00091	0.00171

As we can see in Fig. 1 and Fig. 2, the newly defined Bernstein-Stancu operators present good approximation behaviour in function approximation.

6. Conclusion

In this paper, we investigated Stancu-type generalization of the new modification of Bernstein operators. We examined that the newly defined Bernstein-Stancu operators fix constant and preserve Korovkin's other test functions in limit case. Also, we improved many approximation properties such as the rate of approximation, Voronovskaya-type asymptotic formula. Furthermore, we demonstrated the theoretical results by using graphical representations.

Conflicts of interest

The authors declared there is no conflict of interest associated with this work.

References

[1] Bernstein S.N., Démonstration du théorem de Weierstrass fondée sur le calculu des probabilités, *Commun. Kharkov Math. Soc.*, 13(2) (1912) 1-2.

[2] Stancu D.D., Approximation of function by means of a new generalized Bernstein operator, *Calcolo*, 20(2) (1983) 211-229.

[3] Cai Q.-B., Lian B.-Y., Zhou G., Approximation properties of λ-Bernstein operators, *J. Inequal. Appl.,* 61 (2018) 1-11.

[4] Kajla A., Acar T., Blending type approximation by generalized Bernstein-Durrmeyer type operators, *Miskolc Math. Notes,* 19(1) (2018) 319-336.

[5] Mohiuddine S.A., Özger F., Approximation of functions by Stancu variant of Bernstein-Kantorovich operators based on shape parameter α, *RACSAM,* 114(70) (2020) 1-17.

[6] Srivastava H.M., Özger F., Mohiuddine SA., Construction of Stancu-type Bernstein operators based on Bezier bases with shape parameter λ, *Symmetry*, 11(3) (2019) 1-22.

[7] Cai Q.-B., Dinlemez Kantar Ü., Çekim B., Approximation properties for the genuine modified Bernstein-Durrmeyer-Stancu operators, *Appl. Math. J. Chinese Univ.,* 35(4) *(*2020) 468-478.

[8] Cai Q.-B., Cheng W.-T., Çekim B., Bivariatea α, q-Bernstein-Kantorovich operators and GBS operators of bivariate α, q-Bernstein-Kantorovich type, *Mathematics,* **7**(12) (2019) 1-18.

[9] Usta F., On New Modification of Bernstein Operators: Theory and Applications, *Iran J. Sci. Technol. Trans. Sci.*, 44 (2020) 1119–1124.

[10] Korovkin P.P., On convergence of linear operators in the space of continuous functions (Russian), *Dokl. Akad. Nauk SSSR (N.S.),* 90 (1953) 961-964.

[11] DeVore R.A., Lorentz G.G., Constructive Approximation, Springer, Berlin, (1993) 177.

[12] Voronovskaya E., Determination de la forme asymptotique dapproximation des functions par polynomes de M. Bernstein, *C R Acad. Sci. URSS,* 79 (1932) 79–85.

On the curvatures of the ruled surfaces of b-lift curves

Anıl ALTINKAYA[1],[*] 🆔, *Mustafa ÇALIŞKAN* [1] 🆔

[1] *Gazi University, Faculty of Science, Department of Mathematics, Ankara/TURKEY*

Abstract

In this study, we defined a new curve which is called the B-Lift curve, also obtained the Frenet vectors of the B-Lift curve. The ruled surfaces have been produced by taking base curves B-Lift curves. Moreover, the tangent, normal, and binormal surfaces of the B-Lift curve are introduced. Besides, the Darboux frame of these ruled surfaces is created. The characterizations of these ruled surfaces are also given and the cases of base curves as the asymptotic curve, geodesic curve, principal line are examined. Finally, examples of these ruled surfaces are given and we illustrate them.

1. Introduction

In differential geometry, surfaces have important places and concepts in many disciplines such as kinematics, physics, computer science, etc. One of the most important of these surfaces is the ruled surface. A ruled surface is defined by a straight line that moves along a curve [1]. Many geometers have attracted the attention of ruled surfaces. T. Mert and M. Atçeken studied the ruled surfaces in de-Sitter and Hyperbolic 3-space [2-4]. E. Karaca and M. Çalışkan also studied the ruled surfaces generated by the natural lift curves on the Pseudo-Sphere [5]. E. Ergün and M. Çalışkan created ruled surfaces by accepting the base curve as a natural lift curve and they studied the integral invariants of these ruled surfaces [6]. The definition of the natural lift was given for the first time in Thorpe's book [7]. According to the definition, the natural lift curve is formed by combining the endpoints of the unit tangent vectors of the main curve.

S. Izumiya and N. Takeuchi examined the curves in terms of the geometry on the ruled surfaces. The principal normal surface of a space curve is defined as a ruled surface whose rules are given by the principal normal curve. They said that principal normal surfaces are by definition related to Bertrand curves and studied the general helices and Bertrand curves as curves on the ruled surfaces. General helices are a generalization of circular helices. In other words, the concept of Bertrand curves is a generalization of the concept of circular helices [8]. A curve is called a general helix if the tangent vector of the curve makes a constant angle

with a fixed straight line. If both $\kappa \neq 0$ and $\tau > 0$ are constant, a curve is called a circular helix. M. A. Lancert proved that a curve is a general helix if and only if the ratio of curvatures along the curve is constant [9].

The Darboux frame along surface curves in 3-dimensional Euclidean space is a well-known concept. French mathematician Jean Gaston Darboux gave this field its name. It's an expansion of the Frenet-Serret frame applied to the surface geometry. Darboux frame is a natural moving frame built on a surface. Using this frame, the characteristics of the curve as a geodesic curve, asymptotic curve, or principal line can be given [10].

In this article, based on Thorpe's definition, we defined a new curve which is called the B-Lift curve, also calculated the Frenet vectors of this curve. Besides, introduced the ruled surfaces which are called tangent, principal normal, binormal surfaces by accepting the base curve as a B-Lift curve. After that, the Darboux frame of these surfaces was created and the situation of the geodesic curve, asymptotic curve, principal line of the B-Lift curve was examined.

2. Preliminaries

In this section, basic definitions and theorems for understanding this article are given.

Let $\vec{A} = (a_1, a_2, a_3)$ be a vector in $\mathbb{R}^3$. The norm is defined as $||\vec{A}|| = \sqrt{a_1{}^2 + a_2{}^2 + a_3{}^2}$. If $||\vec{A}||$ is equal to 1, then $\vec{A}$ is called unit vector in $\mathbb{R}^3$. For the vectors

$\vec{A} = (a_1, a_2, a_3)$ and $\vec{B} = (b_1, b_2, b_3)$ in $\mathbb{R}^3$, the inner product is defined as $< \vec{A}, \vec{B} > = a_1 b_1 + a_2 b_2 + a_3 b_3$. If $\gamma'(s) \neq 0$, $\gamma: I \to \mathbb{R}^3$ is called the regular curve, for all $s \in I$. If $\gamma'(s)$ is equal to 1 then the curve $\gamma: I \to \mathbb{R}^3$ is a unit speed curve [1].

Assume that γ is a unit speed curve. $\{T(s), N(s), B(s)\}$ is called Frenet-Serret frame of the curve $\gamma(s)$. $T(s) = \gamma'(s)$ is the unit tangent vector of the curve $\gamma(s)$. The unit principal normal and binormal vectors are defined by $N(s) = \frac{\gamma''(s)}{||\gamma''(s)||}$ and $B(s) = T(s) x N(s)$, respectively. Frenet-Serret formulas of the unit speed curve $\gamma(s)$ are given as follows:

$T'(s) = \kappa(s)N(s)$

$N'(s) = -\kappa(s)T(s) + \tau(s)B(s)$

$B'(s) = -\tau(s)N(s)$,

where $\kappa(s) = \gamma''(s)$ and $\tau(s) = -< B'(s), N(s) >$ are the curvature and torsion of the curve $\gamma(s)$, respectively [6].

Definition 1 [1] Let $\gamma: I \to M$ be a unit speed curve, where $M \subset \mathbb{R}^3$ is a hypersurface. We called an integral curve to the curve γ if

$\gamma'(s) = X(\gamma(s))$,

where X is a differentiable vector field on M.

Definition 2 [6] Let $\gamma: I \to M$ be a unit speed curve. The natural lift curve $\bar{\gamma}: I \to TM$ of the curve γ is defined as follows:

$\bar{\gamma}(s) = (\gamma(s), \gamma'(s)) = \gamma'(s)|_{\gamma(s)}$.

Then, we can write

$\frac{d\bar{\gamma}(s)}{ds} = \frac{d}{ds}(\gamma'(s))|_{\gamma(s)} = D_{\gamma'(s)}\gamma'(s)$,

where D is Levi-Civita connection in $\mathbb{R}^3$.

Definition 3 [1] Let γ be a regular curve and w be a unit direction of a straight line in $\mathbb{R}^3$, then the ruled surface

$\varphi(s, v) = \gamma(s) + vw(s)$.

Definition 4 [6] Let γ be a regular curve in $\mathbb{R}^3$ and the set $\{T(s), N(s), B(s)\}$ be the Frenet vectors of the curve γ. Then the tangent, principal normal and

binormal surfaces of the curve γ are given in the following equalities:

$$\varphi_T(s, v) = \gamma(s) + vT(s)$$

$$\varphi_N(s, v) = \gamma(s) + vN(s)$$

$$\varphi_B(s, v) = \gamma(s) + vB(s)$$

For the unit normal vector of the ruled surface φ, we have $\frac{\varphi_s \times \varphi_v}{||\varphi_s \times \varphi_v||}$.

Definition 5 [1] Let M be a surface in $\mathbb{R}^3$ and γ be a curve on M. Then the set $\{T, V, U\}$ defines a frame which is called Darboux frame, where $T = \gamma'$, U is a unit normal vector of M and $V = U \times T$. Frenet-Serret formulas for the Darboux frame follow as:

$$\begin{pmatrix} T' \\ V' \\ U' \end{pmatrix} = \begin{pmatrix} 0 & k_g & k_n \\ -k_g & 0 & \tau_g \\ -k_n & -\tau_g & 0 \end{pmatrix} \begin{pmatrix} T \\ V \\ U \end{pmatrix},$$

where $k_g = < U \times T, T' >$, $k_n = < \gamma'', U >$ and $\tau_g = < T, U \times U' >$ are the geodesic curvature, normal curvature and geodesic torsion, respectively.

Definition 6 [1] Let a regular curve γ lie on a surface M. Then the followings are provided:

(1) γ is a geodesic curve if and only if $k_g = 0$.

(2) γ is an asymptotic curve if and only if $k_n = 0$.

(3) γ is a principal line if and only if $\tau_g = 0$.

3. Curvatures of the Ruled Surfaces of B-Lift Curves

In this part, defined the B-Lift curve and the Frenet vectors of the B-Lift curve are calculated. Moreover, the tangent, principal normal, binormal surfaces are constructed and the Darboux frames of these surfaces are created. Besides, the geodesic curve, asymptotic curve, principal line of the B-Lift curve are examined.

Definition 7 For any unit speed curve $\gamma: I \to M$, $\gamma_B: I \to TM$ is called the B-Lift curve of γ which provides the following equation:

$\gamma_B(s) = (\gamma(s), B(s)) = B(s)|_{\gamma(s)}$,   (1)

where B is binormal vector of the curve γ.

Theorem 8 Let γ_B be the B-Lift curve of a regular curve γ. Then the following equations are provided:

$T_B(s) = -N(s),$

$N_B(s) = \frac{\kappa(s)}{||W(s)||}T(s) - \frac{\tau(s)}{||W(s)||}B(s),$ (2)

$B_B(s) = \frac{\tau(s)}{||W(s)||}T(s) + \frac{\kappa(s)}{||W(s)||}B(s),$

where $\{T(s), N(s), B(s)\}$ and $\{T_B(s), N_B(s), B_B(s)\}$ are the Frenet vectors of the curve γ and γ_B, respectively. Furthermore, κ is the curvature, τ is the torsion and the Darboux vector $W = \tau T + \kappa B$ of the curve γ. (The torsion will be taken greater than zero.)

(i) Let γ_B be the B-Lift curve of the regular curve γ. Then the tangent surface of the B-Lift curve is

$\varphi_{T_B}(s, v) = \gamma_B(s) + vT_B(s).$ (3)

From (1) and (2), we have

$\varphi_{T_B}(s, v) = B(s) + v(-N(s)),$ (4)

$(\varphi_{T_B})_s = -\tau N + v(\kappa T - \tau B),$ (5)

$(\varphi_{T_B})_v = -N.$ (6)

The unit normal of the ruled surface φ_{T_B} is

$U_{T_B} = \frac{(\varphi_{T_B})_s \times (\varphi_{T_B})_v}{||(\varphi_{T_B})_s \times (\varphi_{T_B})_v||} = \frac{(-v\tau, 0, -v\kappa)}{\sqrt{v^2\kappa^2 + v^2\tau^2}}.$ (7)

1) $k_g = < U_{T_B} \times T_B, T_B' >$

$= -v(\kappa^2 + \tau^2) \neq 0.$

2) $k_n = < \gamma_B'', U_{T_B} >$

$= -v(\kappa\kappa' + \tau\tau').$

3) $\tau_g = < T_B, U_{T_B} \times U_{T_B}' >$

$= v^2(\frac{\tau}{\kappa})'\kappa^2.$

Corollary 9 For the regular curve γ, $(\kappa\kappa' + \tau\tau') = 0$ if and only if γ_B is the asymptotic curve of the ruled surface φ_{T_B}.

Corollary 10 γ is a general helix curve if and only if γ_B is a principal line of the ruled surface φ_{T_B}.

(ii) Let γ_B be the B-Lift curve of the regular curve γ. Then the principal normal surface of the B-Lift curve is

$\varphi_{N_B}(s, v) = \gamma_B(s) + vN_B(s).$ (8)

From (1) and (2), the following equations are hold:

$\varphi_{N_B}(s, v) = B(s) + v(\frac{\kappa(s)}{||W(s)||}T(s) - \frac{\tau(s)}{||W(s)||}B(s)$ (9)

$(\varphi_{N_B})_s = -\tau N + v(\frac{\kappa'}{||W||}T + \frac{\kappa^2 + \tau^2}{||W||}N - \frac{\tau'}{||W||}B),$ (10)

$(\varphi_{N_B})_v = \frac{\kappa}{||W||}T - \frac{\tau}{||W||}B.$ (11)

$(\varphi_{N_B})_s \times (\varphi_{N_B})_v = (-\tau + \frac{\tau^2}{||W||}, \frac{v}{||W||^2}(\kappa'\tau - \kappa\tau'), -\kappa + \frac{\kappa\tau}{||W||})$ (12)

The unit normal of the ruled surface φ_{N_B} is

$U_{N_B} = \frac{(\varphi_{N_B})_s \times (\varphi_{N_B})_v}{||(\varphi_{N_B})_s \times (\varphi_{N_B})_v||}.$ (13)

1) $k_g = < U_{N_B} \times T_B, T_B' >$

$= \frac{(\kappa^2 + \tau^2)(\tau - 1)}{||W||}.$

2) $k_n = < \gamma_B'', U_{N_B} >$

$= -v\frac{\tau'(\kappa'\tau - \kappa\tau')}{||W||^2}.$

3) $\tau_g = < T_B, U_{N_B} \times U_{N_B}' >$

$= (\tau'\kappa - \kappa'\tau) \cdot [1 + \frac{\tau^2}{||W||^2} - \frac{2\tau}{||W||}].$

Corollary 11 For the regular curve γ, $\tau = 1$ if and only if γ_B is the geodesic curve of the ruled surface φ_{N_B}.

Corollary 12 γ is a general helix curve if and only if γ_B is an asymptotic curve of the ruled surface φ_{N_B}.

Corollary 13 γ is a general helix curve if and only if γ_B is a principal line of the ruled surface φ_{N_B}.

(iii) Let γ_B be the B-Lift curve of the regular curve γ. Then the binormal surface of the B-Lift curve is

$\varphi_{B_B}(s, v) = \gamma_B(s) + vB_B(s).$ (14)

From (1) and (2), we know

$\varphi_{B_B}(s, v) = B(s) + v(\frac{\tau(s)}{||W(s)||}T(s) + \frac{\kappa(s)}{||W(s)||}B(s))$ (15)

$(\varphi_{B_B})_s = -\tau N + v(\frac{\tau'}{||W||}T + \frac{\kappa'}{||W||}B),$ (16)

$(\varphi_{B_B})_v = \frac{\tau}{||W||}T + \frac{\kappa}{||W||}B.$ (17)

$$(\varphi_{B_B})_s \times (\varphi_{B_B})_v = (-\frac{\kappa\tau}{||W||}, -v\frac{(\kappa'\tau-\kappa\tau')}{||W||^2}, \frac{\tau^2}{||W||}).$$
(18)

The unit normal of the ruled surface φ_{B_B} is

$$U_{B_B} = \frac{(\varphi_{B_B})_s \times (\varphi_{B_B})_v}{||(\varphi_{B_B})_s \times (\varphi_{B_B})_v||}.$$
(13)

1) $k_g = <U_{B_B} \times T_B, T_B'>$

$= 0.$

2) $k_n = <\gamma_B'', U_{B_B}>$

$= -\frac{\tau^2}{||W||}(\kappa^2+\tau^2) - v\frac{\tau'}{||W||^2}(\kappa'\tau - \kappa\tau').$

3) $\tau_g = <T_B, U_{B_B} \times U_{B_B}'>$

$= \frac{\tau^2(\kappa\tau'-\kappa'\tau)}{||W||^2}.$

Corollary 14 γ_B is the geodesic curve of the ruled surface φ_{B_B}.

Corollary 15 γ is a general helix curve if and only if γ_B is a principal line of the ruled surface φ_{B_B}.

Example 16 Consider the general helix curve given by

$$\gamma(s) = (\frac{1}{3}s^{\frac{3}{2}}, \frac{1}{3}(1-s)^{\frac{3}{2}}, \frac{\sqrt{3}}{2}s).$$

Frenet vectors of the curve $\gamma(s)$ are given as follows:

$$T(s) = \left(\frac{1}{2}s^{\frac{1}{2}}, -\frac{1}{2}(1-s)^{\frac{1}{2}}, \frac{\sqrt{3}}{2}\right)$$

$$N(s) = ((1-s)^{\frac{1}{2}}, s^{\frac{1}{2}}, 0)$$

$$B(s) = (-\frac{\sqrt{3}}{2}s^{\frac{1}{2}}, \frac{\sqrt{3}}{2}(1-s)^{\frac{1}{2}}, \frac{1}{2}).$$

Then the B-Lift curve of the curve $\gamma(s)$ is

$$\gamma_B(s) = (-\frac{\sqrt{3}}{2}s^{\frac{1}{2}}, \frac{\sqrt{3}}{2}(1-s)^{\frac{1}{2}}, \frac{1}{2}).$$

Frenet vectors of the curve γ_B are obtained as follows:

$$T_B(s) = \left(-(1-s)^{\frac{1}{2}}, -s^{\frac{1}{2}}, 0\right)$$

$$N_B(s) = \left(s^{\frac{1}{2}}, -(1-s)^{\frac{1}{2}}, 0\right)$$

$$B_B(s) = (0,0,1).$$

The tangent, principal normal and binormal surfaces of the curve γ_B are

$\varphi_{T_B}(s,v) = \gamma_B(s) + vT_B(s)$

$= (-\frac{\sqrt{3}}{2}s^{\frac{1}{2}}, \frac{\sqrt{3}}{2}(1-s)^{\frac{1}{2}}, \frac{1}{2})$

$+ v\left(-(1-s)^{\frac{1}{2}}, -s^{\frac{1}{2}}, 0\right)$

$\varphi_{N_B}(s,v) = \gamma_B(s) + vN_B(s)$

$= \left(-\frac{\sqrt{3}}{2}s^{\frac{1}{2}}, \frac{\sqrt{3}}{2}(1-s)^{\frac{1}{2}}, \frac{1}{2}\right) +$

$v\left(s^{\frac{1}{2}}, -(1-s)^{\frac{1}{2}}, 0\right)$

$\varphi_{B_B}(s,v) = \gamma_B(s) + vB_B(s)$

$= \left(-\frac{\sqrt{3}}{2}s^{\frac{1}{2}}, \frac{\sqrt{3}}{2}(1-s)^{\frac{1}{2}}, \frac{1}{2}\right) + v(0,0,1).$
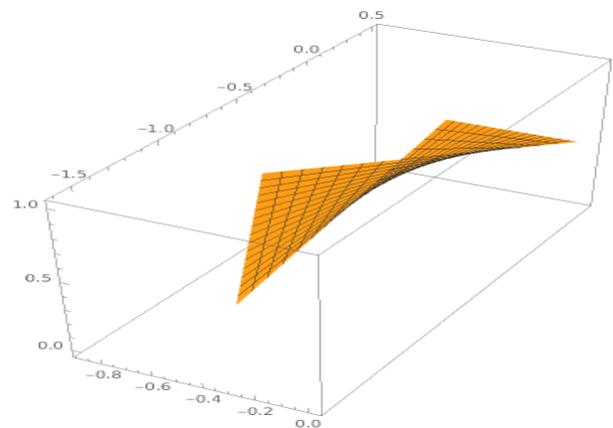
Figure 1. The tangent surface φ_{T_B} of the curve γ_B.
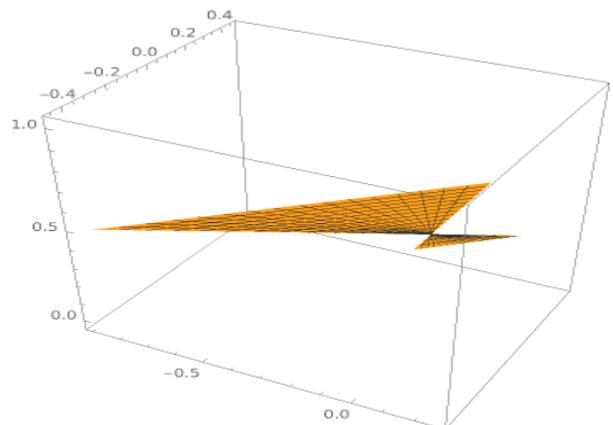
Figure 2. The principal normal surface φ_{N_B} of the curve γ_B.
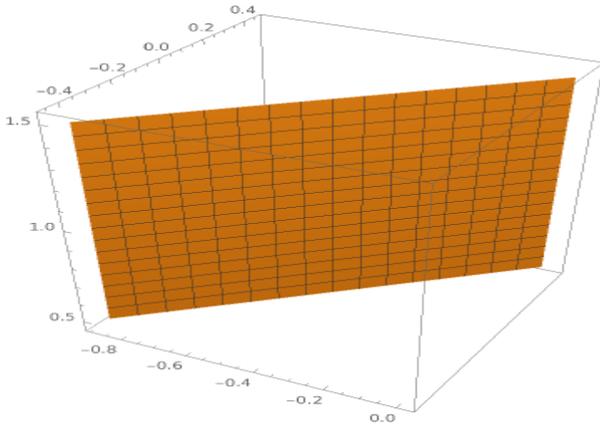
Figure 3. The binormal surface φ_{B_B} of the curve γ_B.

(i) For the ruled surface φ_{T_B}, since γ_B is the general helix, from Corollary 10, γ_B is a principal line of the ruled surface φ_{T_B}.

(ii) For the ruled surface φ_{N_B}, since γ_B is the general helix, from Corollary 12-13, γ_B are an asymptotic curve and principal line of the ruled surface φ_{N_B}.

(iii) For the ruled surface φ_{B_B}, from Corollary 14, γ_B is a geodesic curve of the ruled surface φ_{B_B} and since γ_B is the general helix, from Corollary 15, γ_B is a principal line of the ruled surface φ_{B_B}.

Acknowledgement

The authors are thankful to the referees for their valuable comments, opinions and suggestions.

Conflicts of interest

The authors state that did not have conflict of interests.

References

[1] Carmo M. Do., Differential Geometry of Curves and Surfaces, Prentice- Hall,Inc., Englewood Cliffs, New Jersey, (1976) 1-114.

[2] Mert T., Atçeken M., Some Special Ruled Surfaces in Hyperbolic 3-Space, *Konuralp Journal of Mathematics*, 9 (2) (2021) 298-309.

[3] Mert T., Atçeken M., Special Ruled Surfaces in de-Sitter 3-Space, *Fundamental Journal of Mathematics and Applications* 4 (3) (2021) 195-209.

[4] Mert T., Atçeken M., Spacelike Ruled Surfaces in de-Sitter 3-Space, *Asian Journal of Mathematics and Computer Research*, 27 (4) (2020) 37-53.

[5] Karaca E., Çalışkan M., Ruled Surfaces and Tangent Bundle of Pseudo-Sphere of Natural Lift Curves, *Journal of Science and Arts*, 52 (3) (2020) 573-586.

[6] Ergün E., Çalışkan M., Ruled Surface Pair Generated by a Curve and its Natural Lift in $\mathbb{R}^3$, *Pure Mathematical Sciences*, 1 (2) (2012) 75-80.

[7] Thorpe J. A., Elementary Topics in Differential Geometry, Springer Verlag, New York, Heidelberg-Berlin, (1979) 61.

[8] Izumiya S., Takeuchi N., Special Curves and Ruled Surfaces, *Beitrage zur Algebra und Geometric Contributions to Algebra and Geometry*, 44 (1) (2003) 203-212.

[9] Lancret M. A., Memoire sur les courbes a double courbure, *Memoires presentes a l'Institut*, 1 (1) (1806) 416-454.

[10] O'Neill B., Elementary Differential Geometry, Academic Press New York and London, (1966) 42-187.

[11] Izumiya S., Otani S., Flat Approximations of Surfaces Along Curves, *Demonstratio Mathematica*, 48 (2) (2015) 217-241.

Algebraic operations of virtual fuzzy parameterized soft sets and their application in decision-making

Orhan DALKILIÇ[1,]* ID *, Naime DEMİRTAŞ[1]* ID

[1]*Mersin University, Faculty of Arts and Sciences, Department of Mathematics, Mersin/TURKEY*

Abstract

It is a difficult task for decision-makers to accurately state a membership degree in the range [0,1]. The virtual fuzzy parameterized soft sets (VFPSSs) proposed to overcome this problem is an effective mathematical tool constructed, including the abilities of fuzzy sets and soft sets. In this paper, algebraic operations of VFPSSs are defined and examined these operations' properties. Then, a decision-making algorithm is proposed by the aforesaid operations. Finally, the proposed algorithm is succesfully applied to a decision-making problem.

1. Introduction

It is almost impossible with classical mathematics to express the uncertainty of available data for problems encountered in many fields. Moreover; it is essential to accurately express these data for these areas to obtain accurate results close to the ideal. For this reason, many researchers have tried to construct a mathematical model for fuzzy data encountered in uncertain environments. Two of these studies is the fuzzy sets [1] and rough sets [2]. However; as pointed out by Molodtsov [3], the aforesaid concepts have certain difficulties expressing uncertainty. Molodtsov stated that these difficulties resulted from the lack of a parameterization tool and proposed a new approach, i.e., soft sets, free from these difficulties. Thanks to its success in expressing the uncertainty problems encountered, this concept has been successfully applied to many areas [4-8].

Many hybrid sets [9-17] have been developed using soft sets and the others [1,2,18]. One of them is fuzzy parameterized soft sets [19]. Unlike soft sets, the parameter set of this set theory is a fuzzy set that can express uncertainty better. Therefore, it is preferable in the solution of problems containing such uncertainties. However, it is a difficult task for a decision-maker to express the membership of a parameter fully. In other words, it is uneasy about expressing a value in the range [0,1] correctly. The

virtual fuzzy parameterized soft sets (VFPSSs) [20], which generalize fuzzy parameterized soft sets, overcome the uncertainties. The most important advantages of this concept are as follows:

- The ability of decision-makers to express a decision-making problem by considering their margins of error.
- To be able to observe this change in the case that the margins of error may vary (see ref [20]).

In VFPSSs, the lower and upper parameter sets of a parameter set are defined to express each parameter's membership degrees more clearly. With these advantages, it is a better mathematical model than fuzzy parameterized soft sets for uncertainty. The algebraic operators studied for fuzzy parameterized soft sets are quite successful in constructing a better decision-making process for uncertainty [22]. In this paper, since the virtual fuzzy parameterized soft set theory is still very new, t-norm and s-norm products of this theory are defined. In addition, when we compare the success of the algebraic operators examined for both mathematical models in decision-making processes, it is clear that the algebraic operators proposed in this paper offer better approaches. Because the membership degrees expressed by the decision-makers are given independently in the definition of virtual fuzzy

---

parameterized soft sets, which improves the data transfer received from the decision-makers in terms of increasing the reliability of the results in uncertain environments. Since the mathematical model discussed in our paper makes the decision-makers independent, it is an advantage that makes it more dominant than the contribution of other mathematical models to the decision-making processes. Moreover, beyond this situation, it is aimed to build a better approach with the contribution of algebraic operators. To this end, a decision-making method that can be used in expressing uncertain situations is proposed by using these products. Finally, using the proposed algorithm, the solution to an uncertainty problem is exemplified.

2. Materials and Methods

In this section, some definitions and results are reminded. Detailed explanations related to virtual fuzzy parameterized soft sets can be found in [20].

Throughout this paper, let $U = \{u_1, u_2, \dots, u_n\}$ be a universe set, $P = \{p_1, p_2, \dots, p_m\}$ be a set of parameters and X be a fuzzy set over P. In this case, the lower virtual parameter set and the upper virtual parameter set are expressed as $\underline{P} = \left\{ p_1^{\underline{\alpha_1}}, p_2^{\underline{\alpha_2}}, \dots p_m^{\underline{\alpha_m}} \right\}$ and $\overline{P} = \left\{ p_1^{\overline{\alpha_1}}, p_2^{\overline{\alpha_2}}, \dots, p_m^{\overline{\alpha_m}} \right\}$ respectively. Also, let 2^U denotes the power set of U and $\emptyset \neq A \subseteq P$.

Definition 2.1. [1] A fuzzy set X over U is a set defined by $\mu_X: U \to [0,1]$. μ_X is called the membership function of X, and the value $\mu_X(u)$ is called the grade of membership of $u \in U$. Thus, a fuzzy set X over U can be represented as follows:

$X = \{ (\mu_X(u)/u) : u \in U, \mu_X(u) \in [0,1] \}$

Definition 2.2. [2] A pair (F, P) is called a soft set over U, where F is a mapping given by $F: P \to 2^U$. In other words, a soft set over U is a parameterized family of subsets of U for $p \in P$, $F(p)$ may be considered as the set of p-approximate elements of (F, P).

Definition 2.3. [21] t-norms are associative, monotonic and commutative two valued functions t that map from $[0, 1] \times [0, 1]$ to $[0, 1]$. These properties are formulated with the following conditions:

  i. $t(0,0) = 0$ and $t(\mu_X(p), 1) = t(1, \mu_X(p)) = \mu_X(p)$, $p \in P$,
  ii.   If $\mu_{X_1}(p) \leq \mu_{X_3}(p)$ and $\mu_{X_2}(p) \leq \mu_{X_4}(p)$, then $t\left(\mu_{X_1}(p), \mu_{X_2}(p) \right) \leq t\left(\mu_{X_3}(p), \mu_{X_4}(p) \right)$,
  iii. $t\left(\mu_{X_1}(p), \mu_{X_2}(p) \right) = t\left(\mu_{X_2}(p), \mu_{X_1}(p) \right)$,
  iv. $t\left(\mu_{X_1}(p), t\left(\mu_{X_2}(p), \mu_{X_3}(p) \right) \right) = t\left(t\left(\mu_{X_1}(p), \mu_{X_2}(p) \right), \mu_{X_3}(p) \right)$.

Definition 2.4. [21] t-conorms (s-norms) are associative, monotonic and commutative two placed functions s which map from $[0, 1] \times [0, 1]$ to $[0, 1]$. These properties are formulated with the following conditions:

  i. $s(1,1) = 1$ and $s(\mu_X(p), 0) = s(0, \mu_X(p)) = \mu_X(p)$, $p \in P$,
  ii.   If $\mu_{X_1}(p) \leq \mu_{X_3}(p)$ and $\mu_{X_2}(p) \leq \mu_{X_4}(p)$, then $s\left(\mu_{X_1}(p), \mu_{X_2}(p) \right) \leq s\left(\mu_{X_3}(p), \mu_{X_4}(p) \right)$,
  iii. $s\left(\mu_{X_1}(p), \mu_{X_2}(p) \right) = s\left(\mu_{X_2}(p), \mu_{X_1}(p) \right)$,
  iv. $s\left(\mu_{X_1}(p), s\left(\mu_{X_2}(p), \mu_{X_3}(p) \right) \right) = s\left(s\left(\mu_{X_1}(p), \mu_{X_2}(p) \right), \mu_{X_3}(p) \right)$.

t-norms and t-conorms are related in a sense of logical duality. Typical dual pairs of non parameterized t-norm and t-conorm are complied below:

  i.   Drastic product:

$$t_w \left(\mu_{X_1}(p), \mu_{X_2}(p) \right) = \begin{cases} min\{ \mu_{X_1}(p), \mu_{X_2}(p) \}, & max\{ \mu_{X_1}(p), \mu_{X_2}(p) \} = 1, \\ 0, & otherwise \end{cases} \tag{1}$$

  ii.   Drastic sum:

$$s_w\left(\mu_{X_1}(p),\mu_{X_2}(p)\right) = \begin{cases} max\{\mu_{X_1}(p),\mu_{X_2}(p)\}, & min\{\mu_{X_1}(p),\mu_{X_2}(p)\} = 0, \\ 1, & otherwise \end{cases} \tag{2}$$

iii. Bounded product:
$$t_1\left(\mu_{X_1}(p),\mu_{X_2}(p)\right) = max\{0,\mu_{X_1}(p)+\mu_{X_2}(p)-1\} \tag{3}$$

iv. Bounded sum:
$$s_1\left(\mu_{X_1}(p),\mu_{X_2}(p)\right) = min\{1,\mu_{X_1}(p)+\mu_{X_2}(p)\} \tag{4}$$

v. Einstein product:
$$t_{1.5}\left(\mu_{X_1}(p),\mu_{X_2}(p)\right) = \frac{\mu_{X_1}(p)\mu_{X_2}(p)}{2-[\mu_{X_1}(p)+\mu_{X_2}(p)-\mu_{X_1}(p)\mu_{X_2}(p)]} \tag{5}$$

vi. Einstein sum:
$$s_{1.5}\left(\mu_{X_1}(p),\mu_{X_2}(p)\right) = \frac{\mu_{X_1}(p)+\mu_{X_2}(p)}{1+\mu_{X_1}(p)\mu_{X_2}(p)} \tag{6}$$

vii. Algebraic product:
$$t_2\left(\mu_{X_1}(p),\mu_{X_2}(p)\right) = \mu_{X_1}(p)\mu_{X_2}(p) \tag{7}$$

viii. Algebraic sum:
$$s_2\left(\mu_{X_1}(p),\mu_{X_2}(p)\right) = \mu_{X_1}(p)+\mu_{X_2}(p)-\mu_{X_1}(p)\mu_{X_2}(p) \tag{8}$$

ix. Hamacher product:
$$t_{2.5}\left(\mu_{X_1}(p),\mu_{X_2}(p)\right) = \frac{\mu_{X_1}(p)\mu_{X_2}(p)}{\mu_{X_1}(p)+\mu_{X_2}(p)-\mu_{X_1}(p)\mu_{X_2}(p)} \tag{9}$$

x. Hamacher sum:
$$s_{2.5}\left(\mu_{X_1}(p),\mu_{X_2}(p)\right) = \frac{\mu_{X_1}(p)+\mu_{X_2}(p)-2\cdot\mu_{X_1}(p)\mu_{X_2}(p)}{1-\mu_{X_1}(p)\mu_{X_2}(p)} \tag{10}$$

xi. Minimum:
$$t_3\left(\mu_{X_1}(p),\mu_{X_2}(p)\right) = min\{\mu_{X_1}(p),\mu_{X_2}(p)\} \tag{11}$$

xii. Maximum:
$$s_3\left(\mu_{X_1}(p),\mu_{X_2}(p)\right) = max\{\mu_{X_1}(p),\mu_{X_2}(p)\} \tag{12}$$

Definition 2.5. [20] Let $\underline{X}, X, \overline{X}$ be a fuzzy set over $\underline{P}, P, \overline{P}$, respectively. A virtual fuzzy parameterized soft set Ψ_X over U is defined as follows:

$$\Psi_X = \underline{Y_X} \cup Y_X \cup \overline{Y_X}$$

such that

$$\underline{Y_X} = \left\{\left(\frac{\mu_X(p)-\underline{\alpha}}{p},\underline{\psi_X}(p^{\underline{\alpha}})\right):p^{\underline{\alpha}}\in\underline{P}, p\in P,\mu_X(p)\in[0,1], 0\leq\underline{\alpha}<\mu_X(p)\right\},$$

$$Y_X = \left\{\left(\frac{\mu_X(p)}{p},\psi_X(p)\right):p\in P,\mu_X(p)\in[0,1]\right\},$$

$$\overline{Y_X} = \left\{\left(\frac{\mu_X(p)+\overline{\alpha}}{p},\overline{\psi_X}(p^{\overline{\alpha}})\right):p\in P, p^{\overline{\alpha}}\in\overline{P},\mu_X(p)\in[0,1], 0\leq\overline{\alpha}\leq 1-\mu_X(p)\right\},$$

where the functions $\underline{\psi_X}:\underline{P}\to 2^U$, $\psi_X:P\to 2^U$, $\overline{\psi_X}:\overline{P}\to 2^U$ are called lower approximate function, approximate function, upper approximate function, respectively, and the function $\mu_X:P\to[0,1]$ is called membership function of the set X. Here, $\psi_X(p)=\emptyset$ if $\mu_X(p)=0$. Moreover, $\underline{\psi_X}(p^{\underline{\alpha}})=\emptyset$ if $\mu_X(p)-\underline{\alpha}=0$ and $\overline{\psi_X}(p^{\overline{\alpha}})=\emptyset$ if $\mu_X(p)+\overline{\alpha}=0$.

From now on, $VFPS(U)$ denotes the family of all virtual fuzzy parameterized soft sets over U with P as the set of parameters.

Example 2.1. Let $U = \{u_1, u_2, u_3, u_4, u_5, u_6, u_7\}$ be a universe set, $P = \{p_1, p_2, p_3, p_4\}$ be the set of parameters and $X = \{0.5/p_2, 0.7/p_4\}$ be a fuzzy set over P. If $\underline{X} = \{0.4/p_2, 0.35/p_4\}$, $\overline{X} = \{0.75/p_2, 0.9/p_4\}$, and

$$\underline{\psi_X}(p_2^{0.1}) = \{u_1, u_3, u_4, u_6, u_7\}, \qquad \underline{\psi_X}(p_4^{0.35}) = \{u_2, u_3, u_4, u_5, u_7\},$$

$$\psi_X(p_2) = \{u_1, u_4, u_6, u_7\}, \qquad \psi_X(p_4) = \{u_2, u_4, u_5, u_7\},$$

$$\overline{\psi_X}(p_2^{0.25}) = \{u_1, u_6, u_7\}, \qquad \overline{\psi_X}(p_4^{0.2}) = \{u_2, u_5, u_7\},$$

then the virtual fuzzy parameterized soft set Ψ_X is written by

$$\Psi_X = \left\{ \begin{array}{c} (0.4/p_2, \{u_1, u_3, u_4, u_6, u_7\}), (0.35/p_4, \{u_2, u_3, u_4, u_5, u_7\}) \\ (0.5/p_2, \{u_1, u_4, u_6, u_7\}), (0.7/p_4, \{u_2, u_4, u_5, u_7\}) \\ (0.75/p_2, \{u_1, u_6, u_7\}), (0.9/p_4, \{u_2, u_5, u_7\}) \end{array} \right\}$$

where

$$\underline{Y_X} = \{(0.4/p_2, \{u_1, u_3, u_4, u_6, u_7\}), (0.35/p_4, \{u_2, u_3, u_4, u_5, u_7\})\},$$

$$Y_X = \{(0.5/p_2, \{u_1, u_4, u_6, u_7\}), (0.7/p_4, \{u_2, u_4, u_5, u_7\})\}$$

and

$$\overline{Y_X} = \{(0.75/p_2, \{u_1, u_6, u_7\}), (0.9/p_4, \{u_2, u_5, u_7\})\}.$$

Definition 2.6. [20] Let $\Psi_X \in VFPS(U)$.

(i)   If $\underline{\psi_X}(p^{\underline{\alpha}}) = \psi_X(p) = \overline{\psi_X}(p^{\overline{\alpha}}) = \emptyset$ for all $p^{\underline{\alpha}} \in \underline{P}$, $p \in P$, $p^{\overline{\alpha}} \in \overline{P}$, then virtual fuzzy parameterized soft set Ψ_X is called an X-empty VFPSS, denoted by $\Psi_{\emptyset_X}$. If $X = \emptyset$, then Ψ_X is called an empty virtual fuzzy parameterized soft set, denoted by $\Psi_\emptyset$.

(ii) If $\underline{X}$, X, $\overline{X}$ are crisps subset of $\underline{P}$, P, $\overline{P}$, respectively, and $\underline{\psi_X}(p^{\underline{\alpha}}) = \psi_X(p) = \overline{\psi_X}(p^{\overline{\alpha}}) = U$ for all $p^{\underline{\alpha}} \in \underline{P}$, $p \in P$, $p^{\overline{\alpha}} \in \overline{P}$, then virtual fuzzy parameterized soft set Ψ_X is called an X-universal VFPSS, denoted by $\Psi_{\tilde{X}}$. If $X = P$, then the X-universal virtual fuzzy parameterized soft set is called universal virtual fuzzy parameterized soft set, denoted by $\Psi_{\tilde{P}}$.

Definition 2.7. [20] Let $\Psi_X, \Psi_Y \in VFPS(U)$. Then, Ψ_X is a virtual fuzzy parameterized soft subset of Ψ_Y, denoted by $\Psi_X \widetilde{\subseteq} \Psi_Y$, if

i. $\mu_X(p) - \underline{\alpha} \leq \mu_Y(p) - \underline{\beta}$ and $\underline{\psi_X}(p^{\underline{\alpha}}) \subseteq \underline{\psi_Y}(p^{\underline{\beta}})$ for all $p^{\underline{\alpha}}, p^{\underline{\beta}} \in \underline{P}$,

ii. $\mu_X(p) \leq \mu_Y(p)$ and $\psi_X(p) \subseteq \psi_Y(p)$ for all $p \in P$,

iii. $\mu_X(p) + \overline{\alpha} \leq \mu_Y(p) + \overline{\beta}$ and $\overline{\psi_X}(p^{\overline{\alpha}}) \subseteq \overline{\psi_Y}(p^{\overline{\beta}})$ for all $p^{\overline{\alpha}}, p^{\overline{\beta}} \in \overline{P}$.

Also, Ψ_X is a virtual fuzzy parameterized soft equal to Ψ_Y, denoted by $\Psi_X = \Psi_Y$, if

i. $\mu_X(p) - \underline{\alpha} = \mu_Y(p) - \underline{\beta}$ and $\underline{\psi_X}(p^{\underline{\alpha}}) = \underline{\psi_Y}(p^{\underline{\beta}})$ for all $p^{\underline{\alpha}}, p^{\underline{\beta}} \in \underline{P}$,

   ii. $\mu_X(p) = \mu_Y(p)$ and $\psi_X(p) = \psi_Y(p)$ for all $p \in P$,

   iii. $\mu_X(p) + \overline{\alpha} = \mu_Y(p) + \overline{\beta}$ and $\overline{\psi_X}(p^{\overline{\alpha}}) = \overline{\psi_Y}\left(p^{\overline{\beta}}\right)$ for all $p^{\overline{\alpha}}, p^{\overline{\beta}} \in \overline{P}$.

Proposition 2.1. [20] Let $\Psi_X \in VFPS(U)$. $s\left(\overline{\psi_X}(p^{\overline{\alpha}})\right) \leq s(\psi_Y(p)) \leq s\left(\underline{\psi_X}(p^{\underline{\alpha}})\right)$ is valid for all $p^{\underline{\alpha}} \in \underline{P}, p \in P, p^{\overline{\alpha}} \in \overline{P}$.

Definition 2.8. [20] Let $\Psi_X \in VFPS(U)$. Then, complement Ψ_X, denoted by Ψ_X^c, is a virtual fuzzy parameterized soft set defined by the approximate and membership functions as

   i. $\mu_{X^c}(p) - \underline{\widetilde{\alpha}} = 1 - \left(\mu_X(p) - \underline{\alpha}\right)$ and $\underline{\psi_{X^c}}(p^{\underline{\widetilde{\alpha}}}) = U/\underline{\psi_X}(p^{\underline{\alpha}})$ for all $p^{\underline{\alpha}}, p^{\underline{\widetilde{\alpha}}} \in \underline{P}$,

   ii. $\mu_{X^c}(p) = 1 - \mu_X(p)$ and $\psi_{X^c}(p) = U/\psi_X(p)$ for all $p \in P$,

   iii. $\mu_{X^c}(p) + \overline{\widetilde{\alpha}} = 1 - \left(\mu_X(p) + \overline{\alpha}\right)$ and $\overline{\psi_{X^c}}\left(p^{\overline{\widetilde{\alpha}}}\right) = U/\overline{\psi_X}(p^{\overline{\alpha}})$ for all $p^{\overline{\alpha}}, p^{\overline{\widetilde{\alpha}}} \in \overline{P}$.

Definition 2.9. [20] Let $\Psi_X, \Psi_Y \in VFPS(U)$. Then, union Ψ_X and Ψ_Y, denoted by $\Psi_X \mathbin{\widetilde{\sqcup}} \Psi_Y$, is defined by

   i. $\mu_{X \cup Y}(p) - \underline{\gamma} = max\left\{\mu_X(p) - \underline{\alpha}, \mu_Y(p) - \underline{\beta}\right\}$ and $\underline{\psi_{X \cup Y}}(p^{\underline{\gamma}}) = \underline{\psi_X}(p^{\underline{\alpha}}) \cup \underline{\psi_Y}(p^{\underline{\beta}})$ for all $p^{\underline{\alpha}}, p^{\underline{\beta}}, p^{\underline{\gamma}} \in \underline{P}$,

   ii. $\mu_{X \cup Y}(p) = max\{\mu_X(p), \mu_Y(p)\}$ and $\psi_{X \cup Y}(p) = \psi_X(p) \cup \psi_Y(p)$ for all $p \in P$,

   iii. $\mu_{X \cup Y}(p) + \overline{\gamma} = max\{\mu_X(p) + \overline{\alpha}, \mu_Y(p) + \overline{\beta}\}$ and $\overline{\psi_{X \cup Y}}(p^{\overline{\gamma}}) = \overline{\psi_X}(p^{\overline{\alpha}}) \cup \overline{\psi_Y}\left(p^{\overline{\beta}}\right)$ for all $p^{\overline{\alpha}}, p^{\overline{\beta}}, p^{\overline{\gamma}} \in \overline{P}$.

Definition 2.10. [20] Let $\Psi_X, \Psi_Y \in VFPS(U)$. Then, intersection Ψ_X and Ψ_Y, denoted by $\Psi_X \mathbin{\widetilde{\sqcap}} \Psi_Y$, is defined by

   i. $\mu_{X \cap Y}(p) - \underline{\gamma} = min\left\{\mu_X(p) - \underline{\alpha}, \mu_Y(p) - \underline{\beta}\right\}$ and $\underline{\psi_{X \cap Y}}(p^{\underline{\gamma}}) = \underline{\psi_X}(p^{\underline{\alpha}}) \cap \underline{\psi_Y}(p^{\underline{\beta}})$ for all $p^{\underline{\alpha}}, p^{\underline{\beta}}, p^{\underline{\gamma}} \in \underline{P}$,

   ii. $\mu_{X \cap Y}(p) = min\{\mu_X(p), \mu_Y(p)\}$ and $\psi_{X \cap Y}(p) = \psi_X(p) \cap \psi_Y(p)$ for all $p \in P$,

   iii. $\mu_{X \cap Y}(p) + \overline{\gamma} = min\{\mu_X(p) + \overline{\alpha}, \mu_Y(p) + \overline{\beta}\}$ and $\overline{\psi_{X \cap Y}}(p^{\overline{\gamma}}) = \overline{\psi_X}(p^{\overline{\alpha}}) \cap \overline{\psi_Y}\left(p^{\overline{\beta}}\right)$ for all $p^{\overline{\alpha}}, p^{\overline{\beta}}, p^{\overline{\gamma}} \in \overline{P}$.

3. *t*-Norm and *t*-Conorm Products of Virtual Fuzzy Parameterized Soft Sets

Definition 3.1. Let $\Psi_X, \Psi_Y \in VFPS(U)$. Then, the AND-*t*-norm of Ψ_X and Ψ_Y, denoted by $\Psi_X \mathbin{\overline{\boxtimes}} \Psi_Y$, is the virtual fuzzy parameterized soft set defined as follows:

$$\underline{\mu_{X \overline{\boxtimes} Y}}: \underline{P} \to [0,1], \quad \underline{\mu_{X \overline{\boxtimes} Y}}(p^{\underline{\gamma}}) = \left(\mu_X(p) - \underline{\alpha}\right) \cdot \left(\mu_Y(p) - \underline{\beta}\right), \tag{13}$$

$$\mu_{X \overline{\boxtimes} Y}: P \to [0,1], \quad \mu_{X \overline{\boxtimes} Y}(p) = \mu_X(p) \cdot \mu_Y(p), \tag{14}$$

$$\overline{\mu_{X \overline{\boxtimes} Y}}: P \to [0,1], \quad \overline{\mu_{X \overline{\boxtimes} Y}}(p^{\overline{\gamma}}) = \left(\mu_X(p) + \overline{\alpha}\right) \cdot \left(\mu_Y(p) + \overline{\beta}\right) \tag{15}$$

and

$$\underline{\psi_{X \overline{\boxtimes} Y}}: P \to 2^U, \quad \underline{\psi_{X \overline{\boxtimes} Y}}(p^{\underline{\gamma}}) = \underline{\psi_X}(p^{\underline{\alpha}}) \cap \underline{\psi_Y}(p^{\underline{\beta}}) \tag{16}$$

$$\psi_{X\underline{\boxtimes}Y}: P \to 2^U, \quad \psi_{X\underline{\boxtimes}Y}(p) = \psi_X(p) \cap \psi_Y(p), \tag{17}$$

$$\overline{\psi_{X\underline{\boxtimes}Y}}: P \to 2^U, \quad \overline{\psi_{X\underline{\boxtimes}Y}}(p^{\bar{\gamma}}) = \overline{\psi_X}(p^{\bar{\alpha}}) \cap \overline{\psi_Y}\left(p^{\bar{\beta}}\right) \tag{18}$$

where the functions $\underline{\psi_{X\underline{\boxtimes}Y}}$, $\psi_{X\underline{\boxtimes}Y}$, $\overline{\psi_{X\underline{\boxtimes}Y}}$ are called lower approximate function, approximate function, upper approximate function of $\Psi_X \underline{\boxtimes} \Psi_Y$, respectively, and $\underline{\mu_{X\underline{\boxtimes}Y}}$, $\mu_{X\underline{\boxtimes}Y}$, $\overline{\mu_{X\underline{\boxtimes}Y}}$ are called lower membership function, membership function, upper membership function of $\Psi_X \underline{\boxtimes} \Psi_Y$, respectively.

Definition 3.2. Let $\Psi_X, \Psi_Y \in VFPS(U)$. Then, the OR-$t$-norm of Ψ_X and Ψ_Y, denoted by $\Psi_X \boxtimes \Psi_Y$, is the virtual fuzzy parameterized soft set defined as follows:

$$\underline{\mu_{X\boxtimes Y}}: \underline{P} \to [0,1], \quad \underline{\mu_{X\boxtimes Y}}(p^{\underline{\gamma}}) = \left(\mu_X(p) - \underline{\alpha}\right) \cdot \left(\mu_Y(p) - \underline{\beta}\right), \tag{19}$$

$$\mu_{X\boxtimes Y}: P \to [0,1], \quad \mu_{X\boxtimes Y}(p) = \mu_X(p) \cdot \mu_Y(p), \tag{20}$$

$$\overline{\mu_{X\boxtimes Y}}: P \to [0,1], \quad \overline{\mu_{X\boxtimes Y}}(p^{\bar{\gamma}}) = \left(\mu_X(p) + \bar{\alpha}\right) \cdot \left(\mu_Y(p) + \bar{\beta}\right) \tag{21}$$

and

$$\underline{\psi_{X\boxtimes Y}}: P \to 2^U, \quad \underline{\psi_{X\boxtimes Y}}(p^{\underline{\gamma}}) = \underline{\psi_X}(p^{\underline{\alpha}}) \cup \underline{\psi_Y}(p^{\underline{\beta}}) \tag{22}$$

$$\psi_{X\boxtimes Y}: P \to 2^U, \quad \psi_{X\boxtimes Y}(p) = \psi_X(p) \cup \psi_Y(p), \tag{23}$$

$$\overline{\psi_{X\boxtimes Y}}: P \to 2^U, \quad \overline{\psi_{X\boxtimes Y}}(p^{\bar{\gamma}}) = \overline{\psi_X}(p^{\bar{\alpha}}) \cup \overline{\psi_Y}\left(p^{\bar{\beta}}\right) \tag{24}$$

where the functions $\underline{\psi_{X\boxtimes Y}}$, $\psi_{X\boxtimes Y}$, $\overline{\psi_{X\boxtimes Y}}$ are called lower approximate function, approximate function, upper approximate function of $\Psi_X \boxtimes \Psi_Y$, respectively, and $\underline{\mu_{X\boxtimes Y}}$, $\mu_{X\boxtimes Y}$, $\overline{\mu_{X\boxtimes Y}}$ are called lower membership function, membership function, upper membership function of $\Psi_X \boxtimes \Psi_Y$, respectively.

Definition 3.3. Let $\Psi_X, \Psi_Y \in VFPS(U)$. Then, the OR-$t$-conorm of Ψ_X and Ψ_Y, denoted by $\Psi_X \boxplus \Psi_Y$, is the VFPSS defined as follows:

$$\underline{\mu_{X\boxplus Y}}: \underline{P} \to [0,1], \quad \underline{\mu_{X\boxplus Y}}(p^{\underline{\gamma}}) = \left[\left(\mu_X(p) - \underline{\alpha}\right) + \left(\mu_Y(p) - \underline{\beta}\right)\right] - \left(\mu_X(p) - \underline{\alpha}\right) \cdot \left(\mu_Y(p) - \underline{\beta}\right), \tag{25}$$

$$\mu_{X\boxplus Y}: P \to [0,1], \quad \mu_{X\boxplus Y}(p) = \mu_X(p) + \mu_Y(p) - \mu_X(p) \cdot \mu_Y(p), \tag{26}$$

$$\overline{\mu_{X\boxplus Y}}: P \to [0,1], \quad \overline{\mu_{X\boxplus Y}}(p^{\bar{\gamma}}) = \left[\left(\mu_X(p) + \bar{\alpha}\right) + \left(\mu_Y(p) + \bar{\beta}\right)\right] - \left(\mu_X(p) + \bar{\alpha}\right) \cdot \left(\mu_Y(p) + \bar{\beta}\right) \tag{27}$$

and

$$\underline{\psi_{X\boxplus Y}}: P \to 2^U, \quad \underline{\psi_{X\boxplus Y}}(p^{\underline{\gamma}}) = \underline{\psi_X}(p^{\underline{\alpha}}) \cup \underline{\psi_Y}(p^{\underline{\beta}}) \tag{28}$$

$$\psi_{X\boxplus Y}: P \to 2^U, \quad \psi_{X\boxplus Y}(p) = \psi_X(p) \cup \psi_Y(p), \tag{29}$$

$$\overline{\psi_{X\boxplus Y}}: P \to 2^U, \quad \overline{\psi_{X\boxplus Y}}(p^{\bar{\gamma}}) = \overline{\psi_X}(p^{\bar{\alpha}}) \cup \overline{\psi_Y}\left(p^{\bar{\beta}}\right) \tag{30}$$

where the functions $\underline{\psi_{X\boxplus Y}}$, $\psi_{X\boxplus Y}$, $\overline{\psi_{X\boxplus Y}}$ are called lower approximate function, approximate function, upper approximate function of $\Psi_X \boxplus \Psi_Y$, respectively, and $\underline{\mu_{X\boxplus Y}}$, $\mu_{X\boxplus Y}$, $\overline{\mu_{X\boxplus Y}}$ are called lower membership function, membership function, upper membership function of $\Psi_X \boxplus \Psi_Y$, respectively.

Definition 3.4. Let $\Psi_X, \Psi_Y \in VFPS(U)$. Then, the AND-$t$-conorm of Ψ_X and Ψ_Y, denoted by $\Psi_X \overline{\boxplus} \Psi_Y$, is the VFPSS defined as follows:

$$\underline{\mu_{X\overline{\boxplus}Y}}: \underline{P} \to [0,1], \quad \underline{\mu_{X\overline{\boxplus}Y}}(p^{\underline{\gamma}}) = \left[\left(\mu_X(p) - \underline{\alpha}\right) + \left(\mu_Y(p) - \underline{\beta}\right)\right] - \left(\mu_X(p) - \underline{\alpha}\right) \cdot \left(\mu_Y(p) - \underline{\beta}\right), \tag{31}$$

$$\mu_{X\overline{\boxplus}Y}: P \to [0,1], \quad \mu_{X\overline{\boxplus}Y}(p) = \mu_X(p) + \mu_Y(p) - \mu_X(p) \cdot \mu_Y(p), \tag{32}$$

$$\overline{\mu_{X\boxplus Y}}: P \to [0,1], \quad \overline{\mu_{X\boxplus Y}}(p^{\overline{\gamma}}) = \left[(\mu_X(p) + \overline{\alpha}) + (\mu_Y(p) + \overline{\beta})\right] - (\mu_X(p) + \overline{\alpha}) \cdot (\mu_Y(p) + \overline{\beta}) \tag{33}$$

and

$$\underline{\psi_{X\boxplus Y}}: P \to 2^U, \quad \underline{\psi_{X\boxplus Y}}(p^{\underline{Y}}) = \underline{\psi_X}(p^{\underline{\alpha}}) \cap \underline{\psi_Y}(p^{\underline{\beta}}) \tag{34}$$

$$\psi_{X\boxplus Y}: P \to 2^U, \quad \psi_{X\boxplus Y}(p) = \psi_X(p) \cap \psi_Y(p), \tag{35}$$

$$\overline{\psi_{X\boxplus Y}}: P \to 2^U, \quad \overline{\psi_{X\boxplus Y}}(p^{\overline{\gamma}}) = \overline{\psi_X}(p^{\overline{\alpha}}) \cap \overline{\psi_Y}(p^{\overline{\beta}}) \tag{36}$$

where the functions $\underline{\psi_{X\boxplus Y}}$, $\psi_{X\boxplus Y}$, $\overline{\psi_{X\boxplus Y}}$ are called lower approximate function, approximate function, upper approximate function of $\Psi_X \boxplus \Psi_Y$, respectively, and $\underline{\mu_{X\boxplus Y}}$, $\mu_{X\boxplus Y}$, $\overline{\mu_{X\boxplus Y}}$ are called lower membership function, membership function, upper membership function of $\Psi_X \boxplus \Psi_Y$, respectively.

Example 3.1. Let $U = \{u_1, u_2, u_3, u_4, u_5, u_6, u_7, u_8\}$ be an universe set, $P = \{p_1, p_2, p_3, p_4, p_5\}$ be the set of parameters and $X = \{0.64/p_2, 0.55/p_4\}$, $Y = \{0.3/p_2, 0.48/p_3\}$ are two fuzzy sets over P. If

$$\underline{X} = \{0.42/p_2, 0.45/p_4\}, \quad \overline{X} = \{0.7/p_2, 0.85/p_4\}$$

and

$$\underline{Y} = \{0.2/p_2, 0.3/p_3\}, \quad \overline{Y} = \{0.5/p_2, 0.65/p_3\},$$

then the virtual fuzzy parameterized soft sets Ψ_X and Ψ_Y are written by

$$\Psi_X = \begin{Bmatrix} (0.42/p_2, \{u_1, u_2, u_3, u_7, u_8\}), (0.45/p_4, \{u_1, u_3, u_5, u_6, u_8\}) \\ (0.64/p_2, \{u_2, u_3, u_7, u_8\}), (0.55/p_4, \{u_3, u_5, u_6, u_8\}) \\ (0.7/p_2, \{u_2, u_3, u_8\}), (0.85/p_4, \{u_3, u_6, u_8\}) \end{Bmatrix}$$

and

$$\Psi_Y = \begin{Bmatrix} (0.2/p_2, \{u_1, u_2, u_4, u_5, u_7\}), (0.3/p_3, \{u_1, u_3, u_4, u_5, u_6\}) \\ (0.3/p_2, \{u_2, u_4, u_5, u_7\}), (0.48/p_3, \{u_3, u_4, u_5, u_6\}) \\ (0.5/p_2, \{u_2, u_4, u_5\}), (0.65/p_3, \{u_4, u_5, u_6\}) \end{Bmatrix}.$$

Then,

$$\Psi_X \boxplus \Psi_Y = \begin{Bmatrix} (0.536/p_2, \{u_1, u_2, u_3, u_4, u_5, u_7, u_8\}), (0.3/p_3, \{u_1, u_3, u_4, u_5, u_6\}), \\ (0.45/p_4, \{u_1, u_3, u_5, u_6, u_8\}), (0.748/p_2, \{u_2, u_3, u_4, u_5, u_7, u_8\}), \\ (0.48/p_3, \{u_3, u_4, u_5, u_6\}), (0.55/p_4, \{u_3, u_5, u_6, u_8\}), \\ (0.85/p_2, \{u_2, u_3, u_4, u_5, u_8\}), (0.65/p_3, \{u_4, u_5, u_6\}), (0.85/p_4, \{u_3, u_6, u_8\}) \end{Bmatrix}$$

Proposition 3.1. Let $\Psi_X, \Psi_\emptyset, \Psi_{\tilde{P}} \in VFPS(U)$. Then,

    i. $\Psi_X \boxplus \Psi_{\tilde{P}} = \Psi_{\tilde{P}}$,
    ii. $\Psi_X \boxtimes \Psi_{\tilde{P}} = \Psi_X$,
    iii. $\Psi_X \boxplus \Psi_\emptyset = \Psi_X$,
    iv. $\Psi_X \boxtimes \Psi_\emptyset = \Psi_\emptyset$.

Proof. Straightforward.

Proposition 3.2. Let $\Psi_X, \Psi_Y \in VFPS(U)$. Then,

    i. $(\Psi_X \boxplus \Psi_Y)^c = \Psi_X^c \boxtimes \Psi_Y^c$,

ii. $\left(\Psi_X \; \overline{\boxtimes} \; \Psi_Y\right)^c = \Psi_X^c \; \boxplus \; \Psi_Y^c,$

iii. $(\Psi_X \boxtimes \Psi_Y)^c = \Psi_X^c \; \overline{\boxplus} \; \Psi_Y^c,$

iv. $\left(\Psi_X \; \overline{\boxplus} \; \Psi_Y\right)^c = \Psi_X^c \boxtimes \Psi_Y^c.$

Proof. i. For all $p^{\underline{Y}} \in \underline{P}$,

$$\underline{\mu_{(X\boxplus Y)^c}}(p^{\underline{Y}}) = 1 - \underline{\mu_{X\boxplus Y}}(p^{\underline{Y}})$$
$$= 1 - \left(\left[(\mu_X(p) - \underline{\alpha}) + \left(\mu_Y(p) - \underline{\beta}\right)\right] - (\mu_X(p) - \underline{\alpha}) \cdot \left(\mu_Y(p) - \underline{\beta}\right)\right)$$
$$= 1 - \mu_X(p) + \underline{\alpha} - \mu_Y(p) + \underline{\beta} + (\mu_X(p) - \underline{\alpha}) \cdot \left(\mu_Y(p) - \underline{\beta}\right)$$
$$= \left(1 - \mu_X(p) + \underline{\alpha}\right)\left(1 - \mu_Y(p) + \underline{\beta}\right)$$
$$= \underline{\mu_{X^c \overline{\boxtimes} Y^c}}(p^{\underline{Y}})$$

for all $p \in P$,

$$\mu_{(X\boxplus Y)^c}(p) = 1 - \mu_{X\boxplus Y}(p)$$
$$= 1 - \left(\mu_X(p) + \mu_Y(p) - \mu_X(p) \cdot \mu_Y(p)\right)$$
$$= 1 - \mu_X(p) - \mu_Y(p) + \mu_X(p) \cdot \mu_Y(p)$$
$$= \left(1 - \mu_X(p)\right)\left(1 - \mu_Y(p)\right)$$
$$= \mu_{X^c \overline{\boxtimes} Y^c}(p)$$

for all $p^{\overline{Y}} \in \overline{P}$,

$$\overline{\mu_{(X\boxplus Y)^c}}(p^{\overline{Y}}) = 1 - \overline{\mu_{X\boxplus Y}}(p^{\overline{Y}})$$
$$= 1 - \left(\left[(\mu_X(p) + \overline{\alpha}) + \left(\mu_Y(p) + \overline{\beta}\right)\right] - (\mu_X(p) + \overline{\alpha}) \cdot \left(\mu_Y(p) + \overline{\beta}\right)\right)$$
$$= 1 - \mu_X(p) - \overline{\alpha} - \mu_Y(p) - \overline{\beta} + (\mu_X(p) + \overline{\alpha}) \cdot \left(\mu_Y(p) + \overline{\beta}\right)$$
$$= (1 - \mu_X(p) - \overline{\alpha})\left(1 - \mu_Y(p) - \overline{\beta}\right)$$
$$= \overline{\mu_{X^c \overline{\boxtimes} Y^c}}(p^{\overline{Y}})$$

and for all $p^{\underline{\alpha}}, p^{\underline{\beta}}, p^{\underline{Y}} \in \underline{P}$, $p \in P$ and $p^{\overline{\alpha}}, p^{\overline{\beta}}, p^{\overline{Y}} \in \overline{P}$;

$$\underline{\psi_{(X\boxplus Y)^c}}(p^{\underline{Y}}) = U \setminus \left(\underline{\psi_X}(p^{\underline{\alpha}}) \cup \underline{\psi_Y}(p^{\underline{\beta}})\right) = \left(U \setminus \underline{\psi_X}(p^{\underline{\alpha}})\right) \cup \left(U \setminus \underline{\psi_Y}(p^{\underline{\beta}})\right) = \underline{\psi_{X^c}}(p^{\underline{\alpha}}) \cap \underline{\psi_{Y^c}}(p^{\underline{\beta}}),$$

$$\psi_{(X\boxplus Y)^c}(p) = U \setminus \left(\psi_X(p) \cup \psi_Y(p)\right) = \left(U \setminus \psi_X(p)\right) \cup \left(U \setminus \psi_Y(p)\right) = \psi_{X^c}(p) \cap \psi_{Y^c}(p),$$

$$\overline{\psi_{(X\boxplus Y)^c}}(p^{\overline{Y}}) = U \setminus \left(\overline{\psi_X}(p^{\overline{\alpha}}) \cup \overline{\psi_Y}\left(p^{\overline{\beta}}\right)\right) = \left(U \setminus \overline{\psi_X}(p^{\overline{\alpha}})\right) \cup \left(U \setminus \overline{\psi_Y}\left(p^{\overline{\beta}}\right)\right) = \overline{\psi_{X^c}}(p^{\overline{\alpha}}) \cap \overline{\psi_{Y^c}}\left(p^{\overline{\beta}}\right).$$

The remaining parts can also be proved in a similar way.

Proposition 3.3. Let $\Psi_X, \Psi_Y, \Psi_Z \in VFPS(U)$. Then, for $\star = \left\{\overline{\boxtimes}, \boxtimes, \overline{\boxplus}, \boxplus\right\}$ and $* = \{\cap, \cup\}$,

i. $\Psi_X \star \Psi_Y = \Psi_Y \star \Psi_X$

ii. $\Psi_X \star (\Psi_Y \star \Psi_Z) = (\Psi_X \star \Psi_Y) \star \Psi_Z,$

iii. $\Psi_X \star (\Psi_Y * \Psi_Z) = (\Psi_X \star \Psi_Y) * (\Psi_X \star \Psi_Z),$

Proof. Straightforward.

4. The Proposed Decision-Making Model

In this section, we propose a different decision-making method in expressing uncertainty problems using virtual fuzzy parameterized soft sets. For this, we first define the fuzzy decision sets of a given universe set using the OR-t-norm, AND-t-norm, OR-t-conorm and AND-t-conorm. Then, we propose an algorithm by using the defined fuzzy decision sets.

Definition 4.1. Let $\Psi_X, \Psi_Y \in VFPS(U)$. Then, the OR-fuzzy decision set of $\Psi_X \boxplus \Psi_Y$, denoted $\Xi_{\Psi_X \boxplus \Psi_Y}$, is defined by

$$\Xi_{\Psi_X \boxplus \Psi_Y} = \left\{ \frac{\mu_\boxplus(u_j)}{u_j} : u_j \in U \right\}$$

which is a fuzzy set over U, its membership function $\mu_\boxplus$ is defined by $\mu_\boxplus : U \to [0,1]$,

$$\mu_\boxplus(u_j) = \frac{1}{3n} \sum_{\substack{1 \le i \le m \\ 1 \le j \le n}} \begin{bmatrix} \underline{\mu_{X \boxplus Y}} \left(p_i^\gamma \right) \cdot \chi_{\underline{\psi_{X \boxplus Y}}\left(p_i^\gamma\right)}(u_j) + \\ \mu_{X \boxplus Y}(p_i) \cdot \chi_{\psi_{X \boxplus Y}(p_i)}(u_j) + \\ \overline{\mu_{X \boxplus Y}} \left(p_i^{\overline{\gamma}} \right) \cdot \chi_{\overline{\psi_{X \boxplus Y}}\left(p_i^{\overline{\gamma}}\right)}(u_j) \end{bmatrix} \tag{37}$$

where

$$\chi_{\underline{\psi_{X \boxplus Y}}\left(p_i^\gamma\right)}(u_j) = \begin{cases} 1, & u_j \in \underline{\psi_{X \boxplus Y}} \left(p_i^\gamma \right) \\ 0, & u_j \notin \underline{\psi_{X \boxplus Y}} \left(p_i^\gamma \right)' \end{cases} \tag{38}$$

$$\chi_{\psi_{X \boxplus Y}(p_i)}(u_j) = \begin{cases} 1, & u_j \in \psi_{X \boxplus Y}(p_i) \\ 0, & u_j \notin \psi_{X \boxplus Y}(p_i) \end{cases} \tag{39}$$

and

$$\chi_{\overline{\psi_{X \boxplus Y}}\left(p_i^{\overline{\gamma}}\right)}(u_j) = \begin{cases} 1, & u_j \in \overline{\psi_{X \boxplus Y}} \left(p_i^{\overline{\gamma}} \right) \\ 0, & u_j \notin \overline{\psi_{X \boxplus Y}} \left(p_i^{\overline{\gamma}} \right) \end{cases} \tag{40}$$

Here, the fuzzy decision sets $\Xi_{\Psi_X \overline{\boxtimes} \Psi_Y}$, $\Xi_{\Psi_X \boxtimes \Psi_Y}$ and $\Xi_{\Psi_X \overline{\boxplus} \Psi_Y}$ are defined in a similar way.

Next, we construct the algorithm given below for decision-making (i.e., the application of a virtual fuzzy parameterized soft set):

Algorithm

Step 1: Choose fuzzy subsets X and Y over P, (also "fuzzy subsets $\underline{X}$ and $\underline{Y}$ over $\underline{P}$" and "fuzzy subsets $\overline{X}$ and $\overline{Y}$ over $\overline{P}$")

Step 2: Construct the virtual fuzzy parameterized soft sets Ψ_X and Ψ_Y over U,

Step 3: Find the OR-t-conorm $\Psi_X \boxplus \Psi_Y$,

Step 4: Compute the OR-fuzzy decision set $\Xi_{\Psi_X \boxplus \Psi_Y}$.

Step 5: Find r, for which $\mu_{\Xi_{\Psi_X \boxplus \Psi_Y}}(u_r) = max \left\{ \mu_{\Xi_{\Psi_X \boxplus \Psi_Y}}(u) : u \in U \right\}$.

Note that, for other defined products, an algorithm can be constructed similar to the algorithm given above.

Now, we show the steps and principle of the above algorithm by using the following example. It should also be noted that the examples to be given for algorithms created by using other products can be expressed in a similar way.

Example 4.1. Suppose a school wants to choose the students that best suit its parameters. For this, the school has posted an announcement. According to the announcement, a three-stage exam will be held for candidate students. Then; the set of candidate students applying for admission to the school is $U = \{u_1, u_2, u_3, u_4, u_5, u_6, u_7, u_8, u_9\}$ and the set of parameters the school requires from students is $P = \{p_1, p_2, p_3, p_4\} = \{self-confident, \ successful, \ willing \ to \ learn, \ talented\}$.

Step 1: Suppose that the school administration has selected two experts, *X* and *Y*, who are authorized on this subject. The fuzzy sets in which each expert express his opinion on this subject are as follows:

$$\underline{X} = \{0.5/p_1, 0.65/p_3\}, \quad X = \{0.56/p_1, 0.72/p_3\}, \quad \overline{X} = \{0.76/p_1, 0.84/p_3\}$$

and

$$\underline{Y} = \{0.45/p_3, 0.36/p_4\}, \quad Y = \{0.62/p_3, 0.5/p_4\}, \quad \overline{Y} = \{0.75/p_3, 0.67/p_4\}$$

over $\underline{P}, P, \overline{P}$, respectively.

Step 2: The results obtained based on the opinions of the experts are expressed as virtual fuzzy parameterized soft sets Ψ_X and Ψ_Y over U as follows:

$$\Psi_X = \left\{ \begin{array}{c} (0.5/p_1, \{u_2, u_4, u_5, u_7, u_9\}), (0.65/p_3, \{u_1, u_4, u_6, u_7, u_8\}) \\ (0.56/p_1, \{u_2, u_5, u_7, u_9\}), (0.72/p_3, \{u_1, u_4, u_6, u_8\}) \\ (0.76/p_1, \{u_2, u_7, u_9\}), (0.84/p_3, \{u_1, u_4, u_8\}) \end{array} \right\}$$

$$\Psi_Y = \left\{ \begin{array}{c} (0.45/p_3, \{u_1, u_2, u_4, u_5, u_7\}), (0.36/p_4, \{u_1, u_3, u_4, u_5, u_6\}) \\ (0.62/p_3, \{u_2, u_4, u_5, u_7\}), (0.5/p_4, \{u_3, u_4, u_5, u_6\}) \\ (0.75/p_3, \{u_2, u_4, u_5\}), (0.67/p_4, \{u_4, u_5, u_6\}) \end{array} \right\}.$$

Step 3: The OR-*t*-conorm of Ψ_X and Ψ_Y is formed as,

$$\Psi_X \boxplus \Psi_Y = \left\{ \begin{array}{c} (0.5/p_1, \{u_2, u_4, u_5, u_7, u_9\}), (0.8075/p_3, \{u_1, u_2, u_4, u_5, u_6, u_7, u_8\}), \\ (0.36/p_4, \{u_1, u_3, u_4, u_5, u_6\}), (0.56/p_1, \{u_2, u_5, u_7, u_9\}), \\ (0.8936/p_3, \{u_1, u_2, u_4, u_5, u_6, u_7, u_8\}), (0.5/p_4, \{u_3, u_4, u_5, u_6\}), \\ (0.76/p_1, \{u_2, u_7, u_9\}), (0.96/p_3, \{u_1, u_2, u_4, u_5, u_8\}), (0.67/p_4, \{u_4, u_5, u_6\}) \end{array} \right\}$$

Step 4: The OR-fuzzy decision set of $\Psi_X \boxplus \Psi_Y$ is computed as

$$\Xi_{\Psi_X \boxplus \Psi_Y} = \left\{ \begin{array}{c} \dfrac{0.112}{u_1}, \dfrac{0.166}{u_2}, \dfrac{0.032}{u_3}, \dfrac{0.174}{u_4}, \dfrac{0.194}{u_5} \\ \dfrac{0.120}{u_6}, \dfrac{0.130}{u_7}, \dfrac{0.099}{u_8}, \dfrac{0.067}{u_9} \end{array} \right\}$$

For example, the value $\mu_\boxplus(u_7)$ for u_7 is calculated as follows:

$$\mu_\boxplus(u_7) = \frac{1}{3 \cdot 9} \sum_{\substack{1 \le i \le 4 \\ 1 \le j \le 9}} [0.5 + 0.8075 + 0 + 0.56 + 0.8936 + 0 + 0.76 + 0 + 0] = \frac{3.5211}{27} \cong 0.130$$

Step 5: We conclude from the values of u that $\mu_{\Xi_{\Psi_X \boxplus \Psi_Y}}(u_5) = max\left\{\mu_{\Xi_{\Psi_X \boxplus \Psi_Y}}(u) : u \in U\right\} = 0.194$ and hence $r = 5$. Thus u_5 is the optimal choice candidate and so u_5 is the most suitable student candidate for the desired parameters.

5. Conclusion

To date, many hybrid sets have been constructed by considering fuzzy sets and soft sets. However, these sets have not questioned the margin of error of the decision-maker. For this reason, it is usual to encounter certain problems in solving uncertainty problems. This paper has focused on virtual fuzzy parameterized soft sets, which is the first mathematical model that can detect a possible margin of error in the data expressed by decision-makers. Moreover, the present study has studied the algebraic operations of VFPSSs. Afterward, a decision-making method has been proposed. We think that the approach given in this study can be instrumental in expressing with virtual fuzzy parameterized soft sets, which is a new mathematical model, the uncertainty problems encountered in fields such as current life state, computer science, decision making, etc.

Conflicts of interest

The author state that did not have conflict of interests.

References

[1] Zadeh L.A., Fuzzy sets, *Information and Control*, 8 (1965) 338-353.

[2] Pawlak Z., Rough sets, *International Journal of Computing and Information Sciences*, 11 (1982) 341-356.

[3] Molodtsov D., Soft set theory-first results, *Computers and Mathematics with Applications,* 37 (1999) 19-31.

[4] Zou Y. and Xiao Z., Data analysis approaches of soft sets under incomplete information, *Knowledge-Based Systems*, 21 (2008) 941–945.

[5] Selvakumari K., Solving Game Problem Using Weighted Soft Sets, *Journal of Computer and Mathematical Sciences*, 9(10) (2018) 1307-1311.

[6] Deli I. and Çağman N., Application of soft sets in decision-making based on game theory, *Ann Fuzzy Math Inform*, 11(3) (2016) 425-438.

[7] Kamacı, H., A novel approach to similarity of soft sets, *Adıyaman University Journal of Science*, 9(1) (2019), 23-35.

[8] Aygün, E. and Kamacı, H., Some new algebraic structures of soft sets. *Soft Computing*, 25 (2021) 8609-8626.

[9] Kamacı, H., Interval-valued fuzzy parameterized intuitionistic fuzzy soft sets and their applications, *Cumhuriyet Sci. J.,* 40(2) (2019) 317-331.

[10] Kamacı, H., On Hybrid Structures of Hypersoft Sets and Rough Sets, *International Journal of Modern Science and Technology*, 6(4) (2021) 69-82.

[11] Maji P.K., Roy A.R. and Biswas R., Fuzzy soft sets, *Journal of Fuzzy Mathematics*, 9(3) (2001) 589-602.

[12] Çağman N., Enginoğlu S. and Çıtak F., Fuzzy soft set theory and its applications, *Iranian Journal of Fuzzy Systems*, 8(3) (2011) 137-147.

[13] Demirtaş N. and Dalkılıç O., An application in the diagnosis of prostate cancer with the help of bipolar soft rough sets, *on Mathematics and Mathematics Education (ICMME 2019)*, KONYA, 283, (2019).

[14] Demirtaş N., Hussaın S. and Dalkılıç O., New approaches of inverse soft rough sets and their applications in a decision-making problem, *Journal of Applied Mathematics and Informatics*, 38(3-4) (2020) 335-349.

[15] Dalkılıç O., An Application of VFPFSS's in Decision-Making Problems, *Journal of Polytechnic*,758474 (2020).

[16] Kamal N.L.A.M., Abdullah L., Abdullah I., Alkhazaleh S. and Karaaslan F., Multi-valued interval neutrosophic soft set: Formulation and Theory, *Neutrosophic Sets and Systems*, 30(1) (2019) 12.

[17] Hooda D.S., Kumari R. and Sharma D.K., Intuitionistic Fuzzy Soft Set Theory and Its Application in Medical Diagnosis, *International Journal of Statistics in Medical Research*, 7(3) (2018) 70-76.

[18] Smarandache F, A Unifying Field in Logics: Neutrosophic Logic. Neutrosophy, Neutrosophic Set, Neutrosophic Probability, *American Research Press*, Rehoboth, NM, (1999).

[19] Çağman N., Çıtak F. and Enginoğlu S., FP-soft Set Theory and Its Applications, *Annals of Fuzzy Mathematics and Informatics*, 2 (2011) 219-226.

[20] Dalkılıç O. and Demirtas N., VFP-Soft Sets and Its Application on Decision-Making Problems, *Journal of Polytechnic*, 685634 (2020).

[21] Zimmermann, H., J. Fuzzy Set Theory and Its Applications. 2nd Edition. Dordrecht: Kluwer Academic Publishers, (1991).

[22] Çağman, N. and İrfan, D., Products of FP-soft sets and their applications, *Hacettepe Journal of Mathematics and Statistics,* 41(3) (2012) 365-374.

4-dimensional pseudo-Galilean geometry

Mücahit AKBIYIK[1],* iD, Salim YÜCE[2] iD

[1]*Beykent University, Department of Mathematics, Istanbul/ TURKEY*

[2]*Yildiz Technical University, Department of Mathematics, Istanbul/ TURKEY*

Abstract

According to F. Klein, Geometry is the study of invariant properties of figures, i.e., properties unchanged under all motions. In this article, we introduce 4-dimensional pseudo-Galilean transformations. Moreover, we study invariant properties under translation, shear and Minkowskian rotation motions. We have computed Frenet-Serret formulas of a curve and also we have found the fundamental theorem of curve theory in 4-dimensional pseudo-Galilean geometry.

1. Introduction

Non-Euclidean geometry, literally is any geometry that is not the same as Euclidean geometry. The applications of Non-Euclidean geometry, [1] have been found in a lot of places of our life such as the theory of general relativity, celestial mechanics, cosmology. Another interesting application area is architecture. For example, in 2009, the Tote restaurant in Mumbai was designed with aid of the fractal geometry, [1]. Galilean geometry is a geometry of the Galilean Relativity or shortly a non-Euclidean geometry. It is a bridge from Euclidean geometry to special relativity. It is a theory that is invariant under Galilean transformations stated by Yaglom. Galilean geometry is worked in detail in [2-4].

In 1998, pseudo-Galilean geometry $\mathbb{G}_1^3$ as analog to [2] and [4] is defined by Divjak, [5]. This work [5] also includes the theory of curves in $\mathbb{G}_1^3$. Then, a lot of papers such as [5-12] in pseudo-Galilean geometry $\mathbb{G}_1^3$, have been worked. In this paper, 4-dimensional pseudo-Galilean geometry $\mathbb{G}_1^4$ will be defined and the curves in $\mathbb{G}_1^4$ will be considered.

2. Minkowski Space $\mathbb{R}_1^3$

In this section, we give some fundamental information to construct a new geometry about 3- dimensional Minkowski space. Thus, we will be able to consider Galilean transformations in 3- dimensional Minkowski space. Let us consider $3-$dimensional Minkowski space $\mathbb{R}_1^3 = \left[\mathbb{R}, (+,+,-) \right]$ and let the Lorentzian inner product of $\mathbf{x} = (x_1, x_2, x_3)$ and $\mathbf{y} = (y_1, y_2, y_3) \in \mathbb{R}_1^3$, be

$$\langle \mathbf{x}, \mathbf{y} \rangle = x_1 y_1 + x_2 y_2 - x_3 y_3.$$

The norm of $\mathbf{x} \in \mathbb{R}_1^3$ is denoted by $\|\mathbf{x}\|$ and defined as

$$\|\mathbf{x}\| = \sqrt{|\langle \mathbf{x}, \mathbf{x} \rangle|}.$$

A vector $\mathbf{x} \in \mathbb{R}_1^3$ is called a spacelike, timelike and null (light-like) vector if $\langle \mathbf{x}, \mathbf{x} \rangle > 0$ or $\mathbf{x} = \mathbf{0}$, $\langle \mathbf{x}, \mathbf{x} \rangle < 0$ and $\langle \mathbf{x}, \mathbf{x} \rangle = 0$ for $\mathbf{x} \neq \mathbf{0}$, respectively, [13,14]. A timelike vector is said to be positive (resp. negative) if and only if $x_3 > 0$ (resp. $x_3 < 0$).

Let $\mathbf{x}$ and $\mathbf{y}$ be positive (negative) timelike vectors in $\mathbb{R}_1^3$. There is a unique non-negative real number α such that

$$\langle \mathbf{x}, \mathbf{y} \rangle = \|\mathbf{x}\| \|\mathbf{y}\| \cosh \alpha.$$

This number is called the Lorentzian timelike angle between the vectors $\mathbf{x}$ and $\mathbf{y}$. Let $\mathbf{x}$ and $\mathbf{y}$ be spacelike vectors in $\mathbb{R}_1^3$ that span a spacelike vector subspace. There is a unique nonnegative real number α such that

$$\langle \mathbf{x}, \mathbf{y} \rangle = \|\mathbf{x}\| \|\mathbf{y}\| \cos \alpha.$$

Let $\mathbf{x}$ and $\mathbf{y}$ be spacelike vectors in $\mathbb{R}_1^3$ that span a timelike vector subspace. There is a unique nonnegative real number α such that

$$\langle \mathbf{x}, \mathbf{y} \rangle = \|\mathbf{x}\| \|\mathbf{y}\| \cosh \alpha.$$

Let $\mathbf{x}$ be a spacelike vector and $\mathbf{y}$ be a timelike vector in $\mathbb{R}_1^3$. Then, there is a unique real number $\alpha \geq 0$ such that

$$\langle \mathbf{x}, \mathbf{y} \rangle = \|\mathbf{x}\| \|\mathbf{y}\| \sinh \alpha.$$

Basic rotations (also called the elemental rotation) are rotations about one of the axes of a coordinate system. The following three basic rotation rotate vectors by an angle α about the x, y, or z axis, in $\mathbb{R}_1^3$. The rotation by angle α about the axes x is denoted by $R_x(\alpha)$ and is calculated as

$$R_x(\alpha) = \begin{bmatrix} 1 & 0 & 0 \\ 0 & \cosh \alpha & \sinh \alpha \\ 0 & \sinh \alpha & \cosh \alpha \end{bmatrix},$$

the rotation by angle α about the axes y is denoted by $R_y(\alpha)$ and is obtained by

$$R_y(\alpha) = \begin{bmatrix} \cosh \alpha & 0 & \sinh \alpha \\ 0 & 1 & 0 \\ \sinh \alpha & 0 & \cosh \alpha \end{bmatrix},$$

and the rotation by angle α about the axes z is denoted by $R_z(\alpha)$ and is calculated as:

$$R_z(\alpha) = \begin{bmatrix} \cos \alpha & \sin \alpha & 0 \\ -\sin \alpha & \cos \alpha & 0 \\ 0 & 0 & 1 \end{bmatrix},$$

with the help of the article [15].

However, according to Euler's rotation theorem, any general rotations in space $\mathbb{R}^3$ may be described using three basic rotations. As you see, the elemental rotations can occur about the axes of the fixed coordinate system (extrinsic rotations) or about the axes of a rotating coordinate system, which is initially aligned with the fixed one, and modifies its orientation after each elemental rotation. Without considering the possibility of using two

different conventions for the definition of the rotation axes (intrinsic or extrinsic), there exist twelve possible sequences of rotation axes, divided into two groups: by Proper Euler angles ($R_z R_x R_z$, $R_x R_y R_x$, $R_y R_z R_y$, $R_z R_y R_z$, $R_x R_z R_x$, $R_y R_x R_y$) and by Tait–Bryan angles ($R_x R_y R_z$, $R_y R_z R_x$, $R_z R_x R_y$, $R_x R_z R_y$, $R_z R_y R_x$, $R_y R_x R_z$). Similarly, the rotation matrices in $\mathbb{R}_1^3$ can be obtained from above three using matrix multiplication.

For example, the product

$$R = R_z(\alpha) R_y(\beta) R_x(\gamma) = \begin{bmatrix} \cosh\beta\cos\alpha & \cosh\gamma\sin\alpha + \sinh\beta\sinh\gamma\cos\alpha & \sinh\gamma\sin\alpha + \cosh\gamma\sinh\beta\cos\alpha \\ -\cosh\beta\sin\alpha & \cosh\gamma\cos\alpha - \sinh\beta\sinh\gamma\sin\alpha & \sinh\gamma\cos\alpha - \cosh\gamma\sinh\beta\sin\alpha \\ \sinh\beta & \cosh\beta\sinh\gamma & \cosh\beta\cosh\gamma \end{bmatrix}$$

represents a rotation whose yaw, pitch, and roll angles are α, β and γ about axes z, y, x, respectively. Moreover, the product

$$R = R_z(\alpha) R_x(\gamma) R_z(\beta) = \begin{bmatrix} \cos\alpha\cos\beta - \cosh\gamma\sin\alpha\sin\beta & \cos\alpha\sin\beta + \cosh\gamma\cos\beta\sin\alpha & \sinh\gamma\sin\alpha \\ -\cos\beta\sin\alpha - \cosh\gamma\cos\alpha\sin\beta & \cosh\gamma\cos\alpha\cos\beta - \sin\alpha\sin\beta & \sinh\gamma\cos\alpha \\ -\sinh\gamma\sin\beta & \sinh\gamma\cos\beta & \cosh\gamma \end{bmatrix} \quad (1)$$

represents a rotation whose angles α, β, γ about axes z, x, z.

Also, rotations in Minkowski space, preserve the types of vectors. One can be found more information about Minkowski space in [13-21].

3. Pseudo-Galiean Geometry $\mathbb{G}_1^4$

Let $\{x, y, z\}$ and $\{x', y', z'\}$ be two referance frames in $\mathbb{R}_1^3$. We know that there is the relation

$$\begin{bmatrix} x' \\ y' \\ z' \end{bmatrix} = \begin{bmatrix} \cos\alpha\cos\beta - \cosh\gamma\sin\alpha\sin\beta & \cos\alpha\sin\beta + \cosh\gamma\cos\beta\sin\alpha & \sinh\gamma\sin\alpha \\ -\cos\beta\sin\alpha - \cosh\gamma\cos\alpha\sin\beta & \cosh\gamma\cos\alpha\cos\beta - \sin\alpha\sin\beta & \sinh\gamma\cos\alpha \\ -\sinh\gamma\sin\beta & \sinh\gamma\cos\beta & \cosh\gamma \end{bmatrix} \begin{bmatrix} x \\ y \\ z \end{bmatrix} + \begin{bmatrix} a \\ b \\ c \end{bmatrix}$$

between these two frames from (1). If the origin point O of referans frame $\{x, y, z\}$ with constant velocity $\mathbf{v}$ on a non-null line l moves according to relative frame $\{x', y', z'\}$, then there are two cases with respect to l for coordinates $a(t), b(t)$ and $c(t)$ of point O at the moment t where $x'\hat{O}l = \delta_1$, $y'\hat{O}l = \delta_2$, and $z'\hat{O}l = \delta_3$ by aid of [13]:

Case 1 : if l is timelike, then one can be written

$$\begin{bmatrix} a(t) \\ b(t) \\ c(t) \end{bmatrix} = \begin{bmatrix} a + (v\sinh\delta_1)t \\ b + (v\sinh\delta_2)t \\ c + (v\cosh\delta_3)t \end{bmatrix},$$

where $\sinh^2\delta_1 + \sinh^2\delta_2 - \cosh^3\delta_3 = 1$.

So, the relation between the coordinates (x', y', z') and (x, y, z) of the point A is given by

$$\begin{bmatrix} x' \\ y' \\ z' \end{bmatrix} = \begin{bmatrix} \cos\alpha\cos\beta - \cosh\gamma\sin\alpha\sin\beta & \cos\alpha\sin\beta + \cosh\gamma\cos\beta\sin\alpha & \sinh\gamma\sin\alpha \\ -\cos\beta\sin\alpha - \cosh\gamma\cos\alpha\sin\beta & \cosh\gamma\cos\alpha\cos\beta - \sin\alpha\sin\beta & \sinh\gamma\cos\alpha \\ -\sinh\gamma\sin\beta & \sinh\gamma\cos\beta & \cosh\gamma \end{bmatrix} \begin{bmatrix} x \\ y \\ z \end{bmatrix} + \begin{bmatrix} a + (v\sinh\delta_1)t \\ b + (v\sinh\delta_2)t \\ c + (v\cosh\delta_3)t \end{bmatrix}.$$

By adding the relation $t' = t + d$ which expresses the possibility of shifting the time origin, we arrive at the formulas

$$
\begin{cases}
x' = a + x\left(\cos\alpha\cos\beta - \cosh\gamma\sin\alpha\sin\beta\right) + y\left(\cos\alpha\sin\beta + \cosh\gamma\cos\beta\sin\alpha\right) + t\left(v\sinh\delta_1\right) + z\left(\sinh\gamma\sin\alpha\right) \\
y' = b - x\left(\cos\beta\sin\alpha + \cosh\gamma\cos\alpha\sin\beta\right) - y\left(\sin\alpha\sin\beta - \cosh\gamma\cos\alpha\cos\beta\right) + t\left(v\sinh\delta_2\right) + z\left(\sinh\gamma\cos\alpha\right) \\
z' = c - x\left(\sinh\gamma\sin\beta\right) + y\left(\sinh\gamma\cos\beta\right) + z\left(\cosh\gamma\right) + t\left(v\cosh\delta_3\right) \\
t' = d + t,
\end{cases}
$$

which give the relation between two coordinate systems the pseudo-Galilean motions. The motions can be split into three motions: a rotation about the $t-$axis; a shear in the direction of vector $\mathbf{v} = \left(v\sinh\delta_1, v\sinh\delta_2, v\cosh\delta_3, 0\right)$, and a translation determined by the vector $\left(a, b, c, d\right)$. If the motion is arranged as x instead of time parameter t and y, z, w instead of space parameter x, y, z, respectively, we get

$$
\begin{cases}
x' = d + x \\
y' = a + \left(v\sinh\delta_1\right)x + \left(\cos\alpha\cos\beta - \cosh\gamma\sin\alpha\sin\beta\right)y + \left(\cos\alpha\sin\beta + \cosh\gamma\cos\beta\sin\alpha\right)z + \left(\sinh\gamma\sin\alpha\right)w \\
z' = b + \left(v\sinh\delta_2\right)x - \left(\cos\beta\sin\alpha + \cosh\gamma\cos\alpha\sin\beta y\right) - \left(\sin\alpha\sin\beta - \cosh\gamma\cos\alpha\cos\beta\right)z + \left(\sinh\gamma\cos\alpha\right)w \\
w' = c + \left(v\cosh\delta_3\right)x - \left(\sinh\gamma\sin\beta\right)y + \left(\sinh\gamma\cos\beta\right)z + \left(\cosh\gamma\right)w
\end{cases}
$$

where $\sinh^2\delta_1 + \sinh^2\delta_2 - \cosh^3\delta_3 = 1$.

Case 2: Similary, if l is spacelike, then there are four situations and it can be easily calculated such as above.

Finally, if we calculate the two cases then we obtain the following equations

$$
\begin{cases}
x' = d + x \\
y' = a + vex + \left(\cos\alpha\cos\beta - \cosh\gamma\sin\alpha\sin\beta\right)y + \left(\cos\alpha\sin\beta + \cosh\gamma\cos\beta\sin\alpha\right)z + \left(\sinh\gamma\sin\alpha\right)w \\
z' = b + vfx - \left(\cos\beta\sin\alpha + \cosh\gamma\cos\alpha\sin\beta\right)y - \left(\sin\alpha\sin\beta - \cosh\gamma\cos\alpha\cos\beta\right)z + \left(\sinh\gamma\cos\alpha\right)w \\
w' = c + vgx - \left(\sinh\gamma\sin\beta\right)y + \left(\sinh\gamma\cos\beta\right)z + \left(\cosh\gamma\right)w
\end{cases}
\tag{2}
$$

where the coefficents e, f, g are angles such that $e^2 + f^2 - g^2 = 1$.

So, the above equations are called 4-dimensional pseudo-Galilean transformations. The invariant theory under 4-dimensional pseudo-Galilean transformations is called 4-dimensional pseudo-Galilean geometry and is denoted by $\mathbb{G}_1^4$.

4. Basic Information About $\mathbb{G}_1^4$

Let $\mathbf{a} = (x, y, z, w)$ and $\mathbf{b} = (x_1, y_1, z_1, w_1)$ be vectors in the pseudo-Galilean space $\mathbb{G}_1^4$. The scalar product in the Pseudo-Galilean space $\mathbb{G}_1^4$ is defined by

$< \mathbf{a}, \mathbf{b} >_\mathbb{G} = xx_1$.

A vector $\mathbf{a} = (x, y, z, w)$ is said to be isotropic or special vector if $x = 0$. Otherwise, $\mathbf{a} = (x, y, z, w)$ is called a non-isotropic. All unit non-isotropic vectors and isotropic vectors are of the form $\mathbf{a} = (x, y, z, w)$, $x \neq 0$ and $\mathbf{p} = (0, y, z, w)$, respectively. Let $\mathbf{p} = (0, y, z, w)$ and $\mathbf{q} = (0, y_1, z_1, w_1)$ be two isotropic vectors. Then, the special scalar product of isotropic vectors $\mathbf{p}$ and $\mathbf{q}$ is defined by

$< \mathbf{a}, \mathbf{b} >_\delta = yy_1 + zz_1 - ww_1$.

Along with the study, the special scalar product will be denoted by $\delta-$ product. The orthogonality of vectors in pseudo-Galilean space $\mathbb{G}_1^4$, $\mathbf{a} \perp_{\mathbb{G}} \mathbf{b}$, means that $<\mathbf{a},\mathbf{b}>_{\mathbb{G}}=0$ for $<\mathbf{a},\mathbf{a}>_{\mathbb{G}} \neq 0$. So, all isotropic vectors are orthogonal to the non-isotropic vectors. Also, the δ-orthogonality of isotropic vectors $\mathbf{p}$ and $\mathbf{q}$ means that

$$<\mathbf{p},\mathbf{q}>_\delta=0.$$

The norm of a vector $\mathbf{a}$ is defined by

$$\|\mathbf{a}\|_{\mathbb{G}}=|x|,$$

and $\mathbf{a}$ is called a unit vector if $\|\mathbf{a}\|_{\mathbb{G}}=1$. The norm of an isotropic vector $\mathbf{p}$ is defined by

$$\|\mathbf{p}\|_\delta=\sqrt{\left|y^2+z^2-w^2\right|}$$

and p is called a unit isotropic vector if $\|\mathbf{p}\|_\delta=1$. Briefly, the vectors in $\mathbb{G}_1^4$ are divided into two classes: the non-isotropic vector or the isotropic vectors which are spacelike, timelike or null.

Let $\mathbf{a}=(x,y,z,w)$, $\mathbf{b}=(x_1,y_1,z_1,w_1)$ and $\mathbf{c}=(x_2,y_2,z_2,w_2)$ be at least one non-isotropic vector in the pseudo-Galilean space $\mathbb{G}_1^4$, we introduce the vector product of $\mathbf{a}$, $\mathbf{b}$ and $\mathbf{c}$ as the following:

$$\mathbf{a}\times\mathbf{b}\times\mathbf{c}=-\begin{vmatrix} \mathbf{0} & \mathbf{e}_2 & \mathbf{e}_3 & -\mathbf{e}_4 \\ x & y & z & w \\ x_1 & y_1 & z_1 & w_1 \\ x_2 & y_2 & z_2 & z_2 \end{vmatrix}.$$

Especially, the vector product of isotropic vectors $\mathbf{p}=(0,y,z,w)$, $\mathbf{q}=(0,y_1,z_1,w_1)$ and $\mathbf{r}=(0,y_2,z_2,w_2)$ is introduced

$$\mathbf{p}\times\mathbf{q}\times\mathbf{r}=-\begin{vmatrix} \mathbf{e}_1 & \mathbf{e}_2 & \mathbf{e}_3 & -\mathbf{e}_4 \\ 0 & y & z & w \\ 0 & y_1 & z_1 & w_1 \\ 0 & y_2 & z_2 & z_2 \end{vmatrix}.$$

Here, $\mathbf{e}_1,\mathbf{e}_2,\mathbf{e}_3$ and $\mathbf{e}_4$ are coordinate direction vectors which satisfy at follows:

$$\mathbf{e}_1\times\mathbf{e}_2\times\mathbf{e}_3=\mathbf{e}_4,$$
$$\mathbf{e}_2\times\mathbf{e}_3\times\mathbf{e}_4=\mathbf{e}_1,$$
$$\mathbf{e}_3\times\mathbf{e}_4\times\mathbf{e}_1=\mathbf{e}_2,$$
$$\mathbf{e}_4\times\mathbf{e}_1\times\mathbf{e}_2=-\mathbf{e}_3.$$

Let $\{\mathbf{D},\mathbf{E},\mathbf{F},\mathbf{G}\}$ be vectors in $\mathbb{G}_1^4$.

i) If $\mathbf{D}$ is a unit non-isotropic vector and $\{\mathbf{E},\mathbf{F}\}$ are unit isotropic spacelike vectors and $\mathbf{G}$ is a unit isotropic timelike vector, then $\{\mathbf{D},\mathbf{E},\mathbf{F},\mathbf{G}\}$ is called an orthonormal basis of $\mathbb{G}_1^4$.

ii) If $\mathbf{D}$ is a unit non-isotropic vector and $\mathbf{E}$ is a unit isotropic spacelike vector, $\{\mathbf{F},\mathbf{G}\}$ are unit isotropic lightlike vectors such that $\langle\mathbf{F},\mathbf{G}\rangle_\delta=-1$, $\{\mathbf{D},\mathbf{E},\mathbf{F},\mathbf{G}\}$ is called a null basis (or null frame) of $\mathbb{G}_1^4$.

5. Construction of Frenet-Serret Frame in $\mathbb{G}_1^4$

Let α be a curve in $\mathbb{G}_1^4$ given first by

$$\alpha(t) = (x(t), y(t), z(t), w(t)),$$

where $x(t), y(t), z(t), w(t) \in C^4$ (the set of four-times continuously differentiable functions) and t run through a real interval. If $\dfrac{dx(t)}{dt} \neq 0$, then the curve α is called an admissible curve. Otherwise, the curve α is called a non-admissible curve. From now on, we denote differentiation with respect to t by a dash.

I .

An admissible curve given first by

$$\alpha(t) = (x(t), y(t), z(t), w(t)),$$

where $x'(t) \neq 0$, the parameter of arc length is defined by

$$ds = |x'(t)dt| = |dx|.$$

For briefly, we assume $ds = dx$ and $s = x$ as the arc length of the curve α. Let an admissible curve α of the class C^r $(r \geq 3)$ parameterized by arclength x, given in coordinate form $\alpha(x) = (x, y(x), z(x), w(x))$. The first vector of the Frenet-Serret frame, namely the tangent vector of α is defined by

$$\mathbf{T}(x) = \alpha'(x) = \left(1, y'(x), z'(x), w'(x)\right).$$

Since $\mathbf{T}$ is a unit vector, so, we may express $\langle \mathbf{T}, \mathbf{T} \rangle_\mathbb{G} = 1$. Differentiating the last equation with respect to x, we have $\langle \mathbf{T}', \mathbf{T} \rangle_\mathbb{G} = 0$. Note that $\mathbf{T}'(x)$ can be a timelike, spacelike or null vector:

So, we have computed Frenet-Serret formulas with respect to three conditions of $\mathbf{T}'(x)$.

A. Let $\mathbf{T}'(x)$ be a timelike vector: The vector function $\mathbf{T}'$ gives us the rotation measurement of the curve α. The real valued function

$$k_1 = \|\mathbf{T}'\|_\delta = \sqrt{-\left(y''\right)^2 - \left(z''\right)^2 + \left(w''\right)^2} \tag{3}$$

is called the first curvature of the curve α. Now, we define the principal normal vector

$$\mathbf{N} = \frac{\mathbf{T}'}{k_1} \text{ or } \mathbf{N}(x) = \frac{1}{k_1(x)}\left(0, y''(x), z''(x), w''(x)\right).$$

Since $\mathbf{N}(x)$ is a timelike vector, $\langle \mathbf{N}(x), \mathbf{N}(x) \rangle_\delta = -1$ and $2\langle \mathbf{N}'(x), \mathbf{N}(x) \rangle_\delta = 0$. So, $\mathbf{N}'(x)$ is a spacelike vector. Then, $\mathbf{N}'(x) \neq \mathbf{0}$ is a spacelike vector linearly independent with $\mathbf{N}(x)$. We define second curvature of the curve α as

$$k_2(x) = \|\mathbf{N}'(x)\|_\delta.$$

The third vector field, namely binormal vector field of the curve α which is spacelike vector is defined by

$$\mathbf{B}_1(x) = \frac{1}{k_2(x)}\left(0, \left(\frac{y''(x)}{k_1(x)}\right)', \left(\frac{z''(x)}{k_1(x)}\right)', \left(\frac{w''(x)}{k_1(x)}\right)'\right).$$

Therefore, the vector $\mathbf{B}_1(x)$, is both orthogonal to $\mathbf{T}$ and $\mathbf{N}$. Hence, the fourth unit vector is defined by

$$\mathbf{B}_2(x) = \mathbf{T}(x) \times \mathbf{N}(x) \times \mathbf{B}_1(x).$$

The basis $\{\mathbf{T}, \mathbf{N}, \mathbf{B}_1, \mathbf{B}_2\}$ is positively oriented because $\det(\mathbf{T}, \mathbf{N}, \mathbf{B}_1, \mathbf{B}_2) = 1$. We define the third curvature of the curve α by the inner product

$$k_3 = \langle \mathbf{B}_1', \mathbf{B}_2 \rangle_\delta.$$

Here, as well known, the set $\{\mathbf{T}, \mathbf{N}, \mathbf{B}_1, \mathbf{B}_2, k_1, k_2, k_3\}$ is called the Frenet-Serret apparatus of the curve α. And here, we know that the vectors are mutually orthogonal vectors satisfying

$$\langle \mathbf{T}, \mathbf{T} \rangle_{\mathbb{G}} = -\langle \mathbf{N}, \mathbf{N} \rangle_\delta = \langle \mathbf{B}_1, \mathbf{B}_1 \rangle_\delta = \langle \mathbf{B}_2, \mathbf{B}_2 \rangle_\delta = 1,$$

$$\langle \mathbf{T}, \mathbf{N} \rangle_{\mathbb{G}} = \langle \mathbf{T}, \mathbf{B}_1 \rangle_{\mathbb{G}} = \langle \mathbf{T}, \mathbf{B}_2 \rangle_{\mathbb{G}} = \langle \mathbf{N}, \mathbf{B}_1 \rangle_\delta = \langle \mathbf{N}, \mathbf{B}_2 \rangle_\delta = \langle \mathbf{B}_1, \mathbf{B}_2 \rangle_\delta = 0.$$

Now, let calculate Frenet Serret equations. Considering the definitions above, firstly, we know that

$$\mathbf{T}'(x) = k_1(x)\mathbf{N}(x).$$

It is possible to define the vector $\mathbf{N}'$ according to frame $\{\mathbf{T}, \mathbf{N}, \mathbf{B}_1, \mathbf{B}_2\}$ by

$$\mathbf{N}'(x) = \lambda_1(x)\mathbf{T}(x) + \lambda_2(x)\mathbf{N}(x) + \lambda_3(x)\mathbf{B}_1(x) + \lambda_4(x)\mathbf{B}_2(x),$$

$\lambda_i \in \mathbb{R}$, for $1 \leq i \leq 4$. Multiply both sides by the vectors $\{\mathbf{T}, \mathbf{N}, \mathbf{B}_1, \mathbf{B}_2\}$ and considering above the equations, we have, respectively

$$\lambda_1(x) = \langle \mathbf{N}'(x), \mathbf{T}(x) \rangle_{\mathbb{G}} = 0$$

$$\lambda_2(x) = \langle \mathbf{N}'(x), \mathbf{N}(x) \rangle_\delta = 0$$

$$\lambda_3(x) = \langle \mathbf{N}'(x), \mathbf{B}_1(x) \rangle_\delta = k_2(x)$$

By the definiton the the third vector field $\mathbf{B}_1$, we easily obtain

$$\lambda_4(x) = \langle \mathbf{N}', \mathbf{B}_2 \rangle_\delta = 0.$$

We immediately arrive at

$$\mathbf{N}' = k_2(x)\mathbf{B}_1(x).$$

In order to compute the vector function $\mathbf{B}_1'$, let us decompose

$$\mathbf{B}_1' = \mu_1(x)\mathbf{T}(x) + \mu_2(x)\mathbf{N}(x) + \mu_3(x)\mathbf{B}_1(x) + \mu_4(x)\mathbf{B}_2(x),$$

where $\mu_i \in \mathbb{R}$, for $1 \leq i \leq 4$. Similiar to $\mathbf{N}'$, we express

$$\mu_1(x) = \langle \mathbf{B}_1'(x), \mathbf{T}(x) \rangle_{\mathbb{G}} = 0$$

$$\mu_2(x) = \langle \mathbf{B}_1'(x), \mathbf{N}(x) \rangle_\delta = k_2(x)$$

$$\mu_3(x) = \langle \mathbf{B}_1'(x), \mathbf{B}_1(x) \rangle_\delta = 0$$

$$\mu_4(x) = \langle \mathbf{B}_1'(x), \mathbf{B}_2(x) \rangle_\delta = k_3(x)$$

so we get,

$$\mathbf{B}_1'(x) = k_2(x)\mathbf{N}(x) + k_3(x)\mathbf{B}_2(x). \tag{4}$$

In an analogous way, we can write

$$\mathbf{B}_2'(x) = \xi_1(x)\mathbf{T}(x) + \xi_2(x)\mathbf{N}(x) + \xi_3(x)\mathbf{B}_1(x) + \xi_4(x)\mathbf{B}_2(x),$$

where $\xi_i \in \mathbb{R}$, for $1 \le i \le 4$. Then, with the aid of the equaiton (4), we can find

$$\xi_1(x) = \left\langle \mathbf{B}_2'(x), \mathbf{T}(x) \right\rangle_{\mathbb{G}} = 0$$

$$\xi_2(x) = \left\langle \mathbf{B}_2'(x), \mathbf{N}(x) \right\rangle_{\delta} = 0$$

$$\xi_3(x) = \left\langle \mathbf{B}_2'(x), \mathbf{B}_1(x) \right\rangle_{\delta} = -k_3(x)$$

$$\xi_3(x) = \left\langle \mathbf{B}_2'(x), \mathbf{B}_2(x) \right\rangle_{\delta} = 0.$$

So, we have $\mathbf{B}_2' = -k_3\mathbf{B}_1$. And we obtain the Frenet equations in matrix form

$$\begin{bmatrix} \mathbf{T}' \\ \mathbf{N}' \\ \mathbf{B}_1' \\ \mathbf{B}_2' \end{bmatrix} = \begin{bmatrix} 0 & k_1 & 0 & 0 \\ 0 & 0 & k_2 & 0 \\ 0 & k_2 & 0 & k_3 \\ 0 & 0 & -k_3 & 0 \end{bmatrix} \begin{bmatrix} \mathbf{T} \\ \mathbf{N} \\ \mathbf{B}_1 \\ \mathbf{B}_2 \end{bmatrix}.$$

B.Let $\mathbf{T}'(x)$ be a spacelike vector: The first curvature of α is defined by

$$k_1 = \sqrt{\left(y''\right)^2 + \left(z''\right)^2 - \left(w''\right)^2}.$$

We define the principal normal vector $\mathbf{N}(x) = \dfrac{\mathbf{T}'(x)}{k_1(x)}$ and $\left\langle \mathbf{N}(x), \mathbf{N}(x) \right\rangle_{\delta} = 1$. So, we get $2\left\langle \mathbf{N}'(x), \mathbf{N}(x) \right\rangle_{\delta} = 0$. Since $\mathbf{N}'(x)$ is orthogonal to the spacelike vector $\mathbf{N}(x)$, $\mathbf{N}'(x)$ may be spacelike, timelike or lightlike.

i.Assume that $\mathbf{N}'(x)$ is a spacelike vector. Again we write the second curvature

$$k_2 = \left\| \mathbf{N}' \right\|_{\delta},$$

and

$$\mathbf{B}_1(x) = \frac{1}{k_2(x)} \left(0, \left(\frac{y''(x)}{k_1(x)} \right)', \left(\frac{z''(x)}{k_1(x)} \right)', \left(\frac{w''(x)}{k_1(x)} \right)' \right).$$

Also,

$$\mathbf{B}_2(x) = \mathbf{T}(x) \times \mathbf{N}(x) \times \mathbf{B}_1(x)$$

and

$$k_3 = \left\langle \mathbf{B}_1', \mathbf{B}_2 \right\rangle_{\delta}.$$

$\mathbf{B}_2(x)$ is a timelike vector. Similarly, the Frenet equations are

$$\begin{bmatrix} \mathbf{T}' \\ \mathbf{N}' \\ \mathbf{B}_1' \\ \mathbf{B}_2' \end{bmatrix} = \begin{bmatrix} 0 & k_1 & 0 & 0 \\ 0 & 0 & k_2 & 0 \\ 0 & -k_2 & 0 & k_3 \\ 0 & 0 & k_3 & 0 \end{bmatrix} \begin{bmatrix} \mathbf{T} \\ \mathbf{N} \\ \mathbf{B}_1 \\ \mathbf{B}_2 \end{bmatrix}. \qquad (5)$$

ii.Assume that $\mathbf{N}'(x)$ ***is a* timelike vector.** The second curvature is

$$k_2(x) = \left\| \mathbf{N}'(x) \right\|_\delta$$

and

$$\mathbf{B}_1(x) = \frac{1}{k_2(x)} \left(0, \left(\frac{y''(x)}{k_1(x)} \right)', \left(\frac{z''(x)}{k_1(x)} \right)', \left(\frac{w''(x)}{k_1(x)} \right)' \right).$$

Moreover,

$$\mathbf{B}_2(x) = \mathbf{T}(x) \times \mathbf{N}(x) \times \mathbf{B}_1(x)$$

and

$$k_3 = \left\langle \mathbf{B}_1', \mathbf{B}_2 \right\rangle_\delta. \qquad (6)$$

$\mathbf{B}_2(x)$ is a spacelike vector. The Frenet equations can be easily seen

$$\begin{bmatrix} \mathbf{T}' \\ \mathbf{N}' \\ \mathbf{B}_1' \\ \mathbf{B}_2' \end{bmatrix} = \begin{bmatrix} 0 & k_1 & 0 & 0 \\ 0 & 0 & k_2 & 0 \\ 0 & k_2 & 0 & k_3 \\ 0 & 0 & k_3 & 0 \end{bmatrix} \begin{bmatrix} \mathbf{T} \\ \mathbf{N} \\ \mathbf{B}_1 \\ \mathbf{B}_2 \end{bmatrix}. \qquad (7)$$

iii.Assume that $\mathbf{N}'(x)$ ***is a lightlike vector.*** We define the third vector field as $\mathbf{B}_1(x) = \mathbf{N}'(x)$, which is linearly independent with $\mathbf{N}(x)$. Let $\mathbf{B}_2(x)$ be the unique lightlike vector such that $\left\langle \mathbf{B}_1, \mathbf{B}_2 \right\rangle_\delta = -1$ and it is orthogonal to $\mathbf{N}(x)$. The vector $\mathbf{B}_2(x)$ is the second binormal vector of α. The third curvature of the curve α $k_3 = -\left\langle \mathbf{B}_1', \mathbf{B}_2 \right\rangle_\delta$. The Frenet formulas are similar to above

$$\begin{bmatrix} \mathbf{T}' \\ \mathbf{N}' \\ \mathbf{B}_1' \\ \mathbf{B}_2' \end{bmatrix} = \begin{bmatrix} 0 & k_1 & 0 & 0 \\ 0 & 0 & 1 & 0 \\ 0 & 0 & k_3 & 0 \\ 0 & 1 & 0 & -k_3 \end{bmatrix} \begin{bmatrix} \mathbf{T} \\ \mathbf{N} \\ \mathbf{B}_1 \\ \mathbf{B}_2 \end{bmatrix}.$$

C. Let $\mathbf{T}'(x)$ ***be a lightlike vector:*** The normal vector as $\mathbf{N}(x) = \mathbf{T}'(x)$ and define the first binormal vector as $\mathbf{B}_1(x) = \mathbf{N}'(x)$, which is a unit spacelike vector. The second binormal vector $\mathbf{B}_2(x)$ is unique lightlike vector which is orthogonal to $\mathbf{B}_1(x)$ such that $\left\langle \mathbf{N}(x), \mathbf{B}_2(x) \right\rangle_\delta = -1$. Thus, $\{ \mathbf{T}, \mathbf{N}, \mathbf{B}_1, \mathbf{B}_2 \}$ is null frame. The Frenet formulas are

$$
\begin{bmatrix} \mathbf{T}' \\ \mathbf{N}' \\ \mathbf{B}_1' \\ \mathbf{B}_2' \end{bmatrix} = \begin{bmatrix} 0 & 1 & 0 & 0 \\ 0 & 0 & 1 & 0 \\ 0 & k_3 & 0 & 1 \\ 0 & 0 & k_3 & 0 \end{bmatrix} \begin{bmatrix} \mathbf{T} \\ \mathbf{N} \\ \mathbf{B}_1 \\ \mathbf{B}_2 \end{bmatrix} . \tag{8}
$$

The third curvature of α is $k_3 = -\left\langle \mathbf{B}_1', \mathbf{B}_2 \right\rangle_\delta$.

Corollary 5.1 The admissible curve $\alpha(x)$ in $\mathbb{G}_1^4$ classifies in the following cases:

1) a curve with timelike normal vector $\mathbf{N}$.

2) three curves with spacelike normal vector $\mathbf{N}$ and binormal vector $\mathbf{B}_1$ which is spacelike, timelike or null.

3) a curve with null normal vector $\mathbf{N}$.

II.

A non-admissible curve α is given by the parametrization $\alpha(t) = (c, y(t), z(t), w(t))$, where $c = $ constant. So, a non-admissible curve α classify in the three kinds, spacelike, timelike, null curve, on $3-$dimensional Minkowski Space $x = c$ in $\mathbb{G}_1^4$. Finally, with the help of [19], we can easily find the construction of Frenet-Serret frames for a non-admissible curve α.

6. The Fundamental Theorem

Until now, we can construct the Frenet-Serret apparatus for a given curve. But, we have not yet addressed to what extent we can do inverse. Given some k_1, k_2 and k_3, we would like to know if it is possible to construct a curve to fit these functions. The fundamental theorem of curves says that it is possible to reconstruct the curve from only the curvature functions.

Theorem 6.1 Let $k_1(x) > 0$, $k_2(x) > 0$ and $k_3(x)$, $x \in I$, be three differentiable maps. Then, there exist three differential regular parametrized curves $\alpha : I \to \mathbb{G}_1^4$, $\alpha = \alpha(x)$, with curvatures $k_1(x)$, $k_2(x)$ and $k_3(x)$.

Proof. Let $x_0 \in I$ and let $\{\mathbf{D}, \mathbf{E}, \mathbf{F}, \mathbf{G}\}$ be an orthonormal basis, which it will be the initial conditions of an

ordinary differential equation (ODE) system. Depending on the causal character of the vectors $\mathbf{E}$ and $\mathbf{F}$, we obtain three different cases:

Firstly, if we want to obtain a curve with timelike normal $\mathbf{N}$ and curvatures $k_1(x)$, $k_2(x)$ and $k_3(x)$, respectively, then we consider that $\{\mathbf{D}, \mathbf{E}, \mathbf{F}, \mathbf{G}\}$ is orthonormal basis positively oriented and $\mathbf{E}$ is timelike. In such case, we solve the ODE system of equations

$$\mathbf{T}'(x_0) = k_1(x_0)\mathbf{N}(x_0)$$
$$\mathbf{N}'(x_0) = k_2(x_0)\mathbf{B}_1(x_0)$$
$$\mathbf{B}_1'(x_0) = k_2(x_0)\mathbf{N}(x_0) + k_3(x_0)\mathbf{B}_2(x_0)$$
$$\mathbf{B}_2'(x_0) = -k_3(x_0)\mathbf{B}_1(x_0)$$

with initial condition

$$\mathbf{T}(x_0) = \mathbf{D}$$
$$\mathbf{N}(x_0) = \mathbf{E}$$
$$\mathbf{B}_1(x_0) = \mathbf{F}$$
$$\mathbf{B}_2(x_0) = \mathbf{G}.$$

Let $\{\mathbf{T}, \mathbf{N}, \mathbf{B}_1, \mathbf{B}_2\}$ be the unique solutions and define $\alpha(x) = \int_{x_0}^{x} \mathbf{T}(u)\, du$. We prove that this curve is with timelike normal $\mathbf{N}$ and curvatures $k_1(x)$, $k_2(x)$ and $k_3(x)$, respectively. We show that

$\{\mathbf{T}, \mathbf{N}, \mathbf{B}_1, \mathbf{B}_2\}$ is an orthonormal basis with the same causal properties that initial basis $\{\mathbf{D}, \mathbf{E}, \mathbf{F}, \mathbf{G}\}$. Consider the ODE system:

$$\langle \mathbf{T}, \mathbf{T} \rangle_{\mathbb{G}}' = 2k_1 \langle \mathbf{N}, \mathbf{T} \rangle_{\mathbb{G}}$$

$$\langle \mathbf{N}, \mathbf{N} \rangle_{\delta}' = 2k_2 \langle \mathbf{B}_1, \mathbf{N} \rangle_{\delta}$$

$$\langle \mathbf{B}_1, \mathbf{B}_1 \rangle_{\delta}' = 2k_2 \langle \mathbf{N}, \mathbf{B}_1 \rangle_{\delta} + 2 \langle \mathbf{B}_2, \mathbf{B}_1 \rangle_{\delta}$$

$$\langle \mathbf{B}_2, \mathbf{B}_2 \rangle_{\delta}' = -2k_3 \langle \mathbf{B}_1, \mathbf{B}_2 \rangle_{\delta}$$

$$\langle \mathbf{T}, \mathbf{N} \rangle_{\mathbb{G}}' = k_1 \langle \mathbf{N}, \mathbf{N} \rangle_{\mathbb{G}} + k_2 \langle \mathbf{T}, \mathbf{B}_1 \rangle_{\mathbb{G}}$$

$$\langle \mathbf{T}, \mathbf{B}_1 \rangle_{\mathbb{G}}' = k_1 \langle \mathbf{N}, \mathbf{B}_1 \rangle_{\mathbb{G}}$$

$$\langle \mathbf{T}, \mathbf{B}_2 \rangle_{\mathbb{G}}' n = k_1 \langle \mathbf{N}, \mathbf{B}_1 \rangle_{\mathbb{G}}$$

$$\langle \mathbf{N}, \mathbf{B}_1 \rangle_{\delta}' = k_2 \langle \mathbf{B}_1, \mathbf{B}_1 \rangle_{\delta} + k_2 \langle \mathbf{N}, \mathbf{N} \rangle_{\delta} + k_3 \langle \mathbf{N}, \mathbf{B}_2 \rangle_{\delta}$$

$$\langle \mathbf{N}, \mathbf{B}_2 \rangle_{\delta}' n = k_2 \langle \mathbf{B}_1, \mathbf{B}_2 \rangle_{\delta} - k_3 \langle \mathbf{N}, \mathbf{B}_1 \rangle_{\delta}$$

$$\langle \mathbf{B}_1, \mathbf{B}_2 \rangle_{\delta}' = k_2 \langle \mathbf{N}, \mathbf{B}_2 \rangle_{\delta} + k_3 \langle \mathbf{B}_2, \mathbf{B}_2 \rangle_{\delta} - k_3 \langle \mathbf{B}_1, \mathbf{B}_1 \rangle_{\delta}$$

with initial conditions at $x = x_0$ given by $(1, -1, 1, 1, 0, 0, 0, 0, 0, 0)$. On the other hand, the functions

$f_1 = 1, f_2 = -1, f_3 = 1, f_4 = 1, f_5 = 0, f_6 = 0, f_7 = 0, f_8 = 0, f_9 = 0, f_{10} = 0$ satisfy the same ODE system and initial conditions. By uniqueness,

$$\langle \mathbf{T}, \mathbf{T} \rangle_{\mathbb{G}} = -\langle \mathbf{N}, \mathbf{N} \rangle_{\delta} = \langle \mathbf{B}_1, \mathbf{B}_1 \rangle_{\delta} = \langle \mathbf{B}_2, \mathbf{B}_2 \rangle_{\delta} = 1$$

$$\langle \mathbf{T}, \mathbf{N} \rangle_{\mathbb{G}} = \langle \mathbf{T}, \mathbf{B}_1 \rangle_{\mathbb{G}} = \langle \mathbf{T}, \mathbf{B}_2 \rangle_{\mathbb{G}} = \langle \mathbf{N}, \mathbf{B}_1 \rangle_{\delta} = \langle \mathbf{N}, \mathbf{B}_2 \rangle_{\delta} = \langle \mathbf{B}_1, \mathbf{B}_2 \rangle_{\delta} = 0.$$

So, $\{\mathbf{T}, \mathbf{N}, \mathbf{B}_1, \mathbf{B}_2\}$ is an orthonormal basis of $\mathbb{G}_1^4$, where $\mathbf{N}$ is timelike. From the definition of α,

$\alpha'(x) = \mathbf{T}(x)$ and so α is a curve with timelike normal parametrized by arc lengh and curvatures of α are k_1, k_2 and k_3.

Secondly, if we want to obtain a curve with spacelike normal vector $\mathbf{N}$ and spacelike binormal vector $\mathbf{B}_1$ and curvatures k_1, k_2 and k_3, consider the initial conditions

$$\mathbf{T}(x_0) = \mathbf{D}$$
$$\mathbf{N}(x_0) = \mathbf{E}$$
$$\mathbf{B}_1(x_0) = \mathbf{F}$$
$$\mathbf{B}_2(x_0) = \mathbf{G},$$

where $\{\mathbf{D},\mathbf{E},\mathbf{F},\mathbf{G}\}$ is orthonormal basis and $\mathbf{G}$ is timelike. Considering that the ODE system that we solve is (5), the proof is clear.

Finally, if we are looking for a curve with spacelike normal and timelike binormal vector, the initial condition is an orthonormal basis $\{\mathbf{D},\mathbf{E},\mathbf{F},\mathbf{G}\}$, where $\mathbf{F}$ is timelike and the ODE system (7). And the proof is similar.

Theorem 6.2 Let $k_1(x) > 0$, and $k_3(x)$, $x \in I$, be two smooth maps. Then, there exist a curve with spacelike normal $\mathbf{N}$ and lightlike binormal $\mathbf{B}_1$ with curvatures $k_1(x)$ and $k_3(x)$.

Proof. If we want to obtain a curve with spacelike normal $\mathbf{N}$ and lightlike binormal $\mathbf{B}_1$ with curvatures

$k_1(x)$ and $k_3(x)$, respectively, then we consider that $\{\mathbf{D},\mathbf{E},\mathbf{F},\mathbf{G}\}$ be the null frame of $\mathbb{G}_1^4$ such that $\mathbf{E}$ is spacelike and $\mathbf{F},\mathbf{G}$ are unit isotropic lightlike vectors such that $\langle \mathbf{F},\mathbf{G} \rangle_\delta = -1$. We pose the ODE system (8) with initial conditions

$$\mathbf{T}(x_0) = \mathbf{D},$$
$$\mathbf{N}(x_0) = \mathbf{E},$$
$$\mathbf{B}_1(x_0) = \mathbf{F},$$
$$\mathbf{B}_2(x_0) = \mathbf{G}.$$

Let $\{\mathbf{T},\mathbf{N},\mathbf{B}_1,\mathbf{B}_2\}$ be the unique solution and define $\alpha(x) = \int_{x_0}^{x} \mathbf{T}(u)\,du$. We prove that α is a curve with spacelike normal $\mathbf{N}$ and null binormal vector $\mathbf{B}_1$. First, we consider the next ODE system of 10 equations:

$$\langle \mathbf{T},\mathbf{T} \rangle'_{\mathbb{G}} = 2k_1 \langle \mathbf{N},\mathbf{T} \rangle_{\mathbb{G}}$$
$$\langle \mathbf{N},\mathbf{N} \rangle'_{\delta} = 2 \langle \mathbf{N},\mathbf{B}_1 \rangle_{\delta}$$
$$\langle \mathbf{B}_1,\mathbf{B}_1 \rangle'_{\delta} = 2k_3 \langle \mathbf{B}_1,\mathbf{B}_1 \rangle_{\delta}$$
$$\langle \mathbf{B}_2,\mathbf{B}_2 \rangle'_{\delta} = 2 \langle \mathbf{N},\mathbf{B}_1 \rangle_{\delta} - 2k_3 \langle \mathbf{B}_2,\mathbf{B}_2 \rangle_{\delta}$$
$$\langle \mathbf{T},\mathbf{N} \rangle'_{\mathbb{G}} = k_1 \langle \mathbf{N},\mathbf{N} \rangle_{\mathbb{G}} + k_2 \langle \mathbf{T},\mathbf{B}_1 \rangle_{\mathbb{G}}$$
$$\langle \mathbf{T},\mathbf{B}_1 \rangle'_{\mathbb{G}} = k_1 \langle \mathbf{N},\mathbf{B}_1 \rangle_{\mathbb{G}}$$
$$\langle \mathbf{T},\mathbf{B}_2 \rangle'_{\mathbb{G}} = k_1 \langle \mathbf{N},\mathbf{B}_1 \rangle_{\mathbb{G}}$$
$$\langle \mathbf{N},\mathbf{B}_1 \rangle'_{\delta} = \langle \mathbf{B}_1,\mathbf{B}_1 \rangle_{\delta} + k_3 \langle \mathbf{N},\mathbf{B}_1 \rangle_{\delta}$$
$$\langle \mathbf{N},\mathbf{B}_2 \rangle'_{\delta} = \langle \mathbf{B}_1,\mathbf{B}_2 \rangle_{\delta} + \langle \mathbf{N},\mathbf{N} \rangle_{\delta} - k_3 \langle \mathbf{N},\mathbf{B}_2 \rangle_{\delta}$$
$$\langle \mathbf{B}_1,\mathbf{B}_2 \rangle'_{\delta} = k_3 \langle \mathbf{B}_1,\mathbf{B}_2 \rangle_{\delta} + \langle \mathbf{B}_1,\mathbf{N} \rangle_{\delta} - k_3 \langle \mathbf{B}_1,\mathbf{B}_2 \rangle_{\delta}$$

with initial conditions at $x = x_0$ given by $(1,1,0,0,0,0,0,0,0,-1)$. On the other hand, the functions

$$f_1 = 1, f_2 = 1, f_3 = 0, f_4 = 0, f_5 = 0, f_6 = 0, f_7 = 0, f_8 = 0, f_9 = 0, f_{10} = -1$$

satisfy the same ODE system and initial conditions. By uniqueness,

$$\langle \mathbf{T},\mathbf{T} \rangle_{\mathbb{G}} = \langle \mathbf{N},\mathbf{N} \rangle_{\delta} = 1, \quad \langle \mathbf{B}_1,\mathbf{B}_1 \rangle_{\delta} = \langle \mathbf{B}_2,\mathbf{B}_2 \rangle_{\delta} = 0$$
$$\langle \mathbf{T},\mathbf{N} \rangle_{\mathbb{G}} = \langle \mathbf{T},\mathbf{B}_1 \rangle_{\mathbb{G}} = \langle \mathbf{T},\mathbf{B}_2 \rangle_{\mathbb{G}} = \langle \mathbf{N},\mathbf{B}_1 \rangle_{\delta} = \langle \mathbf{N},\mathbf{B}_2 \rangle_{\delta} = 0, \quad \langle \mathbf{B}_1,\mathbf{B}_2 \rangle_{\delta} = -1.$$

This implies that $\{\mathbf{T}, \mathbf{N}, \mathbf{B}_1, \mathbf{B}_2\}$ is a null basis of $\mathbb{G}_1^4$, where $\mathbf{N}$ is spacelike. From the definition of α,

$\alpha'(x) = \mathbf{T}(x)$ and so α is a curve with spacelike normal $\mathbf{N}$ and lightlike binormal $\mathbf{B}_1$ with curvatures $k_1(x)$ and $k_3(x)$.

Theorem 6.3 Let $k_3(x)$, $x \in I$, be a smooth function. Then, there is a curve with null normal vector $\mathbf{N}(x)$ and curvature $k_3(x)$.

Proof. It can be easily proved from the ODE system (8) as above the theorem.

As we see from Theorem 6.1, we have two different curves having the same curvatures. So, there is not a unique curve with the same curvatures. And also, these curves are not equivalent under pseudo-Galilean motions. Because we don't have any of these motions. But for any two same types orthonormal frame in $\mathbb{G}_1^4$ there is a pseudo-Galilean motion which transforms one frame into the other one and a space curve in $\mathbb{G}_1^4$ under proper pseudo-Galilean motions is transformed in the same type curve. So, we can give the following theorem:

Theorem 6.4 Two admissible same type curves in $\mathbb{G}_1^4$ are equivalent under pseudo-Galilean motions if only if they have the same natural equations for $k_i(x), i = 1, 2, 3$.

7. Applications

Now, we illustrate examples of presented method.

Example 7.1 Let us consider the following curve with spacelike normal vector $\mathbf{N}(x)$ and timelike binormal vector $\mathbf{B}_1(x)$ in the space $\mathbb{G}_1^4$

$$\alpha(x) = (x, 1, \cosh x, \sinh x). \tag{9}$$

By differentiating both sides of (9) with respect to arc length x, we have

$$\alpha'(x) = (1, 0, \sinh x, \cosh x).$$

Thus, we decompose tangent vector of α as follows:

$$\mathbf{T}(x) = (1, 0, \sinh x, \cosh x).$$

And considering the equation (3),

$$k_1(x) = \|\mathbf{T}'(x)\|_\delta = 1.$$

Thereafter, we arrive at $\mathbf{N}(x) = (0, 0, \cosh x, \sinh x)$. So, the curve is a curve with spacelike normal vector.

Moreover, one more differentiating of the normal vector equation, we have

$$\mathbf{N}'(x) = (0, 0, \sinh x, \cosh x).$$

By the aid of the this equation, we have the second curvature function

$$k_2(x) = 1$$

and timelike binormal vector $\mathbf{B}_1(x)$ is obtained

$$\mathbf{B}_1(x) = (0, 0, \sinh x, \cosh x).$$

Furthermore, the cross product of tangent, principal normal, and binormal vectors is formed

$$\mathbf{B}_2(x) = \mathbf{T}(x) \times \mathbf{N}(x) \times \mathbf{B}_1(x) = -\begin{vmatrix} \mathbf{0} & \mathbf{e}_2 & \mathbf{e}_3 & -\mathbf{e}_4 \\ 1 & 0 & \cosh x & \sinh x \\ 0 & 0 & \sinh x & \cosh x \\ 0 & 0 & \cosh x & \sinh x \end{vmatrix}.$$

Thus, we have

$$\mathbf{B}_2(x) = (0,1,0,0).$$

In order to determine the third curvature of the curve, considering the equation (6), we have

$$k_3(x) = 0.$$

So, the curve is a curve with spacelike normal vector $\mathbf{N}(x)$ and timelike binormal vector $\mathbf{B}_1(x)$. Also, the following equations provide

$$\begin{bmatrix} \mathbf{T}' \\ \mathbf{N}' \\ \mathbf{B}_1' \\ \mathbf{B}_2' \end{bmatrix} = \begin{bmatrix} 0 & 1 & 0 & 0 \\ 0 & 0 & 1 & 0 \\ 0 & 1 & 0 & 0 \\ 0 & 0 & 0 & 0 \end{bmatrix} \begin{bmatrix} \mathbf{T} \\ \mathbf{N} \\ \mathbf{B}_1 \\ \mathbf{B}_2 \end{bmatrix}.$$

So, we construct the Frenet-Serret apparatus for the given curve $\alpha(x)$. Now, let reconstruct the curve $\alpha(x)$ from only the curvature functions.

Example 7.2 Let $k_1(x) = 1$, $k_2(x) = 1$ and $k_3(x) = 0$, $x \in I$, and consider the following ordinary differential equation system

$$\mathbf{T}'(x_0) = k_1(x_0)\mathbf{N}(x_0)$$
$$\mathbf{N}'(x_0) = k_2(x_0)\mathbf{B}_1(x_0)$$
$$\mathbf{B}_1'(x_0) = k_2(x_0)\mathbf{N}(x_0) + k_3(x_0)\mathbf{B}_2(x_0)$$
$$\mathbf{B}_2'(x_0) = -k_3(x_0)\mathbf{B}_1(x_0)$$

with initial condition

$$\mathbf{T}(x_0) = (1,0,0,1)$$
$$\mathbf{N}(x_0) = (0,0,1,0)$$
$$\mathbf{B}_1(x_0) = (0,0,0,1)$$
$$\mathbf{B}_2(x_0) = (0,1,0,0).$$

Then we have

$$t_i' = n_i$$
$$n_i' = b_i$$
$$b_{1i}' = n_i$$
$$b_{2i}' = 0,$$

for $i = 1,2,3,4$. If we solve this ODE with method of Laplace transformation, then we obtain

$$\mathbf{T}(x) = (1, 0, \sinh x, \cosh x),$$

$$\mathbf{N}(x) = (0, 0, \cosh x, \sinh x),$$

$$\mathbf{B}_1(x) = (0, 0, \sinh x, \cosh x),$$

$$\mathbf{B}_2(x) = (0, 1, 0, 0).$$

Now, let define $\alpha(x) = \int_0^x \mathbf{T}(u)du$. So, we get $\alpha(x) = (x, 0, \cosh x - 1, \sinh x)$.

Actually, we find the same curve in the equation (9)

$$\alpha(x) = (x, 1, \cosh x, \sinh x)$$

under the translation determined with $\mathbf{u} = (0, -1, 1, 0)$. Finally, the curve is a curve with spacelike normal vector $\mathbf{N}(x)$ and timelike binormal vector $\mathbf{B}_1(x)$ and $k_1(x) = 1$, $k_2(x) = 1$ and $k_3(x) = 0$, $x \in I$ (See **Figure 1**).
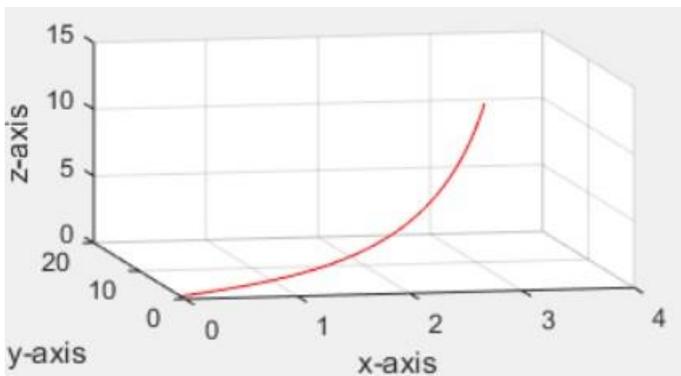

Figure 1. The image of the curve α in 3-dimensional $y = 1$-pseudo-Galilean space or 3-dimensional $xzw-$ pseudo-Galilean space in 4-dimensional pseudo-Galiean geometry

8. Conclusion and Further Remarks

Throughout the presented paper, we define pseudo-Galilean motions and pseudo-Galilean geometry $\mathbb{G}_1^4$. That is, we introduce a new geometry. Also, we present the curve theory in $\mathbb{G}_1^4$. Here, using vector product, we give formulas of frame vectors for curves.

Unlike Euclidean, Minkowskian, and Galilean geometries, the curves in pseudo-Galilean geometry $\mathbb{G}_1^4$ are not enough to classify the curves according to their tangent vectors $\mathbf{T}$. It is also necessary to classify with respect to their normal vector $\mathbf{N}$ and binormal vector $\mathbf{B}_1$. There are actually 8-kinds of curves in $\mathbb{G}_1^4$. So, differences according to other geometries are observed in the calculation of the fundamental theorem of curve theory in $\mathbb{G}_1^4$. However, we can construct the Frenet-Serret apparatus for a given curve and also reconstruct the curve from only the curvature functions.

Via this method, some of classical differential geometry topics can be treated. We hope these results will helpful to mathematicians who are specialized in mathematical modeling.

Conflicts of interest

The authors declared no conflict of interests.

References

[1] Gawell E., Non-Euclidean Geometry in the Modelling of Contemprary Architectural Forms, *The Jour. of Polish Soc. for Geo. and Engin. Graphics*, 24 (2013) 35-43.

[2] Yaglom I.M., A simple non-Euclidean Geometry and its Physical Basis, Springer-Verlag, New York, (1979).

[3] Yilmaz S., Construction of the Frenet-Serret frame of a curve in 4D Galilean space and some applications, *Int. Jour. of the Physical Sciences*, 5(8) (2010) 1284-1289.

[4] Röschel O., Die Geometrie des Galileischen Raumes, PD thesis, Institut für Math. und Angew. Geometrie, Leoben, 1984.

[5] Divjak B., Curves in Pseudo-Galilean Geometry, *Annales Univ. Sci. Budapest*, 41 (1998) 117-128.

[6] Sipus Z.M., Ruled Weingarten surfaces in the Galilean space, *Period. Math. Hungar*., 56 (2008) 213-225.

[7] Sipus Z.M., Divjak B., Surfaces of constant curvature in the pseudo-Galilean space, *International J. Math. Math. Sci.,* 375264 (2012) 1-28.

[8] Divjak B., Sipus Z.M., Special Curves on Ruled Surfaces in Galilean and pseudo-Galilean Spaces, *Acta math. Hungar*, 98 (3) (2003) 203-215.

[9] Divjak B, Sipus Z.M., Some Special Surfaces in the Galilean Surfaces in the pseudo-Galilean Space*, Acta Math. Hungar.*, 118 (3) (2008) 209-226.

[10] Divjak B, Sipus Z.M., Minding isometries of ruled surfaces in pseudo-Galilean space, *Journal of Geometry,* 77 (2003) 35-47.

[11] Yoon D.W., Surfaces of revolution in the three dimensional pseudo-Galilean space, *Glasnik Matematicki*, 48 (2013) 415-428.

[12] Aydin, M.E., Öğrenmiş A.O., Ergüt M., Classification of factorable surfaces in the pseudo-Galilean space, *Glasnik Matematički*, 50 (2) (2015) 441-451.

[13] Ratcliffe, J.G, Foundations of Hyperbolic Manifolds, Foundations of hyperbolic manifolds, Springer Science & Business Media, (1983).

[14] Neill O.B., Semi-Riemannian Geometry with Applications to Relativity, Volume 103 (Pure and Applied Mathematics). Academic Press. New York, (1983).

[15] Kula L., Karacan M.K., Yayli Y., Formulas for the exponential of a semi skew symmetric matrix of order 4, *Mathematical and Computational Applications*, 10 (1) (2015) 99-104.

[16] Formiga J.B., Romero C., On the differential geometry of curves in Minkowski space, arXiv:gr-qc/0601002v1, Retrieved Dec 28, 2020.

[17] El-Ahmedy A.E., Al-Hesiny E., On the Geometry of Curves in Minkowski 3-Space and its Foldings, *Applied Mathematics*, 4 (2013) 746-752.

[18] Ehrlich, P.E., Global Lorentzian Geometry, Nework: Marcel Dekker. Inc., (1981).

[19] Yilmaz S., Özyilmaz E., Turgut M., On the differential geometry of curves in Minkowski space-Time I, *Int. J. Contemp. Math. Sciences*, 3(27) (2008) 1343-1349.

[20] Yilmaz S., Özyilmaz E., Turgut M., On the differential geometry of curves in Minkowski space-Time II, *Word Academy of Science, Engineering and Technology*, 3(11) (2009) 1004-1006.

[21] Lopez R., Differential geometry of curves and Surfaces in Lorentz-Minkowski Space, *Int. Electron. J. Geom*, 7(1) (2014) 44-107.

Special helices on equiform differential geometry of timelike curves in $\mathbb{E}_1^4$

Fatma BULUT[1,]* iD

[1]*Bitlis Eren University, Faculty of Arts and Sciences, Department of Mathematics, Bitlis/TURKEY*

Abstract

In this paper, we introduce the moving Frenet frame along the timelike curve in $\mathbb{E}_1^4$ and then Frenet formulas with the equiform parameter in the equiform geometry of the Minkowski space-time. We obtain k-type helices for equiform differential geometry of timelike curves in Minkowski space-time $\mathbb{E}_1^4$, in terms of their curvature functions. We give some new characterizations for these helices and investigate the special helices in Minkowski space-time. Finally, we establish (k, m)-type slant helices for equiform differential geometry of timelike curves in $\mathbb{E}_1^4$.

1. Introduction

Differential geometry is basically an area where the theory of curves and manifolds are studied. New theories are practically being built on it everyday applications. Especially, since the theory of curves finds application in many disciplines, it has become an important field for both mathematicians and biologists, physics and even engineers and medicine in some fields. However, the geometric structures built on the timelike and spacelike curves and the construction of Frenet vectors opened completely different doors and allowed to work on a very wide platform. Geometricians try to express and prove these and similar issues in various spaces, for example in the Lorentz-Minkowski space in the Euclidean space, and in the Semi-Euclidean space. In particular, the theory of curves in Lorentz-Minkowski and Semi-Euclidean space, and the differences arising from the classification of curves as spacelike, timelike and null have yielded very interesting results.

Recently, Izumiya and Takeuchi introduced the concept of slant helix in Euclidean space. For instance, in [1], the authors presented some necessary and sufficient conditions for a curve to be a slant helix in Euclidean n-space. In [2], the authors established equiform differential geometry of curves in Minkowski space-time. Geometricians [3-5] usually deal with the theoretical part and continue to work with spacelike, timelike curves, involute-evolute curves, helices, and various characterizations. M.Y. Yilmaz and M. Bektaş defined (k, m)-type slant helices in 4-dimensional Euclidean space in [6]. Furthermore, very important theories have been proved in the 4-dimensional Minkowski space, which contains the most interesting and most different curves [7-10] and similar subjects [11-13] have yielded quite remarkable results. Because equiform roofs are expressed in 4-dimensional Euclidean space, each of them has its own unique geometric structures, allowing the study of events in a broad perspective.Additionally, F. Bulut and M. Bektaş obtained helix types for equiform differential geometry of spacelike curves in $\mathbb{E}_1^4$ in [12].

In this paper, we examine the structures of (k, m)-type helices of the distinguished timelike curves and the timelike curves expressed by the s parameter. We present helix types which are called curves as k-type helices and (k, m)-type slant helices for equiform differential geometry of timelike curves in Minkowski space-time.

2. Geometric Preliminaries

The Minkowski space-time $\mathbb{E}_1^4$ is a Euclidean space provided with the indefinite flat metric given by

$$g = -dx_1^2 + dx_2^2 + dx_3^2 + dx_4^2$$

where $x_1^1, x_1^2, x_1^3, x_1^4$ is a rectangular coordinate system of $\mathbb{E}_1^4$. Recall that an arbitrary vector $y \in \mathbb{E}_1^4 - \{0\}$ can be spacelike, timelike or null (lightlike vector), if holds $g\langle y, y \rangle \rangle 0$, $g\langle y, y \rangle \langle 0$ or $g\langle y, y \rangle = 0$ respectively. If y is a timelike vector, then $\| y', y' \| = \sqrt{-\langle y', y' \rangle}$. For an arbitrary the curve $\alpha(s)$ in $\mathbb{E}_1^4$ is named a spacelike, a timelike and a null (lightlike) curve, if all of its velocity vectors $\alpha'(s)$ are spacelike, timelike, and null (lightlike), respectively [13]. The normal vector on the spacelike or the timelike hypersurface is, respectively, a timelike or a spacelike vector.

Let $\alpha: I \subset \mathbb{R} \to \mathbb{E}_1^4$ be a curve in Minkowski space-time. The curve α is said to be a timelike curve if $\langle \dot{\alpha}(t), \dot{\alpha}(t) \rangle < 0$ for each $t \in I$. The arclength of a timelike curve α measured from $\alpha(t_0)(t_0 \in I)$ is

$$s(t) = \int_{t_0}^{t} \| \dot{\alpha}(t) \| \, dt.$$

α is said to be parameterized by the arc-length function s, if $\| \alpha'(s) \| = -1$, where $\alpha'(s) = d\alpha/ds$. Consequently, we say that α is a timelike curve, if $\| \alpha'(s) \| = -1$. For any $x, y, z \in \mathbb{E}_1^4$, we define a vector $x \times y \times z$ by

$$x \times y \times z = \begin{vmatrix} -e_1 & e_2 & e_3 & e_4 \\ x_1^1 & x_1^2 & x_1^3 & x_1^4 \\ x_2^1 & x_2^2 & x_2^3 & x_2^4 \\ x_3^1 & x_3^2 & x_3^3 & x_3^4 \end{vmatrix},$$

where $x_i = (x_i^1, x_i^2, x_i^3, x_i^4)$, $1 \leq i \leq 3$. Let $\alpha: I \to \mathbb{E}_1^4$ be a timelike curve in $\mathbb{E}_1^4$. Let $\{t(s), n(s), b_1(s), b_2(s)\}$ is a pseudo-orthogonal frame which satisfies the following Frenet-Serret formulas of $\mathbb{E}_1^4$ along α.

$$\begin{bmatrix} t \\ n \\ b_1 \\ b_2 \end{bmatrix}' = \begin{bmatrix} 0 & \overline{\kappa}_1 & 0 & 0 \\ \mu_1\overline{\kappa}_1 & 0 & \mu_2\overline{\kappa}_2 & 0 \\ 0 & \mu_3\overline{\kappa}_2 & 0 & \mu_4\overline{\kappa}_3 \\ 0 & 0 & \mu_5\overline{\kappa}_3 & 0 \end{bmatrix} \begin{bmatrix} t \\ n \\ b_1 \\ b_2 \end{bmatrix}, \quad (1)$$

where $\overline{\kappa}_1, \overline{\kappa}_2$ and $\overline{\kappa}_3$ are respectively, first, second and third curvature of the timelike curve α and we have

$$\overline{\kappa}_1(s) = \| \alpha''(s) \|,$$

$$n(s) = \frac{\alpha''(s)}{\overline{\kappa}_1(s)},$$

$$b_1(s) = \frac{n'(s) + \mu_1\overline{\kappa}_1(s)t(s)}{\| n'(s) + \mu_1\overline{\kappa}_1(s)t(s) \|},$$

$$b_2(s) = t(s) \times n(s) \times b_1(s).$$

Denote by $\{t(s), n(s), b_1(s), b_2(s)\}$ the moving Frenet frame along the timelike curve α [1-7]. So, $t(s)$ is a timelike tangent vector and the principal normal vector $n(s)$, the first binormal vector $b_1(s)$ and the second binormal vector $b_2(s)$, then $\mu_i = \mp 1 (1 \leq i \leq 5)$ and we get $\mu_1 = \mu_2 = \mu_4 = 1, \mu_3 = \mu_5 = -1$.

Now, let γ be a timelike curve. Then T is timelike vector and following Frenet formulas is given

$$\begin{bmatrix} T \\ N \\ B_1 \\ B_2 \end{bmatrix}' = \begin{bmatrix} 0 & \overline{\kappa}_1 & 0 & 0 \\ -\overline{\kappa}_1 & 0 & \overline{\kappa}_2 & 0 \\ 0 & -\overline{\kappa}_2 & 0 & \overline{\kappa}_3 \\ 0 & 0 & -\overline{\kappa}_3 & 0 \end{bmatrix} \begin{bmatrix} T \\ N \\ B_1 \\ B_2 \end{bmatrix},$$

where $\overline{\kappa}_1, \overline{\kappa}_2$ and $\overline{\kappa}_3$ denote the first, the second and the third curvature functions according to of γ, respectively. Here, $\{T, N, B_1, B_2\}$ satisfy the following equations

$$\langle N, N \rangle = \langle B_1, B_1 \rangle = \langle B_2, B_2 \rangle = 1, \qquad \langle T, T \rangle = -1.$$

3. Equiform Differential Geometry of Timelike Curves

Let $\alpha: I \to \mathbb{E}_1^4$ be a timelike curve. We define the equiform parameter of $\alpha(s)$ by

$$\sigma = \int \frac{ds}{\rho} = \int \overline{\kappa}_1 \, ds$$

where $\rho = \frac{1}{\kappa_1}$ is the radius of curvature of the curve and $\frac{ds}{d\sigma} = \rho$.

Let's indicate by $\{\mathbf{T}, \mathbf{N}, \mathbf{B_1}, \mathbf{B_2}\}$ the acting Frenet frame along the curve $\alpha(s)$ in the space $\mathbb{E}_1^4$ and so $\{\mathbf{T}, \mathbf{N}, \mathbf{B_1}, \mathbf{B_2}\}$ are, respectively, the unit tangent, the principal normal, the first binormal and the second binormal vector fields. We define the equiform parameter of $\alpha(s)$. Then, we can write

$\mathbf{U_1} = \rho\mathbf{T}$,

$\mathbf{U_2} = \rho\mathbf{N}$,

$\mathbf{U_3} = \rho\mathbf{B_1}$,

$\mathbf{U_4} = \rho\mathbf{B_2}$.

Then, $\{\mathbf{U_1}, \mathbf{U_2}, \mathbf{U_3}, \mathbf{U_4}\}$ is an equiform invariant tetrahedron of the curve α [2]. σ is an equiform invariant parameter of α. The derivatives of these vectors with respect to s can be obtained by the following equations:

$$\mathbf{U_1'} = \frac{d}{d\sigma}(\mathbf{U_1}) = \rho\frac{d}{ds}(\rho\mathbf{T}) = \dot{\rho}\mathbf{U_1} + \mathbf{U_2},$$

$$\mathbf{U_2'} = \frac{d}{d\sigma}(\mathbf{U_2}) = \rho\frac{d}{ds}(\rho\mathbf{N}) = \mathbf{U_1} + \dot{\rho}\mathbf{U_2} + \left(\frac{\overline{\kappa}_2}{\overline{\kappa}_1}\right)\mathbf{U_3},$$

$$\mathbf{U_3'} = \frac{d}{d\sigma}(\mathbf{U_3}) = \rho\frac{d}{ds}(\rho\mathbf{B_1}) = -\left(\frac{\overline{\kappa}_2}{\overline{\kappa}_1}\right)\mathbf{U_2} + \dot{\rho}\mathbf{U_3} + \left(\frac{\overline{\kappa}_3}{\overline{\kappa}_1}\right)\mathbf{U_4},$$

$$\mathbf{U_4'} = \frac{d}{d\sigma}(\mathbf{U_4}) = \rho\frac{d}{ds}(\rho\mathbf{B_2}) = -\left(\frac{\overline{\kappa}_3}{\overline{\kappa}_1}\right)\mathbf{U_3} + \dot{\rho}\mathbf{U_4},$$

where the functions $\overline{\kappa}_1$, $\overline{\kappa}_2$ and $\overline{\kappa}_3$ are the curvatures of α [12]. Then, the Frenet formulas in the equiform geometry of the Minkowski space-time can be written as below:

$\mathbf{U_1'} = \overline{K_1}\mathbf{U_1} + \mathbf{U_2}$,

$\mathbf{U_2'} = \mathbf{U_1} + \overline{K_1}\mathbf{U_2} + \overline{K_2}\mathbf{U_3}$,

$\mathbf{U_3'} = -\overline{K_2}\mathbf{U_2} + \overline{K_1}\mathbf{U_3} + \overline{K_3}\mathbf{U_4}$,

$\mathbf{U_4'} = -\overline{K_3}\mathbf{U_3} + \overline{K_1}\mathbf{U_4}$.

The functions $\overline{K_1}$, $\overline{K_2}$, $\overline{K_3}$ are the equiform curvatures of α.

$$\begin{bmatrix} \mathbf{U_1'} \\ \mathbf{U_2'} \\ \mathbf{U_3'} \\ \mathbf{U_4'} \end{bmatrix} = \begin{bmatrix} \overline{K_1} & 1 & 0 & 0 \\ 1 & \overline{K_1} & \overline{K_2} & 0 \\ 0 & -\overline{K_2} & \overline{K_1} & \overline{K_3} \\ 0 & 0 & -\overline{K_3} & \overline{K_1} \end{bmatrix} \begin{bmatrix} \mathbf{U_1} \\ \mathbf{U_2} \\ \mathbf{U_3} \\ \mathbf{U_4} \end{bmatrix}, \tag{2}$$

where

$$\overline{K_1} = \frac{1}{\rho^2}\langle \mathbf{U_j'}, \mathbf{U_j}\rangle; \quad (j = 1,2,3,4),$$

$$\overline{K_2} = \frac{1}{\rho^2}\langle \mathbf{U_2'}, \mathbf{U_3}\rangle = -\frac{1}{\rho^2}\langle \mathbf{U_3'}, \mathbf{U_2}\rangle, \tag{3}$$

$$\overline{K_3} = \frac{1}{\rho^2}\langle \mathbf{U_3'}, \mathbf{U_4}\rangle = -\frac{1}{\rho^2}\langle \mathbf{U_4'}, \mathbf{U_3}\rangle.$$

4. k-Type Helices in $\mathbb{E}_1^4$

Definition 1. Let α be a timelike curve in $\mathbb{E}_1^4$ with equiform Frenet frame $\{\mathbf{U}_1, \mathbf{U}_2, \mathbf{U}_3, \mathbf{U}_4\}$. If there exists a non-zero constant vector field $\mathbf{U}$ in $\mathbb{E}_1^4$ such that $\langle \mathbf{U}_k, \mathbf{U} \rangle = \mathbf{c}_k$ is a constant for $1 \leq k \leq 4$, α is said to be a $k-$type slant helix and $\mathbf{U}$ is called the slope axis of α.

Theorem 1. Let α be a timelike curve with Frenet formulas in equiform geometry of the Minkowski space-time $\mathbb{E}_1^4$. Then, if the curve α is a 1-type helix (or general helix), then we have

$$\langle \mathbf{U}_2, \mathbf{U} \rangle = -\overline{K}_1 c,$$

where c is a constant.

Proof. Assume that α is a 1-type helix in $\mathbb{E}_1^4$, then for a constant field $\mathbf{U}$, we can write

$$\langle \mathbf{U}_1, \mathbf{U} \rangle = c \tag{4}$$

is a constant and differentiating (4) with respect to σ, we find as below:

$$\langle \mathbf{U}_1', \mathbf{U} \rangle = 0.$$

Using the equiform Frenet equations in equiform geometry, we have the following equation:

$$\langle \overline{K}_1 \mathbf{U}_1 + \mathbf{U}_2, \mathbf{U} \rangle = 0,$$

and it follows that

$$\overline{K}_1 \langle \mathbf{U}_1, \mathbf{U} \rangle + \langle \mathbf{U}_2, \mathbf{U} \rangle = 0.$$

Using (4), we obtain

$$\langle \mathbf{U}_2, \mathbf{U} \rangle = -\overline{K}_1 c.$$

The proof is completed.

Theorem 2. Let α be a timelike curve with Frenet formulas in equiform geometry of the Minkowski space-time $\mathbb{E}_1^4$. Then, if the curve α is a 2-type helix, then we have

$$\langle \mathbf{U}_1, \mathbf{U} \rangle + \overline{K}_2 \langle \mathbf{U}_3, \mathbf{U} \rangle = -\overline{K}_1 c_1,$$

where c_1 is a constant.

Proof. Let the curve α be a 2-type helix in $\mathbb{E}_1^4$, then for a constant field $\mathbf{U}$, in that case, the following equations can be obtained:

$$\langle \mathbf{U}_2, \mathbf{U} \rangle = c_1 \tag{5}$$

is a constant and differentiating this equation with respect to σ, we get

$$\langle \mathbf{U}_2', \mathbf{U} \rangle = 0$$

from the equiform Frenet equations in equiform geometry, we find

$$\langle \mathbf{U}_1 + \overline{K}_1 \mathbf{U}_2 + \overline{K}_2 \mathbf{U}_3, \mathbf{U} \rangle = 0,$$

and

$$\langle \mathbf{U}_1, \mathbf{U} \rangle + \overline{K}_1 \langle \mathbf{U}_2, \mathbf{U} \rangle + \overline{K}_2 \langle \mathbf{U}_3, \mathbf{U} \rangle = 0.$$

Using (5), we obtain the following equation:

$$\langle \mathbf{U}_1, \mathbf{U} \rangle + \overline{K}_2 \langle \mathbf{U}_3, \mathbf{U} \rangle = -\overline{K}_1 c_1.$$

The proof is completed.

Theorem 3. Let α be a timelike curve with Frenet formulas in equiform geometry of the Minkowski space-time $\mathbb{E}_1^4$. In that case, if the curve α is a 3-type helix, then we have

$$-\overline{K}_2 \langle \mathbf{U}_2, \mathbf{U} \rangle + \overline{K}_3 \langle \mathbf{U}_4, \mathbf{U} \rangle = -\overline{K}_1 c_2$$

where c_2 is a constant.

Proof. Let the curve α be a 3-type helix. Thus, for a constant field $\mathbf{U}$ such that

$$\langle \mathbf{U}_3, \mathbf{U} \rangle = c_2 \tag{6}$$

is a constant. Differentiating (6) with respect to σ, we get

$$\langle \mathbf{U}_3', \mathbf{U} \rangle = 0,$$

and using equiform Frenet equations, we have

$$\langle -\overline{K}_2 \mathbf{U}_2 + \overline{K}_1 \mathbf{U}_3 + \overline{K}_3 \mathbf{U}_4, \mathbf{U} \rangle = 0,$$

and it follows that

$$-\overline{K}_2 \langle \mathbf{U}_2, \mathbf{U} \rangle + \overline{K}_1 \langle \mathbf{U}_3, \mathbf{U} \rangle + \overline{K}_3 \langle \mathbf{U}_4, \mathbf{U} \rangle = 0. \tag{7}$$

By setting (6) in (7), we can write

$$-\overline{K}_2 \langle \mathbf{U}_2, \mathbf{U} \rangle + \overline{K}_3 \langle \mathbf{U}_4, \mathbf{U} \rangle = -\overline{K}_1 c_2.$$

The proof is completed.

Theorem 4. Let α be a timelike curve with Frenet formulas in equiform geometry of the Minkowski space-time $\mathbb{E}_1^4$. If the curve α is a 4-type helix, then we have

$$\langle \mathbf{U}_3, \mathbf{U} \rangle = \frac{\overline{K}_1}{\overline{K}_3} c_3,$$

where c_3 is a constant.

Proof. Let the curve α be a 4-type helix in $\mathbb{E}_1^4$, then for a constant field $\mathbf{U}$, we can write the following equation:

$$\langle \mathbf{U}_4, \mathbf{U} \rangle = c_3 \tag{8}$$

is a constant. By differentiating (8) with respect to σ, we get

$$\langle \mathbf{U}_4', \mathbf{U} \rangle = 0$$

and using equiform Frenet equations, we find as below:

$$\langle -\overline{K}_3 \mathbf{U}_3 + \overline{K}_1 \mathbf{U}_4, \mathbf{U} \rangle = 0$$

and we can write

$$-\overline{K}_3 \langle \mathbf{U}_3, \mathbf{U} \rangle + \overline{K}_1 \langle \mathbf{U}_4, \mathbf{U} \rangle = 0.$$

By setting equation (8) in the last equation is written as follows:

$$\langle \mathbf{U}_3, \mathbf{U} \rangle = \frac{\overline{K}_1}{\overline{K}_3} c_3.$$

The proof is completed.

5. (k,m)-Type Slant Helices for Equiform Differential Geometry in $\mathbb{E}_1^4$

In this section, we will define (k,m)-type slant helices for timelike curve with equiform Frenet frame in $\mathbb{E}_1^4$ such as [6].

Definition 2. Let α be a timelike curve in $\mathbb{E}_1^4$ with equiform Frenet frame $\{\mathbf{U}_1, \mathbf{U}_2, \mathbf{U}_3, \mathbf{U}_4\}$. We call α is a (k,m)-type slant helix if there exists a non-zero constant vector field $\mathbf{U} \in \mathbb{E}_1^4$ satisfies $\langle \mathbf{U}_k, \mathbf{U} \rangle = \mathbf{c}_k$, $\langle \mathbf{U}_m, \mathbf{U} \rangle = \mathbf{c}_m$ are constants for $1 \leq k, m \leq 4, k \neq m$. The constant vector $\mathbf{U}$ is an axis of (k,m)-type slant helix.

Theorem 5. If the curve α is a $(1,2)$-type slant helix in $\mathbb{E}_1^4$, then we have

$$\langle \mathbf{U}_3, \mathbf{U} \rangle = \frac{c_2^2 - c_1^2}{c_1} \frac{1}{\overline{K}_2},$$

where $\overline{K}_2 = -\frac{c_2}{c_1}$ is a constant.

Proof. Let the curve α be a $(1,2)$-type slant helix in $\mathbb{E}_1^4$, then for a constant field $\mathbf{U}$, we can write following equations:

$$\langle \mathbf{U}_1, \mathbf{U} \rangle = c_1 \tag{9}$$

is a constant, and

$$\langle \mathbf{U}_2, \mathbf{U} \rangle = c_2 \tag{10}$$

is a constant. Differentiating (9) and (10) with respect to σ, we get

$$\langle \mathbf{U}_1', \mathbf{U} \rangle = 0$$

and

$$\langle \mathbf{U}_2', \mathbf{U} \rangle = 0.$$

Using equiform Frenet equations, we find the following equations:

$$\langle \overline{K}_1 \mathbf{U}_1 + \mathbf{U}_2, \mathbf{U} \rangle = 0$$

and it follows that

$$\langle \mathbf{U}_1 + \overline{K}_1 \mathbf{U}_2 + \overline{K}_2 \mathbf{U}_3, \mathbf{U} \rangle = 0.$$

In that case, we get

$$\overline{K}_1 \langle \mathbf{U}_1, \mathbf{U} \rangle + \langle \mathbf{U}_2, \mathbf{U} \rangle = 0, \tag{11}$$

$$\langle \mathbf{U}_1, \mathbf{U} \rangle + \overline{K}_1 \langle \mathbf{U}_2, \mathbf{U} \rangle + \overline{K}_2 \langle \mathbf{U}_3, \mathbf{U} \rangle = 0. \tag{12}$$

By setting (9) and (10) in (11), we find

$$\overline{K}_1 c_1 + c_2 = 0.$$

Substituting (9) and (10) to (12), we obtain as below:

$$c_1 + \overline{K}_1 c_2 + \overline{K}_2 \langle \mathbf{U}_3, \mathbf{U} \rangle = 0. \tag{13}$$

Finally, we get

$$\overline{K}_1 = -\frac{c_2}{c_1}, \tag{14}$$

and by setting (14) in (13), we get

$$\langle \mathbf{U}_3, \mathbf{U} \rangle = \frac{c_2^2 - c_1^2}{c_1} \frac{1}{\overline{K}_2}.$$

The proof is completed.

Theorem 6. If the curve α is a $(1,3)$-type slant helix in $\mathbb{E}_1^4$, then there exists a constant such that

$$\langle \mathbf{U}_4, \mathbf{U} \rangle = -\frac{\overline{K}_1 \overline{K}_2}{\overline{K}_3} c_1 - \frac{\overline{K}_1}{\overline{K}_3} c_3$$

where c_1, c_3 are constants.

Proof. Let the curve α be a $(1,3)$-type slant helix in $\mathbb{E}_1^4$, then for a constant field $\mathbf{U}$, we can write as below:

$$\langle \mathbf{U}_1, \mathbf{U} \rangle = c_1 \tag{15}$$

is a constant, and

$$\langle \mathbf{U}_3, \mathbf{U} \rangle = c_3 \tag{16}$$

is a constant. Differentiating (15) and (16) with respect to σ, we get

$\langle \mathbf{U}_1', \mathbf{U} \rangle = 0$

and

$\langle \mathbf{U}_3', \mathbf{U} \rangle = 0.$

Using equiform Frenet equations, we obtain the following equations:

$\langle \overline{K}_1 \mathbf{U}_1 + \mathbf{U}_2, \mathbf{U} \rangle = 0,$

and we have that

$\langle -\overline{K}_2 \mathbf{U}_2 + \overline{K}_1 \mathbf{U}_3 + \overline{K}_3 \mathbf{U}_4, \mathbf{U} \rangle = 0.$

(We know that $\mathbf{U}$ is a constant). Thus, we can write as below:

$$\overline{K}_1 \langle \mathbf{U}_1, \mathbf{U} \rangle + \langle \mathbf{U}_2, \mathbf{U} \rangle = 0, \tag{17}$$

$$-\overline{K}_2 \langle \mathbf{U}_2, \mathbf{U} \rangle + \overline{K}_1 \langle \mathbf{U}_3, \mathbf{U} \rangle + \overline{K}_3 \langle \mathbf{U}_4, \mathbf{U} \rangle = 0. \tag{18}$$

By setting equation (15) in equation (17), we get

$$\langle \mathbf{U}_2, \mathbf{U} \rangle = -\overline{K}_1 c_1. \tag{19}$$

Substituting (16) and (19) to (18), we find

$$\langle \mathbf{U}_4, \mathbf{U} \rangle = -\frac{\overline{K}_1 \overline{K}_2}{\overline{K}_3} c_1 - \frac{\overline{K}_1}{\overline{K}_3} c_3.$$

The proof is completed.

Theorem 7. If the curve α is a $(1,4)$-type slant helix in $\mathbb{E}_1^4$, then there exists a constant such that

$\langle \mathbf{U}_2, \mathbf{U} \rangle = -\overline{K}_1 c_1$

and

$\langle \mathbf{U}_3, \mathbf{U} \rangle = \dfrac{\overline{K}_1}{\overline{K}_3} c_4$

where $c_1, \ c_4$ are constants.

Proof. Let the curve α be a $(1,4)$-type slant helix in $\mathbb{E}_1^4$, then for a constant field $\mathbf{U}$, we can write the following equations:

$$\langle \mathbf{U}_1, \mathbf{U} \rangle = c_1 \tag{20}$$

is a constant and

$$\langle \mathbf{U}_4, \mathbf{U} \rangle = c_4 \tag{21}$$

is a constant. Differentiating (20) and (21) with respect to σ, we get

$\langle \mathbf{U}_1', \mathbf{U} \rangle = 0$

and

$\langle \mathbf{U}_4', \mathbf{U} \rangle = 0.$

Using equiform Frenet equations, we find

$\langle \overline{K}_1 \mathbf{U}_1 + \mathbf{U}_2, \mathbf{U} \rangle = 0$

and

$\langle -\overline{K}_3 \mathbf{U}_3 + \overline{K}_1 \mathbf{U}_4, \mathbf{U} \rangle = 0.$

So, the following equations can be obtained:

$$\overline{K}_1 \langle \mathbf{U}_1, \mathbf{U} \rangle + \langle \mathbf{U}_2, \mathbf{U} \rangle = 0, \tag{22}$$

$$-\overline{K}_3 \langle \mathbf{U}_3, \mathbf{U} \rangle + \overline{K}_1 \langle \mathbf{U}_4, \mathbf{U} \rangle = 0. \tag{23}$$

By setting (20) in (22), we have

$$\langle \mathbf{U}_2, \mathbf{U} \rangle = -\overline{K}_1 c_1.$$

Substituting (21) to (23), we get

$$\langle \mathbf{U}_3, \mathbf{U} \rangle = \frac{\overline{K}_1}{\overline{K}_3} c_4.$$

The proof is completed.

Theorem 8. If the curve α is a (2,3)-type slant helix in $\mathbb{E}_1^4$, then there exists a constant such as

$$\langle \mathbf{U}_1, \mathbf{U} \rangle = -\overline{K}_1 c_2 - \overline{K}_2 c_3$$

and

$$\langle \mathbf{U}_4, \mathbf{U} \rangle = \frac{\overline{K}_2}{\overline{K}_3} c_2 - \frac{\overline{K}_1}{\overline{K}_3} c_3.$$

Proof. Let the curve α be a (2,3)-type slant helix in $\mathbb{E}_1^4$, then for a constant field $\mathbf{U}$, we can write

$$\langle \mathbf{U}_2, \mathbf{U} \rangle = c_2 \tag{24}$$

is a constant and

$$\langle \mathbf{U}_3, \mathbf{U} \rangle = c_3 \tag{25}$$

is a constant. Differentiating (24) and (25) with respect to σ, we find

$$\langle \mathbf{U}_2', \mathbf{U} \rangle = 0$$

and

$$\langle \mathbf{U}_3', \mathbf{U} \rangle = 0.$$

Using equiform Frenet formulas, the following equations can be obtained:

$$\langle \mathbf{U}_1, \mathbf{U} \rangle + \overline{K}_1 \langle \mathbf{U}_2, \mathbf{U} \rangle + \overline{K}_2 \langle \mathbf{U}_3, \mathbf{U} \rangle = 0, \tag{26}$$

$$-\overline{K}_2 \langle \mathbf{U}_2, \mathbf{U} \rangle + \overline{K}_1 \langle \mathbf{U}_3, \mathbf{U} \rangle + \overline{K}_3 \langle \mathbf{U}_4, \mathbf{U} \rangle = 0. \tag{27}$$

By setting (24) and (25) in (26), we get

$$\langle \mathbf{U}_1, \mathbf{U} \rangle = -\overline{K}_1 c_2 - \overline{K}_2 c_3,$$

and substituting (24) and (25) to (27), we have

$$\langle \mathbf{U}_4, \mathbf{U} \rangle = \frac{\overline{K}_2}{\overline{K}_3} c_2 - \frac{\overline{K}_1}{\overline{K}_3} c_3.$$

The proof is completed.

Theorem 9. If the curve α is a (2,4)-type slant helix in $\mathbb{E}_1^4$, then there exists a constant such as

$$\langle \mathbf{U}_1, \mathbf{U} \rangle = -\overline{K}_1 c_2 - \overline{K}_2 \frac{\overline{K}_1}{\overline{K}_3} c_4,$$

where c_2, c_4 are constants.

Proof. Let the curve α be a (2,4)-type slant helix in $\mathbb{E}_1^4$, then for a constant field $\mathbf{U}$, we can write the following equations:

$$\langle \mathbf{U}_2, \mathbf{U} \rangle = c_2 \tag{28}$$

and

$$\langle \mathbf{U}_4, \mathbf{U} \rangle = c_4 \tag{29}$$

are constants. By differentiating (28) and (29) with respect to σ, we get the following equations:

$$\langle \mathbf{U}_2', \mathbf{U} \rangle = 0$$

and

$$\langle \mathbf{U}_4', \mathbf{U} \rangle = 0.$$

Using equiform Frenet equations, we find

$$\langle \mathbf{U}_1, \mathbf{U} \rangle + \overline{K}_1 \langle \mathbf{U}_2, \mathbf{U} \rangle + \overline{K}_2 \langle \mathbf{U}_3, \mathbf{U} \rangle = 0, \tag{30}$$

$$-\overline{K}_3 \langle \mathbf{U}_3, \mathbf{U} \rangle + \overline{K}_1 \langle \mathbf{U}_4, \mathbf{U} \rangle = 0. \tag{31}$$

Substituting (28) to (30), we obtain as follows:

$$\langle \mathbf{U}_1, \mathbf{U} \rangle + \overline{K}_2 \langle \mathbf{U}_3, \mathbf{U} \rangle = -\overline{K}_1 c_2. \tag{32}$$

By setting (29) in (31), we have the following equation:

$$\langle \mathbf{U}_3, \mathbf{U} \rangle = \frac{\overline{K}_1}{\overline{K}_3} c_4 \tag{33}$$

and by setting (33) in (32), we obtain

$$\langle \mathbf{U}_1, \mathbf{U} \rangle = -\overline{K}_1 c_2 - \overline{K}_2 \frac{\overline{K}_1}{\overline{K}_3} c_4.$$

The proof is completed.

Theorem 10. If the curve α is a $(3,4)$-type slant helix in $\mathbb{E}_1^4$, then there exists a constant such as

$$\langle \mathbf{U}_2, \mathbf{U} \rangle = \frac{\overline{K}_3}{\overline{K}_2} \left(\frac{c_3^2}{c_4} + c_4 \right)$$

where c_3, c_4 are constants.

Proof. Let the curve α be a $(3,4)$-type slant helix in $\mathbb{E}_1^4$, then for a constant field $\mathbf{U}$, we can write as follows:

$$\langle \mathbf{U}_3, \mathbf{U} \rangle = c_3 \tag{34}$$

is a constant and

$$\langle \mathbf{U}_4, \mathbf{U} \rangle = c_4 \tag{35}$$

is a constant. By differentiating (34) and (35) with respect to σ, we have the following equations:

$$\langle \mathbf{U}_3', \mathbf{U} \rangle = 0$$

and

$$\langle \mathbf{U}_4', \mathbf{U} \rangle = 0.$$

Using equiform Frenet formulas, we find as below:

$$-\overline{K}_2 \langle \mathbf{U}_2, \mathbf{U} \rangle + \overline{K}_1 \langle \mathbf{U}_3, \mathbf{U} \rangle + \overline{K}_3 \langle \mathbf{U}_4, \mathbf{U} \rangle = 0, \tag{36}$$

and

$$-\overline{K}_3 \langle \mathbf{U}_3, \mathbf{U} \rangle + \overline{K}_1 \langle \mathbf{U}_4, \mathbf{U} \rangle = 0. \tag{37}$$

Substituting (34) and (35) to (37), we can write

$$\overline{K}_1 = \overline{K}_3 \frac{c_3}{c_4}, \tag{38}$$

and by setting (34), (35) and (38) in (36), we obtain

$$\langle \mathbf{U}_2, \mathbf{U} \rangle = \frac{\overline{K}_3}{\overline{K}_2} \frac{c_3^2}{c_4} + \frac{\overline{K}_3}{\overline{K}_2} c_4.$$

The proof is completed.

6. Conclusion

In this study we investigate equiform differential geometry of timelike curves and $k-$ and $(k,m)-$type slant helices for equiform differential geometry of timelike curves in the Minkowski space-time.

Acknowledgment

Conflicts of interest

The authors stated that did not have conflict of interests.

References

[1] Ali A.T., Turgut M., Some characterizations of slant helices in the Euclidean space $\mathbb{E}^n$, *Hacet. J. Math. Stat.*, 39 (3) (2010) 327–33.

[2] Abdel-Aziz H.S., Saad M.K., Abdel-Salam A.A., Equiform Differential Geometry of Curves in Minkowski Space-Time, https://arxiv.org/abs/1501.02283, (2015).

[3] İlarslan K., Nešović E., Spacelike and Timelike Normal Curves in Minkowski Space-Time, *Publications de L'Institut Mathematique, Nouvelle série, tome*, 85 (99) (2009) 111-118.

[4] Aydın M.E., Ergüt M., The equiform differential geometry of curves in 4-dimensional Galilean space $\mathbb{G}_4$, *Stud. Univ. Babes-Bolyai Math.*, 58 (3) (2013) 399–406.

[5] Turgut M., Yilmaz S., Characterizations of Some Special Spacelike Curves in Minkowski eg-time, *International J.Math. Combin.*, (2) (2008) 17-22.

[6] Yılmaz M.Y., Bektaş M., Slant helices of (k,m)-type in $\mathbb{E}^4$, *Acta Univ. Sapientiae, Mathematica,* 10 (2) (2018) 395–401.

[7] Yilmaz S., Turgut M., On the characterizations of inclined curves in Minkowski space-time $\mathbb{E}_1^4$, *International Mathematical Forum,* 3 (16) (2008) 783-792.

[8] Gluck H., Higher curvature of curves in Euclidean space, *Amer. Math. Monthly,* 73 (1996) 699–70.

[9] Miroslava P.T., Emilija S., W-curves in Minkowski space-time, *Novi Sad J. Math.,* 32 (2) (2002) 55-65.

[10] Bektas M., Ergüt M., Soylu D., The Characterization of the Spherical Timelike Curves in 3- Dimensional Lorentzian Space, *Bull. Malaysian Math. Soc. (Second Series)*, 21 (1998) 11-125.

[11] İlarslan K., Spacelike normal curves in Minkowski space $\mathbb{E}_1^3$, *Turk J Math.,* 29 (2005) 53-63.

[12] Bulut F., Bektaş M., Special Helices On Equiform Differential Geometry of Spacelike Curves in Minkowski Space-Time, *Commun. Fac. Sci. Univ. Ank. Ser. A1 Math. Stat.,* 69 (2) (2020) 51-62.

[13] O'Neill B., Semi Riemannian geometry, *Academic Press,* New York-London (1983).

Characteristic of gap photodectored plasma cell

Duygu YİĞİT ÜNLÜ[1], * iD   *Hatice Hilal KURT[2]* iD

[1]*Gazi University, Gazi University Institute of Naturel and Applied Science, Ankara/TURKEY*
[2]*Gazi University, Faculty of Science, Department of Physics, Ankara/TURKEY*

Abstract

In the study, it was experimentally investigated the Microelectronic Gas Discharge System (MGDS) with Gallium Phosphate (GaP) cathode. The system was operated in the dark and under different Infrared (IR) illumination intensities. The Current-Voltage Characteristic (CVC) was obtained for different IR illuminations under high-pressure conditions. IR illumination produced different electrical conductivities at high pressures. This reality shows that the system can operate more conveniently at high pressures for optoelectronic applications. It was determined that the system showed Negative Differential Resistance (NDR) and hysteresis behaviors when appropriate experimental parameters were set. It was seen that the pressure and distance between the electrodes has a significant factor in determining the hysteresis value. AVK, Discharge Light Emission (DLE), and hysteresis behaviors were investigated under different illumination intensities using a semiconductor plasma system. It has been observed that IR illumination creates different electrical conductivities at high pressures. This showed that the system can operate more conveniently at high pressures for optoelectronic applications. It has been observed that CVCs are more stable as the distance between the electrodes decreases. In this study, the IR sensitivity of GaP was tested for the first time. According to the experimental results, it was seen that GaP can be optically excited with IR light when the appropriate distance between the electrodes and the appropriate gas pressure was adjusted.

1. Introduction

In recent years, mycoplasma discharge systems have great interest due to their feasibility to environmental and industrial environments. Gas discharge plasmas are extensively utilized in technological applications such as light emission systems, plasma displays and display panels, laser technologies, fusion, atmospheric plasma units, surface coating and sterilization of biological units [1,2]. It is also used as a protective coating in the semiconductor industry, analytical chemistry, etching and deposition of thin films, environmental and biotechnological applications [3,4]. Convert to the IR signals into the visible region it is generally used the gas discharge devices with semiconductor electrodes [5,6]. In the case of gas discharge, any change in the electron property of the cathode may be undesirable and cause temporal and spatial instability in the functions of the system parameters [7].

In the discharge of the gases it is generally used Townsend and Glow discharges. Townsend discharge that can occur at low current value and also it is a weak discharge [8]. The space charge that produced by the Townsend discharge can affect and distort the electric field in the gas GaP [9,10,11]. Because of the Townsend discharge is a complex situation, gas discharge interval *d*, electrode shape, type of gas-filled and pressure *p* play an important role in the character of discharge [12]. However, it was occurred a strong discharge with high space-charge generation in the Glow discharge. In the glow discharge state, the positive space charge accumulates near the cathode. This accumulation is observed as a high luminous layer near the cathode [13].

In this study, MGDS with GaP cathode was investigated experimentally. The system was operated in the dark and under different IR illumination intensities. Firstly, CVCs were obtained for different IR illuminations in high-pressure situations. According to the CVC graphs, it was observed that IR illumination creates different electrical conductivities at high pressures. This reality showed that the system can

operate more conveniently at high pressures for optoelectronic applications. Then it was determined that the distance between the electrodes has an important outcome on the optical and electrical characteristic of the system. Three-dimensional CVC graphs were obtained as a function of pressure for different electrode distanced and cathode diameter D values. It was seen that CVCs were more stable as the distance between the electrodes decreased. In additionally, CVC graphs were obtained as a function of the distance between the electrodes at different p pressure values. Experimental data showed that currents of different magnitudes originate from different electrode spacing. Also, it was observed that maximum current values can be obtained at short distances between the electrodes and at low pressures. The pressure dependence of the recycle plots was investigated when the GaP photodetector was exposed to weak illumination intensity in the forward and feedback condition. In the study, it was observed that the hysteresis width (ΔV) changed depending on the pressure in the forward and feedback conditions, the hysteresis range narrowed with the increase in pressure.

2. Experimental Design

In Figure 1 showed that the setup of the MGDS [14]. The basic element of the discharge cell, GaP, was located at the cathode part of the cell. Total testing system; From right to left, the external light source consists of an optical lens for visible light emitted from the source, a silicon filter, a discharge cell, a CCD camera, a vacuum pump, a black box, and a digital manometer. In Figure 1(b) a detailed schematic diagram of the entire setup was shown with a sandwich-like structure. The gas discharge GaP was located between the two electrodes. One of them consists of a glass layer coated with SnO_2 and the other was composed of a semiconductor (such as GaP, GaAs). This range can be adjusted to different thicknesses from 45 μm to 323 μm. The DLE recorded with the CCD camera was transferred to a PC (Fig. 1(b)). A PC, some interface systems were used to measure the electrical property of the DLE. A Keithley 199 multimeter and a Stanford PS 325 high voltage power supply are used to measuring the electrical current flowing through the cell and the voltage across the cell. These measurements were digitized with software [14].
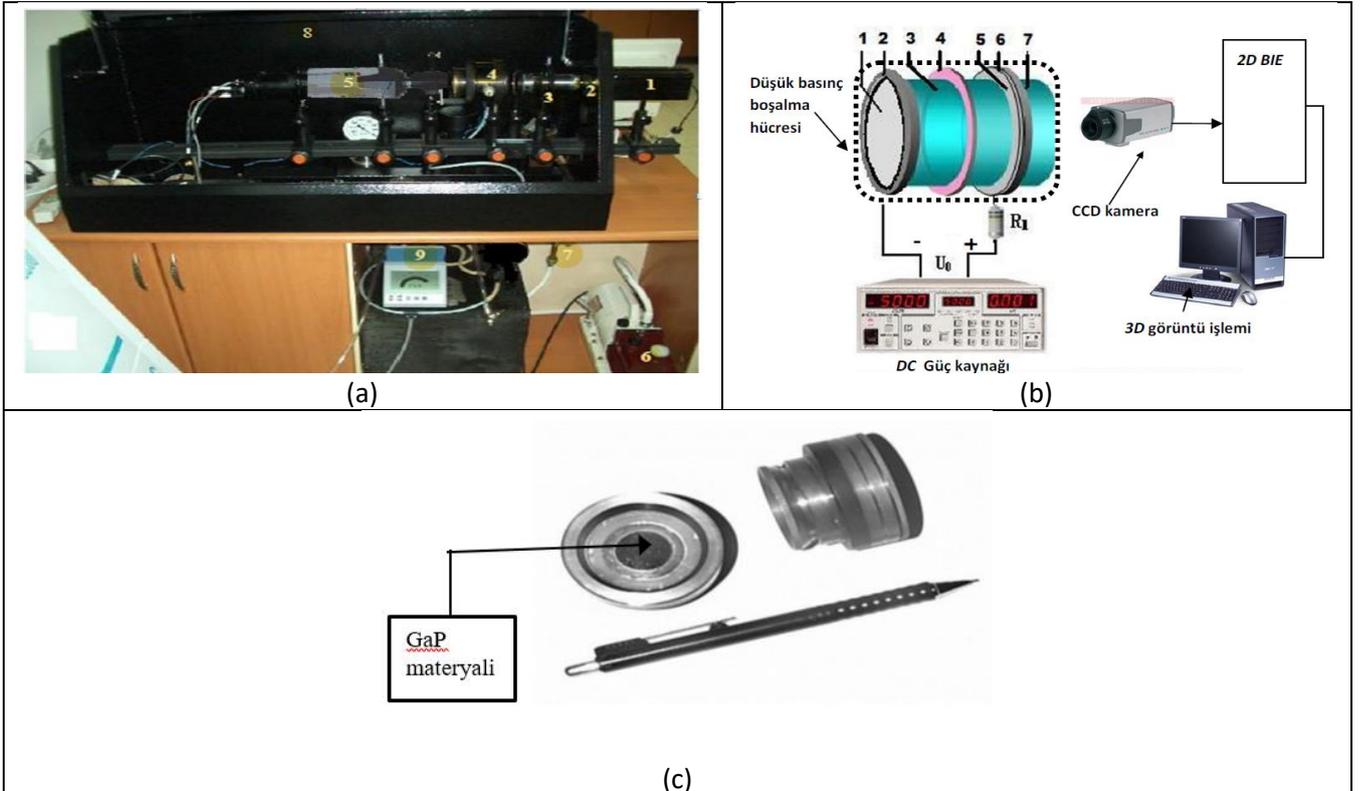

Figure 1. (a) MGDS: 1) Light source; 2) Optical lens; 3) Silicon filter 4) Gas ionization system; 5) CCD camera; 6) Vacuum pump; 7) Vacuum valve; 8) Experiment box and 9) Digital manometer; (b) Diagram of the sandwich-type ionization cell, measuring and recording system: 1) GaAs material; 2) Sample holder; 3) Microrelease spacing; 4) Insulating mica; 5) Transparent conductor SnO_2; 6) Glass disc, 7) Visible light beam. The dotted part is shown in (c). GaP material is located in the middle of the cell. The d distance between the electrodes is the micro distance between GaP and transparent SnO_2 [14].

3. Results and Discussion

In the experimental studies, high resistance semiconductor GaP electrodes, which exhibit linear CVCs at different illumination intensities and are sensitive to IR light, were used in all voltage ranges. The spatial distribution of the current during gas discharge and the luminosity in the vacuum was proportional to the conductivity of the cell. Spatial dispersion leads to visualization of stability within a given parameter range. In plasma systems, optical and electrical prosperities of semiconductor electrodes were the significant importance they work as a control parameter and act as local resistors [15].

In Figure 2, CVCs were obtained for different IR illuminations under high-pressure conditions. IR illumination produced different electrical conductivities at high pressures. This reality shows that the system can operate more conveniently at high pressures for optoelectronic applications. When the IR light source was used in the system, the discharge current was varied through different illuminance intensities.
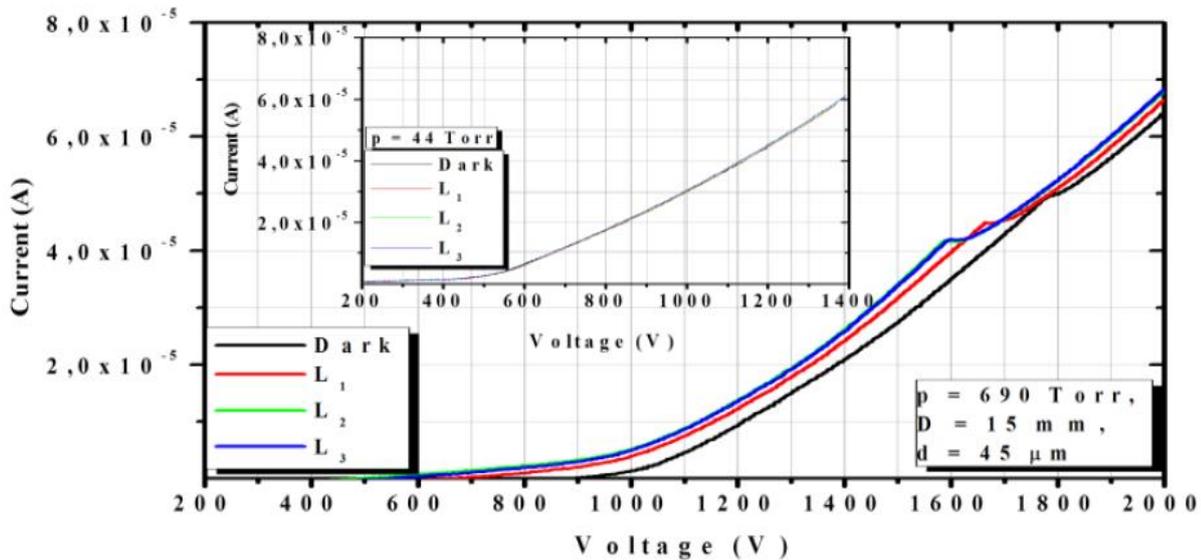
(a)
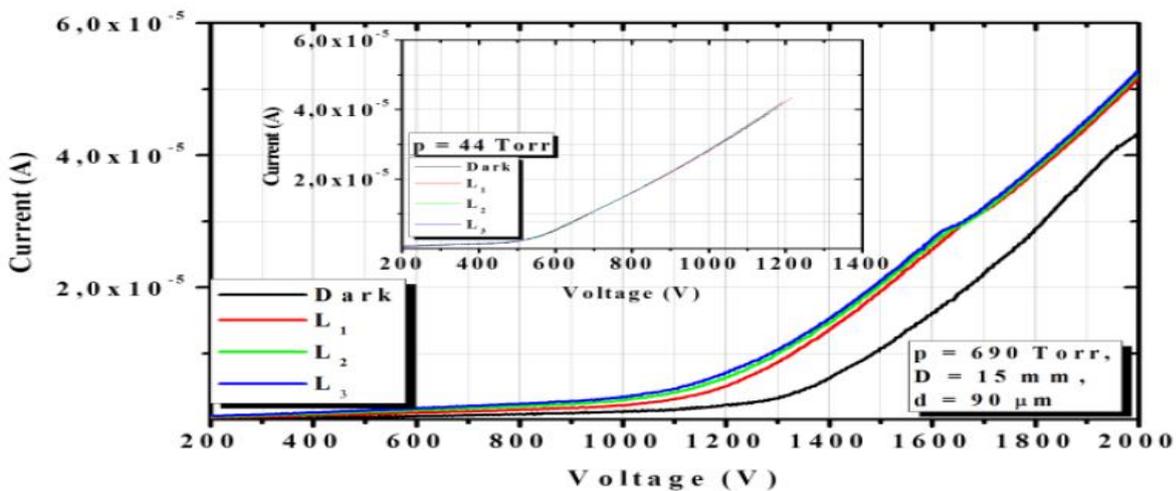
(b)
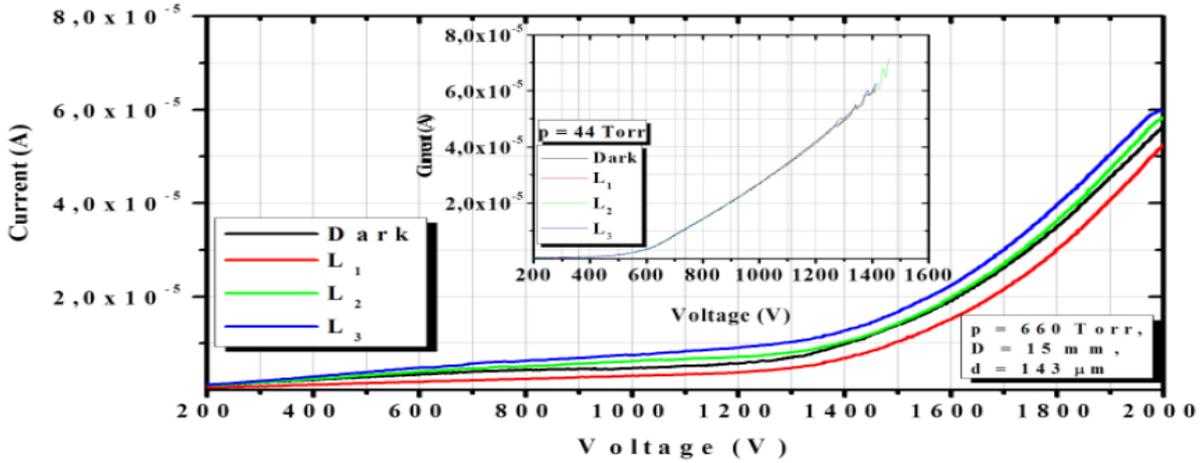
(c)

Figure 2. (a) Current-voltage graph for pressure of 690 torr, electrode diameter of 15 mm, and distance between electrodes of 45 μm. (b) Current-voltage graph for pressure of 690 torr, electrode diameter of 15 mm, and distance between electrodes of 90 μm. (c) Current-voltage graph for pressure of 660 torr, electrode diameter of 15 mm, and distance between electrodes of 143 μm.

The distance of the electrodes has an important result on the electrical and optical characteristics of the system. Figure 3 shows the CVCs measured between d = 240 μm and d = 445 μm as a function of pressure for different cathode diameter values D. It was seen that CVCs are more stable when set to d = 240 μm.

Moreover, due to the plasma behavior inside the cell, the distance between the electrodes leads to differences in the discharge current. The difference in CVCs was due to the presence of electric field domains moving from the cathode to the anode. The pressure dependence of CVC at 240 μm is linear, while its behavior at 445 μm was non-linear.
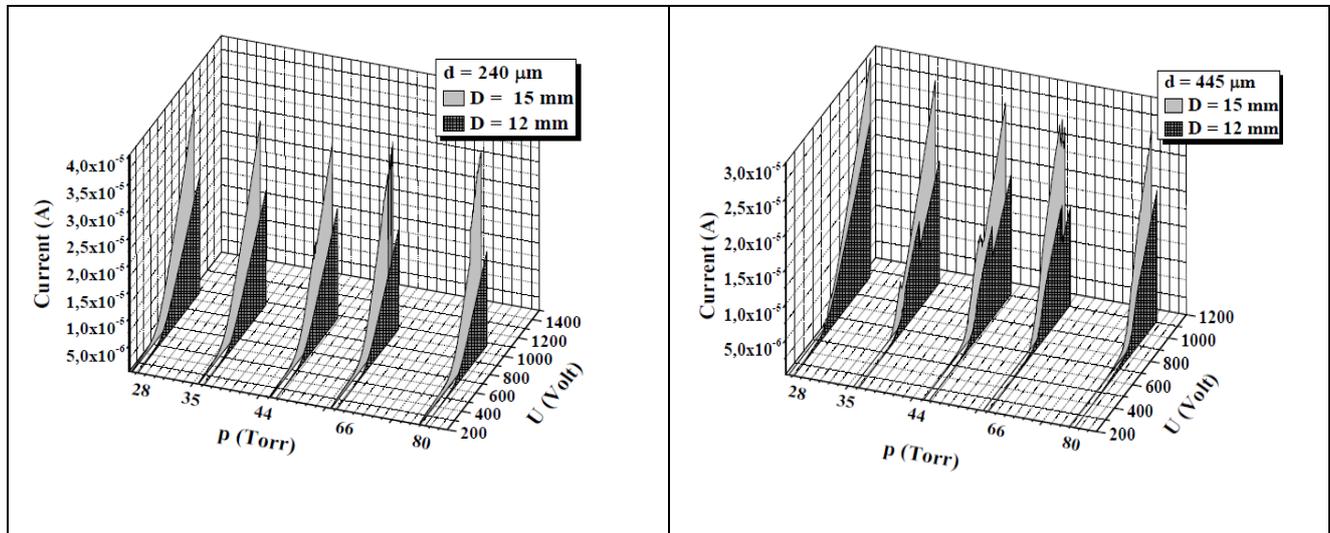

Figure 3. 3D CVC graph as a function of pressure for different d and D values.

It was known that GaP has high sensitivity in the wavelength range of 400-550 nm. Currently, almost all of the studies in the literature belong to the transmittance characteristics in the visible or UV region [1].

In this study, the IR sensitivity of GaP was tested for the first time. While no IR sensitivity was observed at a low-pressure value (p = 44 Torr), it was shown that

GaP can be optically stimulated with IR light when the appropriate inter-electrode distance and the appropriate gas pressure (in the range of 660-690 Torr) are set. As can be seen in Figure 4, different conductivity values were obtained under different IR illumination at high pressures. On the other hand, there is a stable conductivity for low-pressure value. According to the obtained findings, the optical

properties of GaP can be improved and the IR sensitivity of the material can be improved optically when the appropriate pressure value adjusted.

The relationship between current and distance between electrodes at three different pressure regimes is shown in Figure 4. Measurements were made for pressure values of 160, 200 and 360 Torr at distances between electrodes ranging from 50 μm to 525 μm. According to the results obtained; It has been seen that different magnitudes of currents will be obtained for different electrode distances. Accordingly, maximum current values were obtained at low pressures and short distances between electrodes.
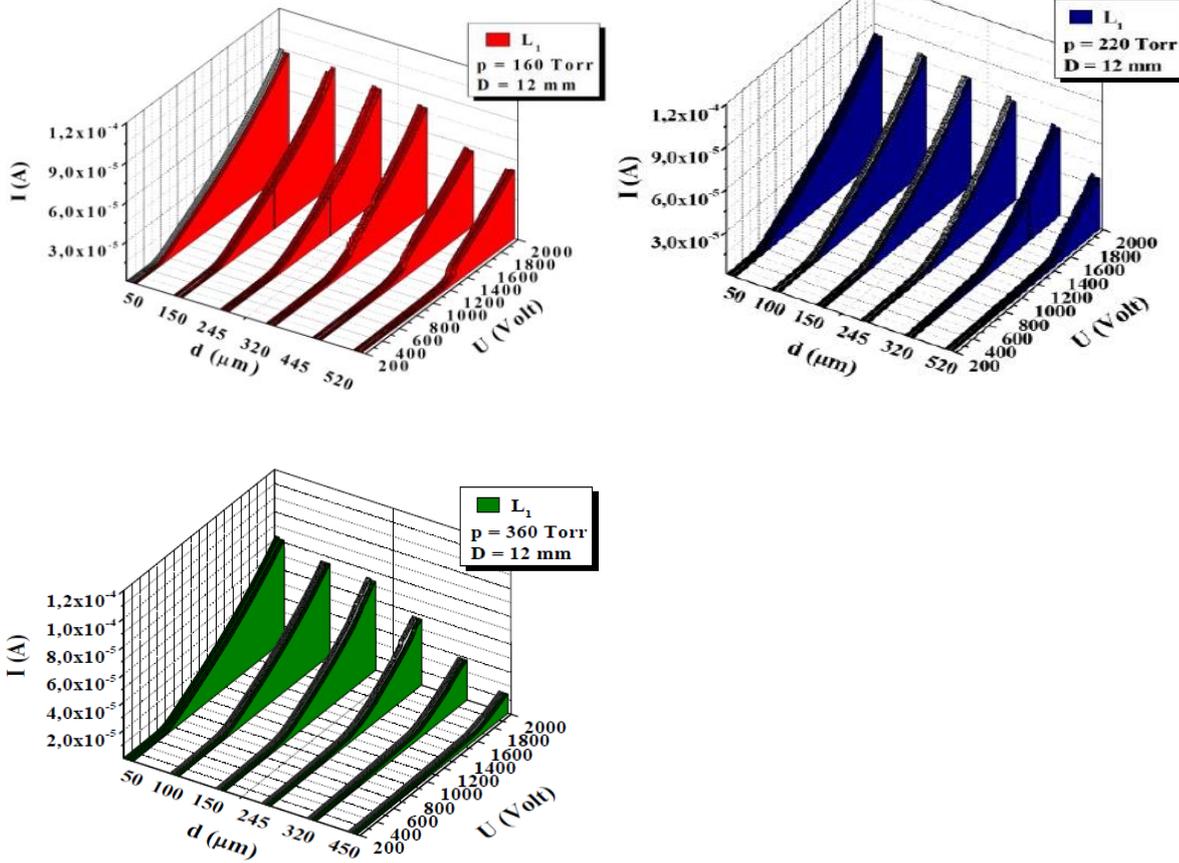
Figure 4. CVC graphs as a function of the d distance between the electrodes at different p pressure values.

Experimental results show that there were trap levels in GaP and these levels have different effects on current under forward and reverse voltage supply. In Figure 5 (a-d), the recycling (hysteresis) behavior of the electrodes depending on the gas saturation was investigated. Hysteresis was an indication of the bstable state of the system. Impurities and traps in the semiconductor affect the hysteresis state [16].

Figure 5 (a-d) CVC measurements applied to show the effect of pressure on hysteresis. It was observed that the function of the pressure in the forward and feedback conditions in the hysteresis width (ΔV) changes. The hysteresis range narrows with the increases in pressure. The pressure and the distance between the electrodes play a significant role in determining the true value of the hysteresis. Likewise, the radiation graphs inside the CVCs confirm the situation.
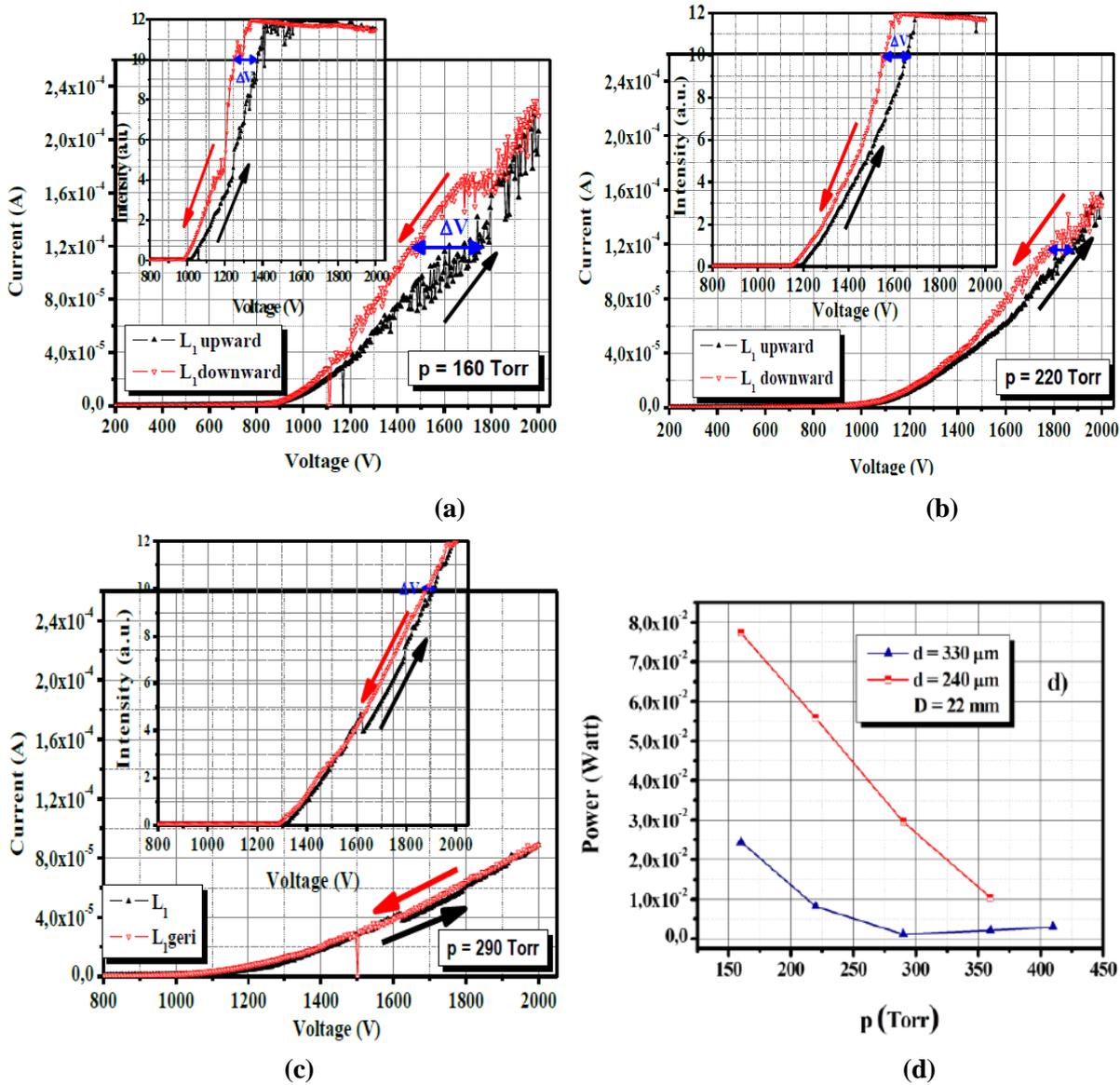
Figure 5. Pressure dependence of recycle graphs in forward and feedback condition when GaP photodetector is exposed to weak illumination; a) for p = 160 Torr; b) for p = 220 Torr; c) for p = 290 Torr; d) variation of force with pressure.

Figure 6 (a, b) shows the effect of the distance between the electrodes on the hysteresis. CVC measurements showed that the trapping centers in the GaP material changed the hysteresis width. This effect was significant evident when the thickness was reduced to a certain value. It was observed that the narrow electrode spacing supported the formation of hysteresis, whereas the wide electrode spacing prevented the hysteresis formation.

(a)   **(b)**
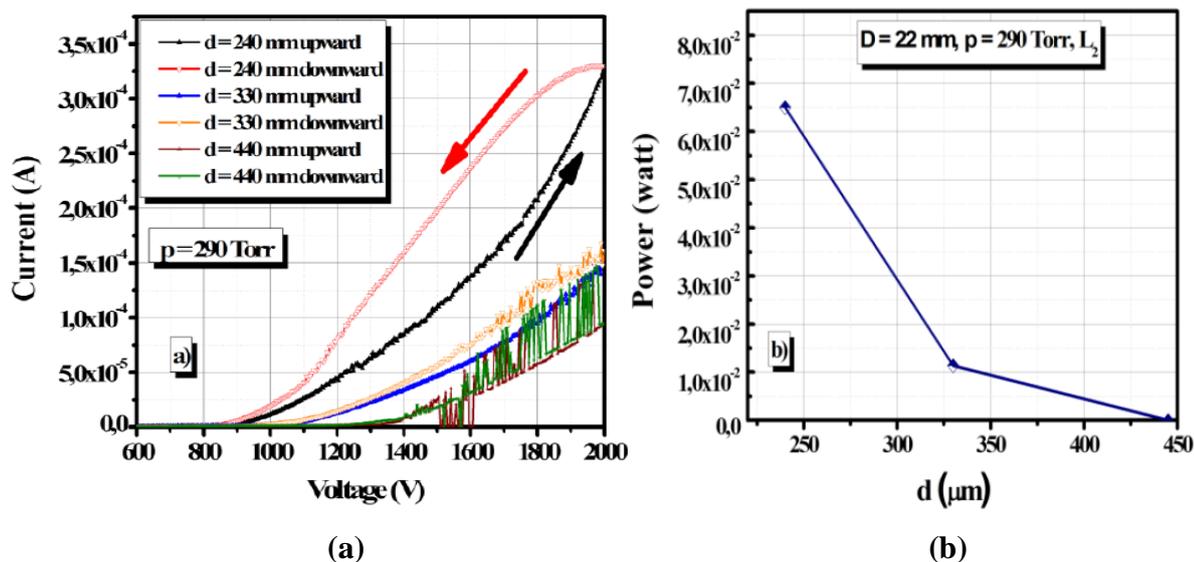
Figure 6. a) Recycle graphs at p= 2900 Torr for different electrode distances; b) Variation of the power according to the distance between the electrodes.

4. Conclusion

In the study, MGDS with GaP cathode was investigated experimentally. The system was operated in the dark and under different IR illumination intensities. The CVC was obtained for different IR illuminations under high-pressure conditions. IR illumination produced different electrical conductivities at high pressures. This reality shows that the system can operate more conveniently at high pressures for optoelectronic applications. It was detected for the first time for GaP that the system showed NDR and hysteresis behaviors when appropriate experimental parameters were set. It was seen that the pressure and the distance between the electrodes played a significant role in find out the hysteresis value. CVC, DLE, and hysteresis behaviors were investigated under different illumination intensities using a semiconductor plasma system. It was observed that IR illumination creates different electrical conductivities at high pressures. This showed that the system can operate more conveniently at high pressures for optoelectronic applications. It was also observed that CVCs were more stable as the distance between the electrodes decreases.

In this study, the IR sensitivity of GaP was tested for the first time in the experimental system. According to the experimental results, it was shown that GaP can be optically excited with IR light when the appropriate distance between the electrodes and the appropriate gas pressure was adjusted. When the experimental data were examined, it was seen that different current values would be obtained at different electrode distances. As a result of the comparison of the currents

at different pressure values, it was seen that in the short distance between electrodes and at low pressure maximum current values can be obtained. Also, it was seen that GaP was important because it works at room temperature and has a wide application area in optoelectronic systems. IR photosensitive photodetectors were used in many applications. These photodetectors have some disadvantages, especially for remote IR regions, as they require a cooling unit. Despite its widespread use, the IR sensitivity of the GaP material has not been satisfactorily studied. It is thought that this study will help to better understand the electrical and optical characteristics of GaP material. In this sense, experiments were carried out to improve the performance of the system. GaP material has some advantages because it works at room temperature. For this purpose, a connection was established between flow and discharge characteristics at different pressure values. According to the experimental results, it can be said that GaP has technological importance as it can be used as an IR detector in IR image converters.

In this study, it was demonstrated by making both CVC and DLE measurements, unlike the studies of other independent authors, that the IR sensitivity of GaP electronic material is due to voltage-dependent electron trapping caused by inherent defects in the semiconductor n-type GaP material. In addition, the effects of various parameters on material characteristics (pressure, voltage, distance between electrodes, cathode diameter, and IR illumination intensity) were experimentally investigated. The change in electrical characteristics of GaP material has a significant effect in optoelectronic applications.

Acknowledgment

Conflicts of Interest

No conflict of interest was stated by the authors.

References

[1] Portsel L. M., Lodygin A. N., Astrov, Y. A., Townsend-like discharge: the suppression of instabilities by a semiconductor electrode, *J. of Phys. D: Appl. Phys.*, 42 (23) (2009): 235208.

[2] Weltmann K. D., Kolb J. F., Holub M., Uhrlandt D., Šimek M., Ostrikov K., Becker K. (2019). The future for plasma science and technology, *Plas. Proc. and Poly.*, *16*(1), 1800118.

[3] Grill A., Cold plasma in materials fabrication, Vol. 151. IEEE Press, New York, 1994.

[4] Lieberman M. A., Lichtenberg A. J., Principles of plasma discharges and materials processing, *MRS Bullet.*, 30(12) (1994) 899-901.

[5] Lodygin A. N., Portsel L. M., Astrov, Y. A., DC Townsend Discharge in Nitrogen: Temperature-Dependent Phenomena, *Contr. to Plasma Phys.*, 52(8) (2012) 682-691.

[6] Salamov B. G., Kurt H. Y., Current instability in a planar gas discharge system with a large-diameter semiconductor cathode, *J. of Phys. D: Appl. Phys.,* 38(5) (2005) 682.

[7] Gurevich E. L., Kittel S., Hergenröder R., Astrov Y. A., Portsel L. M., Lodygin A. N., Ankudinov A. V., Modification of GaAs surface by low-current Townsend discharge, *J. of Phys. D: Appl. Phys.,* 43(27) (2010) 275302.

[8] Raizer Y. P., John E A., Gas discharge physics, Vol. 2. Berlin: Springer, 1997.

[9] Chen Z. G., Cheng L., Lu G. Q. M., Zou J., Sulfur-doped gallium phosphide nanowires and their optoelectronic properties, *Nanotechnolog*y, 21(37) (2010) 375701.

[10] Liu F., Song Y. J., Xing Q. R., Hu M. L., Li Y. F., Wang C. L., ... Wang C. Y., Broadband terahertz pulses generated by a compact femtosecond photonic crystal fiber amplifier, *IEEE Phot. Tech. Let.,* 22(11) (2010) 814-816.

[11] McIntosh D., Zhou Q., Lara F. J., Landers J., Campbell J. C., Flip-chip bonded GaP photodiodes for detection of 400-to 480-nm fluorescence, *IEEE Phot. Tech. Let.,* 23(13) (2011) 878-880.

[12] Zhuo L., Hai-Yun L., Xin-Xin W., Bo L. V., Zhi-Cheng G., Li-Ming W., Determination of ionization coefficient of atmospheric helium in dielectric barrier discharge, *Chinese Phys. Let.,* 25(6) (2008) 2136.

[13] Luo H., Liang Z., Lv B., Wang X., Guan Z., Wang L., Observation of the transition from a Townsend discharge to a glow discharge in helium at atmospheric pressure, *App. Phys. Let.,* 91(22) (2007) 221504.

[14] Kurt H. Y., Exploration of the Townsend regime by discharge light emission in a gas discharge device, *Chinese Phys. B,* 23(1) (2013) 015201.

[15] Kurt H. H., Tanrıverdi E., The Features of GaAs and GaP Semiconductor Cathodes in an Infrared Converter System., *J. of Elect. Mater.,* 46(7) (2017) 4024-4033.

[16] Kurt H. H., Çetin S., Tanriverdi E., Yiğit D., Investigation of infrared GaAs photodetector instabilities, *Gazi Ün. Fen Bil. Der. Part C: Tas. ve Tek.,* 2(3) (2014) 281-288.

Analysing the spatial dynamics of earthquakes using event synchronization method: Anatolian Case

Ahmet ÇELİKOĞLU[1],*

¹ Ege University, Faculty of Science, Department of Physics, Izmir/TURKEY

Abstract

In this study, an earthquake network was created for the Anatolian region by using the event synchronization method. The prominent earthquake zones in Anatolia and some of their possible network properties have been investigated by using local measurements. As a result of the measurements, some patterns draw attention. One starts from the south of the Marmara Sea and extends to the inner and coastal Aegean region. It can be mentioned that there is an earthquake continuity, and almost every cell on the network acts as a possible bridge for stress transfer in this region. Other prominent patterns arise on the Eastern Anatolian Fault and close to Van. As the same earthquake and stress continuity appear on these regions and cells acts as a bridge. The data used in the analysis cover the period between 1999-2017. Earthquakes with magnitudes ranging from 5.5 to 6.9 occurred after 2017 in some prominent regions. On the other hand, some of them still silent. Results showed that these regions have the potential for future activities. On the other hand, the North Anatolian Fault and the south-west strand of the East Anatolian Fault remained silent. However, the part of the Eastern Anatolian Fault between Bingöl and Pötürge is very active.

1. Introduction

It is known that Anatolia faces the risk of earthquake hazards. This tectonic region is driven by three major lithospheric plates. The interaction of Eurasian, Arabian and African plates caused many fragments on the Anatolian Peninsula. Due to Eurasian and Arabian plates collisions, the Anatolian plate moves to the west. After the collision with the African plate, it goes down on the African plate along the Aegean subduction zone. These interactions and collisions create one of the most active and complex tectonic regions on Earth. Major faults and systems in Anatolia are given in Figure 1 in order to help to understand and compare network graphs in the next sections. For more information about the tectonic dynamics of the Anatolian Peninsula see [1].

Despite all efforts to explain and predict earthquakes, limited information has been gained, especially in the last century. This is a result of both the complex nature of the earthquakes and insufficient observations of the earth crust. Gutenberg-Richter, Omori and Bath laws are empirical laws and at the centre of this field [2-4]. To better understand this natural phenomenon, studies on to find different laws or scalings are continuing. Due to the complex nature of the earthquake, this

challenge is not easy. Maybe our pattern recognition abilities help us to understand nature as our ancient ancestors. We can search for new scaling and patterns by using the advantage of new technologies and new tools. The complex network method is a good candidate for this aim. Network theory has been applied in various areas such as power grid [5], internet [6,7], protein interactions [8], metabolic network [9], neural network [10] and as expected on earthquakes [11,12]. Although a few studies in the literature reveal such patterns, they have several deficiencies. On the other hand, linear analysis methods were generally used in these studies [11,12] (for more information, see [13]).

Very few of them handle the problem by using nonlinear methods. One of the good example of these nonlinear methods is the event synchronization method which will be discussed next section. This study aims to create an Anatolian earthquake network by using event synchronization method and analyzing the spatial dynamics of this network to investigate possible active regions and pathways of stress transfer. The same method and measurements were used to analyze to earthquake dynamic of Southern California, and remarkable results have been observed [13].
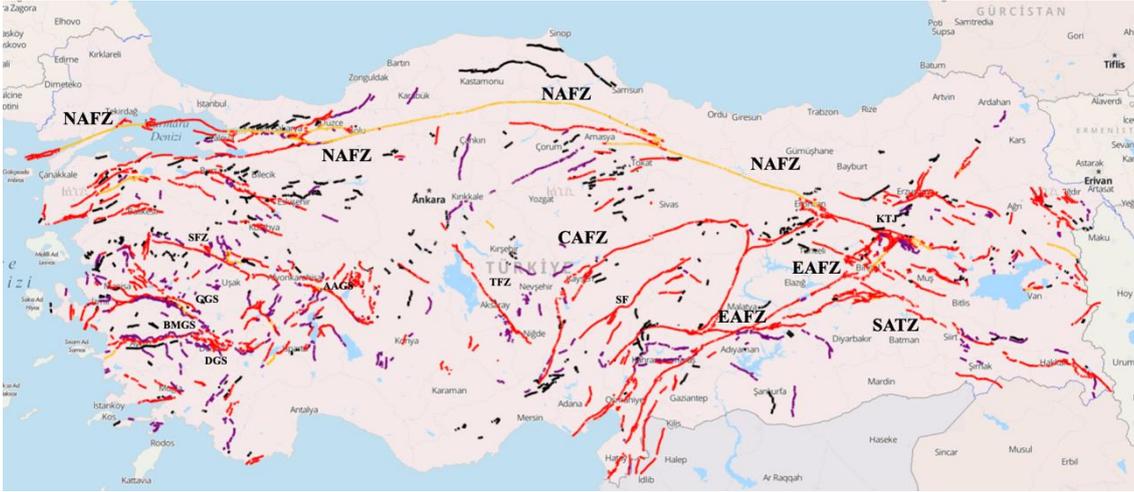
Figure 1. Anatolian major faults and systems. FAULTS: NAFZ: Northern Anatolia Fault Zone; EAFZ: Eastern Anatolia Fault Zone; CAFZ: Central Anatolia Fault Zone; SATZ: Southern Anatolia Trace Zone; SFZ: Simav Fault Zone, GGS: Gediz Graben System, BMGS: Büyük Menderes Graben System, DGS: Denizli Graben System, AAGS: Afyon-Akşehir Graben System; TFZ: Tuzgölü Fault Zone, SF: Sarız Fault, KTJ: Karlıova Triple Junction. Lines in different colours represent that; Yellow: Earthquake Surface Fracture, Red: Holocene Fault, Purple: Quaternary Fault and Black: Possible Quaternary Fault or Lineaments. Fault map is taken from [14].

2. Event Synchronization Method and Construction of Adjacency Matrices

Event synchronization has been introduced to analyze rat electroencephalogram and human EEG signals [15]. The method and its fractions have been applied to various fields such as Indian monsoonal rainfall [16,17]. The method has been applied to this geographical region and heavy rainfall events have been used in this version. Contrary to the EEG signals in the original version, earthquakes are discrete events, and they can be handled as a point process as in [17]. This approach gives advantages for the selection of τ, which is a control parameter in time and determines whether selected two events in different time series have synchronization with each other or not.

For simplicity, suppose we have two time series as x_n and y_n ($n = 1, \ldots, N$) and t_i^x and t_j^y represent the event times in each series. As one can easily guess that these events are earthquakes in our case. If an earthquake occurs at x_n just after an earthquake occurs at y_n, it is called an event pair. τ defines the maximum time interval between these events, which are counted as event pairs. This procedure is given mathematically as;

$$J_{ij}^{\tau} = \begin{cases} 1 & if & 0 < t_i^x - t_j^y \leq \tau \\ \frac{1}{2} & if & t_i^x = t_j^y \\ 0 & & else \end{cases} \tag{1}$$

Since the possibility of two earthquakes occurring simultaneously in both series is almost zero, the second condition has been ignored in this study. One can sum

event pairs by using the summation rule, which is given as;

$$C^{\tau}(x|y) = \sum_i^{m_x} \sum_j^{m_y} J_{ij}^{\tau}, \tag{2}$$

where $c^{\tau}(x|y)$ stands for an event occurs at x_n just after an event occurs at y_n, and the opposite of this case is represented by $c^{\tau}(y|x)$. The strength of event synchronization between these two series can be given as,

$$Q_{xy}^{\tau} = \frac{C^{\tau}(y|x) + C^{\tau}(x|y)}{\sqrt{m_x m_y}} \tag{3}$$

where m_x and m_y refer to the number of events at time series x_n and y_n, respectively. Q^{τ} is defined in $0 \leq Q^{\tau} \leq 1$ and $Q^{\tau} = 1$ ($Q^{\tau} = 0$) means that these two time series are fully synchronized (no synchronization). One can find the synchronization level between parts of the interested region under consideration by using this procedure.

The Anatolian earthquake catalogue is analyzed in our case. The data cover the period from 01/01/1999 to 01/01/2017. This data set is downloaded from the https://udim.koeri.boun.edu.tr/zeqdb/ website with the default area option. The area under consideration is divided into cells and earthquakes in each cell are listed as time series. Event synchronization level between any two cells can be measured by using the procedure mentioned above. If event synchronization between them is greater than a threshold, these two cells linked each other. If this procedure is applied between all cell pairs, the adjacency matrix of the network can be created. This matrix is given as,

$$A_{x,y} = \begin{cases} 1 & if\ Q^{\tau}_{xy} > Q_{thr} \\ 0 & else. \end{cases} \tag{4}$$

After constructing the network, the dynamical properties of the region can be observed by using network measurements.

3. Results

The Anatolian region has many faults and faults zones. The most famous one is the North Anatolian Fault Zone (NAFZ). Although the government, almost all media and many other organizations focus on this region; other parts of Anatolia are also at risk. It is vital to consider the whole picture. For this aim, this manuscript focuses on local measurements of the network to investigate active regions, possible pathways and spatial continuity of earthquakes. As mentioned above, the data cover the period from 01/01/1999 to 01/01/2017. Although the catalogue in https://udim.koeri.boun.edu.tr/zeqdb/ web site (Kandilli Observatory and Earthquake Research Institute catalogue) includes data before 1999, that period has some problems such as insufficient data or different magnitude thresholds, especially for early years. In order to include to Gölcük earthquake, the analyzed data set started in 1999. The catalogue includes $M \geq 2.5$ earthquakes for the early years of the analyzed period, but it includes $M \geq 2.0$ for recent years. The minimum magnitude threshold was chosen as $M_{th} = 2.5$ in terms of consistency and completeness of the analyzes.

Earthquake networks have been created for four different parameter combinations. These parameters are cell size, event synchronization, earthquake magnitude and τ values. As seen from Equation 1, τ value defines the maximum time interval between two events in any two nodes to count them as an event pair. τ values were chosen as 10, 30, 180, 365 days. It is known that the aftershock sequence of small earthquakes generally continues less than 10 days. Some small earthquakes can trigger a big one, but this manuscript handles the problem general perspective and does not count into account the behaviour of individual earthquakes. Also, the number of

earthquakes in the catalogue does not support to create networks with lower values of τ. Because of these reasons, the lower limit of τ was chosen 10 days. Since the aftershock sequence of almost all earthquakes in the catalogue ends less than one year, the upper limit was chosen 365 days. The lower limit of cell size threshold was chosen as small as possible (0.125°) in order to increase the number of nodes. The upper limit of cell size was chosen as 1°, and this size corresponds to approximately the rapture length of a 7.0 magnitude earthquake [18,19]. Another parameter is the magnitude threshold, and it was chosen as 2.5, 3.0 and 3.5. As explained previously, 2.5 is the minimum magnitude in the analyzed data. Since the number of $M > 3.5$ earthquakes does not support creating a network, the upper threshold was chosen $M = 3.5$. The last one is the event synchronization threshold Q_{th}. The interval of this threshold is 0 to 1.0, and the increments are 0.1. The event synchronization method has been used to study earthquake dynamics of the Southern Californian region [13]. It is found that one of the parameter combinations seems to reveal the dynamics of extraordinary earthquakes. Graphs that are created with this parameter combination will be given in results. On the other hand, other parameter combinations will be discussed.

As same in the Southern California region, some long-range links appear in the network. One can think that these kind of long-range links are not so reasonable. On the other hand, long-range interaction is a popular field of study. Also, the authors show that there is stress-stress interaction between nodes in the California region [20,21]. As mentioned above, this study handles the problem general perspective, and measures do not aim to explain the physical dynamics of interactions. The event synchronization value is chosen high to avoid link inflation, which can be obscure important nodes. These higher thresholds decrease the weight of long-range links in the network. So short-range links are dominant in measurements.

Major earthquakes in the analyzed period are given in Figure 2 for comparison results of measurements.
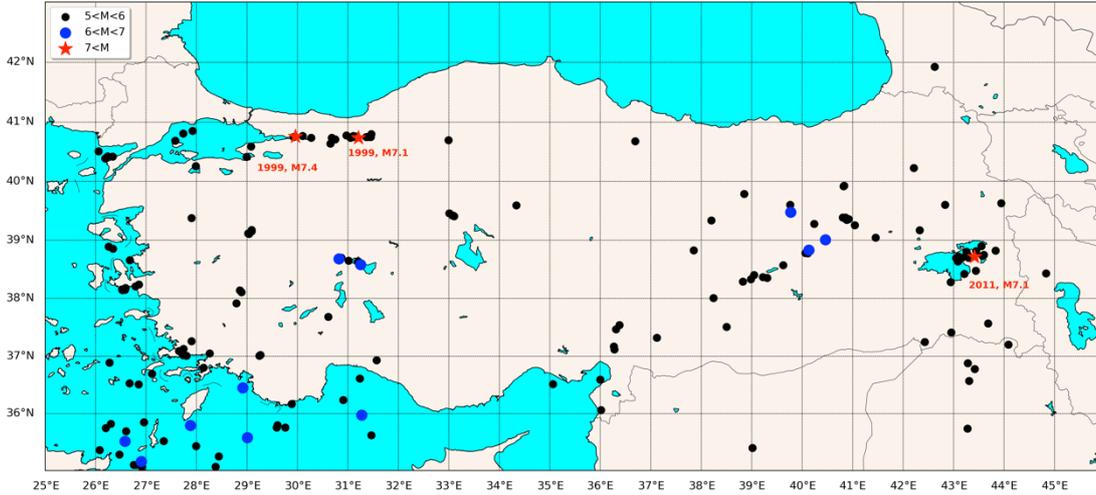
Figure 2. $M \geq 5.0$ Earthquakes between 01/01/1999-01/01/2017 in Turkey and surrounding region.

3.1. Degree centrality

Degree centrality is a good candidate for the observation of active regions. Since any node's degree centrality is related to the number of links of that node, this measurement is an indicator of that node's importance from the network point of view. It is given mathematically as;

$$C_j^D = \frac{\sum_{i=1}^{N} A_{ij}}{N-1} \tag{5}$$

where N is the number of nodes, and A_{ij} is the adjacency matrix. As seen from the equation, any node's degree centrality is the ratio of links of that node to that node's total possible links.

As seen from Figure 3, prominent regions generally correspond to regions where $M > 5.0$ magnitude earthquakes occurred in recent years in Figure 2. The well-known one of these earthquakes is Van Earthquake (October 2011; $M = 7.1$). The aftershock regime of this earthquake increased the activity of the near part region. This activity increases the chance of these cells becoming a part of the network. This situation shows itself as clustering around the northeast at the Van Lake. Another prominent structure in

Eastern Anatolia shows itself as a line. This pattern starts close to Karlıova/Bingöl, follows the Eastern Anatolia Fault Zone (EAFZ) and ends close to Pötürge/Malatya. It is the evidence of activity of the EAFZ in that region. Bingöl earthquake (May 2003, $M = 6.4$), occurred close to the starting point of this pattern. Karlıova Triple Junction (KTJ) is a part of this region, and it is well-known as an active region. This well-known activity has been clearly demonstrated in the network with degree centrality measurement. As same Sivrice earthquake recently happened at the point where this pattern ended. It should be noted that Karlıova-Pötürge part of this fault clearly shows itself in the figure. This fault bifurcates after Çelikhan. The main EAFZ starts from Karlıova and reaches Antakya. It includes the southern strand of the EAFZ. The northern strand between Çelikhan to Iskenderun Gulf called Sürgü-Misis fault system. Both northern and southern strands after Pötürge weekly show themselves in Figure 3. This week representation is a result of relatively few earthquakes on these strands of the fault system. This difference between the two areas of the same fault system can be interpreted as the southwestern part of the fault has not yet taken action, and attention should be paid to this area in the future.
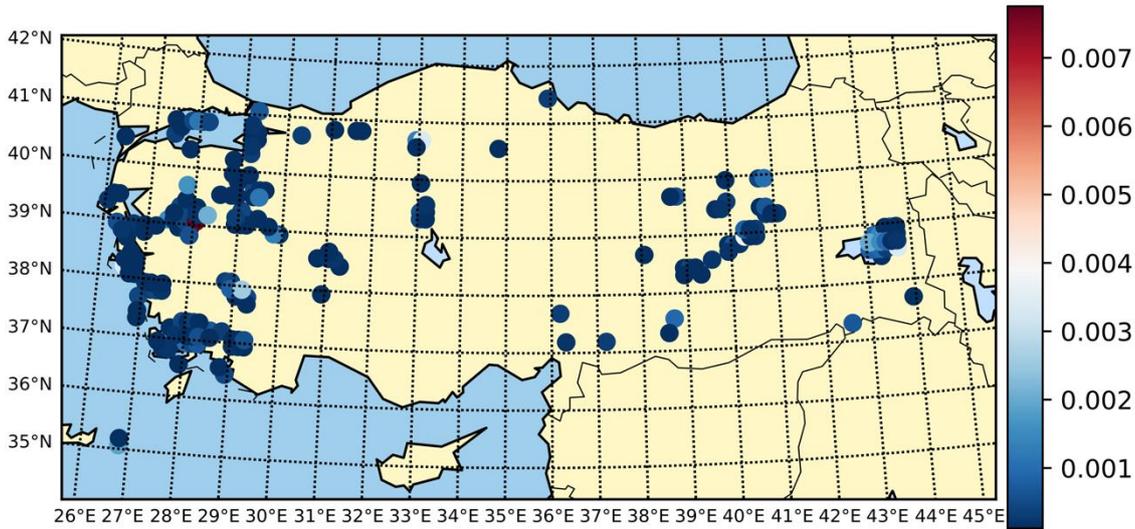
Figure 3. Degree centrality for $M_{th} = 2.5, \tau = 10$ days, $L = 0.125°$ and $Q = 0.9$.

Other prominent regions are the Aegean coasts and the southern Marmara region. The lineaments from İstanbul to Bursa, from Bursa to Balıkesir and Kütahya are trace to Northwest Anatolia Transition Zone. Notably, faults on Manyas-Bursa Bend and Simav Fault are very active, at least for small earthquakes ($M \geq 2.5$). Two different patterns at Aegean cost can be seen in Figure 3. One of them started from Lesbos Island and ended in Kuşadası/Aydın. If one focus on this lineament can see formations perpendicular to Aegean costs. These formations reveal the fault structure of the region. The second lineament can be seen at Gökova Bay. It starts from Kos Island, and it reaches approximately 50 km inside the land. This lineament is a result of frequently occurred earthquakes in that region. It should not be forgotten the effects of the earthquake storm at Gökova Bay. Earthquake storms increase these regions event synchronization levels and help them to be part of the network. It is notable that there are two parallel and long lineaments. On the other hand, there are a few relatively short faults known and drawn in the fault maps. There may be a different fault structure that starts from the inner part of the Aegean Sea and continues on land. These structures show that conducting seismic surveys in the Aegean Sea is essential for understanding the seismicity of the region. These researches should be considered to continue on the land, especially between Köyceğiz and Fethiye.

Apart from these, relatively small clusters or single cells can be seen as a part of the network in degree centrality figure (Figure 3). These active regions are Denizli Graben System (GBS), Afyon-Akşehir Graben System (AAGS), the region at the north to the Tuz Lake, some cells eastern part of the NAFZ close to Erzincan and Erzurum, the western strand of the NAFZ, southern and northern strands of EAFZ and some single cells.

One should note that the magnitude threshold is $M \geq 2.5$ in Figure 3. So the term of activity is related to "How often that cell generates an earthquake which magnitude is greater than 2.5". It is not directly related to "How big an earthquake occurred in that cell". Of course, bigger earthquakes affect their surrounding regions, and its aftershock sequence dominates the catalogue for a certain period at that region and increases the event synchronization level of these cells. We can clearly see effects of $M > 6.0$ earthquakes at its surrounding region such as Van ($M = 7.2$, 2011), Orta ($M = 6.1$, 2000), Çay-Sultandağı ($M = 6.4$, 2002), Pülümür ($M = 6.2$, 2003), Bingöl ($M = 6.4$, 2003), Simav ($M = 5.9$, 2011) earthquakes. On the other hand, if there are frequently occurring $M > 2.5$ earthquakes in any cell, they also increase the event synchronization level of that cell. This means that a cell that regularly generates earthquakes does not need a major earthquake or earthquake storm, to be represented on the network.

If the magnitude threshold increases as $M \geq 3.0$, many cells cannot be part of the network. Only a few of them survive. They are represented as a single cell and small clusters. These small clusters are located at Sığacık Bay, Gökova Bay, Simav, Izmit Bay, Denizli, close to Bala/Ankara, Van, Karlıova/Bitlis and its surrounding region, and a single cell is at the Çorum. It is notable that there are $M > 5.5$ earthquakes in these regions. It can be concluded that many cells in Figure 3 generally generates earthquakes between $2.5 < M < 3.0$. These cells cannot stay to be part of the network for $M \geq 3.0$.

Degree centrality values increase when τ increases. As expected both, new cells join the network, and existing cells make extra connections. Almost all new cells are located aforementioned active regions and, they create more coward clusters step by step as τ increase up to 365 days (10,30,180,365). Especially lineament at Gökova Bay is notable. This lineament is about 200 km long.

The total number of cell degrees for larger cell sizes (0.125°, 0.25°, 0.50°, 1.0°). On the other hand, the number of earthquakes in each cell increase. Is a result of this, degree centrality values increase for these cells. Since we represent the same area with fewer cells, the fault traces appear coarser. This masks the active regions. It is like looking at a photograph with a lower resolution. It seems that (0.125° × 0.125°) cell size is the better option for creating a network with the possible highest resolution. Hereafter, other cell sizes will not be mentioned unless they are necessary.

Another parameter is the event synchronization threshold. Decreasing the event synchronization threshold has the same effect as increasing τ. One can think that using a higher τ and lower event synchronization threshold is an ideal option in order to create a network with higher magnitude thresholds. Although it seems a good option, the number of earthquakes with $M > 3.0$ not enough to realize this opinion. On the other hand, we do not want to decrease the event synchronization threshold so lower values since to avoid the effects of possible random event pairs.

3.2. Betweenness centrality

Betweenness centrality is another measure of the importance of a node. It is based on if a node is on the connection path of any two nodes, this node is important for the communications of these two nodes. From the point of information flow view on a network, these nodes with high betweenness values are important. Due to this advantage, they can receive all information between nodes whose shortest path passes through these nodes. A node with a high betweenness value may have a very low degree centrality or any

other centralities. However, it can be still so important for the network, especially if it is only one node between two parts of the network. Betweenness centrality can be informative in terms of stress propagation paths for an earthquake network. This measurement is given as,

$$C_k^B = \sum_{k \neq i \neq j} \frac{\sigma_k\,(i,j)}{\sigma\,(i,j)}, \tag{6}$$

where $\sigma_k(i,j)$ is the number of shortest paths between i and j passing through k and $\sigma(i,j)$ is the number of all shortest paths between i and j.

As seen from Figure 4 previously mentioned regions draw the attention. If we start from the east, the first pattern can be seen close to the Van Lake and this pattern is probably highly dominated by the 2011 Van Earthquake. Aftershocks of this earthquake increased the possibility of nearby nodes becoming a part of the network. It seems that each node has a role for stress transfer for that region. As same with degree centrality, lineament on EAFZ, clusters at Southern Marmara, Bala, Simav, Sığacık Bay, Denizli, Gökova Bay are other active regions. Cells at these regions may have a role in stress transfer. We think that these patterns are the results of $M > 5.5$ earthquakes in these regions. Aftershock sequences of these earthquakes dominate their surrounding regions. It is thought that the accumulated stress is transferred to others through these cells. Thus, each cell acts as both a new resource and a bridge to stress transfer to its surrounding regions. One red coloured cell close to Gökova Bay has the highest betweenness centrality. However, this cell cannot continue its importance with different parameter combinations. In addition to this, most of the cells have approximately the same betweenness centrality value. It seems that these cells have the same importance for possible stress propagation. Although the energy can separate all directions after an earthquake, stress prefers to transfer along to the fault direction. As a result, almost all cells on this fault are between others and have approximately the same importance for stress propagation. Similar results have been observed in [13].
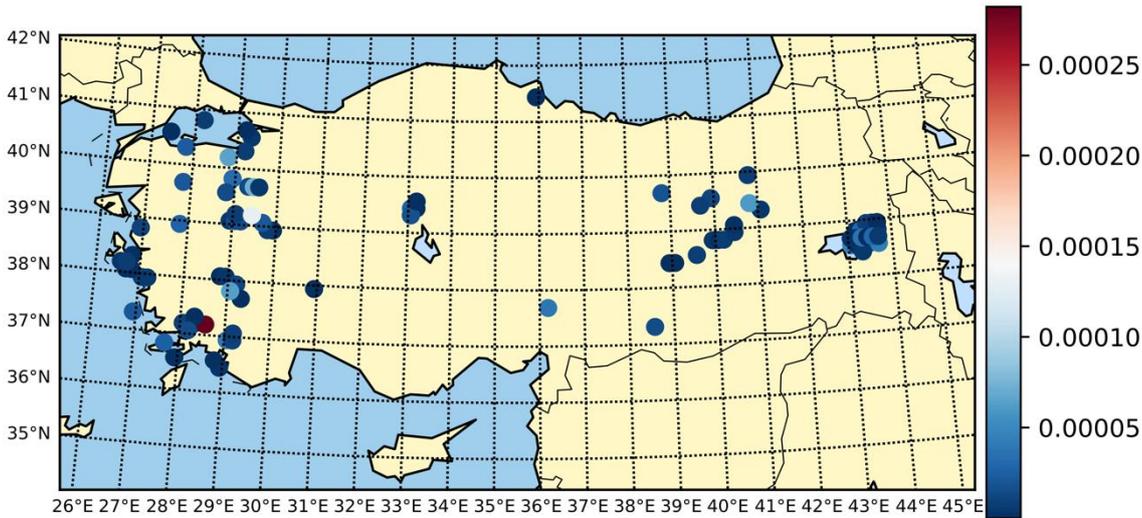
Figure 4. Betweenness centrality for $M_{th} = 2.5, \tau = 10$ days, $L = 0.125°$ and $Q = 0.9$

On the other hand, the number of cells in active regions increases with increasing τ. Especially when it increase 10 days to 30 days, the number of cells in active region clusters is close to the number of cells for 180 days and 365 days. However, it is seen that betweenness values decrease with increasing τ. Of course, as the τ increases, the possibility of occurrence an earthquake at that period of time in each cell increases, so more cells make connections with each other. Thus, many alternative shortest paths can be appeared between any two cells and betweenness values decrease. Besides a lineament along the Marmara Sea draws attention with increasing τ. A network structure goes south perpendicularly to this lineament and then connects to Izmir via Manisa. This structure seems to consist of a lineament from İzmit to Kütahya, a cluster at Manisa and Balıkesir and another lineament from Lesbos Island to Kuşadası. There are many faults and fault zones in the region Southern Marmara, Simav, and Manisa. Although they are considered independent zones, the network structure gives the impression that the NAFZ's effect is carried over the Aegean coast via these faults. It can be interpreted that the stress caused by the NAFZ can be carried to the Aegean shores on a long time scale. Also, Gökova Bay is another important region. The structure in this region become more evident with increasing τ. As mentioned before, it is known that there are many faults in the region, most of which are short. These faults have caused earthquake storms in the recent past. On the other hand, as mentioned before, the long lineament structure, which we consider to be stress continuity, may indicate a different fault mechanism in the region. Another

structure on the EAFZ between Bingöl and Hatay emerged more clearly with increasing τ. In other words, it is thought that there may be a stress transfer along this line. Other prominent regions where cells behaviour as a bridge for possible stress transfer are Denizli, Afyon, north to Tuz Lake and Van Lake. More prominent clusters arise with increasing τ in these regions. Decreasing event synchronization level almost the same effect with increasing τ.

3.3. Local clustering coefficient

The local clustering coefficient is another measurement on a network that has the potential to provide useful information about the regions mentioned above. This measurement has been used to understand spatial continuity of rainfall events for monsoon rainfalls in India [16] and spatial continuity of earthquakes for the Southern California Earthquake region [13]. If two connected nodes are also connected with a third one, it is called a triad. The ratio of the total triads to the possible triads of a node gives its clustering coefficient value. This is a measure of how neighbours of this node are close to a clique. Suppose that there are k_j neighbours of node j. The number of total possible links between neighbours of this node is $k_j(k_j - 1)/2$. On the other hand, this is the maximum value and generally real number of total links between neighbours less than this maximum. If there are ε_j links between neighbours, the local clustering coefficient can be given as,

$$C_j^{LCC} = \frac{2\varepsilon_j}{k_j(k_j-1)}. \tag{7}$$
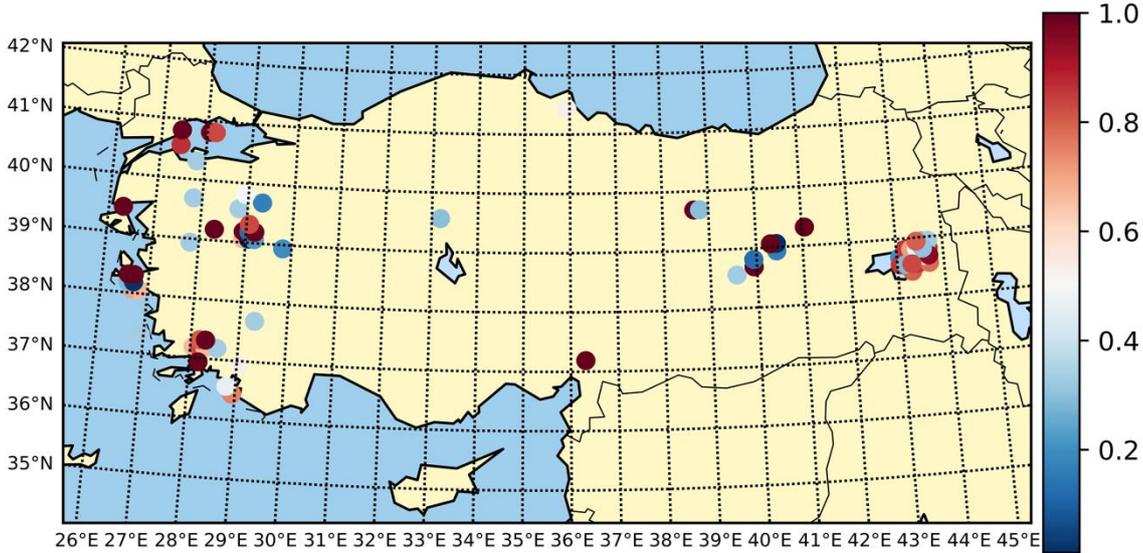
Figure 5. Local clustering coefficient for $M_{th} = 2.5$, $\tau = 10$ days, $L = 0.125°$ and $Q = 0.9$

As seen from Figure 5, almost the same previously mentioned regions have a kind of earthquake continuity. They are KTJ, Van, Kütahya- Manisa, İzmir, Gökova Bay and the Marmara Sea. We think that after an earthquake happens in these regions, another earthquake frequently occurs in their surrounding regions. Hence, it can be interpreted as a stress continuity in the surrounding region of the main earthquake.

The network becomes more crowded with increasing τ. The patterns on to EAFZ and at the Van Lake are noticeable formations at the east. On the other hand, more contribution to the network comes from Marmara and Aegean regions. A lineament starts from Bolu and reaches the west coast of the Maramara Sea. This lineament is the trace of NAFZ in that region. It shows that there is an earthquake continuity at fault direction. Another pattern in the Marmara region starts from the İstanbul-Adapazarı region and reaches Kütahya in the Aegean region. Pattern touches cluster on to Balıkesir-Manisa region. This cluster bounded another lineament which starts from Lesbos Island, passing through Izmir and reaches Kuşadası. These patterns can be interpreted as earthquake continuity and stress continuity in this region. This continuity is an effect of the NAFZ to the western part of this fault at the Marmara Sea and the western part of the Aegean region. Similar to previous findings pattern along to the Gökova Bay, Denizli, Afyon, and the region north to the Tuz Lake draw attention. In light of all these, it can be said that there are earthquake continuity and possible stress continuity in the mentioned regions in long time intervals, which is not clearly seen in a short period.

3.4. Discussion

As previously mentioned, this manuscript focus on local network measurements to understand earthquake network dynamics of the Anatolian region. It is shown that the western part of Anatolia is more active and has earthquake and possible stress continuity. Although it seems to be the result of medium and large-scale earthquakes, small earthquakes that frequently occur in the region have also been effective in the analysis. It is known that there are many faults and fault zones in the western part of Anatolia. These faults and faults zones create independent tectonic structures. There are different patterns as a result of local measurements. The first one is a lineament Bolu to the west coast of the Marmara Sea. The second pattern perpendicular to the first one stars from the east coast of the Marmara Sea and reaches Kütahya. The third one is another lineament that starts from Lesbos Island and reaches Kuşadası/Aydın. Between them, a cluster shows itself at Manisa and Balıkesir. The last one appears at Gökova Bay. These patterns show that there are earthquake activities. Many cells at these regions may serve as a bridge for possible stress transfer to surrounding cells, and there are spatial earthquake continuities. These patterns appear more clear for higher values of τ. These results led us to think that the NAFZ somehow affected the central and western Aegean regions.

Other prominent patterns appear at Van Lake and region between Karlıova/Bingöl and Pötürge/Malatya. Pattern at Van Lake is dominated by Van Earthquake. A cluster appears as a result of aftershocks in the region. Many surrounding cells are part of this cluster, and there is an earthquake continuity in this region.

These cells also serve as bridges. Also, the pattern appears as a lineament on the EAFZ. It seems there are many activities on the Karlıova-Pötürge part of this fault. These activities show that an earthquake continuity appears in this region. It seems that there is possible stress transfer and, many cells serve as bridges on the lineament. It should be noted that activity on the fault after Pötürge is weaker than the Karlıova-Pötürge part. As a result, the west-south part of the fault does not or weakly represented for different parameter combinations. Although the analyzed period (1999−2017) is not so long, that kind of weak activity may not be meaningful for this region. We would like to point out that there may be an accumulation of stress in this part and, there may be possible belated earthquakes.

Other little clusters appear at Denizli, Afyon, Ankara. It seems that clusters at Denizli and Afyon are results of activities on the DGS and AAGS. The cluster that appears at Bala/Ankara is a result of the Bala Earthquakes (2005, 2007, 2008). These earthquakes occurred north end of the Tuzgölü Fault Zone. It should be noted that this project covers the period 1999-2017. It is known that few earthquakes happened in regions mentioned above after January 2017. Their magnitudes are between 5.5 to 6.9. Especially Sığacık Bay is an active region in all three measurements. Also, this region remains part of the network with different parameter combinations. It is one of the two active cells all Anatolia with high parameter combinations. Other cell is in the Van. Contrary to Van there is no major earthquake in the analyzed period. Samos-Izmir earthquake (M=6.9, October 2020) occurred after the analyzed period just close to that cell. We conclude that it may be evidence of other mentioned regions are also at risk.

Acknowledgments

Conflicts of interest

The author state that did not have conflict of interests

References

[1] Emre Ö., Duman T.Y., Özalp S., Şaroğlu F., Olgun Ş., Elmacı H., Çan T., Active fault database of Turkey, *Bull. Earthquake Eng.*, 16 (2018) 3229-3275.

[2] Gutenberg B., Richter C.F., Frequency of earthquakes in California, *Bull. Seismol. Soc. Am.*, 34 (4) (1944) 185–188.

[3] Omori F., On the aftershocks of earthquakes, *J. Coll. Sci., Imp. Tokyo*, 7 (1894) 111-120.

[4] Bath M., Lateral inhomogeneities of the upper mantle, *Tectonophysics*, 2 (1965) 483-514.

[5] Watts D.J., Strogatz S.H., Collective dynamics of 'small-world' networks, *Nature,* 393 (1998) 440-442.

[6] Faloutsos M., Faloutsos P., Faloutsos C., On Power-Law Reltionship of the Internet Topology, *Computer Communications Review*, 29 (1999) 251-262.

[7] Chen Q., Chang H., Govindan R., Jamin S., Shenker S.J., Willinger W., The origin of power laws in internet topologies revisited, *Proceedings of the 21st Annual Joint Conference of the IEEE Computer and Communications Societies, IEEE Computer Society* (2002).

[8] Jeong H., Mason S., Barabasi A.L., Oltvai Z.N., Lethality and centrality in protein networks, *Nature,* 411 (2001) 41-43.

[9] Jeong H., Tombor B., Albert R., Oltvai Z.N., Barabasi A.L., The large scale organization of metabolic networks, *Nature*, (2000) 407-651.

[10] White J.G., Southgate E., Thompson J.N., Brenner S., The structure of the nervous system of the nematode Caenorhabditis elegans, *Phil. Trans. R. Soc. B,* (1986) 314.

[11] Abe S., Suzuki N., Small-word structure of earthquake network, *Physica A,* 337 (2004) 357-362.

[12] Abe S., Suzuki N., Complex-network description of seismicity, *Nonlin. Processes Geophys.*, 13 (2006) 145-150.

[13] Celikoglu A., Earthquake spatial dynamics analysis using event synchronization method, *Phys. Earth Planet. Inter.*, 306 (2020) 106524.

[14] Emre Ö., Duman T.Y., Özalp S., Elmacı H., Olgun Ş., Şaroğlu F., Active Fault Map of Turkey with an Explanatory Text. 1:1,250,000 Scale, General Directorate of Mineral Research and Exploration, Special Publication Series-30, Ankara-Turkey.

[15] Quian Quiroga R., Kreuz T., Grassberger P., Event synchronization: a simple and fast method to measure synchronicity and time delay patterns, *Phys. Rev. E,* 66 (2002) 041904.

[16] Malik N., Marwan N., Kurths J., Spatial structures and directionalities in Monsoon precipitation over South Asia, *Nonlin. Processes Geophys.*, 17 (2010) 371-381.

[17] Malik N., Bookhagen B., Marwan N., Kurths J., Analysis of spatial and temporal extreme monsoonal rainfall over South Asia using complex networks, *Clim. Dyn.*, 39 (2012) 971-987.

[18] Wells D.L., Coppersmith K.J., New empirical relationship among magnitude, rupture length, rupture area and surface displacement, *Bull. Seismol. Soc. Am.*, 84 (4) (1994) 974-1002.

[19] Konstantinou K.I., Papadopoulos G.A., Fokaefs A., Orphanogiannaki K., Emprical relationships between aftershock area dimensions and magnitude for earthquakes in the Mediterranean sea region, *Tectonophysics*, 403 (2005) 95-115.

[20] Efstathiou A., Tzanis A., Vallianatos F., On the nature and dynamics of the seismogenetics systems of North California, USA: An analysis based on Non-Extensive Statistical Physics, *Phys. Earth Planet. Inter.*, 270 (2017) 46-72.

[21] Efstathiou, A., Tzanis A., An examination of the nature and dynamics of seismogenesis in south California, USA, based on Non-Extensive Statistical Physics, *Phys. Earth Planet. Inter.*, 284 (2018) 51-71.

An econometric model for popularrity on media

Orçun AYDIN[1] 🆔 *, Erol TERZİ[2]** 🆔

[1] *Turkish Statistical Institute (TurkStat), Ankara/TURKEY*

[2] *Ondokuz Mayıs University, Faculty of Science, Department of Statistics, Samsun/TURKEY*

Abstract

This paper aims to determine and estimate an econometric model which can be used to forecast media popularity of a governmental organization. Number of media sources monitored was used as regressors while taking types of these sources into account. Some linear models were estimated besides some non-linear models. According to the results, number of national, local, regional newspapers and number of television channels monitored were not found important to estimate number of news caught through media monitoring. On the other hand, number of internet media sources was found important to estimate the dependent variable. Additionally, number of news caught on select subjects in previous year was also found important. In the end an autoregressive panel data model with some additional regressors such as number of monitored sources was suggested to forecast popularity of organization. Any data only accessible to TurkStat members was never used in this paper. TurkStat is not responsible for any inference made in this study.

1. TurkStat and Media Monitoring

Turkish Statistical Institution disseminates more than one hundred press releases each year. On most of the workdays announced press releases attracts wide attention from governmental and academic organizations also from public. In this paper dataset on news between the years 2012 and 2020 was studied. Any data only accessible to TurkStat members was never used in the study. TurkStat is not responsible for any inference made in this study.

Media monitoring is an interesting subject and risks can be minimized with monitoring [1]. To extract the useful information from this mass data, Press and Public Relations Department at TurkStat works on daily cycle agenda and gets the news form selected sources on every morning. Then a team leader attains the news to staff for tagging. The workload of each staff is determined by the consultant by taking their other daily tasks. Then each staff reads the news attained themselves and process them by entering data interested (tagging and classifying). Classification of Negative Information on Socially Significant Topics in Mass Media was also studied before [2]. But TurkStat needs to handle not only comments but also subjects to inference and decide on a detailed communication strategy. Government communication is framed within political communication itself and refers to the exercise that determines the management agenda of institutions, attitudes, and processes [3].

In this paper topmost important subjects were determined and then an econometric forecasting strategy was tried. At first, all the 369,938 news in 2020 are searched and then classified according to the list used by Press and Public Relations Department at TurkStat. However, all the dataset needed was formed and built up from scratch because it is not wanted to use any data only accessible to TurkStat members.
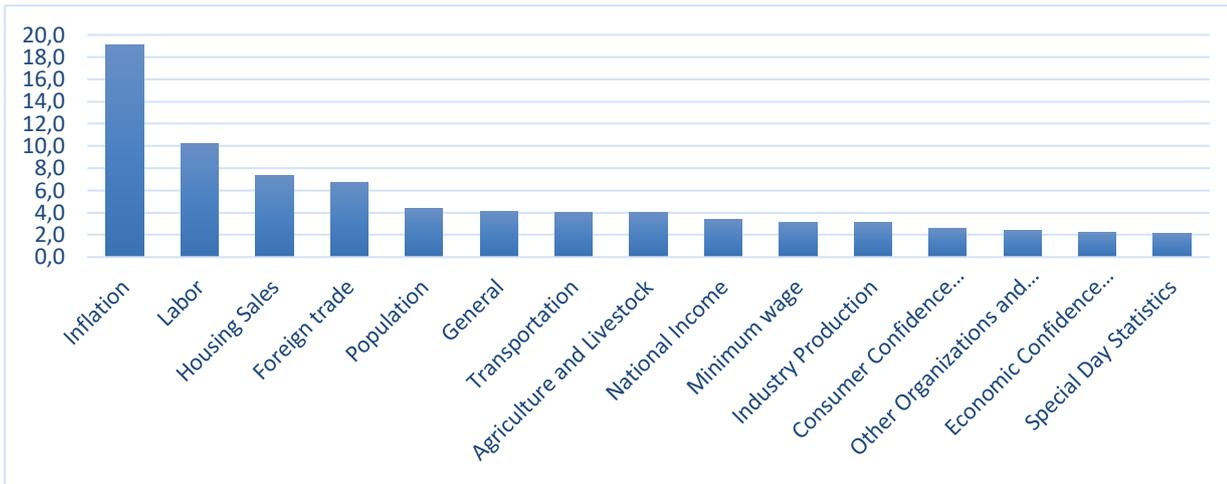
Figure 1. Top fifteen subjects on media in 2020

Then the order of the table was changed in decreasing order according to the amount of news for each subject. It has been seen that the top 12 subjects accounts for more than 70% off all the news in 2020. So, these subjects were chosen as cross-sections to eliminate heterogeneity bias [4].

In the above figure, minimum wage, foreign trade, inflation, labor force, house sales, general (corporation), gross domestic product (GDP), population, industrial production, agriculture, consumer confidence index (CCI), and transportation are the top twelve subjects in 2020.

2. Data and Method

Any data only accessible to TurkStat members was never used in the study. Only the open access data and meta-data were used to analyze the popularity of TurkStat on media. A third-party media monitoring tool was used as a service to search and access texts and media. By using this service news with given uniform resource locaters (URL) were searched with selected keywords above-mentioned. Then, they were classified using the list of subjects. In this process it is seen that some news belongs to more than one class. In such situations, their class is determined by looking the density and meaning, subjectively.

Table 1. Number of news according to selected subjects by year

Subjects	2012	2013	2014	2015	2016	2017	2018	2019	2020	Total
Minimum Legal Wage	270	222	856	2,105	3,924	3,160	6,086	7,235	11,589	35,447
Foreign Trade	2,455	3,024	11,809	14,235	20,060	23,749	26,300	23,510	24,968	150,110
Inflation	2,696	3,116	16,228	23,116	29,711	36,990	48,547	57,937	70,637	288,978
Labour Force	2,249	3,312	11,620	14,270	16,988	24,543	22,491	27,799	37,846	161,118
House Sales	113	699	7,177	11,513	16,565	19,210	21,454	23,762	27,164	127,657
General	404	947	5,495	5,609	12,371	7,613	7,611	5,262	15,179	60,491
GDP	747	1,202	3,491	6,261	11,145	15,469	10,726	9,647	12,532	71,220
Population	1,152	2,023	6,339	5,998	12,136	12,635	14,721	13,339	16,130	84,473
Industry Production	766	1,233	3,782	5,065	1,770	8,326	8,509	8,764	11,477	49,692
Agriculture	1,386	2,136	9,266	12,454	14,834	18,386	15,075	15,223	14,788	103,548
CCI	251	451	1,971	4,000	4,265	4,975	4,887	5,634	9,611	36,045
Transportation	841	1,687	5,484	7,924	12,863	13,163	16,263	12,509	14,811	85,545
Total	13,330	20,052	83,518	112,550	156,632	188,219	202,670	210,621	266,732	1,254,324

In the above table, amount of news by selected subjects and by years can be seen for the time period between years 2012 and 2020. Top twelve subjects are the rows of table. This selection makes analyzing easier as the reduced table accounts for more than 72% of all data. For the year 2020, there are 266,732 news caught on these subjects. Without selection, there are 369,938 news caught on all the subjects including the unclassified ones.

In the below table, number of media sources for media monitoring can be seen. About 1,165 sources were monitored for 2012 while it has increased up to 4,172 in 2020. In this paper, the number of media sources used for monitoring was used as dependent variable and effect of this variable on the popularity of TurkStat on media was investigated. Amount of news was used as a proxy for this popularity.

Table 2. Number of media sources according to media types

Years	National Newspapers	Local N.	Regional N	Magazines	Tv Channels	Internet Media	Total
2012	45	250		800	70		1.165
2013	48	668		1.059	160		1.935
2014	46	503	210	1.489	81	394	2.723
2015	52	378	228	1.137	98	1.098	2.991
2016	51	536	212	1.189	74	1.501	3.563
2017	51	536	212	1.189	75	1.605	3.668
2018	51	536	212	1.189	75	1.605	3.668
2019	57	379	212	1.189	107	2.228	4.172
2020	57	379	212	1.189	107	2.228	4.172

According to the table above, internet as a media source type accounts for most of the sources. Cost of internet press is so less compared to all other traditional ways. Magazines takes the second place however amount of news on this type of source is not so high as expected. Because the time period from 2012 to 2020 is not enough for a time series analysis, a panel data approach is more convenient to apply. So, selected subjects are used as cross sections.

Many researchers illustrated panel data analyses deeply [4-10]. According to them, a general panel data regression model can be represented as below.

$$Y_{it} = \mu + \mu_i + \beta_1 X_{1,it} + \beta_2 X_{2,it} + \cdots + \varepsilon_{it} \qquad (1)$$

Here, the variable Y_{it} is the dependent variable and regressed on $X_{1,it}$, $X_{2,it}$ and so on. The heterogeneity between cross sections is represented by the cross-sectional intercept term μ_i. Here, μ is the general intercept for the panel data regression model. ε_{it} represents errors and $\beta_i's$ are the slope parameters to be estimated.

Covariance analysis for this panel data model was explained to identify the source of sample variance [4]. As mentioned, this method allows the true relation for each individual to depend on the class to which the individual belongs. As explained in panel data regression analysis effects are assumed to be fixed or random [4]. Fixed effects models can be estimated with

dummy variable approach using ordinary least squares method and this estimator is called as covariance estimator.

In this manner, it also includes some advantages of usual analysis of variance [4]. As explained, panel data gives the researcher large number of data points. Suppose researcher has ten individuals and gathered data about them for ten years' time period. So, ten years is not enough for a time series analysis neither for a cross sectional analysis. But in the end with this panel data approach, researchers have one hundred data to use. Additionally, panel data gives the opportunity to investigate some questions impossible to get answers with time-series or cross-sectional data sets. Making dynamic inference is not possible with a cross-sectional data set. Multiple information for an individual decreases the negative effect of measurement errors. Panel data gives the model a chance to learn individual's behavior from other ones' behaviors.

On the other hand, panel data sets have some disadvantages also [4]. Firstly, analyze is more complicated compared to simple cross-sectional or time-series analysis. Unobservable regressors correlated with other regressors in the model can lead to biased estimators as explained.

3. Results and Discussion

At first, data was visualized, descriptive statistics was found for the 2020 data. By this way, the range of the data to be used was discussed to make things simple while keeping study representative. At the figure below, all the news by months can be seen for the year 2020.
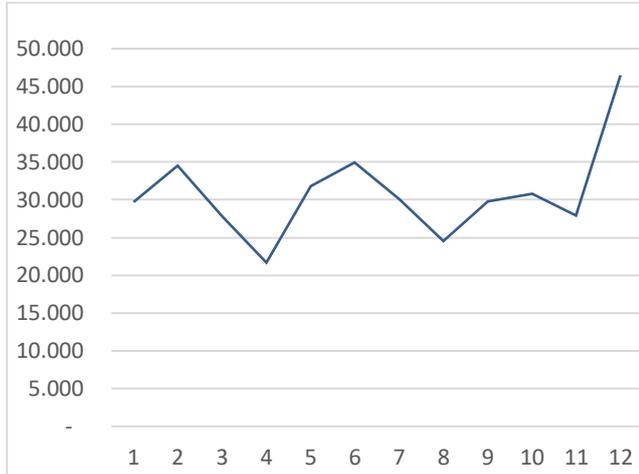

Figure 2. Amount of news by months in 2020

The number of news is not sable among months and follows a fluctuating pattern. Additionally, second, sixth and twelfth months experienced the top three amounts of news.

At the figure below, amount of news by months and by media type can be seen. In total, 369,938 news were caught to our monitoring system. Data for internet media type as 2254 thousand news does worth mentioning for the internet media type. This is the case for all the years from 2012 to 2020. This domination comes from the fact that internet press publishing is much easier compared to traditional arenas as for low costs and also for the effort needed to publish. In the end, it is so wide to publish news with embedding in web pages.
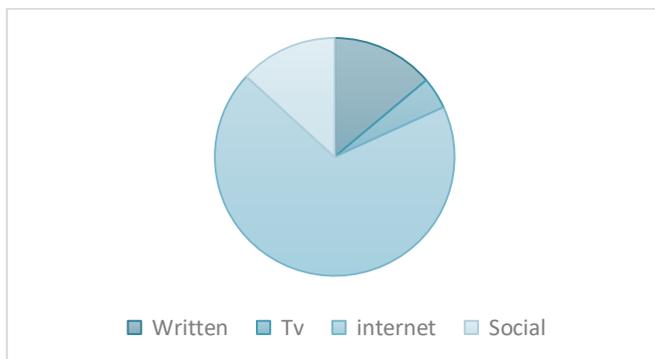
Figure 3. Number of news by nedia types in 2020
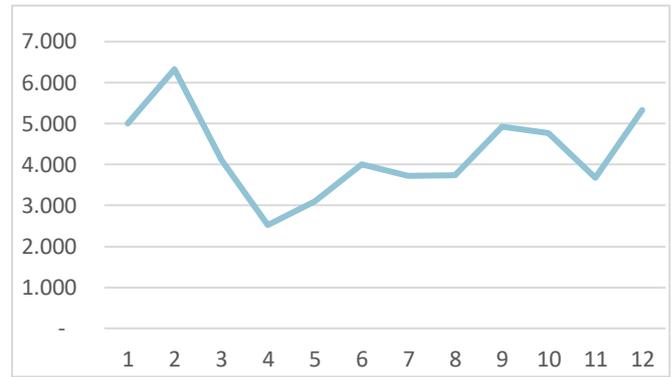
Figure 4. Number of news by months on written sources in 2020

In the figure above, written news caught by our monitoring system shows a different fluctuating pattern from the general line illustrated before. Observation performs a peak in second month with more than six thousand news. However, this trend falls below three thousand news on fourth month. An upward trend can be seen towards to the end of the year 2020. According to these points it can be said that every type of media source performs a different pattern peculiar to themselves.
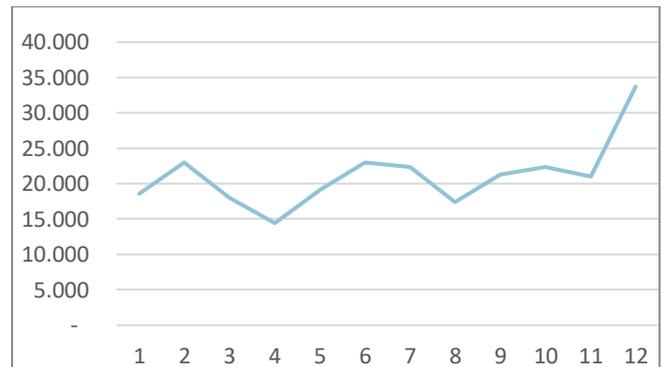

Figure 5. Number of news by months on internet sources in 2020

Internet media type is less volatile between 15,000 and 25,000 news. However, amount of news on internet media sources performs more than ten thousand news on each month. A similar peak and deep can be seen on second and fourth months as other media types.
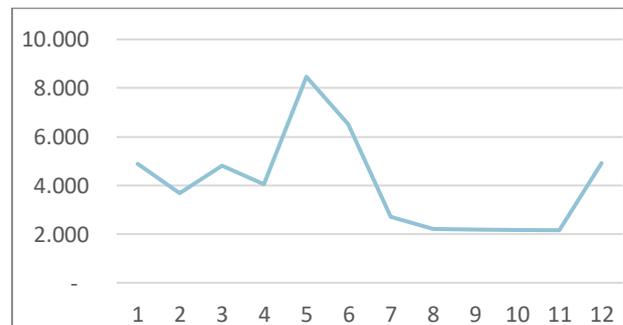

Figure 6. Number of news by months on social media sources in 2020

937

Social media sources perform a different pattern compared to other three types. Number of news fluctuates between two thousand and nine thousand. On the fifth month a strong peak can be seen with more than five thousand news. On the seventh month line falls below three thousand news and goes through an approximately stable level until eleventh month. Towards the end of the year a strong trend shows up again.
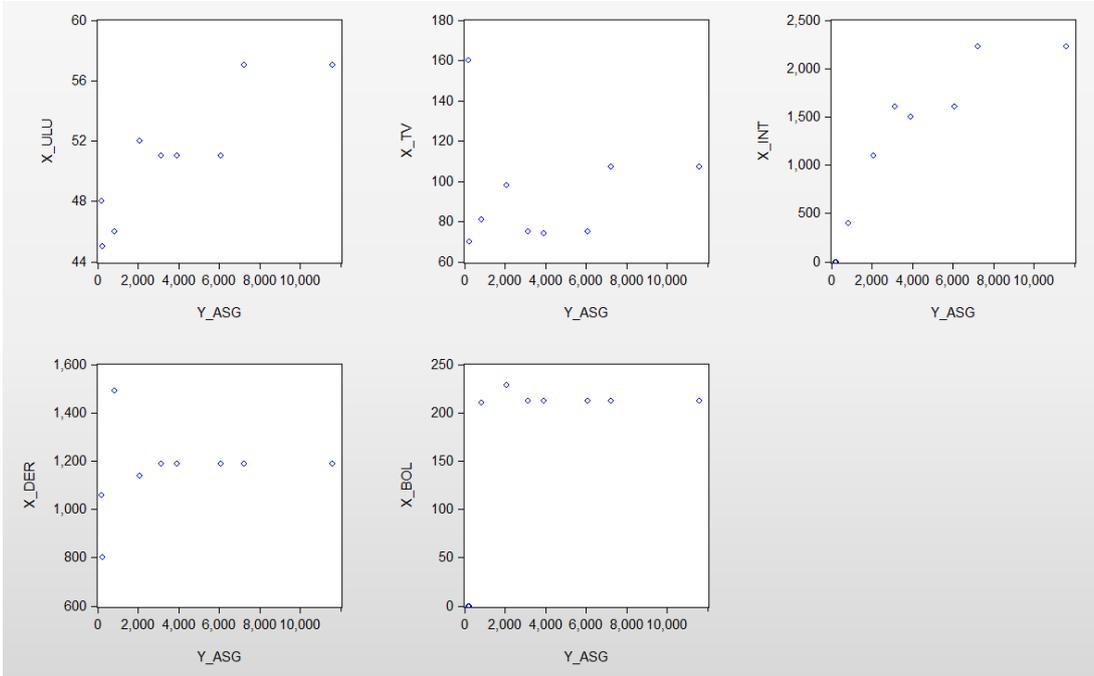

Figure 7. Scatterplot between minimum wage and types of media sources

Scatter plot above shows a nearly linear correlation between national newspapers. A similar linear structure can be seen between minimum wage and Tv's but with a less correlation noticed visually. Correlation between minimum wage and internet media type is like linear but in some scatterplots square like correlation can also be seen. However, magazine and regional media sources visually has not a strong correlation between minimum wage news.
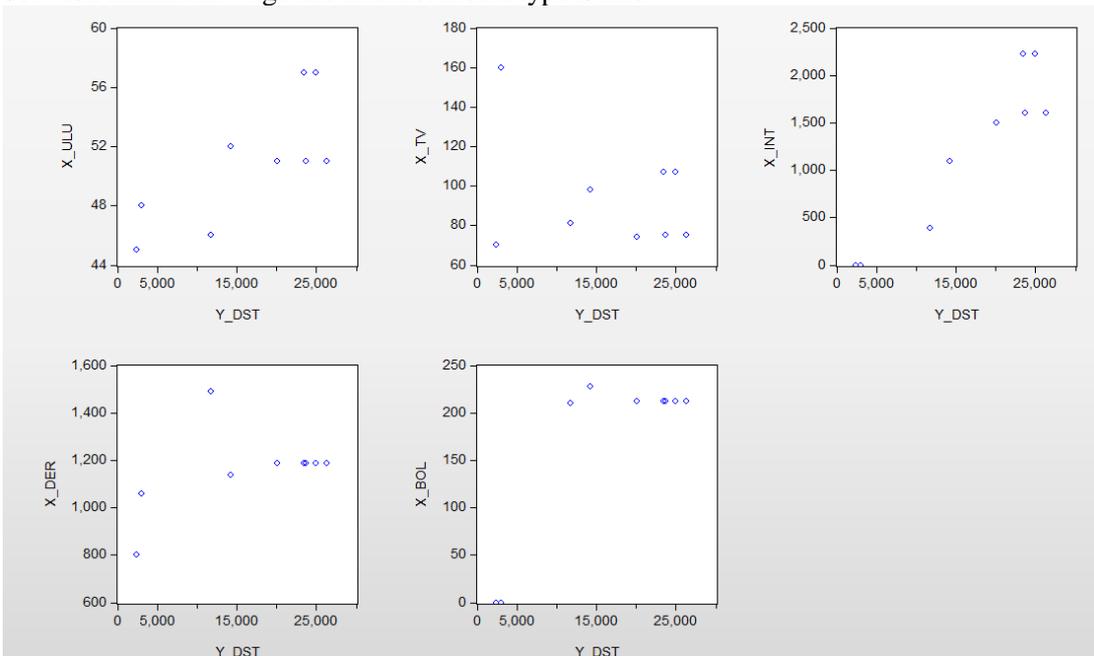

Figure 8. Scatterplot between foreign trade and types of media sources

Scatter plot above shows a nearly linear and positive correlation between national newspapers and foreign trade. A similar linear structure can be seen between foreign trade and internet media sources. Correlation between foreign trade and magazine media type is a square root like correlation. No correlation can be mentioned visually between foreign trade and regional media sources.

As mentioned below while checking scatterplots observed relations can be modelled as linear or square root like relations. In this sense, first model was set as following.

$$Y_{it} = \mu + \beta_1 X\_int_{it} + \beta_2 X\_Bol_{it} + \beta_3 X\_Der_{it} + \beta_4 X\_tv_{it} + \beta_5 X\_ulu_{it} + \varepsilon_{it} \qquad (2)$$

Pooled estimation with Model (2) is found to be significant (P=0.0000) but most of the coefficients found to be insignificant. Only internet media type is significant at 0.10 level. Determination coefficient is so low (%33) and Durbin-Watson (0.159) is not acceptable. That is why Model (3) was estimated below.

$$Y_{it} = \mu + \mu_i + \beta_1 X\_int_{it} + \beta_2 X\_int_{it}^{1/2} + \varepsilon_{it} \quad (3)$$

Model (3) is found to be significant (P=0.0000). Determination coefficient is 0.75 and shows a better fit with this fixed effect approach compared to pooled regression in Model (2). β_1 is estimated as 6,89

(P=0.0345) and β_2 is estimated as 72.15 (P=0.6313). Internet media type was found significant in Model (2) as placed linearly but is found insignificant here in square root form. However, Durbin-Watson is not acceptable (0.0476) and should be seen as signs of autocorrelation.

$$Y_{it} = \mu + \mu_i + \beta_1 X\_int_{it} + \varepsilon_{it} \qquad (4)$$

Model (4) was found to be significant (P=0.0000). Determination coefficient is again 0.75 and shows a good fit with this fixed effect approach. β_1 was estimated as 8,389 (P=0.0000). Internet media type was found insignificant in Model (3), so left aside in this Model (4). However, Durbin-Watson is not acceptable (0.0497) and signs some autocorrelation again as Model (3).

$$Y_{it} = \mu + \mu_i + \beta_1 X\_int_{it} + \beta_{2i} Y_{it-1} + \varepsilon_{it} \qquad (5)$$

Model (5) was found to be significant (P=0.0000). Determination coefficient is better (0.96) with this cross-sectional fixed-effect dummy variable approach. Adjusted-R^2 is found as 0.948 and shows a good determination. Both intercept and slope coefficients are heterogenous in this model and this makes sense. Because each subject has its own trend in media popularity. Estimated values for β_1 and β_2 coefficients are given below. Durbin-Watson is acceptable (2.55) and signs that autocorrelation is removed with autoregressive cross-relational term in this Model (5).

Table 3. Coefficient estimates for Model (5)

Coefficient	Estimate	St. error	t-stat	Prob.
μ	2729.588	609.3685	4.479371	0.0000
β_1	3.673852	0.915684	4.012139	0.0002
β_{2i} (minimum wage)	0.317134	0.471417	0.672725	0.5035
β_{2i} (foreign trade)	0.506766	0.135512	3.739635	0.0004
β_{2i} (inflaton)	0.962326	0.062963	15.28409	0.0000
β_{2i} (labor)	0.750553	0.133379	5.627236	0.0000
β_{2i} (house sales)	0.642272	0.138175	4.648246	0.0000
β_{2i} (corporational)	-0.178859	0.306650	-0.583266	0.5617
β_{2i} (GDP)	0.286263	0.228706	1.251661	0.2152
β_{2i} (industrial production)	0.023742	0.358184	0.066285	0.9474
β_{2i} (agricukture)	0.269409	0.197289	1.365552	0.1768
β_{2i} (CCI)	-0.222603	0.598527	-0.371919	0.7112
β_{2i} (transportation)	0.295716	0.219205	1.349038	0.1820

Most of the coefficient estimates are significant for Model (5). With the assumption of this relationship structure keeps existing for the future period, this model can be used for forecasting. Cross-sectional coefficient estimates are given below.

Table 4. Cross-sectional coefficient estimates for Model(5)

Coefficient	Value
μ_1 (minimum wage)	-4173.183
μ_1 (foreign trade)	2905.119
μ_1 (inflaton)	1896.306
μ_1 (labor)	668.8228
μ_1 (house sales)	250.4876
μ_1 (corporational)	899.3940
μ_1 (GDP)	-915.4359
μ_1 (industrial production)	-1622.200
μ_1 (agricukture)	2156.622
μ_1 (CCI)	-2414.749
μ_1 (transportation)	348.8170

4. Conclusion

In this paper, news published on media about statistics disseminated by Turkish Statistical Institute (TurkStat) were analyzed. More than one million records over years from 2012 to 2020 were studied. All the records were studied by using URL as primary key on database. Texts for all the news were read and then news were classified according to related subjects. This was accomplished by recording interested variables for each while reading news. By this way after reading and before classifying more than six million data gathered. That is why open-source R software was used for this huge dataset. Reading media articles to discuss the popularity is a conventional way but still works [11].

Even countries and international organizations use content analysis in media articles to get a acknowledge on image and popularity [12]. In this study, some keywords adaptive with TurkStat's press release calendar were used for content analysis. By these keywords, news was matched with press releases or other subjects. After this preparation data was aggregated yearly and then modelled by using panel data regression methods. In this manner the effect of number of media sources monitored on popularity of organization was investigated. In the end, an econometric model was suggested for forecasting purposes.

Number of news published on media was used as a proxy for popularity on media. Only number of internet type media sources was found to be important on estimating number of news published. An autoregressive panel data model was used. A percentage increment in number of monitored media sources was found to increase media popularity by 3.67 percent. Previous amount of news on a certain subject was also found to be important on estimating amount of news in current year on selected subject. A percentage increment in number of news published on a certain subject was found heterogenous between subjects.

As in some studies, future popularity on the internet can be predicted by current available data [13]. Differently by the econometric model suggested in this study, number of news could be forecast because future number of sources to be monitored is an accessible information before that year starts. Previous year's number of news is also a variable and value is known beforehand. There is no other study like this for a governmental organization. That is why national statistical offices (NSO) can use this approach to forecast popularity of NSO and set a communication strategy relying on these statistics. Because there is not enough data for a time series approach, panel data method used in this paper can be used to succeed in estimating and forecasting.

Criticism on his study can be made on, no classifying is adopted for comments in texts. In case of a positive or a negative comment in meaning, "whether this effect the popularity or not?" is a nonrespondent question here. Only the absolute numbers by selected subjects are handled in this study. For future researchers inspired by this study it can be suggested to focus more on attitudes of the press staff. Because editors add interpretations while designing and editing texts of news. These interpretations are thought to have important effect on spreading acceleration of these news. This may indirectly determine the popularity of an organization.

Conflicts of interest

The author state that did not have conflict of interests

References

[1] Craufurd Smith R., Monitoring media pluralism in the digital era: application of the Media Pluralism Monitor 2020 in the European Union, Albania and Turkey in the years 2018-2019. Country report: United Kingdom , (2020).

[2] Mukhamediev R. I., Yakunin K., Mussabayev R., Buldybayev T., Kuchin Y., Murzakhmetov S., Yelis M. (2020). Classification of Negative Information on Socially Significant Topics in Mass Media, *Symmetry*, 12(12) (2020) 1945.

[3] Sánchez-Núñez P., Yanez E. R., Cabrera F. E., Peláez-Repiso A., Government Communication Management in Digital Ecosystems: A Real Case of Country Brand Analysis, In 2020 *Seventh International Conference on eDemocracy & eGovernment (ICEDEG)* (pp. 264-268) (2020, April) IEEE.

[4] Hsiao C., Panel data analysis, (2003).

[5] Arellano M., Panel data econometrics. Oxford university press, (2003).

[6] Baltagi B., Econometric analysis of panel data. John Wiley & Sons, (2008).

[7] Frees E. W., Longitudinal and panel data: analysis and applications in the social sciences. Cambridge University Press, (2004).

[8] Hsiao C., Why panel data?. *The Singapore Economic Review*, 50(02) (2005) 143-154.

[9] Hsiao C. Analysis of panel data (No. 54). Cambridge university press, (2014)..

[10] Wooldridge J. M., Econometric analysis of cross section and panel data. MIT press, (2010).

[11] Regusci E., A Content Analysis of News Coverage about Plant-Based Milk, master thesis, Faculty of Texas Tech University, (2020).

[12] Chouliaraki L., Georgiou M., Zaborowski R., Oomen W. A., The European 'migration crisis' and the media: a cross-European press content analysis, (2017).

[13] Trattner C., Moesslang D., Elsweiler D.,. On the predictability of the popularity of online recipes. *EPJ Data Science*, 7(1) (2018) 1-39.

Forecasting the returns of pension investment funds in Turkey with artificial neural network

Fatih ÇEMREK [1,*] , *Özge DEMİR* [2]

[1]*Eskişehir Osmangazi University, Faculty of Science and Letter, Eskişehir/TURKEY*
[2]*Eskişehir Osmangazi University, Graduate School of Natral and Applied Sciences, Eskişehir /TURKEY*

Abstract

Individuals start to experience the retirement period after completing their active working time. During the retirement period, the income generated during the work period is reduced. The Personal Pension System was organized on the basis that both individuals can able to generate additional income during the retirement period and the savings are increased and remain in the system. This system aims to enable individuals to increase their income during the retirement period through their savings. Funds operated according to the religious property principles created to drive investment into savings accumulated in individual pension accounts of participants seeking to retire and build up wealth are called pension funds. Pension investment funds are of great importance to our capital market and the future of our country.

1. Introduction

The Personal Pension System (TPPS) is designed to drive the long-term investment of individuals' wealth throughout their working lives and to provide an income that will improve the living conditions of individuals during retirement. Individuals gain an income in addition to their retirement income by voluntarily and/or automatically participating in this system established The deposits are monitored in individual accounts and are stored in TAKASBANK, which is appropriate by the Capital Markets Board (TPPS). TPPS; is monitored and supervised by the Capital Market Board (SPK), the pension Monitoring Center (EGM), TAKASBANK, independent audit companies, and internal audit elements, especially the Undersecretariat of the Treasury [1].

As a complement to the social security system, TPPS also supports the economic development of countries. In our country, financial assets and markets are improving because the total amount of savings is insufficient. Financial markets have not been able to achieve the desired development due to limited demand for financial instruments. In Turkey, savings are often defined in the form of a cushion, and as a result, the fund accumulation to be

transferred to investments is not sufficient. Therefore, small savings within the country can be assessed in financial markets for use in the growth of funds. More than that, market fluctuations and speculation can be prevented. In this context, the TPPS funds have increased the country's fund savings and have increased the net savings volume in recent years. The inclusion of pension funds among long-term investment funds in financial markets will have a deepening effect on markets. This effect will reduce borrowing costs in the private and public sectors. The need for public financing must be met at the lowest cost in the medium and long term, following developments in the domestic and foreign markets. In this case, pension funds are the most important long-term enterprise investment tools and can be intended for this purpose. With the development of individual pension funds in Turkey, it is expected to reduce the gameplay that may occur in financial markets. These funds have the opportunity to move longer-term, and therefore long-term paper is an important customer that can be sold for the Treasury [2]. Pension investment funds provide liquidity and stability in the market, with a fixed demand for securities, and provide investors

with the opportunity to lower their costs. As a result, investments will become long-term and more return-yielded enterprise investments. The transfer of pension investment funds into capital markets as long-term investments reduces the gameplay in markets, thus enabling a stable growth opportunity.

Significant changes in the financial system may occur as a result of increased funding with TPPS in Turkey. These funds can block financial crises that can arise due to short-term variable capital movements in the country and can reduce the depth of a possible crisis. TPPS is widely used in the world and is a long-term financial resource for country economies. Therefore, it provides significant support for the country's economy in the long term [3].

Key indicators of individual pensions in Turkey are given in Table 1.

Table 1. Number of participants and Fund amounts of Pension companies in Turkey [1]

Retirement Companies	Number of participants	Participants' Fund Amount (TL)
Aegon Life and Retirement	37,671	132,128,516
Allianz Life and Retirement	94,630	2,801,049,763
Allianz Life and Retirement	728,934	12,158,903,088
Anadolu Life and Retirement	1,091,010	16,312,824,287
Avivasa Life and Retirement	787,046	16,801,925,214
Axa Life and Retirement	33,794	426,214,299
Bereket Life and Retirement	93,913	360,296,123
BNP Paribas Cardif Retirement	181,937	2,260,767,911
Cigna Finans Life and Retirement	83,601	707,565,760
Fiba Life and Retirement	91,108	1,614,645,975
Garanti Life and Retirement	1,111,079	12,694,233,683
Halk Life and Retirement	561,547	4,066,235,326
Katılım Life and Retirement	253,288	1,466,479,144
Metlife Life and Retirement	184,525	1,619,012,245
NN Life and Retirement	255,144	3,165,530,598
Vakıf Life and Retirement	547,507	7,224,409,572
Ziraat Life and Retirement	657,702	4,544,494,775
Total	6,794,436	88,356,176

In Turkey, the participants of the pension companies total of 6,794,436 and the funding of the participants is TL 88,356,176 billion. The various and

.

distributions of pension investment funds in Turkey are given in Figure 1
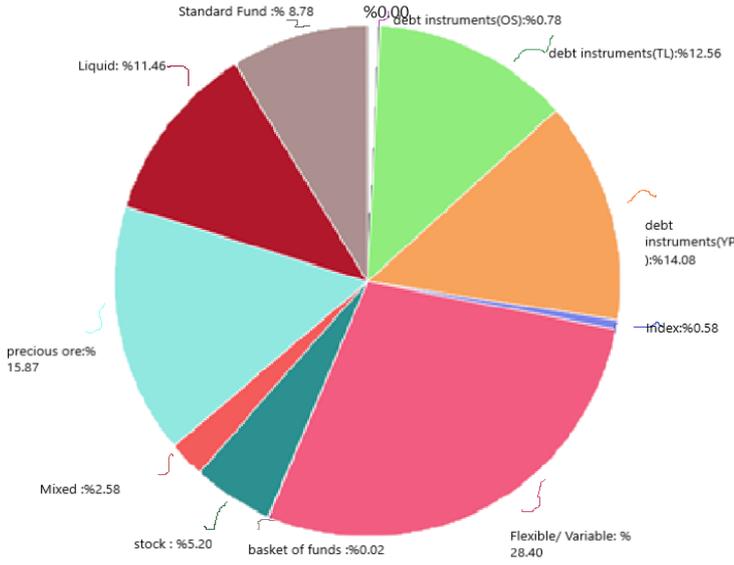
Figure 1. Various and distributions of pension investment funds in Turkey [1]

In the literature, studies have been carried out comparing the ARIMA method and the classic time series method to determine the prediction success of the Artificial Nerve Networks (ANN). In many of these studies, The prediction success of it's models has been determined to be better than conventional time series methods. In some studies, it was determined that the methods examined do not outperform each other.

Qi and Zhang [4], have developed a model and with this model, it is determined that the architectural selection criteria are not sufficient to examine short-term and long-term time series with artificial neural networks.

Eğrioğlu and Aladağ [5] compared architectural selection criteria for using artificial neural networks in predicting long-term dependent time series. In the study, it was stated that the time series in the curve and linear structure can be modeled with the and the biggest problem encountered in ANN was the number of nodes in the plates.

Avcı [6] used the multi-layered artificial neural networks model to predict the daily and seance returns of the National 100 Index, and stated that this method is an effective method. It is also stated that IT is possible to further increase the estimation powers of the model using different variables and model structures.

Wallace [7] examined ANN models from a conceptual point of view and examined the fields used in the finance literature. Wallace (2008) stated that the most basic use of artificial neural networks is financial forecasting. In addition, it is stated that ANN can be used to test the validity of the efficient market theory.

Düzgün [8] worked to estimate the GDP for Turkey in the period 1987 and 2007, and it was stated that the ARIMA model is better in terms of foresight than its model.

Nitin et al [9] used different ARIMA and ANN models for India Stock Exchange data and stated that the ARIMA model's prediction performance is better.

Irmak et al [10] used Winter Exponential Correction method to estimate the number of patients and they indicated that the Winter Exponential Correction method was better.

Akel and Karacameydan [11] have used the Artificial Nerve Networks (ANN) method to estimate the net asset values of investment funds in Turkey. The study used 19 of type a and 19 of type b and 38 of total investment funds for the period January 2001 through December 2008, and six macro-economic variables were used to estimate net asset values for these funds. In the study, if the hedge fund to predict the net asset value, and regression analysis has been used and predictions obtained by

both methods have been compared. According to the analysis results, it has been determined that their models have more successful results.

Keskin Benli and Yıldız [12] used linear time series methods and nonlinear but model and estimated the price of gold. Then, the predictive success performance of the methods used was compared. In the study, the result was that the average of the error squares was more successful than the root of mean square (RMSE) value and the ARIMA model was more successful than the model.

Pekmezci and Dilek [13] ın this study, the performances of cointegration tests, which are frequently used in the literature, were compared for different sample sizes in terms of their empirical power and type I error probabilities. As a result of this study, it was determined that some test applications in testing cointegration in terms of empirical power and type I error probability did not meet.

Ertuğrul and Bekin [14] used time series and artificial neural networks models to estimate some basic food prices in Turkey. As a result, Holt's exponential correction used to estimate wheat and barley prices was determined that box-Jenkins models and their model had similar values in respect of the mean of error squares (MSE), while the estimate for the steel prices was given better estimates.

Kızılkaya [15] used ANN used the ARIMA model to estimate Turkey's inflation and unemployment rates, The period 1923-2014 for unemployment and 1969-2014 for annual inflation have been reviewed and forecasts for the period 2015-2020 have been made.

Koç ve Onacak [16] used the euro purchase rate, US dollar purchase rate, under-the-republic sale price, Stock Exchange Istanbul 100 Index closing price, interest rate applied to TL deposits in banks and Consumer Price Index as input variable. In the study, artificial neural networks were used to forecast estimate the pension investment fund share prices. The analysis reviewed monthly data from January 2003 to October 2017. It has been found that the model of artificial neural networks produces results close to actual values.

2. Materials and Methods

2.1. Dataset

In this study, in January 2016-October 2019, 4 variables were used to estimate the returns of investment funds based on the stock of three separate retirement investment companies, gold and foreign currency. These variables are used in PPI (2003=100), CPI (2003=100), Exchange rate (TL\$), gold exchange. The monthly prices of the monetary market fund of Anatolian life Pension Şti, Ziraat Pension Şti, NN Hayat Pension Company have been studied. In the study, the predictions of the long-term values of pension investment funds were compared with the model of time series and the predictions of the results obtained from artificial neural networks (ANN). The study conducted a time series analysis of artificial neural networks, SPSS 21 with Matlab R2016b. Analytics have been created for each company separately. The logarithm of all input-output data has been taken for use in ANN algorithms and time series analysis.

2.2 Artificial neural networks (ANN)

ANNs can be defined as computer systems inspired by biological neural networks in order to be able to derive and discover new information through learning, which is one of the most basic features of the human brain, without any assistance [17-22].

ANN uses the information obtained from the samples as input, creates their own experiences by processing them, and then they can make similar decisions. The ANN model consists of layers, namely the input layer, the hidden layer, and the output layer, which contain neurons that are in connection with each other. Determining the number of layers in which the network will be formed and the number of neurons in these layers is defined as "network architecture". ANN architecture affects the performance of the network. ANN shows common features with the human brain, such as learning, remembering, and generalizing from experience. A mathematical model for the biological nerve structure was developed by McCulloch and Pitts in 1943, and it was briefly defined as the M-P nerve. This developed model is shown in Figure 2.
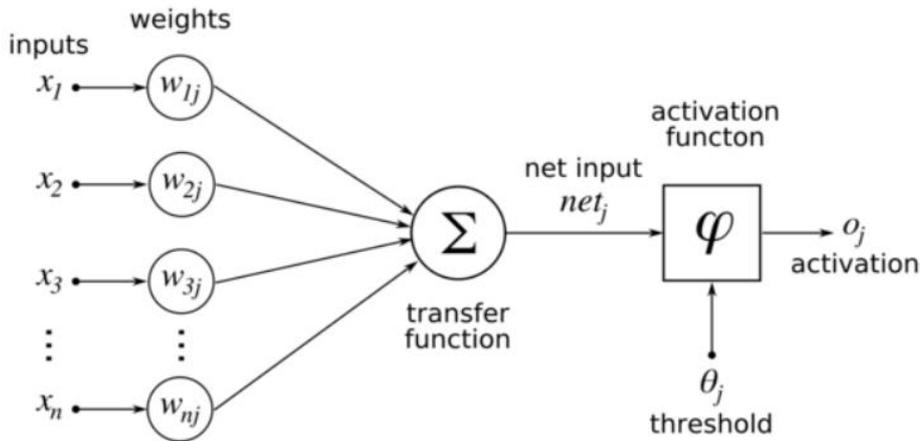
Figure 2. Architectural Structure of Neural Network (McCulloch and Pitts in 1943)

Artificial neural networks are in two classes as feed-forward and feed-back networks based on how they operate. In advanced artificial neural networks, the signals are in one direction, from the input layer to the output layer only. For feedback networks, there is a type of feedback process. In these network structures, the direction of the signal is from the input layer to the output layer.

However, the neurons on a layer can receive signals from themselves, from the neurons on the layer or other layers[21]. In the time series, the three-layer forward feed model is most commonly used. In single-variable time series, the network output is estimated when inputs are past or delayed variables [5]. In use, the learning process is to set the information stored in the weights of the connections generated in the network to perform a desired function. In other words, output is obtained by setting the weight value of the network at the end of the learning process, while initially determining the weight value of the network at random.

Different algorithms are used for learning. These algorithms are divided into two groups, with consultants (supervised) and without consultants (unsupervised). The non-consultative learning algorithm does not specify output variables that correspond to input variables, and weights are adjusted automatically by the network. In the guided learning algorithm, output variables corresponding to input variables are also loaded as information on the network. The network is adjusting the hitch weights so that the difference between network output and target output is minimal. The redistribution algorithm is a learning algorithm that is most commonly used in neural networks using the consulted learning algorithm. It is important to select the learning parameter used in the redistribution algorithm to optimize the performance of the network [18]. The time series analysis uses more back-propagation algorithms.

This study used the reverse-spread algorithm and the model for it is shown in Figure 3.
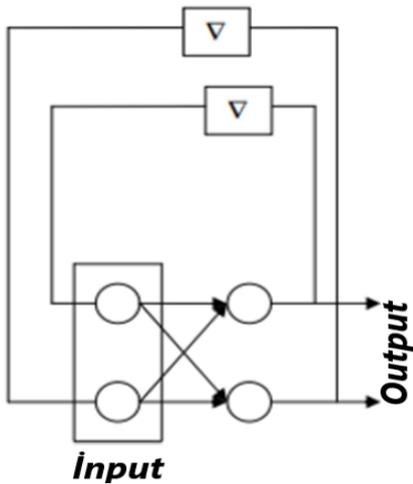
Figure 3. Redistributed network structure.

The developed simplified ANN model is shown in Figure 4.

İnput :Gold, PPI, CPI, $

ARTİFİCAL

OUTPUT : MONEY MARKET FUND

Figure 4. The Developed Based Artificial Neural Network Model

Within a general artificial neural network system, layers are formed by the combination of neurons in the same direction [22]. These layers are the input layer, hidden layer, and output layer. Input variables are made up of the input layer. With the interaction of these input variables, the output variable is formed. Output variables also create the output layer. There is a hidden layer of nerves that is not connected to the external environment. These nerves send signals on the input layer to the output layer with their weight.

2.3. Time series analysis

Time series are often an important practice of statistics and even economies. A time series is a series of measurements that are periodically observed with time intervals. Time series analysis is all over science, but governments are often used to make economic predictions of organizations over economic data.

The time series are divided into stationary and non-stationary series according to deviations from the average. If the average and the variance of the time series being examined shows a symmetrical change of the variance, or if the series is free of periodic fluctuations, these series are called static time series. Statistically, stability is important. The statistical results are taken over the series's stagness assumption.

If a time series is not static, it is made static using some methods (such as differentiation), then analyzes are performed. In the literature, many economic data can be observed to be non-stable. Therefore, it will be appropriate to review the relevant data that is not static. Non-static time series are reviewed in two sections. One is that the average of the series depends on time, the other is that the series autocorrelation depends on time.

3.Results and Discussion

3.1.The results of the time series

The model and forecast strength set out in the time series analysis of the estimate of money market funds for three separate retirement companies are shown in Table 2 below.

Table 2. Specified Model Results

Companies	Model	MSE
Anadolu Life AndRetirement	ARIMA(1,1,0)	0.0001
NN Life And Retirement	ARIMA(1,1,1)	0.0000814
Ziraat Life And Retirement	ARIMA (1,0,0)	0.0000780

Prediction accuracy measurements;

MSE (Mean Square Eror) $=\frac{1}{n}\sum c_t^2$

3.2 The results of artificial neural network

The results found by analyzing the multivariate forward diffused artificial nervous network architecture and MATLAB program are shown in Figure 5.
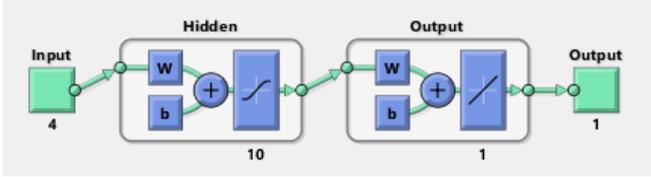

Figure 5. Artificial Neural Networks Model

Artificial Neural Networks Model Results were given in Table 3.

Table 3. Artificial Neural Networks Model Results

Companies	Iteration	MSE
Anadolu Life And Retirement	171	0.0000256
Ziraat Life And Retirement	177	0.0000141
NN Life And Retirement	6	0.0000198

The deviations from the mean are very low compared to the analysis of the time series and are forecasting.
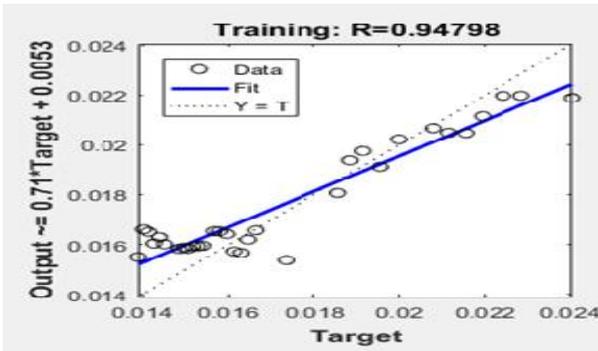
Figure 6: Ziraat Life And Retirement Training And Test Data Regression Result
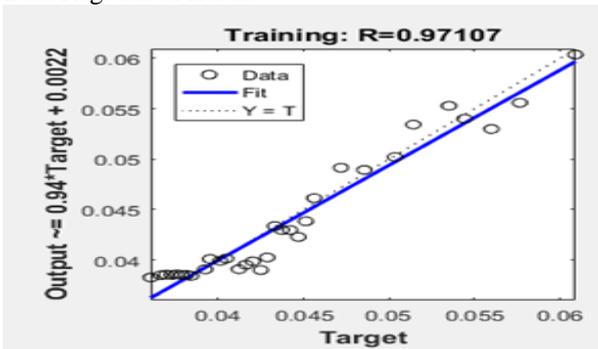
Figure 7. Anadolu Life And Retirement Training And Test Data Regression Result
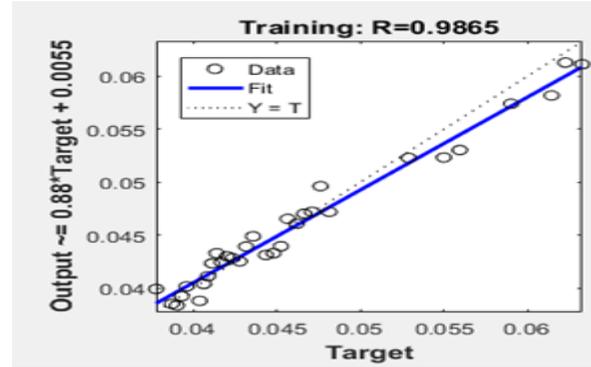
Figure 8..NN Life And Retirement Training And Test Data Regression Result

Prediction and prediction success due to data loss correction in time series analysis are very risky in comparison to the artificial neural network method. MSE values in time series analysis and artificial neural networks have shown superior performance in predicting artificial neural networks compared to Table 4.

Table 4. Forecasting Success Criteria Results

	Time Series Analysis	ANN
	MSE	MSE
Anadolu Life And Retirement	0.0001	0.0000256
NN Life And Retirement	0.0000814	0.0000141
Ziraat Life And Retirement	0.0000780	0.0000198

The 5-month estimate (standardized values) obtained by The Time Series and Artificial Neural Networks method of Anadolu Life And Retirement is shown in Table 5.

Table 5. Time Series Analysis And ANN Forecasting

Period	Forecasting With Time Series	Forecasting With ANN
2019-11	0,06243026	0,0564418
2019-12	0,05601761	0,0561455
2020-01	0,05601398	0,0585714
2020-02	0,05874537	0,0594157
2020-03	0,05929718	0,0568943
2020-04	0,05689785	0,0572886
2020-05	0,05775788	0,0585676

4.Conclusion

With uncertainties in the economy, it is important for decision-makers to determine what economic time series will show in the future. In this case, the values that make up the time series are examined and the model installed and the series are asked to forecast the values that they will receive in the future with high performance.

In this study, it is aimed to present a general framework to compare the working processes and forecasting performances of forecasting methods. For this purpose, a linear time series method and nonlinear ANN model were used and the predictive success performances of the two methods were compared by applying them to Private Pension Mutual Funds in Turkey. As a result of the study, it was determined that the prediction performance of ANN was more successful**.**

It is recommended to use artificial neural networks instead of classical time series analysis in forecasting and forecasting modeling. Those who do the estimation process should use different methods in their work. Thus, the most suitable model for the studied time series is determined. Evaluating the method or model used at each stage may yield better results in case the data set changes.

Acknowledgment

Conflicts of interest

The authors declared no conflict of interests.

References

[1] Emeklilik Gözetim Merkezi, Bireysel-Emeklilik-Nedir? https://www.egm.org.tr/bireysel-emeklilik/bireysel-emeklilik-nedir (2020).

[2] Korkmaz T., Türkiyede'ki Emeklilik Fonlarının Perfonmans Ölçümü ve Fon Yöneticilerinin Zamanlama Yeteneği, *Akdeniz Üniversitesi İ.B.F Dergisi*, (14) (2007) 66-93.

[3] Zor İ., OECD Ülkeleri ve Türkiye Bağlamında Bir Değerlendirme, *Reasürör Dergisi*, 70 (2008) 6-20.

[4] Qi M., Zhang P.G., An Investigation of Model Selection Criteria for Neural Network Time Series Forecasting, *European Journal of Operational Research*, 132 (3) (2001) 666-680.

[5] Eğrioğlu E., Aladağ Ç.H., Yapay Sinir Ağları ve Arıma Modellerin Melez Yaklaşımı ile Zaman Serilerinde Öngörü, İstanbul Üniversitesi VII. Ulusal Ekonometri ve İstatistik Sempozyumu, 26-27 Mayıs 2005, İstanbul.

[6] Avcı E., Forecasting Daily and Sessional Returns of the ISE-100 Index with Neural Networks Models, *Doğuş Üniversitesi Dergisi*, 8 (2) (2007) 128-142.

[7] Wallace M.P., Neural Networks And their Application to Finance, *Business Intelligence Journal*, (July) (2008) 67-76.

[8] Düzgün R., A Comparison of Artificial Neural Networks and ARIMA Models' Success in GDP Forecast, *Marmara Üniversitesi İ.İ.B.F. Dergisi*, 25 (2) (2008) 165-176.

[9] Nitin N.M., Saxena V. P., Pardasani, K. R., Next Day Stock Forecasting An Application of ANN and ARIMA, The IUP, *International Journal of Theoretical and Applied Finance*, 17 (1) (2011) 70-84.

[10] Irmak S., Köksal C.D., Asilkan Ö., Hastanelerin Gelecekteki Hasta Yoğunluklarının Veri Madenciliği Yöntemleri ile Tahmin Edilmesi, *Uluslararası Alanya İşletme Fakültesi Dergisi*, 4 (1) (2012) 101-114.

[11] Akel V., Karacameydan F., Yatırım Fonları Net Varlık Değerlerinin Yapay Sinir Ağları Yöntemiyle Tahmin Edilmesi, *Anadolu Üniversitesi Sosyal Bilimler Dergisi*, 12 (2012) 87-105.

[12] Keskin Benli Y., Yıldız A., Altın Fiyatının Zaman Serisi Yöntemleri ve Yapay Sinir Ağları ile Öngörüsü, *Dumlupınar Üniversitesi Sosyal Bilimler Dergisi*, 42 (2014) 213-224.

[13] Pekmezci A., Dilek M. (2014). The Comparison of Performances of Widely Used Cointegration Tests, *Communications in Statistics- Simulation and Computation*, 45(6) 2070-2080.

[14] Ertuğrul İ. Bekin A., Türkiye'de Bazı Temel Gıda Fiyatları İçin Yapay Sinir Ağları ve Zaman Serisi Tahmin Modellerinin Karşılaştırmalı Analizi,

Kafkas Üniversitesi İktisadi ve İdari Bilimler Fakültesi Dergisi, 7 (13) (2016) 253-280.

[15] Kızılkaya O., Türkiye'nin Enflasyon ve İşsizlik Oranının Yapay Sinir Ağları ve Box-Jenkins Yöntemiyle Tahmini *Social Sciences Studies Journal*, 3 (12) (2017) 2197-2207.

[16] Koç S., Onacak D., Yapay Sinir Ağları ile Emeklilik Yatırım Fonu Hisse Senedi Fiyatlarının Tahmini, *Finans Ekonomi ve Sosyal Araştırmalar Dergisi*, 3 (3) (2018) 590-600.

[17] Fausett L., (1994). Fundamentals of Neural Networks. Prentice Hall USA (1994).

[18] Güneri N., Apaydın A., Öğrenci Başarılarının Sınıflandırılmasında Lojistik Regresyon Analizi ve Sinir Ağları Yaklaşımı, *Ticaret ve Turizm Eğitim Fakültesi Dergisi*, 1 (2004) 170-188.

[19] Indro D.C., Jianga C.X., Patuwo B.E., Zhang G.P., Prediction Mutual Fund Performance Using Artificial Neural Networks, Omega, *International Journal of Management Science*, 27 (3) (1999) 373-380.

[20] Öztemel E., Yapay Sinir Ağları. 2. Basım. Papatya Yayıncılık İstanbul (2006).

[21] Tolon M., Güneri Tosunoğlu N., (2008). Tüketici Tatmini Verilerinin Analizi: Yapay Sinir Ağları ve Regresyon Analizi Karşılaştırması, *Gazi Üniversitesi İktisadi ve İdari Bilimler Fakültesi Dergisi*, 10 (2), 247-259.

[22] Çuhadar M., Güngör, İ., Göksu, A., Turizm Talebinin Yapay Sinir Ağları ile Tahmini ve Zaman Serisi Yöntemleri ile Karşılaştırmalı Analizi: Antalya İline Yönelik Bir Uygulama, *Süleyman Demirel Üniversitesi İktisadi ve İdari Bilimler Fakültesi Dergisi*,14 (1) (2009) 99-114.

Investigation of joining properties of AA 5083 material in MIG and TIG weldings

Hatice VAROL ÖZKAVAK [1],* (ID) *Serdar MERCAN* [2] (ID)

[1] *Isparta University of Applied Science, Mechanical and Metal Tech. Dpt.,32200, Isparta, TURKEY*
[2] *Sivas Cumhuriyet University, Faculty of Technology, Mechatronics Eng. Dpt., 58140, Sivas, TURKEY*

Abstract

AA 5083 Aluminum alloys begin to be replaced steels in automobiles, ships, and high-speed-trains by providing reduced energy consumption and low carbon emissions thanks to their low densities, good weldabilities, and high corrosion resistance. During the production of high-speed trains, which are of special importance for our country, the proper selection of joining method for AA5083 increases the production speed. In this study, AA5083 alloys with 8 mm thickness were butt-welded under different parameters by using MIG and TIG weldings. It was aimed to determine the changes in microstructure and mechanical properties of welded samples, and also to specify the proper welding method. As a result, it was found that samples joined by MIG welding have higher strength and ductility, along with a lower amount of microstructural defects compared to their counterparts joined by TIG welding.

1. Introduction

Aluminum, also known as green material, is the 3rd most commonly found element on Earth [1-3]. Al, the most common material used as an alternative to steel for many applications in design and production, has many important properties as low weight, excellent impact resistance, ideal corrosion resistance, and recyclability [4,5]. For this reason, Al and its alloys have found widespread use in many sectors such as the automotive, railway, aerospace, and shipbuilding industries [6]. 5XXX Al series are widely used for structures in shipbuilding. These alloys have a high strength/weight ratio, good weldability, and excellent corrosion resistance against sea conditions [7,8]. The strength of AA5083 alloy, which contains 4.5% Mg and %1 Mn in its chemical composition, can be increased by strain-hardening or solid solution strengthening in concentrated Mg [9]. In many industrial applications where Al alloy is used, there are complex structures that require highly efficient nondetachable connections. It is determined that, under static and dynamic loadings, welded Al alloys in such complex structures show more efficiency compared to rivet joints [10]. Besides, the use of welded joints in the joining of Al alloys reduces the cost by 60-65%. Metal Inert Gas (MIG) and Tungsten Inert Gas (TIG) welding methods are widely used in joining Al alloys

[11]. When arc-welding methods are used for Al alloys, fatigue damage, brittle fracture, and stress-corrosion cracks occur due to distortion and residual stress [12]. To reduce residual stresses and prevent distortion, pre-/intra-welding [15,16] or post-welding [17,18] mechanical and thermal processes [13,14] were discussed in many studies. In TIG welding, which is widely used for joining Al and its alloys, an electric arc is created between the non-consumable tungsten electrode and the workpiece. In this method, an electrode holder is used to fix the non-consumable tungsten electrode. When electrical power is applied between the electrode and the workpiece, the gas passes through the cylinder and reaches the nozzle around the electrode. The gas surrounds the arc, protecting the welding area from atmospheric effects and preventing defects [19]. On the other hand, MIG welding is performed by feeding a continuous solid wire electrode from a welding gun and weld pool. In both methods, protective gas is sent to the welding gun [20]. MIG welding method is more superior compared to TIG welding in terms of microstructure change, bonding capability, and welding metal deposition ability [21].

In their study, Yang et al. analyzed the electrochemical properties of Al 6082 joined by MIG and friction stir welding and stated that the corrosion rate of FSW

joints was lower than the MIG joints [22]. Schneider et al. aimed to optimize the effects of TIG-MIG/MAG hybrid welding techniques on welding geometry. At the end of the study, the most effective parameters were found as the type of protective gas (MIG-MAG), voltage (MIG-MAG), wire feed speed (MIG-MAG), along with welding speed and density of the electric current (TIG) [23]. Subbaiah investigated the microstructure and mechanical properties of casted Al-Mg-Sc alloy after TIG welding. It was stated that the TIG-welded Al-Mg-Sc alloy casting has improved tensile properties compared to the main material. Furthermore, the author confirmed a decrease in strength due to Mg vaporization [24]. In their study, Zhang et al. compared the joining properties of laser and TIG welding methods for AlSi10Mg samples manufactured by SLM and casting techniques. Welding morphology, defects, microstructure, and mechanical properties were discussed in the study. As the result of the study, it was concluded that the gaps present within SLM samples causes defects during welding, laser shows better welding properties and higher tensile strength than TIG welding for SLM parts. It was also stated that tensile strength of SLM-SLM or SLM-casting joining is superior in comparison with the main material [25]. Shu-Fen studied the effect of welding current on morphology and microstructure of T joints for Al alloys joined by double-pulse MIG welding. The authors stated that the width and depth of the welding seam increase by rising the average current, and the most optimal properties are achieved at a current of 90 A. Singh et al. deduced that tensile strength shows a significant increment by increasing welding current and gas flow rate [26]. In addition to this, Kumar et al. investigated the effect of heat input on the strength of the joining area and found that the tensile strength decreases with heat input increment [27]. Similarly, Jahanzaib et al. concluded that if a high welding current and low welding speed are selected, the quality of the welded connection improves [28]. Raveendra et al. examined the effect of the welding current on the weld seam and obtained a linear increase in the front and back side by increasing the welding current [29]. Gharibshahiyon et al. stated that high heat input causes grain growth along with toughness and impact energy reduction in welded joints [30].

Mg is the main element of 5000 series Al alloys. Thanks to their low densities, good weldabilities, and high corrosion resistance, AA5083 Aluminum alloys begin to be replaced steels in automobiles, ships, and high-speed-trains by providing reduced energy consumption and low carbon emissions [31]. Thus, the joining process of Al alloys plays an important role. In the literature, there are studies on the joining of AA5083 Al alloys. By investigating mechanical properties and microstructure of AA5083 alloy by FSW method, it is seen that reduction in friction heat input leads to high ductility, good formability, and betterment in grain size [32]. In other studies, two different porosity structures that occurred during the laser welding of AA5083 Al alloys were examined, and it was concluded that the number of porosities can be reduced in case of using a double beam source as welding [33,34].

In this study, AA5083 alloys with 8 mm thickness were joined under different parameters by using MIG and TIG weldings. In this study, the gap in the literature has been tried to be closed by considering the values that are not used in the literature in terms of both the thickness of the joined part and the process parameters used. The mechanical properties and microstructure of the welded joints were analyzed.

2. Materials and Methods

In this study, AA5083 Aluminum plates were joined via MIG and TIG weldings. In the experiments, plates with 8 mm thickness were used. Samples were procured from GÖK YAPI AŞ and joined in TÜDEMSAŞ Welding School. After welding, the samples were cooled to room temperature. The chemical composition of the AA5083 alloy selected for this study is given in Table 1, and mechanical properties are given in Table 2.

Table 1. Chemical composition of AA5083 Aluminium alloy

Fe	Si	Cu	Mn	Mg	Zn	Cr	Ti	Other	Al
0,40	0,40	0,10	0,40-1,0	4,0-4,9	0,25	0,05-0,25	0,15	0,15	Balance

Table 2. Mechanical properties of AA5083 Aluminium alloy

Density (gr/cm^3)	Brinell Hardness (HB)	Tensile Strength (MPa)	Yield Strength (MPa)	Elasticity Module (GPa)
2,66	85	317	228	71GPa

The main objective of the study is to determine the optimum welding method by examining the change in microstructure and mechanical properties of AA5083 alloy joined with TIG and MIG methods under different process parameters. The workflow of the study is given in Figure 1.

Welding parameters used in the experiments are given in Table 3. While selecting the welding parameters, the process parameters used in previous studies were evaluated, and originality was ensured in the study by choosing different parameters from these parameters [1,35,38]. Zirconiated Tungsten (98%W+2%Zr) electrode is used with 2,4mm diamaeter for TIG welding proceses. 1,6 mm wire diameter is used for MIG welding process.
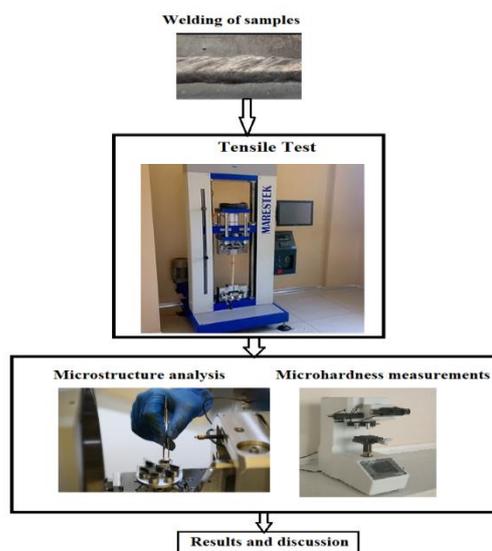
Figure 1. Workflow of the study

Table 3. Welding parameters used in the study

Method	Sample Number	Current (A)	Voltage (V)	Speed (mm/s)	Torch Distance (mm)
MIG	S1	150	18	2,6	
	S2	170	20	2,7	15
	S3	180	22	2,3	
	S4	190	23	2,5	

Method	Sample Number	Current (A)	Tungsten electrode diameter (mm)	Speed (mm/s)	Stand-off distance (mm)
TIG	S5	140		2,4	
	S6	160	2,5	3,1	5
	S7	180		4	
	S8	200		5	

Plate samples joined with different process parameters are given in Figure 2. After the joining process, the samples were prepared for microstructure analysis, microhardness measurement. During the preparation of the samples, the cutting operations were performed in the Electrical discharge machining (EDM) device to prevent the samples from being exposed to any hot or cold deformation. For microstructure analysis of welded samples in the study, test pieces were cut from the cross-section of the weld. Subsequently, the test pieces were sanded by 400,800,1500 grit sandpapers and polished with broadcloth, respectively. Finally, surface polished test pieces were etched in Keller solution (2 ml HF, 3 ml HCl, 5 ml HNO3, and 190 ml H2O) and prepared for microstructure analysis. In addition, SEM examinations were performed on the FEI QUANTA FEG 250 device to determine the grain structure and porosity within the weld area.

Figure 2. Images of plate samples joined by (a) MIG welding (b) TIG welding

To determine the weld area strength of welded samples, a Marestek brand tensile test device was used. The samples used in the tensile test were prepared in accordance with ASTM EN ISO 4136 standards. Analysis of the sample regions is given in Figure 3. Tensile tests were carried out at room temperature with a speed of 0.5 mm.
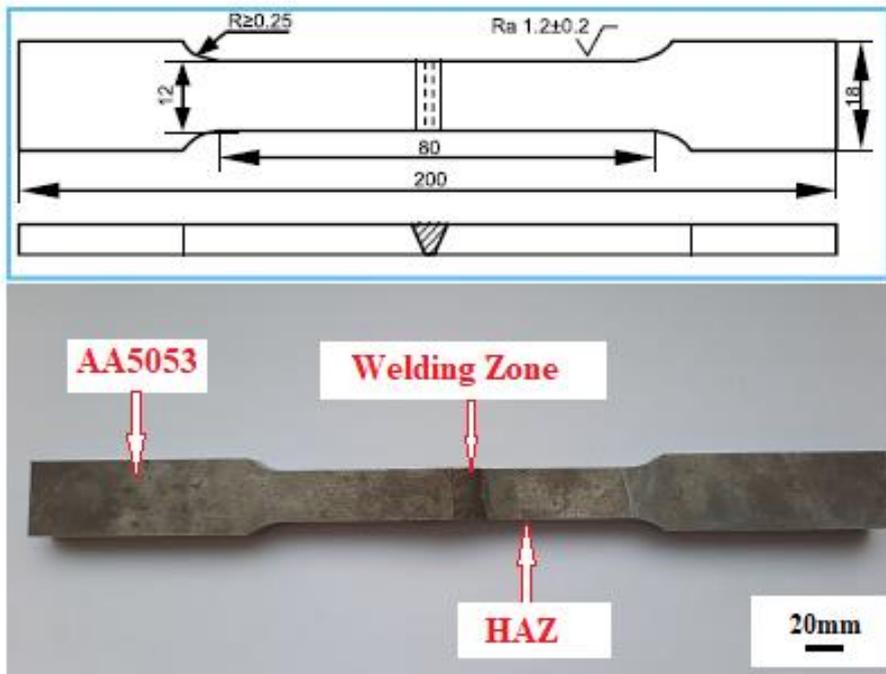

Figure 3. Tensile test specimens used in the study

Vickers microhardness measurement was carried out at 300g load to determine the change in hardness after the joining process. Microhardness measurements were taken from three different points: the heat-affected zone (HAZ), the base material (MB), and the weld zone (WZ). The measurements points are shown in Figure 4. The measuring range is set at 0.5 mm.
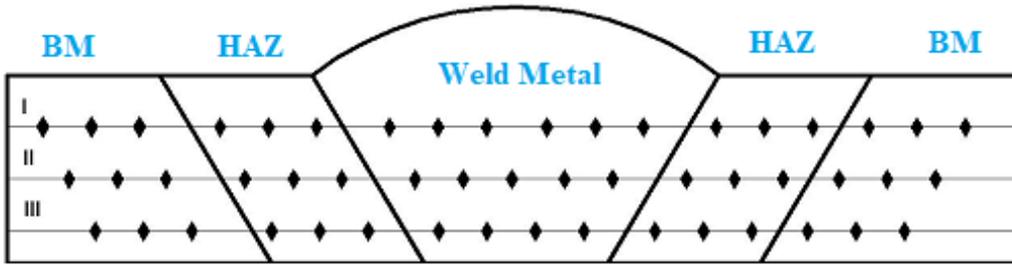
Figure 4. Microhardness measurement points

3. Results and Discussion

3.1. Macro and microstructure analyzes

In the study, 8 mm thick AA5083 alloys were joined by TIG and MIG welding methods using different welding parameters. Macrostructure images of the welded samples are given in Figure 5. In Figure 5, it is seen that defects such as pore and spatter were encountered in samples joined by the TIG welding method. It is thought that incomplete melting causes these specific defects within the welding zone [1].

When the MIG-welded samples are examined, it is clearly observed that the weld root is smoother since the melting is accurately accomplished. This situation can be explained by the fact that the joining is performed perfectly in the MIG welding method. When this situation seen in the macrostructure analysis is evaluated together with the tensile test results, the results overlap with each other.
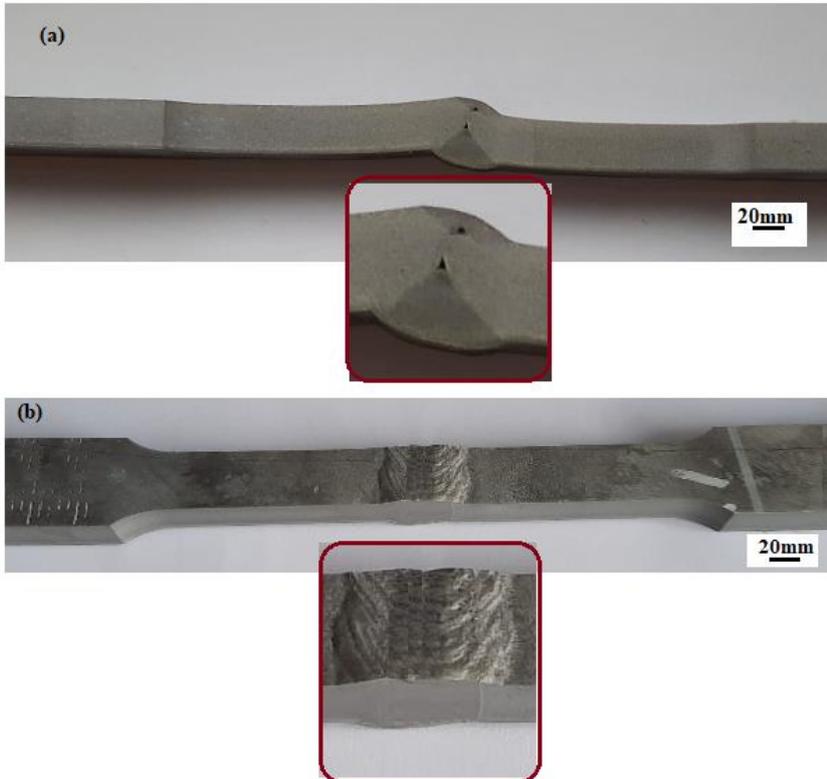
Figure 5. Macro images of welded samples (a) TIG welding (b) MIG welding

The post-tensile test macro structure images of the samples joined by TIG and MIG welding methods are given in Figure 6. When Figure 6 is examined, it is observed that the fracture starts from the porosity region in the TIG welded samples. This situation can be explained as an indication of the low mechanical

properties of the samples joined by the TIG welding method. In Figure 7, macro images of all tensile samples are given. When Figure 7 examined the fractures had occurred in the weld metals for the

samples joined with a lower welding current. This was because a lower welding current leads to poor penetration on the joints [1].
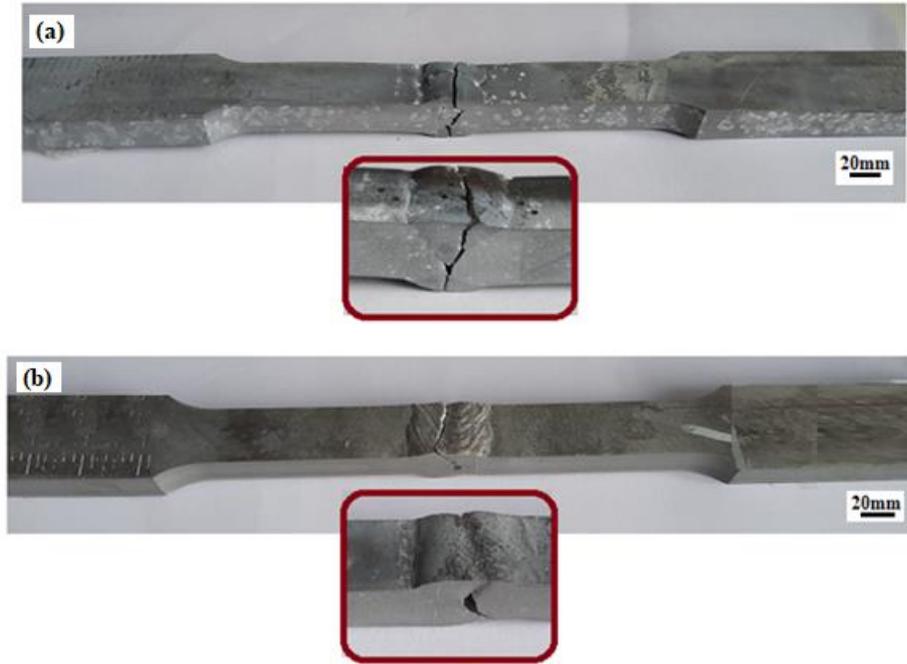

**Figure 6.** Macro images of welded samples (a) TIG welding (b) MIG welding
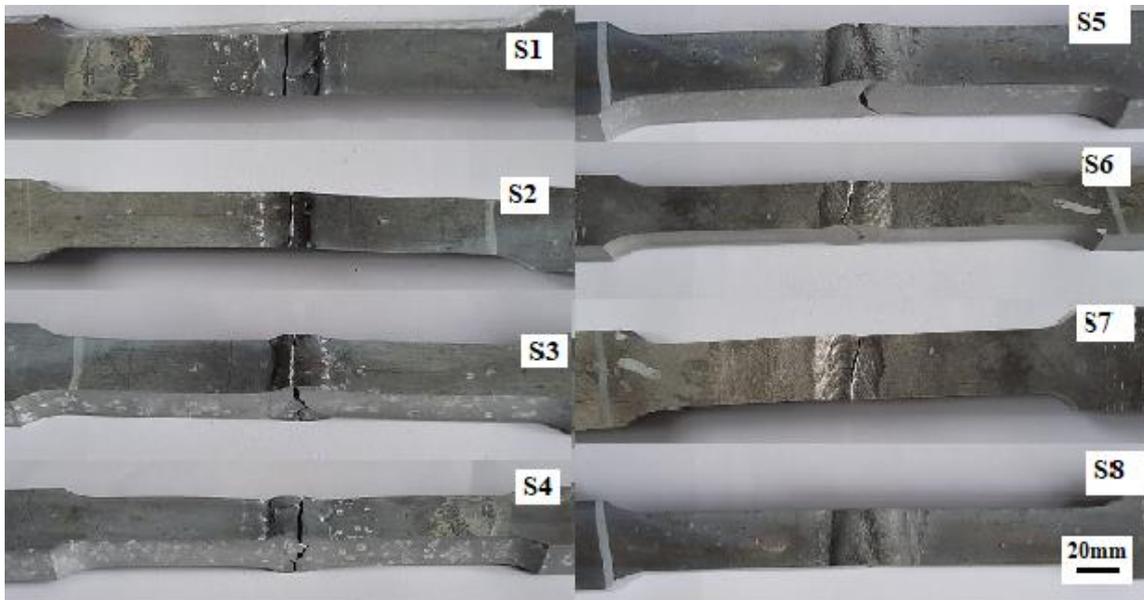
Figure 7. Macro images of tensile samples

In addition to the macrostructural analysis of welded samples, their microstructural analysis was carried out as well. Microstructural analyses were performed in

base metal and weld zone areas, as given in Figure 8. Different weld zone width for each sample was taken into account during the conduction of experiments.

Figure 8. Microstructure analysis areas for the samples

In Figure 9, microstructure images of the welded zone for the MIG welded samples are given. At the S4 sample in Figure 9 (S4), which is processed with the highest welding current, a growth in grain size can be seen. This situation can be explained as the elevation in heat input due to the increasing current. A similar case can be seen for the S3 sample as well. In the S1 sample, for which the welding current was selected as 150 A, and the S2 sample, where the welding current was 170 A, the heat input did not cause grain coarsening, on the contrary, it provided a better grain formation. When Figure 9 is examined, it is possible to talk about a typical one-directional solidified microstructure. Whether this solidified grain structure obtained in the MIG method is columnar or coaxial depends on the solidification rate [36]. Rapid solidification occurs in the MIG method. Fine grain size is formed as a result of rapid solidification in the MIG method. It is also seen that spherical-shaped porosities are found within the samples joined by MIG welding. The formation of these porosities is due to the hydrogen solubility in molten aluminum.
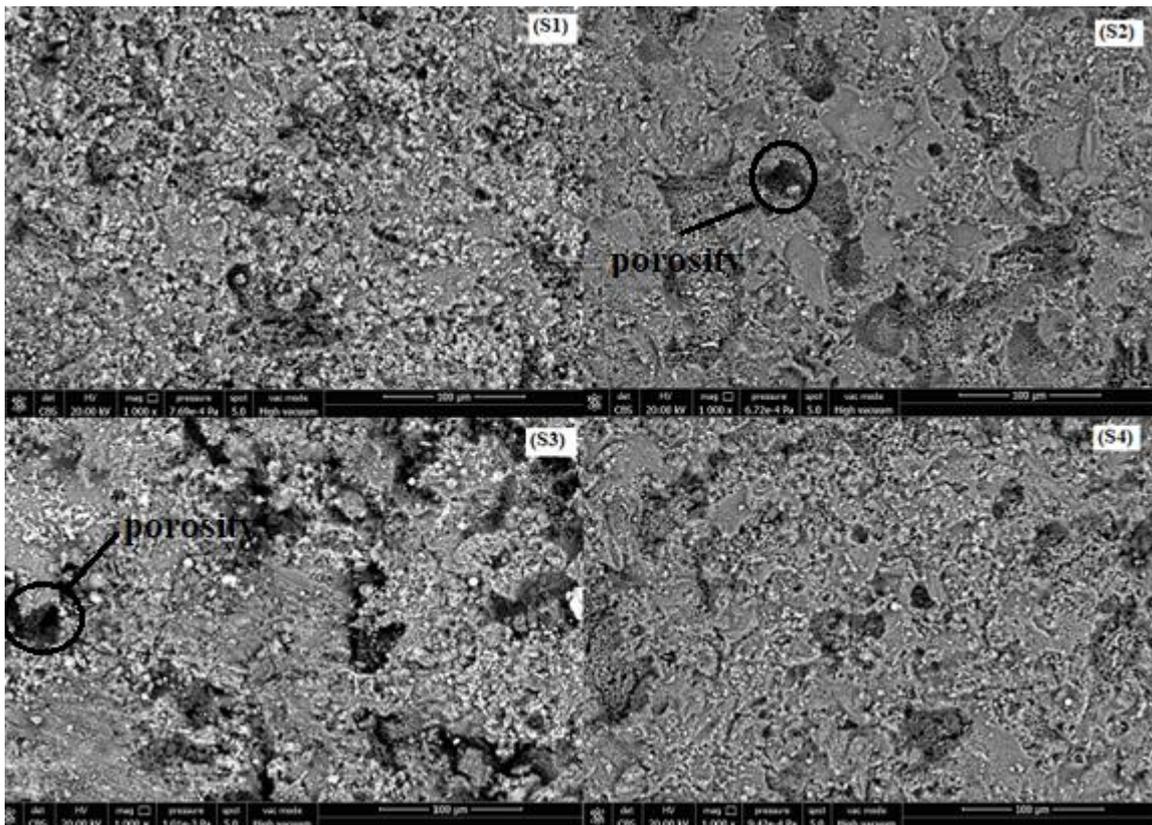

Figure 9. Microstructure images of welding zones of MIG welded samples

Figure 10 shows the microstructure images of the weld area of the samples joined by TIG welding. When TIG-welded samples are examined, it is seen that despite the increment in the welding current decreases the grain growth, the grain size obtained in TIG welding has not reached the size obtained in MIG welding. This is

because the melt convection in TIG welding is slower than in MIG welding [37,38]. The gradient convection of the melting slows down the solidification and causes the grains to grow. With the increase of welding current, solidification moderately accelerates, which eventually decreases the grain size. For this reason, the largest grain size was obtained in the S6 sample where the welding current is 140 A. The temperature gradient

difference in the TIG welding is different compared to MIG welding, which affects recrystallization. The amount of porosity formed in the samples joined by TIG welding is higher than the MIG welding method. The porosities within the samples were formed as a result of inhomogeneous heating and cooling processes.
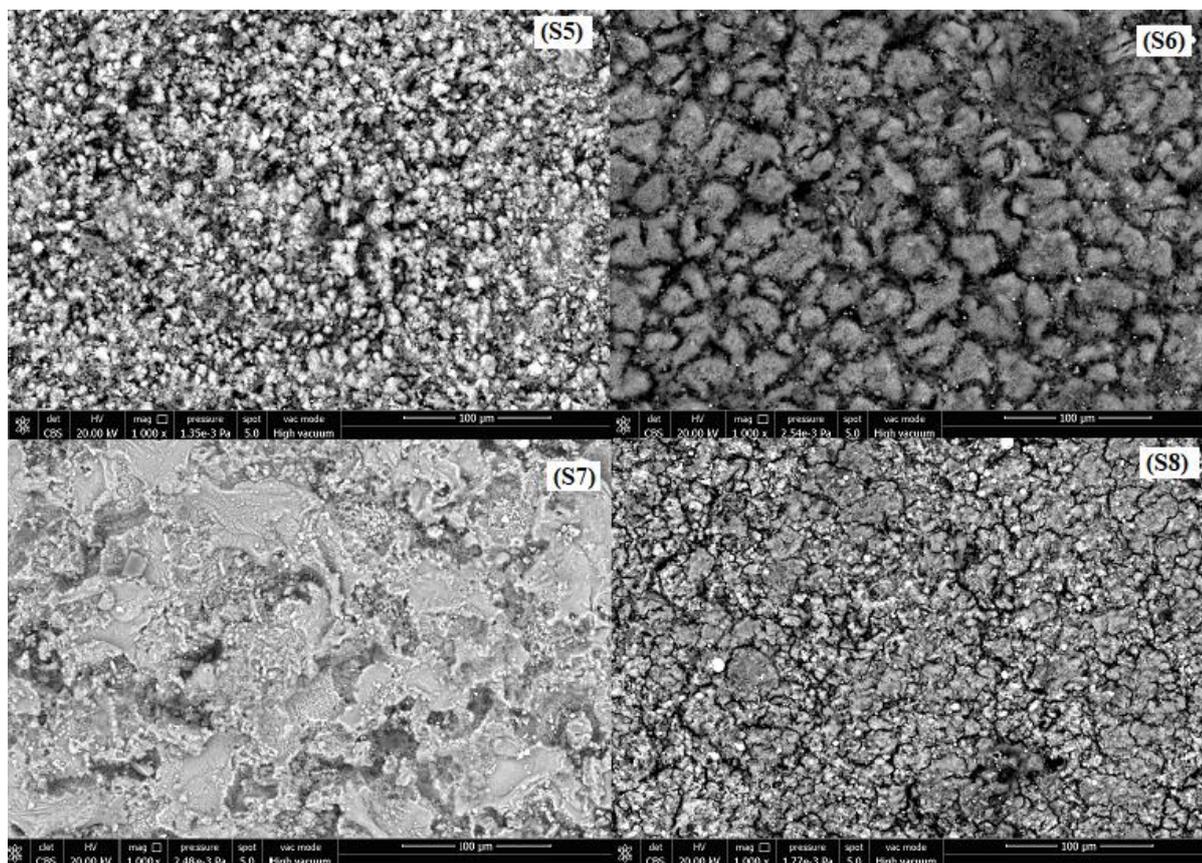
Figure 10. Microstructure images of welding zones of TIG welded samples

As a result of microstructure analyzes, it has been determined that the grain structure in MIG welding is favorable to TIG welding. Besides, it has been also observed that the second phase particles formed within the samples affect the strength and ductility [31].

3.2. Micro-Hardness tests

Microhardness measurements were made on samples joined with TIG and MIG weldings. Hardness values of TIG-welded samples are given in Figure 11, and hardness values of MIG-welded samples are given in Figure 12. By examining the hardness values of MIG-welded samples, it is seen that the average hardness

value of the base metal is HV79±2, while the average hardness value of the weld zone is HV63±3. It is also observed that there is a decrease in hardness from the base metal towards the weld zone [44]. Therefore, the hardness value in the weld zone is 18% lower than the hardness value of the base metal in MIG welding. Along with it, hardness values in the HAZ region are higher than in the weld zone for MIG welded samples (Figure 12). This causes the hardness of the weld metal area to drop, as β-phase deposits occur during the welding process [7]. The β-phase (Figure- dark areas) occurring in the weld zone is due to the distribution of the solute in the structure during solidification and occurs with the formation of a solute-rich local region.
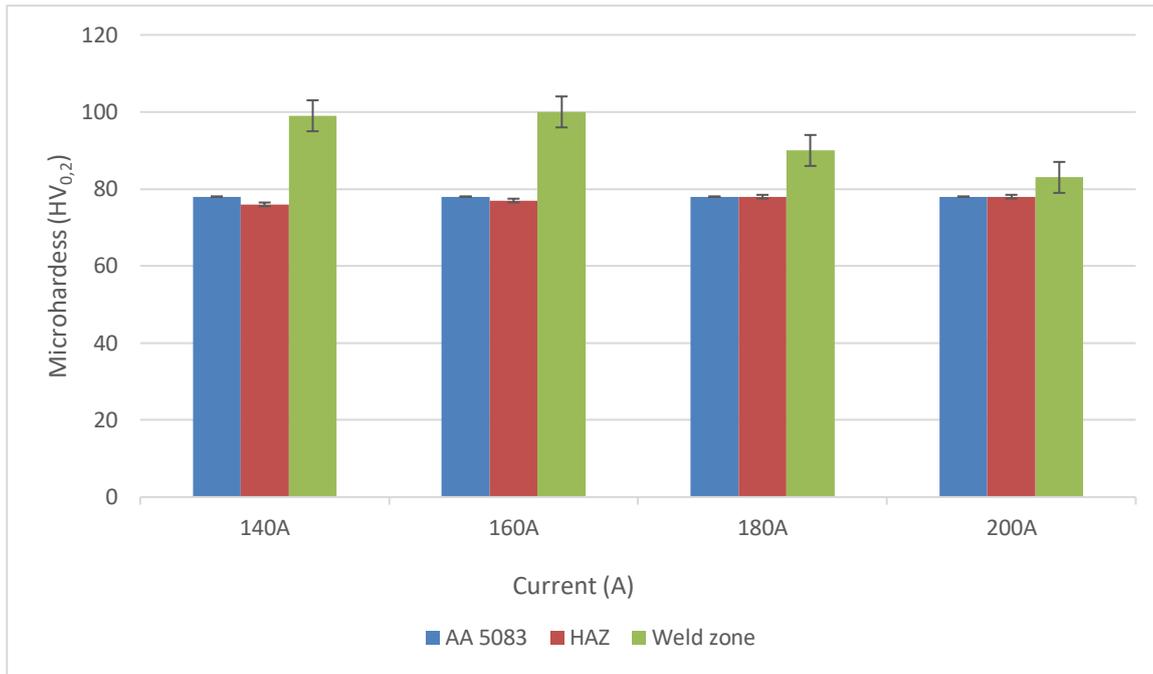
Figure 11. Microhardness values of TIG-welded samples
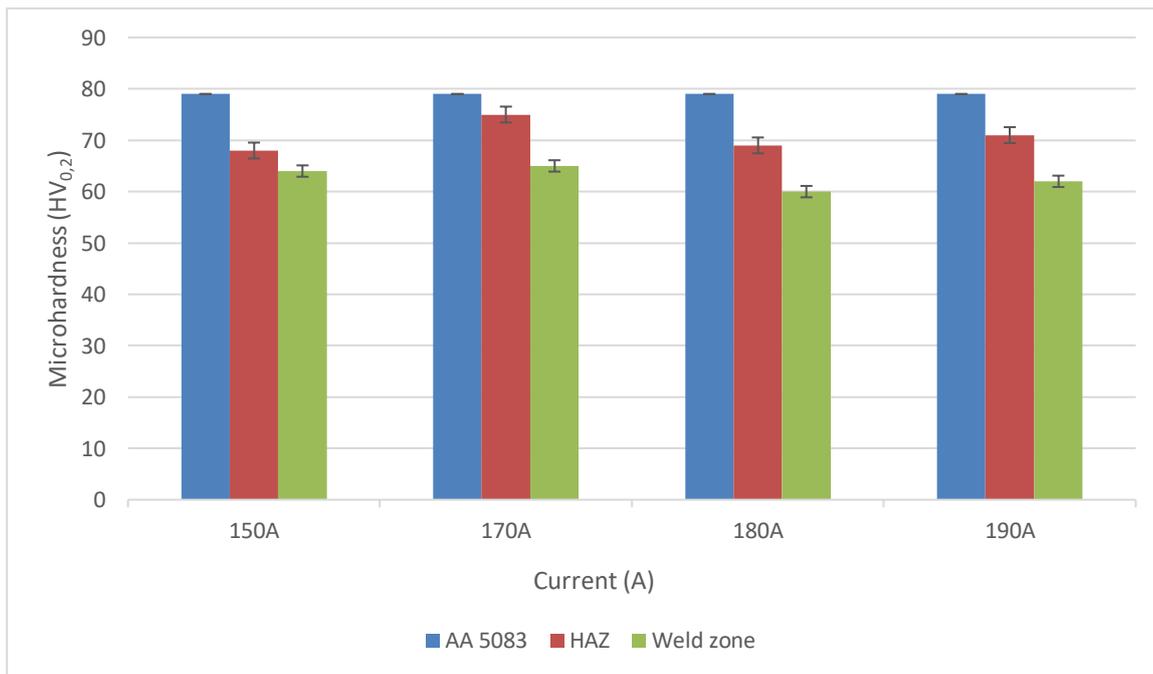

Figure 12. Microhardness values of MIG-welded samples

By examining the hardness values of TIG-welded samples, it appears that the average hardness value of the base metal is HV78±2, while the average hardness value of the weld zone is HV93±4. The hardness values of the HAZ region and the base material were achieved close to each other for the TIG-welded samples. However, the hardness values of the weld zone are higher than the other regions. This situation adversely affects the strength of the joining. With the increase in

welding current, the hardness value of the weld zone decreases. This reduction in hardness leads to a betterment in the strength of the joints. Obtaining the hardness value higher even than the base metal can be explained as an indicator that the weld zone is brittle and fragile. When the macro and microstructures of the fractured surface of the TIG-welded samples are inspected, the brittleness of the fracture type in the weld zone confirms this result.

When the hardness distribution of MIG welding was examined, it was determined that the hardness value of the base metal was the highest. This can be explained as the heat input occurring during the welding process affects the main material properties (grain structure, grain size). In TIG welding, the hardness value of the weld zone was higher than the other zones. This is due to the fact that these regions have become more brittle structures.

3.3. Tensile tests

Tensile tests were applied to the samples in order to determine the mechanical properties after welding. The change in the tensile stress of the TIG-welded samples according to the welding current is given in Figure 13. The tensile test results of the samples combined with AA 5083, 140 A, 160 A, 180 A and 200 A welding currents are 317 MPa, 122 MPa, 105 MPa, 119 MPa and 125 MPa respectively. As Figure 13 indicates, the maximum tensile stress (125 MPa) could be obtained at 200 A. All welded samples were fractured from the weld zone during the tensile tests. This proves that the strength of the weld zone is less than the strength of the base material. Although the weld zone strength increases with the welding current increment, it could never reach the strength of the base material. Porosities formed within the weld zone and microstructural changes that occur during the solidification of the weld pool reduce the strength of the welded parts. In the study, porosities were clearly observed in the TIG-welded samples. Previous studies in literature verify this phenomenon [40-42]. In addition, the strength of the welded joint depends on the penetration depth as well. Welding current increase leads to deeper penetration, therefore the welded joint strengthens with the increasing welding current. Besides, since the root of the weld is partially joined, it acts as a stress formation zone, causing crack initiation and propagation, thus causes the joining strength to weakens [31]. One of the most considerable problems seen in TIG welding is grain coarsening that appears after slow solidification at the interfaces. The grain coarsening formation in the welded area significantly reduces the strength of this specific region.
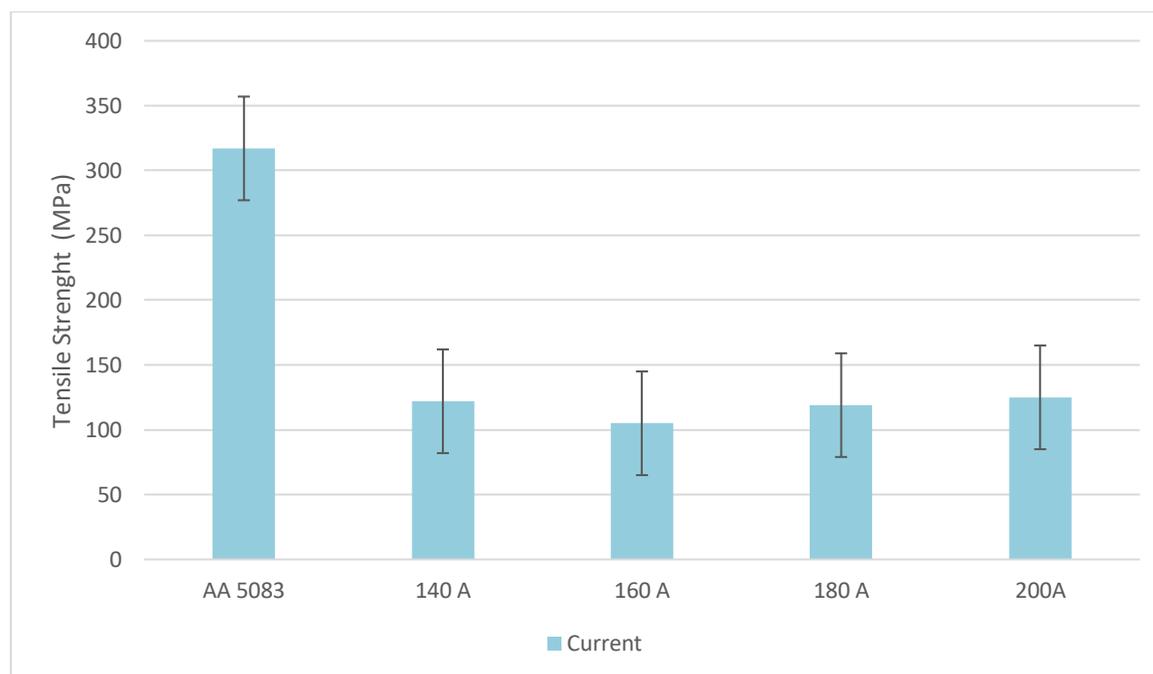

Figure 13. Tensile test results of TIG-welded samples

In this study, tensile tests for AA5083 alloys with 8 mm thickness were carried out to determine the mechanical properties after MIG welding at 150A, 170A, 180A, and 190A. The tensile test results of the samples combined with 150 A, 170 A, 180 A and 190 A welding currents are 301MPa, 305MPa, 270 MPa and 263MPa, respectively, and are given in Figure 14. As the figure indicates, the maximum tensile stress (305 MPa) was obtained at 170 A. In operations where the welding current passes 170 A, the strength of the welded joints decreases again. With the increase of the welding current value, the temperature of the welding zone elevates; thus causes the microstructure of the joint area to deteriorate and its strength to decrease. The grain structure solidified in the weld zone changes depending on the cooling rate. Since cooling is faster

in MIG than TIG, a dendritic internal structure was formed. With the increase of the current in MIG welding the temperature gradient difference, which significantly affects the recrystallization process, leads to a decrease in work-hardening and eventually causes a decrease in strength [43]. Furthermore, it causes coarse-graining due to welding current increment, which also leads to a reduction in strength. For this reason, with the increase of the welding current in MIG welding, a decrease in the strength for welded samples takes place again. The strength values obtained in the process of joining with MIG welding are very close to the yield stress value of the main material (317 MPa). This clearly shows that 170A is the most suitable parameter for MIG welding.
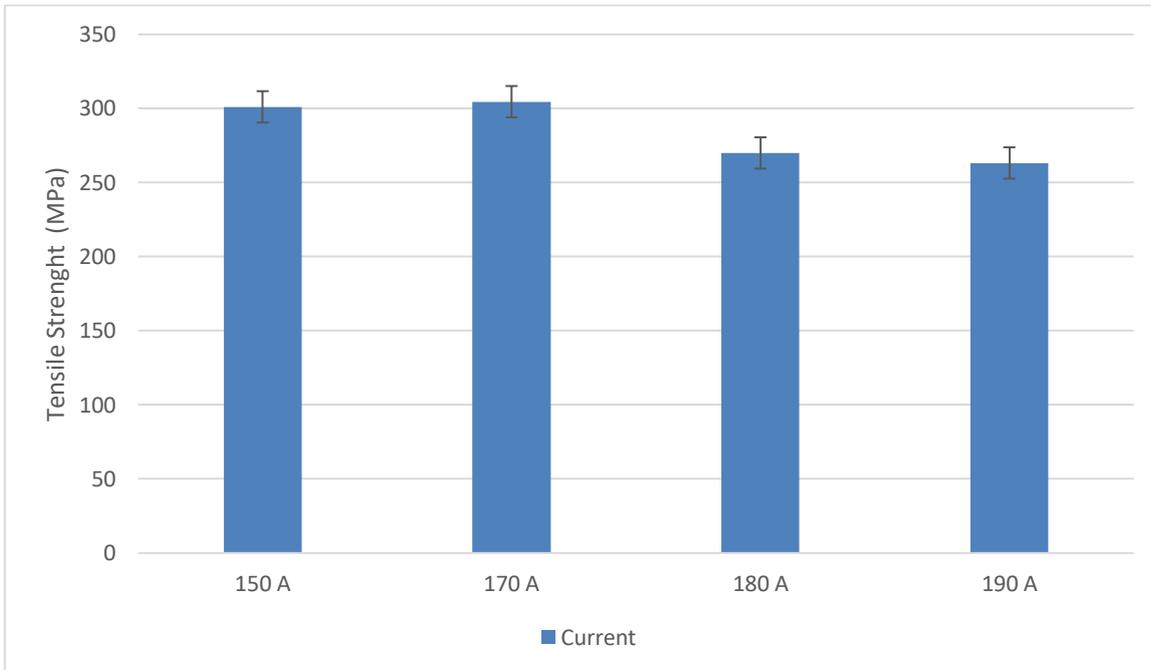

Figure 14. Tensile test results of MIG-welded samples

In the study, microstructure analyzes of the broken surfaces after the tensile test were also made. Broken surface evaluation for S4 and S6 samples, which are the samples with lowest strength values for both welding methods, was taken into consideration. In Figure 15, their microstructure examinations for both TIG ad MIG welding methods are given. Concentric grains exhibiting semi-ductile behavior in the base metal were observed during the AA 5083 core metal internal structure inspections. Dimples formed within the S4 sample are smaller than the ones in the parent material. Furthermore, sample S6 exhibited a fragile behavior. In either method, the main material is more ductile.
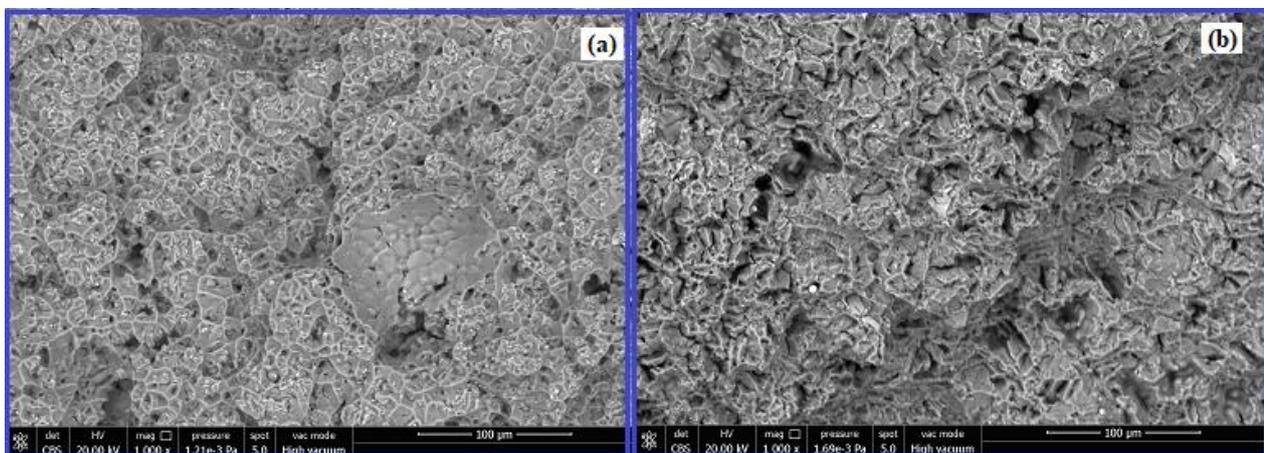

Figure 15. Post-tensile test macro structure images of broken surfaces (a) MIG-welded samples (b) TIG-welded samples

The tensile strength of the samples combined with the TIG method was lower than the samples combined with the MIG method. This is due to the formation of grain coarsening due to slow solidification during the welding process. In the TIG method, porosities occurred in the welding zone and this caused a decrease in strength. If the welding current selected for the MIG method exceeds 170 A, a decrease in strength is obtained; In the TIG method, the strength increases as the current increases.

4. Conclusion

In this study, AA5083 alloys with 8 mm thickness were butt-welded under different current values by using MIG and TIG weldings. The results are as follows:

The slow solidification occurring at the interfaces during the joining process with the TIG welding method leads to a grain growth, which caused the strength values to be lower than the MIG welding method.

The weld zone hardness values of the MIG welding were obtained lower than the TIG welding. On the other hand, the hardness value of the weld zone was higher than the base metal in the TIG welding method. These high hardness values are an indication that the welding zone is brittle and fragile.

Maximum tensile stress of 125 MPa for TIG-welded sampes was acquired at 200 A. It is also concluded that more current value in TIG welding means higher strength.

For MIG-welded samples, maximum tensile stress of 305 MPa was acquired at 170 A. A decrease in tensile strength was seen when the current value exceeded 170 A. For this reason, the most suitable current value for MIG welding method was determined as 170 A.

Acknowledgment

Conflicts of interest

The authors state that did not have conflict of interests

References

[1] Mercan E., Ayan Y., Kahraman N., Investigation on joint properties of AA5754 and AA6013 dissimilar aluminum alloys welded using automatic GMAW, *Engineering Science and Technology, an International Journal,* 23 (2020) 723-731.

[2] Franz D., Szilvasi T., Irran E., Inoue S., A monotopic aluminum telluride with an Al= Te double bond stabilized by N-heterocyclic carbenes, *Nature Communication,* 6 (2015) 1-6.

[3] Zamzami I.A., Susmel L., Nominal and local stress quantities to design aluminium-to-steel thin welded joints against fatigue, *International Journal of Fatigue,* 101 (2) (2017) 137–158.

[4] Heinen P., Wu H., Olowinsky A., GillnerA., Helium-tight laser beam welding of aluminum with brillant laser beam radiation, *Physics Procedia*, 56 (2014) 554–565.

[5] Li J., Xue J., Zhang Z., Hu Y., Effects of thermal frequency on microstructures, *Applied Science,* 8 (4) (2018) 540.

[6] Borrego L.P., J.D. Costa, J.S., Jesus, A.R. Loureiro, J.M. Ferreira., Fatigue life improvement by friction stir processing of 5083 aluminium alloy MIG butt welds, *Theoretical and Applied Fracture Mechanics*,70 (2014)68-74.

[7] Ilman M.N., Triwibowo N.A., Wahyudianto A., Muslih M.R., Environmentally assisted fatigue behaviour of stress relieved metal inert gas (MIG) AA5083 welds in 3.5% NaCl solution, *International Journal of Fatigue,* 100 (2017) 285–295.

[8] Perel V.Y., Misak H.E, Mall S., Jain V.K, Biaxial fatigue crack growth behavior in aluminium alloy 5083-H116 under ambient laboratory and saltwater environments, *Journal of Material Engineering Performance,* 24(4) (2015) 1565–72.

[9] Abkenar M.R., Kihl D.P., Manzari M.T., Fatigue tests on aluminium specimens subjected to constant and random amplitude loadings, *ASME Journal of Materials Technology,* 138(2016) 1–7.

[10] Holtz R.L., Pao P.S., Bayles R.A., Longazel T.M., Goswami R., Corrosion fatigue of aluminium alloy 5083-H131 sensitizes at 448 K (175°C), *Metal Materials Transaction A,* 43 A (2012) 2839–2849.

[11] Miller K.W., Chao Y.J., Wang P.C., Performance Comparison of Spot-Welded, Adhesive Bonded, and Self-Piercing Riveted Aluminium Joints, *ASM proceedings of the international conference: trends in welding research,* (1998) 910–915.

[12] Costa J.D.M, Jesus J.S., Loureiro A., Ferreira J.A.M., Borrego L.P., Fatigue life improvement of mig welded aluminum T-joints by friction stir processing, *Internatinal Journal of Fatigue*, 61 (2014) 244–54.

[13] Messler Jr R.W., Principles of welding: processes, physics, chemistry and metallurgy, 1st ed. New York: John Wiley & Sons, (1999).

[14] Ilman M.N., Kusmono, Muslih M.R., Subeki N., Wibowo H., Mitigating distortion and residual stress by static thermal tensioning to improve fatigue crack growth performance of MIG AA5083 welds, *Materials Design*, 99 (2016) 273–283

[15] Mochizuki M., Toyoda M., Weld distortion control during welding process with reverse-side heating, *ASME Journal of Pressure Vessel Technology,* 129 (2007) 619–29.

[16] Han W.T., Wan F.R., Li G., Dong C.L., Tong J.H., Effect of trailing heat sink on residual stresses and welding distortion in friction stir welding Al sheets, *Science Technology Welding Joint*, 16 (5) (2011) 453–8.

[17] Cheng X., Fisher J.W., Prask H.J., Gnaupel-Herold T., Yen B.T., Roy S., Residual stress modification by post-weld treatment and its beneficial effect on fatigue strength of welded structures, *Internatinal Journal of Fatigue,* 25 (2003) 1259–69.

[18] Ipekoglu G., Cam G., Effects of initial temper condition and post weld heat treatment on the properties of dissimilar friction-stir-welded joints between AA7075 and AA6061 aluminium alloys, *Metal Materials Transactions A,* 45 (2014) 3074–87.

[19] Vijay S., Rajanarayanan S., Ganeshan G.N., Analysis on mechanical properties of gas tungsten arc welded dissimilar aluminium alloy (Al2024 & Al6063), *Materials Today: Proceedings*, 21 (2020) 384–391.

[20] Miller, Equipments.Welders. Available at: https://www.millerwelds.com/equipment/welders /mig-gmaw. Retrieved March 2, 2021.

[21] Bunaziv I., Akselsen O.M., Salminen A., Unt A., Fiber laser-MIG hybrid welding of 5 mm 5083 aluminum alloy, *Journal of Materials Processing Technology* ,233 (2016) 107–114.

[22] Yong P., Changbin S., Yadong Z., Ying C., Comparison of Electrochemical Behaviors between FSW and MIG Joints for 6082 Aluminum Alloy, *Rare Metal Materials and Engineering*, 46(2) (2017) 0344-0348.

[23] Schneider C.F., Lisboa C.P., Silva R.A and Lermen R.T., Optimizing the Parameters of TIG-MIG/MAG Hybrid Welding on the Geometry of Bead Welding Using the Taguchi Method, *Journal of Manufacturing and Materials Processing,* (2017) 1- 14.

[24] Subbaiah K., Microstructure and Mechanical properties of Tungsten Inert Gas Welded Joints of Cast Al-Mg-Sc alloy, *Materials Today: Proceedings*, 16 (2019) 248–25.

[25] Zhang C., Baob Y., Zhua H., Niea X., Zhanga W., Zhanga S., Zeng A. A, comparison between laser and TIG welding of selective laser melted AlSi10Mg, *Optics and Laser Technology*, 120 (2019) 105696.

[26] Singh L., Singh R., Singh N. K., Singh D., Singh P,. An Evaluation of TIG Welding Parametric Influence on Tensile Strength of 5083 aluminium Alloy, International Journal of Mechanical, *Industrial Science and Engineering* (2013) 795-798.

[27] Kumar S., Shahi A. S., Effect of heat input on the microstructure and mechanical properties of gas tungsten arc welded AISI 304 stainless steel joints, *Materials and Design,* (2011) 3617–3623.

[28] Jahanzaib M., Hussain S., Wasim A., Aziz H., Mirza A., Ullah S., Modeling of weld bead geometry on HSLA steel using response surface methodology, *The İnternational Journal of Advance Manufacturing Technology,* (2017) 2087 – 2098.

[29] Raveendra A., Kumar B.V.R.R, Sivakumar A., Reddy V.P K., Influence of Welding Parameters on Weld Characteristics of 5052 Aluminium Alloy sheet Using TIG Welding, *International Journal of Application or Innovation in Engineering & Management (IJAIEM)*, (2014) 186-190.

[30] Gharibshahiyan E., Raouf A.H., Parvin N., Rahimian M., The effect of microstructure on hardness and toughness of low carbon welded steel using inert gas welding, *Materials & Design,* (2011) 2042–2048.

[31] Liu Y., Wang W., Xiea J., Sunb S., Wang L., Qiana Y., Menga Y., Wei Y., Microstructure and mechanical properties of aluminum 5083 weldments by gas tungsten arc and gas metal arc welding, *Materials Science and Engineering A,* 549 (2012) 7-13.

[32] Hirata T., Oguri T., Hagino H., Tanaka T., Chung S.W., Takigawa Y., Higashi K., Influence of friction stir welding parameters on grain size and formability in 5083 aluminum alloy, *Material Science and Engineering A,* 456 (2007) 344–349.

[33] Peel M., Steuwer A, Preuss M., Withers P.J., Microstructure, mechanical properties and residual stresses as a function of welding speed in aluminium AA5083 friction stir welds, *Acta Materilia,* 51 (2003) 4791–4801.

[34] Haboudou A., Peyre P., Vannes A.B., Peix G., Reduction of porosity content generated during Nd: YAG laser welding of A356 and AA5083 aluminium alloys, *Materials Science and Engineering A,* 363 (2003) 40–52.

[35] James M.N., Hughes D.J., Hattingh D.G., Mills G., Webster P.J., Residual stress and strain in MIG butt welds in 5083-H321 aluminium: As-welded and fatigue cycled, *International Journal of Fatigue*, 31 (2009) 28–40.

[36] Spinelli J.E., Ferreira I.L., Garcia A., Influence of melt convection on the columnar to equiaxed transition and microstructure of downward unsteady-state directionally solidified Sn–Pb alloys, *Journal of Alloys and Compounds*, 384 (2004) 217–226.

[37] Wu C.S., Computer Sımulatıon Of Three-Dımensıonal Convectıon In Travellıng Mıg Weld Pools, *Engineering Computations*, 9 (1992) 529–537.

[38] Mutombo K., Toit M.D., Microstructure and mechanical properties of aluminum 5083 weldments by gas tungsten arc and gas metal arc welding, *Materials Science Forum*, 654–656 (2010) 2560–2563.

[39] Moreira P.M.G.P., Figueiredo M.A.V., Castro P.M.S.T., Fatigue behaviour of FSW and MIG weldments for two aluminium alloys., *Theory Application Fracture Mechanics,* 48 (2007) 169–177.

[40] Kumar K., Mohan P., Masanta M., Influence of welding current on the mechanical property of 3 mm thick commercial 1050 aluminium butt joint weld by AC-TIG welding method, *Materials Today: Proceedings,* 5 (2018) 24141–24146.

[41] Ahmad Ibrahim M. F., Bakar S.R.S., Jalar A., Othman N. K., Sharif J., Daud A. R., Rashdi N. M., Effect of porosity on tensile behavior of welded AA6061-T6 aluminium alloy, *Applied Mechanics and Materials,* (2011) 534-53.

[42] Pessoa E. C. P., Bracarense A. Q., Zica E. M., Liu S., Guerrero F. P., Porosity variation along multipass underwater wet welds and its influence on mechanical properties, *Journal of Materials Processing Technology,* (2006) 239-24.

[43] Borrego L.P., Costa, J.D., Jesus, J.S., Loureiro A.R., Ferreira J.M., Fatigue life improvement by friction stir processing of 5083 aluminium alloy MIG butt welds, *Theoretical and Applied Fracture Mechanics,* 70 (2014) 68-74.

[44] Yürük A., Kaya Y., Kahraman N., Alüminyum Alaşımlarının MIG Kaynak Yöntemi ile Kaynak Edilebilirliğinin İncelenmesi, *Bayburt Üniversitesi Fen Bilimleri Dergisi*, 4(1) (2021).

Effects of various heat treatments on microstructure and mechanical properties of investment cast Co-Cr-Mo implants

Kübra ÖZTÜRK [1], * iD *, Onur ERTUĞRUL* [2] iD *, Murat ÖZCAN* [3] iD

[1] *Dokuz Eylül University, Department of Metallurgical and Materials Engineering, İzmir/TURKEY*
[2] *İzmir Katip Çelebi University, Department of Materials Science and Engineering, İzmir/TURKEY*
[3] *Eksen Hassas Dokum, İzmir/Turkey*

Abstract

In this study, the effects of various heat treatments (solutionizing, solutionizing + aging) on the microstructure and mechanical properties of the Co-Cr-Mo based hip implants produced by investment casting were investigated. The solution treatments were carried out at 1125°C, 1175°C and 1225°C for 3 hours under argon atmosphere. The aging treatments were carried at 850°C for 4 hours. The samples were examined under scanning electron microscope (SEM) and optical microscope (OM). Room temperature tensile tests and hardness tests were applied. The results showed that, the process of solutionizing at 1175°C and subsequent aging resulted in the formation of the smallest size precipitates with more homogeneous distribution in the interdendritic space of the as-cast structure compared to other treatments. According to tensile test results of the aged samples, as the solutionizing temperature increased to 1175°C both strength and elongation values increased. However, with the increase of solutionizing temperature to 1225°C, strength and elongation values decreased again. Solutionizing temperature of 1175°C gave the best microstructure-mechanical property relationship. Moreover, hardness values increased with the subsequent aging, yet do not change significantly with the solutionizing temperature.

1. Introduction

Cobalt base alloys (Co–Cr–Mo), conforming to ASTM F-75 standard, are widely used in several medical applications such as knee and hip joint replacement, given their excellent biocompatibility, corrosion and wear resistance, combined with their good mechanical properties [1]. ASTM F-75 grade alloy is generally produced by investment casting method [2]. This method may lead to some defects in the as-cast position such as porosity, large grain size, hard precipitates in interdendritic zones, low ductility, low fatigue strength and inhomogeneties in carbide morphology and their size [2,3]. This is because the microstructures of the as-cast alloys, which indicate solidification segregation (interested to the formation of precipitates), considerably with the casting parameters (e.g., the melt temperature and cooling rate) [3, 4]. Several solutions to this problem have been suggested to decrease defect amount and to develop the mechanical properties such as ductility and strength of this alloy. However, the mechanical properties of these alloys can be improved

by heat treatments by dissolving the wide carbide area and generate a more homogeneous microstructure [5]. Nevertheless, the mechanical properties can be improved with additional heat treatments by dissolving the large carbide network and produce a more homogeneous structure [6]. Lee et al. studied the effect of the addition of N on the microstructure and mechanical properties of the C-free Co-Cr-Mo alloys with various Cr contents. They revealed that Ni-free Co-Cr-Mo alloys with enriched Cr content up to 34 wt%, modified by N addition, are suitable for hip and knee joints that are produced on the basis of the casting process such as investment casting [7]. Their properties such as corrosion resistance, wear resistance, excellent biocompatibility, hardness of Co-Cr-Mo alloy depend mainly on the carbon content and the type of heat treatment applied [8]. The main strengthening mechanism of Co base alloys is the presence of second phase precipitates. The precipitation hardening performance of the alloy is closely related to the phase, size, amount, and distribution of precipitates in the metallic matrix [8,9].

Gomez et al. investigated the effects of casting parameters such as pouring temperature on the microstructure of ASTM-F75 (Co-28%Cr-6%Mo) alloy [10]. They showed that mechanical properties can be optimized through controlling processing parameters. The microstructural study showed that pouring and preheating mold-temperatures affect the evolution of the microstructure during rapid cooling and various microstructures result in a large range of mechanical properties for the alloy ASTM-F75. The preheating mold temperature and the liquid temperature varied between 900, 1000, and 1410, and 1470°C, respectively. According to the results, optimum static strength and ductility were obtained when shrinkage microporosity decreased and the volume fraction of $M_{23}C_6$ type ''eutectic'' carbides precipitated at grain boundaries [10]. It is also found that the as-cast grain size is very sensitive to preheating mold and metal pouring temperatures. Moreover, the formation of ''eutectic'' carbides can be minimized by increasing the preheating mold and metal pouring temperatures [10,11].

Co-Cr-Mo alloys generally consist of a metastable γ (fcc) matrix and ε (hcp) martensite. The ε martensite is formed during quenching, plastic deformation, and isothermal heat treatment. [12]. The as-cast ASTM F-75 alloy consists of two primary phase microstructure: γ-face centered cubic (γ-fcc) phase and ε hexagonal close packed (ε-hcp). γ -face centered cubic (γ-fcc) phase which shows advanced elongation and ultimate tensile strength when temperature is high enough [12]. Another is ε-hcp phase which shows low elongation and brittle fracture on straining when temperature is low [4, 13]. Co-base alloys present a dentritic α-fcc metastable matrix due to tansformation of fcc→hcp so obtained precipitated formed in microstructured by $M_{23}C_6$ carbides, α or M_6C carbide phase σ phase both α and σ phases [13, 14]. Carbide precipitation at grain boundaries and interdendritic regions is the major strengthening mechanism in the as-cast condition. K. Yamanaka et al., studied the the effects of carbon on the relation between the microstructure and the mechanical properties of Ni-free Co–Cr–W-based cast alloys. Result of the study show that adding carbon to the alloys increased the amount of interdendritic precipitates that formed and changed the precipitation behavior [15].

The aim of the study is to investigate the effects of the heat treatment procedure and temperature on microstructure, tensile properties, and hardness of the investment-casted ASTM-F75 alloy. For the first set

of samples, only solution treatment was applied at three different temperatures (1125, 1175 and 1225°C, respectively). Then, aging treatments were applied to the solutionized samples. The solution treatment was applied in order to provide fine and homogenously distributed grain structure, and also to dissolve some of the carbides in the post-casting structure. Additional aging treatments were applied in order to increase the strength and hardness values. With the optimum heat treatment, it is expected that the ductility of the final material will increase significantly compared to as–cast material.

2. Materials and Methods

2.1 Casting process

Cobalt based superalloy in accordance with the standard ASTM F-75 was used in this study which has Cr and Mo as main alloying elements and Ni, Fe, C, Mn and Si as trace elements. The casting is made by ASTM F-75 alloy ingot directly. The compositional limits of this alloy is shown in Table 1 and the spectrometer results of 7 samples produced in this study are listed in Table 2. There are three basic steps required for investment casting. These are wax-based mold preparation, dipping into ceramic slurry and shaping, and finally pouring molten metal into this mold. In the production step, firstly, the wax is melted at 72°C. It is mixed for homogenization. Then, it is injected into aluminum mould with the help of temperature and pressure. After visual and dimensional controls, wax models are being sticked to wax runner with the help of heat. Figure 1a represents the pattern creation step. After assemblying, tree is being coated with refractories. Refractories depend on quality requirements. Zircon, Alumina, various Alumina Silicates, Mahnezia can be used. Wax assemly is being coated with appropriate refractory and allowed to dry for every coating step. Next operations are wax removal with autoclave furnace and ceramic mold sinterring at 1000°C for 25 minutes. The aim of the sintering process is to prevent the thermal shock that may occur when the molten metal is spilled and to facilitate the sweep of the molten metal. While preheating the mould in furnace, the solid metal was placed in the induction furnace, and melted at 1560°C. Figure 1b demonstrates the melted metal in the furnace. The ceramic mold is connected to the furnace and the melt metal mold is poured. After 22 minutes, the casting ends as shown in Figure 1c. The mold is allowed to cool to room temperature as shown below in Figure 1d.

(a)

(b)

(c)

(d)
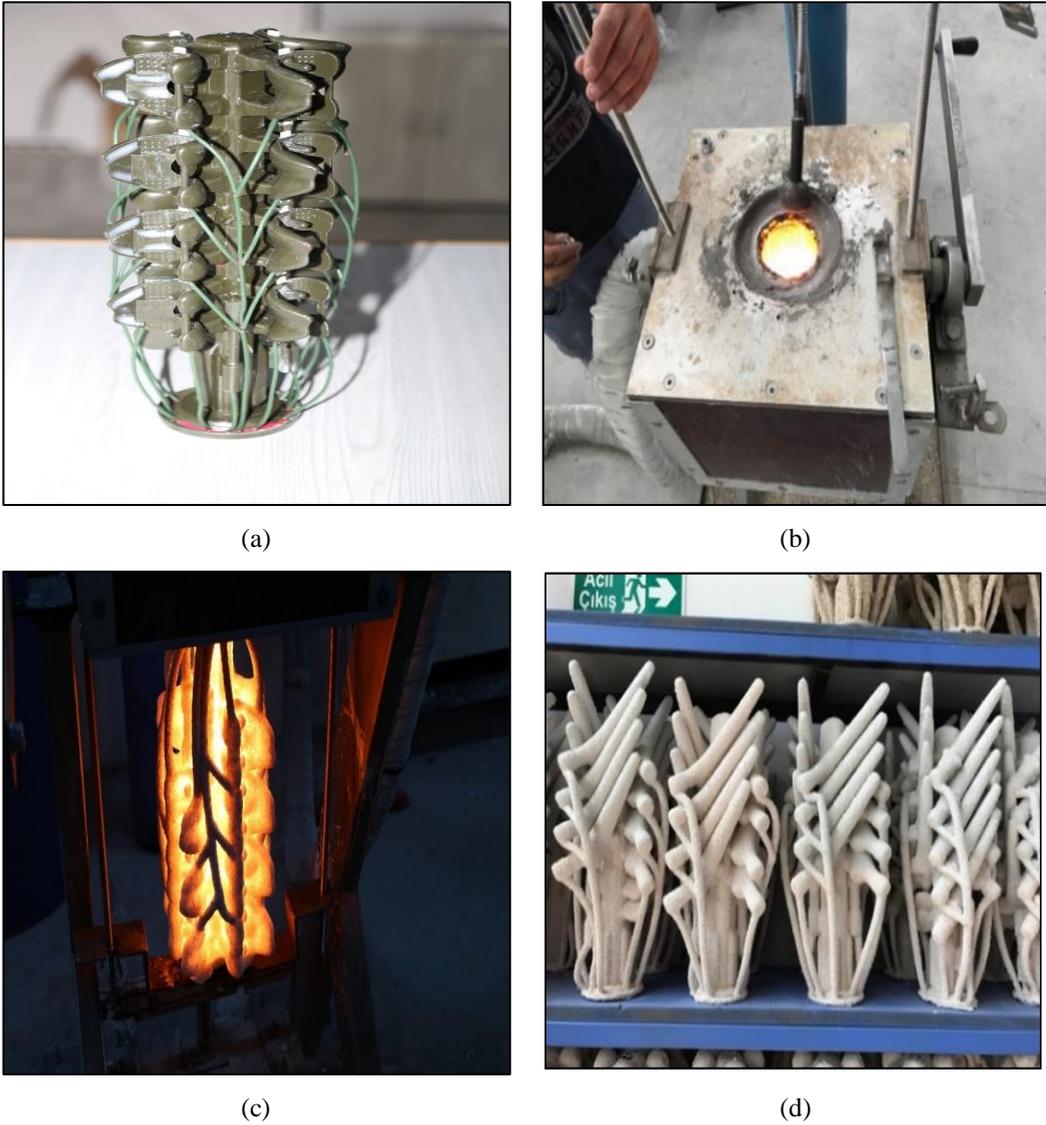
Figure 1. (a) Pattern creation, (b) Melting of ASTM F-75 alloy, (c) Pouring, (d) Cooling of mold

Table 1. The chemical composition of the ASTM F-75 alloy

Element (wt%)	Co	Cr	Mo	Ni	C	Si
ASTM F-75	Bal.	27-30	5-7	<0.50	<0.35	<1.0

Table 2. The spectrometry analysis results of the as-cast samples

Elements (%)	Cr	Mo	Ni	Fe	C	Mn	Si	Co
C1	28,17	5,34	0,23	0,28	0,22	0,59	0,32	64,84
C2	28,61	5,97	0,50	0,40	0,22	0,43	0,33	63,55
C3	27,31	5,83	0,22	0,27	0,27	0,59	0,30	65,21
C4	27,63	5,27	0,23	0,32	0,29	0,70	0,38	65,18
C5	27,78	5,87	0,42	0,39	0,25	0,36	0,59	64,34
C6	28,68	5,54	0,45	0,38	0,23	0,41	0,67	63,65
C7	28,48	5,35	0,23	0,32	0,24	0,59	0,38	64,41

2.2 Solution treatment and aging treatment processes

Six test samples were encoded as C1, C2, C3, C4, C5, and C6. Test samples were undergone to solution treatment (C1, C3, C5) and solution treatment + aging treatment (C2, C4, C6). One set of samples are shown in Figure 2a. The solution treatments were performed at 1125°C, 1175°C and 1225°C temperatures for 3 h, followed by quenching in water. The heat treatments were carried out in a high-temperature tube furnace under an inert gas atmosphere (Argon). The heat treatment setup is shown in Figure 2b. The aging treatment was performed at 850°C for 4h. All samples were applied to solution treatment only whereas the C2, C4, C6 samples were subjected to only aging as shown in Table 3.

(a)

(b)

Figure 2. (a) Tensile test samples together with hardness samples of ASTM F-75 and (b) tubular furnace

Table 3. Sample coding and Experimental parameters used in the present study.

Sample Codes	Heat Treatment
C1	Solutionizing (1125°C)
C2	Solutionizing (1125°C) +Aging
C3	Solutionizing (1175°C)
C4	Solutionizing (1175°C) +Aging
C5	Solutionizing (1225°C)
C6	Solutionizing (1225°C) +Aging
C7	As-Cast (No heat treatment)

2.3 Microstructural study

The preparation of samples for optical microscopy (OM) and scanning electron microscopy (SEM) were carried out using conventional procedures such as grinding and polishing steps. The samples were first grinded with SiC grinding papers. Polish using diamond suspension (1 and 3 µm). Afterwards, the samples were thoroughly cleaned so as to remove any polishing residue. The sample surface was then etched to obtain examination of microstructure. Etching solution consist of 4 g Sodium Hydroxide, 100 ml water, 4 g potassium permanganate. This solution immersed over the surface for 25 seconds. Then the samples were cleaned by rinsing with ethanol. Then, the sample is placed on the optical microscope. The samples were examined also by SEM using a Carl Zeiss 300VP microscope which was operated at an acceleration voltage of 15 kV. Moreover, energy dispersive spectroscopy (EDS) techniques were employed to provide a more accurate characterization of the different precipitated phases, even though the EDS technique provides a semi-quantitative analysis.

2.4 Mechanical testing

Two tensile samples were cut from the produced hip implants. After solution treatment and aging heat treatment processes were applied, tensile samples are machined from the material in the desired orientation. The tensile test samples were 12.5 mm in gauge diameter (D), 10 mm in radius (R), 50 mm in gauge length (G), and 60 mm in reduced section (A). The tensile tests were applied using a crosshead speed of 1.5 mm/min by Zwick Z250 test machine. The technical drawing of the tensile test samples, which is taken from ASTM E8 standard, is given in Figure 3. Macrophotographs of a tensile test samples (a) before and (b) after the tests are given in Figure 4. In the

second mechanical testing phase, two different hardness tests were applied: Rockwell Hardness Test and Vickers Hardness Test (HV_1). A force of 9.8N was applied for an indentation time of 15 s in the microhardness test.
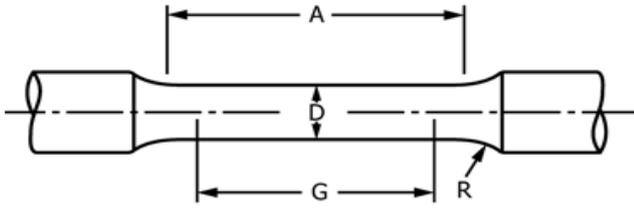

**Figure 3.** The technical drawing of a tensile test sample

(a)   (b)
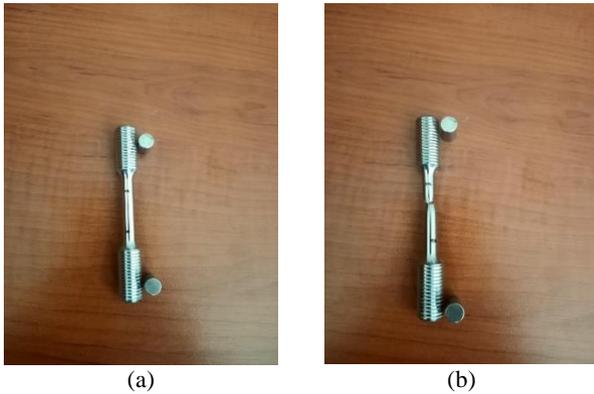
Figure 4. Macrophotographs of a tensile test sample (a)before and (b) after the test.

3. Results and Discussion

3.1 Microstructural evaluation by optical microscopy (OM)

3.1.1 Images of as-cast and solution treated samples

Co-base alloys exhibit a dendritic α-fcc metastable matrix due to the nature of the fcc→hcp transformation and a precipitate formed mainly by $M_{23}C_6$ carbides, and a lamellar phase formed by interlayed plates of $M_{23}C_6$ carbide and a phase [5]. $M_{23}C_6$ carbide initially present in the alloy tends to transform into M_6C carbide. According to microstructure of the various ASTM F-75, all samples showed Co grains with or without carbide precipitates depending on heat treatment conditions. These samples exhibited lameller type carbides on matrix structure. Figure 3 shows that the typical microstructure of as-cast condition with a cobalt matrix (FCC) containing primary lamellar and blocky carbides. Three different structure of the carbides in the as-cast microstructure can be determined. The "eutectic" carbide with lamellar morphology was formed at grain boundaries by interlayer plates of $M_{23}C_6$ carbide and a phase. These

phases has not been clearly identified because it can be maybe σ or both α and σ phases. As-cast cobalt alloys the solidified microstructures consist of a predominantly FCC γ-dendritic structure which is accompanied by segregation, and second phase precipitates within the matrix and along the interdendritic regions [16]. In the case of as-cast alloys present highly inhomogeneous structure is expected to form with large-grained cored dendrites and Co-rich areas [16,17]. The microstructures observed by optical microscopy belong to as-cast condition are shown in Figure 5. This as-cast microstructure is the characteristic one as described above.
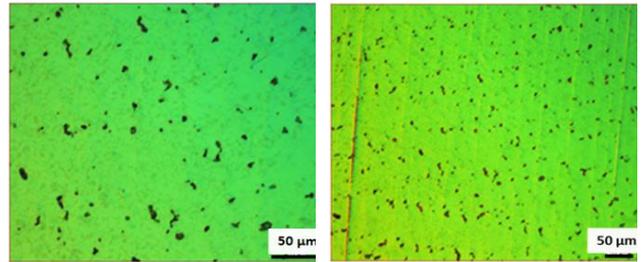

Figure 5. OM images belong to microstructure of the as-cast sample.
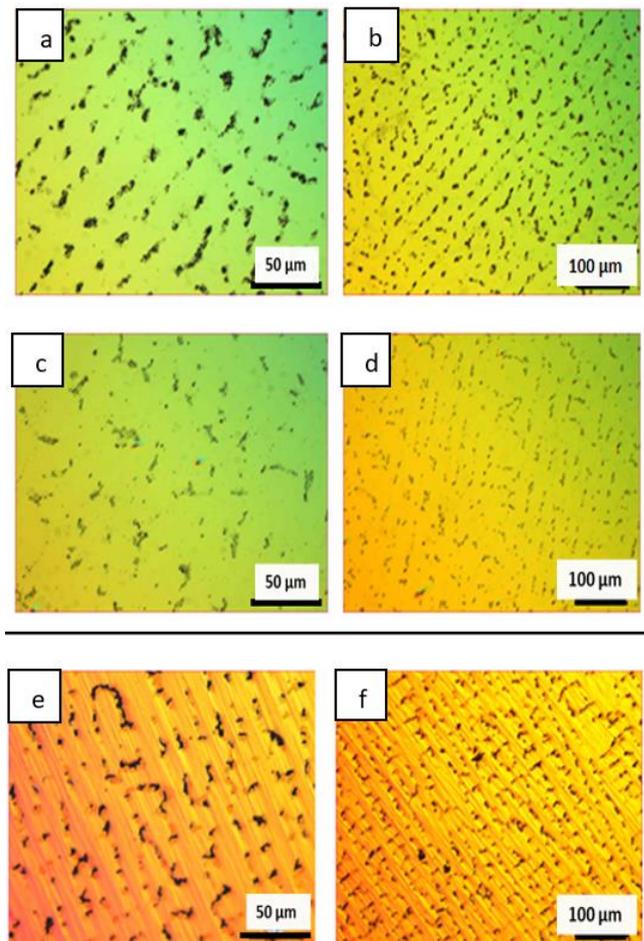

Figure 6. Microstructures of samples solutionized at (a-b) 1125°C (c-d); 1175°C, (e-f) 1225°C

Figure 6a and b show the microstructural evolution for solution treatment at 1125°C (Sample C1). There is a microstructural morphology change from lamellar to a more round-like form of $M_{23}C_6$ carbides as the solution treatment temperature increases. The chemical composition of these carbides corresponds to the $M_{23}C_6$ (M = Co, Cr and Mo) phase. As the $M_{23}C_6$ carbide suffers a spheroidization and sometimes could transform according to the $M_{23}C_6 \rightarrow M_6C$ reaction [8], it can also be noticed in Figure 6c-d and e-f respectively (Samples C3 and C5). It can be seen from these Figures that the morphology of the carbides changed, and the carbides have been shrunk with increasing solution treatment temperature.

3.1.2 Images of solution treated and aged samples

Carbide precipitation at grain boundaries and interdendritic regions is the major strengthening mechanism in the as-cast samples. Moreover, additional fine precipitate carbides are always beneficial in terms of strength and hardness increase in metallic materials.

According to optical microscope images, matrix phase was observed with spheroidized $M_{23}C_6$ carbides in microstructures presented in Figure 7. Carbide precipitates are seen through the grain boundaries and also in the matrix structure. As a result, the strength of the material is increased significantly in C2 and C4 samples. In addition to that lamellar carbides, precipitations into the grains became more evident due to the aging process in all three conditions (C2, C4 and C6).

3.2 XRD analysis

Figure 8 shows the XRD patterns belong to the C7, C1 and C2 samples. Here, patterns belong to C1 and C2 samples were given as representative since the patterns for the samples C3-C4 and C5-C6 give similar results parallel to C1-C2. The pattern of the as-cast sample shows that both γ matrix phase with fcc crystal structure and ε phase with hcp structure are present. Also, the structure contains $M_{23}C_6$ type carbide phase. The structure of the as-solutionized condition contains γ and ε phases together, as seen in Figure 8b. After the subsequent aging process, the structure contains mainly a high intensity ε phase together with $M_{23}C_6$ type carbides and the matrix phase (γ).


Figure 7. Microstructures of samples (a,b) solutionized at 1125°C and aged, (c,d) solitonized at 1175°C and aged and (e,f) solutionized at 1225°C and aged.
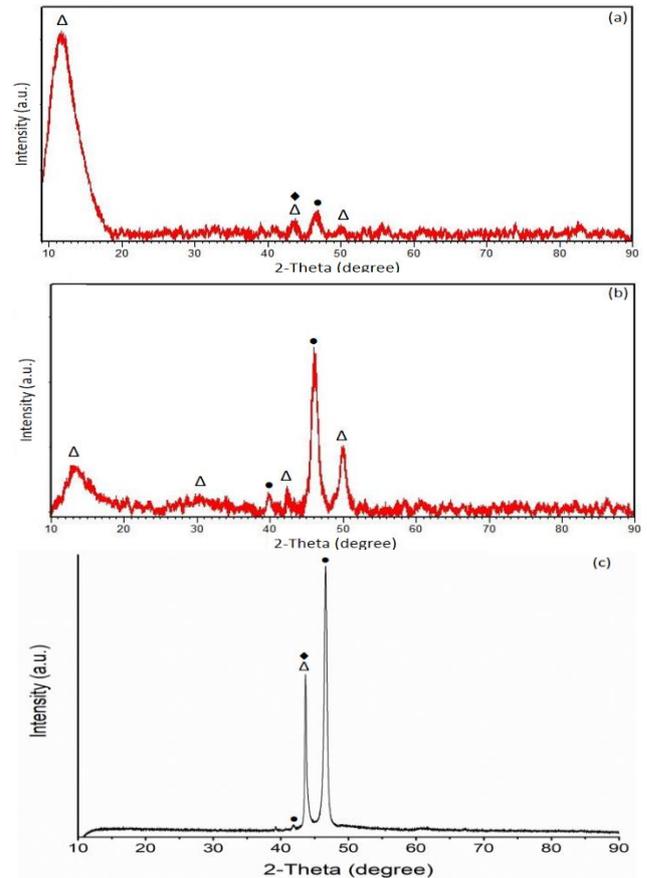
Figure 8. XRD patterns of the samples: (a) as-cast, (b) solutionized at 1125°C, (c) solutionized at 1125°C and aged (the symbols represent; Δ: fcc γ phase, •: hcp ε phase, ♦: $M_{23}C_6$ phase).

3.3 SEM study

3.3.1 As-cast and solution sreated samples

The as-cast microstructure corresponding to sample C7 is shown in Figure 9. The typical microstructure of as-cast alloy consists of a cobalt matrix (FCC) containing primary lamellar and carbides. It is showed a solid solution of Co as a matrix and also carbides as secondary phase. Figure 10a and b present the microstructure of the sample C1 showing the matrix and carbide phases together. The microstructure consists of a dendritic Co-rich fcc matrix and interdendritic precipitates. The SEM images show that the $M_{23}C_6$ carbide spheroidization tends to transformed M_6C carbide and also carbide size reduction, carbides homogeneously distributed and smaller in size when increased heat treatment temperature. These Figures show an electron backscattered SEM image of all samples, so bright area indicate that high atomic number and dark areas indicate that low atomic number of phase and also bright area representing solid matrix of phase; Co grains.
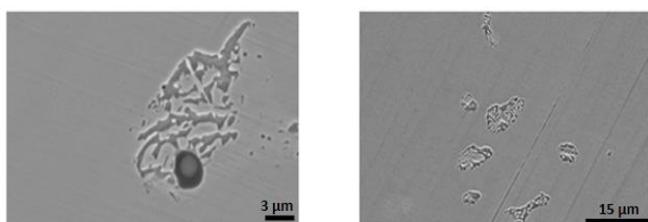

**Figure 9.** Microstructure of as-cast alloy.
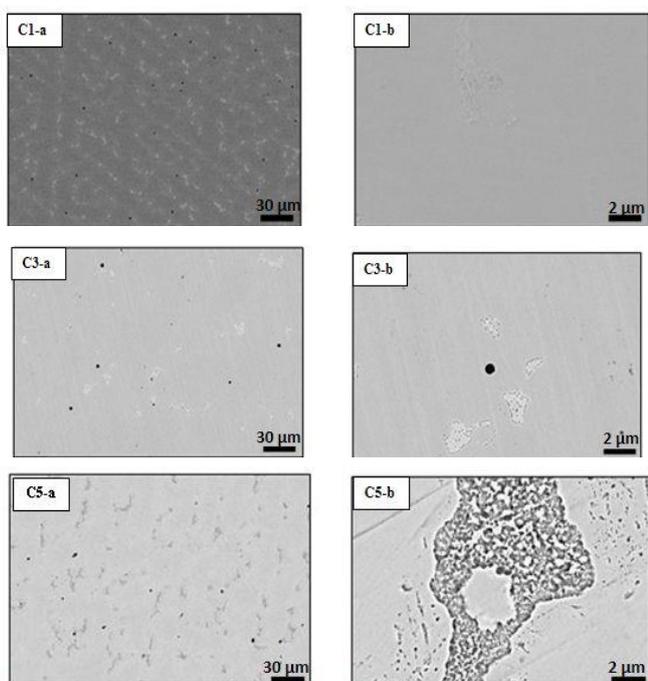
Figure 10. SEM images samples solutionized at C1 (a-b); 1125°C, C3 (a-b); 1175°C, C5 (a-b) 1225°C

Three areas were selected as shown in Figure 11 and Table 4. Selected area 1 show the Co-rich matrix composition with a 67.04 mass% of Co content. EDS Spot 1 analyse indicated that the secondary phase of Co-Cr-Mo phase occurs in the structure which is in accordance with the chemical composition of Co-Cr-Mo (ASTM F-75). EDS Spot 2 shows the higher concentration of Cr (46.96%), Mn (17.26%) and Si (30.51%) and also some amount of C. According to this result, Si-rich inclusions are within carbides in the middle of the interdendritic zones. Manganese and silicon are mainly in solution and are not segregated toward grain boundaries, and they are difficult to reveal. Co–Cr–Mo alloys with low and medium C content, as in this case, typically show very little grain boundary attack [10,18].
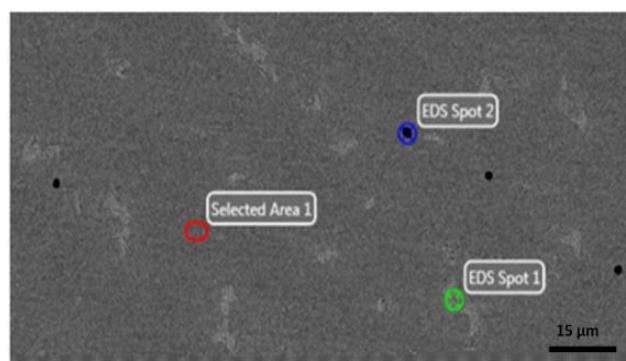

Figure 11. SEM micrograph corresponding to C1 and three regions were selected for analysis, selected area, EDS spot 1, EDS spot 2.

Table 4. Composition of elemental analysis for selected Area 1, EDS spot 1, EDS spot 2.

	Co	Cr	Mo	Mn	Si	C
Selected area 1	67,04	26.39	2.99	1,04	0.75	0.001
EDS Spot 1	46,51	34,86	13,37	1,05	1,50	1,67
EDS Spot 2	1,16	46,96	0,16	17,26	30,51	3,94

The EDS analysis corresponding to sample C3 belong to the areas spotted in Figure 12. Three area were selected as in the Table 5. From the obtained results, the higher concentration of Co rich matrix means that it is Co enriched and reaches the composition of 65.62 mass%. EDS Spot 2 and spot 3 analysis indicate that there is a secondary (eutectic) phase composed of Co, Cr and Mo elements as also found in the sample C1. From the result of Spot 1 analysis, it may be a Si-rich inclusion within the carbide in the middle of inter dendritic zones.
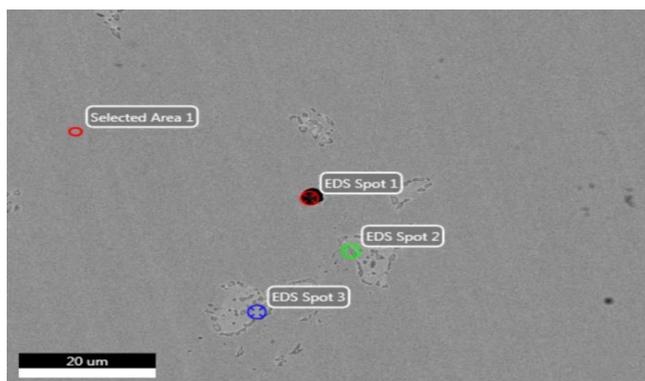
Figure 12. SEM micrograph corresponding to C3 and four regions were selected for analysis, EDS spot 1, EDS spot 2, EDS spot 3, selected area 1.

Table 5. Composition of elemental analysis for selected area 1, EDS spot 1, EDS spot 2, EDS spot 3.

	Co	Cr	Mo	Mn	Si	C
Selected area 1	65,62	27,08	3,89	1,03	0,92	0
EDS Spot 1	29,50	23,39	1,81	4,60	38,81	0
EDS Spot 2	57,45	27,43	10,22	1,09	1,81	0,33
EDS Spot 3	49,57	35,36	11,66	0,85	1,22	0

The EDS analysis corresponding to sample C5 are taken from the areas shown in the backscattered electron image of C5 (Figure 13). Three area were selected as in the Table 6. The higher concentration of Co found in bright area in the selected area 1, so it means that Co-rich matrix is Co enriched and reaches the composition of 82.27 wt.%. Here, all three EDS analysis indicate the famous intermetallic Co-Cr-Mo matrix phase with bright colour. Also, EDS spot 2 indicates a higher concentration of chromium compared to the other two which can be attributed to another secondary precipitation-like phase with dark colour.

Table 6. Composition of elemental analysis for selected area 1, EDS spot 1 and EDS spot 2.

|	Co	Cr	Mo	Mn	Si	C
Selected area 1	82,27	14,99	1,94	0	0,80	0
EDS Spot 1	63,60	33,16	1,05	0,12	0,31	0
EDS Spot 2	79,62	15,68	3,65	0	0,87	0
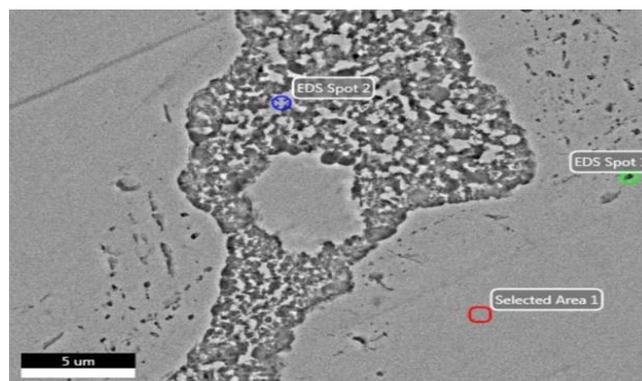
Figure 13. SEM micrograph corresponding to C5 and three regions were selected for analysing, EDS spot 1, EDS spot 2 and selected area 1.

3.3.2 Solution treated and aged samples

The typical microstructure of as cast-condition with a cobalt matrix (FCC) containing primary lamellar and blocky carbides. In general the as-cast microstructure is a Co-fcc dendritic matrix with the presence of a secondary phase, such as the $M_{23}C_6$ carbides precipitated at grain boundaries and at interdendritic zones. These precipitates are the main strengthening mechanism in this type of alloys [7]. Figure 14 represented that sample C2 has obvious $M_{23}C_6$ carbide and some possible M_6C carbide. The carbides in the shape of small dot like areas seen in C4 and C6 samples can be attributed to M_6C carbide presence.
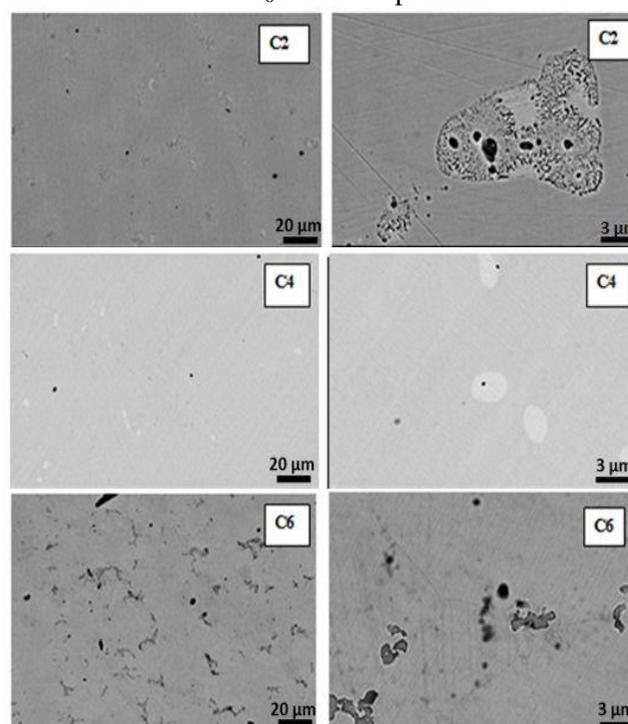

Figure 14. SEM micrograph of (a-b) C2, (c-d) C4 and (e-f) C6 samples.

C6 which is solution treated at 1225°C and aged, reveals lamellar type of carbides along are along within grain boundaries.

The EDS analysis taken from the areas shown in Figure 15 are belong to sample C2. Four different areas were selected as in the Table 7. Comments can easily be made that selected area 1 represents the matrix phase having the values of Co (82.80%) Cr (14.80%) and Mo (2.16%) which is in accordance with ASTM F-75 standard. Same result can be said for the selected area 2. Small black dots are detected in EDS spot 1 and EDS spot 2, which are mostly $M_{23}C_6$ type carbide. As the solution treatment progresses, the $M_{23}C_6$ carbide suffers a spheroidization and could transform according to the $M_{23}C_6 \rightarrow M_6C$ reaction [8].

Therefore, it should be noticed that some amount of these carbides could be transformed to M_6C type carbides.
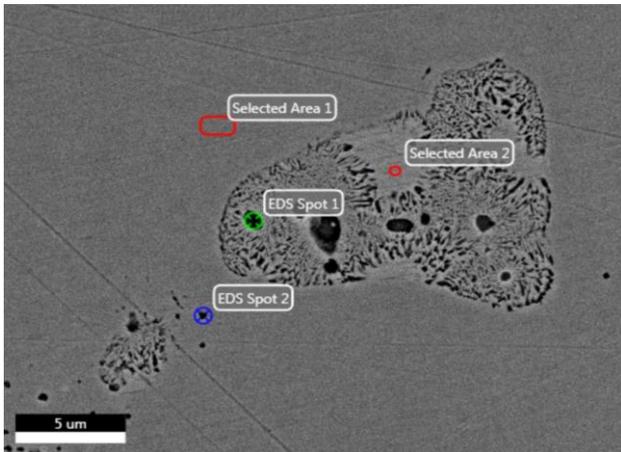

Figure 15. SEM micrograph corresponding to C2 and three regions were selected for analysis. (selected area 1, selected area 2, EDS spot 1, EDS spot 2)

Table 7. Composition of elemental analysis for selected area 1, selected area 2, EDS spot 1 and EDS spot 2.

	Co	Cr	Mo	Mn	Si	C
Selected area 1	82,80	14,80	2,16	0	0,84	0
EDS Spot 1	72,27	20,03	6,54	0	1,15	0
EDS Spot 2	71,19	21,32	6,26	0	1,10	0,07
EDS Spot 3	65,40	31,71	1,27	0	0,34	0

The EDS analysis taken from the areas shown in Figure 16 are belong to sample C4. Three areas were selected as in the Table 8. M_6C carbide phase detected in EDS spot 1. EDS spot 2 shows $M_{23}C_6$ carbide phase. It embraces EDS spot 1 which is M_6C carbide phase. Comments can easily be made that selected area 1 is the α phase so it evinces to higher value of Co (62.34%) Cr (28.74%) and Mo (4.85%) which is base matrix of ASTM F-75.
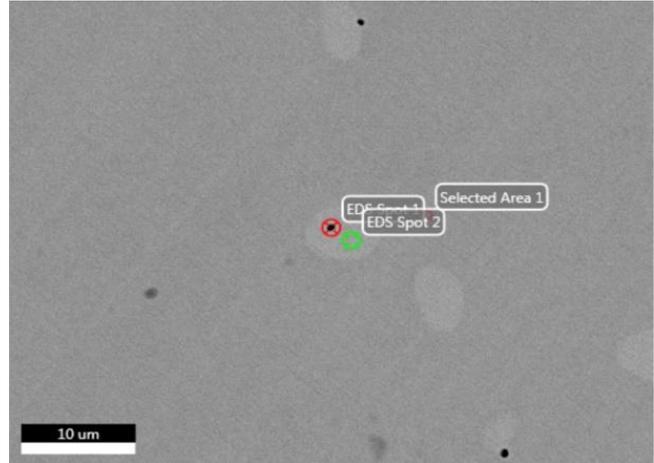

Figure 16. SEM micrograph corresponding to C4 and three regions were selected for analysis. (selected area 1, EDS spot 1, EDS spot 2)

Table 8. Composition of elemental analysis for selected area 1, EDS spot 1 and EDS spot 2.

	Co	Cr	Mo	Mn	Si	C
Selected area 1	62,34	28,74	4,85	0,96	0,94	0
EDS Spot 1	27,07	31,46	21,59	14,51	2,77	1,29
EDS Spot 2	49,79	34,63	11,40	1,07	1,21	0,21

The EDS analysis taken from the areas shown in Figure 17 are belong to sample C6. Four different areas were selected as in the Table 9. Different from C2 and C4 samples, there is one Cr-rich area (selected area 1) consists of higher amounts of Cr and C. The result confirms the presence of the $M_{23}C_6$ carbide phase.
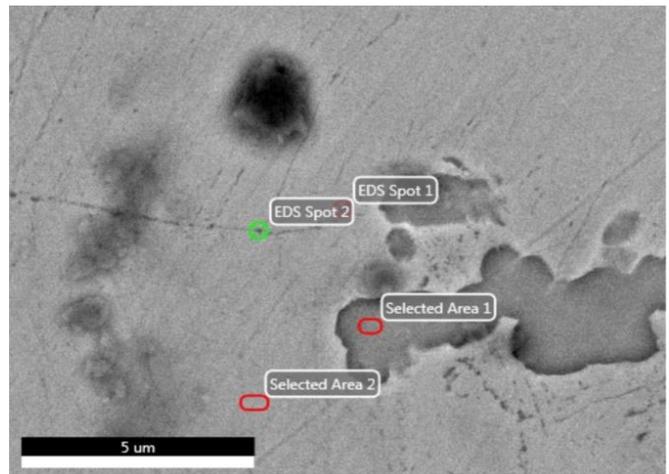

Figure 17. SEM micrograph corresponding to C6 and three regions were selected for analysis. (selected area 1, selected area 2, EDS spot 1, EDS spot 2)

Table 9. Composition of elemental analysis for selected area 1, EDS spot 1 and EDS spot 2.

	Co	Cr	Mo	Mn	Si	C
Selected area 1	18,21	67,87	7,64	0	0,74	5,44
Selected area 2	81,04	16,04	2,09	0	0,77	0
EDS Spot 1	80,65	16,42	2,14	0	0,78	0
EDS Spot 2	82,27	14,84	2,11	0	0,78	0

3.4 Mechanical test results

Table 10 shows mechanical test results of the samples. As can be seen from the table, solution treatment + aging conditions (C2, C4, C6) possess higher yield strength values than only solution treated samples (C1, C3, C5) and also higher than the as-cast condition. The solutionizing temperature of 1175°C gives the highest yield strength values both solutionized and solutionized + aged conditions; 649 MPa and 683 MPa, respectively. When heat treatment temperature is increased to 1225°C, yield strength was decreased for C5 and C6. From result of these observation; the highest value of yield strength was obtained by aged samples, specially C4 at 1175°C (683 MPa).

Table 10. Mechanical properties of the samples.

Sample Codes	Heat Treatment	YTS(Mpa)	UTS (MPa)	Elongation (%)	HV$_1$
ASTM F-75 *	-	450	665	8	-
C1	Solutionizing (1125°C)	521±23	742±37	9.3±0.5	355
C2	Solutionizing (1125°C) +Aging	613±21	763±62	8.4±0.1	365
C3	Solutionizing (1175°C)	649±56	826±56	9.05±0.65	350
C4	Solutionizing (1175°C) +Aging	683±23	829±58	9.75±0.25	364
C5	Solutionizing (1225°C)	521±19	716±8	8.6±0.2	351
C6	Solutionizing (1225°C) +Aging	635±65	738±20	8.5±0.5	362
C7	As-Cast	550±11	719±3	8.7±0.3	300

Table 10 also shows the effect of solutionizing temperature (1125°C, 1175°C, 1225°C) on tensile strength of for all heat treated conditions. As can be seen from the table 10, solution treatment + aging conditions (C2, C4, C6) possess higher yield strength values than only solution treated samples (C1, C3, C5) and also higher than as-cast condition. It is worth noting that, In the experiment carried out at 1175 degrees, a second phase was formed in the structure of the sample, which is soluble at high temperatures and has limited solubility at low temperatures. The precipitates of the microstructures interact with dislocations and tend to hinder their movement The presence of secondary phase grains increased the strength. We could observe fine precipitates in Fig. 7, in which grain size was a small size appears. As the temperature of the solution treatment was increased, the carbides reduced. The solutionizing temperature of 1175°C gives the highest yield strength values both solutionized and solutionized + aged conditions; 826 MPa and 829 MPa, respectively. Owing to lamellar carbides that exist in the microstructure have led to the strength of the material increased significantly in C2

and C4 samples. As the heat treatment temperature was increased to 1225°C, tensile strength was decreased significantly for C5 and C6. As a result; the highest value of tensile strength was obtained by aged samples, specially C4 at 1175°C (829 MPa).

When the elongation values are considered, the as–cast sample has the elongation value of 8.7 %. The sample which solution treated at 1125°C temperature results similar value as as-cast sample. 1175°C solutionized sample represents a lower elongation value of 9.05%. There has been decrease for 1225°C solutionized sample which is the lowest elongation value for solution treated conditions. For aged samples (C2, C4, C6), C2 and C6 shows lower elongation values than all other conditions (8.4 and 8.5 % respectively). However, the C4 condition (both solutionized and aged at 1175°C) gives the best result of 9.75% elongation value which is remarkable among all samples.

The hardness values of the samples are given in the Figure 18. There is obvious increment value of hardness results ever then as-cast sample. Only heat treated samples showed the results of C1 (355 HV1),

C3 (350 HV1), C5 (351 HV1) values. It was clear from the results that aging temperature has an impact on hardness of the samples. The hardness values of aged samples is higher compared to that of solution-treated samples, aged samples gave higher hardness values than solutionized samples. Also, as the solutionizing temperature increases the hardness values stay constant with having C2 (365 HV$_1$), C4 (364 HV$_1$) and C6 (362 HV$_1$) hardness, respectively.
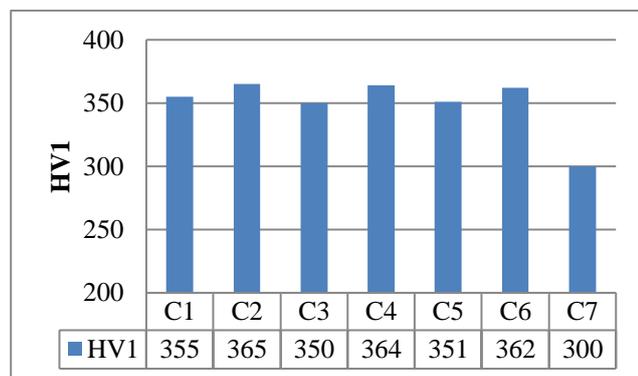

Figure 18. The hardness values of the samples

4. Conclusion

This paper presents the results of processing-microstructure and mechanical properties for ASTM F-75 alloy after applying both solution treatment and aging processes. The results obtained in this study can act as guidelines for tuning the microstructure of Co-Cr-based hip implants materials in order to increase their mechanical properties. The different phases present were identified using XRD and SEM EDX analysis. In all conditions, the microstructures agreed with the literature. As a result;

- The undissolved carbides of Cr, Mo, and Co have major effects on the microstructural and mechanical properties of the solution treated and aged samples. $M_{23}C_6$ type carbides and intermetallic phase were detected at grain boundaries and interdendritic zones. $M_{23}C_6$ carbides tend to spheroidize and also carbide size reduces. With increased heat treatment temperature, carbides are homogeneously distributed and begin to be smaller.

- The tensile tests showed that all heat treatments improved mechanical properties as both strength and ductility increased. For the as-solutionized samples, the best strength and ductility values have been obtained by solutionizing at 1175°C. Elongation values of solution treated and solution treated+aging samples exists in the range of 8.5 to 9.7 %.

- As the temperature increases to 1225°C, tensile strength and also yield strength decreased. Similar to this treatment, solutionizing at 1175°C and subsequent aging increased both yield, tensile strength and elongation. This treatment gives the highest mechanical properties as considerably high values have been obtained (e.g yield strength of 683 MPa, tensile strength of 829 MPa and an elongation of 9.75 %).

- Hardness values also increased with the subsequent aging process as hardness values are similar for three different solutionizing temperatures.

- It was demonstrated that samples from C4 alloy showed precipitates, much smaller size and with a more homogeneous distribution in the interdendritic space of the as-cast structure with respect to the other six alloys studied. Grain size is also effective in increasing the mechanical strength. This effect could be the result of the applied optimum heat treatment temperature (1175°C) and aging conditions when compared to other samples.

Conflicts of interest

The author declares that there is no conflict of interest.

References

[1] Giacchi J., V, Morando C.N., Fornaro O., Palacio H.A., Microstructural characterization of as-cast biocompatible Co–Cr–Mo alloys, *Materials Characterization*, 62(1) (2011) 53-61.

[2] Zangeneh S.H., Lashgari H.R., Saghafİ M., Karshenas M., Effect of isothermal aging on the microstructural evolution of Co–Cr–Mo–C alloy, *Materials Science and Engineering*, 527(24-25) (2010) 6494–6500.

[3] Montero O.C., Talavera M., Lopez H., Effect of alloy preheating on the mechanical properties of as-cast CoCrMoC alloys, *Metallurgical Materials Transactions*, 30 (1999) 611–20.

[4] Dobbs H.S., Robertson J.L.M., Heat treatment of cast Co–Cr–Mo for orthopaedic implant use, *J Mater Sci.*, 18 (1983) 391–401.

[5] Yamanaka K., Mori M., Chiba A., Influence of carbon addition on mechanical properties and microstructures of Ni-free Co–28Cr–9 W–1Si–C alloys subjected to thermomechanical processing, *J. Mech. Behav. Biomed. Mater*., 37 (2014) 274–85.

[6] Youdelis W.V., Kwon O., Carbide phases in cobalt of subsize tensile test specimens and the traditional base superalloy: Role of nucleation entropy in refine- method of measuring % elongation to fracture by joinment, *Metal Sci*., 17(8) (1983) 379–384.

[7] Lee S.H., Nomura N., Chiba A., Significant improvement in mechanical properties of biomedical Co-Cr-Mo alloys with combination of N addition and Cr enrichment, *Mater. Trans*., 49(2) (2008) 260–264.

[8] Yamanaka K., Mori M., Chiba A., Assessment of precipitation behavior in dental castings of a Co–Cr–Mo alloy, *Mechanical Behavior Biomedical Materials*, 50 (2015) 268–27.

[9] Li S.J., Niinomi M., Akahori T., Kasuga T., Yang R., Hao Y.O., Fatigue characteristics of bioactive glass-ceramic-coated Ti–29Nb–13Ta–4.6Zr for biomedical application, *Biomaterials*, 25(17) (2004) 3369-3378.

[10] Gomez M., Mancha H., Salinas A., Rodryguez J.L., Escobedo J., Castro M., Mendez M., Relationship between microstructure and ductility of investment cast ASTM F-75 implant alloy, *Journal of Biomedical Materials Research*, 34(2) (1997), 157–163.

[11] Sims C.T, Hagel W., Stoloff N., The Superalloys II: High temperature materials for aerospace and industrial power, 2nd ed. New York: Wiley & Sons, (1987).

[12] Ramírez V.L.E., Castro R.M., Herrera T.M., García L.C.V., Almanza C.E., Cooling rate and carbon content effect on the fraction of secondary phases precipitate in as-cast microstructure of ASTM F75 alloy, *J Material Process Technology*, 209(4) (2009) 1681–1687.

[13] Rosenthal R., Cardoso B.R., Bott I.S., Paranhos R.P.R., Carvalho E.A., Phase characterization in as-cast F-75 Co-Cr-Mo-C alloy, *J. Mater. Sci*., 45(15) (2010) 4021–4028.

[14] Yamanaka K., Mori M., Sato K., Chiba A., Characterisation of nanoscale carbide precipitation in as-cast Co–Cr–W-based dental alloys, *J. Mater. Chem. B*., 4(10) (2016) 1778–1786.

[15] Yamanaka K., Mori M., Chiba A., Effects of carbon concentration on microstructure and mechanical properties of as-cast nickel-free Co–28Cr–9W-based dental alloys, *Mater. Sci. Eng*., 40(7) (2014) 127–134.

[16] Ledesma A.L.R., Lopez H.F., Islas J.A.J., Evaluation of chill cast Co-Cr alloys for biomedical applications, *Metals*, 6(8) (2016) 188.

[17] Salam S., Hou P.Y., Zhang Y.D., Zhang X.H., Wang H.F., Zhang C., Yang Z.G., Microstructural modelling solution for complex Co based alloys and coatings, *Surf. Coat. Technol*., 236 (2013) 510–517.

[18] Herrera T.M., Espinoza A., Méndez J., Castro M., López J., Rendón J., Effect of C content on the mechanical properties of solution treated as-cast ASTM F75 alloys, *J Mater Sci Mater Med*., 16(7) (2005) 607–11.

AUTHOR GUIDELINES

Thank you for choosing to submit your paper to Cumhuriyet Science Journal. The following instructions will ensure we have everything required so your paper can move through pre-evaluating, peer review, production and publication smoothly. Please take the time to read and follow them as closely as possible, as doing so will ensure your paper matches the journal's requirements.

Submission

Cumhuriyet Science Journal is an international, peer-reviewed, free of charge journal covering the full scope of both natural and engineering sciences. Manuscripts should be submitted by one of the authors of the manuscript as online submission after registration to the Cumhuriyet Sciences Journal. Microsoft Word (.doc, .docx, .rtf), files can be submitted. There is no page limit. If there is a problem while uploading the files of manuscript, please try to reduce their file size, especially manuscripts including embedded figures. Submissions by anyone other than one of the authors will not be accepted. The submitting author takes responsibility for the paper during submission and peer review. If for some technical reason submission through the online submission systme is not possible, the author can contact csj@cumhuriyet.edu.tr for support.

Submission or processing charges

Cumhuriyet Science Journal does not charge any article submission, processing charges, and printing charge from the authors.

Terms of Submission

Papers must be submitted on the understanding that they have not been published elsewhere (except in the form of an abstract or as part of a published lecture, review, or thesis) and are not currently under consideration by another journal. The submitting author is responsible for ensuring that the article's publication has been approved by all the other coauthors. It is also the authors' responsibility to ensure that the articles emanating from a particular institution are submitted with the approval of the necessary institution. Only an acknowledgment from the editorial office officially establishes the date of receipt. Further correspondence and proofs will be sent to the author(s) before publication unless otherwise indicated. It is a condition of submission of a paper that the corresponding author permit editing of the paper for readability. All enquiries concerning the publication of accepted papers should be addressed to csj@cumhuriyet.edu.tr. Please note that Cumhuriyet Science Journal uses iThenticate software to screen papers for unoriginal material. By submitting your paper to Cumhuriyet Science Journal are agreeing to any necessary originality checks your paper may have to undergo during the peer review and production processes. Upon receiving a new manuscript, the Editorial office conducts initial pre-refereeing checks to ensure the article is legible, complete, correctly formatted, original, within the scope of the journal in question, in the style of a scientific article and written in clear English. Any article that has problems with any of the journal criteria may be rejected at this stage.

Peer Review

This journal operates a single blind review process. All contributions will be initially assessed by the editor for suitability for the journal. Papers deemed suitable are then typically sent to a minimum of two independent expert reviewer to assess the scientific quality of the paper. The author is required to upload the revised article to the system within 15 days by making the corrections suggested by the referee. The article will be rejected if there are no fixes in it. The Editor is responsible for the final decision regarding acceptance or rejection of articles. The Editor's decision is final

Title and Authorship Information

The following information should be included

Paper title

Full author names

Full institutional mailing addresses

Corresponding address

Email address

Abstract

The manuscript should contain an abstract. The researchers who are native speakers of Turkish have to add Turkish title and abstract as well. The abstract should be self-contained and citation-free and should be 250-300 words.

Keywords

Keywords of the scientific articles should be selected from the web address of www.bilimadresleri.com

Introduction

This section should be succinct, with no subheadings.

Materials and Methods

This part should contain sufficient detail so that all procedures can be repeated. It can be divided into subsections if required.

Conflicts of interest

Sample sentence if there is no conflict of interest: The authors stated that did not have conflict of interests.

References

References to cited literature should be identified by number in the text in square brackets and grouped at the end of the paper in numerical order of appearance. Each reference must be cited in the text. Always give inclusive page numbers for references to journal articles and a page range or chapter number for books. References should be styled and punctuated according to the following examples

[1] Karaca E., Ulusoy S., Morgül Ü., Ulusoy H.I., Development of Analytical Method for Sensitive Determination of Streptozotocin based on Solid Phase Extraction, Cumhuriyet Sci. J., 41 (4) (2020) 826-831. (sample reference for journals)

[2] Keskin B., Ozkan A.S., Inverse Spectral Problems for Dirac Operator with Eigenvalue Dependent Boundary and Jump Conditions, Acta Math. Hungar., 130 (2011) 150-159(sample reference for journals)

[3] Mazur M.T., Kurman R.J., Dysfunctional Uterine Bleeding. In: Mazur M.T., Kurman R.J., (Eds). Diagnosis of endometrial biopsies   and curettings, A practical approach. 2nd ed. Berlin: Springer, (2005) 100-120. (sample reference for book chapters)

[4] Mazur M.T., Kurman R.J.,Diagnosis of endometrial biopsies   and curettings, A practical approach. 2nd ed. Berlin, (2005) 100-120. (sample reference for book)

[5] National Cancer Institute, Surveillance Epidemiology and End Results. Cancer of the Corpus and Uterus, NOS. Available   at: http://seer.cancer.gov/statfacts/html/corp.html?statfacts_page=corp. Retrieved March 2, 2008. (sample reference for websites)

[6] Surname N., Title of thesis, PD or master thesis, Name of university, name of institue, year. (sample reference for thesis)

[7] Surname N., Title of fulltext conference paper, name of conference, city, year, pages. (sample reference for Abstratcs in conferences are not accepted as a valid reference except full text)

Preparation of Figures

Each figure can be integrated in the paper body or separately uploaded and should be cited in a consecutive order. Figure widths can be 4-6 inch as 300 dpi. The labels of the figures should be clear and informative. The name and the subtitles of the figures must be 9-point font.

Preparation of Tables

Tables should be cited consecutively in the text. Every table must have a descriptive title and if numerical measurements are given, the units should be included in the column heading. Tables should be simple with simple borders and text written as left text. The name and the subtitle of the tables must be 9-point font

Proofs

Corrected proofs must be returned to the publisher within 2 weeks of receipt. The publisher will do everything possible to ensure prompt publication. It will therefore be appreciated if the manuscripts and figures conform from the outset to the style of the journal.

Copyright

The use of general descriptive names, trade names, trademarks, and so forth in this publication, even if not specifically identified, does not imply that these names are not protected by the relevant laws and regulations.

While the advice and information in this journal are believed to be true and accurate on the date of its going to press, neither the authors, the editors, nor the publisher can accept any legal responsibility for any errors or omissions that may be made. The publisher makes no warranty, express or implied, with respect to the material contained herein.

Ethical Guidelines

New methods and ethically relevant aspects must be described in detail, bearing in mind the following:

Human Experiments. All work must be conducted in accordance with the Declaration of Helsinki (1964). Papers describing experimental work on human subjects who carry a risk of harm must include:

A statement that the experiment was conducted with the understanding and the consent of the human subject.

A statement that the responsible Ethical Committee has approved the experiments.

Animal Experiments. Papers describing experiments on living animals should provide:

A full description of any anaesthetic and surgical procedure used.

Evidence that all possible steps were taken to avoid animal suffering at each stage of the experiment. Papers describing experiments on isolated tissues must indicate precisely how the donor tissues were obtained.

Submission Preparation Checklist

As part of the submission process, authors are required to check off their submission's compliance with all of the following items, and submissions may be rejected that do not adhere to these guidelines.

The submission has not been previously published, nor is it before another journal for consideration (or an explanation has been provided in Comments to the Editor).

The submission file is in Microsoft Word document file (Times New Roman) format.

Where available, URLs for the references have been provided.

The text is single-spaced; uses a 11-point font; employs italics, rather than underlining (except with URL addresses); and all illustrations, figures, and tables are placed within the text at the appropriate points, rather than at the end.

The text adheres to the stylistic and bibliographic requirements outlined in the Author Guidelines, which is found in About the Journal.

If submitting to a peer-reviewed section of the journal, the instructions in Ensuring a Double-Blind Review have been followed.